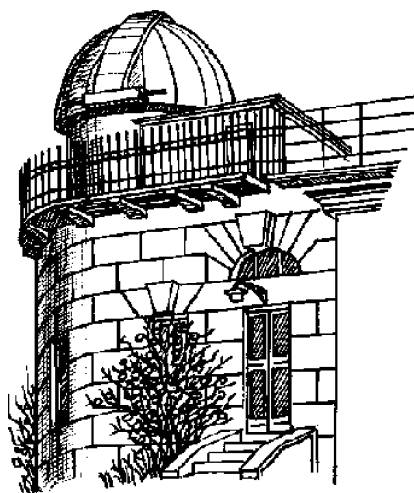


ODESSA ASTRONOMICAL PUBLICATIONS

**Volume 31
(2018)**



Astronomical Observatory
of I. I. Mechnikov Odessa National University

**ODESSA ASTRONOMICAL
PUBLICATIONS**

Volume 31
(2018)

Editorial Board:

- Editor-in-Chief* – Andrievsky S.M., Prof., RI "Astronomical Observatory"
Odessa I.I.Mechnikov National University
Executive Secretary – Kovtyukh V.V., ScD, RI "Astronomical Observatory"
Odessa I.I.Mechnikov National University
Associate Editor – PhD Garbuzov G.A.
Technical editing – PhD Dragunova A.V., Strakhova S.L.

Advisory Editors:

Andronov I.L., ScD (Ukraine); Bagrov A.V., ScD (Russia); Bazey A.A., PhD (Ukraine); Georgieva K., PhD (Bulgaria); Ismailov N., PhD (Azerbaijan); Kim Y., ScD (Republic Korea); Koshkin N.I., PhD (Ukraine); Kučinskas A., PhD (Lithuania); Kudzej I., PhD (Slovakia); Lozitskiy V.G., ScD (Ukraine); Mishenina T.V., ScD (Ukraine); Niarchos P., PhD (Greece); Novosyadlyj B.S., ScD (Ukraine); Picazzio E., PhD (Brasil); Pilyugin L.S., ScD (Ukraine); Turner D., PhD (Canada); Udovichenko S.N., PhD (Ukraine); Ulyanov O.M., PhD (Ukraine); Vavilova I.B., PhD (Ukraine); Yushchenko A., PhD (Republic Korea); Zakhzhay V., ScD (Ukraine); Zhuk A.I., ScD (Ukraine).

Address:

Astronomical Observatory, Odessa National University, E-mail: astronomical_observatory@onu.edu.ua
T. G. Shevchenko Park, Odessa, 65014, UKRAINE <http://www.astro-observ-odessa0.1gb.ua>
Tel.: + 38 048 722-84-42

The electronic version of the journal is on the web page: <http://oap.onu.edu.ua>

Одесские Астрономические Публикации
Издается с 1946 года (издание возобновлено в 1993 г., №6)

Свидетельство о государственной регистрации печатного средства массовой информации:
серия КВ № 14722-3693Р от 30.10.2008 г.

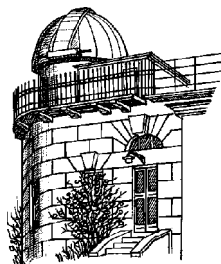
Журнал включен в список МОН Украины приказом МОНУ № 996 от 11.07.2017 г.

Печатается по решению Ученого совета НИИ "Астрономическая обсерватория" Одесского
национального университета имени И.И.Мечникова от 20 сентября 2018 г., протокол №9

Printed in UKRAINE
BAITE PUBLISHING COMPANY

ODESSA ASTRONOMICAL PUBLICATIONS

Volume 31
(2018)



CONTENTS

Cosmology, gravitation, astroparticle physics, high energy physics

| | |
|---|----|
| Bronza S.D., Svyrydova Ju.V., Kotvytska L.A. THE ANALYSIS OF IMAGES OF A CIRCULAR SOURCE IN N-POINT GRAVITATIONAL LENSES | 6 |
| Chernin A.D., Karachentsev I.D., Emelyanov N.V. ZELDOVICH LOCAL PANCAKE: DARK ENERGY DOMINATION..... | 11 |
| Gladush V.D. ON THE CONFIGURATION SPACE OF A SPHERICALLY SYMMETRIC SYSTEM OF GRAVITATIONAL AND ELECTROMAGNETIC FIELDS | 15 |
| Holovko M.G., Gladush V.D. SUPERSPACE APPROACH TO THE QUANTIZATION OF CHARGED BLACK HOLES WITH ALLOWANCE FOR THE COSMOLOGICAL CONSTANT | 20 |
| Kotvytskiy A.T., Shablenko V.Yu., Bronza E.S. FIXED POINTS OF MAPPING OF N-POINT GRAVITATIONAL LENSES | 24 |
| Panko E., Sirginava A., Stepaniuk A. DETAILED MORPHOLOGY OF THE RICH CONCENTRATED GALAXY CLUSTERS | 29 |
| Ryazantsev G.B., Lavrenchenko G.K., Beckman I.N., Buntseva I.M., Nedovesov S.S. CONDENSATION OF COLD NEUTRONS – IDEA OF G.A.GAMOW. CHEMICAL PROPERTIES OF THE NEUTRON MATTER AND ITS PLACE IN THE PERIODIC SYSTEM OF ELEMENTS | 33 |
| Sergijenko O. 2-FIELD MODEL OF DARK ENERGY WITH CANONICAL AND NON-CANONICAL KINETIC TERMS | 38 |
| Tugay A.V., Pulatova N.G., Zhoga A.D. NUMERICAL ESTIMATOR FOR LARGE-SCALE COSMIC STRUCTURES..... | 42 |
| Voitsekhovskiy V.V., Tugay A.V., Tkachuk V.V., Shevchenko S.Yu. X-RAY EMISSION OF ICRF SOURCES | 47 |
| Voitsekhovskiy V.V., Tugay A.V. SIMULATION OF LARGE-SCALE STRUCTURE OF UNIVERSE BY GAUSSIAN RANDOM FIELDS | 52 |
| Zakhozhay V.A. HIERARCHICAL STRUCTURE OF THE UNIVERSE | 56 |

Astrophysics

| | |
|--|-----|
| Doikov D.N. POSITRON ANNIHILATION SPECTROSCOPY OF YOUNG SUPERNOVA REMNANTS | 62 |
| Eglitis I., Sokolova A. DISTRIBUTION OF CARBON STARS IN THE GALAXY | 70 |
| Gorbaneva T.I., Mishenina T.V. HAFNIUM ABUNDANCES IN FGK DWARF OF GALACTIC DISK | 75 |
| Mishenina T.V., Gorbaneva T.I. MOLYBDENUM AND RUTHENIUM IN THE GALAXY..... | 78 |
| Mishenina T., Usenko I., Kniazev A., Kovtyukh V. STATUS REFINEMENT OF METAL-POOR STAR HD 6268..... | 84 |
| Nazarenko V.V. THE DEPENDENCE OF ON- AND OFF-STATE GENERATIONS IN CLASSICAL MICROQUASARS FROM THE DISK DENSITY. 3-D NUMERICAL HYDRODYNAMICAL SIMULATIONS OF THE HIGH AND LOW MASS ACCRETION RATE IN ACCRETION DISK IN MICROQUASAR CYG X-1 | 90 |
| Oknyansky V.L., Shenavrin V.I., Metlova N.V., Gaskell C.M. ADDITIONAL SUPPORT FOR RELATIVE WAVELENGTH INDEPENDENCE OF IR LAGS IN NGC 4151 OVER THE PAST DECADE | 94 |
| Shereta E., Carraro G., Gorbaneva T., Mishenina T. MOLYBDENUM ABUNDANCE IN SOME OPEN CLUSTERS | 100 |
| Tvardovskiy D.E., Marsakova V.I., Andronov I.L., Shakun L.S. PERIOD VARIATIONS AND POSSIBLE THIRD COMPONENTS IN THE ECLIPSING BINARIES AH TAURI AND ZZ CASSIOPEIAE..... | 103 |
| Udovichenko S.N., Keir L.E. ON THE IRREGULAR VARIATIONS IN THE LIGHT CURVES OF RY Vul | 110 |

| | |
|--|-----|
| Usenko I.A., Miroshnichenko A.S., Danford S., Kovtyukh V.V., Turner D.G., Shul'ga A.V., Protsyuk Yu.I. SPECTROSCOPIC INVESTIGATIONS OF GALACTIC CLUSTERS WITH ASSOCIATED CEPHEID VARIABLES. I. POLARIS CLUSTER AND α UMI..... | 113 |
| Usenko I.A., Kniazev A.Yu., Kovtyukh V.V., Mishenina T.V., Miroshnichenko A.S., Turner D.G., Protsyuk Yu.I. SPECTROSCOPIC INVESTIGATIONS OF GALACTIC CLUSTERS WITH ASSOCIATED CEPHEID VARIABLES. II. NGC 5662 AND V CEN | 117 |
| Velichko A.B., Fedorov P.N. KINEMATICS OF THE MILKY WAY FROM VELOCITIES OF YOUNG RED CLUMP GIANTS USING THE PMA AND GAIA DR2 DATA | 123 |

Radioastronomy

| | |
|--|-----|
| Galanin V.V., Lytvynenko O.A., Derevyagin V.G., Kravetz R.O. RADIO TELESCOPE URAN-4 AND THE PROBLEM OF RADIO INTERFERENCE | 128 |
| Isaeva E.A. THE RELATIONSHIP OF THE SCR WITH PARAMETERS OF RADIO BURSTS AND CME..... | 132 |
| Orlov V.V., Lytvynenko O.A., Galanin V.V. ALGORITHMS OF MULTI FREQUENCY RADIOMETRY IN THE CONDITIONS OF BROADBAND INTERFERENCE | 137 |
| Tsvyk N.O. ON THE INFLUENCE OF MHD TURBULENCE ON THE STRUCTURE OF THE RADIOGALAXY LOBES .. | 142 |

Sun, solar activity and astrobiology

| | |
|--|-----|
| Isaeva E.A. NEW APPROXIMATION OF THE ENERGY SPECTRUM OF PROTON SCR | 147 |
| Lozitsky V.G., Yurchyshyn V.B., Ahn K., Wang H., Lozitska N.I. PROBLEM OF SUPER-STRONG MAGNETIC FIELDS ON THE SUN: BRIEF CHRONOLOGY AND NEW OBSERVATIONAL DATA | 152 |
| Shepelev V.A., Melnik V.N., Vashchishin R.V. PRELIMINARY RESULTS OF INTERFEROMETRIC OBSERVATIONS OF THE QUIET SUN AT THE FREQUENCIES 8–32 MHZ..... | 159 |
| Sobitnyak L.I., Ryabov M.I., Sukharev A.L., Orlyuk M.I., Romenets A.O., Sumaruk Yu.P. THE CATALOG OF MAGNETIC STORMS FOR ODESSA MAGNETIC ANOMALY ZONE | 163 |

Solar system

| | |
|--|-----|
| Bushuev F., Kaliuzhnyi M., Khalaley M., Kryuchkovskiy V., Kulichenko M., Shulga O. DOPPLER STATION FOR ORBITAL TRACKING OF LOW-ORBIT SPACECRAFTS BY THEIR RADIO BEACON SIGNALS | 167 |
| Bushuev F., Kaliuzhnyi M., Mazhaev O., Shulga O., Shakun L., Bezrukovs V., Reznichenko O., Moskalenko S., Malynovskiy Ye. EXTERNAL COMPARISON SATELLITE POSITIONS OBTAINED BY THE NETWORK OF PASSIVE CORRELATION RANGING OF GESTATIONARY TELECOMMUNICATION SATELLITES | 171 |
| Konovalova N.A., Gorbanev Yu.M., Davruqov N.H. THE EXISTENCE OF GROUPS OF METEORITE-PRODUCING FIRE-BALLS AND METEORITES IN COMET-LIKE ORBITS | 174 |
| Koshkin N., Shakun L., Korobeinikova E., Melikyants S., Strakhova S., Dragomiretsky V., Ryabov A., Golubovskaya T., Terpan S. MONITORING OF SPACE DEBRIS ROTATION BASED ON PHOTOMETRY | 179 |
| Kulichenko M.O., Shulga O.V. RADIANTS AND ORBITAL DISTRIBUTION OF TV FAINT SPORADIC METEORS..... | 186 |
| Shakun L.S. FEATURES OF KOTLIN ORBIT ESTIMATION LIBRARY | 191 |
| Velichko S.F., Andreev M.V. PHOTOMETRY OF COMET C/2009 P1 (GARRADD) BEFORE AND AFTER PERIHELION..... | 196 |

Astroinformatics

| | |
|--|-----|
| Akhmetov V.S., Khlamov S.V., Andruk V.M., Protsyuk Yu. I. THE CATALOGUES ANALYSIS OF STARS EQUATORIAL COORDINATES AND B-MAGNITUDE OF THE FON PROJECT | 199 |
| Eglitis I. ASTEROIDS EXPLORATION WITH BALDONE SCHMIDT TELE-SCOPE | 204 |
| Eglitis I., Eglite V., Andruk V., Protsyuk Yu., Protsyuk S., Kovylanska O. BALDONE 1.2M TELESCOPE PLATE ARCHIVE – HIDDEN RESERVES OF THE FON PROJECT..... | 208 |
| Khlamov S.V., Savanevych V.E., Briukhovetskyi O.B., Dikov E.N., Vavilova I.B. DEVELOPMENT AND IMPROVEMENTS OF COMPUTATIONAL METHODS IMPLEMENTED TO THE COLITEC SOFTWARE | 211 |
| Maigurova N.V., Pomazan A.V., Shulga A.V. HIGH-PRECISION FOLLOW-UP OBSERVATIONS OF NEAR-EARTH OBJECTS | 216 |
| Maigurova N.V., Protsyuk Yu.I., Bondarchuk L.E. ASTROMETRIC CCD OBSERVATIONS OF SELECTED WDS MULTIPLE STAR SYSTEMS..... | 220 |
| Mullo-Abdolv A., Relke H., Kokhirova G., Yuldoshev Q., Protsyuk Yu., Andruk V. PROGRESS IN THE REALIZATION OF THE PROJECT FON-DUSHANBE CATALOGUE | 224 |
| Protsyuk Yu., Kovalchuk O. ANALYSIS OF MASS CCD OBSERVATIONS TO IMPROVE THE ACCURACY OF ASTROMETRIC PROCESSING | 228 |
| Protsyuk Yu.I., Shukhratov Sh.Sh., Kovalchuk O.M., Muminov M.M., Yuldoshev Q.H., Abdurakhimov R.R., Andruk V.M. RESULTS OF PROCESSING OF CCD OBSERVATIONS OF SELECTED OPEN CLUSTERS ON MAIDANAK..... | 231 |
| Shatokhina S.V., Relke H., Yuldoshev Q., Andruk V.M., Protsyuk Yu.I., Muminov M. ASTEROIDS SEARCH RESULTS IN DIGITIZED OBSERVATIONS OF THE NORTHERN SKY SURVEY PROJECT (KITAB PART)..... | 235 |
| Vavilova I.B., Babyk Iu.V. NEW APPROACH FOR ANALYSIS OF THE X-RAY DATA IN CORES OF GALAXY CLUSTERS: BINNING ON THE CONCENTRATION RINGS, CONTOUR BINNING, AND WAVELET TRANSFORMS.. | 239 |
| Yizhakevych O.M., Mullo-Abdolv A.Sh., Relke H.V., Kokhirova G.I., Pakuliak L.K., Andruk V.M. FIRST RESULTS OF THE SEARCHING OF ASTEROIDS BASED ON THE DATA OF FON-DUSHANBE PROCESSED PLATES | 247 |
| Yizhakevych O.M., Andruk V.M., Yuldoshev Q., Pakuliak L.K., Muminov M.M. THE FIRST RESULTS OF PROCESSING OBSERVATIONS OF SS BODIES FROM UBAI PHOTOGRAPHIC PLATE COLLECTION USING THE NEW TECHNIQUE | 251 |

COSMOLOGY, GRAVITATION, ASTROPARTICLE PHYSICS, HIGH ENERGY PHYSICS

DOI: <http://dx.doi.org/10.18524/1810-4215.2018.31.144434>THE ANALYSIS OF IMAGES OF A CIRCULAR SOURCE
IN N-POINT GRAVITATIONAL LENSESBronza S.D.¹, Svyrydova Ju.V.², Kotvytska L.A.³¹ Department of Further Mathematics, Ukrainian State University of Railway Transport, Kharkiv, Ukraine, bronza.sem@gmail.com² Faculty of Construction, Ukrainian State University of Railway Transport, Kharkiv, Ukraine, julietca@meta.ua³ Department of Low-Temperature Physics, V. N. Karazin Kharkiv National University, Kharkiv, Ukraine, lilya18kotv@gmail.com

ABSTRACT. Currently, in the field of computer processing, there are difficulties. When processing astrophysical experimental data, the difficulties are connected, on the one hand, with a large amount of information that requires processing, and, on the other hand, with the technical capabilities of computers. The use of analytical methods can significantly reduce information processing time. The information that is entered is recorded in an analytical form, more convenient for processing. Information is processed analytically (Kotvytskiy & Bronza, 2016), and not by methods of the Ray Tracing type. Some results were obtained strictly analytically, and they do not need further computer processing (Kotvytskiy et al., 2016). The goal of this paper is to analyze images in N -point gravitational lenses by:

- reduction of research of an arbitrary source to the study of a circular source;
- reduction of research of a circular source in an N -point gravitational line to its study in the Schwarzschild lens and other few-point lenses;
- analytical study of a circular source in the Schwarzschild lens and other few-point gravity lenses;
- research of the place of the Schwarzschild lens, in the set of N -point gravitational lenses.

Using the methods of algebraic geometry, algebraic topology and the theory of functions, we have prepared a problem for computer modeling: finding images of arbitrary sources in an N -point gravitational lens. We researched the images of a circular source in the Schwarzschild lens and proved that the study of images of any other sources is combinatorial reduced to this case.

АБСТРАКТ. В теперішній час в області обробки комп'ютерної інформації, спостерігаються труднощі. При обробці астрофізичних експериментальних даних, труднощі пов'язані з одного боку з великою кількістю інформації, яка потребує обробки, а з іншого боку з технічними можливостями комп'ютерів. Застосування аналітичних методів дозволяє значно скоротити час обробки інформації. Інформація, яка вводиться, записується в аналітичному вигляді, більш зручному для обробки. Інформація обробляється аналітично (Kotvytskiy & Bronza, 2016), а не методами типу Ray

Tracing. Деякі результати вдалося отримати строго аналітично, і вони не потребують подальшої комп'ютерної обробки (Kotvytskiy et al., 2016).

Метою даної роботи є аналітичне дослідження зображень в N -точкових гравітаційних лінзах шляхом:

- редукції досліджень довільного джерела до вивчення кругового джерела;
- редукції досліджень кругового джерела в N -точковій гравітаційній лінзі до його дослідження в лінзі Шварцшильда та інших мало-точкових лінзах;
- аналітичного дослідження кругового джерела в лінзі Шварцшильда і інших мало-точкових гравітаційних лінзах;
- дослідження місця лінзи Шварцшильда, в множині N -точкових гравітаційних лінз.

Методами алгебраїчної геометрії, алгебраїчної топології та геометричної теорії функцій ми підготували задачу знаходження зображень довільних джерел в N -точкових гравітаційних лінзах до комп'ютерного моделювання. Аналітично досліджені зображення кругового джерела в лінзі Шварцшильда і деяких інших мало-точкових гравітаційних лінзах. Показано, що дослідження зображень будь-яких інших джерел комбінаторно зводиться до цього випадку.

Keywords: Gravitational lens, algebraic geometry, phases of images.

1. Introduction

Let R_X^2 and R_Y^2 be vector spaces. It is known, (Kotvytskiy & Bronza, 2017), (Kotvytskiy et al., 2017) that N -point gravitational lens sets a single-valued mapping

$$L : (R_X^2 \setminus \Lambda) \rightarrow R_Y^2, \quad (1)$$

where $\Lambda = \{l_i \mid i = 1, 2, \dots, N\}$ - set of radius - vectors \vec{l}_i point masses. The mapping L can be written in the coordinate form (Weinberg, 2008):

$$\begin{cases} y_1 = x_1 - \sum_{i=1}^N m_i \frac{x_1 - a_i}{(x_1 - a_i)^2 + (x_2 - b_i)^2} \\ y_2 = x_2 - \sum_{i=1}^N m_i \frac{x_2 - b_i}{(x_1 - a_i)^2 + (x_2 - b_i)^2} \end{cases}, \quad (2)$$

were $\bar{x} = (x_1, x_2)$, $\bar{y} = (y_1, y_2)$, $\bar{l}_i = (a_i, b_i)$, and m_i normalized, dimensionless point masses satisfying the relation $\sum m_i = 1$. We add the vector spaces R_X^2 and R_Y^2 to affine ones. We will define orthonormal bases in them. For the unit of rationing, we take the Einstein-Chvolson radius. The resulting affine spaces R_X^2 and R_Y^2 are called the lens plane and the source plane, respectively. For some researches, they are combined and called the picture plane. The mapping L^{-1} inverse to (1) is, in general, multivalued (Kotvytskiy, et al., 2017), (Kotvytskiy, et al., 2017). It can, naturally, be continued from $(R_X^2 \setminus \Lambda)$ to all R_X^2 (we will leave the same notation behind the continued mapping), i.e.

$$L^{-1} : R_Y^2 \rightarrow R_X^2 \quad (3)$$

Some authors call this mapping as a lens mapping, see, for example, (Schneider et al., 1999). A special case of the N -point gravitational lens is the Schwarzschild lens, (Weinberg, 2008), (Schneider et al., 1999), which is determined by the condition $N = 1$, $a_1 = 0$, $b_1 = 0$, and $m = 1$.

From the algebraic point of view, system (2) is a system of two rational equations, which are given over the field of real numbers. System (2) can also be considered over the field of complex numbers. If the coordinates of the source are fixed, the set of real solutions of the system is the set of its images in the lens.

In this note, system (2) is researched by methods of algebraic geometry, mathematical analysis and the theory of functions. This allows us to obtain analytical expressions for describing sources and images and to construct efficient algorithms for solving problems using computer algebra methods. In some cases, it is possible to accurately obtain an analytical solution.

2. Description of sources by the analytical method

In this article, we assume that the source is flat and located in the plane R_Y^2 . Sources can be classified according to various criteria, for example: physical, homogeneous and non-homogeneous; topological, on:

- zero-dimensional, consisting of a finite number of points;
- one-dimensional, consisting of a finite number of lines;
- two-dimensional, consisting of a finite number of two-dimensional regions;
- combined.

Due to the physical nature of the problem, we restrict ourselves to considering sources with a finite number of connected components, and we assume that any compo-

nent or:

- point;
- arc piecewise smooth curve;
- of course – a connected domain, the boundary of which consists of a finite number of arcs of smooth curves.

From the definition of mapping (1) by the system of equations (2), it follows that the source image is the union of the images of its connected components. It can also be assumed that the boundary of each connected component (a multiply connected domain) consists of a finite set of closed Jordan curves. From here follows: the image of a multiply-connected region can be represented as a finite combination of simply-connected regions. This combinatorial problem is effectively solvable in the framework of algebraic topology. The reduction of research of an arbitrary source to the study of a circular source provides

Riemann's theorem. For any simply connected domain G (the boundary of the region has at least two points), there is analytic function $\zeta = f(z)$ in the domain G , which conformally maps the G to the unit circle $|z| < 1$. In addition, if a is a certain point of the G domain, then the function $\zeta = f(z)$ is uniquely determined by the conditions: $f(a) = 0$, $f'(a) > 0$.

Thus, at the first stage, it suffices to study the image of a point, a Jordan curve and a circle.

Note also that the trajectory of a point source, also, can be considered as the union of Jordan curves. When considering inhomogeneous sources, the functions by which they are given can be approximated by step functions given by level lines. Due to the physical nature of the problem, each level line can also be considered as a Jordan curve, or their union.

To set:

- point source is enough to set the coordinates of the point;
- an extended one-dimensional source, it suffices to specify a Jordan curve (for our purposes, for example, as an irreducible polynomial in two y_1, y_2 variables, or as a parametric curve $y_1 = y_1(t)$, $y_2 = y_2(t)$);
- an extended two-dimensional source, set, its boundaries, as Jordan curves, and the region itself, as a system of inequalities relative to its boundaries.

3. Asymptotic behaviour of a mapping

The direct task of the theory of gravitational lensing is the task of constructing images from a given source.

We make some assumptions regarding the source. We will assume that the source is homogeneous, flat and has a clear boundary. In topological terms, a source is a connected, finitely connected domain whose boundary is rectifiable, or in general, is an algebraic set (Lavrentiev & Shabat, 1973), (Gurvits & Kurant, 1968). The image of an S source in a lens, in topological terms, is an open set, generally speaking, consisting of several connected components.

We define some concepts necessary for further presentation.

The diameter of the S source is called the diameter of the minimum circle to which it belongs, and the center of the source S is the center O_S of this circle. We say that the source of S is small, if its diameter d_S is significantly less than the unit $d_S \ll 1$, and deleted (located far away) if the module $|\vec{O}_S|$ of the radius-vector \vec{O}_S is significantly greater than one, i.e. $|\vec{O}_S| \gg 1$. Similarly, we define the concept: the diameter and center of the connected components of the image, and the remote image.

Occurs

Theorem 1. Let the source S and its images be viewed in the picture plane. If the source is small and deleted, then its image has:

- remote component of connectivity S_1 , such that $|O_{S_1}| > |O_S|$;
- each point S_1 , with $|O_S| \rightarrow \infty$, tends to its image in S_1 ;
- restriction of the mapping L to S_1 is a bijection of S_1 to S .

First we prove the lemma

Lemma 2. The remote image of a remote point source in N -point gravitational lens tends to its remote image in the Schwarzschild lens.

Proof. Let points $(a_i, b_i) \in R_X^2$ and $\delta = \sqrt{x_1^2 + x_2^2}$. Let $\delta \rightarrow \infty$. Where we have:

$$x_1 - \sum_{i=1}^N m_i \frac{x_1 - a_i}{(x_1 - a_i)^2 + (x_2 - b_i)^2} = x_1 - \frac{x_1}{x_1^2 + x_2^2} + o(\delta). \quad (4)$$

A similar relation holds for the right side of the second equation of system (2).

For system (2), with $\delta \rightarrow \infty$, we have:

$$\begin{cases} y_1 = x_1 - \sum_{i=1}^N m_i \frac{x_1 - a_i}{(x_1 - a_i)^2 + (x_2 - b_i)^2} \\ y_2 = x_2 - \sum_{i=1}^N m_i \frac{x_2 - b_i}{(x_1 - a_i)^2 + (x_2 - b_i)^2} \end{cases} \Rightarrow \begin{cases} y_1 = x_1 - \frac{x_1}{x_1^2 + x_2^2} \\ y_2 = x_2 - \frac{x_2}{x_1^2 + x_2^2} \end{cases} \quad (5)$$

Thus, when the image is removed from the origin of coordinates in an N -point lens, it differs little from the images in the Schwarzschild lens.

But for the Schwarzschild lens, it is known that the points of the remote source are close to the points of the remote component of the image. Indeed, if $y_1^2 + y_2^2 \rightarrow \infty$, then:

$$x = \frac{1}{2} \left(y_1 \pm y_1 \sqrt{1 + \frac{4}{y_1^2 + y_2^2}} \right) \rightarrow x_1 = \begin{cases} y_1 \\ 0 \end{cases}, \quad (6)$$

thus, the abscissa S_1 tends to abscissa S . The same is true for ordinates.

The proof is complete.

Proof of Theorem 1.

We show that the points of the S_1 (the remote component of the image of the source of the S in the Schwarzschild lens) tend to their images, if $|O_S| \rightarrow \infty$. For the Schwarzschild lens we have: $\sqrt{(x_1 - y_1)^2 + (x_2 - y_2)^2} = 1/\sqrt{x_1^2 + x_2^2} = 1/\delta$. In addition, from $|O_S| \rightarrow \infty \Rightarrow r \rightarrow \infty$, and therefore $\sqrt{(x_1 - y_1)^2 + (x_2 - y_2)^2} = 1/\delta \rightarrow 0$.

The restriction of the mapping L to S_1 is a bijection of S_1 to S . Indeed, a point from S has two pre-images, one of which belongs to the remote image S_1 , and the second is in the unit circle. Considering the lemma, we have: the assertions of Theorem 1 are true.

4. Images of a circular source in the Schwarzschild lens

The Riemann theorem and Theorem 1 show the need to investigate images of a point and circular source in the Schwarzschild lens.

It is known that each point source located not at the origin of coordinates has two points (further conjugate) images in the Schwarzschild lens, one of which is in the unit circle and the other outside it.

Occurs

Theorem 2. If g_1, g_2 is the coordinates of one of the conjugate images in the Schwarzschild lens, then the coordinates of the second image are $-g_1(g_1^2 + g_2^2)^{-1}, -g_2(g_1^2 + g_2^2)^{-1}$.

Proof. Let's substitute the coordinates of each of the images into the lens equation. Both images have the same source.

The theorem is proved.

Corollary of Theorem 2. Let the source be small, simply connected, and not containing the origin. Then, in the Schwarzschild lens, it has two images. The points of the images are conjugate and their coordinates satisfy Theorem 2. We will call such images conjugate.

Let us turn to the study of images of a circular source. Let the source be a disk $D_\varepsilon = D_\varepsilon(a)$ of radius ε with the center at the point $(a, 0)$, and its boundary ∂D_ε :

$$\begin{cases} y_1 = t \\ y_2 = \pm \sqrt{\varepsilon^2 - (t_1 - a)^2} \end{cases}. \quad (7)$$

We substitute (7) into the system of equations that describes the Schwarzschild lens and exclude t . We have:

$$(x_1^2 + x_2^2 - 1)^2 - 2ax_1(x_1^2 + x_2^2 - 1) + (a^2 - \varepsilon^2)(x_1^2 + x_2^2) = 0 \quad (8)$$

We turn in (8) to the polar coordinates, we have:

$$(r^2 - 1)^2 - 2a(r^2 - 1)r \cos \phi + (a^2 - \varepsilon^2)r^2 = 0. \quad (9)$$

We research the equation (8) and (9), for which we consider special cases:

I) $a = 0$; **II)** $|a| = \varepsilon$; **III)** $|a| < \varepsilon$; **IV)** $|a| > \varepsilon$.

Case I).

From (9) we have: the image of the disk D_ε under the mapping L^{-1} is the ring k_ε . The ring is formed by circles:

$$r_1 = (\sqrt{\varepsilon^2 + 4} + \varepsilon) / 2, \quad r_2 = (\sqrt{\varepsilon^2 + 4} - \varepsilon) / 2. \quad (10)$$

The radii of the circles are reciprocal, i.e. $r_1 = 1 / r_2$.

Case II).

If $|a| = \varepsilon \Rightarrow a = \pm \varepsilon$. Consider the case of $a = \varepsilon$. We substitute $a = \varepsilon$ into (8). We have: the equation is divided into two:

$$x_1^2 + x_2^2 = 1, \quad (x_1 - \varepsilon)^2 + x_2^2 = 1 + \varepsilon^2 \quad (11)$$

Equations (11) are equations of circles. Therefore, the image of the $D_\varepsilon = \{(y_1, y_2) | y_1^2 + y_2^2 \leq \varepsilon^2\}$ disk, when displaying $L^{-1} : R_Y^2 \rightarrow R_X^2$, will be two circular wells. The wells are formed by circles (11), are conjugate and have the following areas:

$$S_I = \frac{\pi}{2} + \varepsilon - (1 + \varepsilon^2) \operatorname{arccctg} \varepsilon, \quad (12)$$

$$S_{II} = \frac{\pi}{2} + \pi \varepsilon^2 + \varepsilon - (1 + \varepsilon^2) \operatorname{arccctg} \varepsilon \quad (13)$$

Similarly, we consider the case of $a = -\varepsilon$.

Case III). $|a| < \varepsilon$.

The value of the polar radius $r \geq 0$. From (9) we have: if $a < \varepsilon$ we have two ovals, which are one in the other and are the boundary of a doubly connected domain homeomorphisms to the K_1 ring.

Internal and external ovals:

$$r_{\mp} = \frac{1}{2} \left(a \cos \varphi \mp \sqrt{\varepsilon^2 - a^2 \sin^2 \varphi} + \sqrt{\left(a \cos \varphi - \sqrt{\varepsilon^2 - a^2 \sin^2 \varphi} \right)^2 + 4} \right), \quad (14)$$

The area of this K_1 is

$$S = \int_0^\pi (r_+ - r_-)(r_+ + r_-) d\varphi. \quad (15)$$

Case IV). $|a| > \varepsilon$.

If $a > \varepsilon$, then we have: two closed, disjoint, conjugate curves (ovals). The curves are one outside the other and are the boundaries of simply connected regions. Each of the areas is homeomorphism to a disk. Curves are defined if $\varepsilon^2 - a^2 \sin^2 \varphi \geq 0$. Where do we get:

$$-\arcsin \frac{\varepsilon}{|a|} \leq \varphi \leq \arcsin \frac{\varepsilon}{|a|}, \quad \pi - \arcsin \frac{\varepsilon}{|a|} \leq \varphi \leq \pi + \arcsin \frac{\varepsilon}{|a|}. \quad (16)$$

The ovals in the right and left half-planes are given for constraints (16) by the equation (14).

The far (near) arc of the right oval is associated with the far (near) arc of the left oval. The area of the area bounded by the right oval:

$$S = \int_0^{\arcsin \frac{\varepsilon}{a}} (r_+ - r_-)(r_+ + r_-) d\varphi. \quad (17)$$

5. Classification of circular images source in the Schwarzschild lens

Without loss of generality, we can assume that the center of the circular source is on the x-axis, and the radius of the source is small.

For images of a circular source, a classification theorem holds in the Schwarzschild lens.

Theorem 3. Images of a circular source in the Schwarzschild lens belong to only one of the sets defined below (we will call the sets phases, the circular source and the image of the circular source will be depicted in the picture plane).

Let the radius of the circular source ε , and the center is at point $(a, 0)$.

Phases and parameters by which they are defined:

phase «-7»: $a < \varepsilon - \frac{1}{2\varepsilon}$; phase «-6»: $a = \varepsilon - \frac{1}{2\varepsilon}$;

phase «-5»: $\varepsilon - \frac{1}{2\varepsilon} < a < -1 + \varepsilon$; phase «-4»:

$a = -1 + \varepsilon$; phase «-3»: $-1 + \varepsilon < a < -\varepsilon$; phase «-2»:

$a = -\varepsilon$; phase «-1»: $-\varepsilon < a < 0$; phase «0»: $a = 0$;

phase «1»: $0 < a < \varepsilon$; phase «2»: $a = \varepsilon$; phase

«3»: $\varepsilon < a < 1 - \varepsilon$; phase «4»: $a = 1 - \varepsilon$; phase «5»:

$1 - \varepsilon < a < \frac{1}{2\varepsilon} - \varepsilon$; phase «6»: $a = \frac{1}{2\varepsilon} - \varepsilon$; phase

«7»: $a > \frac{1}{2\varepsilon} - \varepsilon$.

Corollary 1, Theorem 3. The classification of phases, in Theorem 3, is linear, has 15 phases, including 7 point and 8 intervals. The phases are symmetrical with respect to the central phase - the Einstein ring. Each of the phases is completely determined by the values of two parameters: the coordinates of the center of the circular source, and its radius. Parameters are phase invariants.

Corollary 2, Theorem 3. Any small simply connected source containing the origin has a Schwarzschild lens, a single doubly connected image that contains a unit circle. The points of the image outside and inside the unit circle are conjugate and their coordinates satisfy Theorem 2.

6. Research of images in a N - point gravitational lens

The Schwarzschild Lens holds a special place in the set of point gravitational lenses:

- the point source has a long image - the Einstein ring;
- to it reduce other H-point gravitational lenses.

For a sufficiently complete study it is necessary to study the typical representatives of the set N - point gravitational lenses: binary, 3-ary, etc. Also interesting are lenses with symmetries. The equation for specifying im-

ages of a circular source in an N-point gravitational lens, generally follows from (2) and (7).

Let the source be a disk $D_\varepsilon = D_\varepsilon(a)$ of radius ε centered at point (a, b) and its boundary ∂D_ε is given by parametric equations. Then the borders of the images are described by the equation:

$$\left(x_1 - \sum_{i=1}^N m_i \frac{x_1 - a_i}{(x_1 - a_i)^2 + (x_2 - b_i)^2} - a \right)^2 + \left(x_2 - \sum_{i=1}^N m_i \frac{x_2 - a_i b_i}{(x_1 - a_i)^2 + (x_2 - b_i)^2} - b \right)^2 = \varepsilon^2 \quad (18)$$

Equation (18) is sufficient for computer modeling of images in small - point lenses. Thus, for the direct problem there is a constructive, quasi-analytical solution. For special cases, it is possible to solve the direct problem analytically.

Example.

Let the point source is on axis OY_1 , that is $y_2 = 0$. Binary symmetric gravitational lens with masses $m_1 = 1/2$, $m_2 = 1/2$. For any real y_1 , there are always three real solutions that are determined by the equation

$$x_1^3 - y_1 x_1^2 - (b^2 + 1)x_1 + b^2 y_1 = 0. \quad (19)$$

In addition, with some ratios of parameters two more solutions can be implemented. For example, if $y_1 = 0$ and $b \leq 1$, then we have the following, additional, pair of solutions $\vec{x} = (0, \pm\sqrt{1-b^2})$.

7. Conclusion

In this paper, in the proof of the theorems, topological methods and the Riemann theorem on conformal equivalence of simply connected domains were used. It was proved that the study of images of any sources combinatorial reduces to the study of images of a circular source. It has been analytically proven that the Schwarzschild lens is a "limit" lens in the family of N-point gravitational lenses. The features of the Schwarzschild lens as a limiting lens are investigated, the classification of its images is proposed.

References

- Kotvytskiy A.T., Bronza S.D.: 2016, *Odessa Astron. Publ.*, **29**, 31.
- Kotvytskiy A.T., Bronza S.D., Vovk S.R.: 2016, *Bulletin of Kharkiv Karazin National University "Physics"*, **24**, 55 (arXiv:1809.05392).
- Bronza S.D., Kotvytskiy A.T.: 2017, *Bulletin of Kharkiv Karazin National University "Physics"*, **26**, 6.
- Kotvytskiy A.T., Bronza S.D., Shablenko V.Yu.: 2017, *Acta Polytechnica*, **57**(6), 404.
- Weinberg S.: 2008, *Cosmology* (Oxford Univ. Press, Oxford), 593.
- Kotvytskiy A., Bronza S., Shablenko V. et al.: 2017, *Zbirnyk naukovykh prac'*, Vinnitsa, 198 (in Ukrainian)
- Kotvytskiy A.T., Bronza S.D., Shablenko V. Yu.: 2017, *Odessa Astron. Publ.*, **30**, 35.
- Schneider P., Ehlers J., Falco E.E.: 1999, *Gravitational lenses*. (Springer-Verlag Berlin Heidelberg), 560.
- Lavrentiev M.A., Shabat B.V.: 1973, *Metody teorii funkcij kompleksnogo peremennogo* (Moscow), 716. (in Russian)
- Gurvits A., Kurant R.: 1968, *Teorija funkcij* (Moscow), 648. (in Russian)

DOI: <http://dx.doi.org/10.18524/1810-4215.2018.31.144435>

ZELDOVICH LOCAL PANCAKE: DARK ENERGY DOMINATION

A. D. Chernin¹, I. D. Karachentsev², N. V. Emelyanov¹¹ Sternberg Astronomical Institute, Moscow University, Moscow, Russia
Arthur.Chernin1@gmail.com,² Special Astrophysical Observatory, Russian Academy of Sciences, Nizhniy Arkhys, Russia

ABSTRACT. Zeldovich Local Pancake is a two-dimensional system of 15 giant galaxies nearest to us. Two of the galaxies, the Milky Way and the Andromeda Galaxy, move to each other in the Local Group, while the rest of the galaxies are located around the group at the distances up to 10 Mpc from the group barycenter and move away from it forming a local expansion outflow. We use recent Hubble Space Telescope data on local giants and their numerous fainter companions to study the dynamical structure and evolutionary trends of the expanding system. N-body computer model, which reproduces the observed kinematics of the flow, is constructed under the assumption that the system as a whole is embedded in the universal dark energy background. In the model, the motions of the flow bodies are controlled by their mutual attraction force and the repulsion force produced by the dark energy. It is found that the repulsion dominates the force field of the system. Because of this, the the system expands with acceleration. The dark energy domination increases with time and introduces to the expansion flow an asymptotically linear velocity-distance relation with the universal time-rate (the Hubble constant) that depends on the dark energy density only.

Key words: galaxies: groups: general, galaxies: kinematics and dynamics, dark energy.

АБСТРАКТ. Локальний млинець Зельдовича – двовимірна система, яка утворена 15 найближчими до нас гігантськими галактиками. Дві з них, Чумацький Шлях і галактика в Андромеді, рухаються назустріч один одному в Місцевій Групі галактик, тоді як інші галактики знаходяться навколо групи на відстанях до 10 Мпс від її барицентра і рухаються геть від неї, утворюючи місцевий потік розбігання. Ми спираємося на свіжі дані спостережень космічного телескопа “Хаббл” для місцевих гігантських галактик і їх чисельних і менших за розмірами компаньонів,

для вивчення сучасної динамічної структури потоку розбігання і тенденцій його еволюції. Ми будуємо також чисельну модель задачі декількох тел, яка відтворює спостережану кинематику і динаміку потоку в припущенні, що система як ціле занурена в універсальний фон темної енергії. У цій моделі рух тел потоку управляється силою їх взаємного тяжіння і силою відштовхування, яка створюється темною енергією. Встановлено, що сила відштовхування домінує в силовому полі системи. З цієї причини розширення системи відбувається з прискоренням. Домінування темної енергії посилюється з часом і асимптотично привносить в систему лінійну залежність швидкості від відстані з універсальним коефіцієнтом (постійної Хаббла), що залежать тільки від щільності темної енергії.

Ключові слова: галактики, групи галактик, кинематика і динаміка галактик, темна енергія.

1. Introduction

A half century ago, the notion of cosmic pancakes was introduced by Ya. B. Zeldovich in his famous theory of galaxy formation (Zeldovich, 1970). Initially, pancakes were considered as flattened clouds of protogalactic gas produced by gravitational instability in the early Universe. Now the pancake concept is treated in a wider context with not only gasdynamical processes, but also motions of two-dimensional (2D) cosmic N-body systems which is applicable to nonlinear stages of gravitational instability (Chernin et al., 2015 and references therein). It is important that such 2D systems are really observed in the Cosmic Web on the spatial scales from several to hundreds megaparsec (Mpc). The nearest to the Milky Way 2D system is the N-body ensemble of 15 giant galaxies observed at distances up to 10 Mpc from the barycentre of the Local Group. Following the suggestion by one of us (I.K.), we refer to this system as Zeldovich Local Pancake (ZLP). The

ZLP galaxies and their numerous fainter companions have recently been observed (Karachentsev & Kudrya, 2013; Karachentsev et al., 2013, 2014) with the Hubble Space Telescope (HST). Two of the local giants of the ensemble, which are the Milky Way and the Andromeda Nebula, are moving towards each other inside the Local Group, while a dozen others are moving away from the group with radial velocities from 100 to 900 km/s. Each of the ZLP members contributes more or less equally to the system's total matter mass which is estimated as 10^{14} solar masses.

The physics behind the observed properties of the systems is also enriched now compared to the original pancake dynamics: it includes both gravity of matter and anti-gravity produced by universal dark energy. All the cosmic systems and the Cosmic Web as a whole are embedded in the dark energy background. We adopt that the dark energy is represented by Einstein's cosmological constant Λ , as in the currently standard Λ CDM cosmology. The constant is positive, which implies that the dark energy produces a repulsive force of anti-gravity. The cosmic repulsion acts not only on the global cosmological distances where it was originally discovered in observations (Riess et al., 1998; Perlmutter et al., 1999), but actually everywhere in space. We will use the works on the local dark energy effects (Chernin, 2001) to show below that in the volume of the observed Local Group ($R \approx 1$ Mpc), the dark energy anti-gravity is weaker than the gravity produced by the matter mass of the group; but the anti-gravity repulsion (described in the reference frame of the group barycentre) dominates at distances > 13 Mpc from group's barycentre. The anti-gravity domination makes the ZLP expand with acceleration. Because of this, the ZLP is cooling with time and its time-rate ("the Hubble constant") $H(t)$ tends to the current cosmological value $H_0 = 70 \text{ km}/(\text{sMpc})$.

We describe the motions of the ZLP giants with the use of the N-body computer model in combination with the HST data (Karachentsev et al., 2013, 2014; Karachentsev, Kaisina & Makarov, 2014). The anti-gravity of dark energy effects at the present epoch, as well as in the future, are in the focus of our discussion here. We do not discuss, however, the origin and early evolution of the ZLP in its past. The observed present-day velocities and distances of the giants are used as initial conditions in our model.

2. ZLP: Basic HST data

The observation data on the local giant galaxies and their companions are presented in the recently published Updated Nearby Galaxy Catalogue (UNGC) by Karachentsev et al. (2013); see also Karachentsev & Kudrya (2014) and Karachentsev et al. (2014). The catalogue contains systematic and homogeneous data

on coordinates, distances, radial velocities and other basic physical parameters of about 800 galaxies at distances up to 10 Mpc. More than 300 UNGC galaxies at these distances have been observed with the HST for about 330 HST orbits. The unique resolution available in the HST observations allowed us to use the Tip of the Red Giant Branch (TRGB) method for precise measurements of distances to more than 300 nearby galaxies with an accuracy from 10 to 30 per cent. Precise data on the radial velocities of the galaxies have also been compiled in the UNGC.

According to Karachentsev et al. (2013, 2014), there are 15 nearby giant galaxies at distances up to 10 Mpc: they are the Milky Way and the Andromeda Nebula (gravitationally bound in the Local Group), and galaxies M81, NGC 5128, IC342, NGC 253, NGC 4736, NGC 5236, NGC 6946, M101, NGC 4258, NGC 4594, NGC 3115, NGC 3627 and NGC 3368. Each of the giants of the ZLP is actually the main galaxy of a group (similar to the Local Group), which includes the galaxy itself and its extended dark matter halo together with companion galaxies therein. The mass M of the system is the total orbital mass of the group. The UNGC data are used to estimate the masses of the groups via motions of their 351 less-massive companions (Karachentsev & Kudrya, 2014). The distance R of a giant and its radial velocity V are calculated relative to the barycentre of the Local Group.

The nearest to the Local Group is M81 galaxy with a distance of 3.6 Mpc. Its recession velocity (relative to the Local Group barycentre) is about 100 km/s, the lowest in the ZLP. The mass of the galaxy is 5×10^{12} solar masses (we give here rounded numbers, the exact figures with error bars may be found in the paper by Karachentsev & Kudrya, 2014). The most distant from us is the galaxy NGC 3368 at 10.4 Mpc with the radial velocity 740 km/s which is the second largest velocity in the ZLP. Its mass is 2×10^{13} solar masses, which is the second largest mass in the ZLP. The most massive galaxy is probably NGC 4594 at 9.3 Mpc; its mass is 3×10^{13} solar masses, but with an error of 2×10^{13} solar masses, the largest error in the data. The major gross parameter of the ZLP is its total mass $M_{tot} = 8 \times 10^{13}$ solar masses, which is the sum of the matter (dark matter and baryons) masses of the ZLP member. (2014).

3. ZLP: N-body model

The structure and evolution of the ZLP may be studied with a computer model which treats it as a two-dimensional (2D) gravitational N-body system embedded in the dark energy background. This is a non-relativistic isolated conservative system of point-like masses interacting with each other via Newton's mutual gravity and undergoing Einstein's anti-gravity pro-

duced by the universal - dark energy background. Dark energy is considered as continuous medium with the density $\rho_\Lambda = c^2\Lambda/(8\pi G)$, which is positive and constant in space and time in any reference frame (here G is the Newtonian gravitational constant and c is the speed of light). The currently adopted value of the universal dark energy density is $\rho_\Lambda = 0.7 \times 10^{29} \text{ g/cm}^3$. The dynamical effects of dark energy in the model are described by relations that come from General Relativity with Einstein non-zero cosmological constant Λ and the currently standard Λ CDM cosmology (see for details Chernin, 2001; Byrd et al., 2012). As macroscopic medium, dark energy is characterized by the equation of state

$$p_\Lambda = -\rho_\Lambda c^2, \quad (1)$$

where p_Λ is the dark energy pressure. Dark energy cannot serve as a reference frame, and it is co-moving to any like trivial emptiness.

In General Relativity, the effective gravitating density is determined by both density and pressure of any medium:

$$\rho_{eff} = \rho_\Lambda + 3p_\Lambda c^2. \quad (2)$$

For dark energy, the effective density, $\rho_{eff} = -2\rho_\Lambda < 0$, is negative, and because of this dark energy produces the repulsion, or anti-gravity. General Relativity indicates also that the passive gravitational density is the sum $\rho_{pass} = \rho + p/c^2$ for any fluid. The value ρ_{pass} is zero for dark energy. According to the equivalence principle, the passive gravitational mass is equal to the inertial density. Thus, the inertial density of dark energy is also zero. This implies that dark energy is affected neither by the external gravity of matter nor by its own anti-gravity.

In the ZLP, the local dynamical effects of dark energy are treated in terms of Newtonian mechanics; this is possible because the velocities of the local galaxies are small compared to the speed of light, and the spatial differences in both gravity and anti-gravity potentials are much smaller (in absolute value) compared to the speed of light squared. According to this weak field approximation, Einstein's law of anti-gravitation states that any body in the Universe is affected by the repulsive force, which is proportional to the dark energy density ρ_Λ and to the distance R of the body from the origin of the adopted reference frame:

$$F_\Lambda = 8\pi/3G\rho_\Lambda R. \quad (3)$$

This force acts along the direction from the origin, and it gives the force per unit mass of the body (i.e. acceleration) in the projection on the body radius-vector. This relation can be rewritten in the form

$$F_\Lambda = H_\Lambda^2 \Lambda R, \quad (4)$$

where $H_\Lambda = (8\pi/3G\rho_\Lambda)^{1/2} = 61 \text{ km}/(\text{sMpc})$ is the cosmic universal Hubble constant, which is valid on both

global and local spatial scales everywhere in space and at any moment of time.

The equations of motion for the ZLP bodies are based on the relations (3) and (4) with the initial conditions specified at the present moment of cosmic time $t = t_0 = 13.7 \text{ Myr}$. These are the observed positions of the flow bodies and their measured radial velocities recalculated to the barycentre of the Local Group. The model has strong limitations: (i) it is valid only when and where the distances between the system bodies (giant galaxies with their dark matter haloes) are large enough compared to the sizes of the bodies; (ii) it does not describe the origin and early evolution of the flow. As it may be seen from the data above, the first limitation is well satisfied for the observed present-day state of the flow; it is clearly satisfied as well in the future states of the system. The second limitation comes from the first one and also from the account of complex physical processes responsible for the formation and evolution of the local systems in their early history. Observations provide us with the radial velocities of the galaxies, but say nothing about their tangential (transverse) velocities. This is an obvious flaw in any dynamical model of extragalactic astronomy where the full velocity vector is needed for correct formulation of initial conditions. Fortunately, the coordinate origin of our model is located close to the barycentre of the ZLP, so that most measured velocities are actually radial. Having this in mind, we assume that the transversal velocities are zero in the initial conditions for the model.

The numerical integration of equations of motions for the ZLP bodies are made with the use of the standard computer method with the automatic choice of the integration step. The result reproduces the motions of the ZLP bodies from the Local Group barycentre as functions of time from $t = 13 \text{ Gyr}$ to $t = 25 \text{ Gyr}$. The major features of the state and evolution of the system are proving to be as follows:

- 1) the ZLP bodies are moving away from the initial position, so that the system as a whole is expanding with time;
- 2) the recession velocities of the ZLP bodies are growing with time, which indicates that the expansion of the system proceeds with acceleration;
- 3) the accelerating expansion means that the dark energy anti-gravity is stronger than the mutual gravity attraction of the ZLP bodies;
- 4) the domination of the dark energy anti-gravity in the ZLP dynamics is similar to the cosmological effect of the global accelerating expansion at the present-day state of the whole Universe.
- 5) with their growth with time, the ZLP trajectories converge to the straight line $V = H_\Lambda R$ going from the coordinate origin in the (V to R) phase space;
- 6) accordingly, the mean radial velocity dispersion decreases in ZLP with the trajectories growth, and the

system becomes increasingly regular and “cold”.

As we may see now, the dark energy domination is the major factor of the ZLP state and dynamical evolution at $t > t_0$. The dark energy anti-gravity becomes stronger, while the mutual gravity of the galaxies vanishes with the system expansion. These findings have become possible due to a recent combination of the HST observational data (Karachentsev et al., 2013, 2014; Karachentsev & Kudrya, 2014) with a computer model for the ZLP.

4. Conclusions

The ZLP and some other known local expanding systems and flows are observed at advanced stages of their evolution when they have already reached a certain degree of regularity. At these stages, the anti-gravity domination became the key factor of the system evolution. Earlier in the cosmic times, the dynamical effects of the dark energy were insignificantly weak and the cosmic structures of various spatial scales formed due to gravitational collapse driven mostly by dark matter. These evolutionary stages were studied by Zeldovich in 1970. It would be interesting to study also the transition epoch when the dark energy anti-gravity becomes strong enough to terminate collapse. That kind of gravity vs. anti-gravity interplay may be one of the important aspects of general theory of cosmic structure formation.

Acknowledgements. We are grateful to G. Bisnovatyi-Kogan, G. Byrd, Yu. Efremov, M. Pruzhinskaya, P. Teerikorpi, M. Valtonen and A. Zasov for helpful discussions.

References

- Byrd G.G., Chernin A.D., Teerikorpi P., Valtonen M.J.: 2012 *Paths to Dark Energy* Berlin/Boston De Gruyter
- Chernin A.D.: 2001, **Phys.-Usp.**, **44**, 1099.
- Chernin A.D., Emelyanov N.V., Karachentsev I.D.: 2015, *MNRAS*, **449**, 2069.
- Karachentsev I.D., Makarov D.I. Kaisina E.I.: 2013, *AJ*, **145**, 101.
- Karachentsev I.D., Kudrya Yu.N.: 2014, *AJ*, **148**, 50.
- Karachentsev I.D., Kaisina E.I., Makarov D.I.: 2014, *AJ*, **147**, 13.
- Perlmutter S. et al.: 1999, *ApJ*, **517**, 565.
- Riess A.G. et al.: 1998, *AJ*, **116**, 1009.
- Zeldovich Ya.B.: 1970, *A&A*, **5**, 84.

DOI: <http://dx.doi.org/10.18524/1810-4215.2018.31.144461>

ON THE CONFIGURATION SPACE OF A SPHERICALLY SYMMETRIC SYSTEM OF GRAVITATIONAL AND ELECTROMAGNETIC FIELDS

V.D. Gladush

Oles Honchar Dnipro National University, Dnipro, Ukraine,
vgladush@gmail.com

ABSTRACT. We study some classical and quantum aspects of the configuration space for a spherically-symmetric (SS) system of gravitational and electromagnetic fields. Note that this fields configurations, which are stationary respect to external observer, have regions of space-time (S-T) with dynamic behavior. This means that in these regions there exists an evolution of the S-T geometry in time, which is responsible for both classical and quantum mechanical properties of the model. From the standard action, we construct the reduced action and conserved total mass and charge. In view of a Hamiltonian constraint the non-dynamic degree of freedom from the action is excluded. This leads to the action in the minisuperspace. Therefore, the classical investigation stage of the Einstein equations solutions reduces to the study of solutions of the Einstein-Hamilton-Jacobi equation in the minisuperspace. It turns out that minisuperspace is flat therefore solutions of the Einstein equations correspond to a pencil of lines in the minisuperspace. Their intersections with the light cone of the minisuperspace correspond to the event horizons in the S-T of the charged BH. The consideration of the quantum aspects is formally reduced to the quantization of a particle in a three-dimensional pseudo-Euclidean space. Using the compatibility condition of the DeWitt and the eigenvalue equations for the operators of mass and charge the configuration wave function is constructed. Thus, we obtain a model of a charged BH with a continuous spectrum of masses and charge.

Keywords: spherical-symmetric configurations, minisuperspace, Hamilton operator, mass and charge operators, compatibility condition

АБСТРАКТ. Досліджуються деякі класичні і квантові аспекти фізики і геометрії мінісуперпростору сферично-симетричної системи гравітаційного та електромагнітного полів. Відзначимо, що такі класичні конфігурації, які є стаціонарними з точки зору зовнішнього

спостерігача, мають певні області простору-часу (ПЧ) з динамічним поведінкою (Т-області). Це означає, що в цих областях існує еволюція геометрії ПЧ в часі, яка відповідає, як за класичні, так і за квантово-механічні властивості моделі. Зі стандартної дії будується дія для зазначеної системи полів в Т-області, вводяться повна маса і заряд системи, які зберігаються. За допомогою гамільтонової в'язі, з отриманої скороченої дії виключається нединамічна ступінь вільності. Це призводить до дії в конфігураційному просторі (мінісуперпросторі). Виявляється, що рівняння геодезичних в мінісуперпросторі разом з в'яззю еквівалентні рівнянням Ейнштейна. Тому, класичний етап дослідження рішення рівнянь Ейнштейна зводиться до дослідження розв'язків рівняння Ейнштейна-Гамільтона-Якобі в мінісуперпросторі. Виявляється, що мінісуперпростор є плоским, тому розв'язкам рівнянь Ейнштейна відповідає пучок прямих в мінісуперпросторі. Їх перетин зі світловим конусом мінісуперпростору відповідають горизонтам подій в ПЧ зарядженої ЧД. Перетин цих прямих у пучку відповідає центральній сингулярності ПЧ. Розгляд квантових аспектів системи формально зводиться до квантування вільної частинки в тривимірному псевдоевклідовому мінісуперпросторі. Використовуючи умову сумісності рівнянь Девітта і проблеми на власні значення квантових операторів маси і заряду, будується хвильова функція сферично-симетричної конфігурації гравітаційного і електромагнітного полів. Таким чином, ми отримуємо модель зарядженої чорної діри із безперервним спектром мас і заряду.

Ключові слова: сферично-симетричні конфігурації, конфігураційний простір, оператор Гамільтона, оператори маси і заряду, умова сумісності

1. Introduction

It is known that the classical and quantum aspects of the behavior of the gravitational field is determined by a superspace metric so that superspace is the action arena of classical and quantum geometrodynamics. By studying the superspace geometry we can obtain important information about the classical and quantum manifestations of the dynamical system under consideration. However, the study of superspace in the general case meets with insurmountable mathematical difficulties (Anderson 2015, Giulini 2009). Therefore, reduced models are widely used, among which spherically symmetric (SS) configurations are popular and simplest models used for studying the problems of quantum gravity in a simpler setting. The general geometrodynamics approach to studying of the SS gravitational field of the black hole (BH) was developed in work of Kuchař 1994, the case of the electromagnetic and gravitational fields configuration of the charged BH, was considered by Louko et al. 1996 and Nakamura et al. 1993.

The present work is devoted to studying of the minisuperspace of the electromagnetic and gravitational fields SS configurations and the search for a correspondence between space-time and the minisuperspace, with the subsequent transition to quantization. We consider the class of SS configurations with diagonal S-T metrics. The model is based on the observation that the classical SS configurations of the electromagnetic and gravitational fields, which are stationary from the point of view of an external observer, have certain S-T regions (T-regions) with dynamic behavior. This means that in these regions there is an evolution of the S-T geometry over time, which is responsible for the quantum mechanical properties of the considered charged BH model.

2. Classical description of the spherically-symmetric configuration of the gravitational and electromagnetic fields

Consider the SS space-time $M^{(4)}$ with the metric

$$ds^2 = g_{\mu\nu} dx^\mu dx^\nu = \gamma_{ab} dx^a dx^b - R^2 d\sigma^2. \quad (1)$$

Here $d\sigma^2 = d\theta^2 + \sin^2\theta d\alpha^2$, $R = R(x^a)$, $\gamma_{ab} = \gamma_{ab}(x^a) - 2D$ metric tensor, $\sqrt{-g} = \sqrt{-\gamma}R^2 \sin\theta$, где $g = \det|g_{\mu\nu}|$, $\gamma = \det|\gamma_{ab}|$, $\mu, \nu = 0, 1, 2, 3$; $a, b = 0, 1$. The action for a system of gravitational and electromagnetic fields has the form

$$S = -\frac{1}{16\pi c} \int \left(\frac{c^4}{\kappa} {}^{(4)}R + F^{\mu\nu} F_{\mu\nu} \right) \sqrt{-g} d^4x, \quad (2)$$

where ${}^{(4)}R$ is the scalar curvature, $F_{\mu\nu} = A_{\nu,\mu} - A_{\mu,\nu}$ is the electromagnetic field tensor, $A_\mu = \{A_a, 0, 0\}$ is vector potential.

Note that information about the structure of SS space is contained in the square of the gradient (see Berezin 2003)

$$(\nabla R)^2 = \gamma^{ab} R_{,a} R_{,b}. \quad (3)$$

The surfaces $R(r, x^0) = \text{const}$, for which $(\nabla R)^2 = 0$, divide $M^{(4)}$ into

$$\begin{aligned} \text{R-regions } M_R^{(4)} \subset M^{(4)}, \text{ when } ((\nabla R)^2 < 0 \text{ and} \\ \text{T-regions } M_T^{(4)} \subset M^{(4)}, \text{ when } ((\nabla R)^2 > 0. \end{aligned}$$

In the R-region the surface $R(r, x^0) = \text{const}$ are time-like, and in the T-region is spacelike. Using the generalized Birkhoff theorem, in the R-region we can choose a coordinate system in which γ_{ab} and R depend only on the space-like coordinate r . Similarly, in the T-region, there exists a system in which γ_{ab} and R depend on the time-like coordinate x^0 .

In work of Gladush (2017) it is shown that the metric (1) and action (2) in the T-region can be presented in the form

$$\begin{aligned} ds_T^2 = h^{-1}(N dx^0)^2 - h(dx^1)^2 - R^2 d\sigma^2 \\ = R\xi^{-1} (N dx^0)^2 - \xi R^{-1} (dx^1)^2 - R^2 d\sigma^2. \end{aligned} \quad (4)$$

$$S_T = \int L_T dx^0 = \int \frac{l}{2c} \left\{ \frac{\mathfrak{T}}{N} + \frac{c^4}{\kappa} N \right\} dx^0, \quad (5)$$

where L_T is the Lagrange function of the reduced system with a kinetic term

$$\mathfrak{T} = -\frac{c^4}{\kappa} \xi_{,0} R_{,0} + R^2 \phi_{,0}^2. \quad (6)$$

Here $R_{,0} = \partial R / \partial x^0$, $\xi_{,0} = \partial \xi / \partial x^0$. In the R-region, the action S_R has a similar form, the evolutionary coordinate x^0 is space-like here.

From the Lagrangian L_T the primary constraint $P_N = \partial L / \partial \dot{N} = 0$ and momenta $P_i = \partial L / \partial \dot{q}^i$ follow:

$$P_\xi = -\frac{c^3 l}{2\kappa N} \dot{R}, \quad P_R = -\frac{c^3 l}{2\kappa N} \dot{\xi}, \quad P_\phi = \frac{l}{cN} R^2 \dot{\phi}. \quad (7)$$

From the Lagrange-Euler equation we obtain the secondary constraint

$$\frac{\delta L_T}{\delta N} = \frac{\partial L_T}{\partial N} = \frac{l}{2c} \left\{ -\frac{\mathfrak{T}}{N^2} + \frac{c^4}{\kappa} \right\} = 0. \quad (8)$$

So the Hamiltonian function $H = P_\xi \dot{\xi} + P_R \dot{R} + P_\phi \dot{\phi} - L$ leads to the Hamiltonian constraint in the T-region

$$H = \frac{Nc}{2l} \left\{ -\frac{4\kappa}{c^4} P_\xi P_R + \frac{1}{R^2} P_\phi^2 - \mu^2 \right\} \sim 0, \quad (9)$$

where $\mu = cl / \sqrt{\kappa}$.

In addition the system has the following conserved values:

Charge function is equal to the charge inside the region of radius R

$$Q(N, R, \phi, 0) = \frac{R^2}{N} \phi, 0 = \frac{c}{l} P_\phi. \quad (10)$$

Total mass function taking into account the contribution of the electromagnetic field is (see Gladush 2017)

$$M_{tot} = \frac{c^2}{2\kappa} R (1 + \gamma^{ab} R_{,a} R_{,b}) + \frac{Q^2}{2c^2 R}, \quad (11)$$

In the considered variables, as well as through momenta, it has the form

$$M_{tot} = \frac{c^2}{2\kappa} \left[R + \frac{1}{N^2} \left(\xi \dot{R}^2 + \frac{\kappa R^3 \dot{\phi}^2}{c^4} \right) \right], \quad (12)$$

$$M_{tot} = \frac{1}{2l^2} \left[\frac{l^2 c^2}{\kappa} R + \frac{4\kappa}{c^4} \xi P_\xi^2 + \frac{1}{R} P_\phi^2 \right]. \quad (13)$$

We also write out the Poisson brackets of dynamic quantities:

$$\{H, M_{tot}\} = \frac{2\kappa}{l^2 c^4} P_\xi H \sim 0, \quad \{H, Q\} = \{M_{tot}, Q\} = 0.$$

3. The configuration space of the SS system of gravitational and electromagnetic fields and its geometry

The factor N can be excluded from the action (5), while the original variational principle is transformed into a variational principle in the configuration space. Indeed, (8) implies $N = \sqrt{\kappa \mathfrak{T}}/c^2$. Substituting this expression into (5) we get

$$S_{\mathfrak{R}} = \int L_{\mathfrak{R}} dx^0 = \mu \int \sqrt{\mathfrak{T}} dx^0 = \mu \int d\Omega, \quad (14)$$

where

$$d\Omega^2 = \mathfrak{T}(dx^0)^2 = -\frac{c^4}{\kappa} d\xi dR + R^2 d\phi^2 > 0 \quad (15)$$

is the metric minisuperspace \mathfrak{R} . We see that $S_{\mathfrak{R}}$ is the action for a geodesic in the configuration space. The geodesic equations derived from this, together with the equation for N, are equivalent to the original Einstein equations. Definitions of the momenta (7) can now be rewritten in the standard form

$$P_a = \mu \Omega_{ab} \frac{dq^a}{d\Omega}, \quad (16)$$

as momenta of the particle with mass μ and 3-velocity $dq^a/d\Omega = \{d\xi/d\Omega, dR/d\Omega, d\phi/d\Omega\}$, moving along the geodesic in a minisuperspace.

It turns out that the minisuperspace with the metric (15) is flat. Therefore, there are transformations of field functions, for example,

$$\xi = \frac{\kappa}{c^4} \left(c\tau - x - \frac{y^2}{c\tau + x} \right), \quad (17)$$

$$\phi = \frac{y}{c\tau + x}, \quad R = c\tau + x,$$

leading metrics (15) to Lorentz form

$$d\Omega^2 = -c^2 d\tau^2 + dx^2 + dy^2. \quad (18)$$

Substituting $P_\xi = \partial S/\partial \xi, P_R = \partial S/\partial R, P_\phi = \partial S/\partial \phi$ into the Hamiltonian constraint (9), we arrive at the Einstein-Hamilton-Jacobi (EHJ) equation

$$-\frac{4\kappa}{c^4} \frac{\partial S}{\partial \xi} \frac{\partial S}{\partial R} + \frac{1}{R^2} \left(\frac{\partial S}{\partial \phi} \right)^2 = \frac{l^2 c^2}{\kappa}. \quad (19)$$

His solution is

$$S = \frac{l}{c} Q\phi + P_\xi \xi - \frac{l^2 c^6}{4\kappa^2 P_\xi} \left(\frac{\kappa Q^2}{c^4 R} + R \right). \quad (20)$$

We define the BH mass by the equation $M_{tot} = m$. Then

$$P_\xi = \pm l c^2 \sqrt{\frac{m}{2\kappa \xi_0}}. \quad (21)$$

As a result, the trajectories equations in the minisuperspace take the form

$$\phi(T) = \sqrt{\frac{\xi_0}{2\kappa m}} \frac{Q}{T}, \quad \xi(T) = \frac{c^3}{2\kappa m} \xi_0 T F_T(T, m, Q), \quad (22)$$

where in the T-region $R = cT$ and

$$F_T(T, m, Q) = -1 + \frac{2\kappa m}{c^3 T} - \frac{\kappa Q^2}{c^6 R^2}. \quad (23)$$

For the metric function in (4) we find

$$h = \frac{c^2 \xi_0}{2\kappa m} F_T(T, m, q), \quad h = -\frac{c^2 \xi_0}{2\kappa m} F_R(R, m, q) \quad (24)$$

for the T- and R-regions, respectively, and $F_R(R, m, q) = -F_T(T = R/c, m, q)$. These expressions lead to standard representations of the Reissner-Nordstrom metric. in the T- and R-regions.

Consider the trajectories structure in the configuration space. The region of admissible motions corresponding to a solution in a T-region is determined by the conditions $\xi > 0, R > 0$ or

$$-\Omega^2 = c^2 \tau^2 - x^2 - y^2 > 0, \quad R = c\tau + x > 0, \quad (25)$$

which correspond to the upper interior of the cone $\Omega^2 = 0$ in coordinates $\{c\tau, x, y\}$ (see fig. 1). In these

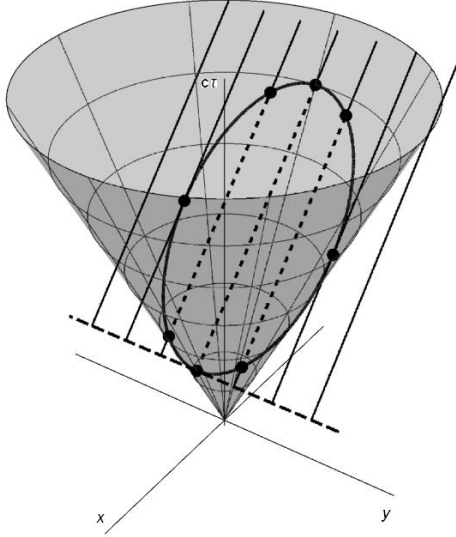


Figure 1: Mini-superspace SS configuration of gravitational and electromagnetic fields in coordinates $\{c\tau, x, y\}$.

coordinates, solutions (22) are described by straight lines:

$$\begin{aligned} c\tau(R) &= \frac{1}{2} \left[\left(1 - \frac{a}{R_g}\right) R + a \right], \\ x(R) &= \frac{1}{2} \left[\left(1 + \frac{a}{R_g}\right) R - a \right], \\ y &= \sqrt{\frac{\xi_0}{R_g}} Q, \quad R_g = \frac{2\kappa m}{c^2}, \quad a = \frac{\xi_0 c^4}{\kappa} \end{aligned} \quad (26)$$

The evolution of the system in configuration space, for given M and Q , can be represented as motion along a straight of the family (26), starting outside the cone $\Omega^2 = 0$ on the line $c\tau(0) = a/2, x(0) = -a/2, y = \sqrt{\xi_0/R_g}Q$, (central singularity). Further, the straight intersects the cone $\Omega^2 = 0$ with $R = R_1$ (inner horizon), comes upon inside the cone, crosses it with $R = R_2$ (outer horizon) and leaves to infinity of the minisuperspace. The motion inside the cone $\Omega^2 = 0$ of the minisuperspace corresponds to the solution for the T-region of the S-T, to the motion outside the cone corresponds to the solution for the R-regions of the S-T (see Fig. 1). For an extremely charged BH, when $|Q| = m\sqrt{\kappa}$, the corresponding straight of the family (26) touches the cone $\Omega^2 = 0$ at the point $R_1 = R_2 = m\kappa$. For superextremal charges $|Q| > m\sqrt{\kappa}$ these straight lie outside the cone $\Omega^2 = 0$.

4. Quantization of a spherically symmetric configuration of the gravitational and electromagnetic fields

The quantum states of the field configuration under consideration are determined by the wave function $\Psi(R, \xi, \phi)$ on the minisuperspace with the coordinates $\{R, \xi, \phi\}$. The corresponding momentum operators in this representation have the form:

$$\hat{P}_R = -i\hbar \frac{\partial}{\partial R}, \quad \hat{P}_\xi = -i\hbar \frac{\partial}{\partial \xi}, \quad \hat{P}_\phi = -i\hbar \frac{\partial}{\partial \phi}. \quad (27)$$

The classical Hamiltonian, the total mass and charge functions lead to operators

$$\hat{H} = \frac{Nc}{2l} \left\{ \frac{4\kappa\hbar^2}{c^4} \frac{\partial^2}{\partial R \partial \xi} - \frac{\hbar^2}{R^2} \frac{\partial^2}{\partial \phi^2} - \frac{c^2 l^2}{\kappa} \right\}, \quad (28)$$

$$\hat{M} = \frac{1}{2l^2} \left(\frac{l^2 c^2}{\kappa} R - \frac{4\kappa\hbar^2}{c^4} \frac{\partial}{\partial \xi} \xi \frac{\partial}{\partial \xi} - \frac{\hbar^2}{R} \frac{\partial^2}{\partial \phi^2} \right). \quad (29)$$

$$\hat{Q} = \frac{c}{l} \hat{P}_\phi = -i \frac{c\hbar}{l} \frac{\partial}{\partial \phi}. \quad (30)$$

For the Hermitian operator of the total mass, in the configuration space we use the following ordering of the operators: $\hat{P}_\xi \xi \hat{P}_\xi$. The following commutation relations hold

$$[\hat{H}, \hat{M}] = -\frac{2\kappa\hbar^2}{l^2 c^4} \frac{\partial}{\partial \xi} \hat{H} \sim 0, \quad [\hat{H}, \hat{Q}] = [\hat{Q}, \hat{M}] = 0.$$

States with a certain total mass and charge correspond to eigenfunctions and eigenvalues of the operators of total mass and charge:

$$\hat{M}\Psi_m = m\Psi_m, \quad \hat{Q}\Psi_q = q\Psi_q. \quad (31)$$

They reduce to the following equations

$$\left\{ \frac{c^2 l^2}{\kappa} R - \frac{4\kappa\hbar^2}{c^4} \frac{\partial}{\partial \xi} \xi \frac{\partial}{\partial \xi} - \frac{\hbar^2}{R} \frac{\partial^2}{\partial \phi^2} \right\} \Psi_m = 2l^2 m \Psi_m. \quad (32)$$

$$\frac{\partial}{\partial \phi} \Psi_q = \frac{iq l}{c\hbar} \Psi_q. \quad (33)$$

From the last equation we obtain $\Psi_q = A e^{i(q l / c\hbar)\phi}$. The general wave functions of the DeWitt equation $\hat{H}\Psi = 0$ and the charge operator, also as general wave functions of the operators total mass and charge, can be represented in the form

$$\Psi = \psi(\xi, R) e^{i(q l / c\hbar)\phi}, \quad \Psi_m = \psi_m(\xi, R) e^{i(q l / c\hbar)\phi}.$$

The functions ψ and ψ_m satisfy the equations

$$\left(\frac{4\partial^2}{\partial R \partial \xi} + \frac{c^2 q^2 l^2}{\kappa \hbar^2} \frac{1}{R^2} \right) \psi = \frac{c^6 l^2}{\kappa^2 \hbar^2} \psi,$$

$$\left\{ \frac{l^2 c^2}{\kappa} R - \frac{4\kappa\hbar^2}{c^4} \frac{\partial}{\partial \xi} \xi \frac{\partial}{\partial \xi} + \frac{1}{R} \frac{q^2 l^2}{c^2} \right\} \psi_m = 2ml^2 \psi_m.$$

Using the compatibility condition for the DeWitt and eigenvalues equations for the mass operator, we construct a regular solution of this system on the horizon,

which leads to a wave function of a configuration in a state with given mass m and charge q for a T-region:

$$\Psi_{m,q}^T = C J_0 \left(\frac{lc}{l_{pl}^2} T \sqrt{h F_T(T, m, q)} \right) e^{i(ql/c\hbar)\phi}, \quad (34)$$

where J_0 is the Bessel function of the first kind of zero order. The functions $F_T(T, m, q) > 0$ is defined in (23). Note that h and T are positive independent values here. For the classical Reissner-Nordstrom solution, the variables h and $R = cT$ enter the initial metric (4), at that in the T-region, the value of h depends on T , according to (24). We note that for the metric mini-superspace (15), signature conditions are not violated in both the T- and R-regions of the S-T. At that the evolution of the system in configuration space in all cases occurs within the direction $d\Omega^2 > 0$. Therefore quantum equations constructed in a minisuperspace are performed independently of the type of the region of the S-T. Thus, the wave function of the system in the R-region has the form similar (34) and can be written out by formally replacing $hF_T(T, m, q) \rightarrow -hF_R(R, m, q)$:

$$\Psi_{m,q}^R = C J_0 \left(\frac{l}{l_{pl}^2} R \sqrt{-h F_R(R, m, q)} \right) e^{i(ql/c\hbar)\phi}. \quad (35)$$

Here $R > 0$ and $h < 0$. Since $F_R(R, m, q) > 0$, then the value under the radical is positive. In the classical case, the value of h is determined by the value of R through the function $F_R(R, m, q)$, according to (24). The wave function (35) can be formally obtained based on the metric (4) and the Lagrangian of the configuration L_R in the R-region, where the evolutionary parameter x^0 is spacelike. Therefore, the solution (35) can be considered an analytic continuation of the solution (34) through the horizons $F_R(R, m, q) = F_T(T, m, q) = 0$. Note that the coefficient N is not included in the wave function $\Psi_{m,q}(h, T, \phi)$, which determines the probability amplitude of the configuration $\{h, T, \phi; m, q\}$, that is, the points $\{h, T, \phi\}$ of a minisuperspace, for given observables m, q . The mass and charge spectra of the BH in this approach are continuous.

4. Discussion and conclusions

As it has been shown, the configuration space of the SS system of electromagnetic and gravitational fields is flat, therefore to solutions of the Einstein equations there correspond straight lines in minisuperspace with the metrics(18). This greatly simplifies the differential-geometric structure of EHJ equations solutions. In addition, metric functions can be expressed in terms of the natural invariant parameter corresponding to the geodesic in the minisuperspace. As a result, classical solutions for S-T metrics can be constructed without fixing the calibration, for an arbitrary lapse function.

We note also that the used differential equations determines only the local structure of the space, while the global structure needs to be redefine. Thus, the question of the mass spectrum is not solved at local approach, since the nature of the spectrum depends on the global properties of the geometry of the S-T and superspace, their structure as a whole, as well as the structure of the phase space of the system. Therefore, to obtain a discrete spectrum, additional differential-geometric and algebraic (group) structures are introduced on the space-time, configuration or phase spaces (see, for example, Barvinsky et al. 2001, Das et al. 2003 and references therein). As a rule, a discrete spectrum occurs in the presence of a potential well or compact geometry of the configuration or phase space leading to the finite motions.

References

- Anderson E.: 2015, ArXiv:1412.0239v2, 29.
 Giulini D.: 2009, *Gen.Rel.Grav.* **41**, 785.
 Kuchař K.: 1994, *Phys. Rev.* **D50**, 3961.
 Louko J., Winters-Hilt S.: 1996, *Phys. Rev.* **D54**, 2647.
 Nakamura K., Konno S., Oshiro Y., Tomimatsu A.: 1993, *Prog. Theor. Phys.* **90**, 861.
 Berezin B.A.: 2003, *Физика элементарных частиц и атомного ядра* **34**, 49.
 Gladush V.D.: 2017, *Odessa Astr. Publ.*, **30**, 19.
 Barvinsky A., Das S., Kunstatter G.: 2001, *Class. Quantum Grav.*, **18**, 4845.
 Das S., Ramadev P., Yajnik U. A., Sule A.: 2003, *Phys. Lett.* **B565**, 201.

DOI: <http://dx.doi.org/10.18524/1810-4215.2018.31.144503>

SUPERSPACE APPROACH TO THE QUANTIZATION OF CHARGED BLACK HOLES WITH ALLOWANCE FOR THE COSMOLOGICAL CONSTANT

M.G. Holovko, V.D. Gladush

Dnipro National University, Gagarin Ave, 725014, Ukraine,
dilmendar@gmail.com, vgladush@gmail.com

ABSTRACT. In the present paper, we study the geometry of a mini-superspace and its relation to the corresponding space-time geometry of a spherically symmetric configuration of electromagnetic and gravitational fields, taking into account the cosmological constant, and the construction of the wave function of a quantum system. By the generalized Birkhoff theorem, for this configuration we can introduce the R- and T-regions, which simplifies the description of the dynamical system. Proceeding from the standard classical Einstein-Hilbert action, a Lagrangian of the fields configuration is constructed for a spherically symmetric space-time. The Lagrangian of the system is degenerate and contains a non-dynamic degree of freedom, which leads to a constraint. After eliminating the constraints, we proceed to the description of the dynamic system in the configuration space (minisuperspace). We consider additional conserved physical quantities: the total mass and the charge of the system. We note that the geometry of the minisuperspace turns out to be conformally flat. In addition to the standard horizons inherent in a charged black hole, space-time has an additional cosmological horizon. In the configuration space the simplest invariants of the curvature tensor: the scalar curvature, the square of the Ricci tensor, the Kretschmann invariant, are vanish, while the components of the Ricci tensor and the curvature tensor diverge on the minisuperspace analogue of the cosmological horizon.

Within the framework of canonical quantum gravity with material sources, physical states are found by solving the Hamiltonian constraint in the operator form for the wave function of the system defined on the minisuperspace, taking into account conserved additional quantities. Formal quantization in the R-region can be regarded as an analytic continuation of solutions from the T-region. In this approach, taking into account the mass and charge operators leads to a continuous spectra of mass and charge.

Keywords: charged black holes, cosmological constant, mass and charge function, Hamiltonian constraint, quantization, mass and charge operators.

АНОТАЦІЯ. В даній роботі розглядається задача вивчення геометрії мінісуперпростору та його зв'язок із відповідною геометрією простору-часу сферично-симетричної конфігурації електромагнітного та гравітаційного полів з урахуванням космологічної сталої та побудова хвильової функції відповідної квантової системи. З узагальненої теореми Біркгоффа випливає, що для даної системи можна визначити R- та T-області, що спрощує опис динамічної системи. Виходячи зі стандартної класичної дії Ейнштейна-Гільберта, будується лагранжіан конфігурації полів для сферично-симетричного простору-часу. Лагранжіан системи є виродженим та містить нединамічну ступінь вільності що призводить до в'язі. Виключаючи в'язь, можна перейти до опису динамічної системи в конфігураційному просторі (мінісуперпросторі). Розглядаються додаткові фізичні величини, що зберігаються: повна маса і заряд системи. Відзначимо, що геометрія мінісуперпростору є конформно-пласкою. Крім стандартних горизонтів, властивих зарядженим чорним дірам, простір-час має додатковий космологічний горизонт. В конфігураційному просторі найпростіші інваріанти тензора кривини такі як скалярна кривина, квадрат тензора Річі, інваріант Кречмана, дорівнюють нулю, в той час як ненульові компоненти тензора Річі і тензора кривини розбігаються на аналозі космологічного горизонту.

В рамках канонічної квантової гравітації з матеріальними джерелами, фізичні стани знаходяться шляхом розв'язання гамільтонової в'язі в операторній формі для хвильової функції системи, визначеної на мінісуперпросторі, з урахуванням додаткових величин, що зберігаються. Формальне квантування в R-області при цьому можна розглядати як аналітичне продовження розв'язків із T-області. В обраному підході, врахування операторів маси і заряду призводить до неперервного спектру маси і заряду.

Ключові слова: заряджені чорні діри, космологічна стала, масова і зарядова функція, Гамільтонова в'язь, квантування, оператори маси і заряду.

1. Introduction

The study of the canonical formalism of general relativity shows that all dynamic information about the gravitational field is contained in constraints. After replacing momenta $P_{ij} = \delta S / \delta \gamma_{ij}$ they lead to the Einstein-Hamilton-Jacobi equations (EHJ) for action functional S :

$$G_{ijkl} \frac{\delta S}{\delta \gamma_{ij}} \frac{\delta S}{\delta \gamma_{kl}} - \sqrt{\gamma} R^{(3)} = 0,$$

where $G_{ijkl} = (1/2)(\gamma)^{-1/2} (\gamma_{ik}\gamma_{jl} + \gamma_{il}\gamma_{jk} - \gamma_{ij}\gamma_{kl})$ is supermetric of configuration space and conditions of invariance $(\delta S / \delta \gamma_{ij})_{;j} = 0$.

When quantized, in accordance with the Dirac approach, constraints become conditions on the state vector (Dirac, 1979; Gitman, 1986). After replacement $\hat{P}_{ij} = -i\delta / \delta \gamma_{ij}$ momenta constraints leads to the relations of invariance of the state vector: $(\delta / \delta \gamma_{ij} \Psi)_{;j} = 0$. In this case, the Hamiltonian constraint leads to the Wheeler-DeWitt equation

$$\left\{ G_{ijkl} \frac{\delta}{\delta \gamma_{ij}} \frac{\delta}{\delta \gamma_{kl}} - \sqrt{\gamma} R^{(3)} \right\} |\Psi\rangle = 0.$$

(See, for example, Schulz 2014 and references therein.)

We see that both classical and quantum aspects of the behavior of a gravitational field are determined by the metric of superspace so that superspace is an arena of action classical and quantum geometrodynamics. Studying the geometry of a general superspace, one can obtain important information about the classical and quantum manifestations of the dynamical system under consideration. However, the study of superspace in general is faced with great mathematical difficulties. Therefore, reduced models are widely used, among which spherically symmetric configurations are popular and simplest models used to study the problems of quantum gravity.

The work is devoted to the study of the minisuperspace of spherically-symmetric configurations of the electromagnetic and gravitational fields with a cosmological constant and the search for a correspondence between the space-time and minisuperspace phenomena, and their quantization. Here we consider the class of configurations with diagonal space-time metrics. We are based on the observation that the considered configurations that are stationary from the point of view of the external observer, there are certain regions of the space-time with dynamic behavior. This means that in these regions there is an evolution of the space-time geometry in time, which is responsible for the quantum mechanical properties of the considered black hole model (Nakamura, 1993; Gladush, 2016).

2. Classic description of CBH with Λ

The action for the gravitational and electromagnetic fields with cosmological constant in space-time $V^{(4)}$ has

the form

$$S_{tot} = -\frac{1}{16\pi} \int_{V^{(4)}} \left(\frac{c^3}{\kappa} (R^{(4)} + 2\Lambda) + \frac{1}{c} F_{\mu\nu} F^{\mu\nu} \right) \sqrt{-g^{(4)}} d^4x. \quad (1)$$

For a spherically symmetric configuration, the electromagnetic field tensor and the interval have the forms

$$F_{\mu\nu} = A_{\nu,\mu} - A_{\mu,\nu} \rightarrow F_{ab} = A_{b,a} - A_{a,b}, \quad (2)$$

$$ds^2 = h(x^0, r) (dx^0)^2 - g(x^0, r) dr^2 - R^2(x^0, r) d\sigma^2, \quad (3)$$

where $d\sigma^2 = d\theta^2 + \sin\theta d\alpha^2$ is the angular part of the metric; a, b = 0, 1. After integrating over the angles and discarding the surface term, the action (1) can be reduced to the form

$$S = \int_{V^2} \left(\frac{c^3}{2\kappa} \sqrt{gh} \left[1 + \frac{RR_{,1}}{g} (\ln Rh)_{,1} - \Lambda R^2 - \frac{RR_{,0}}{h} (\ln(gR))_{,0} \right] + \frac{1}{2c} \frac{(A_{1,0} - A_{0,1})^2 R^2}{\sqrt{gh}} \right) dx^2. \quad (4)$$

Here $X_{,0} \equiv \partial X / \partial x^0$, $X_{,1} \equiv \partial X / \partial r$ denote the derivatives with respect to x^0 and x^1 . Information on the structure of space is contained in the quantity $(\nabla R)^2 = g^{ab} R_{,a} R_{,b}$ (see Berezin, 2003). The surface $R(x^0, r) = R_g = const$ for which $(\nabla R)^2 = 0$ divides V^4 into two T- and two R-regions. Moreover, $(\nabla R)^2 > 0$ in the T-region, and $(\nabla R)^2 < 0$ in the R-region. Using the generalized Birkhoff theorem, we can choose a coordinate system in the R-region in which h, g and R depend only on the spacelike coordinate r. Similarly, in the T-region there exists a coordinate system in which h, g and R depend only on the timelike coordinate x^0 . Then the metrics in the R- and T-regions take the form:

$$ds_R^2 = h(r) (dx^0)^2 - g(r) dr^2 - R^2(r) d\sigma^2, \quad (5)$$

$$ds_T^2 = h(x^0) (dx^0)^2 - g(x^0) dr^2 - R^2(x^0) d\sigma^2. \quad (6)$$

In this case, the action (4) is divided in the sum $S = S_R + S_T$, where S_R and S_T are the actions defined in the R and T regions respectively. The Lagrangians corresponding to them have the form

$$L_R = \frac{\chi_T}{2c} \frac{A_{0,1}^2 R^2}{\sqrt{gh}} + \frac{\chi_T c^3}{\kappa} \sqrt{gh} \left[1 - \Lambda R^2 + \frac{RR_{,1}}{g} (\ln Rh)_{,1} \right], \quad (7)$$

$$L_T = \frac{\chi_R}{2c} \frac{A_{1,0}^2 R^2}{\sqrt{gh}} + \frac{\chi_R c^3}{\kappa} \sqrt{gh} \left[1 - \Lambda R^2 - \frac{RR_{,0}}{h} (\ln Rg)_{,0} \right]. \quad (8)$$

Here χ_T and χ_R - constants, obtained by integration of the action over coordinate x^0 in R-region and coordinate r in T-region. Since the Lagrangian is defined up to a constant factor, we further assume that $\chi_R = \chi_T = 1$ (meter).

It is convenient to introduce new variables in the R- and T- regions:

$$\begin{aligned} \phi_R &= -A_0, & \xi_R &= -Rh, & N_R &= \sqrt{gh}, \\ \phi_T &= A_1, & \xi_T &= Rg, & N_T &= \sqrt{gh}. \end{aligned} \quad (9)$$

In these variables, the Lagrangians (7) and (8) take a uniform form:

$$L = \frac{F_{,\alpha}^2 R^2}{2cN} + sN \left(1 - \Lambda R^2 + \frac{R_{,\alpha} U_\alpha}{N^2} \right). \quad (10)$$

where $s = c^3/\kappa$, α - is the evolutionary parameter, which in each of the regions takes the form $\alpha = x^0 = ct$ or $\alpha = r$ respectively. From the Lagrange-Euler equation for variable N in (10) it follows that $\partial L/\partial N = 0$. It means that N is Lagrange multiplier and there is the constraint applied to system:

$$-\frac{\phi_{,\alpha}^2 R^2}{2cN^2} + \frac{s}{2} \left(1 - \Lambda R^2 + \frac{\xi_{,\alpha} R_{,\alpha}}{N^2} \right) = 0. \quad (11)$$

Expressing N from (11) and substituting it in (10), we obtain new Lagrangian and action of the system:

$$L = s \sqrt{(1 - \Lambda R^2) \left(-R_{,\alpha} \xi_{,\alpha} + \frac{R^2}{sc} \phi_{,\alpha}^2 \right)}, \quad (12)$$

$$S = s \int \sqrt{(1 - \Lambda R^2) \left(-dRd\xi + \frac{R^2}{sc} d\phi^2 \right)}. \quad (13)$$

Thus, the action (13) for the system is an action for geodesic in a minisuperspace with a metric

$$d\Omega^2 = (1 - \Lambda R^2) \left(-dRd\xi + \frac{R^2}{sc} d\phi^2 \right). \quad (14)$$

It appears that minisuperspace is conformally flat, which leads to the fact, that the scalar curvature, the square of the Ricci tensor, the Kretschmann invariant, are vanish, while the components of the Ricci tensor and the curvature tensor diverge on the minisuperspace analogue of the cosmological horizon ($c\tau + x = 1/\sqrt{\Lambda}$). This can be seen by following transition to new variables:

$$\begin{aligned} \xi &= \frac{1}{sc} \left(c\tau - x - \frac{y^2}{c\tau+x} \right), \\ R &= c\tau + x, & \phi &= \frac{y}{c\tau+x}. \end{aligned} \quad (15)$$

In these variables metric (14) takes form:

$$d\Omega^2 = (1 - \Lambda(c\tau + x)) \left(-c^2 d\tau^2 - dx^2 - dy^2 \right). \quad (16)$$

Introducing generalized momenta as $P_i = \frac{\partial L}{\partial Q_{i,\alpha}^i}$ where L is lagrangian (10), we define Hamiltonian of the system:

$$\begin{aligned} H &= P_i Q_{i,\alpha}^i - L = \\ &= \frac{N}{2s} \left(-4P_R P_\xi + \frac{sc}{R^2} P_\phi - s^2(1 - \Lambda R^2) \right) = -N \frac{\partial L}{\partial N}. \end{aligned} \quad (17)$$

Thus, we obtain Hamilton constraint: $H = 0$. Therefore, for further consideration, it's expediently to introduce additional physical quantities - the mass and charge of the system. In the classical case, the charge is determined by the charge function as follows (Gladush, 2017):

$$Q = \frac{R^2}{\sqrt{gh}} (A_{0,1} - A_{1,0}). \quad (18)$$

The total mass of the configuration has the form (Gladush, 2012):

$$M = \frac{s}{c} R \left(1 - \frac{\Lambda}{3} R^2 + \frac{R_{,0}^2}{h} - \frac{R_{,1}^2}{g} \right) + \frac{Q^2}{2c^2 R}. \quad (19)$$

In new variables these functions have following form:

$$Q = cP_\phi, \quad M = \frac{s}{2c} \left(R - \frac{\Lambda}{3} R^3 + \frac{4\xi P_\xi^2}{s^2} \right) + \frac{P_\phi^2}{2R}. \quad (20)$$

In order to obtain classical solution, we substitute following relations in Hamilton constraint (17) and mass and charge functions:

$$P_\xi = \frac{\partial S}{\partial \xi}, \quad P_R = \frac{\partial S}{\partial R}, \quad P_\phi = \frac{\partial S}{\partial \phi}, \quad (21)$$

This leads to the Einstein-Hamilton-Jacobi equation and equations for total mass and charge of the system:

$$-4 \frac{\partial S}{\partial \xi} \frac{\partial S}{\partial R} + \frac{sc}{R^2} \left(\frac{\partial S}{\partial \phi} \right)^2 + s^2(1 - \Lambda R^2) = 0, \quad (22)$$

$$c \frac{\partial S}{\partial \phi} = q, \quad \frac{s}{2c} \left(R - \frac{\Lambda}{3} R^3 + \frac{4\xi}{s^2} \left(\frac{\partial S}{\partial \xi} \right)^2 \right) = m. \quad (23)$$

This equations have following solution:

$$S = \frac{q}{c} \phi + p_\xi \xi - \frac{s^2}{4p_\xi} \left(R - \frac{\Lambda}{3} R^3 + \frac{q^2}{2cR} \right). \quad (24)$$

Here it is taken into account that from the canonical equations for momenta P_ξ and P_ϕ it follows, that they are integrals of motion. In particular, $cP_\phi = q$ - charge of the system. Calculating derivatives $\partial S/\partial q$ and $\partial S/\partial p_\xi$ and equating them to constant, we find trajectories:

$$\xi = \xi_0 - \frac{s^2}{4p_\xi^2} \left(R - \frac{\Lambda}{3} R^3 + \frac{q^2}{2cR} \right), \quad \phi = \frac{sq}{2cp_\xi R}. \quad (25)$$

From mass function we find out that $p_\xi = \sqrt{\frac{msc}{2\xi_0}}$. Finally, we get:

$$\xi = \xi_0 \left(1 - \frac{s}{2mc} \left(R - \frac{\Lambda}{3} R^3 + \frac{q^2}{scR} \right) \right), \quad \phi = \sqrt{\frac{s\xi_0}{2mc^3}} \frac{q}{R}. \quad (26)$$

Performing reverse transformation to (9), we obtain following metric coefficients:

$$\begin{aligned} h_R &= \frac{2mc\xi_0}{s} \left(1 - \frac{2mc}{sR} + \frac{q^2}{scR^2} - \frac{\Lambda}{3}R^3 \right), \\ g_R &= \frac{N_R^2}{h_R}, \quad h_T = \frac{N_T^2}{g_T}, \\ g_T &= -\frac{2mc\xi_0}{s} \left(1 - \frac{2mc}{sR} + \frac{q^2}{scR^2} - \frac{\Lambda}{3}R^3 \right). \end{aligned} \quad (27)$$

Assuming $N_R = N_T = 1$, $\xi_0 = s/2mc$, we obtain classical result for Reissner-Nordström-de Sitter metrics. Solution (26) can be written in terms of minisuperspace variables $(c\tau, x, y)$ in parametric form:

$$\begin{aligned} c\tau &= \frac{1}{2} \left(\left(1 - \frac{a}{R_g} \right) R + a + \frac{a}{R_g} \frac{\Lambda}{3} R^3 \right), \\ x &= \frac{1}{2} \left(\left(1 + \frac{a}{R_g} \right) R - a - \frac{a}{R_g} \frac{\Lambda}{3} R^3 \right), \\ y &= \sqrt{\frac{\xi_0}{R_g}} q. \end{aligned} \quad (28)$$

Here $a = sc\xi_0$, $R_g = 2mc/s$. The curves that are described by (28) are third-order curves. Their intersection with the light cone in the minisuperspace correspond to the event horizons in space-time, while the interior of the cone corresponds to the T-regions. Further, after second intersection with a conus, they move outside the light cone of the minisuperspace, which corresponds to the spatial evolution of fields in the outer R-region. Then they are returning again to the T-region. For extremal and superextremal charged black holes, the corresponding curves are tangent to or pass by the cone, respectively. All this points us to the connection between the geometry of the minisuperspace and the geometry of spherically-symmetric space-time configurations.

3. Quantum description of CBH with Λ

In order to build quantum description of the system, we proceed from functions of physical quantities to their operators. Defining coordinates and momenta operators as

$$\hat{q}^i = q^i, \quad \hat{p}_i = -i\hbar \frac{\partial}{\partial q^i}, \quad (29)$$

we obtain following Hamilton, mass and charge operators:

$$\begin{aligned} \hat{H} &= -\frac{N}{2s} \left(4\hbar^2 \frac{\partial^2}{\partial \xi \partial R} + \hbar^2 \frac{sc}{R^2} \frac{\partial^2}{\partial \phi^2} + s^2(1 - \Lambda R^2) \right), \\ \hat{M} &= \frac{s}{c} \left(R - \frac{\Lambda}{3} R^3 - 4 \frac{\hbar^2}{s^2} \frac{\partial}{\partial \xi} \xi \frac{\partial}{\partial \xi} \right) - \frac{\hbar^2}{2R} \frac{\partial^2}{\partial \phi^2}, \\ \hat{Q} &= -i\hbar c \frac{\partial}{\partial \phi}. \end{aligned} \quad (30)$$

In order for the total mass operator to be Hermitian, we use the following ordering of the operators: $p_\xi \xi p_\xi$. Obtained operators have following commutators:

$$[\hat{M}, \hat{Q}] = 0, \quad [\hat{H}, \hat{Q}] = 0, \quad [\hat{H}, \hat{M}] = \frac{\hbar^2}{sc} \frac{\partial}{\partial \xi} \hat{H} \sim 0. \quad (31)$$

By (31) we can require that the wave function of the system satisfy following system of equations:

$$\begin{cases} \hat{H}\Psi = 0, \\ \hat{M}\Psi = m\Psi, \\ \hat{Q}\Psi = q\Psi. \end{cases} \quad (32)$$

Jointly solving (32), we obtain wave function of the system, which is regular on horizons:

$$\Psi(\xi, R, \phi) = C J_0 \left(\sqrt{\xi R \left[-1 + \frac{2mc}{sR} - \frac{q^2}{scR^2} + \frac{\Lambda}{3} R^3 \right]} \right). \quad (33)$$

Since system (32) has a solution for any values of m and q , the mass and the charge spectra of black hole are continuous.

4. Conclusion

Obtained result is consistent with the previous result of one of the authors (Gladush, 2016; Gladush, 2017) and turns into it at $\Lambda = 0$. Considered approach leads to continuous spectra of mass and charge, what is coincides with results of other authors (Kuchař, 1994; Louko, 1996; Nakamura, 1993). Also quantization was carried out in uniform way, for R- and T-regions simultaneously. Since quantization has physical sense only in T-regions, the results obtained for the R-regions can be considered an analytical continuation of the T-regions solutions. Without the imposition of additional differential-geometric and group structures on the space-time, configuration or phase spaces, it is impossible to obtain a discrete spectrum. The reason for this is that the above differential equations determine only the local structure of the space, whereas the global structure needs to be defined. Thus, the question of the mass and charge spectra is not solved by a local approach, since the properties of the spectra depend on the global properties of the space-time and minisuperspace geometry, and the structure of the phase space of the considered system.

References

- Dirac P.: 1979, *Lectures on quantum mechanics*, in Principles of quantum mechanics, (Nauka, Moscow).
- Gitman D., Tyutin I.: 1986, *Canonical quantization of fields with constraints*, (Nauka, Moscow), 216.
- Schulz B.: 2014, arXiv:1409.7977, 100.
- Berezin B.A.: 2003, *Fizika Elementarnykh Chastits i Atomnogo Yadra* **34**, 49.
- Nakamura K., Konno S., Oshiro Y., Tomimatsu A.: 1993, *Prog. Theor. Phys.* **90**, 861.
- Gladush V.: 2016, *Visn. Dnipr. univ.*, **24**, 31.
- Kuchař K.: 1994, *Phys. Rev.*, **D50**, 3961.
- Louko J., Winters-Hilt S.: 1996, *Phys. Rev.*, **D54**, 2647.
- Gladush V.D.: 2012, *STFI*, **1**, 48.
- Gladush V.D.: 2017, *Odessa Astr. Publ.*, **30**, 19.

DOI: <http://dx.doi.org/10.18524/1810-4215.2018.31.144558>

FIXED POINTS OF MAPPING OF N-POINT GRAVITATIONAL LENSES

A.T. Kotvytskiy¹, V.Yu. Shablenko², E.S. Bronza³

¹ Department of Theoretical Physics, V.N. Karazin Kharkiv National University, Kharkiv, Ukraine, kotvytskiy@gmail.com

² Department of Theoretical Physics, V.N. Karazin Kharkiv National University, Kharkiv, Ukraine, shablenkov@gmail.com

³ Faculty of Computer Science, Kharkiv National University of Radio Electronics, Kharkiv, Ukraine, eugene.bronza@gmail.com

ABSTRACT. In this paper, we study fixed points of N -point gravitational lenses. We use complex form of lens mapping to study fixed points. Complex form has an advantage over coordinate one because we can describe N -point gravitational lens by system of two equations in coordinate form and we can describe it by one equation in complex form. We can easily transform the equation, which describe N -point gravitational lens, into polynomial equation that is convenient to use for our research. In our work, we present lens mapping as a linear combination of two mappings: complex analytical and identity mapping. Analytical mapping is specified by analytical function (deflection function). We studied necessary and sufficient conditions for the existence of deflection function and proved some theorems. Deflection function is analytical, rational, its zeroes are fixed points of lens mapping and their number is from 1 to $N-1$, poles of deflection function are coordinates of point masses, all poles are simple, the residues at the poles are equal to the value of point masses.

We used Gauss-Lucas theorem and proved that all fixed points of lens mapping are in the convex polygon. Vertices of the polygon consist of point masses. We proved theorem that can be used to find all fixed point of lens mapping. On the basis of the above, we conclude that one-point gravitational lens has no fixed points, 2-point lens has only 1 fixed point, 3-point lens has 1 or 2 fixed points. Also we present expressions to calculate fixed points in 2-point and 3-point gravitational lenses. We present some examples of parametrization of point masses and distribution of fixed points for this parametrization.

Keywords: gravitational lensing; lens mapping, fixed points, deflection function; complex analysis.

АННОТАЦІЯ. В роботі досліджуються нерухомі точки в N -точкових гравітаційних лінзах. Для їх дослідження була використана комплексна форма

лінзового відображення. Комплексна форма має перевагу над координатною: в координатному вигляді N -точкова гравітаційна лінза описується системою з двох рівнянь, а в комплексному вигляді досить одного рівняння. Це рівняння легко перетвориться в поліноміальне, яке зручне для дослідження. В роботі лінзове відображення представлено у вигляді лінійної комбінації двох відображень: комплексно-аналітичного і тотожного. Аналітичне відображення задає функція відхилення. Ми вивчили необхідні і достатні умови існування функції відхилення і довели деякі теореми. Функція відхилення: аналітична, раціональна, її нулі є нерухомими точками лінзового відображення, їх число лежить в проміжку від 1 до $N-1$, її полюса є координатами точкових мас, всі полюса прості, лишки в полюсах рівні величинам безрозмірних мас в них.

Ми застосували теорему Гаусса-Люка і довели, що всі нерухомі точки лінзового відображення належать мінімальному випуклому багатокутнику. Вершинами мінімального випуклого багатокутника є точки, в яких знаходяться безрозмірні точкові маси. Довели теорему, за допомогою якої можна знайти всі нерухомі точки лінзового відображення. На підставі вище отриманих результатів, ми зробили висновок, що в одноточковій лінзі нерухомих точок немає, в двухточковій лінзі є тільки одна нерухома точка, в трьохточковій лінзі може бути одна або дві нерухомі точки. Також в роботі приведені вираження для обчислення нерухомих точок в одноточковій і двухточковій гравітаційних лінзах. Наведені деякі приклади параметричного завдання точкових мас і розподілу нерухомих точок.

Ключові слова: гравітаційне лінзування; лінзове відображення, нерухомі точки, функція відхилення; комплексний аналіз.

1. Introduction

Gravitational lensing is a phenomenon of deflection of light ray in a gravity field (Bliokh&Minakov,1989; Zakharov,1997;Schneider,1999). With gravitational lensing, star systems and planets in star systems can be found. Recently, astronomers have observed a large number of gravitational lenses. In addition to one-point lenses, lenses with more than two components were also detected. In this paper, we show that such objects can have fixed points. In physical terms, fixed point of gravitational lens is a point in a picture plane that has such property: if we place source in fixed point, one of images is in this point.

2. General information and formulation of the problem

An N-point gravitational lens can be described by means of the following equation (Zakharov,1997; Schneider,1999):

$$\vec{y} = \vec{x} - \sum_n m_n \frac{\vec{x} - \vec{l}_n}{|\vec{x} - \vec{l}_n|^2}, \tag{1}$$

where m_n are dimensionless masses whose position in the plane of the lens is determined by the normalized radius-vectors \vec{l}_n . It is plain, that $\sum_n m_n = 1$.

We denote the set of radius-vectors \vec{l}_n as $\Lambda = \{l_i | i = 1, 2, \dots, N\}$. Vector equation (1) specifies single-valued mapping

$$L : (R_X^2 \setminus \Lambda) \rightarrow R_Y^2, \tag{2}$$

from vector space R_X^2 to vector space R_Y^2 .

We introduce Cartesian coordinates, that transforms R_X^2 and R_Y^2 spaces into coordinate planes. Coordinate planes R_Y^2 and R_X^2 are source plane and image plane respectively. Source plane R_Y^2 and image plane R_X^2 are often united and called picture plane in astrophysical literature.

Mapping (2) can be described by system of equations:

$$\begin{cases} y_1 = (x_1 - \sum_{n=1}^N m_i \frac{x_1 - a_n}{(x_1 - a_n)^2 + (x_2 - b_n)^2}) \\ y_2 = (x_2 - \sum_{n=1}^N m_i \frac{x_2 - b_n}{(x_1 - a_n)^2 + (x_2 - b_n)^2}) \end{cases}, \tag{3}$$

where (a_n, b_n) are coordinates of point C_n of radius-vector \vec{l}_n in plane R_X^2 .

Analytical research of (3) was in (Kotvytskiy&Bronza&Vovk, 2016; Bronza&Kotvytskiy, 2017; Kotvytskiy&Bronza&Shablenko, 2017), and quasianalytical method of image construction was offered in (Kotvytskiy&Bronza, 2016).

A point of single-valued mapping L is fixed, if each of point coordinates is invariant of L .

We need to substitute $y_1 = x_1$ and $y_2 = x_2$ and into system of equations (3) and solve it to find fixed points.

$$\begin{cases} \sum_{n=1}^N m_i \frac{x_1 - a_n}{(x_1 - a_n)^2 + (x_2 - b_n)^2} = 0 \\ \sum_{n=1}^N m_i \frac{x_2 - b_n}{(x_1 - a_n)^2 + (x_2 - b_n)^2} = 0 \end{cases} \tag{4}$$

Mapping L is surjective. Inverse mapping

$$L^{-1} : R_Y^2 \rightarrow (R_X^2 \setminus \Lambda), \tag{5}$$

is multivalued. If A_0 - is a fixed point of single-valued mapping L , then image of its image, when the mapping is reversed, is not coincide with it, but includes it.

$$A_0 \in L^{-1}(L(A_0)). \tag{6}$$

In this paper we study the set Ξ of fixed points of mapping L .

We set the mapping L in complex form for effective application of mathematical tool.

3. Complexification of lens mapping L

Let define mapping (3) in complex form. We introduce complex structure for R_X^2 and R_Y^2 , that transforms them into complex planes \mathbb{C}_z and \mathbb{C}_ζ respectively.

We introduce new complex variables z and ζ . Let

$$\text{Re } z = x_1, \text{Im } z = x_2, \text{Re } \zeta = y_1, \text{Im } \zeta = y_2. \tag{7}$$

New variables related to old ones as

$$\begin{cases} x_1 = \frac{z + \bar{z}}{2} \\ x_2 = \frac{z - \bar{z}}{2} \end{cases} \text{ and } \begin{cases} y_1 = \frac{\zeta + \bar{\zeta}}{2} \\ y_2 = \frac{\zeta - \bar{\zeta}}{2} \end{cases}, \tag{8}$$

Now system (3) can be written as

$$\zeta = z - \sum_{n=1}^N m_n \frac{1}{\bar{z} - A_n}, \tag{9}$$

where $\sum_{n=1}^N m_n = 1$ and $A_n = a_n + ib_n; n = 1, 2, \dots, N$.

We introduce function $\omega = \sum_{n=1}^N m_n \frac{1}{\bar{z} - A_n}$ and call it deflection function. Function is complex conjugated to ω and defined:

$$w = \sum_{n=1}^N m_n \frac{1}{z - A_n} \tag{10}$$

Functions ω and w contain all the information about N-point gravitational lens. Except that it is convenient to use function w , rather than ω , for application of methods of geometric function theory.

We have:

$$\zeta = z - \bar{w}(\bar{z}) = z - \overline{w(z)}. \quad (11)$$

Or:

$$\bar{\zeta} = \bar{z} - w(z). \quad (12)$$

Thus, N-point lens can be described not only by the system of equation (3) but also by the single equation (9). Mapping (2) can be written as

$$L : (\mathbb{C}_X \setminus \Lambda) \rightarrow \mathbb{C}_Y, \quad (13)$$

mapping of complex plane \mathbb{C}_X into complex plane \mathbb{C}_Y .

We can obtain equation (12) in another way. We can use equation (1) (Witt, 1990).

4. Some properties of $\zeta = \zeta(z)$ and $w = w(z)$.

Statement 4.1. Function $\zeta = \zeta(z)$ is not an analytic function.

Proof. Derivative of $\zeta = \zeta(z)$

$$\frac{\partial \zeta}{\partial \bar{z}} = \frac{\partial}{\partial \bar{z}} (z - \bar{w}(\bar{z})) = 1 - \frac{\partial \bar{w}}{\partial \bar{z}} \neq 0$$

is not identity equal zero, therefore ζ is not analytic function.

Statement 4.2. Deflection function $w = w(z)$ is an analytic function.

Proof. Derivative of $w = w(z)$

$$\frac{\partial w}{\partial \bar{z}} = \frac{\partial}{\partial \bar{z}} \left(\sum_{n=1}^N m_n \frac{1}{z - A_n} \right) = \sum_{n=1}^N m_n \frac{\partial}{\partial \bar{z}} \frac{1}{z - A_n} \equiv 0$$

is identity equal zero, therefore w in an analytic function.

Statement 4.3. Deflection function $w = w(z)$ is:

- rational function, i.e. $w = \frac{A(z)}{B(z)}$, where $A(z)$ and $B(z)$ are polynomials;
- the denominator is a degree $\deg B(z) = N$, the numerator is a degree $\deg A(z) = N - 1$;
- leading coefficients of $A(z)$ and $B(z)$ are equal 1.

Proof. We reduce the sum to common denominator

$$w = \sum_{n=1}^N m_n \frac{1}{z - A_n}. \quad (14)$$

Denominator of deflection function $B(z) = \prod_{n=1}^N (z - A_n)$ is a degree $\deg B(z) = N$ leading coefficient equals 1. Numerator $A(z) = \sum_{n=1}^N m_n z^{N-1} + \dots$ is a degree $\deg A(z) = N - 1$, leading coefficient of $A(z)$ equals $\sum_{n=1}^N m_n = 1$.

Theorem 4.4. Deflection function w can be written in form:

$$a) w = \frac{Q'(z)}{Q(z)}, \quad (15)$$

where $Q(z) = \prod_{n=1}^N (z - A_n)^{m_n}$;

$$b) w = \frac{1}{\deg P(z)} \frac{P'(z)}{P(z)}, \quad (16)$$

where $P(z)$ is polynomial;

Proof. a) $w = \sum_{n=1}^N m_n \frac{1}{z - A_n} = \sum_{n=1}^N (m_n \frac{d}{dz} (\ln(z - A_n))) = \sum_{n=1}^N \frac{d}{dz} (\ln(z - A_n)^{m_n}) = \frac{d}{dz} \left(\ln \left(\prod_{n=1}^N (z - A_n)^{m_n} \right) \right) = \frac{d}{dz} (\ln Q(z)) = \frac{Q'(z)}{Q(z)}$.

We note, that function $Q(z)$ is not a polynomial.

Proof. b) $w = \frac{Q'(z)}{Q(z)} = \frac{d}{dz} (\ln Q(z)) = \frac{d}{dz} \left(\ln \left(\prod_{n=1}^N (z - A_n)^{m_n} \right) \right)$.

Assume without loss of generality, that numbers m_n are rational.

Let $m_n = \frac{p_n}{q_n}$, where p_n and q_n are natural numbers and coprime integers.

We substitute that into equation and transform it. Whence, we have:

$$w = \frac{d}{dz} \left(\frac{1}{h} \ln \left(\prod_{n=1}^N (z - A_n)^{\frac{p_n h}{q_n}} \right) \right), \quad (17)$$

where $h = \prod_{n=1}^N q_n$. Let $s_n = \frac{p_n h}{q_n}$. Numbers s_n are natural numbers.

After transformation (17) we have:

$$w = \frac{d}{dz} \left(\frac{1}{h} \ln P(z) \right) = \frac{d}{dz} \left(\frac{1}{h} P(z) \right) = \frac{1}{h} \frac{P'}{P}, \quad (18)$$

where $P(z) = \prod_{n=1}^N (z - A_n)^{s_n}$ is polynomial. But then

$$w = \frac{1}{h} \frac{1}{h} \frac{P'(z)}{P(z)}. \quad (19)$$

As well, leading coefficients of $A(z)$ and $B(z)$ are equal 1 and leading coefficient of $P'(z)$ equal $\deg P(z)$. We have: $h = \deg P(z)$, i.e. we have (16). QED.

Remark 1 (to theorem 4.4). Polynomials $P(z)$ and $P'(z)$ have the same roots as $B(z) = \prod_{n=1}^N (z - A_n)$, but with different multiplicity.

Remark 2 (to theorem 4.4). Then since function ω is complex conjugate to w , we obviously have:

$$\begin{aligned} \omega = \bar{w} &= \overline{\left(\frac{1}{h} \frac{P'(z)}{P(z)} \right)} = \frac{1}{h} \frac{\overline{P'(z)}}{\overline{P(z)}} = \\ &= \frac{1}{h} \frac{\left(\overline{P(z)} \right)'}{h \overline{P(z)}} = \frac{1}{h} \frac{\overline{P'(z)}}{\overline{P(z)}}. \end{aligned} \quad (20)$$

Function ω , exactly as w , can be expressed in form of ratio of two polynomials. Numerator of the ratio is a derivative of denominator up to an unessential constant multiplier.

Remark 3 (to theorem 4.4). Polynomials $P(z)$ and $P'(z)$ are not coprime. Fraction $\frac{P'(z)}{P(z)}$ can be reduced. Polynomials $P(z)$ and $P'(z)$ are coprime, if and only if $m_n = \frac{1}{N}, n = 1, 2, \dots, N$.

Theorem 4.6. Poles of function w are A_n points, which are coordinates of masses. All poles are simple. For any poles are always true: pole residue equal normalized mass at that point. The sum of residues at finite points into complex plane equal one. At infinity equal minus one.

Proof. Obviously.

5. Fixed points of a lens mapping

Theorem 5.1. (About quantity) By n_0 denote a quantity of a fixed points of mapping $L : (\mathbb{C}_X \setminus \Lambda) \rightarrow \mathbb{C}_Y$, then $n_0 : 1 \leq n_0 \leq N - 1$.

Proof. Fixed points of function $\zeta = z - \bar{w}(\bar{z})$ are roots of equation $z = z - \bar{w}(\bar{z})$, i.e. $\bar{w}(\bar{z}) = 0$. We have $w(z) = 0$, if we complex conjugate it.

Therefore, we have $\deg P'(z) = N - 1$ from the representation (16). Hence, the number of zeroes of function w with regard to multiplicity is $N - 1$. Polynomial $P'(z)$ can have multiple zeroes. The number of different zeroes of polynomial $P'(z)$ is from 1 to $N - 1$.

We have the theorem about distribution of a fixed points of mapping L .

Theorem (main) 5.2. (About distribution) Fixed points of mapping L are in the convex polygon that consists of point masses.

Proof. We use Gauss-Lucas theorem: if P is a polynomial with complex coefficients, all zeros of P' belong to the convex hull of the set of zeros of P .

By theorem 5.1, fixed points of mapping L are zeroes of the function w . By theorem 4.5 we have representation (16).

Since $P(z) = \prod_{n=1}^N (z - A_n)^{s_n}$, roots of $P'(z)$, are in the convex polygon that consists of set $\{A_n\}$, because of Gauss-Lucas theorem (Prasolov, 2014; Davydov, 1964).

Theorem 5.3. (of finding fixed points and its number) Fixed points of mapping L for $N \geq 2$ are roots of:

$$H(z) = \frac{P(z)}{\gcd(P(z), P'(z))}, \quad (21)$$

their number $n_0 = \deg H(z)$, and estimation $n_0 : 1 \leq n_0 \leq N - 1$ is achieved.

Proof. The polynomial $P(z)$ is divided by the polynomial $\gcd(P(z), P'(z))$. Therefore $B(z)$ is a polynomial. Polynomial $\gcd(P(z), P'(z))$ has only multiple

roots. Multiplicity of roots of $\gcd(P(z), P'(z))$ is one less than multiplicity of $P(z)$. Hence all roots of polynomial $H(z)$ are different and $n_0 = \deg H(z)$.

2-point gravitational lens has one fixed point.

In general situation the number of fixed points is $n_0 = N - 1$.

For $N > 2$, we have only one fixed point, if and only if all point masses are equal and located at the vertexes of regular polygon.

Remark 4 (to theorem 5.3). Fixed points are missing from point gravitational lens.

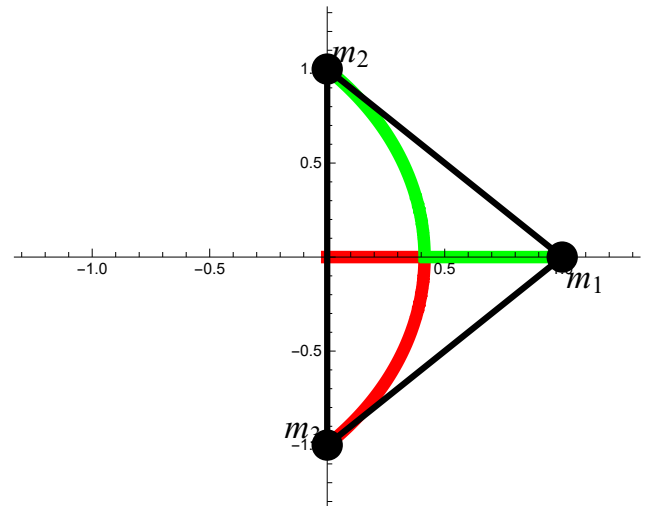


Figure 1: 3-point lens with $m_1 = 1 - s, m_2 = \frac{s}{2}, m_3 = \frac{s}{2}, A_1 = 1, A_2 = i, A_3 = -i$

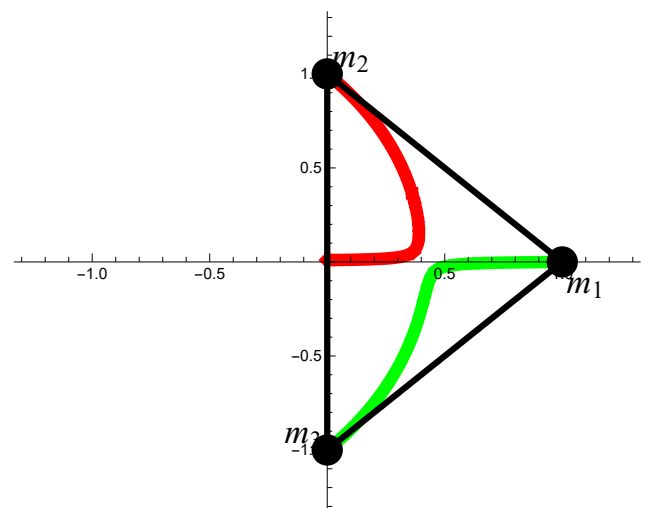


Figure 2: 3-point lens with $m_1 = 1 - s, m_2 = 0.495s, m_3 = 0.505s, A_1 = 1, A_2 = i, A_3 = -i$

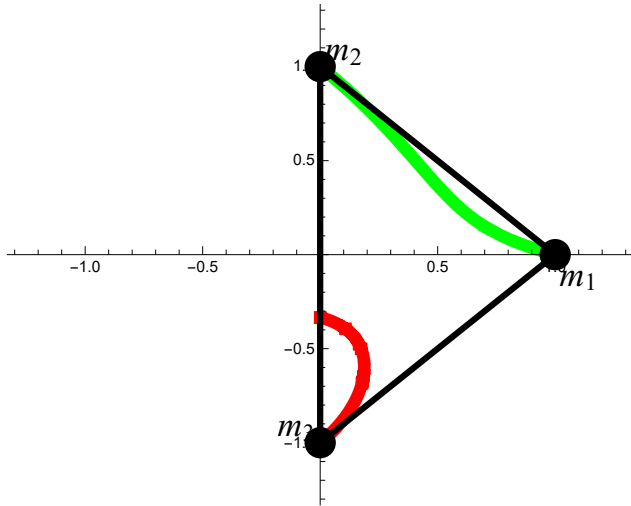


Figure 3: 3-point lens with $m_1 = 1 - s, m_2 = \frac{2s}{3}, m_3 = \frac{s}{3}, A_1 = 1, A_2 = i, A_3 = -i$

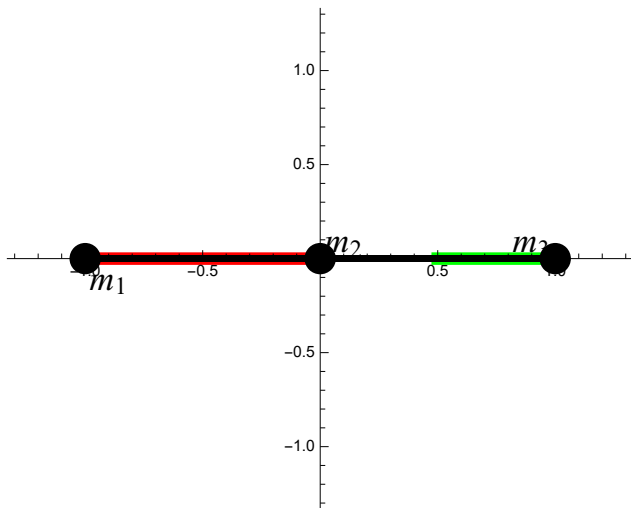


Figure 4: 3-point lens with $m_1 = 1 - s, m_2 = \frac{s}{2}, m_3 = \frac{s}{2}, A_1 = -1, A_2 = 0, A_3 = 1$

6. Examples

For 1-point lens we have deflection function

$$w = \sum_{n=1}^N \frac{m_n}{z - A_n} = \frac{m_1}{z - A_1},$$

where $m_1 = 1$ and $A_1 = 0$.

For 2-point lens we have deflection function

$$w = \frac{m_1}{z - A_1} + \frac{m_2}{z - A_2}$$

where A_1 and A_2 are coordinates of point masses and $m_1 + m_2 = 1$.

With $m_1 = s, m_2 = 1 - s$ and $s \in [0, 1]$ we have

$$z_{st} = A_1 + (A_2 - A_1) s$$

For 3-point lens we have deflection function

$$w = \frac{m_1}{z - A_1} + \frac{m_2}{z - A_2} + \frac{m_3}{z - A_3}$$

where A_1, A_2, A_3 are coordinates of point masses and $m_1 + m_2 + m_3 = 1$.

We have an equation for fixed points

$$z^2 + A_2 A_3 m_1 + A_1 A_3 m_2 + A_1 A_2 m_3 - (A_2 m_1 + A_3 m_1 + A_1 m_2 + A_3 m_2 + A_1 m_3 + A_2 m_3) z = 0$$

Acknowledgements. Albert Kotvytskiy and Volodymyr Shablenko thank for support SFFR, Ukraine, Project No. 32367.

References

Bliokh P.V., Minakov A.A.: 1989, Gravitational Lenses [in Russian]. (Naukova Dumka, Kiev), 240.
 Zakharov A.F.: 1997, Gravitacionnye linzy i mikrolinzy [in Russian]. (Janus-K, Moscow), 328.
 Schneider P., Ehlers J., Falco E.E.: 1999, Gravitational Lenses. (Springer-Verlag Berlin Heidelberg), 560.
 Kotvytskiy A.T., Bronza S.D., Vovk S.R.: 2016, Bulletin of Kharkiv Karazin National University "Physics", **24**, 55 (arXiv:1809.05392).
 Bronza S.D., Kotvytskiy A.T.: 2017, Bulletin of Kharkiv Karazin National University "Physics", **26**, 6.
 Kotvytskiy A.T., Bronza S.D., Shablenko V.Yu.: 2017, Odessa Astron. Publ., **30**, 35.
 Kotvytskiy A.T., Bronza S.D.: 2016, Odessa Astron. Publ., **29**, 31.
 Witt H.J.: 1990, A&A, **236**, 311.
 Praslov V.V.: 2014, Polynomials[in Russian]. MCCME, 336.
 Davydov N.A.: 1964, USSR Computational Mathematics and Mathematical Physics, **4**, No.2, 257.

DOI: <http://dx.doi.org/10.18524/1810-4215.2018.31.145315>

DETAILED MORPHOLOGY OF THE RICH CONCENTRATED GALAXY CLUSTERS

E. Panko¹, A. Sirginava¹, & A. Stepaniuk²

¹ Department of Theoretical Physics and Astronomy,
I. I. Mechnikov Odessa National University Odessa, Ukraine
panko.elena@gmail.com

² Lohika Company, Odessa, Ukraine

ABSTRACT. The results of the detailed analysis of the 2D distribution of galaxies in 28 rich galaxy clusters with significant concentration to the cluster center are present. The analysis was executed in these directions: the detection of regular substructures and peculiarities in the galaxy distribution. The role of brightest cluster members was taken into account too. The input data were selected from “The Catalogue of Galaxy Clusters and Groups” and list of galaxies of Muenster Red Sky Survey. Concentrated galaxy clusters are evolved, virialized structures. Substructures in this type of clusters must be feeble marked. Nevertheless we detected significant part of concentrated galaxy clusters having different kinds of peculiarities, namely crossing and divaricating filaments or X and Y-type peculiarities, as well as curved strips and short dense chains. 2 clusters having extremely density of galaxies were attributed as superconcentrated/compact type.

Key words: Galaxies: clusters: morphology, peculiarities

АБСТРАКТ. Ми представляємо результати детального аналізу 2D розподілу галактик у 28 багатих скупченнях галактик зі значущою концентрацією до центру (С-тип). Спостережною основою для дослідження був "Каталог скупчень та груп галактик", створений на базі Списку галактик Мюнстерського Червоного Огляду Неба. У "Каталозі скупчень та груп галактик" є 460 скупчень, у полі яких знаходиться 100 та більше галактик. Вдосконалена схема морфологічної класифікації скупчень галактик, враховує концентрацію до центру скупчення, наявність у скупченні виділеної смуги – широкої (F-тип) або вузької (L-тип). Роль найяскравіших галактик також приймається до уваги. Відповідно до попереднього розподілу на концентровані С, проміжні І та розсіяні О скупчення, набір

концентрованих скупчень є найменшим.

Під час дослідження для кожного скупчення біло побудовано його мапу у проєкції на картину площину у ідеальних координатах та проаналізовано варіації поверхневої густини галактик. Крім наявності статистично значущих стандартних особливостей, які у морфологічній схемі відповідають типам з виділеною смугою, було знайдено також інші значущі пекулярності. Скупчення галактик з великою концентрацією до центру, відповідно до сучасних уявлень, повинні бути віріалізованими структурами. Підструктури в цьому типі скупчень, скоріш за все, є слабо вираженими. Проте ми виявили, що серед скупчень, що досліджувалися, понад 40

Ключові слова: Галактики: скупчення: морфологія, пекулярності.

1. Introduction

Distribution of galaxies both in the space and on the celestial sphere reflected the primordial adiabatic fluctuations in beginning moments of Universe, as it shown in big number of works from Silk (1968), Peebles & Yu (1970), Sunyaew & Zeldovich (1970) to well quoted *Millennium Simulation* (Springel et al., 2005), *Illustris Project* (Vogelsberger et al., 2014; Artale et al., 2017). The galaxy clusters are the essential component of large-scale structure of Universe in the chain galaxies \Rightarrow galaxy groups \Rightarrow galaxy clusters \Rightarrow galaxy superclusters. From the other hand, galaxy clusters are the special component of large-scale structure because time of virialization of biggest ones is only one order less than age of Universe. Taking into consideration the results of different numerical simulations (from Springel et al., 2005 to, for example, Cui et al., 2018) described arising the knots, filaments, sheets and voids, the galaxy clusters are evolving and colliding objects. The evidences of collisions of galaxy clusters are

detected and analyzed. The collided and interacted galaxy clusters show different distribution of intercluster galaxies, hot gas and DM (Markevitch et al., 2004, Pearce et al., 2017).

The evolution of non-collided galaxy clusters is determined mainly own gravitation. For this case the signs of cluster evolution can be defined according their morphological type. Evidently, galaxy population is not main component in a clusters, however galaxy fraction is seen in optic, and the presence or absence the peculiarities in distribution of galaxies inside the cluster can be easily detected.

Proposed by Panko (2013) classical schemes summarizes the classical approach (Abell, 1958; Zwicky et al., 1961 – 1968, Bautz & Morgan, 1970; Rood & Sastry, 1971 and López-Cruz, 2003). The improved types correspond to concentration to the center (C – compact, I – intermediate, and O – open), preferential line presence (L – line, F – flat, and no symbol if no indication of flatness is present) and the role of bright cluster members, namely cD or BG if the bright cluster’s members (BCMs) role is significant. Other peculiarities are noted as P. The special kinds of regular peculiarities, such as X-type (crossed bands) and Y-type (divaricate filaments) with corresponding positions and orientations of the BCMs; curved strips and short chains were detected in open rich clusters (Panko & Emelyanov, 2017; Panko et al., 2018).

According to idea Rood & Sastry (1971) and Struble & Rood (1982) confirmed in simulations (for example, Vogelsberger et al., 2014; Artale et al., 2017) the galaxy clusters evolve form open to concentrated types. We suppose the influence of neighbours becomes apparent as regular peculiarities.

The paper is organized in the standard manner. Section 2 contains the description of the observational data and the cluster mapping, section 3 presents the characters of substructures, distribution clusters according to subtypes and its analysis, and section 4 conclusions and analysis is given at the end.

2. Observational Data and Mapping

The present study is the part of common analysis of properties of rich galaxy clusters selected from “A Catalogue of Galaxy Clusters and Groups” (Panko & Flin, 2006, hereafter PF). The PF Catalogue contains 460 galaxy clusters with richness 100 and more. According previous classification the set contains 28 concentrated, 178 intermediate and 254 open galaxy clusters. The last subset was analyzed by Panko & Emelyanov (2017). The 178 intermediate clusters were studied by Zabolotnii et al. (in preparation). The difference between O-type and other ones was established by Panko et al. (2016) on subset of rich PF galaxy clusters coinciding to ACO objects (Abell, Corwin & Olowin, 1989).

The information about individual galaxies in the cluster field is obtained from Münster Red Sky Survey Galaxy Catalogue (Ungue et al., 2003). For determination of morphological type we used improved program “The Cluster Cartography set” (Panko & Emelyanov, 2015, hereafter CC). The CC allows to construct cluster map in rectangular coordinates in arcseconds recalculated from standard equatorial. The symbols on the map illustrate the galaxy shape and orientation in the projection on the celestial sphere, but size of symbol corresponds to galaxy magnitude; calculation bases on MRSS data. Additional brightest galaxies can be marked by darker shades of gray.

CC allows us to find the overdense regions as circles on case of C- and I-types of clusters or as belts/strips for L and F clusters. In the last case the clusters field is divided to N bands. N can be 3, 5, 7, 9 or 11 and the width of each band is $1/N$ part of diameter of cluster. The numbers of galaxies in the bands are recalculated to weighted densities of galaxies (Panko & Emelyanov, 2015). It allows to describe overdense features as $L11$ or $L9$ for L-cluster and $F7$ or $F5$ for F-clusters (the numeral part corresponds N). For C and I types the central part of cluster was excluded from overdense features search. The crossing bands, divaricate filaments, curved strips and short chains inside the cluster can be detected according to weighted densities in the sectors.

4. The Subtypes and Peculiarities in Concentration Galaxy Clusters

Our detailed analysis of the distribution of galaxies in concentrated galaxy clusters allows to confirm attribution to C-type without signs of the preferential band only for 15 clusters.

Table 1: The distribution C-type PF galaxy clusters by subtypes

| Type | N | cD | BG | P | PX | PY | P shc | P crv |
|------|-----|----|----|----|----|----|----------|----------|
| C | 12 | 4 | 5 | 4 | | 2 | 1 | 1 |
| CF | 9 | 1 | 5 | 5 | | 2 | 2 | 1 |
| CL | 3 | | 1 | 2 | 1 | 1 | | |
| SC | 2 | | | | | | | |
| CI | 2 | 1 | 1 | 1 | | 1 | 1 | |
| All | 28 | 6 | 15 | 12 | 1 | 5 | 4 | 2 |

These 2 clusters show a special level of overdensity and can be described as compact or superconcentrated (SC-type). The example of SC-type cluster is shown in Fig 1, left panel. SC-type clusters have no peculiarities. At the same time in SC-type clusters we found

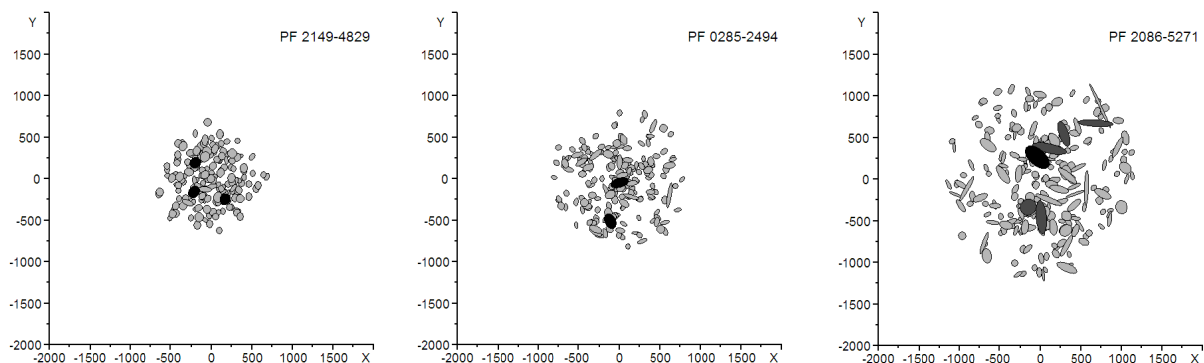


Figure 1: The map of galaxy cluster PF 2149-4829 SC-type and clusters with Y-type peculiarities: PF 0285-2494 and PF 2086-5271 with 2 centers of concentration. Axes labels are given in *arcseconds*.

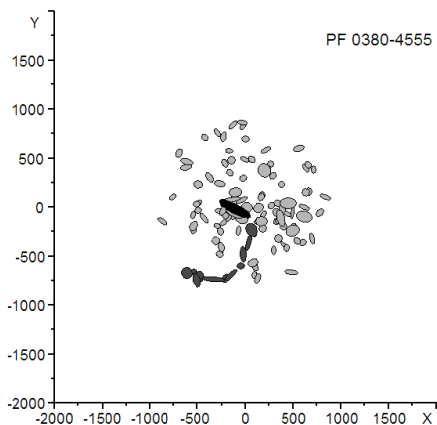


Figure 2: The map of galaxy cluster PF 0380-4555 with curved strip. The galaxies in the filamentary substructure are shown as light grey symbols, brightest galaxy is black one.

extremely big part of galaxies with small ellipticities.

2 C-type clusters from 12 have Y-type substructures underscore the positions of BCMs (Fig 1, central and right panels). For another 2 C-type clusters we found short chain (*shc*) and curved strip (*crv*) peculiarities. The curved strip in PF 0380-4555 is shown in Fig. 2. The founded filamentary substructure requires separate study.

12 clusters having preferential bands were attributed as CF or CL types and 2 clusters were determined as CI-type. The distribution of galaxy clusters of our data subset is shown in Table 1.

The part of galaxies with big and small ellipticities (as way to estimation E/S ratio) is different in normal and peculiar clusters. At the same time, peculiar clusters have essential part of galaxies with big ellipticity and a small part of E galaxies correspondingly.

4. Discussion and conclusions

From the previous study the morphology of galaxy clusters (Panko et al., 2016) based on 247 Rich PF Galaxy Clusters we established the special role of concentrated galaxy clusters - Regular ones according to Abell (1958) and Compact in Zwicky et al. (1968) schemes. The alignment of the brightest galaxy according to parent cluster is statistically significant in C-type clusters. Nevertheless we found the presence of overdense belt in about 40% clusters in our data set. For these clusters alignment of brightest galaxy as well as positions and orientations for 2 or 3 BCMs corresponds to direction of found belt.

The X-type (crossed belts) peculiarity was detected only in 1 case in contrary to Y-type discovered in 5 clusters. The E/S ratio points out the dependence of Hubble mix from interactions between galaxies in substructures. It confirmed the result Panko & Flin (2014) which was not find the hard connection E/S ratio with basic morphology types. In Panko & Flin (2014) paper the presence of peculiarities was not considered.

The orientation of low mass galaxies in filamentary substructures corresponds to Binggeli (1982) effect (Fig. 2), in contrary to high-mass galaxies (Fig. 1, right pane). High-mass galaxies tend to alignment crosswise to overdense strip direction.

We studied the morphological characters of 28 concentrated galaxy clusters. We obtained the list of galaxy clusters with regular substructures of different kinds. We showed the signs of interactions and/or evolution in concentrated galaxy clusters are present. We detected the special types of regular substructures namely curved and short strips in the concentrated galaxy clusters. We detected the alignment of galaxies in regular substructures according to preferential direction or direction to neighbours. We found the vari-

ations of E/S ratio for galaxies in cluster is connected with presence of peculiarities and can be explained by interactions between galaxies in substructures.

Acknowledgements. This research has made use of NASA's Astrophysics Data System.

References

- Abell G. O.: 1958, *ApJS*, **3**, 211.
- Abell G. O., Corwin H. G. & Olowin R. P.: 1989, *ApJS* **70**, 1.
- Artale M. C., Pedrosa S. E., Trayford J. W. et al.: 2017, *MNRAS* **470**, 1771.
- Bautz L. P. & Morgan W. W.: 1970, *ApJ* **162**, L149.
- Binggeli B.: 1982 *A&A*, **107**, 338.
- Cui W., Knebe A., Yepes G.: 2018, *MNRAS*, **473**, 68.
- López-Cruz O., "The Classification of Clusters of Galaxies: Comments on the Proposal of a New Subclass", in: "The Garrison Festschrift: Contribution of the Institute for Space Observations", No 20, R. O. Gray, C. J. Corbally, A. G. D. Philip (eds.): 2003, 109.
- Markevitch M., Gonzalez A. H., Clowe D., et al.: 2004, *ApJ*, **606**, 819.
- Panko E. & Flin P.: 2006, *Journal of Astronomical Data*, **12**, 1.
- Panko E. A.: 2013, *Odessa Astr. Publ.*, **26**, 90.
- Panko E. A & Flin P.: 2014, *Odessa Astr. Publ.*, **27**, 32.
- Panko E. A & Emelyanov S. I.: 2015, *Odessa Astr. Publ.*, **28**, 135.
- Panko E., Bajan K., Flin P. & Gotsulyak A., "Morphological Types of 247 PF Galaxy Clusters", in: "The Zeldovich Universe: Genesis and Growth of the Cosmic Web", Proceedings of the International Astronomical Union, IAU Symposium, Volume 308, R. van de Weygaert, S. Shandarin, E. Saar & J. Einasto (eds.):2016, 213.
- Panko E. A & Emelyanov S. I.: 2017, *Odessa Astr. Publ.*, **30**, 121.
- Panko E., Andrievsky S., Yemelianov S. & Stepaniuk A.: 2018, *Astronomy Reports, in press*.
- Pearce C. J. J., van Weeren R. J., Andrade-Santos F., et al.: 2017, *ApJ*, **845**, 81.
- Peebles P. J. E. & Yu J. T.: 1970, *ApJ*, **162**, 815.
- Rood H. J. & Sastry G. N.: 1971, *PASP*, **83**, 313.
- Silk J.: 1968, *ApJ*, **151**, 459.
- Springel V., White S. D., Jenkins A., et al.: 2005, *Nature*, **435**, 629.
- Struble M. F. & Rood H. J.: 1982, *ApJ*, **87**, 7.
- Sunyaev R. A. & Zeldovich Ya. B.: 1970, *ApSS*, **7**, 3.
- Ungruhe R., Saitter W. C. & Durbeck H. W.: 2003, *Journal of Astronomical Data*, **9**, 1.
- Vogelsberger M., Genel Shy, Springel V., et al.:2014, *MNRAS*, **444**, 1518.
- Zabolotnii V., Panko E. & Yemelianov S., (*in preparation*).
- Zwicky F., Herzog E., Wild P., "Catalogue of galaxies and of clusters of galaxies" (1961 - 1968).

DOI: <http://dx.doi.org/10.18524/1810-4215.2018.31.145079>

CONDENSATION OF COLD NEUTRONS – IDEA OF G. A. GAMOW. CHEMICAL PROPERTIES OF THE NEUTRON MATTER AND ITS PLACE IN THE PERIODIC SYSTEM OF ELEMENTS

G. B. Ryazantsev¹, G. K. Lavrenchenko², I. N. Beckman¹, I. M. Buntseva¹, S. S. Nedovesov³¹ Lomonosov Moscow State University, Leninskie Gory, Moscow, Russia,
*anis-mgu@rambler.ru*² LLC «Institute of Low Temperature Energy Technology», POB188, Odessa, Ukraine,
*lavrenchenko.g.k.@gmail.com*³ Shevchenko National University of Kyiv, Ukraine, *pc.remont.tk@gmail.com*

ABSTRACT. Today, the neutron matter and neutron stars are already substantially rooted in the nuclear physics and astrophysics, and it is logical to have their consideration of them in terms of chemical properties and principles of general chemistry. The formation of a neutron substance, in addition to gravitational neutronization, is considered, other mechanisms, such as the condensation of ultracold neutrons (UCN) and neutronization due to a critical increase in the atomic number in the Periodic system of elements (PS). The stability of the neutron substance is substantiated already at the micro level due to Tamm interaction and not only at the macro level due to the gravitational interaction, as it is now considered in astrophysics. A neutron substance is a very concrete physical reality, urgently demanding its rightful place in the PS and studying not only physical, but also chemical, and possibly even in the near future, engineering and technical properties. We also consider the possibility of a "chemical" interaction of UCN with molecules of substances with an odd number of electrons. It is proposed to extend the PS beyond the limits of classical chemical substances and to cover a much wider range of matter in the universe, based on the forgotten ideas of D.I. Mendeleev. Moreover, PS begins with neutron and its isotopes (dineutron, tetra-neutrone, etc.) and ends the neutron stellar substance.

Keywords: neutron, neutron stars, neutron substance, periodic system of elements, neutronization, Tamm interaction, condensation of UCN.

Сьогодні нейтронна матерія та нейтронні зірки вже істотно вкоренилися в ядерній фізиці і астрофізиці, і логічно їх розглядати з точки зору хімічних властивостей і принципів загальної хімії.

Розглянуто створення нейтронної речовини на додаток до гравітаційної нейтронізації, по іншим механізмам, таким як конденсація ультрахолодних нейтронів (УХН) і нейтронізації через критичне збільшення атомного номера в Періодичній системі елементів (ПС). Стійкість нейтронної речовини затверджується вже на мікрорівні завдяки взаємодії Тамма, а не тільки на макрорівні, зумовленого гравітаційною взаємодією, як це зараз розглядається в астрофізиці.

Слід зазначити, що Г. Гамов вперше розповів про конденсації холодних нейтронів (1946). Рідко згадується ця ідея, яка з часом знайшла застосування в теорії нейтронних зірок. Гамов в 1937-38 рр. Показав, що при стисненні нейтронного газу виникає новий надщільний стан речовини.

Нейтронна речовина – це дуже конкретна фізична реальність, що вимагає законного місця в ПС і вивчення не тільки фізичних, а й хімічних і, можливо, навіть в найближчому майбутньому інженерних і технічних властивостей. Ми також розглядаємо можливість «хімічної» взаємодії УХН з молекулами речовин з непарним числом електронів.

Пропонується розширити ПС за межі класичних хімічних речовин і охопити набагато ширше коло матерії у Всесвіті, заснований на забутих ідеях Д.І. Менделєєва. Більш того, ПС починається з нейтрона і його ізотопів (дінейтрон, тетранейтронів і т. д.) і закінчується нейтронною зоряною речовиною.

Ключові слова: нейтрон, нейтронні зірки, нейтронна речовина, періодична система елементів, нейтронізація, взаємодія Тамма, конденсація УХН.

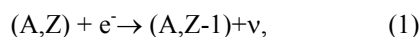
1. Introduction

Neutron matter, from the point of view of General Chemistry, can be formally attributed to chemically simple (i.e., it can not be decomposed further into simpler by chemical means), then inevitably the question arises about the Element, it corresponds to, and its place in the Periodic System (PS). Based on the logic of the Periodic Law (PL) – (atomic number = electric charge) – atomic number of neutron matter will correspond to zero, which brings to mind the Dmitri Ivanovich Mendeleev's idea of the zero group and period. D.I. Mendeleev assumed existence before the hydrogen elements X and Y. Element X (Mendeleev calls it "Newtonium") got its place in the periodic system – in the zero period of the zero group, as the lightest analog of inert gases. In addition, Mendeleev allowed the existence of one more element lighter than hydrogen – the element Y, "Koroniya" (Mendeleev, 1905; Ryazantsev et al., 2014). It should be noted that even after D.I. Mendeleev's question about "zero" elements was repeat-

edly raised by many authors both in the past and in the present centuries, however, for brevity we mention only the very first and famous: for example, Ernest Rutherford in 1920 (Ryazantsev et al., 2014; Kikoin, 1991) and Andreas von Antropoff in 1926 (before the discovery of the neutron itself) as a designation for a hypothetical element with an atomic number zero, which he placed at the beginning of the periodic table (Antropoff, 1926). A. Antropov also proposed the term "Neutronium" for the first time, although at that time this term was understood only by the yet not discovered, but already expected neutron. At the present time, both the dineutron, tetraneutrone, and octaneutron can claim this place in the PS, the information about which has already appeared in the press (Marques et al., 2012; Aleksandrov et al., 2005) and which can formally be considered as neutron isotopes. It's not difficult to see that the very substance of neutron stars, which in 1937 predicted L. D. Landau and discovered in 1968 by astronomers from Cambridge, can be considered from the point of view of the isotopy of the element Neutronium.

2. Neutronization

Thus, the zero position in the PS corresponds to the notion of it as a "**singular point**" in which to unite the micro- and mega-worlds, about the unity of which many philosophers and outstanding natural scientists have repeatedly spoken. The process of transformation of ordinary matter into neutrons under the influence of gravitational forces in the process of the evolution of certain stars was called **Neutronization**. The reaction of electron capture by atomic nuclei (A, Z) (A is the mass number, Z is the order number of the element) has the form:



The energy threshold of the reaction is large, therefore, only at high material densities, characteristic of the final stages of the evolution of some stars, the electron energy may exceed the critical value of the Neutronization threshold. Gravitational neutronization is widely described and discussed in detail, but other mechanisms for the formation of neutron matter are possible, for example, condensation of ultracold neutrons (UCN) and neutronization due to a critical increase in the atomic number of the elements in the PS. First we turn to the consideration of neutronization due to a critical increase in the ordinal number of the elements in the PS. In general, the question of the "ultimate element" was repeatedly raised by different authors and has its interesting "intrigue". The final element was initially assumed to be from the "drip" model of the nucleus with Z slightly more than 100, then it was shifted to the "mysterious" number of 137, passionate admirers of many well-known physicists and among them Richard Feynman, through which 137 elements even got the unofficial name "Feynmanium". It was believed that this element is "finite" because of the uncritical use of the Bohr model of the atom for superheavy elements, when the light velocities for the orbital electrons were obtained at Z = 137. The development of the quantum theory shifted the finite element beyond Z > 170. Let's consider this question

in more detail. The problem of the stability of superheavy atoms was described by Zeldovich Ya. B. and Popov V. S. back in 1971. The question of the electronic structure of an atom in a supercritical nuclear charge (Z > 170) is of great fundamental interest. In 1928, Paul Dirac showed that in the Coulomb field of a point charge Ze the solution of the relativistic equation for an electron becomes singular for Z = 137. Introducing the finite dimensions of the nuclear, I. Ya. Pomeranchuk and Ya. A. Smorodinsky in 1945 showed that an accurate calculation leads to a critical charge (Zc = 170). In the work of S. S. Gerstein and Ya. B. Zeldovich in 1969, it was assumed that, with a supercritical charge Z > Zc, a bare nucleus Z spontaneously emits positrons. An atom with a filled K shell, with an increase in the charge of the nucleus Z > Zc (with increasing Z, the internal electronic levels continue to drop, and the size of the nuclei grow) directly passes to the critical state Z = Zc, not emitting positrons, but by trapping the electrons by the nucleus. The authors also consider the possible contribution of the phenomenon of vacuum polarization and the production of pairs of particles and antiparticles in the field of critical nuclei.

However, we can not but make a few critical remarks:

1. With the unconditional heuristic value of the article by Zeldovich and Popov, they did not go any further – they did not make a direct conclusion about the almost complete neutronization of supercritical nuclei, although they laid the groundwork for this.
2. Their conclusion (the 4th conclusion on p. 410) that the properties of the outer shells of an atom (which determine, in particular, Mendeleev's periodicity of chemical properties) naturally continue to the supercritical region is questionable.
3. They underestimated the role of vacuum polarization. Although there were papers (Panchapakesan, 1971), which state that the vacuum polarization grows unboundedly at Z → Zc. This contradicted their conclusions, however, in our opinion, this is closer to the truth and this leads to the inevitable and almost complete neutronization of supercritical nuclei.

Of the modern works specifying the value of the quantity Zc, we can indicate the work "New method for solving the problem Z > 137" and determining the energy levels of hydrogen-like atoms" V.P. Neznamov and I.I. Safronov in "Advances in Physical Sciences" in 2014.

The gradual neutronization of the element nuclei is observed long before the critical value of Zc are reached, the average index of the ratio of the number of neutrons and protons in the nuclei of chemical elements is steadily increasing already in all periods of the PS.

3. Proton-neutron diagram

Qualitatively, the growth of the neutronization degree of nuclei can be well observed by extrapolating the course

of the curve on a proton-neutron diagram if from the whole set of known elements and their isotopes choose stable and long-lived ones.

It's clear that for quantitative conclusions from the extrapolation of the diagram, it is necessary to carry out a thorough statistical analysis of the curve for the dependence $p - n$ for a very wide range of nuclides. What is the nature of the mathematical dependence of $p - n$? It can be assumed that if in the limit a neutron substance is practically only a set of neutrons, then one should expect a hyperbolic dependence and an asymptotic tendency of the curve to some limit, if there always remains a definite, albeit decreasing, fraction of the protons in the neutron matter, then we should expect a parabolic or exponential dependence.

The statistical processing was carried out by **Mathcad** and **ORIGIN** programs: both methods yielded the same result. The proton-neutron diagram for stable and long-lived isotopes is best described by a quadratic polynomial: $y = ax^2 + bx + c$, where $a = 0.004982$, $b = 1.122$, $c = -1.003$ for Mathcad and $a = 0.005$, $b = 1.126$, $c = -1.0034$ by ORIGIN. Thus, the dependence of $p - n$ best corresponds to a quadratic parabola, rather than to a hyperbola and an exponential, as one would expect from a "drip" nuclear model on the one hand, and on the other, indicates that there is always a residual in the neutron matter fraction of protons.

4. Weizsäcker formula

Additional information can be obtained from the dependence of the specific binding energy of nucleons in the atomic nucleus on their atomic mass A , which is well described by the Weizsäcker formula. Carl Friedrich von Weizsäcker obtained the semi-empirical equation for the binding energy:

$$E_B = \alpha A - \beta A^{2/3} - \gamma Z^2 A^{-1/3} - \xi(N-Z)^2/A + \delta A^{-3/4}, \quad (2)$$

Where, $\alpha = 15,75$ MeV; $\beta = 17,8$ MeV; $\gamma = 0,71$ MeV; $\xi = 22$ MeV; $\delta = + 34$ MeV for even-even, $\delta = 0$ MeV for odd, $\delta = -34$ MeV for odd-odd, A – atomic weight.

It can be seen that with increasing A , the Coulomb energy of repulsion of protons makes the largest contribution to the decrease in the binding energy, while the contribution of the surface energy decreases, and the energy of symmetry is not decisive. Let's try to continue Weizsäcker's dependence on supercritical nuclei.

Because of the process of almost complete neutronization and growth of sizes for supercritical nuclei, the contribution of the surface energy will be leveled, and the Coulomb repulsion will cease to increase when supercriticality is reached, which will result in the stabilization of the neutron substance and reduce the probability of its decay by some mechanism (fission, β^+ -decay). It is necessary to consider in more detail the β^- -decay, which, it would seem, should be dominant with such "overloading" by neutrons.

However, the paradox of neutron matter leads to the fact that starting from a certain critical mass and size (when the path of β -electron in a neutron matter becomes

smaller than the size of the matter), β^- -decay from the destabilizing factor becomes a significant factor of stability. There is always some residual content of the proton matter in the neutron matter, and beta-electron emitted by decayed neutron is not able to leave the neutron matter of sufficient size (larger than the path of beta-electron in it).

5. Tamm interaction

The emitted electron is absorbed by the remaining protons, which in turn are converted into neutrons, thus the dynamic equilibrium of the system is maintained. In fact, it corresponds to the theory of Tamm (1975), which he put forward in his time (1934) to explain the mechanism of nuclear forces for ordinary nuclei. It should be noted that his theory was not satisfactory for ordinary atoms (Tamm appreciated his "unsuccessful" theory of nuclear forces more than his Nobel work on Cherenkov radiation), but it can be realized for the neutron matter of appropriate scale (200-300 and more femtometers), giving it additional stability.

In strongly interacting systems, there are many virtual particles and all kinds of interactions that are allowed by considerations of invariance are realized. So, in our view, the "age-old" theory of exchange β -nuclear forces Tamm (e-exchange of nucleons), and not just its modification by Hideki Yukawa (π -exchange of nucleons), still awaits its recognition (because besides the meson cloud around the nucleon there are certainly other particles) and "dominates" in the neutron matter of the Universe, ensuring its stability and wide space distribution.

An initial study of this problem was given by Frederick Hund in 1936 in the first microscopic description of the equation of state of nuclear matter in beta equilibrium in the article "*The substance at very high pressures and temperatures*" only if Tamm has virtual electrons, Hund realizes a beta-equilibrium of completely real particles, but most importantly, both mechanisms contribute to the stability of supercritical nuclear matter, and in strongly interacting systems there is no fundamental difference between virtual and real particles.

Another factor of additional stability of the neutron matter during the significant increase of its mass (up to a macro scale) will be the ever-increasing contribution to the gravitational interaction. Thus, we obtain a modified Weizsäcker equation for the neutron matter, which describes the main factors of its stability and the real existence in the Universe:

$$E_B = \alpha A - \beta A^{2/3} + \tau A^t + \lambda A^l, \quad (3)$$

Where, $\alpha = 15.75$ MeV; $\beta = 17.8$ MeV; τ – Tamm – interaction; λ – the gravitational interaction. The parameters of equation 3 (τ , λ , t , l) need to be clarified in the course of further research in this area.

It's namely Tamm interaction, due to nuclear β – force, confers resistance to neutron substance already on the micro-level, not just at the macro-level due to the gravitational interaction, as it is now considered to be in astrophysics!

The existence, in addition to the forces of Yukawa, of Tamm-interaction for a neutron substance, allows one to

expect a technology for its production in terrestrial laboratory conditions, which, based on nuclear dimensions, can be called **Femtotechnology**. One of the directions of femtotechnology can be the study of collisions of nuclei of heavy elements, which in sum give a compound nucleus falling into the supercritical region, i.e. $Z_c > 170-175$, which, apart from fission, can be stabilized by the production of various pairs of particles and antiparticles in the field of supercritical nuclei, and in the case of electron-positron pairs, the electrons will be absorbed by the supercritical nucleus and positrons emit as the charge of the nucleus decreases to critical values of Z_c . A detailed study of such systems will become possible after the implementation of the NICA Project (NICA, English Nuclotron-based Ion Collider facility) in Russia.

The possibility of the existence of superdense neutron nuclei was considered in the work of A. B. Migdal's "*Theory of finite Fermi systems and properties of atomic nuclei*" in the section: "*Application of TC FS in nuclear physics*" (1983). Migdal believed: "... neutron nuclei can be stable with respect to beta decay and fission, with $Z \ll N$ and $N > 10^3 - 10^5$. Such nuclei could be observed in cosmic rays in the form of large fragments." Thus, A.B. Migdal proposed that neutron cores be searched for exotic tracks in photographic emulsions after exposure to cosmic rays.

6. Ultracold neutrons

From the Cosmos we will go down to Earth and once again we will see where it's possible to find a neutron substance here? Usually we are dealing with neutron radiation of various energies, but not with neutron matter. This was until 1968, when an experiment was conducted at the Laboratory of Neutron Physics under the guidance of the member of the USSR Academy of Sciences, Fyodor Lvovich Shapiro (1976; [Ignatovich, 1996], in which the phenomenon of retention in vessels of very slow neutrons, predicted by academician Ya. B. Zeldovich. The behavior of neutrons held in vacuumed vessels is reminiscent of the behavior of a highly rarefied gas in the vessel. Such neutrons are called ultracold (UCN). The retention of UCN in the vessels attracts researchers the opportunity (longer than a single neutron flight through the experimental volume) to observe longer this elementary particle in the experimental setup, which gives a significant increase in the sensitivity and accuracy of experiments on the interaction of neutrons with fields and matter. For example, the use of UCN has made it possible to significantly omit the limit of the existence of the electric dipole moment of a neutron, necessary for testing the law of conservation of time parity, to more accurately measure the lifetime of a free neutron to β decay. The most important feature of UCN is that they behave not as radiation, but as a substance and work with them as with a substance similar to a discharged inert gas. Moreover, one can study both physical and chemical properties. Physical properties are already being studied, but the question of the chemistry of UCN seems to be that the question is not even raised; by default somehow it seems obvious that they should be similar to inert gases.

It's look like the truth, but now we already know that inert gases, albeit with difficulty, enter into chemical reactions and form, albeit not stable, but chemical compounds.

Can this happen with UCN? If one assumes that Chemistry is only the interaction of the electron shells of atoms, as many believe, a categorical negative answer follows. But if under Chemistry is understood, more generally, the ability of micro (nano, pico or even femto) – objects to interact and form relatively stable compounds, then why not? Yes, neutrons do not have electric charge and free electrons, so that all ideas about possible classical chemical bonds (ionic, covalent, etc.) immediately disappear. But, neutrons have exactly a magnetic moment and perhaps an electric dipole moment, can not this serve the ability to interact with other objects and form, even if not stable, yet observable connections? For example, the interaction of a neutron with molecules of substances with an odd number of electrons is entirely possible (Serebrov et al., 2011; Ryazantsev et al., 2016). The development of new UCN sources is actively carried out worldwide, some of them are based on the use of solid deuterium at a temperature of 4.5 K (LANL, USA, PSI, Switzerland), and others on the accumulation of UCN in superfluid helium (KEK-RCNP-TRIUMF, Japan-Canada, ILL, France) (Serebrov et al., 2011). Similar work is being intensively carried out in Russia: The neutron laboratory at the Joint Institute for Nuclear Research (Dubna), the Petersburg Nuclear Physics Institute (PNPI), in Gatchina, is working on the creation of a high-intensity UCN source. With its help, they hope to obtain data that will provide answers to the most important questions of modern physics.

The projected source will make it possible to obtain a flux of ultracold neutrons (UCN) with a density of 10^4 cm^{-3} , which is many times greater than the maximum density now reached (Serebrov et al., 2011). This problem – obtaining intensive UCN fluxes – is now considered one of the priority in neutron physics. An increasing and larger increase in the density of ultracold neutrons inevitably leads to the formulation of the question of their possible condensation and the production of a condensed neutron substance in laboratory conditions similar to the cosmic one. It should be noted that G.A. Gamow first spoke about the condensation of cold neutrons (1946). Rarely mention this idea, which over time has found application in the theory of neutron stars. Gamow in 1937–38 showed that when a neutron gas is compressed, a new superdense state of matter arises. Gamow's key hypothesis: "*We can anticipate that neutrons forming this comparatively cold cloud were gradually coagulating into larger and larger neutral complexes ...*"

Not so long ago a decisive breakthrough was made to a new area: a radically new kind of matter, the so-called Bose condensates of the atoms of matter, was created.

Are condensate neutrons possible? Condensates, density and strength of which will be comparable to the density and strength of atomic nuclei. In other words, how close are we today to the point of creation of a cosmic neutron substance in the laboratory?

The Nobel Prize in Physics in 2001 was awarded to researchers Eric A. Cornell, Wolfgang Ketterle and Carl E. Wieman for obtaining and investigating the properties of the fifth state of matter – the Bose-Einstein condensate, they were able to get the first Bose condensate (Cornell et al., 2001). This could be done with the help of methods

developed recently for the supercooling of particles by laser beams and a magnetic field.

The Bose condensate of atoms was obtained in a form convenient for research and laboratory analysis. Soon reports of the receipt of Bose condensates of various atoms showered from everywhere. The activity of scientists was also greatly facilitated by the fact that the facilities for obtaining Bose condensates turned out to be relatively inexpensive – experiments were in full swing in many countries. Soon, methods were also found for obtaining Bose condensates of particles of half-integer spin, fermions, whose class includes neutrons. In them, the particles are connected in pairs, then gathering in a Bose condensate. In many respects, neutrons are close to the lightest atoms. For example, the mass of a neutron is practically equal to the mass of a hydrogen atom, the Bose condensate of which was obtained by Ketterle in 1997.

But, in contrast to atomic Bose condensates, to natural compression of which under Bose condensation an electronic barrier is an irresistible obstacle, nothing can prevent the compression of the neutron Bose condensate. In such a condensate, UCN gas forms pairs with opposite spins, when the critical density and temperature are reached, will in itself shrink to near nuclear density when nuclear forces enter into the matter, forming a stable state – a condensed neutron matter.

7. Conclusions

Thus, the neutron matter in our time is a very concrete physical reality, urgently demanding its rightful place in the PS and studying not only physical, but also chemical, and possibly even in the near future, engineering and technical properties! A neutron substance, or rather an element corresponding to it, begins (zero period) and ends (supercritical atoms) of the PS elements. The neutron substance is given stability already at the micro level due to Tamm-interaction, and not only at the macro level due to the gravitational interaction, as is now believed in astrophysics. The possibility of neutronization is shown not only because of the gravitational interaction, but also in other mechanisms (supercritical increase in the atomic number of the elements and UCN condensation), so there is a fundamental possibility of obtaining a neutron substance even under terrestrial conditions. Neutron matter is a necessary link connecting the microcosm with the macro- and megaworld, from a free neutron to neutron stars and black holes. **The neutron substance is consistent with the original concept of the Periodic Law and the system put forward by Dmitri Ivanovich Mendeleev** (Mendeleev, 1905; Ryazantsev et al., 2014, 2016, 2017, 2018).

References

Aleksandrov D.V., Nikol'skii E.Yu., Novatskii B.G. et al.: 2005, *JETP LETTERS*, **81** (2), 43–46.

- Antropoff A.: 1926, *Zeitschrift für Angewandte Chemie*, **39** (23), 722–725.
- Dirac P.A.M.: 1928, *Proc. Roy. Soc.*, **117**, 610; **118**, 341.
- Gamow G.: 1946, *Phys. Rev.*, **70**, 572.
- Gershtein S.S., Zel'dovich Ya.B.: 1970, *Soviet Physics JETP*, **30**, № 2, 358–361.
- Hund F.: 1936, *Ergebn. Exakt. Naturwiss.* **15**, 189.
- Ignatovich V.K.: 1996, *Advances in Physical Sciences*, **166**, 303–324.
- Kikoin A.K.: 1991, *Quant*, № 1, 38, 39, 42–44.
- Cornell E.A., Wieman K.E., Ketterle W.: 2001, *Advances in Physical Sciences*, **173**, 1319.
- Marques F.M., Orr N.A., Achouri N.L., et al.: 2012, *Phys. Rev. Lett.*, **109**, 239201.
- Mendeleev D.I.: 1905, Separate edition: “*An Attempt of Chemical Understanding of the World Ether*”, St. Petersburg., Typolithography of M. P. Frolova, 5–40.
- Migdal A.B.: 1983, *Theory of Finite Fermi Systems and Properties of Atomic Nuclei*, second edition, revised and augmented, M.: Nauka, Main editors of physical and mathematical literature, 54.
- Neznamov V.P., Safronov I.I.: 2014, *Advances in Physical Sciences*, **184**, № 2, 200–205.
- Panchapakesan N.: 1971, *Phys. Lett.* **35B**, 522.
- Pomeranchuk I.Ya., Smorodinsky Y.A.: 1945, *J. Phys. USSR*, **9**, 97.
- Ryazantsev G.B., Lavrenchenko G.K.: 2014, *Technical gases*, №1, 3–10.
- Ryazantsev G.B., Lavrenchenko G.K.: 2016, *Technical gases*, №4, 41–49.
- Ryazantsev G.B.: 2014, *Science and Life*, №2, 76–80.
- Ryazantsev G.B., Khaskov M.A., Beckman I.N.: 2016, *ISINN-24. 24 International Seminar on Interaction of Neutron with Nucl.* Dubna: JINR, Russia, Abstracts, 71.
- Ryazantsev G.B., Lavrenchenko G.K., Khaskov M.A., Beckman I.N.: 2017, *ISINN-24. 24 International Seminar on Interaction of Neutron with Nucl.* Dubna: JINR, Russia, Article, 65–74.
- Ryazantsev G.B., Khaskov M.A., Beckman I.N., Lavrenchenko G.K.: 2017, *ISINN-25. 25 International Seminar on Interaction of Neutron with Nucl.* Dubna: JINR, Russia, Abstracts, 79.
- Ryazantsev G.B., Lavrenchenko G.K., Beckman I.N.: 2018, *18-th Gamow Summer School “ASTRONOMY AND BEYOND: ASTROPHYSICS, COSMOLOGY, COSMOMICROPHYSICS, ASTROPARTICLE PHYSICS, RADIOASTRONOMY AND ASTROBIOLOGY”* Odessa, Ukraine, Abstracts, 15.
- Shapiro F.L.: 1976, *Collected Works*. M., Science, **2**, 348.
- Serebrov A.P., Boldarev S.T., Erykalov A.N. et al.: 2011, *Physics Procedia*, **17**, 251–258.
- Tamm I.E.: 1975, *Collection of scientific works*, M., Science, **1**, 283–326.
- Zel'dovich Ya.B., Popov V.S.: 1971, *Advances in the physical sciences*, **105**, 403–440.

DOI: <http://dx.doi.org/10.18524/1810-4215.2018.31.144667>

2-FIELD MODEL OF DARK ENERGY WITH CANONICAL AND NON-CANONICAL KINETIC TERMS

O. Sergijenko

Astronomical Observatory, Taras Shevchenko National University of Kyiv,
Observatorna str. 3, Kyiv, 04053, Ukraine, olga.sergijenko.astro@gmail.com

ABSTRACT. For some parametrizations of the dark energy equation of state that varies in time there is transition from quintessence to phantom or vice versa at a certain redshift. Quintom – the 2-field model with 2 canonical kinetic terms (one with the “+” sign for quintessence and one with the “-” sign for phantom) and a potential $U(\phi, \xi)$ in Lagrangian – is one of the most popular scalar field models allowing for such behavior. We generalize quintom to include the tachyonic kinetic term along with the classical one. For such a model we obtain the expressions for energy density and pressure. For the spatially flat, homogeneous and isotropic Universe with Friedmann-Robertson-Walker metric of 4-space we derive the equations of motion for the fields. We discuss in detail the reconstruction of the scalar fields potential $U(\phi, \xi)$. Such a reconstruction cannot be done unambiguously, so we consider 3 simplest forms of $U(\phi, \xi)$: the product of $\Phi(\phi)$ and $\Xi(\xi)$, the sum of $\Phi(\phi)$ and $\Xi(\xi)$ and the sum of $\Phi(\phi)$ and $\Xi(\xi)$ to the κ th power. The second additional assumption that should be made is about the dependence of either kinetic term X_ϕ or X_ξ on the scale factor a . For each case we obtain the reconstructed potentials in the parametric form. If it is possible to invert dependences of the fields ϕ and ξ on the scale factor a and obtain the analytical expressions for $a(\phi)$ and $a(\xi)$ then we can find the potentials $U(\phi, \xi)$ in explicit form. From the obtained explicit expressions it is clear that they are not suitable for practical use for the multicomponent cosmological models with realistic parametrizations of the dark energy equation of state crossing -1 . On the other hand, the parametric dependences which define the potential $U(\phi, \xi)$ are suitable for multicomponent cosmological models and all parametrizations of the dark energy equation of state.

Keywords: Cosmology: dark energy.

АБСТРАКТ. Для ряду параметризацій рівняння стану темної енергії, що змінюється з часом, на деякому червоному зміщенні є можливим перехід від квінтесценції до фантома або навпаки. Квінтом – 2-польова модель з 2 канонічними

кінетичними членами (один зі знаком “+” для квінтесценції та один зі знаком “-” для фантома) та потенціал $U(\phi, \xi)$ в лагранжіані – є однією з найпопулярніших скалярно-польових моделей, що дозволяють таку поведінку. Ми пропонуємо узагальнення квінтюма, що включає тахіонний кінетичний член поряд з класичним. Для такої моделі ми отримуємо вирази для густини енергії та тиску темної енергії. Для просторово плоского однорідного ізотропного Всесвіту з метрикою 4-простору Фрідмана-Робертсона-Уокера ми виводимо рівняння руху для полів. Ми детально обговорюємо реконструкцію потенціалу скалярних полів $U(\phi, \xi)$. Така реконструкція не може бути зроблена однозначно, отже, ми розглядаємо 3 найпростіші форми $U(\phi, \xi)$: добуток $\Phi(\phi)$ та $\Xi(\xi)$, сума $\Phi(\phi)$ та $\Xi(\xi)$ та сума $\Phi(\phi)$ та $\Xi(\xi)$ у степені κ . Друге додаткове припущення, яке необхідно зробити, стосується залежності кінетичного члена X_ϕ або X_ξ від масштабного множника a . Для кожної з комбінацій цих 2 припущень ми отримуємо реконструйовані потенціали в параметричній формі. В тих випадках, коли можливо обернути залежності полів ϕ та ξ від масштабного множника a та отримати аналітичні вирази для $a(\phi)$ та $a(\xi)$, ми можемо знайти потенціали $U(\phi, \xi)$ в явній формі. З отриманих явних виразів очевидно, що вони не підходять для практичного використання для багатоконпонентних космологічних моделей з реалістичними параметризаціями рівняння стану темної енергії, що переходять через -1 . З іншого боку, параметричні залежності, що визначають потенціал $U(\phi, \xi)$, є придатними для багатоконпонентних космологічних моделей та всіх параметризацій рівняння стану темної енергії.

Ключові слова: Космологія: темна енергія.

1. Introduction

20 years ago the accelerated expansion of the Universe was discovered. The cosmological constant in Einstein equations (equation of state parameter $w = -1$)

is the simplest explanation of it. The dark energy in form of a scalar field is the most popular alternative to Λ . Its equation of state parameter can either be constant or vary in time. Dark energy with $w > -1$ is called quintessence, with $w < -1$ – phantom. For several widely used parametrizations of $w(z)$, e.g. Chevallier & Polarski (2001) and Linder (2003) (CPL), Komatsu et al. (2009) (WMAP5), at a certain redshift there is transition from quintessence to phantom or vice versa. Such behavior is forbidden for a single minimally coupled scalar field, as it was shown for the first time by Vikman A. (2005) (see also Easson D.A. & Vikman A. (2016)). However, crossing of the phantom divide is possible in the cases of kinetic gravity braiding (Deffayet C. et al. (2010)), sound speed vanishing in phantom domain (Creminelli P. et al. (2009)) or non-minimal couplings (Amendola L. (2000), Pettorino V. & Baccigalupi C. (2008)).

The most popular scalar field model allowing for $w = -1$ crossing is quintom proposed by Feng B. et al. (2005). It is the 2-field model with 2 canonical kinetic terms – one with the “+” sign for quintessence and one with the “-” sign for phantom – and a potential $U(\phi, \xi)$ in Lagrangian.

Quintom can be generalized to include a non-canonical kinetic term. The simplest physically motivated Lagrangian with the non-canonical kinetic term is the tachyon one. So, we propose the 2-field model of dark energy with classical and tachyonic kinetic terms.

2. 2-field model with classical and tachyonic kinetic terms

We consider the spatially flat, homogeneous and isotropic Universe with Friedmann-Robertson-Walker (FRW) metric of 4-space

$$ds^2 = g_{ij}dx^i dx^j = a^2(\eta)(d\eta^2 - \delta_{\alpha\beta}dx^\alpha dx^\beta) \quad (1)$$

(here $i, j = 0, 1, 2, 3$, $\alpha, \beta = 1, 2, 3$, a is the scale factor, η is the conformal time and $c = 1$). The Universe is filled with relativistic (radiation, neutrinos), non-relativistic (baryons, dark matter) matter and dark energy. The latter is modeled by 2 scalar fields with the Lagrangian:

$$L = -X_\phi - U(\phi, \xi)\sqrt{1 - 2X_\xi}, \quad (2)$$

where

$$X_\phi = \frac{1}{2}\phi_{,i}\phi^{,i} = \frac{\dot{\phi}^2}{2},$$

$$X_\xi = \frac{1}{2}\xi_{,i}\xi^{,i} = \frac{\dot{\xi}^2}{2}$$

are the kinetic terms. This Lagrangian is classical (Klein-Gordon) with respect to the field ϕ which corresponds to phantom and tachyon (Dirac-Born-Infeld)

with respect to the field ξ which corresponds to quintessence.

The energy density and pressure for such a model are as follows:

$$\rho_{de} = -X_\phi + \frac{U(\phi, \xi)}{\sqrt{1 - 2X_\xi}}, \quad (3)$$

$$p_{de} = -X_\phi - U(\phi, \xi)\sqrt{1 - 2X_\xi}. \quad (4)$$

The dark energy equation of state (EoS) parameter is defined as $w(a) = p_{de}/\rho_{de}$.

For the metric (1) the Lagrangian (2) yields the following equations of motion:

$$\ddot{\phi} + 2aH\dot{\phi} - \frac{\partial U}{\partial \phi}a^2\sqrt{1 - \frac{\dot{\xi}^2}{a^2}} = 0, \quad (5)$$

$$\ddot{\xi} + 2aH\dot{\xi} - 3aH\dot{\xi}\frac{\dot{\xi}^2}{a^2} + \frac{1}{U}\left(\frac{\partial U}{\partial \phi}\dot{\phi}\dot{\xi} + a^2\frac{\partial U}{\partial \xi}\right)\left(1 - \frac{\dot{\xi}^2}{a^2}\right) = 0. \quad (6)$$

Here a dot denotes the derivative with respect to η and $H \equiv \dot{a}/a$ is the Hubble parameter.

From (3)-(4) it is clear that reconstruction of the potential $U(\phi, \xi)$ cannot be done unambiguously and requires additional assumptions. First of all, we should choose a form of $U(\phi, \xi)$. We restrict our consideration to 3 simplest ansatzes from Andrianov et al. (2008):

- $U(\phi, \xi) = \Phi(\phi)\Xi(\xi)$,
- $U(\phi, \xi) = \Phi(\phi) + \Xi(\xi)$ and
- $U(\phi, \xi) = [\Phi(\phi) + \Xi(\xi)]^\kappa$, $\kappa = const.$

Secondly, we should assume either X_ϕ or X_ξ to be a known function of the scale factor. Then for $X_\xi = \alpha(a)$ we get:

$$U(a) = \frac{1}{2}\frac{1-w}{1-\alpha}\sqrt{1-2\alpha\rho}, \quad (7)$$

$$X_\phi(a) = -\frac{1}{2}\frac{1-2\alpha+w}{1-\alpha}\rho \quad (8)$$

and for $X_\phi = \beta(a)$:

$$U(a) = \sqrt{-(\rho w + \beta)(\rho + \beta)}, \quad (9)$$

$$X_\xi(a) = \frac{1}{2}\frac{\rho(1+w) + 2\beta}{\rho + \beta}. \quad (10)$$

Dependences of the fields ϕ and ξ on the scale factor a are determined from $X_\xi = \alpha$ and (8):

$$\xi(a) = \pm \int \frac{da}{aH}\sqrt{2\alpha}, \quad (11)$$

$$\phi(a) = \pm \int \frac{da}{aH}\sqrt{-\frac{1}{2}\frac{1-2\alpha+w}{1-\alpha}\rho} \quad (12)$$

or $X_\phi = \beta$ and (10):

$$\phi(a) = \pm \int \frac{da}{aH} \sqrt{2\beta}, \quad (13)$$

$$\xi(a) = \pm \int \frac{da}{aH} \sqrt{\frac{1}{2} \frac{\rho(1+w) + 2\beta}{\rho + \beta}}. \quad (14)$$

These expressions together with either (7) or (9) define $U(\phi)$ in the parametric form. This allows us to reconstruct the potential even if the integrals in (11)-(14) cannot be solved analytically.

3. Reconstructed potentials in an explicit form

If it is possible to invert the analytical dependences (11)-(12) or (13)-(14) then we can obtain the explicit expressions for potentials (as it has been done for single-field models in e.g. Sergijenko & Novosyadlyj (2008), Novosyadlyj & Sergijenko (2009)). For $U(\phi, \xi) = \Phi(\phi)\Xi(\xi)$, $X_\xi = \alpha$ the potential is reconstructed as:

$$\begin{aligned} U(\phi, \xi) = \exp \left\{ \pm \int d\phi \left[\frac{1}{a} \sqrt{-\frac{(1-\alpha)(1-2\alpha+w)}{\rho}} \right. \right. \\ \times \frac{1}{(1-w)(1-1-2\alpha)} \left(\frac{\dot{w}-2\dot{\alpha}}{1-2\alpha+w} + \frac{\dot{\alpha}}{1-\alpha} \right. \\ \left. \left. + 3aH(1-w) \right) \right] (a(\phi)) \mp \int d\xi \left[\frac{1}{2a} \frac{\sqrt{2\alpha}}{1-2\alpha} \left(\frac{1}{2} \frac{\dot{\alpha}}{\alpha} \right. \right. \\ \left. \left. + \frac{\dot{\alpha}}{1-\alpha} \frac{1-2\alpha+w}{1-w} + \frac{\dot{w}-2\dot{\alpha}}{1-w} \right. \right. \\ \left. \left. + 3aH(2-4\alpha+w) \right) \right] (a(\xi)) \right\}, \end{aligned}$$

for $U(\phi, \xi) = \Phi(\phi)\Xi(\xi)$, $X_\phi = \beta$ it is as follows:

$$\begin{aligned} U(\phi, \xi) = \exp \left\{ \pm \int d\phi \left[\frac{1}{a} \frac{\sqrt{2\beta}}{\rho w + \beta} \left(3aH + \frac{1}{2} \frac{\dot{\beta}}{\beta} \right) \right] \right. \\ \times (a(\phi)) \pm \int d\xi \left[\frac{1}{2a} \frac{\sqrt{(\rho(1+w) + 2\beta)(\rho + \beta)}}{\rho w + \beta} \right. \\ \times \left(\frac{\rho(\dot{w} - 3aH(1+w)^2) + 2\dot{\beta}}{\rho(1+w) + 2\beta} \right. \\ \left. \left. + 3 \frac{aH(1-w)\rho - 6aH\beta - \dot{\beta}}{\rho + \beta} \right) \right] (a(\xi)) \right\}. \end{aligned}$$

For $U(\phi, \xi) = \Phi(\phi) + \Xi(\xi)$, $X_\xi = \alpha$ we get:

$$\begin{aligned} U(\phi, \xi) = \pm \int d\phi \left[\frac{1}{2a} \sqrt{-\frac{1-2\alpha+w}{(1-\alpha)(1-2\alpha)}} \rho \right. \\ \times \left(\frac{\dot{w}-2\dot{\alpha}}{1-2\alpha+w} + \frac{\dot{\alpha}}{1-\alpha} + 3aH(1-w) \right) \right] (a(\phi)) \\ \mp \int d\xi \left[\frac{1}{2a} \sqrt{\frac{2\alpha}{1-2\alpha}} \frac{1-w}{1-\alpha} \rho \left(\frac{1}{2} \frac{\dot{\alpha}}{\alpha} + \frac{\dot{\alpha}}{1-\alpha} \right. \right. \end{aligned}$$

$$\begin{aligned} \times \frac{1-2\alpha+w}{1-w} + \frac{\dot{w}-2\dot{\alpha}}{1-w} + 3aH \\ \left. \left. \times (2-4\alpha+w) \right) \right] (a(\xi)), \end{aligned}$$

while for $U(\phi, \xi) = \Phi(\phi) + \Xi(\xi)$, $X_\phi = \beta$:

$$\begin{aligned} U(\phi, \xi) = \pm \int d\phi \left[\frac{1}{a} \sqrt{2\beta} \sqrt{-\frac{\rho + \beta}{\rho w + \beta}} (3aH \right. \\ \left. + \frac{1}{2} \frac{\dot{\beta}}{\beta} \right) \right] (a(\phi)) \pm \int d\xi \left[\frac{1}{2a} \sqrt{\frac{\rho(1+w) + 2\beta}{\rho w + \beta}} \right. \\ \times (\rho + \beta) \left(\frac{\rho(\dot{w} - 3aH(1+w)^2) + 2\dot{\beta}}{\rho(1+w) + 2\beta} \right. \\ \left. \left. + 3 \frac{aH(1-w)\rho - 6aH\beta - \dot{\beta}}{\rho + \beta} \right) \right] (a(\xi)). \end{aligned}$$

In the case of $U(\phi, \xi) = [\Phi(\phi) + \Xi(\xi)]^\kappa$, $\kappa = const$, $X_\xi = \alpha$ the potential reads:

$$\begin{aligned} U(\phi, \xi) = \frac{1}{(2\kappa)^\kappa} \left\{ \pm \int d\phi \left[\frac{1}{a} \sqrt{-(1-2\alpha+w)} \rho^{\frac{1}{\kappa}-\frac{1}{2}} \right. \right. \\ \times (1-w)^{\frac{1-\kappa}{\kappa}} (1-\alpha)^{\frac{1}{2}-\frac{1}{\kappa}} (1-2\alpha)^{\frac{1}{2\kappa}-1} \left(\frac{\dot{w}-2\dot{\alpha}}{1-2\alpha+w} \right. \\ \left. \left. + \frac{\dot{\alpha}}{1-\alpha} + 3aH(1-w) \right) \right] (a(\phi)) \mp \int d\xi \left[\frac{1}{2a} \sqrt{2\alpha} \right. \\ \times (1-2\alpha)^{\frac{1}{2\kappa}-1} \left(\frac{1-w}{1-\alpha} \rho \right)^{\frac{1}{\kappa}} \left(\frac{1}{2} \frac{\dot{\alpha}}{\alpha} + \frac{\dot{\alpha}}{1-\alpha} \right. \\ \left. \left. \times \frac{1-2\alpha+w}{1-w} + \frac{\dot{w}-2\dot{\alpha}}{1-w} + 3aH(2-4\alpha+w) \right) \right] \\ \left. \times (a(\xi)) \right\} \end{aligned}$$

and $U(\phi, \xi) = [\Phi(\phi) + \Xi(\xi)]^\kappa$, $\kappa = const$, $X_\phi = \beta$ yields:

$$\begin{aligned} U(\phi, \xi) = \frac{1}{\kappa^\kappa} \left\{ \pm \int d\phi \left[\frac{1}{a} \sqrt{2\beta} (\rho + \beta)^{\frac{1}{2\kappa}} \right. \right. \\ \times (-\rho w + \beta)^{\frac{1}{2\kappa}-1} \left(3aH + \frac{1}{2} \frac{\dot{\beta}}{\beta} \right) \right] (a(\phi)) \\ \mp \int d\xi \left[\frac{1}{2a} \sqrt{\rho(1+w) + 2\beta} (\rho + \beta)^{\frac{\kappa+1}{2\kappa}} \right. \\ \times (-\rho w + \beta)^{\frac{1}{2\kappa}-1} \left(\frac{\rho(\dot{w} - 3aH(1+w)^2) + 2\dot{\beta}}{\rho(1+w) + 2\beta} \right. \\ \left. \left. + 3 \frac{aH(1-w)\rho - 6aH\beta - \dot{\beta}}{\rho + \beta} \right) \right] (a(\xi)) \right\}. \end{aligned}$$

It is clear that for the multicomponent cosmological models with realistic parametrizations of the dark energy EoS crossing -1 (CPL, WMAP5) these expressions are not suitable for practical use since even for $\alpha = const$ or $\beta = const$ the integrals cannot be solved analytically. Thus, to reconstruct the potentials for certain values of cosmological parameters and

dependences $w(a)$ and $\alpha(a)$ or $\beta(a)$ we have to use the parametric dependences (7), (11), (12) or (9), (13), (14) which define the potential $U(\phi, \xi)$.

4. Conclusion

In the reconstruction of potential of the proposed 2-field model of dark energy with classical and tachyonic kinetic terms there are 2 ambiguities requiring additional assumptions: about the form of $U(\phi, \xi)$ and about the dependence of a kinetic term on the scale factor. The third ambiguity – a sign in front of the integrals in (11)-(14) – is less important since the potentials with “+” and “-” are symmetric with respect to $\phi = 0$ and $\xi = 0$. For 3 ansatzes for the form of $U(\phi, \xi)$ we obtained the reconstructed potentials in explicit form and in parametric one that is suitable for multicomponent cosmological models and all parametrizations of the dark energy equation of state.

Acknowledgements. This work has been supported in part by the Department of target training of Taras Shevchenko National University of Kyiv under National Academy of Sciences of Ukraine (project 6Φ).

References

- Andrianov A.A., Cannata F., Kamenshchik A.Y. et al. 2008, *J. Cosmol. Astropart. Phys.*, **02**, 015.
 Amendola L. 2000, *Phys. Rev. D*, **62**, 043511.
 Chevallier M. & Polarski D. 2001, *Int. J. Mod. Phys. D*, **10**, 213.
 Creminelli P., D’Amico G., Norena J. et al. 2009, *J. Cosmol. Astropart. Phys.*, **02**, 018.
 Deffayet C., Pujolas O., Sawicki I. et al. 2010, *J. Cosmol. Astropart. Phys.*, **10**, 026.
 Easson D.A. & Vikman A. 2016, arXiv:1607.00996 [gr-qc].
 Feng B., Wang X., Zhang X. 2005, *Phys. Lett. B*, **607**, 35.
 Komatsu E., Dunkley J., Nolta M.R. et al. 2009, *Astrophys. J. Suppl. Ser.*, **180**, 330.
 Linder E.V. 2003, *Phys. Rev. Lett.*, **90**, 091301.
 Novosyadlyj B. & Sergijenko O. 2009, *Journal of Physical Studies*, **13**, 1902.
 Pettorino V. & Baccigalupi C. 2008, *Phys. Rev. D*, **77**, 103003.
 Sergijenko O. & Novosyadlyj B. 2008, *Kinematics and Physics of Celestial Bodies*, **24**, 259.
 Vikman A. 2005, *Phys. Rev. D*, **71**, 023515.

DOI: <http://dx.doi.org/10.18524/1810-4215.2018.31.144738>

NUMERICAL ESTIMATOR FOR LARGE-SCALE COSMIC STRUCTURES

A. V. Tugay¹, N. G. Pulatova², A. D. Zhoga¹

¹ Taras Shevchenko National University of Kyiv,
Glushkova 4, Kyiv, 03022, Ukraine, tugay.anatoliy@gmail.com

² Main Astronomical Observatory,
Zabolotnogo, 27, Kyiv, 03143, Ukraine, nadya@mao.kiev.ua

ABSTRACT. Components of large-scale structure (LSS) of Universe includes galaxy clusters, walls, filaments, groups and field galaxies. The question of spatial organization of all these components remains open despite of a number of recently developed methods of LSS analysis. In this paper we introduce new continuous structural parameter of galaxy distribution for the determining of the type of LSS surrounding. This parameter is based on comparison of the radial distribution of galaxies around the certain point with the uniform one. Our method for structure parameter calculation is based on the distribution of 1000 closets galaxies to the selected one. Such number was selected because most galaxy clusters contains up to 1000 galaxies. When we exceed 1000th closest galaxy we will leave possible cluster or filament and will pass to another type of LSS. We suppose that in uniform distribution of galaxies their number should increase as third power a distance, similar to luminosity. Therefore the inverse dependence of galaxy distance from number should be cubic root. New structural parameter was introduced as the difference of this dependence of cubic root.

The main type of cosmic surrounding for a galaxy is defined by the value and the sign of such structural parameter. If a galaxy lie in a cluster the distances of nearby galaxies will be less than cubic root. We integrated distance difference for all 1000 galaxies and get negative structural parameter in this case. If a galaxy lie in a void, the distances of surrounding galaxies will be larger than cubic root. In such case the structural parameter will be positive.

New parameter was calculated for sky distribution of SDSS galaxies at distances from 50 to 150 Mpc. Analysing obtained values, we come to conclusion that our structural parameter can be used for the division of LSS components and extragalactic filament detection.

Keywords: large-scale structure of Universe, galaxies, filaments.

АБСТРАКТ. Компоненти великомасштабної структури Всесвіту (ВМС) включають скупчення галактик, стіни, філаменти, групи і галактики поля. Питання про просторове розташування всіх цих компонент залишається відкритим незважаючи на велику кількість сучасних методів аналізу ВМС. У даній роботі ми вводимо новий неперервний структурний параметр розподілу галактик для визначення типу оточення у ВМС. Визначення параметру полягає у порівнянні радіального розподілу галактик навколо заданої точки з однорідним розподілом. При обчисленні структурного параметра для обраної галактики використовується розподіл тисячі найближчих до неї галактик. Таке число було вибрано оскільки більшість скупчень містять до тисячі галактик. Після вичерпання тисячі найближчих галактик можливе скупчення або філамент має закінчитися і ми перейдемо до інших елементів ВМС. Ми припускаємо, що у випадку однорідного розподілу кількість галактик (а також їх повна світність) має зростати пропорційно кубу відстані. Отже, обернена залежність відстані галактики від її порядкового номера має бути близька до кубічного кореня. Новий структурний параметр вводиться як інтеграл відхилення цієї залежності від кубічного кореня.

Тип великомасштабного оточення галактики визначається величиною і знаком структурного параметра. Якщо галактика знаходиться у скупченні, відстані сусідніх галактик будуть менші, ніж за усередненою залежністю з кубічним коренем. При додаванні різниць двох залежностей для тисячі галактик отримується від'ємний структурний параметр. Якщо ж галактика знаходиться у voidі, відстані сусідніх галактик будуть більші за кубічний корінь з номера. У цьому випадку структурний параметр буде додатним.

Новий параметр був обчислений для розподілу по небу галактик SDSS на відстанях від 50 до 150 Мпк. Аналіз отриманих значень дозволяє зробити

висновок про те, що такий параметр може бути використаний для розділення компонентів ВМС і виявлення міжгалактичних філаментів.

Ключові слова: великомасштабна структура Всесвіту, галактики, філаменти.

1. Introduction

Large-scale structure (LSS) of Universe is complex but mostly covered from direct optical observations. Galaxies are the only type of light emitting sources at cosmological scale, but they possess minor part of total mass of matter. In some special cases it is possible to find the distribution of dark matter in galaxy clusters by peculiar velocities or gravitational lensing (Kaiser, 1993; Parnovsky, 2004). There are different views on distribution of LSS elements. Results of analysis of observations and simulations are controversial. The most common view on LSS is to consider voids bordered by walls, walls consisting from filaments and filaments which has clusters, groups and field galaxies. In this work we propose a method for numerical evaluating the type of LSS element for any point of extragalactic space based on the coordinates of nearby galaxies. The method was tested with modern catalogs of isolated galaxies (Karachentseva, 2010; Karachentsev, 2011).

2. Types of LSS elements and methods of their description

In the first case of uniform distribution of galaxies in space we will consider the luminosity of galaxies as the main observable parameter. For physical analysis of LSS evolution the mass is more important, but it can be evaluated correct for very little part of galaxies. The study of mass/luminosity ratio is wide and complex direction of extragalactic astronomy (Girardy, 2000) but in this work we will explain LSS only by the distribution of visible light of galaxies. Moreover, in the current paper we will assume that all galaxies has the same luminosity and hence the large-scale cosmic structures will be analysed only by galaxy positions and density. If all galaxies are identical and little enough, their total number and luminosity will increase as the third power of radial distance. Such uniform distribution should be tested for observable Universe at the scales much less and larger than 100 Mpc, the main scale of cosmic web. If the number of galaxies around the chosen point grow as the first power of distance, nearby LSS should be considered as one-dimensional, i.e. filament. If luminosity increase as squared radius, such region will be called a wall.

To determine the morphological type of local LSS we build the cumulative luminosity function (CLF) for the

chosen point. As it was mentioned before, we count only the number of galaxies but not magnitudes and M/L relation for CLF estimation. An excess or depression could be found for CLF at lower scales. If there is an excess we can say that chosen point (or central galaxy) lies in cluster. If there is a depression, then the galaxy should be located in the void. Now we introduce the large-scale structural parameter as normalized depression at cumulative luminosity function. It should have largest values for isolated galaxies and low (negative) values for cluster galaxies. The main cases of possible usage of structural parameter are the following.

1. One LSS element in uniform matter distribution. We can find its type by local power index of CLF and the value of the structural parameter. The shape of CLS is important for detailed description of current structure. For example, it is possible to detect galaxy cluster and to select appropriate radial profile of dark matter distribution for it. For detailed description of each LSS element a number of numerical structural parameters are needed, but even two parameters can not be calculated for real data of galaxy observations.

2. Complex system of LSS elements repeating periodically in the space. Suppose that void has radius R and walls are thin. Then we should not build CLF for distances larger than $2R$. We can expect large number of observable galaxies at this range for the Local Universe. By the CLF shape it is possible to describe LSS in details. But in the ultimate worst case there could be no galaxies at all. Such opposite situations lead to the following issues. It was supposed above that all galaxies are similar. But if we will consider the brightest galaxies (for periodic LSS), each of them will be the central galaxy of a cluster at the intersection of some number of voids, walls and filaments. For example, in graphite-like spatial grate each cluster is the point of connection of 4 voids, 6 walls and 4 filaments. The number of mentioned brightest galaxies should be proportional to the number of voids. For the current state of observational astronomy it is easy to find a distance at which even one observed galaxy per void or cluster can not be guaranteed. This distance is a limit of any assumption of uniform distribution of galaxy positions and luminosities.

3. Discrete distribution of different single galaxies behind the mentioned limit. That galaxies are very bright and tends to have random distribution. Is it possible calculate their structural parameters and put them to some place in LSS? Consider a galaxy, its nearest neighbour and the luminosities of these two. It is important to measure the minimal distance between galaxies in the units of void radius. This parameter can be used for the description of distant Universe instead of CLF shape. The brightest galaxies in the Universe will appear once per many LSS cells. Very probably they will be beamed AGNs and this is only one from a

number of selection effects at such large distances. In this extreme case of many cells between two uniquely bright galaxies we can fill space between them with normal distribution of faint galaxies with some upper luminosity limit. It will be some kind of model of distant galaxy distribution with apriori parameters. In the rest part of a paper we will consider parameters of galaxy distribution from much closer region.

In this paper we describe LSS by special structural parameter anticorrelated with density contrast of dark matter mass and galaxy luminosity. Consider a list of cosmic structures in the order of increasing isolation.

1. Central galaxy of a cluster
2. Galaxy near the cluster center
3. Galaxy in the periphery of cluster
4. Galaxy in a group
5. Galaxy in a pair or triplet
6. Field galaxy in the filament
7. Isolated galaxy in the wall
8. Isolated galaxy in the void

We suppose here that LSS consist from cells with walls at the borders and voids inside the cells. Walls themselves consist from filaments. Groups and clusters may appear in the filaments according to necklace model. The largest clusters tends to be found at the intersection of filaments. In this work we will consider the following LSS elements:

1. Cluster. Galaxy is counted as galaxy in cluster if it can pass cluster diameter at Hubble time. Galaxies in cluster are tied by common gravity field. So groups, triplets, pairs and interacting galaxies are considered as clusters. Cluster is compact overdensity in spatial galaxy distribution. It can be surrounded by ellipsoid with some limit ellipticity.

2. Filament. It is one-dimensional galaxy overdensity. Filament can be curved but we can not describe the shape of filament with our structural parameter. According to inconsistency of different methods for filament detection from observational data, the locations and forms of certain real filaments seems to be doubtful. Structural parameter, introduced in the present work, is the next attempt to distinguish filaments from visible galaxy distribution.

3. Wall. Although filaments may not so obvious, there are well defined underdensities in the Universe i.e. voids. The volume between voids is much larger than the volume of clusters. This volume is generally referenced as walls. It is natural to consider the walls as two-dimensional overdensities.

4. Voids should contain isolated and field galaxies but not clusters and groups. There is a problem to locate the border between void and wall. For example, in the case of two nearby maximums in the distribution of structural parameter, then they should be assigned as voids and the space between them should include the wall.

These elements describe a medium in which the structural parameter is calculated. Its value increases from cluster to void. The method of normalization of our structural parameter is the following. To reduce the effect of peculiar velocities in redshift space, we take a sample of galaxies in 100 Mpc redshift span and don't use their distances at the next stages. This corresponds to suggestion that all galaxies of our sample lie in a single layer of LSS. Hence all galaxies are placed on celestial sphere with the radius equal to unity. Then the normalized distances were found from one selected galaxy to another $N=1000$ nearby galaxies. Such distances (R) are measured in angular units i.e. radians. The averaged angular distance of nearby galaxies is an extra value for local LSS description. The value of the structural parameter is an integrated difference of cubic root function from $R(N)$ dependence. So this value is the excess of average angular distance above uniform distribution.

3. Distribution of structural parameter for real galaxies

To estimate optimal distance range for CLF and structural parameter calculation we found the following bounds. HyperLeda extragalactic database contains 18619 galaxies within $v_{3k}=3500$ km/s that corresponds Local Supercluster. We illustrate the completeness of current observational data with D/L relation, where D is average distance between nearest observable galaxies and $L=100$ Mpc - the size of cosmic web cell. At $z=0.2$ (6 layers of superclusters) the ratio $D/L=0.2$ and at $z=1$ $D/L=4$. There are 3 layers and 180 voids at low redshift ($z<0.1$) with 1000 galaxies per void. According such relations we concluded that the method of CLF analysis is correct at distances up to 1000 Mpc.

In this work we selected from HyperLeda database redshift region from 3000 to 10000 km/s that corresponds to Coma supercluster position. It is the most appropriate sample of galaxies for LSS study (Tugay, 2012; Tugay, 2014).

We find three main types of $R(N)$ dependences.

1. Cluster-like galaxy surrounding. The most galaxies has distances less than cubic root and structural parameter is negative. An example of such dependence is shown in a Fig. 1.

2. Void-like surrounding. The most galaxies has distances larger than cubic root and structural parameter is positive (Fig. 2).

3. Intermediate case in which $N(R)$ dependence intersect cubic root one or more times (Fig. 3). In such case structural parameter may lie in wide range of positive and negative values. The distribution of number of intersections from structural parameter is shown at Fig. 4. The value of structural parameter is the difference of galaxy angular distance (in radians) from cubic

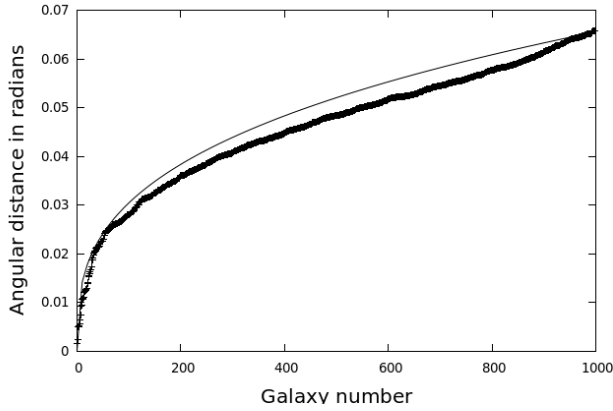


Figure 1: Cumulative luminosity function for a galaxy in cluster-like surrounding.

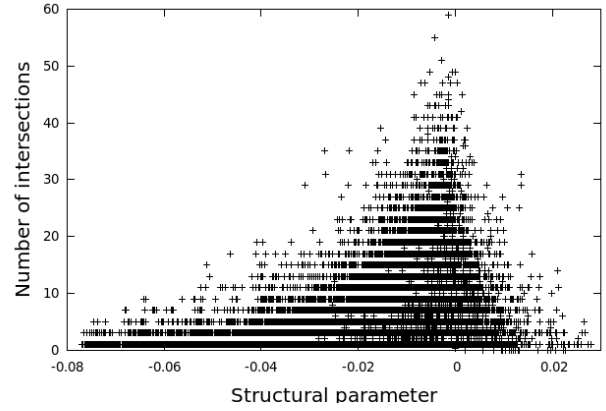


Figure 4: Distribution of number of intersections from structural parameter.

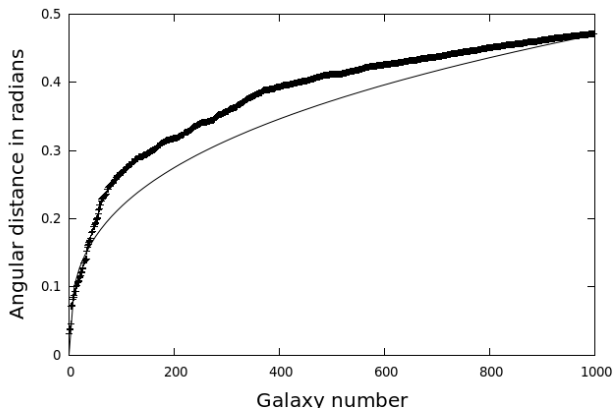


Figure 2: CLF for a galaxy in void-like surrounding.

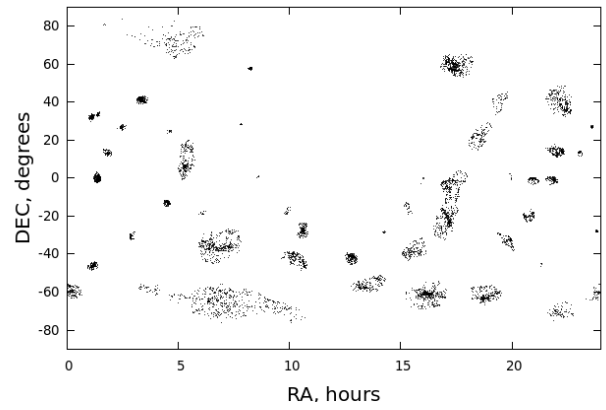


Figure 5: Sky distribution of HyperLeda galaxies with lowest value of structural parameters.

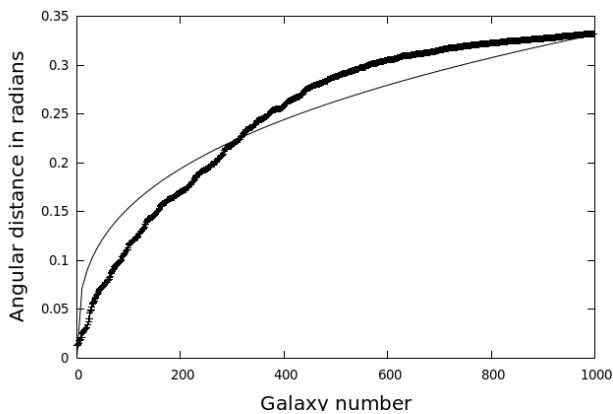


Figure 3: The intersection of uniform relation by CLF should be referred as wall or filament.

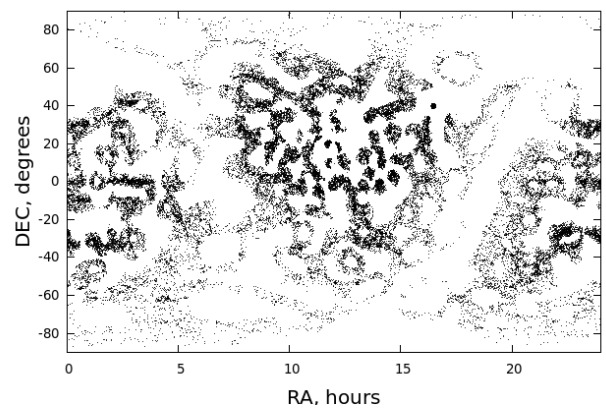


Figure 6: Regions with possible filaments.

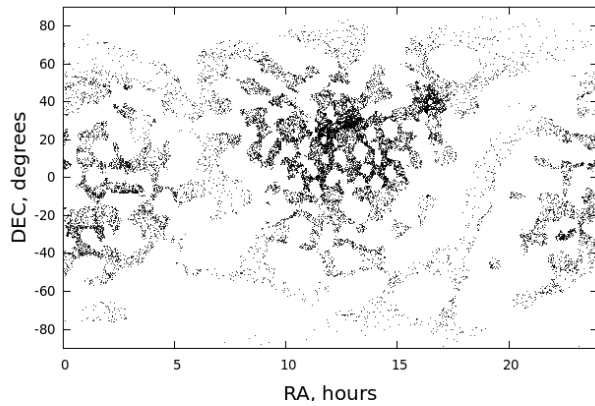


Figure 7: Void candidates according to largest values of structural parameter.

root function averaged for one thousand nearby galaxies. To distinguish void-like regions we selected the values of structural parameter less than -0.03 . Negative values from -0.03 to 0 were considered as corresponding to filament, wall or group regions.

Galaxies in void-like surrounding has much larger distances to neighbours. We analysed the distances to 1000th closest galaxy as secondary structural parameter (SSP). To estimate how CLF characterise isolated galaxies, SSP was also calculated for 2MASS selected isolated galaxy catalog 2MIG (Karachentseva, 2010). Results are presented in Table 1. SSP is systematically larger for 2MIG galaxies.

Table 1: Secondary structural parameter for HyperLeda and 2MIG galaxies measured in centiradians (34 arcmin). SSP is angular distance to 1000th nearest galaxy. HL-2MIG is HyperLeda sample without 3227 galaxies with largest SSP. Only minor part of these galaxies are 2MIG members.

| Sample | HyperLeda | 2MIG | HL-2MIG |
|------------------|-----------|---------|---------|
| Num. of galaxies | 89904 | 3227 | 86677 |
| Minimal SP | 1.1 | 4.5 | 1.1 |
| Average SP | 11.1496 | 16.8932 | 10.9358 |
| Error of avg.SP | 0.0161 | 0.1171 | 0.0159 |
| Scatter | 4.8 | 6.7 | 5.0 |
| Maximal SP | 38.1 | 38.1 | 22.4 |

Sky distributions of galaxies with different values of structural parameter are presented at Fig 5-7. These distributions leads to the following conclusions.

1. Structural parameter is smooth continuous value. Largest clusters, such as Coma at Fig. 7, can not be detected with it.

2. Cluster-like regions represents systematical effects of HyperLeda sky coverage and has minor correlation with real clusters.

3. The most clear picture of cosmic web can be seen only in the zone of SDSS coverage ($120 < RA < 240$ deg, $0 < DEC < 60$ deg), where observational data are the most dense and uniform. Regions of intermediate values of structural parameter could be used for filament detection.

4. Conclusion

We developed a new method for LSS description by the distribution galaxy positions. New structural parameter can be used for defining LSS elements at distances up to 1000 Mpc.

References

- Girardi M., Borgani S., Giuricin G. et al.: 2000, *ApJ*, **530**, 62.
 Kaiser N., Squires G.: 1993, *ApJ*, **404**, 441.
 Karachentsev I.D., Makarov D.I., Karachentseva V.E., Melnyk O.V.: 2011, *Astrophysical Bulletin*, **66**, 1.
 Karachentseva V.E., Mitronova S.N., Melnyk O.V. & Karachentsev I.D.: 2010, *ASPC*, **421**, 11.
 Parnovsky S.L., Tugay A.V.: 2004, *AstL*, **30**, 357.
 Tugay A.V.: 2012, *Odessa Astron. Publ.*, **25**, 142.
 Tugay A.V.: 2014, *Advances in Astronomy and Space Physics*, **4**, 42.

DOI: <http://dx.doi.org/10.18524/1810-4215.2018.31.144692>

X-RAY EMISSION OF ICRF SOURCES

V. V. Voitsekhovskiy¹, A. V. Tugay¹, V. V. Tkachuk¹, S. Yu. Shevchenko²¹ Taras Shevchenko National University of Kyiv, Kyiv, Ukraine,
*tugay.anatoliy@gmail.com*² Schmalhausen Institute of Zoology, Kyiv, Ukraine,
astromott@gmail.com

ABSTRACT. Considering increasing requirements to the coordinates measurement precision by the end of XX century International Astronomical Union commenced implementation of the new astrometric system ICRF (International Celestial Reference Frame). This quasi-inertial reference frame system centered in the barycenter of the Solar System and has axes defined by the positions of distant extragalactic sources – frames. Unlike equatorial system ICRF has no shortcomings of the coordinates identification due to the Earth axis precession, stellar proper motions and other factors. Extragalactic frames of the ICRF system are mostly quasars, radio galaxies, blazars and Seyfert galaxies i.e. different types of the active galaxy nuclei (AGN). Active galaxy nuclei are characterized by processes with significant. Such processes quite often are followed by X-ray emission generation. The purpose of this work is to consider X-ray emission of ICRF sources and features of their possible proper motions. Among 295 selected reference frames of the system we identified 54 X-ray sources which were observed by space observatory XMM Newton and noticed rapid variability of the blazars 2E 2673 (W Com) and 2E 1802 which enables to conclude that they have some very active processes in the sources centers. With regards to the future more detailed analysis we believe that evidences of the objects proper motion could be found in their spectra. Based on the constructed luminosity and spectral graphs we could conclude that apart from above mentioned AGNs rest 52 objects do not show variability and special attention should be paid to blazars within ICRF system development and use. Major part of the X-ray sources between the reference frames are stable.

Keywords: ICRF, reference systems, galaxies: active, X-rays: galaxies.

АБСТРАКТ. Зважаючи на зростаючі вимоги до точності вимірювання координат, наприкінці XX століття Міжнародний Астрономічний союз запровадив нову астрометричну систему ICRF (International Celestial Reference Frame). Ця

квазіінерціальна система координат має центр в барицентрі Сонячної системи та її вісі визначаються положенням віддалених позагалактичних джерел – фреймів. На відміну від екваторіальної системи, ICRF позбавлена недоліків визначення координат, що пов'язані з прецесією, власним рухом зірок та іншими факторами. Позагалактичні джерела системи ICRF являють собою, як правило, квазари, радіогалактики, блазари і сейфертівські галактики, тобто різні типи активних ядер галактик. Активні ядра галактик (АЯГ) характеризуються процесами з значними швидкими рухами. Такі процеси часто супроводжуються виникненням рентгенівського випромінювання. Метою даної роботи є вивчення рентгенівського випромінювання джерел ICRF та особливості їх можливого власного руху. Серед 295 визначених опорних фреймів системи ми знайшли 54 рентгенівських джерела, які спостерігалися космічною обсерваторією XMM-Newton та встановили, що швидку мінливість спектру мають блазари 2E 2673 (W Com) та 2E 1802, що дозволяє зробити висновок про дуже активні процеси в центрі джерел. З огляду на проведення більш повного аналізу ми вважаємо, що можуть знайтися свідчення власних рухів в їх спектрах. Базуючись на побудованих кривих блиску та спектрах можна зазначити, що окрім вищенаведених активних ядер галактик 52 об'єкти не демонструють змінності. Ми прийшли до висновку, що в рамках розробки та використання системи ICRF необхідно приділяти особливу увагу блазарам. Більшість рентгенівських джерел в опорних фреймах системи є стабільними.

Ключові слова: ICRF, система опорних координат, галактики: активні, рентгенівське випромінювання: галактики.

1. Introduction

ICRF is a frame of reference defined by the positions of extragalactic sources. The most appropriate extragalactic sources should be very luminous so it is

obvious that many of them are active galactic nuclei (AGNs). They always has some active processes and rapid motion in the center.

Active galactic nuclei are complex phenomena. At the heart of an AGN there is a relativistic accretion disk around the spinning supermassive black hole. In the center of the galaxy the emissions of relativistic particles occurs as narrow and uniform brightness jets. Curious that, their observation may indicate that the center of image is moving with speed over the speed of light (Schneider, 2006). The explanation of this effect is that we can only observe the movement of a projection on area perpendicular to the field of vision. The effect of "superluminal" expansion is observed in jets moving toward the observer at a small angle to the line of sight. Blazars has the smallest value of this angle among other types of AGNs, so we considered to check spectra for available BL Lacs in ICRF to identify possible motion.

The accuracy of ICRF is 40 microarcsec¹. AGN with typical redshift $z=1$ may have relativistic radiojet with knots passing through this angle in few years. Such relativistic motion in the AGNs could be detected by astrometric methods in the nearest future. Some signs of these processes can be checked in X-ray band. X-ray emission is generated in the very center of AGN and is influenced by the fastest motion of the matter. The aim of this work is to consider X-ray emission of ICRF sources and to look for signs of their possible proper motion. For this purpose we used 3XMM-DR4 catalog (Rosen et al., 2015) of X-ray sources based on observational data from modern space observatory XMM-Newton. We checked light curves of all X-ray ICRF sources and made certain conclusions about their stability.

2. Identification and analysis of X-ray ICRF sources

Initial phase of our work was to find ICRF sources in 3XMM-DR4 catalog. Current version of ICRF (ICRF2) composed by 3414 sources² and 3XMM-DR4 catalog contains 372728 individual sources. Using X-ray and optical galaxies from cross-identification sample (Tugay, 2012) we found that 54 of ICRF sources are listed in the 3XMM-DR4 catalog. 33 sources of the sample have only one XMM observation and the rest 21 sources have two observations each. General parameters of these sources are presented in the Table 1 below. We reviewed X-ray light curves of these sources using LEDAS database and found that most of them are constant. The deviation of mean X-ray flux of 52 objects during the whole observation does not exceed the half of rms scatter. The example

¹<http://hpiers.obspm.fr/icrs-pc/>, 'ICRF2' chapter

²<http://rorf.usno.navy.mil/ICRF2/>

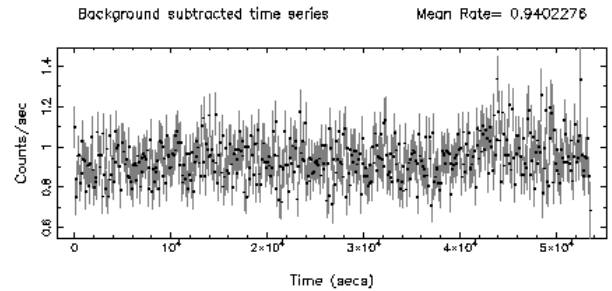


Figure 1: Light curve of OJ287. Example of stable X-ray source.

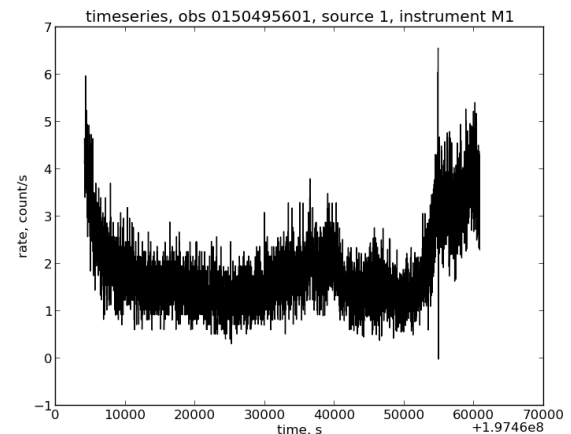


Figure 2: Light curve of 2E 1802 from MOS1 camera. The time at Fig. 2 and 3 is measured in seconds from 01.01.1998.

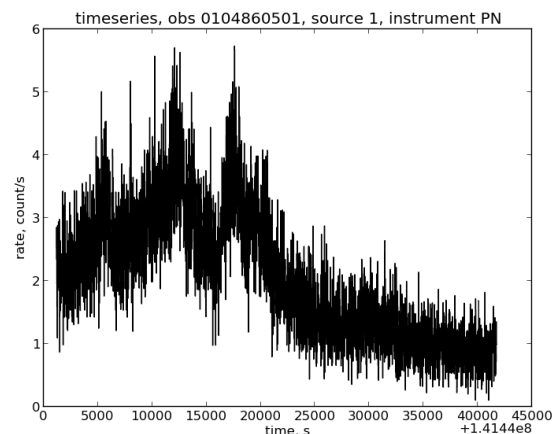


Figure 3: Light curve of W Com from PN camera.

of constant X-ray light curve is presented at Fig. 1. However, we found X-ray variability of 2E 1802 and

Table 1: List of X-ray ICRF sources.

| N | XMM ID | SIMBAD type | Name | z |
|-----|------------------|--------------|----------------|--------|
| 1. | J001031.0+105829 | Seyfert 1 | Mrk 1501 | 0.090 |
| 2. | J003824.8+413706 | Quasar | 5C 3.50 | 1.353 |
| 3. | J005748.8+302108 | Galaxy | IAU 0057+3021 | 0.016 |
| 4. | J012642.7+255901 | Quasar | 4C 25.05 | 2.358 |
| 5. | J014922.3+055553 | Quasar | QSO B0146+056 | 2.347 |
| 6. | J015002.6-072548 | Seyfert 2 | IAU 0150-0725 | 0.017 |
| 7. | J022239.6+430207 | BL Lac | 3C 66A | 0.340 |
| 8. | J023838.9+163659 | BL Lac | 2E 618 | 0.940 |
| 9. | J024008.1-230915 | Quasar | 2E 638 | 2.225 |
| 10. | J024457.6+622806 | Seyfert 1 | 2E 653 | 0.044 |
| 11. | J031155.2-765150 | BL Lac | 2E 746 | 0.223 |
| 12. | J031301.9+412001 | Seyfert 1 | QSO B0309+411 | 0.136 |
| 13. | J040748.4-121136 | Seyfert 1 | 2E 938 | 0.572 |
| 14. | J044017.1-433308 | Quasar | 2E 1127 | 2.852 |
| 15. | J052257.9-362730 | BL Lac | 2E 1263 | 0.055 |
| 16. | J053056.4+133155 | Quasar | 2E 1289 | 2.070 |
| 17. | J053954.2-283955 | Quasar | 2E 1496 | 3.103 |
| 18. | J072153.4+712036 | BL Lac | 2E 1802 | 0.300 |
| 19. | J084124.3+705342 | Quasar | 4C 71.0 | 2.172 |
| 20. | J085448.8+200630 | BL Lac | OJ 287 | 0.306 |
| 21. | J095456.8+174331 | Quasar | QSO B0952+179 | 1.475 |
| 22. | J095524.7+690113 | Super Nova | SN 1993J | 0.0001 |
| 23. | J104117.1+061016 | Quasar | 2E 2303 | 1.270 |
| 24. | J105829.6+013358 | BL Lac | 4C 01.28 | 0.185 |
| 25. | J112027.8+142054 | LINER | 4C 14.41 | 0.362 |
| 26. | J113007.0-144927 | Quasar | 2E 2471 | 1.189 |
| 27. | J121923.2+054929 | LINER | NGC 4261 | 0.007 |
| 28. | J122006.8+291650 | LINER | NGC 4278 | 0.002 |
| 29. | J122131.6+281358 | BL Lac | 2E 2673 | 0.102 |
| 30. | J122222.5+041315 | Quasar | 4C 04.42 | 0.965 |
| 31. | J122906.6+020308 | BL Lac | 3C 273 | 0.173 |
| 32. | J123959.4-113722 | LINER | M 104 | 0.003 |
| 33. | J124646.8-254749 | Quasar | QSO B1244-25 | 0.638 |
| 34. | J125359.5-405930 | Quasar | QSO B1251-407 | 4.464 |
| 35. | J125611.1-054721 | Quasar | 3C 279 | 0.536 |
| 36. | J130533.0-103319 | Seyfert 1 | 2E 2966 | 0.278 |
| 37. | J131028.6+322043 | BL Lac | 2E 2979 | 0.997 |
| 38. | J132527.6-430108 | Seyfert 2 | CENTAURUS A | 0.001 |
| 39. | J132616.5+315409 | Radio Galaxy | 4C 32.44 | 0.370 |
| 40. | J140700.3+282714 | BL Lac | Mrk 668 | 0.076 |
| 41. | J140856.4-075226 | Quasar | QSO B1406-076 | 1.493 |
| 42. | J143023.7+420436 | Quasar | 7C 1428+4218 | 4.705 |
| 43. | J151002.9+570243 | Quasar | 1E 1508.7+5714 | 3.880 |
| 44. | J160913.3+264129 | Radio Galaxy | PKS 1607+268 | 0.473 |
| 45. | J165352.2+394536 | BL Lac | Mrk 501 | 0.033 |
| 46. | J170934.3-172853 | Quasar | IAU 1709-1728 | 0.560 |
| 47. | J184208.9+794617 | Seyfert 1 | 2E 4136 | 0.056 |
| 48. | J201114.2-064403 | Radio Galaxy | PKS 2008-068 | 0.547 |
| 49. | J212912.1-153841 | Quasar | 2E 4479 | 3.268 |
| 50. | J213032.8+050217 | Quasar | IAU 2130+0502 | 0.990 |
| 51. | J215155.5-302753 | Quasar | QSO B2149-307 | 2.344 |
| 52. | J220314.9+314538 | BL Lac | 4C 31.63 | 0.295 |
| 53. | J225357.7+160853 | Quasar | 3C 454.3 | 0.859 |
| 54. | J235509.4+495008 | Seyfert 2 | IAU 2355+4950 | 0.237 |

Table 2: Spectral properties of ICRF BL Lacs. Normalisation unit is $10^{-5} \text{cm}^{-2} \text{s}^{-1} \text{keV}^{-1}$

| <i>Object</i> | $n_H, 10^{20} \text{cm}^{-2}$ | Normalisation | <i>PhotonIndex</i> | $\chi^2/\text{d.o.f.}$ |
|---------------------------------------|-------------------------------|----------------|--------------------|------------------------|
| 3C66A | 7.47 ± 0.49 | 66.2 ± 2.9 | 2.5 ± 0.04 | 1.0698 / 173 |
| 2E618 (Grandi, 2006) | 1.34 ± 0.03 | | 1.55 ± 0.02 | 0.857 / 109 |
| 2E1263 (Winter, 2010; Cusumano, 2010) | 6 ± 1 | | 2.14 ± 0.01 | 3.65 / 336 |
| 2E1802 (Baumgartner, 2012) | 3.81 ± 0.42 | | 2.7 ± 0.01 | 9.22 / 89 |
| OJ287 | 20 ± 4 | 44.6 ± 1.1 | 1.75 ± 0.01 | 3.046 / 324 |
| 4C01.28 | 1.89 ± 0.23 | 55.8 ± 1.5 | 1.814 ± 0.018 | 1.0073 / 305 |
| 2E2673 (Piconcelli, 2002) | 0.64 ± 0.37 | | 1.32 ± 0.09 | 1.73 / 196 |
| 3C273 (Reeves, 2000; Donato, 2001) | 1.79 ± 0.2 | | 1.55 ± 0.02 | 0.857 / 1093 |
| 2E2979 | 0.432 ± 1.28 | 74.5 ± 1.3 | 1.668 ± 0.011 | 1.0655 / 399 |
| Mrk668 | <0.01 | 2.2 ± 0.66 | 0.98 ± 0.13 | 2.905 / 8 |
| Mrk501 | 2.70 ± 0.07 | 991 ± 40 | 2.49 ± 0.06 | 1.7800 / 316 |

2E 2673 (W Com) blazars during XMM observations dated 04.04.2004 and 22.06.2002 respectively (Fig. 2-3). Such variability can not be explained by soft proton solar flares which were observed for a number of other ICRF sources. So these two blazars are typical examples of the most active galactic nuclei with rapid and powerful processes in the center. Other blazars may also have variability out of XMM observation time. We analyzed spectra of all blazars from our sample to check any possible special features and to reveal some additional unusual objects. We applied standard XMM SAS software to fit two-parametric power law model of X-ray continuum with hydrogen absorption at low energies. The results of spectral fitting are given in the Table 2 and some examples of spectra are shown on Figs. 4-6. All blazar spectra have a good approximation by our simple model. We assume that if the spectrum of any blazar is not fitted by such simple model then there is a reason to expect some complex structure of the source and possible variability. Otherwise, we consider the blazar as a typical source and appropriate for ICRF usage.

Spectral parameters are constant in all available XMM observations. So we have found out that X-ray spectra makes no reasons to expect any image motion of these sources in the nearest future. We conclude that current state of spectral analysis doesn't allow to predict a correlation between the spectra parameters and variability.

3. Results and conclusions

In the result of our analysis of light curves and spectral characteristics of ICRF blazars in X-ray band we found rapid variability for 2E 2673 (W Com) and 2E 1802 but no special features in the spectra.

Assuming that the variability of a source in any band should be connected with possible motion of the source (and the center of its image) we might predict that stable source should not have significant motion.

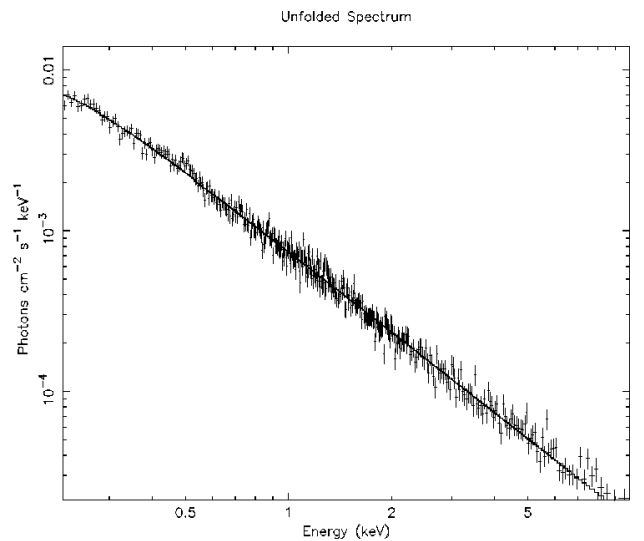


Figure 4: Spectrum of 2E 2979. Example of unabsorbed source.

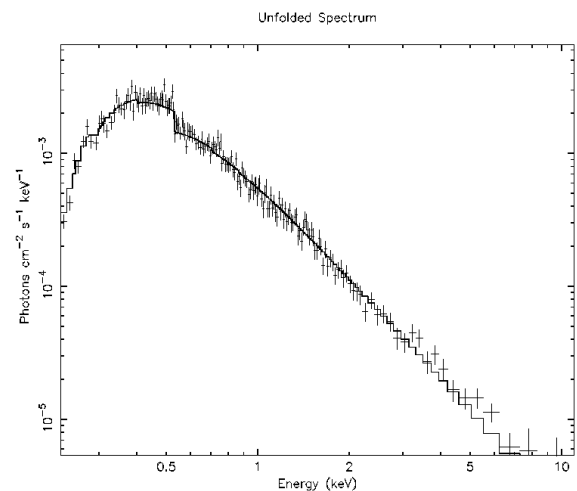


Figure 5: Spectrum of 4C 01.28. Example of absorbed source.

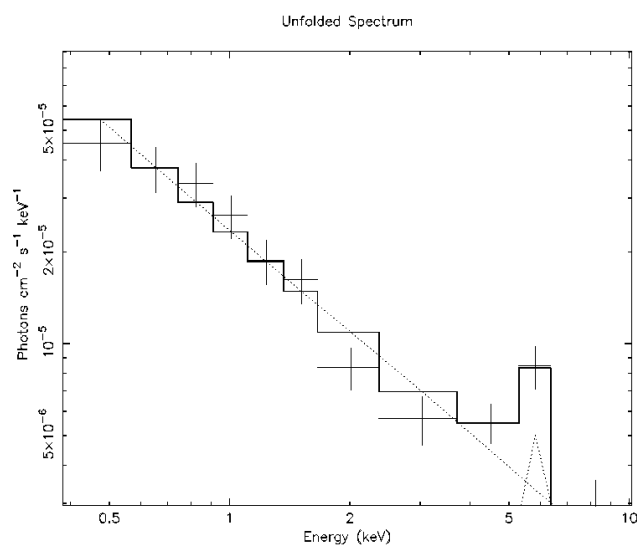


Figure 6: Spectrum of Mrk 668. Example of faint source.

So we conclude (for the moment) that the most of ICRF sources are stable and appropriate as defined sources for astrometric reference systems. Keeping in mind all possible extreme physical processes related to active galactic nuclei, the issue of possible image motion of ICRF sources remains persistent. W Com and 2E 1802 should still be considered as 'suspicious' ICRF sources. Their X-ray variability reveals fast processes in the very center of AGN that could cause detection of the image shift in the future. Future radiotelescopic studies of astrometric defined sources should review more thoroughly not only these two objects but any blazars, since the luminosity variability or even a motion could be detected.

Acknowledgements. The authors are thankful to Vasyly Choliy for motivation to such interesting and actual task.

References

- Baumgartner W. H., Tueller J., Markwardt C. et al.: 2012, *ApJ SS*, **207**, 19.
- Cusumano G., LaParola V., Segreto A. et al.: 2010, *A&A*, **524**, A64.
- Donato D., Ghisellini G., Tagliaferri G. et al.: 2001, *A&A*, **375**, 739.
- Grandi P. & Malaguti G. 2006, *ApJ*, **642**, 113.
- Ma C., Arias E.F., Eubanks T.F. et al. 1998, *ApJ*, **116**, 516.
- Piconcelli E., Cappi M., Bassani L. et al.: 2002, *A&A*, **394**, 835.
- Reeves J.N. & Turner M.L.: 2000, *Mon. Not. R. Astron. Soc.*, **316**, 234.
- Rosen S., Watson M., Pye J. et al.: 2015, *ADASS XXIV Proc.*, 319.
- Schneider P. 2006. 'Extragalactic Astronomy and Cosmology', Springer, Berlin Heidelberg New York.
- Tugay A. 2012. *Odessa Astron. Publ.*, **25**, 142.
- Winter L., Muschoztky R., Reynolds C.R. et al.: 2010, *AIP Conference Proceedings*, **369**, 1248.

DOI: <http://dx.doi.org/10.18524/1810-4215.2018.31.144752>

SIMULATION OF LARGE-SCALE STRUCTURE OF UNIVERSE BY GAUSSIAN RANDOM FIELDS

V. V. Voitsekhovskiy, A. V. Tugay

Taras Shevchenko National University of Kyiv,
Kyiv, Ukraine, tugay.anatoliy@gmail.com

ABSTRACT. Large-scale structure of Universe includes galaxy clusters connected by filaments. Voids occupy the rest of cosmic volume. The search of any dependencies in filament structure can give answer to more general questions about origin of structures in the Universe. This becomes possible because, according to current picture of Universe, one could simulate the evolution of Universe until its very beginning or vice versa. One of the theories which describe the shape of large-scale structures is adiabatic Zeldovich theory. This theory explain three-dimensional galaxy distribution as a set of thin pancakes which were formed from hot primordial gas under own gravitational pressure in the cosmological period of acoustic oscillations. According to cosmological hydrodynamical theories a number of computer simulations of LSS were performed to describe its properties. In this work we consider alternative variant of simulating the distribution of matter that is very similar to real. We simulated two-dimensional galaxy distribution on the sky using random distributions of clusters and single galaxies. The main assumption was that matter clusterised to initial density fluctuations with uniform distribution. According to Zeldovich theory, low-dimensional anisotropies should increase, that corresponds to appearance of filaments in 2D case. Thus we generated a net of filaments between clusters with certain length limits. Real galaxy distribution was simulated by random changing galaxy positions in filaments and clusters. We generated radial distributions of galaxies in clusters taking into account the surrounding and add uniform distribution of isolated galaxies in voids. Our model has been coordinated with SDSS galaxy distribution with using two-point angular correlation function. Parameters of random distributions were found for the case of equality of correlation function slope for the model and for observational data.

Keywords: large-scale structure of Universe, galaxies, filaments.

АБСТРАКТ. Великомасштабна структура Всесвіту включає скупчення галактик, що з'єднані філаменатами. Войди займають решту космічного простору. Пошуки закономірностей у структурі

філаментів можуть дати відповіді на питання щодо походження структур у Всесвіті. Це можливо завдяки чисельним моделюванням Всесвіту від його народження до сучасності і навпаки. Форми великомасштабних структур пояснюються у адіабатичній теорії Зельдовича. В цій теорії тривимірний розподіл галактик утворює сукупність тонких "млинців", що формуються з первинного гарячого газу під дією гравітації у космологічний період домінування акустичних осциляцій. Для опису великомасштабних структур були виконані багаточисленні комп'ютерні симуляції з використанням космологічних гідродинамічних теорій. У даній роботі ми пропонуємо альтернативний метод моделювання розподілу матерії, що дає результат досить близький до реального. Був змодельований двовимірний розподіл галактик по небу на основі випадкових розподілів скупчень і окремих галактик. Використано припущення про те, що матерія збирається у скупчення до первинних флуктуацій густини, що мають рівномірний розподіл. Відповідно до теорії Зельдовича, анізотропія структур нижчої розмірності повинна зростати, що відповідає утворенню філаментів у двовимірному випадку. Тому у даній роботі пропонується генерування мережі філаментів між скупченнями з визначеними обмеженнями довжини. Реальний розподіл галактик був змодельований випадковими зміщеннями положень галактик у філаментах і скупченнях. Радіальні розподіли галактик у скупченнях були згенеровані з врахуванням оточення; додатково був згенерований однорідний розподіл ізольованих галактик. Нова модель була узгоджена з розподілом галактик SDSS шляхом порівняння утової двоточкової кореляційної функції. Параметри випадкових розподілів були визначені для випадку рівності нахилу кореляційної функції моделі і спостережних даних.

Ключові слова: великомасштабна структура Всесвіту, галактики, філаменти.

1. Introduction

Large-scale structure of Universe represents clusters of galaxies divided by large voids. In general it appears as needles-like structure. Non-Hubble galaxy velocities lead to distortion of galaxy distribution in redshift space. A handy way to study LSS is to consider 2D concentric layers (Tugay, 2012). Thickness of the layer is 100 Mpc that are responsible for one galaxy supercluster. In this work we performed two-dimensional simulation of large-scale structure of Universe in one 100 Mpc-thick layer corresponding to single supercluster. A combination of random functions was selected and implemented to simulate SDSS-like galaxy distribution. Resulting distribution was tested with two-point angular correlation function.

2. Description of new method of LSS simulation

We started with random uniform distribution of points which are considered as galaxy groups or clusters. The points were connected with straight filaments if the distance between them lies in some definite range. Then we generated spherical distribution of galaxies in each cluster. The number of galaxies in cluster was selected as power function of number of filaments pointing to this cluster. We find that isolated galaxies are not generated by this method so we generated additional random distribution of galaxies in all volume.

Physical argumentation of our method is the following. Starting points simulate the largest initial density fluctuations. They grow fastest and become interconnected by filaments. If there are a region with a number of fluctuations with many connections that means that it is large overdensity and there should be larger number of galaxies (Doroshkevich, 1980; Kim, 2009). Also there should be small density fluctuations that form isolated galaxies. So we can divide galaxies by three groups: galaxies in clusters, galaxies in filaments and isolated galaxies. If we will exclude from real volume observed clusters and isolated galaxies, only filament galaxies will remain. This gives us general picture of structure and interconnection of different elements of large-scale structure.

3. Realisation of new method

We chose a layer with a thickness of 100 Mpc and filled it with galaxy clusters, filaments and isolated galaxies. Galaxies in clusters and filaments hold a Gaussian distribution. The resulting model has the following parameters.

1. r_1 and r_2 – minimal and maximal distances for filament construction. Filament is constructed if distance between cluster is less then r_2 and larger then r_1 .

This parameters were selected proportional to average distance r between clusters. Initial bounding distances were selected as following:

$$r_1 = \frac{Ar}{2} \quad (1)$$

$$r_2 = 2Ar \quad (2)$$

where A is additional multiplicative factor that was changed from 1 to 0.8 and 1.2. So we used parameter A to set the values of r_1 and r_2 .

2. We change the quantity of galaxies in a cluster – n . Initial value of n is given by formula

$$n = \frac{z^5}{1000} \quad (3)$$

where z is number of filaments that are connected to a cluster. This value was multiplied by factor B close to unity.

3. I – number of field galaxies including isolated.

4. F – number of galaxies in filament. This value is proportional to mass of filament.

5. D – radius of cluster. The distance of galaxy from cluster center was calculated as tangent of random number from 0 to $\pi/2$ multiplied to radius coefficient D . So the half of cluster galaxies lie at the distance no more then D from center. Our initial value for D was 1.4 degrees.

6. N – total number of clusters.

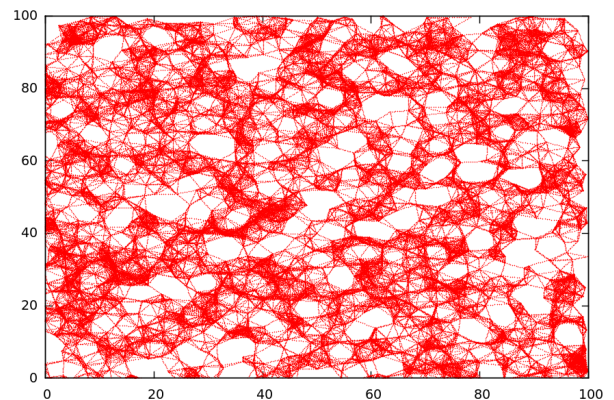


Figure 1: Hexagonal point grid or other simple distribution.

Fig. 1 demonstrate random distribution of points, which coordinates depends on distance between this points and are connected with straight filaments. There are some tendency towards the accumulation and void formation as we can see from this picture of random points distribution. At first we simulated distribution according to initial conditions which reflect cellular structure of Universe. Results obtained by such way are demonstrated at Fig. 1. As we can

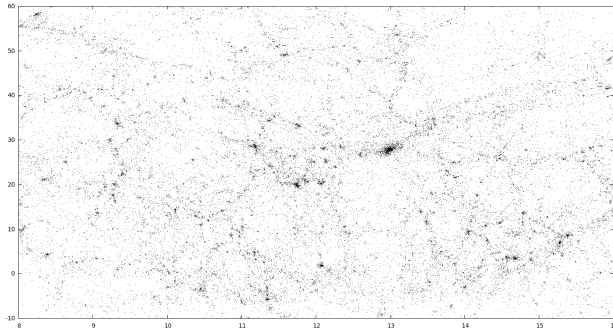


Figure 2: Real distribution of galaxies.

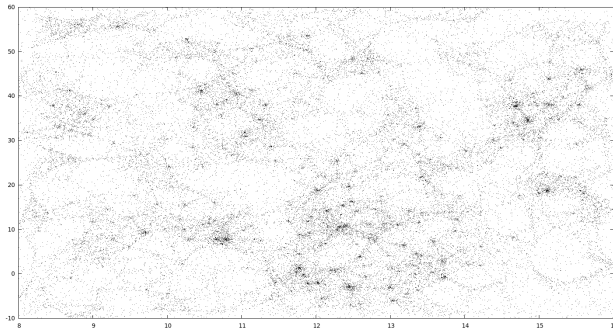


Figure 3: Our model of galaxy distribution.

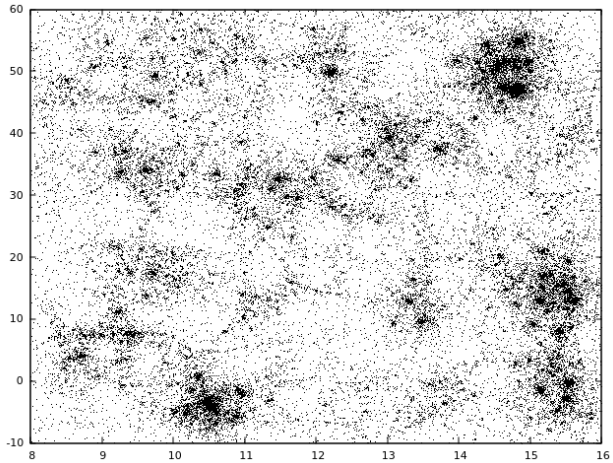


Figure 4: Model with reduced coefficients.

see from this graph, result is quite rough and does not reflect real picture of situation. The second stage of work was the attempt to simulate large-scale structure of Universe with the help of random distribution of single galaxies.

We used the distribution of galaxies modeled using Gaussian random fields depending on the mass of filaments (the number of galaxies present there) and

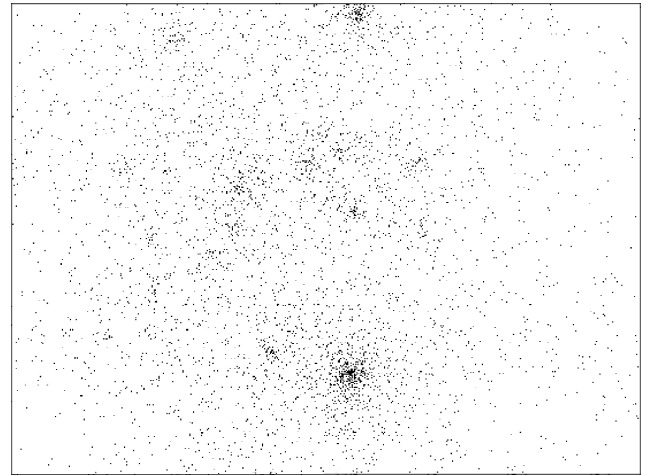


Figure 5: Enlarged part of distribution.

boundary distances between them, with addition of isolated galaxies. The resulting distribution is presented on Fig. 2.

Fig. 3 represent observable distribution of galaxies based on the SDSS sampling for radial velocity range from 4000 to 11000 km/s. Comparing it with Fig. 2 one can see unquestioning similarity, that can be estimated quantitatively, by calculating the angular two-point correlation function. We used Landy-Szalay estimator (4) for calculate correlation between SDSS and our models (Vargas-Megana, 2012).

$$\xi = \frac{DD - 2DR + RR}{RR} \quad (4)$$

DD is the number of pair of galaxies in certain angular range in the considered sample, RR is the same value for randomised sample and DR is the number of pairs of one real galaxy and one point from randomised sample. We approximate the correlation function by power law with two parameters: power index α and normalisation factor. In Table 1, there are demonstrated different values of power indicator and rate of normalization, that was obtained by changing several parameters in our model. If mass of filament, isolated galaxies quantity and radius of cluster are reduced by 40%, we got power indicator similar to SDSS survey. Fig. 4 demonstrate how this reduced model looks like. Visualization effect is responsible for such unlikely appearance, Fig. 5 shows enlarged part of this picture with the following coordinate ranges: $14 < x < 15.5$ and $45 < y < 55$. X coordinate corresponds to right ascension in hours and Y corresponds to declination in degree for obvious comparison with SDSS galaxy distribution. It should be noted that the simulation of other observational samples, including SDSS galaxies at larger distances, should apply different parameters or even some algorithm details.

Table 1: Approximation parameters.

| Sample | SDSS | M1 | M2 (-40%) | M3 (-45%) |
|----------|---------|---------|-----------|-----------|
| α | -1.4963 | -1.2747 | -1.4743 | -1.5228 |
| Norm | 11.15 | 11.48 | 10.93 | 11.24 |
| F | - | 5 | 3 | 2.75 |
| I | - | 32400 | 19440 | 17820 |
| D | - | 2 | 1.2 | 1.1 |

4. Results and conclusions

We had simulated the matter distribution that in result gives results close to observed. This two dimensional visualisation in its general features is similar to real structure of filaments, galaxy clusters and voids. We compared our model with SDSS catalog by angular two-point correlation function. Changing initial conditions led our distribution to quantitative similarity with SDSS observable data.

Table 2: Changed parameters.

| Parameter change | α | Normalization |
|------------------|----------|---------------|
| N -20% | -1.2420 | 9.304 |
| N +20% | -1.2532 | 9.559 |
| A -20% | -1.2115 | 9.54 |
| A +20% | -1.1892 | 8.835 |
| F -20% | -1.2756 | 9.548 |
| F +20% | -1.2274 | 9.371 |
| B -20% | -1.275 | 9.763 |
| B +20% | -1.1761 | 9.064 |
| D -20% | -1.2964 | 9.722 |
| D +20% | -1.2137 | 9.247 |
| I -20% | -1.2847 | 9.723 |
| I +20% | -1.244 | 9.366 |

References

- Doroshkevich A. G., Kotok E. V., Poliudov A. V. et al.: 1980, *MNRAS*, **192**, 321.
 Kim J. P., Park C., Gott J. R., Dubinski J.: 2009, *ApJ*, **701**, 1547.
 Tugay A.: 2012, *Odessa Astron. Publ.*, **25**, 142.
 Vargas-Megana M. et al.: arXiv:1211.6211v2.

DOI: <http://dx.doi.org/10.18524/1810-4215.2018.31.148048>

HIERARCHICAL STRUCTURE OF THE UNIVERSE

V.A. Zakhzhay

V.N. Karazin Kharkiv National University, Kharkiv, Ukraine

zkhvladimir@mail.ru

ABSTRACT. The modern understanding of the structure of the Universe is discussed. The Solar System is viewed as an ordinary planetary system. The neighbourhood of the Sun is specified starting with the nearest stars and nearby clusters and working outward through the Local system of stars, in particular, Gould's belt. The subgroups of the Milky Way, our stellar system, and Andromeda are examined as components of the Local Group of galaxies. Special attention is paid to their astrophysical, kinematic and dynamic properties. A larger agglomeration of galaxies, called the Local Supercluster, which contains the Local Group and its immediate neighbourhood is analysed. And finally, the Laniakea hypercluster to which the Local Supercluster and its environment belong is described along with its neighbours, namely the Perseus-Pisces hypercluster and the Local Void.

Keywords: Universe structure; hierarchy; star clusters; galaxy clusters; hyperclusters

АБСТРАКТ. Аналізуються сучасні уявлення про устрій Всесвіту по мірі віддалення від Сонця. Сонячна система представлена як рядова планетна система. Далі характеризуються околиці Сонця: від найближчих зір і їх скупчень до устрою Місцевої зоряної системи (МЗС – поясу Гулда). Аналізується гіпотеза щодо припущення, що за структурою і астрофізичними показниками МЗС схожа на маленьку галактику, яка нагадує об'єкт Ходжа в спіральній галактиці NGC 6946.

Будова Галактики, Нашої зоряної системи, підгрупи Андромеди аналізуються з точки зору складових частин Місцевої групи галактик (МГГ). Приділяється увага їх астрофізичним і кінематичним властивостям. За межами МГГ аналізується їх безпосереднє оточення та більш крупна структура – Місцеве Надскупчення (МН), до якої вона належить. Далі розглядається гіперскупчення Ланіакєя, в якому містяться МН і його околиці. Характеризуються сусіди гіперскупчення Ланіакєя: гіперскупчення Персея-Риб і Місцевий вайд.

Аналізуються прояви просторово-часового устрою Всесвіту та його коміркова структура. Обмірковується область Всесвіту, обмежена хабблівським радіусом і її властивості. Робиться висновок, що основними складовими серед об'єднань зоряних систем різної ієрархії слід вважати групи, надскупчення та гіперскупчення, оскільки проглядається закономірність, за якою, як правило, більш вищий рівень об'єднання галактик включає на два порядки більше об'єктів

нижчої ланки. За такої класифікації, підгрупи та скупчення галактик є проміжними елементами крупномасштабної ієрархії об'єднань галактик.

Остаточний висновок: на теперішній час встановлено повну «адресу», де знаходиться землянин у Всесвіті. Наступною незвіданою структурою світу може бути лише місце нашого Всесвіту серед інших всесвітів, якщо вони існують.

1. Hypotheses and evidence of a hierarchical structure of the Universe

The picture of the universe formed in the early days of telescopic astronomy was restricted to the structure of the Solar System. At that time, there was just conjecture about the stellar origin of the Milky Way and philosophic speculations about the presence of planets orbiting stars like those orbiting the Sun [3]. The discovery of the laws of motion and gravity by Isaac Newton definitely established the validity of heliocentric model of the Universe [31]. Systematic telescopic observations initiated accumulation of data on the universe beyond the Solar System and scientific substantiation of the suggested hypotheses about its structure.

1.1. First scientific hypotheses

The analysis of the accumulated telescopic astronomical observations allowed making first hypotheses about hierarchical structure of the Universe in the middle of the eighteenth century. In 1750, Thomas Wright proposed a new concept of the Universe consisting of hierarchically arranged systems with one of the components being the disc-shaped Milky Way [44]. In 1755, Immanuel Kant also came to the conclusion that the Solar System formed from gaseous cosmic matter was a constituent part of the Milky Way [21]. In 1771, Johann Lambert hypothesized that our Solar System was a member of one of those larger intermediate stellar systems which constitute the Milky Way [24].

Validation of the suggested hypotheses required further telescopic observations of celestial bodies. Such surveys of the structure of the Universe were pioneered by William Herschel. He found clumping of nebulae and resolved the richest of them in the constellation Coma Berenices [11] incorporated into a rather narrow region extending through the constellations Virgo, Ursa Major and Andromeda. Since the middle of the twentieth century this region has been identified as a part of the Local Supercluster. In 1785, based on the results of careful

observations and calculations of stellar parameters, Herschel presented the first model of the Galaxy shaped as a flattened disc in the first-order approximation [12]. Herschel's Catalogue of One Thousand New Nebulae and Clusters of Stars [13] published in 1786 gave an impetus to systematic survey of star clusters.

1.2. First findings of surveys of the arrangement of stellar systems

Increasing diameters of telescope mirrors, usage of clock drives to compensate for the celestial sphere rotation, introduction of spectral analysis and its implementation into observational astronomy in the nineteenth hundreds enabled to initiate systematic studies of the stellar systems, such as multiple star systems and star clusters, discovered by that time. Determination of the orbital period of the double star Castor by Herschel in 1803 resulted in the establishment of its physical duplicity and allowed application of Kepler's third law to its investigation [14]. The discovery of the Doppler effect in 1842 marked the start of its implementation in astronomical observations. In particular, it enabled the detection of spectroscopic binaries (Edward Pickering, 1890; [33]). There were a total of about 10 thousand of double and multiple stars comprised of three to sixteen components found at that time. The compiled catalogues of double and multiple stars laid the foundation of their systematic investigation.

The discovery of the first spiral structure in the stellar system Messier 51 (M51) made by William Parsons in 1845 with a six-foot (72 inch) reflecting telescope, which was the largest in the world back then, marked the beginning of surveys of the structure of such stellar systems. By the late nineteenth century, spirality was detected in at least 10 "stellar nebulae"; the existence of elliptical, lenticular and annular structures was also reported [29]. In 1847, John Herschel found out that the brightest stars were concentrated in a narrow region on the celestial sphere; later on, in 1879, having studied that pattern Benjamin Gould established that the ring was inclined to the plane of the Milky Way at an angle of 18° . That finding refuted the arrangement of the Milky Way systematised by the Herschels in the early nineteenth century. Estimates of distances of the investigated stars were needed to evaluate the significance of that discovery. The studies aimed at the stellar parallax determination initiated by Friedrich Struve in 1835 and Friedrich Bessel in 1840 were confined to the immediate solar vicinity. Innovative approach which could allow the estimation of distances of open star clusters and nebulae, as well as determination of the dimensions of the Galaxy, were required.

1.3. Investigation and systematisation of data in the 20th-21st centuries

The accumulation of data on the stellar distances, as well as the demand for introduction of the concept of luminosity as a measure of intrinsic brightness of stars irrelevant to their distances, actuated Einar Hertzsprung to introduce the concept of absolute magnitude in 1905 and enabled him to establish its dependence on the star's colour [15, 16]. Later on, in 1910-1913, Henry Russel

independently elaborated that idea and inferred a relationship between the stars' spectra and absolute magnitudes [34-36]. The plotted relationship was called the Hertzsprung-Russel diagram, and since then it is of great importance for studying stellar systems.

The detection of the correlation between the luminosity and period of Cepheids in the Small Magellanic Cloud by Henrietta Leavitt in 1908-1912 [26, 27] contributed to the determination of distances to the remotest stellar systems. It enabled Harlow Shapley to deduce the dimensions of the Galaxy from the distribution of globular clusters on the celestial sphere relative to the Milky Way and from the presence of RR Lyrae variable stars in the relevant clusters [38]. It turned out that all discovered star clusters and nebulae could be split into two groups, namely those within and those beyond the Galaxy. Further analysis of extragalactic nebulae revealed that they consisted of stars, and that there was a correlation between their redshifts and distances (Edwin Hubble, 1929; [18-20]). Thus, a real reference framework needed for the determination of the scales of the Universe and its three-dimensional structure became available.

The analysis of spatial arrangement of galaxies made it possible to establish their inhomogeneous distribution in the universe over a given range of scales. They combine into certain structures which tend to have a common feature – namely, that larger structures consist of those which are smaller and contain fewer galaxies. As a result, galaxy groupings were classified based on different levels of hierarchy from groups and clusters of galaxies to galaxy superclusters. In the second half of the twentieth century, it became clear that such hierarchical structures are confined to hyperclusters which along with galaxy superclusters constitute the cellular space-time structure of the Universe. As regards the distribution of galaxies and different levels of their arrangement, the concept of homogeneous spatial distribution of galaxies can only be employed for cosmological distances.

2. Distinctive features of the Solar System and its immediate neighbourhood

There is no clear definition of the immediate solar neighbourhood to date. A sphere centred on the Sun thus ruling out the existence of any star clusters within itself may be chosen as such a region. In this case, such a region should be limited to the radius of about 20 pc.

2.1. Solar System

Our planetary system is one of the lowest ranked in the hierarchy of multiple systems with only single stars and substars ranked lower. It contains a central main-sequence star, eight planets, two asteroid belts and possibly a cloud of comets. Planets in the Solar System reflect the existing planet classification [47] – namely, that inner planets are referred to as silicate and metal planets while giants are equally split into hydrogen-helium and ice planets. Dwarf planets are more similar to silicate ones; they are present in the main asteroid belt and seen among moons of giant planets. Among moons of giants and Kuiper belt components there are icy and silicate-ice dwarfs. The total number of dwarf planets known so far is 92 [48]. It is supposed that our Solar System is surrounded by a cloud

of comets whose outer edge is likely to be at one quarter of the distance of the nearest triple-star system Alpha Centauri.

2.2. Multiple stars and planetary systems nearest to the Sun

As far as within the boundaries of the nearest five stellar systems their significant diversity manifests itself. The triple-star system Alpha Centauri, which is at the distance $d = 1.30\text{--}1.34$ pc from the Sun, includes two solar-like G and K components and a red dwarf ($d = 1.30$ pc) with a silicate planet slightly larger than Earth ($\approx 1.3 M_{\odot}$) that lies in the habitable zone of Proxima Centauri. Barnard's Star ($d = 1.83$ pc) is an individual red dwarf for which the presence of planetary system was claimed earlier [40–42]. However, this claim has never been lent credence with up-to-date exoplanet search methods [7]. Both components of the binary system Luhman 16 ($d = 2.02$ pc) are L-type dwarfs, i.e. substars. Wolf 359 ($d = 2.39$ pc) is a single M-type dwarf. It should be noted that there is one more object in the investigated region, namely WISE 0855–0714 ($d = 2.20$ pc), which is formally not reckoned as a stellar system as its mass is below the brown-dwarf limit [47]. This is grounds for classifying this Y-dwarf as a rogue planet, i.e. single planet with no central star. All the above listed dwarfs are main-sequence stars. Sirius B ($d = 2.20$ pc) is the closest white dwarf to the Sun while Arcturus ($d = 11.24$ pc) is the nearest red giant. Epsilon Eridani is the closest planetary system to the Sun ($d = 3.32$ pc) with two belts of asteroids (debris discs); its structure is similar to that of the Solar System, though ϵ Eridani is 10 times younger.

Meanwhile, planetary systems formed longer ago also resemble the Solar System. For instance, within 10 pc there are about 70 planets found around 23 stars, including the Solar System. Among those planetary systems, there are planets of different types, in particular, Jupiter-like planets account for 20 per cent, ice giants – 20 per cent, and Earth-sized planets, including super-Earths, comprise 60 per cent. Such distribution is the same as that in the Solar System.

3. Local system of stars

The immediate solar neighbourhood is a part of the Local system of stars, the central region of which is called Gould's belt. Today, the Local system is associated with a region twice (or even four times) as large as the Gould belt distinguished earlier.

3.1. Star clusters and associations nearest to the Sun

Five of seven bright stars in the constellation Ursa Major, namely Alioth, Mizar, Merak, Megrez and Phecda, are associated with the closest stellar moving group (also known as Collinder 285) which is at $d \approx 25$ pc from the Sun. The total number of stars in the Ursa Major association is about 100; its diameter is 7 pc. The estimated age of this stellar association is 400 Myr.

The Pleiades are the second nearest star cluster ($d = 135$ pc). It includes about a thousand stars and substars (which account for 25 per cent of the total population) within $110'$ (4 pc). Its age is estimated to be 100 Myr. This

star cluster is close to the centre of Gould's belt whose distinctive spatial feature is the presence of the so-called doughnut-shaped ring with stellar associations along its outline. These stellar associations contain main-sequence stars, giants, bright giants and supergiants. There is extensive ongoing star formation in these regions.

The Scorpius–Centaurus association is the nearest OB association to the Sun. It consists of three subgroups, namely Upper Scorpius, Upper Centaurus-Lupus and Lower Centaurus-Crux. The mean distances to these subgroups range from 380 pc to 470 pc. Each subgroup has a diameter of about 90 pc; the total number of components in this stellar association is $\sim 5,000$; its estimated age is 11–15 Myr. It is this stellar association to which Antares, the most massive red supergiant, belongs.

The nearest active star-forming region is associated with the Orion Nebula ($d \approx 410$ pc) which is 10 pc in diameter. Apart from young stars, a protoplanetary disc and several substars have been found there.

3.2. General description of the Local system of stars

The Local system of stars is 8 pc away from the galactic centre. Its inner region is associated with the Gould belt whose radius is ≈ 500 pc. There are about 15 nebulae, more than 20 stellar associations and a few tens of star clusters in that region.

The astrometrically determined radius of the Local system can be traced out to 1 kpc [1]. The mass of this region is 20 million solar masses [32]; it includes several hundred of star clusters and a few tens of stellar associations comprised of more than 500 OBA type stars and T Tauri stars [2]. The Local system disc of a thickness less than 380 pc is inclined to the galactic plane at an angle of 18° towards the centre of the Galaxy and North Galactic Pole. There are two stellar populations detected in the Local system – namely, the old population with age of about 600 Myr and the second population which is of an order of magnitude younger. A spike-like formation consisting of $\approx 4,500$ young stars has been found in the outskirts; it can be traced out to 2 kpc [30]. The Local system rotates differentially at the velocity of 3 ± 1 km s⁻¹ (maximum 6 km s⁻¹). The Sun was also gravitationally bound to the Local system 100 Myr ago when moving at a distance of about 100 pc from its centre at an orbital velocity of 4 km s⁻¹ [32].

How should we classify the Local system? As is seen from its afore-mentioned features, the Local system has got all the properties of a small galaxy such as, for instance, the Hodge complex in the spiral galaxy NGC 6946 [9, 17, 25].

4. The Milky Way subgroup

The galactic disc immersed in the spherical component wherein satellite galaxies are clustered is called our stellar system [45] or the Milky Way subgroup (sometimes family).

4.1. Our Galaxy

The Milky Way consists of a flattened structure and constituents of the spherical and intermediate components

[45]. The flattened structural component of the Galaxy includes the thick and thin discs within the galactocentric radius $R_{GC} = 15$ kpc. The visible ring (with the radius $R_{GC} = 8$ kpc) is embedded into the inner (old) halo ($R_{GC} = 9$ kpc), which is one of the constituents of the spherical component. The bulge ($R_{GC} = 3$ kpc), 2 pc thick, is considered as an intermediate structural component with a bar-shaped structure while its very centre contains a black hole with a mass equivalent to 4 million Suns. Two major stellar arms, each with one loose spiral spur, extend from the central bulge outwards. The next constituent of the spherical component is the young halo ($R_{GC} = 9-20$ kpc); moving outwards it is followed by the outer halo ($R_{GC} = 20-120$ kpc) and the outskirts ($R_{GC} = 120-254$ kpc) confined to the orbit of the remotest satellite galaxy Leo I [45, 47]. The Local system, which contains the Solar System, resides between the Carina-Sagittarius and Perseus Arms. Sometimes this location is related to the Orion spur.

4.2. The Milky Way's satellite galaxies

There are 15 known smaller companion galaxies of the Milky Way concentrated in three belts. In the inner belt, there are three satellite galaxies which are highly susceptible to the gravitational tidal interaction with the Milky Way. All these companions lie within the young halo [45, 47]. The second belt with satellites is associated with the Magellanic Stream. It contains seven satellite galaxies, including the Large and Small Magellanic Clouds, within 90 pc from the centre of the Galaxy. These companions are projected as an elongated ellipse outline on the celestial sphere. They are clustered mainly towards the plane inclined to the galactic equator at an angle of 70° [28, 43]. Five satellite galaxies are found in the third belt beyond the central 90 kpc; they are also concentrated towards the plane inclined to the galactic equator at an angle of 50° [46]. There is also an object with no detected emission having a mass equivalent to that of the Large and Small Magellanic Clouds found in the galactic equator plane 90 pc away from the galactic centre [4, 5]. The origin of this object has not been clarified so far.

5. Local Group of galaxies

Our stellar system is a member of the Local Group of galaxies which is also home to the Andromeda subgroup. Galaxies which do not belong to any of these subgroups are reckoned as those in the outskirts of the Local Group. There are 50 galaxies in the Local Group known so far.

5.1. The Andromeda subgroup

The internal structure of the Andromeda Galaxy (also known as Messier 31) resembles that of the Milky Way. However, since its luminous mass is half as much again as that of the Milky Way, the estimated number of its constituents (i.e. stars, star clusters, stellar associations and smaller companion galaxies) is greater. The mass of its central black hole is 15 times that of the Milky Way. The Andromeda nebula is an unbarred spiral galaxy. It has less dark matter than the Galaxy, though considering its presence these two subgroups are of the same mass which is corroborated by similar plateaux in their rotation curves [10].

As of today, there are 18 satellite galaxies known in the Messier 31 subgroup, the most distant of which (LGC III and And VI) are 280 kpc away from its centre thus constraining the scale of this subgroup.

Satellite galaxies are concentrated towards two planes inclined to the equator of M31. Most of them are inclined to the galactic plane at an angle of 30° while spheroidal dwarf satellites are inclined at an angle of 80° [47]. Unlike our stellar system, wherein the largest satellite galaxies, namely the Large and Small Magellanic Clouds, are located relatively close to the Milky Way, in the Andromeda subgroup the most massive satellites (M33 and IC 10) reside in the outer reaches (225 kpc and 250 kpc away from the centre of M31, respectively).

5.2. Galaxies in the Local Group outskirts

Fourteen galaxies do not belong to any of the subgroups of the Local Group, and 17 more galaxies are potentially to be classified likewise [47]. Their distances from the Sun range from 400 kpc to 1,360 kpc. Most galaxies in the outskirts of the Local Group are irregular with seven of ten irregulars being barred ones (IB type). Two galaxies in the constellations Cetus and Tucana are classified as elliptical; another two galaxies (in Hydra and Antlia) are contiguous and interact with each other. The Sagittarius Dwarf Irregular Galaxy (SagDIG) is the most distant from the Sun.

5.3. Kinematics of the Local Group galaxies

Hubble's law does not hold within the Local Group. The Milky Way and M31 subgroups are approaching each other at a radial speed of about 120 km s^{-1} . However, as far as beyond the Local Group Hubble's law starts being applicable. A rather plausible explanation of such behaviour of the law is that the subgroup dimensions are governed by the balance between the forces of attractive and repulsion (dark energy) [6]. It means that attraction dominates within subgroups while repulsion prevails beyond their boundaries. Therefore, it would be more reasonable to interpret Hubble's law with respect to the recession of galaxy subgroups rather than that of galaxies.

6. Local Supercluster

Based on the analysis of 1,250 galaxies from the Harvard Survey of Galaxies Brighter than the Thirteenth Magnitude (Shapley & Ames, 1932; [37]), Gerard de Vaucouleurs [8] deduced the existence of the next level of the hierarchical structure, namely the Local Supercluster, comprising the Local Group. In fact, it was a re-discovery of what William Herschel had noticed more than 150 years earlier [11] since the richest portion of clumping which he had detected (with no photo available!) in Coma Berenices turned out to be a constituent part of the supercluster discovered later by de Vaucouleurs.

6.1. The Local Group surroundings

There are five groups of galaxies in the immediate surroundings of the Local Group (< 5 Mpc), namely the Sculptor group (at a distance $d = 2.8$ Mpc), IC 342/Maffei ($d = 3.1$ Mpc), M81 ($d = 3.7$ Mpc), M94/Canes Venatici I

($d = 4.0$ Mpc) and Centaurus A/NGC 5128 ($d = 4.3$ Mpc) groups [47]. Thus, the Sculptore group of galaxies is the closest to the Local Group. Five of these six groups of galaxies (along with the Local Group) have two subgroups each [47]; these subgroups are well-defined with pronounced dominant galaxies, and at least one dominant galaxy in each pair of subgroups is spiral. In general, the largest of these dominant galaxies are smaller than the Milky Way. The Andromeda galaxy is the largest in this region while the Milky Way is the fourth in size. The discussed region comprises about 200 galaxies (a quarter of which belong to the Local Group); it is a component of the Local volume which contains more than 630 galaxies detected within 10 Mpc from the Local Group [22, 23].

6.2. Structure and kinematics of the Local Supercluster

The Local Supercluster encompasses more than 30 thousand galaxies, classified into about 100 groups and clusters of galaxies [47]. About 60 per cent of galaxies belonging to the Local supercluster are concentrated in a narrow disc of 50 Mpc in diameter and 3 Mpc thick (which is twice the diameter of the Local Group). Almost 98 per cent of all the galaxies are members of 11 galactic clouds; they are well-separated and constitute 5 per cent of the Virgo supercluster volume.

The central region of the Local Supercluster comprises three galaxy clusters, the closest of which ($d = 16$ Mpc) is found in the constellation Virgo. Virgo A (M87) galaxy is an cD galaxy dominant in this region. The diameter of the Virgo cluster is 5 Mpc; its spatial number density is an order of magnitude higher than that observed in the groups of galaxies (500 galaxies Mpc^{-3}). There are about 200 galaxies with high and moderate luminosities observed in this cluster, and two thirds of them are spiral galaxies. A total of ≈ 2000 galaxies are expected to be detected in this region.

The Local Group moves at a speed of 300 km s^{-1} relative to the Local Supercluster and at a velocity of 620 km s^{-1} with respect to the cosmic microwave background [47]. Employing the composite velocity vector allowed the detection of the so-called ‘‘Great Attractor’’ [39] estimated to be a much more massive structure as compared to the Local Supercluster. It has emerged that in the Local Universe such massive agglomerations have an impact on the local value of the Hubble parameter; hence, the local velocity field is characterised by the following values of the Hubble tensor depending on the directions towards the Local Supercluster: $81 \text{ km s}^{-1} \text{ Mpc}^{-1}$ towards its nucleus; $48 \text{ km s}^{-1} \text{ Mpc}^{-1}$ towards its polar axis and $62 \text{ km s}^{-1} \text{ Mpc}^{-1}$ towards the plane perpendicular to the direction towards the Local Supercluster [22, 23].

7. Large-scale structure of the Universe

Superclusters of galaxies assemble into larger structures which are referred to as hyperclusters. These enormous hyperclusters, in their turn, aggregate into the large-scale three-dimensional cosmic web of thickness reckoned by its constituent superclusters of galaxies. Such a complex arrangement is referred to as the cellular

structure of the Universe while the formed vast spaces are called the voids.

7.1. The Laniakea hypercluster and Local Void

As it has turned out, both the Local Supercluster and the Great Attractor are members of the Laniakea hypercluster (the name ‘‘Laniakea’’ means ‘‘immense heaven’’ in Hawaiian). This aggregation stretches out over 160 Mpc, encompasses ~ 100 thousand galaxies and consists of about 100 superclusters of galaxies (including the Local Supercluster). Laniakea neighbours another huge grouping, namely the Perseus-Pisces hypercluster; they are separated from each other by the Local Void, which is the nearest vast empty region of space with the cross-section extent of more than 45 Mpc. This void comprises three separate sectors separated by ‘‘filament bridges’’ and lies adjacent to the Local Group (at $d = 23$ Mpc from Earth); one of its boundaries is delineated by the Local Sheet which is a galaxy filament containing the Local Group.

7.2. Cellular structure of the Universe within the Hubble length

The cellular structure of the Universe becomes apparent on the scales of an order of billions of light-years. It is possible to distinguish large-scale filaments comprised of super- and hyperclusters of galaxies spaced by voids. Such an arrangement is also typical for larger scales, for which another specific rule holds: the more distant an object is, the earlier in its evolution the object can be surveyed. The most distant structures tend to show main features of the early Universe. Features of galaxies and large-scale structures into which they combine differ from those observed at noticeably shorter distances. This is the manifestation of the space-time structure of the Universe.

In compliance with Hubble’s law, the increase in the velocity of the observed objects is limited by relativity to the speed of light. Substituting the speed of light for the recessional velocity in the equation for Hubble’s law yields the Hubble distance to the objects currently receding at the speed of light. This distance is referred to as the radius of the Hubble sphere (or the Hubble length). Any objects beyond the Hubble length cannot be seen by observed from Earth. On the other hand, any quant of light of our universe cannot get outside the Hubble sphere. It means that for an external observer our universe appears to be as a black hole. Is there such an external observer? Nobody knows. Certain cosmologists allow for the existence of wormholes where the mouth of each is a black hole; if this were true, it would be a chance to survey other universes since theoretically a photon could traverse from one universe to other ones through such wormholes. And perhaps, if a spatial resolution of an interferometer with an extremely large database sufficient to clearly resolve the Schwarzschild radius of supermassive black holes (for which such radius should be immense) is reached one day, these black holes will serve as peculiar windows through which we will be able to take a look at other universes.

8. Conclusions

As can be seen from the brief analysis of the observed stellar systems and their groupings of different levels of complexity, their general hierarchy is quite evident with simple systems being included into larger structures.

There are three levels of the stellar system hierarchy:

- 1) multiple stars and planetary systems;
- 2) star clusters and associations;
- 3) galaxies.

On a larger scale, galaxies combine into

- 1) groups;
- 2) clusters;
- 3) superclusters;
- 4) hyperclusters.

For the latter, the following pattern of arrangement is assumed:

- a) ~ 100 groups form a supercluster;
- b) ~ 100 superclusters form a hypercluster.

Therefore, subgroups and clusters of galaxies are intermediate structural components of a large-scale hierarchy of the assembly of galaxies.

So far, for us, Earth's inhabitants, the full address has been established according to our location in the Universe – namely, that from the residence in the Solar System in our Galaxy to the Laniakea hypercluster beyond which the large-scale space-time cosmic web only exists. The next aspect of the universe structure to be explored is the position of our Universe among other universes if they exist...

References

- Bobylev V. V.: 2004, *Astron. Let.*, **30**, 159.
- Bochkarev, N. G.: 1990, *The local interstellar medium.* – M.: Nauka, 191 p. (USSR).
- Bruno G.: 1584, *On the Infinite, the Universe, and Worlds.* – J Charlewood, Venice (London).
- Chakrabarti S., Blitz L.: 2011, *Astrophys. J.*, **731**, 40.
- Chakrabarti S., Bigil F., Chang P., Blitz L.: 2011, *Astrophys. J.*, **743**, 35.
- Chernin, A. D.: 2008, *Phys. Usp.*, **51**, 253.
- Choi J., McCarthy C., Marcy G.W. et al: 2013, *Astrophys. J.*, **764**, 131.
- De Vaucouleurs G.: 1959, *Sov. Astron.*, **3**, No. 6, 897.
- Efremov Yu. N.: 2004, *Astrophysics*, **47**, 273.
- Fich M., Blitz L., Stark A.A.: 1989, *Astrophys. J.*, **342**, 272.
- Herschel W.: 1784, *Phil. Transact. Roy. Soc. London*, **74**, 437.
- Herschel W.: 1785, *Phil. Transact. Roy. Soc. London*, **75**, 213.
- Herschel W.: 1785, *Phil. Transact. Roy. Soc. London*, **76**, 457.
- Herschel W.: 1785, *Phil. Transact. Roy. Soc. London*, **93**, 339.
- Hertzsprung E.: 1905, *Zeit. Wissensch. Photogr.*, **3**, 442.
- Hertzsprung E.: 1911, *Publ. Astrophys. Obs. Potsdam*, **22**, A1.
- Hodge P.W.: 1967, *Publ. Astron. Soc. Pac.*, **79**, No. 466, 29.
- Hubble E.P.: 1929, *Contrib. Mount Wilson Observ.*, **3**, 23.
- Hubble E.P.: 1929, *Astron. Soc. Pac. Leaf.*, **1**, No. 23, 93.
- Hubble E.P.: 1929, *Proc. Nat. Acad. Sci. USA*, **15**, 168.
- Kant I.: 1755, *Allgemeine Naturgeschichte und Theorie des Himmels.*– Königsberg und Leipzig, bey Johann Friederich Petersen.
- Karachentsev I.D., Karachentseva V.E., Huchtmeier W.K., Makarov D.I.: 2004, *Astron. J.*, **127**, 2031.
- Karachentsev I.D., Makarov D.I.: 1996, *Astron. J.*, **111**, No. 2, 794.
- Lambert J.H.: 1771, *Anlage zur Architektonik oder Theorie des Einfachen und Ersten in der philosophischen und mathematischen Erkenntnis.* – Riga.
- Larsen S., Richtler T.: 2000, *Astron. Astrophys.*, **354**, 836.
- Leavitt H.S.: 1908, *Ann. Harv. Coll. Observ.*, **60**, 87.
- Leavitt, H.S., Pickering, E.C.: 1912, *Harv. Coll. Observ. Circ.*, **173**, 1.
- Marochnik L.S., Suchkov A.A.: 1984, *The Galaxy.* – M.: Nauka, 392 p. (USSR)
- Mayer M.V.: 1896, *The Universe. Astronomy in popular statement.* – St-Pb: Prosveshchenie, 684 p. (Rus).
- Miyamoto M., Sôma M., Yoshizawa M.: 1993, *Astron. J.*, **105**, No. 6, 2138.
- Newton I.: 1686, *Philosophiae Naturalis Principia Mathematica.* – Trin. Coll. Cantab. Soc.
- Olano C.A.: 2001, *Astron. J.*, **121**, 295.
- Pickering, E. C.: 1890, *Mon. Not. Roy. Astron. Soc.*, **50**, 296.
- Russell, H.N.: 1910, *Astron. J.*, **26**, 147.
- Russell, H.N.: 1910, *Science*, **32**, 883.
- Russell, H.N.: 2013, *Observ.*, **36**, 324.
- Shapley, H., Ames A.: 1932, *Ann. Harv. Coll. Observ.*, **88**, No. 2, 41.
- Shapley H., Curtis, H.D.: 1921, *Bull. Nat. Res. Coun.*, **2**, Part 3, No. 11, 171.
- Smoot G.F.: 2007, *Rev. Mod. Phys.*, **79**, 1349.
- Van de Kamp P.: 1963, *Astron. J.*, **68**, No. 7, 515.
- Van de Kamp P.: 1969, *Astron. J.*, **74**, No. 6, 751.
- Van de Kamp P.: 1975, *Ann. Rev. Astr. Ap.*, **13**, 295.
- Vorontsov-Vel'yaminov B.A.: 1978, *Extragalactic astronomy.* – M.: Nauka, 479 p. (USSR).
- Wright T.: 1750, *An original theory or new hypothesis of the Universe.* – Manuscript.
- Zakhozhay V.A.: 2005, *Kinem. Phys. Celest. Bod.*, **21**, No. 6, 283.
- Zakhozhay V.A.: 2007, *Sc.D. thesis*, Kharkiv: V.N. Karazin Kh. Nat. Univ., 317 p. (Rus)
- Zakhozhay V.A.: 2017, *Introduction to the Astrophysics and Cosmogony.* – Kharkiv: V.N. Karazin Kh. Nat. Univ., 208 p. (Ukr)
- Zakhozhay O.V., Zakhozhay V.A., Krugly Yu.N.: 2006, *Proc. 13th Open Young Sci. Conf. Astron. Sp. Phys.*– April 25-29, 2006, Kyiv. – Kyiv Nat. Taras Shevchenko Univ., 122.

ASTROPHYSICS

DOI: <http://dx.doi.org/10.18524/1810-4215.2018.31.144437>

POSITRON ANNIHILATION SPECTROSCOPY OF YOUNG SUPERNOVA REMNANTS

D.N. Doikov

Odessa National Maritime University, Dep. of Mathematics, Physics and Astronomy
doikov@mail.bg

ABSTRACT. This paper discusses radiative and thermodynamic properties of cold rarefied aggregates of non-uniformly distributed gas and dust through which high fluxes of positrons with energies of 0.011-3.6 MeV pass. The investigated gas is in the form of a nebula with densities of $1-10^8 \text{ cm}^{-3}$ and temperatures ranging from 30-100 K. We estimated the energy input into thermodynamic temperatures of the ejecta components. Additional heating and γ -ray luminosity of all the components of the examined ejecta were factored in. The structure of the radiation field $S(E,r)$ and electron velocity distribution function $F(E,r)$ were determined depending on the energies of quanta and electrons, respectively. The ejecta of SN 1987A was considered as an ideal object to investigate the positron impact on the nebula. The interaction of positrons with solids, atoms and molecules was examined separately. Traveling of positrons in solids typically results in their enhanced amorphous state, heating and annihilation with free electrons of solid-state grains with emission of two photons each of the energy $E_\gamma = 0.511 \text{ MeV}$. Consequently, a characteristic excessive luminescence of dust particles, namely astronomical silicates and graphite, occurs. In fact, the energy loss of fast positrons due to ionisation leads to consecutive creation of K-L-M vacancies, which is followed by cascade transitions with the transfer of the remaining energy to the Auger electrons rather than to surrounding atoms which make up a solid. In this case, in a solid particle, the energy released in cascade transitions is either used to change the lattice structure or converted into γ -quanta emission upon the annihilation of positrons and K-L electrons. The estimated energy used to heat a solid particle itself makes up a half of the energy released in the downward M-L-K cascades, which is indicative of a significant contribution to the energy balance of the ejecta dust. This contribution exceeds the energy estimates from the net radiation loss of particles in the matter. In the nebular atomic-molecular plasma of the supernova ejecta, the conservation of energy dictates that the energy lost to create a K-vacancy is allocated to the subsequent cascade transitions and the Auger electrons while the one-photon annihilation of positrons and K-electrons of atoms and molecules yields characteristic γ -quanta with energies close to their own values - $E_\gamma \approx 1.022 \text{ MeV}$. The study of annihilation of positrons and K-electrons with emission of a single photon revealed a relationship between the energy of the emitted γ -quanta with the recoil energies of nuclei - E_n , binding energies of K-electrons of different atoms - E_b and energies of incident positrons E_p . The cross-sections

for interactions of positrons and atoms in the investigated young supernova remnants were calculated and scaling of electron arrangements of the atoms involved in those interactions was performed. We pointed out that for the iron-peak atoms the cross-section for the positron-atom interaction increases by four orders of magnitude, thus making the interaction between positrons and electrons in the K-L shells the most probable. It is shown that in astrophysics the positron annihilation spectroscopy of matter yielding a characteristic radiative response has opened up new opportunities for studying young supernova remnants and active galactic nuclei. In particular, it is now possible to independently determine the mass ratio of dust and gas-molecular components by the strength ratio of annihilation γ -lines I (0.511)/I (1.022). We report the estimated contribution of various elements to the profiles of the indicated γ -lines and conclude that it is not related to the proper dynamic motions of the supernova remnants. This is a crucial factor in the study of bulges in active galactic nuclei wherein the physical conditions are assumed to be steady-state in relatively large scales.

Keywords: II type SN remnants, radioactive elements, positron spectroscopy of remnants dust and gas.

АБСТРАКТ. В даній роботі розглянуто радіаційні і термодинамічні властивості холодних розріджених агрегатів, які містять неоднорідно розподілені газ і пил, що зазнають інтенсивного проходження потоків позитронів з енергіями 0.011-3.6 MeV. Розглянутий газ перебуває в небулярному стані зі щільністю $1-10^8 \text{ cm}^{-3}$ і температурою 30-100K. Отримано енергетичний внесок у термодинамічну температуру компонентів оболонки. Враховано енергетичний внесок у додаткове нагрівання і світіння в γ -області спектру усіх компонентів випромінювання оболонки. Визначено структуру поля випромінювання $S(E,r)$ і функцію розподілу електронів за швидкостями $F(E,r)$ в залежності від енергій квантів або електронів. Оболонку SN 1987A розглянуто як ідеальний об'єкт впливу позитронів на небулярне середовище. Окремо розглянуто взаємодії позитронів з пилом, атомами і молекулами. Характерними наслідками руху позитронів у твердих частках є збільшення їх аморфності, нагрів і двухфотонна анігіляція з вільними електронами твердотільних утворень енергією квантів $E_\gamma = 0,511 \text{ MeV}$, внаслідок чого виникає характерне надлишкове світіння пилу – астрономічних силікатів і графіту. Іонізаційні втрати енергії швидких позитронів по суті не

приводять до послідовних процесів утворення K-L-M вакансій, каскадних переходів і передачі залишкової енергії Оже-електронам, а викликають нагрів пилу. У цьому випадку енергія від каскадних переходів у твердій частці більшою мірою пов'язана з витратами на зміну кристалічної структури і будують γ -кванти від анігіляції позитрона з K-L-електронами. Енергію, витрачену саме на нагрів пилу, оцінено як половина енергії N-M-K каскадів. У цьому випадку знайдена суттєва складова у енергобаланс пилових часток оболонки, яка перевищує оцінки по чистим радіаційним втратам часток у речовині. В небулярній атомно-молекулярній плазмі оболонки наднової енергія, яка утворена позитроном K-вакансії перерозподіляється між каскадними переходами і Оже-електронами, а однофотонна анігіляція позитронів з K-електронами атомів і молекул продукує характерні γ -кванти з енергіями значень близько $E_\gamma \approx 1,022$ MeV. В роботі, під час дослідження однофотонної анігіляції позитронів з K-електронами виявлено зв'язок енергій утворених γ -квантів з енергіями віддачі ядер E_n , енергіями зв'язка електронів з K-оболонки – E_b різних атомів і енергіями позитронів – E_p . Обчислені перетини взаємодій позитронів з атомами розглянутих молодих оболонки наднових і отримані масштаби атомних електронних структур, що залучено у цю взаємодію. Визначено, що для атомів залізного піку перетини взаємодій позитронів з атомами зростає на 4 порядки і утворює взаємодії позитронів з оболонки K-L-електронів найбільш вірогідними. Доведено, що позитронна спектроскопія речовини у вигляді його характерного радіаційного відгуку розкриває для астрофізики нові можливості у дослідженні молодих залишків наднових та активних ядер галактик. Зокрема, у відношенні інтенсивності анігіляційних γ -ліній $I(0,511)/I(1,022)$ виявляється можливим незалежно визначення відношення пилової маси до маси газово-молекулярної складової. Зроблено висновки з приводу вкладу у профілі зазначених γ -ліній, які викликані різними елементами. Показано, що цей внесок не пов'язаний з власними динамічними рухами оболонки наднових. Вищезазначена обставина є особливо важливою при дослідженні Балджа активних ядер галактик, де фізичні умови вважаються стаціонарними на відносно великих масштабах.

Ключові слова: Наднові II типу, радіоактивні елементи, позитронна спектроскопія газу та пилу залишків наднових.

1. Introduction

The motion of fast particle streams through matter has always been used for studying of media. In the age of the first experiments of Ernest Rutherford and his apprentices, it had been already evident that the quantum structure of matter reacted differently to such particles. In those experiments, the motion of fragments of radioactive nuclei after their decay could trigger different energy responses for one and the same matter, depending on its phase state. For solids and even for liquids, the loss of energy results in the least radiative response. After a fragment resulted from

the decay creates a vacant K-L-M energy level in an atom in a solid phase, the energy conserved in this transition to the excited state is re-allocated between consecutive cascades and change of the lattice structure of the solid. In addition, the stronger the interatomic bond in a solid is, the more efficient the latter route is. For a perfect diamond-lattice the radioactive emission results in the change of its spectral properties (i.e. colour, absorption coefficient, conductivity, Young's modulus, etc.). This is why dust particles in young supernova remnants change their optical and structural properties even during relatively short observations. A decrease in Young's modulus is indicative of their amorphisation, as well as accelerated disintegration and sputtering of these particles in the interstellar medium. Liquids behave similarly to solids, with the only exception being that the released energy is converted predominantly into emission and dissociation of molecules which leads to an effective increase in the temperature of the liquid. In astrophysics, the nebulae have never been observed as liquid gas-and-dust aggregates. Therefore, it is more reasonable to focus on studying the radiative properties of gas and dust being traversed by positrons. The presence of strong fluxes of hard radiation in the interstellar gas, supernova remnants and upper atmosphere of some stars results in qualitatively new effects and appearance of spectra of these media. In such media, as a result of vacant K energy levels created due to positron traveling, atoms undergo consecutive cascade transitions with the transfer of the remaining energy to the Auger electrons. In some cases, hard radiation produced in supernova remnants passes through very cold (30-80 K) gas and dust of the nebula. In these circumstances, we have got dual-mode source functions $S(E,r)$ and electron velocity distribution functions $F(E,r)$ depending on the energies E of photons and electrons, respectively, as well as on the current position r in the Type II SN 1987A remnant (Jerkstrand *et al.*, 2001; Doikov & Andrievskii, 2017; Doikov *et al.*, 2018). The low probability of recombination of the excited atoms and molecules, along with the given specific values $S(E,r)$ and $f(E,r)$, indicates that the excited state of atoms of the supernova ejecta due to their ionisation is being maintained. As a consequence, the lifespans of a certain portion of atomic ions are long and comparable with the typical half-lives of radioactive elements injecting respective fast particles. A new method of distinguishing between isotopes using the ratio of integrated strengths of their lines $I(^{44}\text{CaI})/I(^{40}\text{CaI})$ was reported in the afore-mentioned papers. $^{44}\text{CaII}$ is a final product of radioactive decay chain $^{44}_{22}\text{Ti} \xrightarrow{85\text{y}} ^{44}_{21}\text{Sc} \xrightarrow{6\text{h}} ^{44}_{20}\text{Ca}$ while ^{40}CaI is the end-product of synthesis in the progenitor star. Line profiles of neutral and ionised atoms are well studied for both isotopes. Spectroscopic response to the positron fluxes in the ejecta of SN 1987A was observed with the Hubble Space Telescope on 07th of January, 1995, eight years after the supernova explosion. Optical transitions in the neutral and ionised calcium atoms were observed among others (Jerkstrand *et al.*, 2011). Over several years of the infrared studies of this supernova, it has become evident that its ejecta consist of fragments (clumps) in which heavy elements that comprised the progenitor core before the explosion are concentrated

(Doikov *et al.*, 2018). These clumps contain dust particles which produce mid- and far-IR emission spectra typical for astronomical silicates. Graphite and other carbon-containing particles are less abundant and may have formed in the clumps originated from the C/O region of the progenitor star (Woosley *et al.*, 1991).

The mere fact of the optical emission spectra from the ejecta clumps is indicative of the presence of astronomical silicates therein. The inter-clump medium, as well as the frontal regions of the remnant, is rich in hydrogen and helium which together comprise 70% of the supernova ejecta matter. The density of hydrogen and helium in the clumps in the inner part of the ejecta is 10^4 cm^{-3} while in the inter-clump medium it is close to the interstellar value of 1 cm^{-3} . The presence of clumps in the interior of the ejecta is associated with their inertness. Major portion of hydrogen and helium (90% of their total abundance) is concentrated in front of these clumps, i.e. in the outer part of the ejecta. According to Varosi & Dwek (1999), the minimum number of clumps in the ejecta with the elemental distribution as specified above may be set to 100. Such distribution of the ejecta fragments, i.e. clumps, was suggested on the basis of high-precision measurements of the IR emission from the dust concentrated in those clumps. Thus, there is a problem set out to solve, which is to semi-empirically determine the spectroscopic response within the clumps containing the radioactive isotope of titanium - $^{44}_{22}\text{Ti}$. The total amount of this isotope derived from the measurements of the radiation component of the products of a series of radioactive transformations $^{44}_{22}\text{Ti} \xrightarrow{85 \text{ y}} ^{44}_{21}\text{Sc} \xrightarrow{6 \text{ h}} ^{44}_{20}\text{Ca}$ is 10^{27} kg (Grebenev *et al.*, 2012). With the half-life of 85 years, the standardised number of positrons within the bulk of the ejecta is 10^{51} . Prior to their annihilation, positrons in the clumps undergo 10^3 collisions on average. In the H/He of the outer part of the ejecta, this number averages $10^4 - 10^5$ collisions. It means that over last 28 years after the hydrogen recombination the radioactive decay of $^{44}_{22}\text{Ti}$ has been a significant source of excitation of atoms and molecules. This paper focuses on the study of γ -emission spectra resulted from the positron annihilation in the gas and dust components of young supernova remnants. There are qualitative physical differences in the positron interaction with solid dust fraction and individual atoms and molecules. When a positron moving through matter is slowing down and losing energy by ionisation, it will decelerate until its energy is down to the thermal energy of free or atomic loosely-bound electrons in the solid. As a result, the positron and an electron form a pair which further annihilate with the emission of two γ -quanta each with the energy $E_\gamma = 0,511 \text{ MeV}$. Another mode of electromagnetic interaction between positrons and bound K-electrons results in the annihilation with emission of a single photon. This process will be discussed below in section 2 which proves its relevance to the study of young supernova remnants after the hydrogen recombination. The dependence of the cross-section for the one-photon annihilation on the energies of incident positrons and main characteristics of atoms and their nuclei will be considered separately in the same section. In this case, given the preliminary determined De Broglie wavelengths for positrons, it is possible to identify the

atomic energy levels in which positrons enter into annihilation interactions with electrons. Average thermodynamic quantities of supernova remnants, unlike those of the active galactic nuclei, change with time as described in sub-section 1.2. Time-varying chemical composition due to radioactive decay is another specific feature of such physical systems. Positron annihilation spectroscopy, combined with the findings reported by Doikov *et al.* (2018), allows obtaining information about the chemical evolution of supernova remnants using γ -lines produced by different elements. The kinetic energy of recoiling nuclei released upon the investigated single-photon annihilation will be derived in the same section. We suggest considering the relationship between the calculated kinetic energy and characteristics of the recoiling nuclei spectral lines, including their Doppler broadening. These aspects have been discussed in more detail in Doikov *et al.* (2018). The γ -line profiles in astrophysical systems of a given type have been understudied; however, the improved accuracy of γ -detectors along with the results obtained in this research make it possible to adopt them for the quantitative study of diffuse nebulae which include supernova remnants.

2. Positron annihilation spectroscopy of young supernova remnants. Energy loss of positrons due to ionisation without annihilation in the nebular gas.

The main reason for the luminescence of cold gas and dust in young supernova remnants is the ionisation by positrons moving in the matter. Positrons diffuse the ejecta and trigger the luminescence emission throughout its entire volume which can be observed in different spectral regions at the current epoch. Let us consider such supernova remnant as a closed system with an attached moving reference frame. The law of total charge conservation for the ejecta should imply the equal number of positrons produced and annihilated per unit time. Otherwise, the condition of zero net charge of all ions, electrons and positrons is not met. In the afore-mentioned radioactive decay series, one 1s electron of the $^{44}_{22}\text{Ti}$ isotope atom is captured while another one is shed as an Auger electron following the positron emission of the unstable isotope $^{44}_{22}\text{Ti}$. As noted in Doikov *et al.* (2017), in the supernova remnants positrons are more likely to annihilate with atomic K-electrons rather than with free thermal electrons. This statement has been corroborated by the International Gamma-Ray Astrophysics Laboratory (INTEGRAL) observations (Grebenev *et al.*, 2012). The energy loss of positrons due to ionisation adds new cascade transitions to the detailed static balance equation; and the Auger effect is factored in in the Saha ionization equation factors. As a result, the supernova remnant is supplemented with the radiation field of hard photons and high-energy Auger electrons. These emergent quanta of hard radiation and especially the ejected Auger electrons proceed to excite the surrounding atoms of metals and give rise to copious number of transitions thereby filling the supernova ejecta with the diffusive radiation. The respective transitions triggered in such a manner were observed in optical and IR regions with the Hubble Space Telescope in January, 1995. At the current epoch, this physical system is at the

nebular phase. It means that quanta and electrons have energies which are sufficiently high to excite atoms and molecules within the entire volume of the ejecta. Since radioactive decay serves as an extra source of energy, we consider certain elementary steps of the ${}^{44}_{22}\text{Ti}$ radioactive transformations which are valuable for further calculations of estimates in compliance with the radioactive decay law.

$$N = N_0 e^{-\lambda t} = N_0 e^{-\frac{0.698}{T_{1/2}} t}, \quad (1)$$

where $T_{1/2}$ is the half-life of ${}^{44}_{22}\text{Ti}$; N_0 is the initial number of atoms of this radioactive isotope. It is more efficient to use the rate of decay, i.e. the activity of the radioactive isotope, expressed as A , which is the number of decays per second and equal to the time derivative of N . In other words,

$$A = \frac{dN}{dt} = -N_0 \frac{0.698}{T_{1/2}} e^{-\frac{0.698}{T_{1/2}} t}. \quad (2)$$

Taking into account the total amount of the titanium isotope ${}^{44}_{22}\text{Ti}$, which has been estimated from the observations by Grebenev *et al.* (2012) and is 10^{27} kg, it may be deduced that at the current epoch on average one to three decays fall on each 1 cm^3 . It means that every second one to three positrons is ejected. The density of matter in the regions where the clumps are located is of the order of 10^4 particles per 1 cm^3 or 10^4 cm^{-3} . In the outer H/He envelope in front of the clumps, the density reaches 10^8 cm^{-3} . When an ejected positron just starts traveling, its maximum energy is of the order of 3.6 MeV; then, it loses 0.1% of its energy in each collision with the ejecta atoms. The kinetic energy loss of such a positron by ionisation is due to its annihilation with predominantly K-electrons, resulting in the creation of the respective core hole and transition of the atom to a highly excited state.

Prior to annihilation with a bound atomic electron, a positron undergoes at least 10^3 collisions with heavy atoms and up to 10^4 collisions with light atoms. In other words, in the SN 1987A remnant at the current nebular phase, positrons are promoting transitions to the excited states throughout the entire ejecta, rather than just within clumps wherefrom they have been ejected (Doikov *et al.*, 2018). Let us calculate the specific energy of such collisional excitation by positrons. To this end, the chemical composition of the supernova ejecta should be specified. Having defined the elemental distribution of the matter in the ejecta clumps, we can calculate the initial rates of the elementary processes required to comply with the basic laws of conservation. First of all, we should take into account the Kirchhoff's law which states that in thermodynamic equilibrium the emissivity of matter is equal to its absorptivity. The thermal radiation coefficient $\eta(\nu)$ should be correlated with the coefficient of thermal energy (heat) absorption $k(\nu)$ and intensity of thermal radiation $I(n, \nu)$:

$$\eta(\nu) = k(\nu)I(n, \nu). \quad (3)$$

This formula does not require factoring in the dissipation of energy of incident positrons due to its minor contribution to the kinetic energy dissipation coefficient as compared to the reduction of energy due to positron scat-

tering (or deflection). According to the preliminary estimates reported by Kaastra & Mewe (1993) upon the results of quantum-mechanical computations, for the iron-group elements about a half of the energy conserved upon the creation of a K-L vacancy is spent on triggering a cascade of radiative transitions while the rest is converted into the kinetic energy of the Auger electrons. In this case, equation (3) may be written as follows:

$$\eta(\nu) = 0,5 k(\nu)I(n, \nu). \quad (4)$$

The energy carried away by the Auger electrons should be then reduced by the total ionisation potential of all principal energy levels which these electrons occupied before the ejection. (Figures 1-3 in Doikov *et al.* (2018) illustrate the results of precise calculations of kinematic and radiative properties of the ejecta for different regions of the SN 1987A remnant, given its clumpiness as postulated by Woosley *et al.* (1988). The spectroscopy of nebulae is feasible if there is a central compact source of radiation or if the nebula itself contain any sources of excitation of radiation components (gas, molecules and dust). Among various codes used to simulate conditions in planetary nebulae, the most popular is the Cloudy code developed by Ferland (1998) and its modifications by Melech (2015). Note that the incoming flux of hard radiation from the central source to the planetary nebula does not affect the charge neutrality of the medium. Hard radiation promotes both light elements and metals to multiple excited states. In other words, one hard UV quantum when hitting, for instance, an iron atom, promotes several low-lying excited states. Subsequently, the de-excitation of the atom occurs via numerous allowed transitions through intermediate excited states. The nebula eventually luminesces producing a characteristic emission spectrum. The progress in examining spectra of planetary nebulae made it possible to accurately specify their physical properties and distinguish the CNO (carbon-nitrogen-oxygen) ions sensitive to the electron density and temperature, as well as to other important characteristics of the nebula. In particular, the fluxes and spectra produced by the central source can be adequately separated from the secondary, the so-called diffuse components of the spectra of planetary nebulae. When the sources of excitation are present in the ejecta being diffusively distributed therein, it seems feasible to study it using the Osterbrock-Lucy equations (formulae 8-12 here below). Employment of these formulae requires determination of the cross-sections for absorption, dissipation and emission in the nebular gas of the ejecta, as well as densities of atoms of different chemical elements and geometric parameters of the clumpy structure of the ejecta.

Earlier mentioned cascade transitions in atoms throughout the ejecta are constrained on their characteristics by the selection rules. Basically, there is only one allowed electron transition to the K shell (2p-1s) in the CNO elements. In the iron-peak elements after Sc, two electron transitions are allowed (3d-2p and 2p-1s). In other atoms, if the vacancy-filling transition is forbidden, the vacant energy level can only be filled by the recombination through allowed intermediate transitions (e.g. through f-levels) rather than via cascade transitions. At the current epoch, the primary radiation field is formed with-

out significant conversion of the short-wave quanta emission to optical one, with the only exception being the intrinsic IR-emission of the ejecta dust particles, which are astronomical silicates. According to the findings by Doikov et al. (2018), the presence of the graphite dust in the SN 1987A debris should have resulted in blocking out the optical radiation, though, in fact, it was recorded during the Hubble Space Telescope observations in 2005, in the eighth year after the supernova explosion.

3. Young supernova remnants. Gas dynamics in the supernova ejecta.

Today, the most extensively studied supernova remnant is SNR 1987A. As all supernova remnants, it has already passed the stage of free expansion after the supernova explosion 31 year ago, and is reckoned to be in the form of a nebula. Due to exponential relationship between the key thermodynamic and kinematic parameters of the supernova ejecta, the gas-dynamic structure of intense explosions during the adiabatic phase of its expansion makes it possible to describe the remnant by the similarity and dimensional methods. In so doing, given a sufficient set of observations, the power-law indices in the equations of gas dynamics for the spherically expanding ejecta can be determined semi-empirically and written as the following simple expressions:

$$\begin{aligned} \rho(M_r, t) &= \rho(M_0, t_0) \left(\frac{t}{t_0}\right)^{-3}, \\ T(M_r, t) &= T(M_0, t_0) \left(\frac{t}{t_0}\right)^{-3(1-\gamma)} \end{aligned} \quad (5)$$

where $M_0 = 20M_\odot$, $\gamma = 1.25 - 1.30$. The temperature $T(M_r, t)$ and density (M_r, t) of the ejecta depends on the distance from the explosion site r and timescale of the process t . With the knowledge of the law of variations in the mean thermodynamic values it became possible to calculate the amount of dust resulted from the ejecta expansion. According to various estimates, the mass of the dust reaches one solar mass. Assuming the clumpy structure of the supernova ejecta, it may be deduced that astronomical silicates and graphite dust were formed in different regions of the ejecta at different times (within one to two years after the explosion as per observations). The presence of the dust particles, which radiate via luminescence being exposed to the emission from the shock fronts, made it possible to study the interstellar medium at the front of the forward shock, as well as the supernova ejecta undergoing shock cooling described by formulae (5), over two decades after the explosion. However, reduced X-ray emission from the forward shock, which has been observed since 2015, should have resulted in the disappearance of the intrinsic emission of the dust; though, in fact, the X-ray emission has decreased to a lesser extent than predicted by the calculations of the dust energy balance. The self-emission of gas and dust in the ejecta observed over last 20 years has called for the presence of extra sources of energy, to which, earlier in the introduction, we have attributed the radioactive transformations of the ^{44}Ti isotope. Thus, for the supernova ejecta

we can postulate the presence of a nebula with inner sources of energy. Observations in recent years have also shown that the supernova ejecta are clumpy. Dust and heavy elements, which are the supernova nucleosynthesis products, are concentrated in the ejecta clumps. The number of such clumps is of the order of 100. The clumps are surrounded by hydrogen and helium; these elements being concentrated mainly in the outer regions of the ejecta make a significant fraction of its total mass.

The mean relative abundances of chemical elements in this study were estimated from the pair of equations (5). The total number of positrons in the ejecta is 10^{51} , which is equivalent to one positron per 1 cm^3 . The volume of the ejecta expands with time while the number of positrons per 1 cm^3 of the ejecta decreases; in any case, it results in the reduction in the emissivity within the entire bulk of the ejecta. The total luminosity of the ejecta may be taken as a constant value, which is valuable for the observations at short wavelengths, including the γ -rays. Another important aspect is that the shape of the remnant is not of significance for the integrated observations of sufficiently distant young supernova remnants. In this case, the remnant is considered to be spherically symmetric. It is also important for mapping the supernova ejecta.

4. Radiative transfer in the ejecta

A specific feature of the Type II supernova remnants is the distribution of emitters within the entire bulk of the ejecta clumps. In this case, the motion of radiative fluxes is diffusive and isotropic rather than directed. This problem has been first considered for the active galactic nuclei. The excited state of atoms, molecules and dust resulting in their own radiation within large volumes of gas-and-dust aggregates was associated with the ejection of high-energy particles, i.e. cosmic rays, and exposure to hard X-rays and γ -rays. A solution to the equation of radiative transfer for volumetrically distributed emitters, i.e. dust particles, was proposed in the monograph by Osterbrock (1989). Later, Lucy et al (1991) modified the relations obtained by Osterbrock in order to simultaneously factor in the absorption and dissipation of the volumetrically emitted quanta. The resulting relations, which are important for our study, bear the name the Osterbrock-Lucy equations:

$$\mathcal{P}_{esc}^{unif}(\tau, \omega) \equiv \frac{P_e(\tau)}{1 - \omega[1 - P_e(\tau)]}, \quad (6)$$

$$P_e(\tau) = \frac{3}{4\pi} \left[1 - \frac{1}{2\tau^3} + \left(\frac{1}{\tau} + \frac{1}{2\tau^2} \right) e^{-2\tau} \right] \quad (7)$$

where $\tau_{ext} = \tau_{abs} + \tau_{scat}$, $\omega = \tau_{scat}/\tau_{ext}$.

Assuming that ε is the emission per unit volume of a clump and adopting equations (18) and (19), Varosi & Dwek (1998) derived formulae of the intensity $I_{out}(\tau, \theta)$ and total emerging flux $F_{out}(\tau)$, which will be convenient for further calculations:

$$I_{out}(\tau, \theta) = \frac{\varepsilon}{\rho\kappa} (1 - e^{-2\tau \cos(\theta)}), \quad (8)$$

$$F_{out}(\tau) = \frac{\pi\varepsilon}{\rho\kappa} \left(1 - \frac{1}{2\tau^3} + \left(\frac{1}{\tau} + \frac{1}{2\tau^2} \right) e^{-2\tau} \right) \quad (9)$$

For the ejecta clumps with different composition the total emerging flux $F_{out}(\tau)$ depends on the ratio between

the scattering, absorption and emission coefficients. The structure of the radiation field of clumps containing no dust was described by Doikov *et al.* (2018). In particular, the source function $S(E,r)$ was defined. The presence of a substantial amount of the graphite dust in the ejecta should have noticeably suppressed the short-wavelength portion of the source function $S(E,r)$ that could have made the production of the remnant atomic spectra, de facto observed in 1995, impossible. The graphite dust contributes to the emission from the shock fronts of SN 1987A whereas the silicate dust emission fits better to explain the spectroscopic features of the ejecta. The particle-size distribution function $n(a) \approx a^{-3.5}$; $10^{-9}m < a < 0.25 \cdot 10^{-6}m$ is typical for the silicate dust. When interpreting the spectroscopic data on the interstellar medium and supernova remnants, we consider the so-called astronomical silicates. Apart from their intrinsic emission, these particles scatter the short-wavelength component of $S(E,r)$ and let the optical and partially IR emission through. When calculating monochromatic optical depth of a clump for a given $S(E,r)$, we can add the expression for the emerging flux produced exclusively by astronomical silicates to formula (21) for the total emerging flux $F_{out}(\tau)$:

$$F_{\lambda}^{sil}(\lambda) = 4\pi m_d k(\lambda) B_{\lambda}(T_d) \quad (10)$$

In this formula, m_d is the mass of the silicate dust in an ejecta clump; $k(\lambda)$ is the absorption coefficient for a given type of astronomical silicates; $B_{\lambda}(T_d)$ is the Planck function for particles with the temperature T_d . Unlike active galactic nuclei wherein particles which promote excitation, as well as quanta, widely range in their energies, the SN 1987A ejecta contain positrons serving as an excitation source with energies constrained by the nuclear transmutation laws which can reach 3.6 MeV. As mentioned earlier, the satellite observations provided a rather accurate estimate of the amount of the titanium radioactive isotope in the SN 1987A ejecta – 10^{27} kg. It means that the energetic activity of the radioactive titanium is strictly determined at a given instant of time. The spectroscopic response of cold gas and dust in the ejecta, through which the fluxes of positrons pass, is no different from the analogous spectroscopic response to the flux of electrons. The differences appear at low intrinsic energies of positrons, i.e. at the stage of positron annihilation. Since the density of matter of the ejecta at the nebular phase is exceptionally low, it may be postulated that the probability of annihilation of positrons and free electrons within this nebula is low. The electron density is orders of magnitude lower than the atomic one. Hence, the annihilation of a positron with a bound atomic electron would be more probable. Low-energy positrons within the ejecta clumps annihilate mainly with K-L electrons of atoms. As will be shown below, upon such annihilation event, following the laws of conservation of energy and momentum, the atom is allowed to emit a single γ -quantum with the energy of the order of 1.0-2.79 MeV. Annihilation of positrons with free electrons yields two γ -quanta each with the energy of 0.511 MeV. It is the positron annihilation with bound electrons resulting in the emission of a 1.022 MeV quantum that has been detected by the INTEGRAL observations. It is problematic to suppose that there is a stable production of a certain amount of primary electrons with

the given narrow range of energies similar to that one of positrons in the absence of a compact relativistic source in the supernova remnant. Therefore, young supernova remnants may be considered as unique objects with respect of their γ -ray spectroscopic measurements. The improved resolution of the γ -spectra of young supernova remnants allows considering the problem of differentiation of these spectra by the chemical composition. The optical thickness of matter factoring in the energy distribution of quanta in the γ -ray region of the ejecta spectrum will be derived in the next section.

5. Determination of the SN composition by the positron annihilation spectroscopy methods. Annihilation γ -lines.

The determination of the field of positron velocities (kinetic energies) in the ejecta, as well as the elemental electronic arrangement, enables us to set the problem of their identification. The radioactive transformation of the ${}^{44}_{22}\text{Ti}$ yields positrons with low Lorentz factor. In this case, the problem on the interaction and further annihilation of a positron with a K-electron of the target atom can be solved in the boundary approximation of low energies (Doikov *et al.*, 2018; Mikhaylov *et al.*, 1998; Anshu *et al.* 2010). To this end, first, it is necessary to calculate the cross-section for the single-photon annihilation of a positron with an atomic K-electron by the following formula:

$$\sigma_{e^+} = \sigma_0 Z^5 \alpha^4 \varphi(E_{e^+}), \quad (11)$$

$$\varphi(E_{e^+}) = \frac{4m_e^3}{p_{e^+}(E_{e^+}+m_e)} \left(\frac{E_{e^+}^2}{m_e^2} + \frac{2E_{e^+}}{3m_e} + \frac{4}{3} - \frac{E_{e^+}+2m_e}{p_{e^+}} \ln \frac{E_{e^+}+p_{e^+}}{m_e} \right), \quad (12)$$

where E_{e^+}, p_{e^+} are the energy and momentum of an incident positron, respectively; m_e is the mass of a core electron; Z is the atomic number of the core electron; σ_0 is the cross-section of dissipation of the electron energy. Further, the monochromatic optical depth of the investigated gas-and-dust medium should be expressed as follows:

$$\tau_{\gamma} = n \sigma_{e^+} \Delta x, \quad (13)$$

where n is the gas density; Δx is the thickness of the absorbing layer. In order to derive the γ -ray spectra of young supernova remnants and active galactic nuclei, as well as to perform their mapping, the obtained values τ_{γ} should be plugged in formulae (8) и (9). The dependence of the cross-section σ_{e^+} on the nucleus charge (expressed in relativistic units and equal to the atomic number of the chemical element Z) is illustrated in Table 1. The units of measurement for the cross-section are cm^2 . The cross-section for the light elements is comparable to the mean geometric cross-section of the K-shells of the target atoms. However, for the iron-peak elements the probability of positron annihilation with an L-electron is 10%.

Next, we should take into account that when a positron slows down to the K-electron velocity, the single-photon annihilation with a K-electron occurs. In this case, the set of equations of conservation of energy and momentum can be written as follows:

Table 1: Dynamic characteristics of the elements relevant to the employment of positron annihilation spectroscopy methods for the one-photon annihilation of positrons and K-electrons in young supernova remnants

| El-nt | At. Wgt | E _b (eV) | Lgσ _{e⁺} | E _γ (MeV) | E _n (MeV) |
|------------------------------|------------|---------------------|------------------------------|----------------------|----------------------|
| ¹ ₁ H | 1.0081 | 13.602 | -26.8551 | 1.026533 | 0.000564 |
| ² ₁ H | 2.01410178 | 13.602 | -26.8551 | 1.026629 | 0.000467 |
| ³ ₂ He | 3.01602932 | 24.586 | -25.6339 | 1.026818 | 0.000267 |
| ⁴ ₂ He | 4.00260325 | 24.587 | -25.634 | 1.026873 | 0.000213 |
| ⁶ ₃ Li | 6.01512280 | 64.40 | -25.2194 | 1.026932 | 0.000114 |
| ⁷ ₃ Li | 7.01600456 | 64.40 | -25.2194 | 1.026912 | 0.000134 |
| ⁷ ₄ Be | 7.01692983 | 123,6 | -24.9133 | 1.026908 | 7.84E-05 |
| ⁹ ₄ Be | 9.01218224 | 123,6 | -24.9133 | 1.026908 | 7.84E-05 |
| ¹² ₆ C | 12.0 | 296 | -24.4648 | 1.026767 | 4.74E-05 |
| ¹³ ₆ C | 13.0033548 | 296 | -24.4648 | 1.026783 | 3.1E-05 |
| ¹⁴ ₇ N | 14.0030740 | 403 | -24.2843 | 1.021399 | 0.005308 |
| ¹⁵ ₇ N | 15.0001089 | 403 | -24.2843 | 1.025435 | 0.001272 |
| ¹⁶ ₈ O | 15.9949146 | 538 | -24.1397 | 1.025731 | 0.000841 |
| ¹⁷ ₈ O | 16.9991317 | 538 | -24.1397 | 1.026539 | 3.34E-05 |

$$\begin{cases} E_p + 2m_e c^2 = E_\gamma + E_n + E_b \\ P_p = P_\gamma + P_n \end{cases} \quad (14)$$

Alternatively, by squaring the second equation (the equation of conservation of momentum) and replacing the momentum moduli with the appropriate values of energy and mass from the expression $P^2 = 2mE$, we obtain a set of equations which is more convenient for the calculations:

$$\begin{cases} E_p + 2m_e c^2 = E_\gamma + E_n + E_b \\ 2m_e E_p = \left(\frac{E_\gamma}{c}\right)^2 + 2\left[\frac{E_\gamma}{c}\right]\sqrt{2m_n E_n} \cos\alpha + 2m_n E_n \end{cases} \quad (15)$$

Here E_p , E_b are the incident positron energy and binding energy of a K-electron of the target atom, respectively; m_e is the electron (positron) mass; E_γ is the sought value of the energy of the γ -quantum emitted upon annihilation; E_n is the recoil energy of the nucleus. In the second equation of the set of equations (14), α is the emission angle between the atom and γ -quantum upon the annihilation of a positron and a K-electron. In the investigated positron low-energy limit, the angles α range from 0 to $\pi/2$ rad. Then, the mean value of $\cos \alpha = 1/2$.

The cross-sections for the annihilation of positrons and K – electrons are the greatest when their kinetic energies are equal to E_b . The numerical solution to the set of equations (11) is four pair of values for the recoil momentum of the nucleus P_n and frequencies ν_γ of the emergent γ -quanta. The equation presented below was derived with adoption of the Hartree atomic unit system Hartree (1957). The electron or positron rest energy $E = m_e c^2 = 1$ was chosen as a unit of energy. The other physical quantities expressed in relativistic units are defined by the sequence of relations $\hbar=c=m_e=1$. Finally, we will solve the following set of equations:

$$\begin{cases} E_p + 2 = E_\gamma + E_n + E_b \\ 2E_p = E_\gamma^2 + [E_\gamma]\sqrt{2m_n E_n} + 2m_n E_n \end{cases} \quad (16)$$

In case of positron deflection (scattering) at small angles ≈ 0 rad, the previous set of equations shall be re-written as follows:

$$\begin{cases} E_p + 2 = E_\gamma + E_n + E_b \\ 2E_p = E_\gamma^2 + 2[E_\gamma]\sqrt{2m_n E_n} + 2m_n E_n \end{cases} \quad (17)$$

The solution for this set of equations will be expressed as follows:

$$AE_\gamma^4 + BE_\gamma^3 + CE_\gamma^2 + DE_\gamma + E = 0 \quad (18)$$

Here $A = 1$; $B = 2m_n$; $C = 4[(m_n^2 - m_n(E_p + 2 - E_b)) - 4E_p]$; $D = 8m_n(E_p - 2m_n(E_p + 2 - E_b))$; $E = 4[E_p - m_n(E_p + 2 - E_b)]^2$; m_n is the mass of the nucleus or its isotope; E_n is the recoil energy of the given nucleus. Table 1 presents these values expressed in relativistic non-system units. In Table 1, the chemical elements produced in the supernova explosion and present in the SNR 1987A, as well as the respective values E_n and E_γ were adopted from the studies by Woosley (1991) and Popov *et al.* (2014). The obtained results allow not only comparing P_n and E_γ for the target atoms, but also detecting any correlation between the recoil momentum of nuclei and the associated Doppler broadening of their emission lines in the spectra of young supernova remnants and active galactic nuclei.

6. Summary and discussion of the findings

The following characteristic features of the radiative response described by Doikov *et al.* (2018) appear in the media exposed to the positron fluxes:

1. The presence of a characteristic non-thermal radiation field with its source function.
2. Non-thermal dual-mode electron energy distribution function associated with the injection of the Auger electrons into the medium.
3. The presence of characteristic γ -lines in the spectrum of the nebular ejecta.
4. The presence of a correlation between the energies of γ -quanta, binding energies of nuclei and their recoil energies upon the single-photon annihilation of K-electrons in the respective atoms and incident positrons.
5. The calculations by formulae (16) have yielded γ -quanta energies which are not consistent with the results of experiments in the one-photon annihilation and physical properties of the interacting quantum systems predicted by the Feynman diagrams; hence, their adoption in solving the indicated problems is not reasonable.

6. The calculations by formulae (17) are important for the description of young supernova remnants and active galactic nuclei as they show the relationship between the recoil energy of the nucleus E_n and the energy of the emitted γ -quantum E_γ given the energy of the incident positron of 0.01MeV. The given values E_γ are physically significant.

7. Molecular spectra

Active radio observations of young supernova remnants have been carried out for a long time, which allowed collecting extensive observational data. Potter *et al.* (2015)

reported data on the strengthening of the fluxes of radio emission from the H_2 molecule generated in the supernova ejecta. Generation of such fluxes requires the fulfilment of two conditions, such as sufficiently high amount of molecular hydrogen and the presence of an efficient source of energy. The first condition was met just after a three-year period of recombination of atomic hydrogen. With regard to the sources of excitation, the mapping of the images has shown that a source of hydrogen excitation is located in the supernova ejecta. As mentioned above, either positrons or the Auger electrons may serve as such a source. Non-optical photons are likely to destroy molecules. The Auger electrons or positrons should have energies of the order of 100 eV to be able to excite the molecular hydrogen lines. The probability of the presence of positrons with such energies is low since as early as at such energies they efficiently annihilate with bound atomic electrons. In contrast, according to the functions of the electron energy distribution in the supernova ejecta $F(E,r)$ reported by Doikov *et al.* (2018), the likelihood of the presence of the Auger electrons with such energies is high. In these functions, E is the energy of electrons, and r is the current position of the examined unit volume of the ejecta relative to the explosion site. The increased emission flux from the H_2 molecule confirms a substantial increase in the density (and proportion) of the Auger electrons with the indicated energies.

8. Conclusions

The presence of positron fluxes in the gas-and-dust aggregates of supernova remnants allows detecting their luminosity across various spectral bands.

1. The decay of proton-rich nuclei of the radioactive isotope ${}^{44}_{22}\text{Ti}$ via a series of transformations ${}^{44}_{22}\text{Ti} \xrightarrow{85\text{ y}} {}^{44}_{21}\text{Sc} \xrightarrow{6\text{ h}} {}^{44}_{20}\text{Ca}$ is a source of positrons in the supernova ejecta. The energy loss of positrons due to ionisation results in the creation of vacant K energy levels in atoms, followed by cascade transitions and ejecting of the Auger electrons. The hard UV and soft X-ray radiation field is formed; this radiation promotes further excitation of atoms and molecules.

2. Positron annihilation in the ejecta dust particles yields two γ -quanta each with the energy of 0.511 MeV.

3. If the positron energy E_p is close to the binding energy E_b of the atomic K-electron, the annihilation occurs with the emission of a single photon upon which the nucleus gains the recoil energy E_n . The data given in Table 1 enable to estimate the kinetic energy of atoms gained in the annihilation events.

4. The Doppler broadening is expected for the spectral lines of atoms involved in both radioactive decay and annihilation processes.

5. The cross-sections for annihilation with the emission of a single photon for various atoms of astrophysical relevance were obtained. From the preliminary determined cross-sections and De Broglie wavelengths for positrons, we have deduced which atomic electrons enter into annihilation with positrons.

6. The author suggests considering the established correlation between E_n and E_γ to be a basis for the determi-

nation of the chemical composition of the target supernova remnants and active galactic nuclei.

7. Using accurate positions of the γ -lines, it is feasible to specify the velocity range for positrons which contribute to these lines.

In summary, this study has shown the relationship between manifestations of the positron motion in the γ -region of the spectrum and the appropriate characteristics of the radiation field in cold gas-and-dust aggregates.

References

- Grebenev S.A., Lutovinov, A.A., Tsygankov, S.S.: 2012, *Nature*, **490**, 373.
- Jerkstrand A., Branson C. and Korma C. T.: 2011, *A. & Ap.*, **530**, A45, pp. 1-23.
- Kaastra J.S. & Mewe R.: 1993, *A & Ap. Sp. Ser.*, **97**, 443.
- Hayakava S. Cosmic Ray Physics. Nuclear and Astrophysics Aspects. John Wiley and Sons. New York, 1969.
- Anshu S., Helmana S., Priyanka A.: 2010, *Applied Physics Research*, **2**, No 2, 176.
- Gould R. J.: 1990, *Ap.J.*, **362**, 284.
- Mikhailov A.I., Mikhailov I.A.: 1998, *JETP*, **113**, N3, 786.
- Doikov D.N., Andrievsky S.M., Yushchenko A.V.: 2018, *Journ. of Phys. Studies*, **22**, 2.
- Doikov D.N., Andrievsky S.M.: 2017, *Odessa Astron. Publ.*, **30**, 63.
- Doikov D.N., Andrievsky S.M., Yushchenko A.V.: 2018, *Phys. Sciences and Technology*, **5**, No1, 60.
- Potter T.M., Staneley-Smith L., Reville B. et al.: 2014, *Ap. J.*, **794**, 174.
- Varosi F., Dwek E.: 1999, *Ap. J.*, **523**, 265.
- Lucy, L. B., Danziger I. J., Gouiffes C. et al.: 1991, in Supernovae, ed. Woosley (N.Y., Springer), 82.
- Popov M.V., Filina A.A., Baranov A.A., Chardonet P. and V.M.Chechetkin: 2014, *Ap. J.*, **783**, 43.
- Woosley S.E. & Hoffman R.D.: 1991, *Ap. J.*, **308**, L31.
- Hartree D.R. The calculation of atomic structures. (1957), John Wiley and Sons, New York. 251p.
- Ferland et al.: 1998, *PASP.*, **110**, 749-761.
- Meleh B.: 2014, Full doctor dissertation, Lviv University.

DOI: <http://dx.doi.org/10.18524/1810-4215.2018.31.144459>

DISTRIBUTION OF CARBON STARS IN THE GALAXY

I.Eglitis¹, A.Sokolova^{1,2}¹ Institute of Astronomy of the University of Latvia,
Riga, Latvia, ilgmars.eglitis@lu.lv² Faculty of Physics and Mathematics of the University of Latvia,
Riga, Latvia, ilgmars.eglitis@lu.lv

ABSTRACT. A search for new faint carbon (C) stars in the Polar region $\delta > 55^\circ$ has been accomplished by obtaining objective prism spectra in the visual and near infrared 550 -- 900 nm on images of CCD camera of Baldone Schmidt telescope of Astrophysical observatory of University of Latvia obtained from May 2006 till June 2015. The positions of stars having color indices $(J - K) > 1.3$ mag were selected in Two Micron All Sky Infrared Survey – 2MASS to pick out potential carbon stars.

Our survey is limited in brightness by $J < 10$ mag. Identification of observed lines and molecular bands in mentioned region are given. The comparison of low resolution spectra of M, C and Zr-type stars are given.

24 new carbon stars were found. Using distribution of absolute magnitudes of carbon stars in Large Magellanic Cloud (LMC) was evaluated the M_k for newly discovered C stars. Various spectral gradients of carbon stars with known effective temperatures obtained by other methods are studied, and a correlation is found between T_{eff} and the spectral gradient [757 – 685]. The accuracy of effective temperature is ± 350 K. The interstellar absorption was calculated from reddening, which is taken from infrared full-sky dust maps. Such characteristics as true color index $(J - K)_0$, effective temperature T_{eff} , distance from the Sun in kpc, absolute magnitude M_k bolometric magnitude, were obtained for newly discovered carbon stars. The accuracy of distances is small and mainly depends on dispersion of M_k in LMC and reaches 30%.

Keywords: circumstellar mater, near infrared, carbon stars, absolute magnitude, distance

АБСТРАКТ. Пошук нових слабких вуглецевих (C) зорь в Полярній області $\delta > 55^\circ$ був досягнутий шляхом отримання спектрів з об'єктивною призмою в області візуального і ближнього інфрачервоного випромінювання в діапазоні 550-900 нм на зображеннях ПЗЗ-камери телескопа Шмідта Астрофізичної обсерваторії Університету Латвії в Балдоне, які були отримані з травня 2006 року по червень 2015 року. Позиції зорь з кольоровими індексами $(J - K) > 1,3$ були відібрані, використовуючи дво-мікрохвильовий інфрачервоний обзор всього неба (2MASS) для виявлення потенційних кандидатів вуглецевих зорь.

Наш огляд обмежений яскравістю в системі $J < 10$ mag. Приведена ідентифікація спостережуваних ліній і молекулярних смуг у вказаній області спектру. Дано

порівняння спектрів зорь спектральних класів M, C і Zr низької роздільної здатності.

Було виявлено 24 нові вуглецеві зорі. Використовуючи розподіл абсолютних величин вуглецевих зорь у Великій Магеллановій Хмарі (LMC), була оцінена M_k для знов відкритих C-зорь. Досліджуються різні спектральні градієнти вуглецевих зорь з відомими ефективними температурами, отриманими іншими методами, виявлений кореляційний зв'язок між T_{eff} і спектральним градієнтом [757 – 685]. Точність визначення ефективного температури, використовуючи знайдену кореляцію, складає ± 350 K. Міжзоряне поглинання розраховувалося по почерво-нінню, яке запозичене з інфрачервоного огляду пилевих хмар Галактики. Для знов виявлених вуглецевих зорь були отримані такі характеристики, як дійсний індекс кольору $(J - K)_0$, ефективна температура T_{eff} , відстань від Сонця в крс, абсолютна світність M_k , болометрична величина. Точність відстаней маленька і в основному залежить від дисперсії M_k в LMC і досягає 30%.

Ключові слова: межзоряна матерія, ближній інфрачервоний діапазон, вуглецеві зірки, абсолютна зоряна величина, відстань

1. Introduction

Carbon stars (C) – one of the reddest stars in the sky – since the fifties of the previous century attract great attention of astronomers. Considerable efforts have been devoted to discover distant and faint carbon stars in the Galaxy. Carbon stars are interesting not only from the stellar evolution point of view, but as it has been revealed in the first summarizing studies they also delineate the spiral structure of the Galaxy. The results of searches do-nen till now are summed up in the General Catalogue of Cool Carbon Stars (CGCS) (Alksnis et al., 2001) contain-ing 6991 entries. Most of the findings have been made using objective prism spectra recorded on photographic plates in the visual spectral region with wide field tele-scopes. The distinguishing indication of C stars is the presence of the Swan band system of the C2 in the spectra. However, the search could be done more efficiently in the near infrared region where the radiation maximum of carbon stars is localized and fainter objects come in reach. The pioneering investigation in this direc-tion has been made by Nassau & Velghe (1964) who reached the wavelength of 880 nm.

A new perspective in the carbon stars spectrophotometry at low resolution opens by using CCD's – they have more sensitivity than photoplates, giving possibilities of quantitative measurement of spectral details and reaching further in the infrared region. However, a serious drawback is a reduction of the available field area. Searching for new carbon stars may overcome this obstacle using the 2MASS catalogue by Skrutskie et al. (2006) containing J, H, and K magnitudes for thousands of very faint red stars.

Comparing the catalogued carbon stars in CGCS with 2MASS survey shows that (except few infrared objects) they are mostly objects brighter than $J = 8.5$ mag. Our intention is to encompass fainter objects. We take objective prism spectra with the CCD camera of all northern sky 2MASS objects brighter than $J = 10$ mag with $(J - K) > 1.5$ mag, to check which of them may be new cool carbon stars. The limit on $(J - K)$ is chosen, to exclude prevalent numerous early M-type stars. As it is shown in article by Dzervitis and Egilitis (2005), where color index distribution of known carbon stars has been analyzed, approximately this $J - K$ value is the boundary in which cool carbon stars come in light. In some regions of the sky the bound on $(J - K)$ is reduced to 1.3 mag to check the previous statement. A range of 550 nm – 900 nm, where carbon stars are brighter than in blue, has been used for the search.

2. Observations

Observations were made with Schmidt system telescope (240 x 120 x 80 cm) of Baldone Astrophysical observatory with a four degrees objective prism and CCD ST – 10XME (2184 x 1472 pixels; size of pixel is 6,8 x 6,8 μ). The spectral range extends from 550 to 900 nm with a spectral resolution of about 500 and maximum sensitivity of the system at 650 nm. Observations were made from May 2006 till June 2015. At first we chose high declination fields which are rarely populated by stars. Observation fields are chosen to the north from $\delta > 60^\circ$. Observation list contains more than 2000 stars from 2MASS with indices $(J - K)$ greater than 1.3 mag and with J magnitude mainly brighter than 10 mag.

2.1. Spectral features of the late stars in 550 nm – 900 nm

Due to a low atmospheric temperature of cool red stars their objective prism spectra main details are molecular bands originated from transitions from the lowest electron levels of molecules. Discrimination among the three spectral types of cool giant stars – M, S and C is based on the fact that the main discriminating molecular bands in their spectra in each case belong to different molecular species and thus are located at different wavelengths. Hence, a characteristic spectral pattern is formed.

Bands seen in carbon star spectra mainly belong to the CN molecule red system excepting the earth atmospheric O₂ A band (approximately at 765 nm) which unlike M and S types happens to lay outside from stellar molecular bands and is therefore distinctly seen as an isolated spectral feature. Visible band sets of the red CN system originated from transitions between vibration levels with quantum number difference $\Delta v = +2, +3, +4$, where in each set +3, +4 the reddest overlapping bands are evident with heads as indicated in Table 1. The first column of table

contains absorbing molecule and band system designation, the second – quantum number difference, the third – band head assignment and then subsequently wavelength of corresponding band head follows.

In total the late C star spectrum consists of symmetric pattern with atmospheric O₂ band in the centre enclosed by two band sets of CN molecules. From the red side spectra is shortened by abrupt termination of very strong CN (0,1) band head at 914 nm and from the blue side it is usually depressed by C₂ of Swan band head (0,1) at 564 nm. From atomic lines only Na I doublet in the blue part and Ca II triplet in the red part sometimes are seen as faint details in spectra of C stars.

Spectra of M-type stars are dominated by triplet γ and γ' system bands of the titan oxide (TiO), forming a very specific pattern of isolated bands. In addition at the red side of singlet δ, ϵ bands are also visible. Late M-type spectra involve bands of the vanadium oxide molecule but they overlap with TiO bands and can't be seen as separate details. Just O₂ atmospheric A band coincides with TiO γ system $\Delta v = -1$ band.

Table 1: Atomic lines and molecular bands seen in low resolution carbon star spectra

| Band | Δv | v', v'' | λ (nm) |
|----------------------------|------------|-----------|----------------|
| CaII, CaII | blend | | 852 |
| CaII | | | 866 |
| NaI doublet | blend | | 589 |
| CN red system | b.h. +2 | (2,0) | 790 |
| CN red system | b.h. +2 | (3,1) | 809 |
| CN red system | b.h. +2 | (4,2) | 830 |
| CN red system | b.h. +3 | (3,0) | 694 |
| CN red system | b.h. +3 | (4,1) | 711 |
| CN red system | b.h. +3 | (5,2) | 728 |
| CN red system | b.h. +3 | (6,3) | 745 |
| CN red system | b.h. +4 | (5,1) | 635 |
| CN red system | b.h. +4 | (6,2) | 649 |
| CN red system | b.h. +4 | (7,3) | 665 |
| C ₂ Swan band | b.h. -1 | (0,1) | 564 |
| O ₂ atmospheric | A band | | 765 |

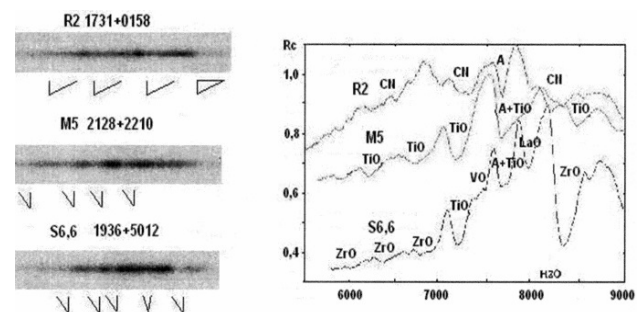


Figure 1: Comparing the spectra of C-type star BL Ori (at the bottom; axis of intensity shifted by -0.1), M-type star M3III 18^h11^m36^s +56°52' 38" (2000) (at the top; axis of intensity shifted by +0.3) and S-type star CCS 1053=V530 Lyr (in the middle). The left panel present objective prism spectra of same stars obtained in Baldone.

S star spectra are similar to M type. The difference lies in some spectral details – bands originated between two lowest level transition of zirconium oxide at 649 nm and at 585 nm, and lanthanum oxide band at 788 nm. Other LaO band at 737 nm overlaps with atmospheric A band.

Examples of all three type of stars are presented in Fig. 1.

3. Some characteristics of discovered carbon stars

2.1. Effective temperatures

Bergeat et al. (2001) gives the new effective temperature scale for late carbon stars which statistically is in a good agreement with the sample of directly determined temperature values from the observed angular diameters and with temperature estimates from the infrared flux method. Since the study is broad and covers 390 C stars, it was possible to check whether the effective temperature scale is used in the case of low resolution. At Baldone observatory it is possible to observe 191 carbon stars of Bergeat et al. (2001) list. Other Bergeat's stars were situated in the sky too low to be seen in Baldone.

Spectra was normalized to the most intensive point of spectrum (usually 783 nm) to make a comparison of the spectrophotometric gradients of various stars.

Spectrophotometric gradients: [685 – 575], [757 – 685], [775 – 685], [775 – 885] were correlated with the effective temperatures from Bergeat's list. Only gradient [757 – 685] shows the correlation with T_{eff} (see Fig. 2). and is confirmed for 191 bright carbon stars. It reveals possibility to classify carbon stars by temperature indices and to detect effective temperatures of stars with accuracy ± 350 K at spectral resolution 500.

2.2. Interstellar absorption

Magnitudes and colour indices have been corrected for interstellar extinction and reddening.

The interstellar absorption A_k and $(J - K)_0$ can be calculated from interstellar reddening. $A_k = 0.302E(B - V)$ and $(J - K)_0 = (J - K) - 0.405E(B - V)$, where $E(B - V)$ is taken from infrared full-sky dust maps obtained by Schlafly and Finkbeiner (2011).

2.3. Distances

Our chosen absolute magnitudes of carbon stars are based on the investigations of C stars in LMC. Maun (2008) showed that absolute magnitude of late carbon stars vary in a small range of magnitude from -8.1 to -7.4 depending on $(J - K)_0$ color indices. Correlation between $(J - K)_0$ color indices and absolute magnitude M_k in LMC were used in this paper to obtain this value for discovered C stars.

The distance r was calculated from the equation:

$$M_k - m_k + 5 \lg r + A_k + 10 = 0,$$

where r in kpc.

The distances r are evaluated taking absolute magnitudes from relation between M_k and $(J - K)_0$ given by Maun (2008) using calculated $(J - K)_0$ for discovered carbon stars. Results of obtained characteristics are collected in Table 2.

2.3. Bolometric magnitudes

Bolometric magnitudes are derived by equation:

$$M_{\text{bol}} = M_k + BC$$

Correlation between bolometric correction between BC and $(J - K)_0$ is presented in paper by Gullieuszik et al. (2012). He showed that BC is weakly depends on colour index $(J - K)_0$ for late type C stars. This correction is used for the acquisition of the M_{bol} .

4. Conclusion

24 new carbon stars (numbered as BIC) have been found at declinations greater than 55° . Carbon stars discovered in Baldone have temperatures in range between 1840 K and 3630 K. Distances till them are between 2.8 kpc and 7.9 kpc. According to distances and galactic latitudes they are located in Orion and Perseus arms. Three of stars BIC 7, BIC 11 and BIC 13 are located 13.3 kpc, 13.2 kpc and 16.1 kpc away, much further away than the outer arm of Galaxy. If we assume that the metallicity in our Galaxy and the Sgr subgalaxy is similar, then the absolute

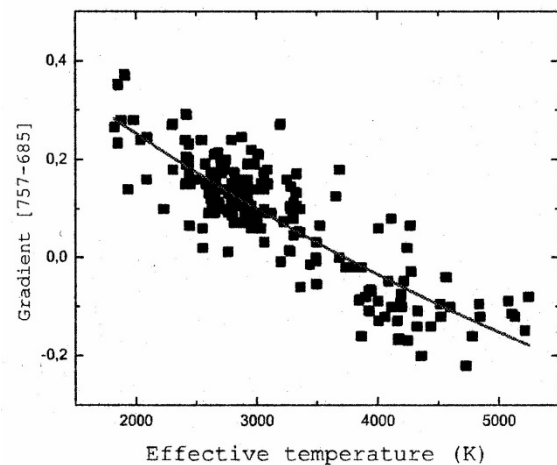


Figure 2: Relation between effective temperatures (Bergeat et al. 2001) and spectrophotometric gradient [757 – 685] obtained from low resolution spectra.

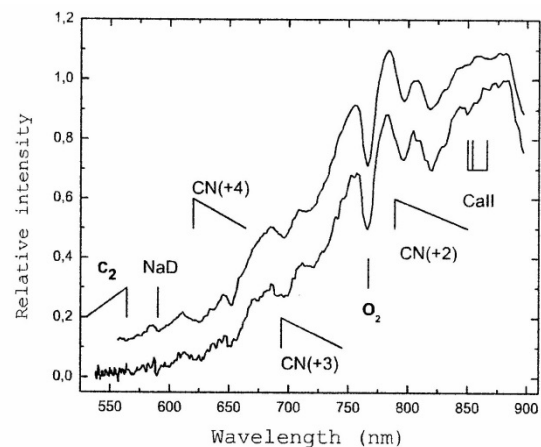


Figure 3: Spectra of discovered carbon star BIC 15 (at the bottom) and BIC 16 (at the top; gradient axis shifted by +0.1)

Table 2: Characteristics of carbon stars discovered in Baldone

| Designation | α (2000) | δ (2000) | K | (J - K) ₀ | E(B - V) | M _k | r (kps) | T _{eff} | M _{bol} |
|-------------|-----------------|-----------------|------|----------------------|----------|----------------|---------|------------------|------------------|
| BIC 14 | 001336.30 | +652710.2 | 6.54 | 1.61 | 1.78 | -8.02 | 6.39 | 2230 | -5.02 |
| BIC 1 | 003627.38 | +654014.1 | 6.59 | 1.35 | 1.89 | -7.65 | 5.47 | 2300 | -4.75 |
| BIC 15 | 010028.67 | +661639,8 | 5.91 | 1.38 | 1.79 | -7.70 | 4.12 | 1920: | -4.80 |
| BIC 2 | 013348.57 | +702623.5 | 6.61 | 1.72 | 0.52 | -8.14 | 8.28 | 2260 | -5.14 |
| BIC 3 | 031829.28 | +653820.9 | 6.63 | 1.29 | 1.09 | -7.54 | 5.86 | 2410 | -4.64 |
| BIC 4 | 040949.55 | +664155.1 | 5.80 | 1.78 | 0.61 | -8.16 | 5.68 | 2410 | -5.16 |
| BIC 5 | 210522.23 | +780116.2 | 6.12 | 3.47 | 0.48 | -7.55 | 5.06 | 2560 | -3.75 |
| BIC 6 | 213542.71 | +683907.1 | 4.91 | 3.35 | 0.91 | -7.59 | 2.79 | 2170 | -3.79 |
| BIC 7 | 214149.53 | +663409.9 | 7.74 | 1.02 | 0.46 | -6.71 | 7.27 | 3630 | -4.01 |
| BIC 8 | 214446.47 | +662710.8 | 6.71 | 1.30 | 0.69 | -7.56 | 6.49 | 2970 | -4.66 |
| BIC 9 | 215304.85 | +650210.2 | 5.68 | 1.94 | 0.72 | -8.14 | 5.25 | 2170 | -4.94 |
| BIC 10 | 215413.43 | +683511.4 | 6.76 | 1.63 | 0.31 | -8.05 | 8.78 | 3020 | -5.05 |
| BIC 11 | 221138.04 | +782812.6 | 8.07 | 2.22 | 0.36 | -8.02 | 15.7 | 3070 | -4.82 |
| BIC 12 | 230801.05 | +801016.7 | 7.66 | 2.38 | 0.13 | -7.90 | 13.1 | 2560 | -4.70 |
| BIC 16 | 233958.74 | +632054.7 | 6.51 | 1.40 | 1.26 | -7.75 | 2.0 | 1840: | -4.85 |
| BIC 12 | 235742.23 | +690134.0 | 5.31 | 2.93 | 0.99 | -7.97 | 4.0 | 2200 | -4.97 |
| BIC 17 | 205607,40 | +564156,8 | 7.96 | 2.16 | 0.08 | -8.04 | 15.7 | 2230 | -4.84 |
| BIC 18 | 205710,47 | +542811,0 | 4.09 | 2.03 | 2.17 | -8.09 | 2.0 | 1969 | -4.89 |
| BIC 19 | 205814,90 | +552342,6 | 5.39 | 1.80 | 0.06 | -8.16 | 5.1 | 2197 | -5.06 |
| BIC 20 | 205820,97 | +555808,9 | 9.16 | 1.19 | 0.06 | -7.33 | 19.7 | 3168 | 4.53 |
| BIC 21 | 210108,27 | +552140,7 | 7.87 | 1.08 | 0.21 | -6.94 | 8.9 | 2197 | 4.14 |
| BIC 22 | 232939,07 | +650337,9 | 6.49 | 3.31 | 0.06 | -7.61 | 6.5 | 1994 | -4.71 |
| BIC 23 | 234142,94 | +624202,3 | 7.25 | 1.72 | 0.03 | -8.14 | 11.9 | 2263 | -5.24 |
| BIC 24 | 234226,63 | +624401,3 | 5.71 | 1.84 | 1.80 | -8.16 | 4.6 | 2298 | -5.26 |

magnitude of C stars which we calculated using M_k distribution LMC should be reduced by 0.5 mag (Mauron 2008). Than distances which are given in Table 2 should be reduced by 20 percent for nearer C stars and by 26 percent for further C stars.

Two of discovered stars BIC 15, BIC 16 (Fig. 3), BIC 18 and BIC 22 have largest gradients and accordingly lowest temperatures. Whereas C stars BIC 7, BIC 10, BIC 11 and BIC 20 have smallest gradients and highest temperatures.

The errors for distances mainly depend on error of evaluation of absolute magnitude and can be obtained by equation:

$$\sigma = \pm \sqrt{\left(\frac{dr}{dM}\right)^2 + \left(\frac{dr}{dK}\right)^2 + \left(\frac{dr}{dE(B-V)}\right)^2}$$

As follow from Mauron (2008) paper the average error of absolute magnitude is close to ± 0.4 mag. It means that error of distances are close to 30%.

Its important is checking of our methodology comparing to distances obtained with other methods. For example using relation between absolute magnitudes and period of light variability or using GAIA parallax measurements.

Future investigations are associated with increasing of accuracy of absolute magnitude determination.

References

- Alksnis A., Balklavs A., Dzervitis U. et al.: 2001, *Baltic Astronomy*, **10**, 1.
- Bergeat J., Knapik A., Rutily B.: 2001, *A&A*, **369**, 178.
- Dzervitis U., Eglitis I.: 2005, *Baltic Astronomy*, **14**, 167.
- Gullieuszik M., Groenewegen M.A.T., Cioni M.-R.L.: 2012, *A&A*, **537**, 105.
- Mauron N.: 2008, *A&A*, **482**, 151.
- Nassau J.J., Velghe A.G.: 1964, *ApJ*, **139**, 190.
- Schlafly E.F., Finkbeiner D.P.: 2011, *ApJ*, **737**, 103.
- Skrutskie M.F., Cutri R.M., Stiening R. et al.: 2006, *AJ*, **131**, 1163.

DOI: <http://dx.doi.org/10.18524/1810-4215.2018.31.144500>

HAFNIUM ABUNDANCES IN FGK DWARF OF GALACTIC DISK

T.I. Gorbaneva, T.V. Mishenina

Astronomical Observatory, Odessa National University, Odessa, Ukraine

clumpstars@ukr.net, tmishenina@ukr.net

ABSTRACT. In this work we present new observational data for hafnium (72). Hf is an important element that is between the lightest rare-earth elements (e.g., La, $Z = 57$) with elements of the third r-process peak (Os, Ir, Pt, $Z = 76-78$). Hafnium is the heaviest ($Z = 72$) stable element represented by low-excitation (<1.5 eV) ionized lines in the spectra of the cool stars (Lawler et al., 2007). This element is important as a stable reference element for nucleocosmochronometry, and also to study of the sources of its production and enrichment with n (neutron)-capture elements of Galactic disc. We provide the analysis of the spectra of 126 FGK dwarfs in metallicity range from $-1.0 < [\text{Fe}/\text{H}] < +0.3$ that were taken from our starting sample of 276 stars (Mishenina et al. 2013). The observed stars belong to the substructures of the Galaxy disc. The observations were conducted using the 1.93 m telescope at Observatoire de Haute-Provence (OHP, France) equipped with the echelle type spectrographs ELODIE and SOPHIE. The results are based on analyses of spectra that have a typical $S/N \sim 100-300$ and a resolution of 42 000 (ELODIE) and 75 000 (SOPHIE). The hafnium abundance was derived by comparing the observed and synthetic spectra in the region of two Hf II line ($\lambda 4080.437 \text{ \AA}$ and $\lambda 4093.155 \text{ \AA}$), making use of the LTE approximation. The obtained hafnium abundance decrease with increasing metallicity in both discs, and have a big scatter at all metallicities. The dependence of our Hf abundance on metallicity and their comparison with those of other authors is presented. It corresponds to typical behavior of the elements behind the iron peak, the elements formed in the processes of neutron capture. The sources of the Hf enrichment of Galactic disc are considered.

Keywords: stars: abundances – stars: late-type – Galaxy: disc – Galaxy: evolution – abundances, nucleosynthesis

РЕФЕРАТ. У цій роботі ми представляємо нові спостережні дані для гафнію (72). Hf є важливим елементом, який знаходиться між найлегшими рідкоземельними елементами (наприклад, La, $Z = 57$) та елементами третього піку r-процесу (Os, Ir, Pt, $Z = 76-78$). Гафній – це найважчий ($Z = 72$) стійкий елемент, представлений іонізованими лініями з низьким потенціалом збудження (<1.5 eV) у спектрах холодних зір (Lawler et al., 2007). Цей елемент важливий як стійкий еталонний елемент для нуклеокосмохронометрії, а також вивчення джерел його виготовлення та збагачення елементами захвату нейтронів галактичного диску. Ми провели аналіз спектрів 126 FGK-карликів ($-1.0 < [\text{Fe}/\text{H}] < +0.3$). Зорі в нашій вибірці належать до підструктур

диска Галактики. Спостереження проводилися за допомогою телескопа 1,93 м на Обсерваторії Верхнього Провансу (ОHP, Франція), оснащеного ешельними спектрографами ELODIE та SOPHIE. Результати базуються на аналізі спектрів, що мають типовий $S/N \sim 100-300$ та роздільну здатність 42 000 (ELODIE) і 75 000 (SOPHIE). Вміст гафнію було отримано шляхом співставлення спостережуваних та синтетичних спектрів в області двох ліній Hf II ($\lambda 4080.437 \text{ \AA}$ та $\lambda 4093.155 \text{ \AA}$), з використанням наближення Локальної Термодинамічної Рівноваги (ЛТР). Отриманий вміст гафнію зменшується зі збільшенням металічності для обох дисків і має великий розкид на всіх металічностях. Представлено залежність наших значень вмісту Hf від металічності та їх порівняння з даними інших авторів. Вона відповідає типовій поведінці елементів, що утворюються в процесах захоплення нейтронів. Розглядаються джерела збагачення Hf галактичного диска.

Ключові слова: зорі: вміст – зорі: пізній тип – галактика: диск – галактика: еволюція – вміст, нуклеосинтез

1. Atmospheric parameters

The effective temperatures T_{eff} , the surface gravities $\log g$, the microturbulent velocity V_t , and metallicities of the studied stars were determined earlier in our paper (Mishenina et al., 2013). Effective temperatures T_{eff} were estimated by the line depth ratio method (Kovtyukh et al., 2003). Surface gravities $\log g$ was determined by two methods: parallaxes and ionization balance of iron.

The microturbulent velocity V_t was derived considering that the iron abundance $\log A(\text{Fe})$ obtained from the given Fe I line is not correlated with the EW of that line.

The metallicity $[\text{Fe}/\text{H}]$ accepted as the iron abundance obtained from Fe I lines.

2. Abundances

In the solar spectrum we found two Hf II lines to be good abundance indicators: $\lambda 4080.44$ and $\lambda 4093.15$. The $\log gf$ source was the Vienna Atomic Line Database (VALD, Kupka et al., 1999). Determination of the Hf abundances was made by new version of STARS LTE spectral synthesis code (Tsymbal, 1996). We used lines, which are weak and do not require to take into account the hyperfine or isotopic structure. The examples of comparison of synthetic and observed spectra for Hf II are shown in Fig. 1(a,b).

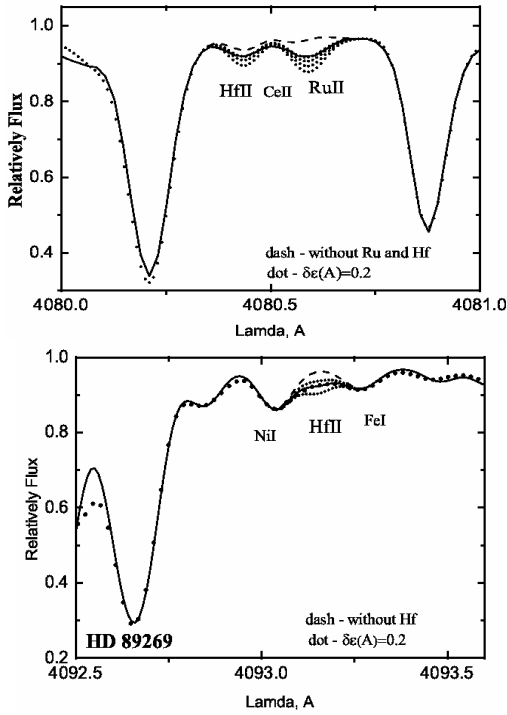


Figure 1(a,b): Comparison of synthetic and observed spectra in the region of Hf II lines. Dotted line: observations; solid black lines marked the spectra calculated for the resulted abundances. The dashed line shows the synthetic spectra without taken into account the contribution from Hf.

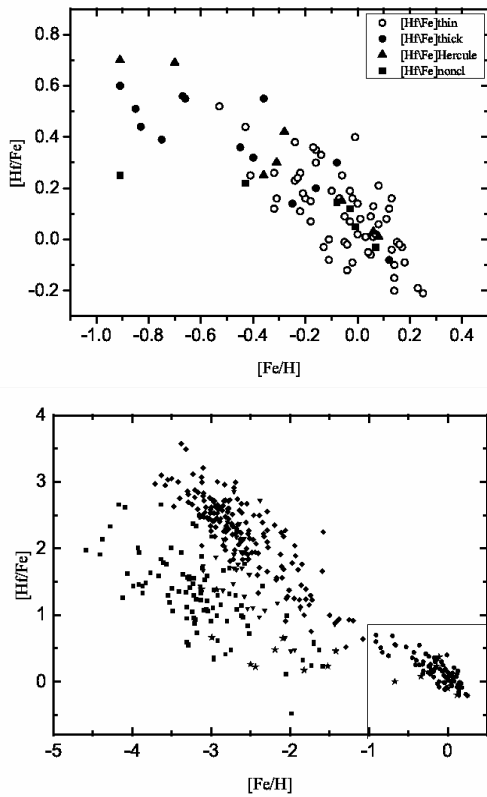


Figure 2(a,b): a) Dependences of $[Hf/Fe]$ on $[Fe/H]$ for the stars of the thick disk (filled symbol), of the thin disk (open circle), the Hercules stream (open triangles), and unclassified stars (square), b) comparison with those of other authors.

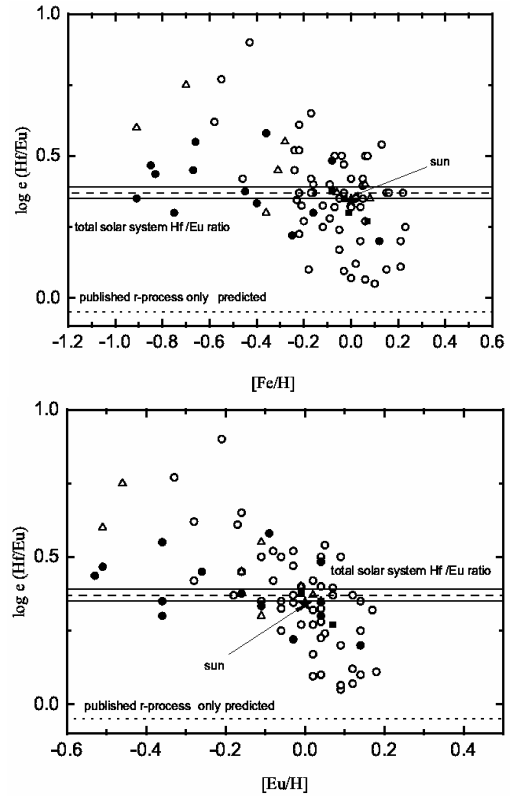


Figure 3(a,b): Abundance comparisons of $\log \epsilon(Hf/Eu)$ vs. $[Fe/H]$ and $[Eu/H]$. The dotted lines define the range of the solar system r-process only, the dashed line is the total solar system ratio (see in details, Lawler et al. 2007) and the solid line is the mean ratio of the stars in our sample.

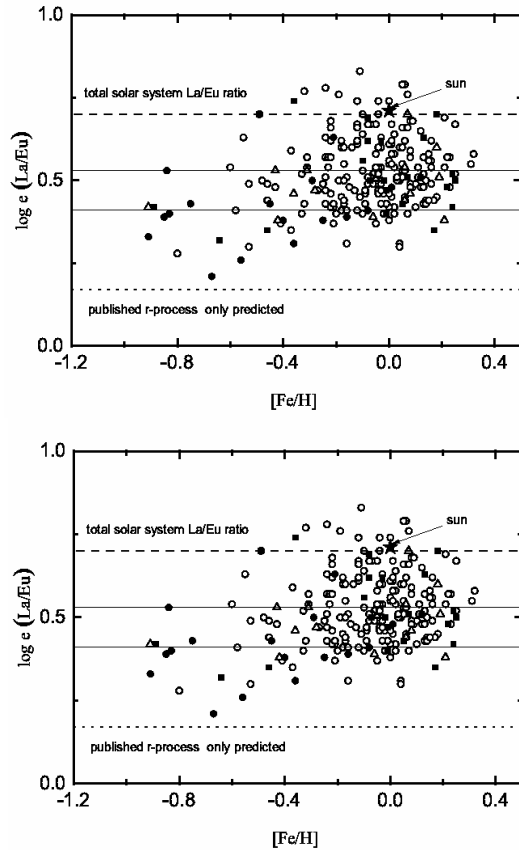


Figure 4(a,b): Abundance comparisons of $\log \epsilon(La/Eu)$ vs. $[Fe/H]$ and $[Eu/H]$. the notation is the same as in Fig. 3.

3. Results

We have determined the abundance of hafnium for 126 stars. As can be seen from Fig. 2a, the hafnium abundance decrease with increasing metallicity in both discs. The dependence of our Hf abundances on metallicity and their comparison with those of other authors (Lawler et al., 2007; Roederer et al., 2014) are presented in Fig. 2b. This is the typical behavior of the elements behind the iron peak, the elements formed in the processes of neutron capture.

To estimate the contribution of the s- (slow), and r- (rapid) processes to the Hf abundance, we compare La и Hf, which are predominantly an s-process element in solar system, with the element Eu (Fig. 3,4), having the prevailing contributions of the r- processes. The dotted lines define the range of the solar system r-process only values based on the published deconvolution of the solar system abundances (Simmerer et al., 2004), and the dashed line is the total solar system ratio based on the stellar value for the r-process (see in details Lawler et al., 2007).

4. Conclusions

We obtained the hafnium abundance for 126 FGK dwarfs belonging to different Galactic substructures. The behavior of Hf abundance with metallicity like as other

elements of n-capture. The observed stellar abundance ratios of Hf/Eu and La/Eu are coincident with previous estimates of the solar system s-, r-processes. The comparison of Hf abundance with those of La (s-element) and Eu (r-element) support that Hf is s-element.

References

- Kovtyukh, V.V., Soubiran, C., Belik, S.I., Gorlova, N.I.: 2003, *A&A*, **411**, 559.
- Kupka F., Piskunov N., Ryabchikova T. A. et al.: 1999, *A&AS*, **138**, 119.
- Lawler J.E., Den Hartog E.A., Labby Z.E. et al.: 2007, *ApJ*, **169**, 120.
- Mishenina T., Pignatari M., Korotin S. et al.: 2013, *A&A*, **552**, 128.
- Roederer I.U., Presto G.W., Thompson I.B. et al.: 2014, *AJ*, **147**, 136.
- Simmerer J., Sneden C., Cowan J.J. et al.: 2004, *ApJ*, **617**, 1091.
- Tsymbal V.V.: 1996, *ASP Conf. Ser.*, **108**, 198.

DOI: <http://dx.doi.org/10.18524/1810-4215.2018.31.145080>

MOLYBDENUM AND RUTHENIUM IN THE GALAXY

T.V. Mishenina, T.I. Gorbaneva

Astronomical Observatory, Odessa National University, 65014-UA Odessa, Ukraine

tmishenina@ukr.net

ABSTRACT. We present a brief overview of the molybdenum and ruthenium present-day nucleosynthesis calculations and abundance determinations in stars belonging to different substructures (populations) in the Galaxy. The following sources of Mo, Ru production were considered: the Asymptotic Giant Branch (AGB) stars of different masses (main s-process), massive stars (weak s-process), neutrino-induced winds from the core-collapse supernova CCSNe (weak r-process), merging of neutron stars (main r-process). Many production sites of the p-nuclei have been proposed: the Type II and Ia supernovae (at the pre-supernova phase, during and after the supernova explosion), the rp-process in neutrino-driven winds, the high-entropy wind (HEW), the vp-process; inside in a supercritical accretion disk (SSAD), in the He-accreting CO white dwarfs of sub-Chandrasekhar mass, and in the carbon deflagration model for Type Ia. We also emphasize on some additional processes such as the i-process in rapidly accreting white dwarfs (RAWDs), the lighter element primary process LEPP as well as another formation channel, namely the charged-particle process (r-process). The contribution to the solar abundance of neutron capture elements and the Galactic Chemical Evolution (GCE) models for n-capture elements were considered.

The Mo and Ru observations in metal-poor stars, Ba stars, globular clusters, meteoritic matter (presolar grains) as well as our new Mo and Ru determinations in Galactic disc are presented. Having analysed our data in the near solar metallicities we found out that there are different sources contributing to the Mo and Ru abundances, and that the main s-process contribution to the Mo and Ru abundances is lower than to the predominant s-element (Y, Zr and Ba) solar abundances.

By comparing the behavior of Mo and Ru in the wide range of $[Fe/H]$ with GCE models one can see that the theoretical description of the galactic behavior of Mo not depicts sufficient and we are faced with the underproduction of molybdenum in the sources and in processes that used at the GCE creation. Additional sources may be the p-process (SN Ia and/or SN II), vp-process (massive stars) or several more exotic processes.

Keywords: stars: abundances – stars: late-type – Galaxy: disc – Galaxy: evolution

АБСТРАКТ. Наведено короткий огляд нуклеосинтезу молибдену та рутенію та методів визначення їх вмісту у зорях, що належать до різних субструктур (популяцій) Галактики. Були розглянуті наступні джерела виробництва Mo, Ru: зірки асимптотичної гілки гігантів (AGB) різної маси (основний s-процес), масивні зірки

(слабкий s-процес), нейтрино-індуковані вітри з ядра-колапсу супернової CCSNe (слабкий r-процес), злиття нейтронних зірок (основний r-процес). Було розглянуто декілька місць утворення p-ядер: наднові типу II і Ia (на фазі до наднової, під час і після вибуху наднової), rp-процес в нейтрино-керованих вітрах, високо-ентропійний вітер (HEW), vp-процес; всередині надкритичного акреційного диску (SSAD), у He-акреції CO білих карликів суб-Чандрасекарових мас, а також у моделі вуглецевого дефлагранта для наднових типу Ia. Ми також акцентуємо увагу на деяких додаткових процесах, таких як i-процес в акретуючих з великою швидкістю білих карликах (RAWDs), в легкому первинному процесі LEPP, а також в іншому каналі формування, а саме процесі зарядженої частинки (r-процес). Розглянуто внесок у сонячний вміст елементів захоплення нейтронів та моделі галактичної хімічної еволюції (GCE) для елементів n-захоплення.

Представлені спостереження Mo і Ru в бідних на метали зорях, в барієвих зорях, в кульових скупченнях, в метеоритній речовині (досонячні зерна), а також представлені нові визначення вмісту Mo і Ru в галактичному диску. Проаналізувавши наші данні для зорь з приблизно сонячною металічністю, ми з'ясували, що існують різні джерела, що сприяють збільшенню кількості Mo і Ru, і що основний внесок s-процеса у вміст Mo і Ru є меншим, ніж у елементів переважно s-процеса (Y, Zr та Ba).

Порівнюючи поведінку Mo і Ru у широкому діапазоні $[Fe/H]$ з моделями GCE, можна побачити, що теоретичний опис галактичної поведінки Mo не є достатнім, і ми зіткнулися з недостатнім виробництвом молибдену в джерелах і в процесах, які використовуються при створенні GCE. Додатковими джерелами можуть бути p-процес (SN Ia та / або SN II), vp-процес (масивні зорі) або ще кілька екзотичних процесів.

Ключові слова: зірки: вміст – зірки: пізній тип – Галактика: диск – Галактика: еволюція

1. Introduction

The study of the enrichment of different substructures of the Galaxy with various elements is essential and crucial for understanding of the evolution of the Galaxy, especially its chemical evolution and structure, and may be a good test system for the processes and sources of nucleosynthesis. The Mo and Ru abundance allows the verification of modern calculations of nucleosynthesis and model Galactic evolution since underabundance of these elements remains an enigma and open issue of nucleosynthesis.

2. Mo and Ru nucleosynthesis

The nucleosynthesis of molybdenum and ruthenium has a long, rich history. Mo and Ru are the light trans-Fe elements produced in different processes, including the slow, rapid and intermediate neutron capture processes (respectively, the s- (main, weak, strong), r- (main, weak), and i-processes) and the proton capture process (the p-process) which, in turn, take place in various nucleosynthesis events in stars of different types.

Kappeler *et al.* (1989) proposed that the main component of the s-process is responsible for production of elements between Sr and Pb (included Mo and Ru). At the near-solar metallicity, asymptotic giant branch (AGB) stars produce the main components of the s-process (e.g., Busso *et al.*, 1999, Gallino *et al.*, 1998). Most neutrons are provided by the $^{13}\text{C}(\alpha, n)^{16}\text{O}$ reaction in the radiative ^{13}C -pocket formed right after the third dredged-up event TDU (Straniero *et al.*, 2003), with a relevant contribution from the partial activation of the $^{22}\text{Ne}(\alpha, n)^{25}\text{Mg}$ in the convective thermal pulse (Serminato *et al.*, 2009).

In massive stars, the weak s-process yields most of the s-process isotopes between iron and strontium. Neutrons are provided by the $^{22}\text{Ne}(\alpha, n)^{25}\text{Mg}$ reaction, which is activated at the end of the convective He-burning core and in the subsequent convective C-burning shell (e.g. Rauscher *et al.*, 2002, Pignatari *et al.*, 2010), in fast-rotating massive stars (e.g. Frischknecht *et al.*, 2012, 2016, Choplin *et al.*, 2018).

The origin of the r-process elements (with $A > 56$) has not been clearly defined yet, nor has it been studied or discussed. Several sources of these elements have been proposed so far:

1) the neutrino-induced winds from the CCSNe (Woosley *et al.*, 1994, Hoffman *et al.*, 1997, Wanajo *et al.*, 2001, Arcones & Montes 2011 etc), or electron-capture supernovae (ECSNe) collapsing on O-Mg-Ne cores (Wanajo *et al.*, 2011), representing a **weak r-process**;

2) the enriched neutron matter resulted from merging of neutron stars (Freiburghaus *et al.*, 1999, Goriely *et al.*, 2011 etc) and/or neutron-star/black hole mergers (Surman *et al.*, 2008), a **main r-process**;

3) polar jets from rotating MHD CCSNe (Nishimura *et al.*, 2006 etc).

Some additional sources of r-process have also been proposed, including the neutron-rich high entropy winds (HEW) (Farouqi *et al.*, 2009), the lighter element primary process LEPP (Travaglio *et al.*, 2004), or another formation channel namely the charged-particle process described in Qian & Wasserburg (2008).

However, the underproduction of light isotopes of molybdenum and ruthenium, ($^{92,94}\text{Mo}$ and $^{96,98}\text{Ru}$) and also lanthanum ^{138}La and ^{115}Sn , in the process of proton capture, which takes place in massive supernovae (Woosley *et al.*, 1978) is a stumbling block indeed. The (classical) p-process is identified with explosive Ne/O-burning in outer zones of the progenitor star. It is initiated by the passage of the supernova shock wave and acts via photodisintegration reactions which produces neighboring (proton-rich) isotopes from pre-existing heavy nuclei (Thielemann *et al.*, 2011). Many production sites of the p-nuclei have been proposed, though to date it is not clear what type of

the p-processes in supernovae is responsible for their nucleosynthesis. In the Type II supernovae, it may be the oxygen/neon layers of highly evolved massive stars during their presupernova phase (Arnould 1976, Rayet *et al.*, 1995). The p-nuclei are synthesized by the photodisintegration of s-nuclei (s-process seeds) produced in the layers during the core He-burning in the progenitor. Photodisintegration (γ, n) reactions are followed by (γ, p) and/or (γ, α) reactions; and also during their supernova explosion (Woosley & Howard 1978).

Neutrino processes have been invoked to explain the abundant production of such p-nuclei (Woosley *et al.*, 1990; Goriely *et al.*, 2001), in particular the neutrino-driven winds originating from a nascent neutron star shortly after supernova (SN II and SN Ia) explosion (Hoffman *et al.*, 1994, 1996); They included ν_e and $\bar{\nu}_e$ capture reactions on free nucleons and heavy nuclei during the freeze out from nuclear statistical equilibrium NSE. As a result, the problem shifts to that one of moderate production of some long-sought p-process nuclei, including ^{92}Mo , and ^{96}Ru .

In the Type Ia supernova, the p-nuclei are produced during explosion (Howard, Meyer, & Woosley 1991); inside in a supercritical accretion disk (SSAD) (Fujiimoto *et al.*, 2003), and He-accreting CO white dwarfs of sub-Chandrasekhar mass (Goriely *et al.*, 2002). The carbon deflagration model for Type Ia supernovae predicts that Mo and Ru isotopes are enhanced and the authors deduce that the SNe I contribution to the solar system content of p-nuclei could be larger than that of SNe II (Kusakabe *et al.*, 2011) etc.

A notable breakthrough in solving this problem occurred when Farouqi *et al.* (2009) proposed co-production of light p-, s- and r-process isotopes in the high-entropy wind (HEW) of Type II Supernovae and Wanajo (2006) has studied the rp-process in neutrino-driven winds. Comparing of the obtained yields to the solar compositions proposes that the neutrino-driven winds can potentially be the origin of light p-nuclei up to $A \sim 110$, including $^{92,94}\text{Mo}$ and $^{96,98}\text{Ru}$, that cannot be explained by other astrophysical sites; vp-process (Frohlich *et al.*, 2006), is related to the innermost ejecta, the neutrino wind expelled from the hot proto-neutron star after core collapse and the supernova explosion, when strong neutrino fluxes create proton-rich ejecta.

Recently, the researchers have found out that in the He-shell of CCSNe (15, 20 and 25 M_{\odot}), some supernova models show excesses of $^{95,97}\text{Mo}$ and depletion of ^{96}Mo relative to solar values (the weak s-process, Pignatari *et al.*, 2018). The i-process in rapidly accreting white dwarfs (RAWDs) have been proposed as contributors to the GCE, as they produces efficiently the Mo stable isotopes ^{95}Mo and ^{97}Mo (Côté *et al.*, 2018). With regard to the production of p-isotope production, e.g. the p-isotope ^{92}Mo in CCSNe of 27 M_{\odot} , they are made, up to production factors of ≈ 30 (Wanajo *et al.*, 2018), and in the neutrino-driven winds associated with over a wide range of neutron- and proton-rich conditions (Bliss *et al.*, 2018). The authors have found out that proton-rich winds may be predominant contributors to the solar abundance of ^{98}Ru , significant contributions to those of ^{96}Ru ($\leq 40\%$) and ^{92}Mo

($\leq 27\%$), and relatively minor contributions to that of ^{94}Mo ($\leq 14\%$). The production of ^{92}Mo and ^{94}Mo is observed in slightly neutron-rich conditions in 11 and 17 M_{\odot} simulations, $^{96,98}\text{Ru}$ can only be produced efficiently via the vp-process and heavily depends on the presence of very proton-rich material in the ejecta (Eichler *et al.*, 2018). SNIa have been suggested as a site for the production of p-nuclides for the abundance ratios $^{92}\text{Mo}/^{94}\text{Mo}$ (Travaglio *et al.*, 2015, Nishimura *et al.*, 2018). SNIa are responsible for at least 50% of the p-nuclei abundances in the solar system (with the exception of ^{94}Mo , Travaglio *et al.*, 2015), but the CCSNe contribute less than 10% of the solar p-nuclide abundances, with only a few exceptions, including ^{92}Mo may either still be completely or only partially produced in CCSNe, but in other sites such as neutrino winds or α -rich freeze out (Travaglio *et al.*, 2018).

3. Solar abundance and Galactic evolution models

AGB stars with low initial mass are mainly responsible for the nucleosynthesis of solar s-isotopes with $A > 90$ (Busso *et al.*, 1999). The main neutron source of low-mass AGB models is the $^{13}\text{C}(\alpha, n)^{16}\text{O}$ reaction, which burns radiatively during the inter-pulse in a thin layer of the He intershell, the so-called ^{13}C pocket (Straniero *et al.*, 1995). The formation of the ^{13}C pocket calls for an unknown mixing mechanism that allows partial mixing of a few protons from the convective envelope into the top layers of the radiative He- and C-rich intershell. The solar s-process abundances must account for the complex chemical evolution of the Galaxy, which includes AGB yields of various masses and metallicities. A number of papers are devoted to an estimate of the contribution to the solar abundance of neutron capture elements (Kapeller *et al.*, 1989, Arlandini *et al.*, 1999, Travaglio *et al.*, 2004, Serminato *et al.*, 2009, Bisterzo *et al.*, 2014). So, Arlandini *et al.* (1999) using the stellar (n, γ) cross sections of neutron magic nuclei at $N = 82$, provide significantly better agreement between the solar abundance distribution of s-nuclei and the predictions of models for low-mass AGB stars.

Since enrichment with any element at solar metallicities is not a single event, the application of models of galactic evolution allows us to take into account the various sources of enrichment and accumulation of an element with time. For example, Serminato *et al.* (2009) or Bisterzo *et al.* (2014) considered Y, Zr, Ba, La, Eu abundance with r-, s- process yields as the s-process (pure AGB s-process production including s-process contribution from massive stars) and the r-process (for elements heavier than Ba). The solar r- process contribution is derived by subtracting the s fractions from the solar abundances (the so-called r-process residuals method), and then the r-contribution to a primary process occurring in SNIi with a limited range of progenitor masses, $M = 8-10 M_{\odot}$ (Travaglio *et al.*, 1999). For Sr, Y, Zr was derive an r-fraction of 10% from observations of very metal-poor r-rich stars (Mashonkina & Christlieb, 2014; Roederer *et al.*, 2014). The authors have employed the chemical evolution code by Ferrini *et al.* (1992) and used the yields from Travaglio *et al.* (1999, 2001, 2004) with a grid of

AGB yields (Chieffi *et al.*, 1998). The solar s-process abundances have been analyzed in the framework of a Galactic Chemical Evolution (GCE) model with the impact of the ^{13}C -pocket structure on the s-process distribution and an additional weak s-process contribution from fast-rotating massive stars (Bisterzo *et al.*, 2017). Recently Prantzos *et al.* (2018) have examined the different contributing sources: i) LIM (low and intermediate mass AGB) stars, rotating massive stars plus their fiduciary r-process (the baseline model, orange continuous curve); ii) LIM stars, non-rotating massive stars and r-process (green dashed curve); iii) LIM stars plus rotating massive stars without the r-process contribution (orange dashed curve); iv) LIM stars and non-rotating massive stars without r-process contribution (gray dashed curve, Fig. 1).

The authors noted, that globally, the computed $[\text{X}/\text{Fe}]$ vs. $[\text{Fe}/\text{H}]$ evolution for the s-elements agrees with those obtained in previous studies (Travaglio *et al.*, 2004; Bisterzo *et al.*, 2017) for metallicities typical of the disk ($[\text{Fe}/\text{H}] \geq -1.0$). The weak s-process in rotating massive stars plays a key role in the evolution of the s-elements at low metallicity (Prantzos *et al.*, 2018).

4. Mo and Ru observations

Observations of Mo and Ru abundances have been performed in stars of different types : Ba stars (Allen & Porto de Mello, 2007), metal-poor stars (Hill *et al.*, 2002, Sneden *et al.*, 2003; Ivans *et al.*, 2006; Honda *et al.*, 2006; Mashonkina *et al.*, 2010; Siqueira Mello *et al.*, 2013, 2014, Peterson 2011, 2013, Hansen *et al.*, 2014, Roederer *et al.*, 2014, Aoki *et al.*, 2017, Sakari *et al.*, 2018, Spite *et al.*, 2018 etc); globular clusters (Yong *et al.*, 2008, Lai *et al.*, 2011, Roederer *et al.*, 2011, Thygesen *et al.*, 2014). In meteoritic matter (presolar grains) the different anomalies of Mo, Ru isotopes are found from presolar nanodiamonds (Xe-HL component, e.g., Lewis *et al.*, 1987), in single SiC-X grains (e.g., Pellin *et al.*, 2006, Pignatari *et al.*, 2016) and SiC AB grains (Savina *et al.*, 2003).

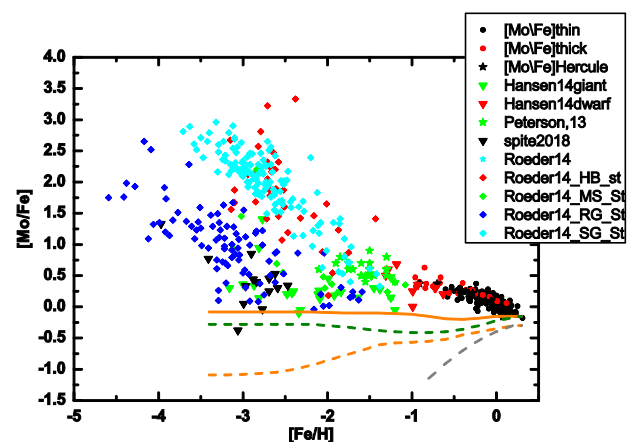


Figure 1: A comparison of our data and other authors for Mo abundances with GCE computations of Prantzos *et al.*, 2018. The notations are at the panel.

4.1. Mo and Ru in metal-poor stars

The extreme overabundance of Mo and Ru with respect to iron in two metal-poor stars (HD 94028, HD 160617) were detected by Ruth Peterson (2011). The author suggested that the low-entropy regime of a high-entropy wind (HEW) above the neutron star formed in a Type II supernova (e.g., Farouqi *et al.*, 2009) produced Mo and Ru in these two moderately metal-poor ($[\text{Fe}/\text{H}] \sim -1.5$) turn off (TO) stars, implying that only a few distinct nucleosynthesis events produced the light trans-Fe elements. The analysis the other elements (e.g. Sr, Y, Zr, and Pd) has shown that Mo and Ru are enhanced in similar manner, by an average factor of four, but Zr and Pd are always less overabundant. This substantiates that only the low-entropy regime of HEW predicts the sizable overproduction of just these elements.

At that, the lower $[\text{Mo}/\text{Fe}]$ values previously obtained for giants, using the same Mo I lines, remain puzzle. In particular, the giants of GCs demonstrate the smaller values of Mo excess. The difference might equally well result from a dependence of low-entropy regime HEW production on metallicity, or on the field halo versus globular-cluster environment. Later Peterson (2013) found the Mo, Ru overabundance for 26 stars with moderate $[\text{Fe}/\text{H}]$ and now, since high molybdenum and ruthenium abundances are typical of moderately metal-poor TO stars, exceptionally few nucleosynthesis events are not required to interpret the high values that Peterson (2011) found for HD 94028 ($[\text{Mo}/\text{Fe}] = 1.0$, $[\text{Ru}/\text{Fe}] = 0.7$) and HD 160617 ($[\text{Mo}/\text{Fe}] = 0.8$, $[\text{Ru}/\text{Fe}] = 0.6$).

Hansen *et al.* (2014) have investigated the Mo and Ru abundances in 71 galactic metal-poor field stars, dwarfs and giants at $-0.63 > [\text{Fe}/\text{H}] > -3.16$. The authors detected a wide spread in the Mo and Ru abundances, and have confirmed earlier discovered of Mo enhanced at stars around $[\text{Fe}/\text{H}] = -1.5$, and they added 15 stars, both dwarfs and giants, with small excess (<0.3 dex) of Mo and Ru abundances to iron, as well as more than 15 stars with Mo and Ru enhanced (>0.5 dex) to the known stellar sample at that time. Why such a difference has been observed, taking into account that the ISM on this metallicity is sufficiently well mixed? This question is still open. Hansen *et al.* (2014) compared the behaviour of the Mo and Ru abundances with that of Sr, Zr, Pd, Ag, Ba and Eu, for which the production sources were well known. To extract the similarity in formation processes, absolute ($\log A$) abundances of Mo and Ru were compared to those of other trace elements. If the two compared elements were produced in the same process, the ratio was expected to be 1:1; in other words, the fitted line should have a slope of 1.0. For instance, the authors reported that the ratio between Mo and Sr close to 1:1 at lower metallicity could indicate that the weak s-process yields occurred in stars with the metallicities below $[\text{Fe}/\text{H}] = -1.83$. As can be seen from Table (Arlandini *et al.*, 1999), 15% of Sr is created by a process that is different from the weak s-process. It is no the weak r-process (Ag, 79 %), but it could be a sort of lighter element primary process (LEPP), such as an α -process or a vp-process (Frohlich *et al.*, 2006) or the charged-particle process described in Qian & Wasserburg (2008). At higher $[\text{Fe}/\text{H}]$ the slope clearly deviates from

unity (1.29), and the uncertainty (star-to-star scatter) is large that could indicate that there are several formation processes creating Mo at higher $[\text{Fe}/\text{H}]$. One option would be the p-process or the earlier mentioned α -/vp-process, which would explain the correlation between Mo and Ru at higher $[\text{Fe}/\text{H}]$ since their lightest isotopes are created by a p-process. As a result, the authors have deduced that Mo is a highly convolved (composite) element that receives contributions from both the s-process and the p-process and less from the main and weak r-processes, whereas Ru is mainly formed by the weak r-process as is silver, for stars within the investigated range of $[\text{Fe}/\text{H}]$. There are a several production processes, in addition to high entropy wind as mentioned in Peterson (2011, 2013), namely the p-process, and the slow (s-), and rapid (r-) neutron-capture processes.

4.2. Mo and Ru in presolar grains

Hansen *et al.* (2014) analyzed the meteoritic enrichment as presolar grains trace the nucleosynthetic origin of Mo and Ru. The absolute elemental stellar abundances were compared to the relative isotopic abundances of presolar grains extracted from meteorites. The comparison with the elemental abundances in presolar grains showed that the r-/s-process ratios from the presolar grains matched the total elemental chemical composition derived from metal-poor halo stars with $[\text{Fe}/\text{H}]$ around -1.5 to -1.1 dex. This may be indicative of the fact that both grains and stars with metallicities around $[\text{Fe}/\text{H}] = -1.5$ and above are equally (well) mixed and hence do not support a heterogeneous presolar nebula. An inhomogeneous interstellar medium (ISM) should only be expected at lower metallicities. The stellar data, combined with the abundance ratios of presolar grains, may indicate that the AGB yields are less efficiently mixed into stars than into presolar grains.

Travaglio *et al.* (2018) showed, however, a non-solar pattern for presolar grains, likely carrying the signature of not well-mixed ejecta from single CCSNe. On the other hand, terrestrial and meteoritic p abundances have to be derived from GCE models, integrating the production of different sites over the history of the Galaxy. The solar composition might also not be representative of the average galactic composition as calculated in GCE models.

Despite the extensive set of observational data for metal-poor stars, solar abundances and presolar grains, there is no sufficient number of observations for the disc stars.

4.3. Mo and Ru in disc stars

In our first study, performed by Komarov&Mishenina (1989), the Mo and Ru abundance determinations were carried out in the atmosphere of K giant stars using the spectral synthesis methods and 5.6 Å/mm photographic spectra obtained with the 6-meter telescope at the SAO of AS of the USSR. Those Mo and Ru abundances coincided with the solar data within the errors. The next study by Gopka *et al.* (1991) was focused on the abundances of the r- and s-process elements in the atmospheres of K-giants. Since then, we have studied the enrichment of the thin and thick disc stars, in the

α -elements, n-capture elements and Mn (Mishenina *et al.*, 2004; 2013a; 2015b), as well as open cluster stars (Mishenina *et al.*, 2013b; 2015a), and performed comparison of the results with a number of the Galactic Chemical Evolution simulations (Mishenina *et al.*, 2017).

The present study focuses on the Mo and Ru enrichment of the Galactic disc. The spectra of more than 200 stars have been obtained using the 1.93 m telescope at Observatoire de Haute-Provence (OHP, France) equipped with the echelle type spectrographs ELODIE ($R = 42000$) and SOPHIE ($R = 75000$) for the wavelengths range 4400 – 6800 Å and signal to noise S/N more than 100. The atmospheric parameters were determined earlier using homogeneous methods for all the target stars (Mishenina *et al.*, 2004; 2013). The abundances were determined in the LTE approximation using the models by Castelli & Kurucz (2004) and the modified STARSP LTE spectral synthesis code (Tsymbol, 1996). The Mo I lines 5506, 5533 Å and Ru I lines 4080, 4584, and 4757 Å are used in our investigation.

In order to find possible sources of contribution to the Mo and Ru abundances, we established correlations of our estimated abundances of Mo and Ru with those of Y, Zr, Ba, Sm, Eu (Mishenina *et al.*, 2013) and Sr (still under preparation) and compared them with the known data on the AGB s-process contribution to the solar abundance. In particular, we have compared the correlations between our determinations of the Ru and Mo abundances, these are 0.48 ± 0.06 (thin disc) and 0.76 ± 0.14 (thick disc) with those reported by Hansen *et al.* (2014) for two groups of low and high metallicity stars: $\sim 0.87 \pm 0.12$ and 1.03 ± 0.08 , respectively. While our estimates for the thick disk are consistent with those of Hansen *et al.* (2014) within the reported errors, the values for the thin disc are indicative of remarkably different sources of enrichment in thin disc stars, though they supported a general conclusion by Hansen about different sources for these two elements. Upon analysis of the correlation between different elements at the near-solar metallicities, we have found out that it is different sources which contribute to Mo and Ru. In particular, the contribution of the main s-process to the Mo and Ru abundances is lower than that to the predominant s-element (Y, Zr and Ba) solar abundance; some additional sources may be contribute as the weak s-process (massive rotation stars), p-process (SN Ia and/or SN II), vp-process (massive stars) or several more exotic processes.

5. Results and discussions. Comparison of the chemical evolution pattern.

Observational data on the Mo and Ru abundances in many stars within the wide range of metallicity, including our new data, are presented in Fig. 1 and 2. We have compared the ratios $[\text{Mo}/\text{Fe}]$ vs. $[\text{Fe}/\text{H}]$ only with the calculations from Prantzos *et al.* (2018; Fig.1) since those for Ru are missing.

As can be seen from Fig. 1, the nucleosynthesis sources suggested and used in this model (AGB and fast-rotation massive stars) do not describe well the observational tendency. This allows deducing that many sources listed in the section on nucleosynthesis may contribute to the enrichment in Mo and Ru, and this should be taken into account.

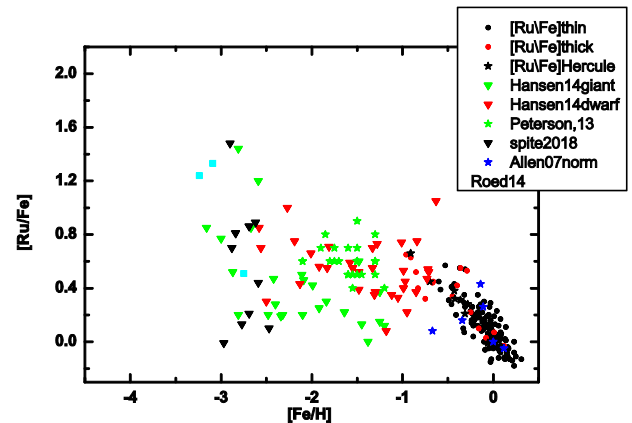


Figure 2: A $[\text{Ru}/\text{Fe}]$ vs. $[\text{Fe}/\text{H}]$. The notation is at the panel.

However, we have noted that very metal-poor stars ($[\text{Fe}/\text{H}] < -2.5$) demonstrate a very large scatter in the abundances of neutron-capture elements, including molybdenum (e.g., Roederer *et al.*, 2014; 331 stars were investigated). At the same time, Aoki *et al.* (2017) who studied the stars with similar metallicities ($[\text{Fe}/\text{H}] < -2.5$) to determine the effect of a weak r-process, have shown that their target stars do not exhibit appreciable overabundance of molybdenum or ruthenium (< 0.25 dex).

The observed scatter pattern for strontium and barium at low $[\text{Fe}/\text{H}]$ was analysed by Cescutti *et al.* (2013) with regard to the stochastic models of galactic evolution taking into account contributions of fast rotating stars to the enrichment. Their model (combining contributions from an r-process and an s-process in fast-rotating massive stars) is able to reproduce the observed scatter in the $[\text{Sr}/\text{Ba}]$ ratio at $[\text{Fe}/\text{H}] < -2.5$. With higher metallicities, the stochasticity of the star formation fades away due to increasing number of exploding and enriching stars, which results in the decrease in the predicted scatter. Perhaps, stochastic models should also be used to explain the spread of molybdenum abundances at very low metallicities.

6. Conclusion

We presented a brief overview of the current state of the Mo and Ru nucleosynthesis, including the s-process contribution to the solar abundances.

We reviewed the Mo and Ru observations in stars of different types performed earlier.

For the first time, we carried out observations of Mo and Ru in the galactic disc.

Having analysed the correlation between different elements at the near solar metallicities, we found out that the sources of contribution to Mo and Ru are different; we also detected that the main s-process contribution to the Mo and Ru abundances was lower than the predominant s-contribution to the abundances of other elements (Y, Zr and Ba).

The comparison of the behaviour of Mo in the Galaxy with the GCE predictions (Prantzos *et al.*, 2018) revealed underproduction of Mo in the adopted sources (AGB stars and fast rotation massive stars); thus, some alternative sources of the Mo enrichment should be factored in, such

as the p-process (SN Ia and/or II), vp-process (massive stars) or several other exotic processes.

References

- Allen D. M., Porto de Mello G. F.: 2007, *A&A*, **474**, 221.
 Aoki M., Ishimaru Y., Aoki W., Wanajo S.: 2017, *ApJ*, **837**, 8.
 Arcones A., Montes F.: 2011, *ApJ*, **731**, 5.
 Arlandini C., Kappeler F., Wisshak K. et al.: 1999, *ApJ*, **525**, 886.
 Arnett W. D., Thielemann F.-K.: 1985, *ApJ*, **295**, 589.
 Arnould M.: 1976, *A&A*, **46**, 117.
 Bisterzo S., Travaglio C., Gallino R. et al.: 2014, *ApJ*, **787**, 10.
 Bisterzo S., Travaglio C., Wiescher M. et al.: 2017, *ApJ*, **835**, 97.
 Bliss J., Arcones A., Qian Y.-Z.: 2018, *ArXiv e-prints*.
 Busso M., Gallino R., Wasserburg G. J.: 1999, *ARA&A*, **37**, 239.
 Castelli F., Kurucz R.: 2004, preprint (ArXiv:0405087).
 Cescutti, G., Chiappini, C., Hirschi, R. et al.: 2013, *A&A*, **553**, A51.
 Chieffi, A., Limongi, M., Straniero, O.: 1998, *ApJ*, **502**, 737.
 Choplin, A., Hirschi, R., Meynet, G., et al.: 2018, eprint arXiv:1807.06974.
 Côté B., Denissenkov P., Herwig F. et al.: 2018, *ApJ*, **854**, 105.
 Eichler M. et al.: 2018, *Journal of Physics G Nuclear Physics*, **45**, 014001.
 Farouqi K., Kratz K.-L., Mashonkina L. I. et al.: 2009, *ApJ*, **694**, L49.
 Ferrini F., Matteucci F., Pardi C., Penco U. 1992, *ApJ*, **387**, 138.
 Freiburghaus C., Rosswog S., Thielemann F.-K.: 1999, *ApJ*, **525**, L121.
 Frischknecht U., Hirschi R., Thielemann F.-K.: 2012, *A&A*, **538**, L2.
 Frischknecht U. et al.: 2016, *MNRAS*, **456**, 1803.
 Frohlich C., Hix W. R., Marturuz-Pinedo G. et al.: 2006, *New Astr. Rev.*, **50**, 496.
 Fujimoto S-i., Hashimoto M-a, Koike O. et al. 2003, *ApJ*, **585**, 418.
 Gallino R., Arlandini C., Busso M. et al.: 1998, *ApJ*, **497**, 388.
 Gopka V.F., Komarov N.S., Mishenina T.V., Yushchenko A.V.: 1991, *PAZH*, **17**, 368.
 Goriely, S., Arnould, M., Borzov, I., Rayet, M.: 2001, *A&A*, **375**, L35.
 Goriely S., Bauswein A., Janka H.-T.: 2011, *ApJ*, **738**, L32.
 Goriely S., Joser J., Hernanz M. et al.: 2002, *A&A*, **383**, L27.
 Hansen C. J., Andersen A. C., Christlieb N.: 2014, *A&A*, **568**, A47.
 Hill et al.: 2002, *A&A*, **387**, 560.
 Hoffman R.D., Woosley S.E., Fuller G.M., Meyer B.S.: 1994, *BAS*, **26**, 1363.
 Hoffman R.D., Woosley S.E., Fuller G.M., Meyer B.S.: 1996, *ApJ*, **460**, 478.
 Hoffman R.D., Woosley S.E., Qian Y.-Z.: 1997, *ApJ*, **482**, 951.
 Howard W., Meyer B., Woosley S.: 1991, *ApJ*, **373**, L5.
 Honda S., Aoki W., Ishimaru Y. et al.: 2006, *ApJ*, **643**, 1180.
 Ivans I.I., Simmerer J., Sneden C. et al.: 2006, *ApJ*, **645**, 613.
 Kappeler F., Beer H., Wisshak K.: 1989, *Reports on Progress in Physics*, **52**, 945.
 Komarov N.S., Mishenina T.V.: *Astrofizika*, **28**, 682.
 Kusakabe, M., Iwamoto, N., & Nomoto, K. 2011, *ApJ*, **726**, 25.
 Lai D.K., Smith G.H., Bolte M. et al.: 2011, *AJ*, **141**, 62.
 Lewis, R.S., Ming, T., Wacker, J.F. et al.: 1987, *Nature*, **326**, 160.
 Maeder A., Meynet G., Chiappini C.: 2015, *A&A*, **576**, A56.
 Mashonkina L. & Christlieb N.: 2014, *A&A*, **565**, 123.
 Mashonkina, L., Christlieb, N., Barklem, P. S., et al.: 2010, *A&A*, **516**, A46.
 Mishenina T., Gorbaneva T., Pignatari M. et al.: 2015b, *MNRAS*, **454**, 1585.
 Mishenina T. et al.: 2017, *MNRAS*, **469**, 4378.
 Mishenina T. V., Kovtyukh V. V.: 2001, *A&A*, **370**, 951.
 Mishenina T.V., Pignatari M., Korotin S.A.: 2013a, *A&A*, **552**, A128.
 Mishenina T.V., Korotin S.A, Pignatari M.: 2013b, *MNRAS*, **433**, 143.
 Mishenina T., Pignatari M., Carraro G. et al.: 2015a, *MNRAS*, **446**, 3651.
 Mishenina T.V., Soubiran C., Kovtyukh V.V., Korotin S.A.: 2004, *A&A*, **418**, 551.
 Nishimura N., Rauscher T., Hirschi R. et al.: 2018, *MNRAS*, **474**, 3133.
 Nishimura S., Kotake K., Hashimoto M.-A.: 2006, *ApJ*, **642**, 410.
 Pellin, M. J. et al.: 2006, *Lunar and Planetary Science LPI*, **37**, 2041.
 Peterson R.C.: 2011, *ApJ*, **742**, 21.
 Peterson R.C.: 2013, *ApJ*, **768**, L13.
 Pignatari M., Gallino R., Heil M. et al.: 2010, *ApJ*, **710**, 1557.
 Pignatari, M. et al.: 2016, *ApJS*, **225**, 24.
 Pignatari M., Hoppe P., Trappitsch R.: 2018, *Geochim. Cosmochim. Acta*, **221**, 37.
 Prantzos N., Abia C., Limongi M., Chieffi A., Cristallo S.: 2018, *MNRAS*, **476**, 3432.
 Qian Y.-Z., Wasserburg G. J.: 2008, *ApJ*, **687**, 272.
 Rauscher, T., Heger, A., Hoffman, R. D., Woosley, S. E. 2002, *ApJ*, **576**, 323.
 Rayet M., Arnould M., Hashimoto M.: 1995, *A&A*, **298**, 517.
 Roederer I.U., Marino A.F., Sneden C.: 2011, *ApJ*, **742**, 37.
 Roederer I. U. et al.: 2012, *ApJS*, **203**, 27.
 Roederer I. U. et al.: 2014, *AJ*, **147**, 136.
 Sakari C. M. et al.: 2018, *ApJ*, **854**, L20.
 Savina, M. R. et al.: 2003, *Geochim. Cosmochim. Acta Suppl.*, **67**, 418.
 Serminato A., Gallino R., Travaglio C.: 2009, *PASA*, **26**, 153.
 Siqueira Mello, C., Spite, M., Barbuy, B., et al.: 2013, *A&A*, **550**, A122.
 Siqueira Mello Jr.C., Hill V., Barbuy B. et al.: 2014, *A&A*, **565**, 93.
 Sneden, C., Cowan, J. J., Lawler, J. E., et al.: 2003, *ApJ*, **591**, 936.
 Straniero, O., Gallino, R., Busso, M., et al.: 1995, *ApJ*, **440**, L85.
 Straniero, O., Dominguez, I., Imbriani, G., & Piersanti, L.: 2003, *ApJ*, **583**, 878.
 Spite F., Spite M., Barbuy B.: 2018, *A&A*, **611**, A30.
 Surman R., McLaughlin G.C., Ruffert M. et al.: 2008, *ApJ*, **679**, L117.
 Thielemann F.-K. et al.: 2011, *Progress in Particle and Nuclear Physics*, **66**, 346.
 Thygesen A.O. et al.: 2014, *A&A*, **572**, A108.
 Travaglio C, Galli D., Gallino R., Busso M.: 1999, *ApJ*, **521**, 691.
 Travaglio, C., Gallino, R., Busso, M., & Gratton, R.: 2001, *ApJ*, **549**, 346.
 Travaglio C., Gallino R., Arnone E. et al.: 2004, *ApJ*, **601**, 864.
 Travaglio C., Gallino R., Rauscher T. et al.: 2015, *ApJ*, **799**, 54.
 Travaglio C., Rauscher T., Heger A., Pignatari M., West C.: 2018, *ApJ*, **854**, 18.
 Tsymbal V.: 1996, *ASP Conf. Ser.*, **108**, 198.
 Wanajo S., Janka H.-T., Kubono S.: 2011, *ApJ*, **729**, 46.
 Wanajo S., Kajino T., Mathews G. J., Otsuki K.: 2001, *ApJ*, **554**, 578.
 Wanajo S., Muller B., Janka H.-T., Heger A.: 2018, *ApJ*, **852**, 40.
 Woosley S. E., Hartmann D. H., Hoffman R. D., Haxton W. C.: 1990, *ApJ*, **356**, 272.
 Woosley S. E., Howard W. M.: 1978, *ApJS*, **36**, 285.
 Woosley, S.E., Wilson, J.R., Mathews, G.J. et al.: 1994, *ApJ*, **433**, 229.
 Yong, D., Karakas, A. I., Lambert, D. L. et al.: 2008, *ApJ*, **689**, 1031.

DOI: <http://dx.doi.org/10.18524/1810-4215.2018.31.145081>

STATUS REFINEMENT OF METAL-POOR STAR HD 6268

T. Mishenina¹, I. Usenko^{1,2}, A. Kniazev³, V. Kovtyukh¹

¹ Astronomical Observatory, Odessa National University, 65014-UA Odessa, Ukraine, tmishenina@ukr.net

² Mykolaiv Astronomical Observatory, Obsevatorna 1, Mykolaiv 54030, Ukraine

³ South African Astronomical Observatory, P.O. 7925, Cape Town, South Africa

ABSTRACT. Metal-poor stars in the Galaxy enable observations of the light and neutron-capture (n-capture) elements produced by their progenitors and deduction of the characteristics of the early Galaxy from the elemental abundances in these stars. Stars with deficiency of metals ($[Fe/H] < -2$) vary significantly in their chemical composition, in particular, in their content of CNO elements, as well as the iron-peak and n-capture elements. A detailed study of the elemental abundances in these stars makes it possible to test experimental models of stellar evolution, nucleosynthesis, homogeneity (the degree of mixing) of interstellar matter, etc., at low metallicity in the Galaxy.

The metal-poor star HD 6268 with $[Fe/H]$ close to -2.5 and low carbon abundance was selected as a target one for this study. The spectral material was collected using the Southern African Large Telescope (SALT) fibre-fed echelle-spectrograph HRS in the medium resolution mode ($R \sim 31000-41000$) with a high S/N ratio near 100-200 within the range from 3900 to 8700 Å. The atmospheric stellar parameters and abundances of 30 chemical elements in the metal-poor star HD 6268 were determined under the LTE approximation using the atmosphere models by Kurucz & Castelli (2003), as well as the equivalent widths EWs and WIDH9 code developed by Kurucz. The abundances of C, Na, Mg, K, Ba, La, Ce, Pr, Sm and Eu were obtained by the synthetic spectrum method factoring in the hyperfine structure (HFS) for the Eu II line 4129 Å. The carbon abundance was determined by the molecular synthesis fitting in the region of CH (4300-4330 Å). For the abundances of Na, Mg, K and Ba, we applied the NLTE corrections.

As a result, we found out that the abundances of C and N confirm their changes associated with canonical extra mixing proposed by Denissenkov & Pinsonneault (2008). The Na-O correlation is open to question unlike the Na-Si correlation which is likely to exist. The Al-Mg and Al-Na correlations are consistent with the data obtained for the field giants with $[C/Fe] < -0.5$ (Roederer *et al.*, 2014).

According to the distribution of elements depending on their atomic numbers in the atmosphere of HD 6268, it is a metal-poor main r-process enriched star.

Keywords: stars: abundances – stars: atmospheres – stars: Population II – stars: individual: HD 6268

АБСТРАКТ. Бідні металами зорі Галактики дають змогу спостерігати легкі елементи та елементи нейтронного захвату, що вироблені їхніми зорями-попередниками, і через їх вміст вивести характеристики ранньої Галактики. Зорі з дефіцитом металів ($[Fe/H] < -2$) показують помітну різноманітність хімічного складу, це стосується як CNO-елементів, так і елементів залізного піку та n-захвату. Детальне вивчення вмісту елементів у цих зорях дозволяє перевіряти (тестувати) моделі зоряної еволюції, нуклеосинтезу, однорідності (ступінь змішування) міжзоряної речовини тощо при низькій металічності в Галактиці.

Малометалічна зоря HD 6268 з $[Fe/H]$ близько $-2,5$ і малим вмістом вуглецю була вибрана для нашого дослідження. Спектральний матеріал був отриманий з ешелє-спектрографом HRS, який розміщений на Південно-Африканському Великому Телескопі (SALT) в режимі середньої роздільної здатності ($R \sim 31000-41000$) з високим співвідношенням сигнал/шум (S/N близько 100-200) у діапазоні від 3900 до 8700 Å. Зоряні параметри та вміст 30 хімічних елементів в атмосфері HD 6268 були визначені в наближенні локальної термодинамічної рівноваги (ЛТР), використовуючи моделі атмосфери Куруца та Кастеллі (2003), еквівалентні ширини EW ліній та код WIDH9 Куруца. Вміст C, Na, Mg, K, Ba, La, Ce, Pr, Sm, Eu, отримано методом синтетичного спектру з урахуванням надтонкої структури (HFS) для лінії Eu II 4129 Å. Вміст вуглецю визначався за молекулярним синтезом пристосування профілей в районі CH (4300-4330 Å). Для вмісту Na, Mg, K, Ba ми використовували виправлення (корекції) за рахунок відхилень від ЛТР.

З отриманих результатів було виявлено, що вмісти вуглецю C і та азоту N підтверджують, що зміни їх вмісту відбулися шляхом канонічного додаткового змішування, запропонованого Денисенковим і Пінсоннео (2008); наявність співвідношення Na-O під сумнівом, на відміну від співвідношення Na-Si, що може бути. Відношення Al-Mg, Al-Na співпадають з даними, отриманими для гігантів галактичного поля з $[C/Fe] < -0.5$ (Roederer *et al.*, 2014).

HD 6268 є зорею, яка демонструє збагачення основним r-процесом відповідно до розподілу вмісту елементів з атомним номером в її атмосфері.

Ключові слова: зірки: вміст хімічних елементів – зірки: атмосфери – зірки: Населення II – зірки: індивідуальні: HD 6268

1. Introduction

Metal-poor stars in the Galaxy enable us to observe CNO elements, as well as the alpha-, iron-peak and neutron-capture (n-capture) elements, produced by their progenitors and deduce the evolution and features of the early Galaxy from the abundances in these stars.

Besides, the stars in the advanced stages of their evolution (e.g. giants, AGB stars, etc.) allow us studying peculiarities of stellar evolution at low metallicity. Stars with deficiency of metals ($[\text{Fe}/\text{H}] < -2$) vary significantly in their chemical composition, in particular, in their content of CNO and n-capture elements (e.g., McWilliam *et al.*, 1995; Burris *et al.*, 2000; Sneden *et al.*, 2003; Honda *et al.*, 2006; Frebel *et al.*, 2008; Roederer *et al.*, 2014, etc.). While the carbon deficiency and excess of nitrogen detected in giants has been traditionally interpreted within the framework of their own evolution, a lot of attention has been paid recently to the stars enriched in carbon, such as carbon-enhanced metal-poor stars (CEMP).

The star **HD 6268** does not exhibit any excess of carbon; the contrary is the case as it is a giant with underabundant carbon and overabundant nitrogen having $[\text{Fe}/\text{H}]$ of about -2.5 (see, e.g., McWilliam *et al.*, 1995; Roederer *et al.*, 2014), which is likely due to the mixing processes within the star, as well as due to different mechanisms of matter transfer over the course of its evolution.

In this regard, it is very important to analyse the chemical composition and, in particular, the correlation of CNO elements with Na, Mg and Al, whose abundances change as a result of nuclear reactions and hydrogen burning in the advanced cycles (e.g., Gratton *et al.*, 2000; Spite *et al.*, 2006). Stellar models predict that as a low mass star evolves up the red-giant branch (RGB), the outer convective envelope expands inward and penetrates into the CN-cycle processed inner regions. The ensuing mixing episode, called the first dredge-up, is expected to alter the abundance of light elements on the star's surface (Iben, 1964).

The first dredge up is expected to be less efficient in metal-poor stars (VandenBerg & Smith, 1988; Charbonnel, 1994): the C and N abundances change insignificantly, and the $^{12}\text{C}/^{13}\text{C}$ ratio is expected to remain > 30 . The theoretical studies (e.g., Charbonnel, 1994; 1995) have demonstrated that some further mixing is possible in the latest phases of the RGB: in fact, after the end of the dredge-up phase is reached, the convective envelope begins to recede, leaving behind a chemical discontinuity; the corresponding change in molecular weight prevents further mixing.

In this study, we have investigated the atmospheric parameters and elemental abundances in HD 6268 aiming at clarifying its status on the basis of accurate determination of its chemical composition.

2. Observations and spectrum processing, radial velocities

The main characteristics of HD 6268 (HIP 4933) were taken from the SIMBAD database, in particular: Equatorial coordinates: $\alpha = 01\ 03\ 18$; $\delta = -27\ 52\ 49$ (2000) (GAIA DR2); Galactic coordinates: 229.57 ; -87.26 (2000).

Stellar magnitudes: $B = 9.725$; $V = 9.046$ (Zacharias *et al.*, 2012; UCAC4); distance = 705.9156 pc (GAIA DR2); parallax (mas): 1.4166 [0.0440] (GAIA DR2); radial velocity (RV) in km/s = 39.52 [0.15] (GAIA DR2).

The spectral material for the target star was collected in 2017 with the 11-metre Southern African Large Telescope (SALT) fibre-fed echelle-spectrograph HRS. The spectra were obtained in the medium resolution mode (R~31000-41000) with a high S/N ratio near 100-200 within the range from 3900 to 8700 Å. All the data were processed using the software package developed by the authors based on the standard system of astronomical data reduction MIDAS. Further spectra processing, such as the continuum establishment, line depth and equivalent width (EW) measurements, etc., was conducted using the DECH30 software package by G.A. Galazutdinov (2007).

3. Determination of parameters

We used spectroscopic methods for determination of the stellar parameters of HD6268, because we found out a contradiction in the photometric data, in particular, the stellar magnitude V obtained earlier in the Johnson system ($V = 8.16$) differed from the latest value $V = 9.046$ given in the SIMBAD database (Zacharias *et al.*, UCAC4). Nevertheless, in the first approximation, in order to determine the effective temperature T_{eff} of the target star, we used the photometric data ($V = 8.16$ and $B-V = 0.813$) and photometric calibration given in McWilliam *et al.* (1995). Then, we refined the T_{eff} value based on the independence of the iron abundance determined from a given line on the lower-level potential E_{low} of that line (Fig. 1). To determine the gravity $\log g$, we employed the iron ionisation balance technique for the Fe I and Fe II abundances. The microturbulent velocity V_t was determined from the condition of independence of the iron abundance determined from a given line on its equivalent width EW (Fig. 2).

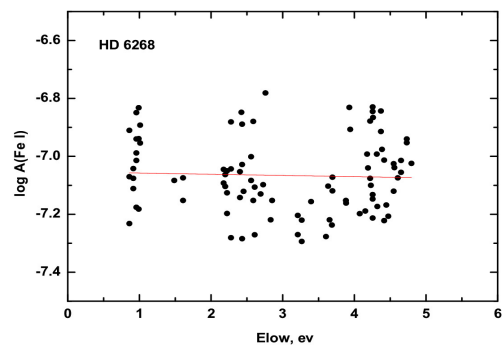


Figure 1: The dependence of $\log A(\text{Fe I})$ on E_{low}

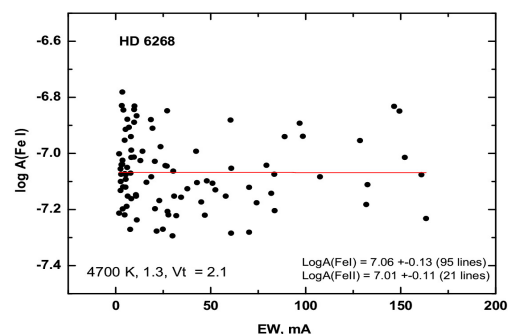


Figure 2: The dependence of $\log A(\text{FeI})$ on EW

Table 1. Parameter's comparison with those obtained in different papers

| T_{eff} | $\log g$ | [Fe/H] | V_t , km/s | reference |
|------------------|----------|--------|-----------------|----------------------------------|
| 4700 | 1.3 | -2.56 | 2.1 | our |
| 4818 | 0.84 | -2.40 | 1.5 | Gratton, 1989 |
| 4670 | 0.75 | -2.58 | 2.73 | McWilliam <i>et al.</i> , 1995 |
| 4700 | 1.6 | -2.36 | 1.3 | Pilachowski <i>et al.</i> , 1996 |
| 4800 | 0.84 | -2.56 | 2.5 | Francois, 1996 |
| 4700 | 1.6 | -2.36 | 1.6 | Burris <i>et al.</i> , 2000 |
| 4740 | 1.20 | -2.32 | - | Cenarro <i>et al.</i> , 2007 |
| 4696 | 1.2 | -2.74 | - | Yong <i>et al.</i> , 2013 |
| 4570 | 0.70 | -2.89 | 1.85 | Roederer <i>et al.</i> , 2014 |
| 4696 | 1.2 | -2.74 | 2.75 | Placco <i>et al.</i> , 2014 |
| 4726 | 1.14 | -2.63 | 2.05 | Wu <i>et al.</i> , 2015 |

The metallicity [Fe/H] was adopted as the iron abundance determined from the Fe I lines. The selection of the parameters was performed using an iterative procedure. Finally, the following parameters were adopted: $T_{\text{eff}} = 4700$ K; $\log g = 1.3$; $V_t = 2.1$ km/s.

Table 1 presents the results of the comparison of our data with the findings of other researchers. As can be seen in Table 1, there is a good agreement between T_{eff} and [Fe/H] obtained by different authors. However, noticeable discrepancies can be observed for the gravity $\log g$ and turbulent velocity V_t .

Our determinations corroborate with the mean values of the parameters within the errors: $\langle T_{\text{eff}} \rangle = 4710 \pm 65$ K; $\langle \log g \rangle = 1.12 \pm 0.30$; $\langle [\text{Fe}/\text{H}] \rangle = -2.56 \pm 0.18$; $\langle V_t \rangle = 2.04 \pm 0.53$ km/s.

It should be noted that for the metallicities close to that one of the target star, the deviations from the Local Thermodynamic Equilibrium (LTE) may influence the stellar parameters and iron abundance (see, e.g., Lind *et al.*, 2012). However, Roederer *et al.* (2014) have investigated metal-poor stars and found out that the Fe II abundance determined by the LTE calculations is close to its estimates under non-LTE approximations within 0.02 dex. The obtained results enabled Roederer *et al.* (2014) to adopt the iron abundance derived from the Fe II lines as an indicator of metallicity [Fe/H]. The effect of the non-LTE deviations on the iron abundance determination from the Fe I lines is stronger, but it does not exceed 0.2 dex as reported by different authors (e.g., Thévenin & Idiart, 1999; Asplund, 2005). Our estimates of the iron abundance obtained from the Fe I and Fe II lines are almost similar, hence our decision to take the Fe I abundance as [Fe/H] does not contribute significantly to the error in determination of the parameters and iron abundance. To verify our $\log g$ determined by the Fe I/Fe II ionization balance, we adopted our estimated surface gravity $\log g$ (as well as T_{eff}) in the theoretical isochrones in the Y2 grid (Demarque *et al.*, 2004) for the relevant metallicity ([Fe/H] = -2.5). As can be seen, there is an agreement between our $\log g$ and the position in the corresponding theoretical track, which corroborates our gravity determination and allow us assuming the age of the target star to be 12 Gyr (Fig. 3).

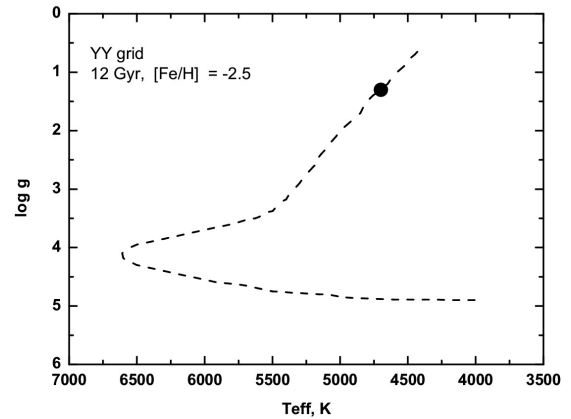


Figure 3: Position of HD 6258 on the theoretical isochrones of the Y2 grid (Demarque *et al.* 2004)

4. Abundance determination

For HD 6268, the abundances of the investigated elements were determined under the LTE approximation with the atmosphere models by Kurucz & Castelli (2003). The stellar model was selected by means of a standard interpolation for T_{eff} and $\log g$. Elemental abundances were determined using the equivalent widths EWs and WIDH9 code by Kurucz. The latest version of the modified STARS code (Tsymbal, 1996) and VALD line list (Kupka *et al.*, 1999) were employed for the LTE determination of the abundances of C, Na, Mg, K, Ba, La, Ce, Pr, Sm and Eu. The Eu abundance was calculated from the Eu II line 4129 Å factoring in the HFS (Ivans *et al.*, 2006). The carbon abundance was determined using the molecular synthesis fitting in the region of CH (4300-4330 Å).

For the Na, Mg, K and Ba abundances we used the NLTE corrections computed by Sergei Korotin: the NLTE correction for the employed Ba lines at [Fe/H] close to -2 was about 0.1 dex (Korotin *et al.*, 2015); and the NLTE departures for Na, Mg and Al at [Fe/H] ~ -2.0 varied from 0.03 to 0.2 dex depending on T_{eff} and $\log g$ (Andrievsky *et al.*, 2010); for D lines Na ~ 0.5 dex.

The spectrum synthesis fitting of the C and Ba lines to the observed profiles for star is shown in Figs. 4,5.

To determine the systematic errors in the abundance estimates due to uncertainties in the atmospheric parameter determinations, we have derived the elemental abundances for the target star from several models with modified parameters ($\delta T_{\text{eff}} = \pm 100$ K; $\delta \log g = \pm 0.2$; $\delta V_t = \pm 0.1$). The total uncertainty due to the parameter and EW errors for the Fe I and Fe II are 0.11 and 0.12, respectively. The determination accuracy for other elements varies from 0.10 to 0.18 dex.

We compared our abundance determinations with those obtained by other authors (Burris *et al.*, 2001; Roederer *et al.*, 2014). The elemental abundances [E/Fe] as a function of the relevant atomic numbers for HD 6268 are depicted in Fig. 6.

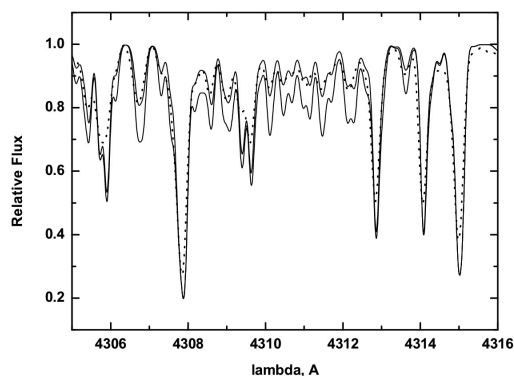


Figure 4: Observed (dotted line) and calculated (solid lines) spectra in the region of CH lines

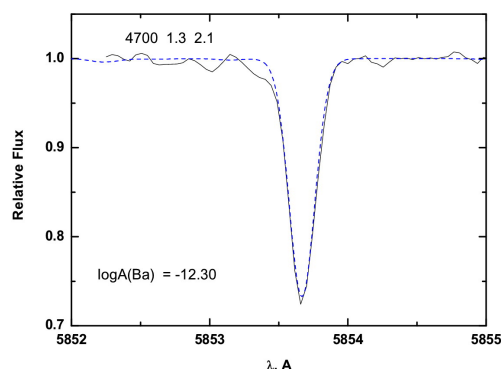


Figure 5: Observed (dashed line) and calculated (solid line) spectra in the region of Ba I line 5853 Å

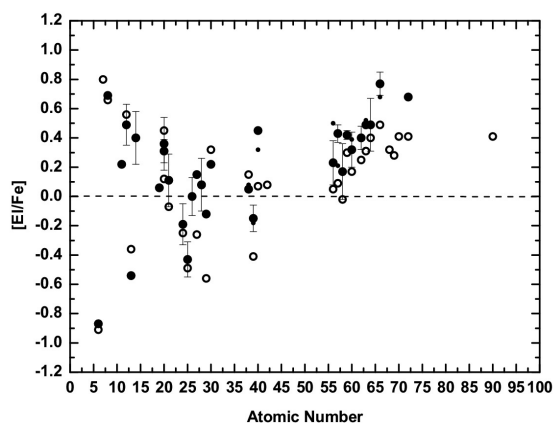


Figure 6: $[E/Fe]$ vs. Atomic Number. Our determination marked as black circles, those of Burris *et al.* (2001) as small circles and Roederer *et al.* (2014) as open circles

5. Results and discussions

The study of HD 6258 star is important in two aspects: from the point of view of the advanced stages of stellar evolution of metal-deficient stars, and in the context of galactic chemical evolution.

5.1. Stellar evolutionary effects (on CNO, Na, Mg, Al)

Stars in the advanced stages of their evolution exhibit variations in the abundances of certain chemical elements.

Table 2: CNO, Na, Mg, Al, and Si abundances

| Elem | our | Roederer et al., 2014 | McWilliam et al., 1996 |
|---------|--------------|-----------------------|------------------------|
| [C/Fe] | -0.87 | -0.91 | -0.68 |
| [O/Fe] | 0.69 | 0.66 | - |
| [Na/Fe] | 0.12 | - | 0.22 (LTE) |
| [Mg/Fe] | 0.49 | 0.56 | 0.44 |
| [Al/Fe] | -0.54 | -0.36 | +0.48 |
| [Si/Fe] | 0.40 | - | 0.50 |

In case of stars of the giant branch, a change in the abundances of Li, CNO, Na, Mg and Al may be expected, which is the subject of many years research in the giants of globular clusters. Table 2 presents the abundances of the listed elements obtained in our study, as well as those reported in McWilliam *et al.* (1996) and Roederer *et al.* (2014).

The abundances are in good agreement with the only exception being the aluminium abundance, though it may be due to a misprint in the paper by McWilliam *et al.* (1996).

Gratton *et al.* (2000) carried out a detailed analysis of mixing along the red-giant branch in 62 field stars within the metallicity range of $-2 \leq [Fe/H] \leq -1$. The abundances of light elements in lower-RGB stars (i.e. stars brighter than those with the first dredge-up luminosity and fainter than the RGB bump) are in agreement with the predictions made using classical evolutionary models. A second dredge-up, which is a distinct mixing episode, occurs in most (perhaps in all) low mass metal-poor stars just after the RGB bump. In the field stars, this second mixing episode only reaches regions of incomplete CNO burning: it causes a depletion of the surface ^{12}C by about a factor of 2.5 with a corresponding increase in the N abundance by about a factor of 4. However, any O-Na anti-correlation which is typically found in the globular cluster stars is observed in the field stars.

Spite *et al.* (2006) performed an LTE analysis of 32 extreme metal-poor (EMP) giants in order to understand the CNO abundance variations found in some, but not all EMP field giants, considering mixing beyond the first dredge-up in the standard stellar models. They found out a C-N anti-correlation that corroborated the hypothesis that the surface abundances could be modified by the CNO processed material from the inner regions.

Our findings, in particular, the carbon underabundance and nitrogen overabundance, may be consistent with the stellar evolution calculations and associated with canonical extra mixing (e.g., Denissenkov & Pinsonneault, 2008; for the CMEP stars). In the mentioned paper, Fig. 5 illustrated variations in the surface C and N abundances (black curve) due to canonical extra mixing with the depth $rmix = 0.045 R_{sol}$ and rate $Dmix = 0.04K$ in the RGB model with $M = 0.83 M_{sol}$ and $Z = 0.0001$. Earlier, Denissenkov & Vandenberg (2003) have shown that at least the extra mixing depth does not seem to depend strongly on metallicity. Therefore, they have suggested calling this universal non-convective mixing process “canonical extra mixing”. They also hypothesised that some of the upper RGB stars (of GCs) may experience “enhanced extra mixing”, which is much faster (by a factor of ~ 100) and to a

some extent deeper than canonical extra mixing. However, the proposed process of enhanced extra mixing leads to the depletion of oxygen and may also contribute to the O-Na and Mg-Al anti-correlations observed in some globular cluster red giants. The turbulent diffusion or/and rotation-induced meridional circulation may be an alternative mechanism of extra mixing in the upper RGB stars. In this case, enhanced extra mixing requires rotational velocities to be ~ 10 times as high as those which are sufficient for canonical extra mixing to occur.

The value $\log L/L_{\odot} = 2.71$ for HD 6268 was calculated via the classical formula:

$$\log L/L_{\odot} = \log M^*/M_{\odot} + 4\log \text{Teff}^*/\text{Teff}_{\odot} - \log g^*/g_{\odot},$$

where $\text{Teff}_{\odot} = 5780$ K, $\log g_{\odot} = 4.44$ and assuming a stellar mass $M^* = 0.85M_{\odot}$.

Figs. 7 and 8 illustrate the computations by Denissenkov & Pinsonneault (2008) for canonical extra mixing at $\log L/L_{\odot} > 2.2$ (these figures correspond to black curves in Figures 2 and 5 in the cited paper). If we compare our values of $[C/H] = -3.43$ and $\log L/L_{\odot} = 2.71$ with the prediction reported in the afore-mentioned study, we can see that our star is located in the black curve which corresponds to canonical extra mixing for non-C-enhanced extremely metal-poor stars (Fig. 7).

If we adopt $[N/Fe] = 0.8$ (Roederer *et al.*, 2014) and $[C/Fe] = -0.87$ (our determination), these values are close to the black curve which shows variations in the surface C and N abundances due to canonical extra mixing (Fig. 8). The C and N abundances, as well as the luminosity of HD 6268, corroborate the presence of canonical extra mixing (Denissenkov & Pinsonneault, 2008) in this star.

We compared our data with those reported by Roederer *et al.* (2014) for the field giants with $[C/Fe] < -0.5$ for different relationships, such as $[Na/Fe]$ vs. $[O/Fe]$, $[Na/Fe]$ vs. $[Al/Fe]$, $[Al/Fe]$ vs. $[Mg/Fe]$ and $[Na/Fe]$ vs. $[Si/Fe]$. Our determinations fall into the area of the listed relations plotted using the values from Roederer *et al.* (2014); however, no clear correlations between these data can be seen, with the only exception being the Al – Mg anti-correlation and to a smaller extent the Na-Al anti-correlation. It should be noted that our data are in good agreement with the respective dependencies (the Na-O correlations and Al-Mg, Na-Al, Si anti-correlations) reported in Marino *et al.* (2015) for the globular cluster NGC 5286. Unfortunately, the number of observations is not sufficient to enable us to draw more reliable conclusions.

5.2. Galactic enrichment

The obtained pattern of the abundances of elements depending on their atomic numbers (for the elements with $AN > 50$, the abundance increases with increasing atomic number) is in agreement with the results obtained by Sneden *et al.* (2003) for the star CS 22892-052 exhibiting a scaled solar system r-process abundance (as stars with the main r-process); meanwhile, it is not consistent with the findings for HD 122563 (Honda *et al.*, 2006) wherein an excess of light neutron-capture elements is observed without an enhancement of heavy elements (as stars with the weak r-process).

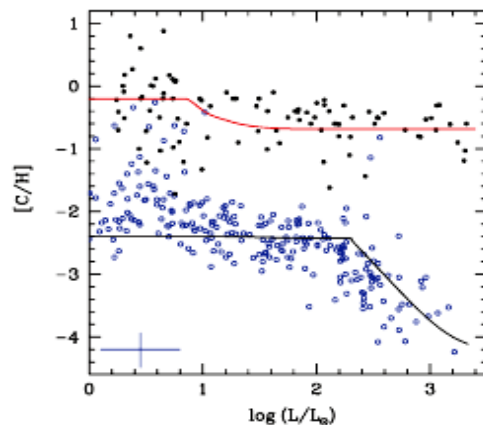


Figure 7: The carbon abundance vs. $\log L/L_{\odot}$; the figure corresponds to Figure 2 in Denissenkov&Pinsonneault (2008)

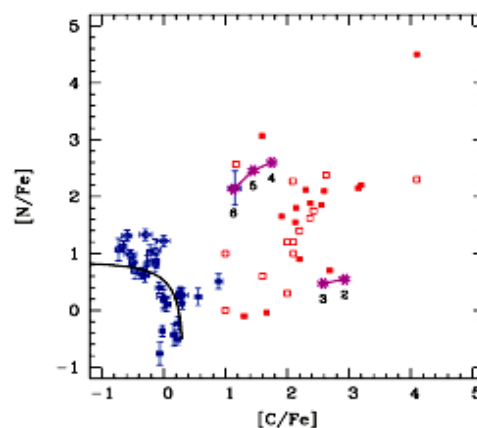


Figure 8: $[N/Fe]$ vs. $[C/Fe]$; the figure correspond to Figure 5 in Denissenkov&Pinsonneault (2008). The black curve depicts variations in the surface C and N abundances associated with canonical extra mixing with the depth $r_{mix} = 0.045 R_{sun}$ and rate $D_{mix} = 0.04 K$ in the RGB model with $M = 0.83 M_{\odot}$ and $Z = 0.0001$.

6. Conclusion

- The C and N abundances confirm their changes due to canonical extra mixing (Denissenkov & Pinsonneault, 2008).
- The Na-O correlation is open to question unlike the Na-Si correlation which is likely to exist.
- The correlations between Al – Mg and Al – Na confirm the data obtained for the field giants (Roederer *et al.*, 2014).
- According to the distribution of elements depending on their atomic numbers, HD 6268 is a metal-poor main r-process enriched star.

References

- Andrievsky S.M. et al.: 2010, *A&A*, **509**, id. A88.
 Asplund M.: 2005, *ARA&A*, **43**, 481.
 Burris et al.: 2000, *ApJ* **554**, 302.
 Castelli & Kurucz: 2004, *ArXiv Astrophysics e-prints* astro-ph/0405087.

- Cenarro et al.: 2007, *MNRAS*, **374**, 664.
Charbonnel C.: 1994, *A&A*, **282**, 811.
Charbonnel C.: 1995, *ApJ*, **453**, 41.
Demarque et al.: 2004, *ApJS*, **155**, 667.
Denissenkov P., Pinsonneault: 2008, *ApJ* **679**, 1541.
Denissenkov P., Vandenberg D.A.: 2003, *ApJ*, **593**, 509.
Gaia Collaboration: 2018, Gaia DR2, Cat.1345.
Galazutdinov G.: 2007, <http://gazinur.com/DECH-software.html>.
Gratton, R.: 1989, *A&A* **208**, 171.
Francois P.: 1996, *A&A* **213**, 229.
Frebel et al.: 2008, *ApJ*, **684**, 588.
Honda et al.: 2006, *ApJ*, **643**, 1180.
Iben I.: 1964, *ApJ*, **140**, 1631.
Ivans et al.: 2006, *ApJ*, **645**, 613.
Korotin et al.: 2015, *A&A* **581**, 70.
Lind et al.: 2012, *MNRAS*, **427**, 50.
McWilliam et al.: 1995, *AJ*, **109**, 2757.
Kupka et al.: 1999, *A&ASuppl.*, **138**, 119.
Marino et al.: 2015, *MNRAS*, **450**, 815.
Pilachowski et al.: 1996, *AJ*, **111**, 1689.
Placco et al.: 2014, *ApJ*, **797**, 21.
Roederer et al.: 2014, *AJ*, **147**, 136.
Snedden et al.: 2003, *ApJ*, **591**, 936.
Spite et al.: 2006, *A&A*, **455**, 291.
Thévenin, F., Idiart, T. P.: 1999, *ApJ*, **521**, 753.
Tsymbal V.: 1996, *ASP Conf. Ser.*, **108**, 198.
Vandenberg D., Smith G.: 1988, *PASP*, **100**, 314.
Wu et al.: 2015, *A&A*, **579**, A8.
Yong et al.: 2013, *ApJ*, **762**, 26.
Zacharias et al.: 2012, *The fourth US Naval Observatory CCD Astrogaph Catalog (UCAC4)*.

DOI: <http://dx.doi.org/10.18524/1810-4215.2018.31.144615>

THE DEPENDENCE OF ON- AND OFF-STATE GENERATIONS IN CLASSICAL MICROQUASARS FROM THE DISK DENSITY. 3-D NUMERICAL HYDRODYNAMICAL SIMULATIONS OF THE HIGH AND LOW MASS ACCRETION RATE IN ACCRETION DISK IN MICROQUASAR CYG X-1

V.V. Nazarenko

Astronomical Observatory, Odessa National University,
Shevchenko Park, Odessa, 65014, Ukraine, nazaret@te.net.ua

ABSTRACT. In the present work we have computed and have compared the on- and off- generations in low and high mass accretion rate accretion disks. The comparison shows that in the case of low mass accretion rate in disk (10^{-10} solar mass per year) the ON-state time interval is very short, order of $0.2 \div 0.4$ of precession period; in the case of high mass accretion rate in disk (10^{-9} solar mass per year) the ON-state time interval is relatively long, order of $0.7 \div 0.9$ of precession period. This shows that in the case more dense disk ON-states are relatively very long time interval because of high mass accretion rate in disk. This result is natural for classical microquasar (CYG X-1) in which the on-states are corresponding high mass accretion rates. For comparison we may also write that the time intervals of OFF-states in the present calculations are order of $1.3 \div 1.5$ of precession periods. The calculations also show that in OFF-states the accretion disk have the low specific viscosity and on contrary have the high specific angular momentum. In ON-states the disk have to contrary to OFF-states the high specific viscosity and low specific angular momentum. It shows that in OFF-states the disk is very rapidly rotating with low viscosity. In ON-states the situation is on contrary. Such the disk time-behaviour is true for both low and high mass accretion rate. The calculations also show that in ON-states the disk radius is very small, order of 0.08 of the orbital separations and on contrary in OFF-states the disk radius is relatively large, order of 0.25 of the orbital separations. The stated above shows that the disk is strong transformed from ON- to OFF-states.

Keywords: Stars: binaries - stars: jets - methods: numerical - hydrodynamics.

АБСТРАКТ. В представленій роботі ми виконали обчислення та порівняння включених та виключених станів з низькою та високою швидкостями акреції в диску. Порівняння

показують, що у випадку низької швидкості акреції в диску (10^{-10} Сонячних мас на рік) часовий інтервал включеного стану є дуже коротким, близько $0.2 \div 0.4$ прецесійного періоду, тоді як у випадку високої швидкості акреції в диску (10^{-9} Сонячних мас на рік) часовий інтервал включеного стану відносно довший, близько $0.7 \div 0.9$ прецесійного періоду. Це показує, що у випадку більш густого диску включені стани відносно довші завдяки високій швидкості акреції в диску. Такий результат є природнім для класичного мікроквасара (CYG X-1), у якого включені стани відповідають високій швидкості акреції в диску. Для порівняння ми можемо також відзначити, що часові інтервали виключених станів в представлених обчисленнях складають $1.3 \div 1.5$ прецесійних періодів. Обчислення також показують, що у виключених станах акреційний диск має низьку питому в'язкість в протилежність високому питомому кутовому моменту. У включених станах диск має в протилежність виключених станів високу питому в'язкість та низький питомий кутовий момент. Це показує, що у виключених станах диск швидко обертається з низькою в'язкістю. У включених станах ситуація є протилежною. Така часова поведінка диску виконується як для високих, так і для низьких швидкостей акреції в диску. Обчислення також показують, що у випадку включених станів радіус диску становить дуже невелику величину, близько 0.08 орбітальних розділень, тоді як у випадку виключених станів радіус диску відносно більший та складає величину близько 0.25 орбітальних розділень. Заявлене вище показує, що диск дуже трансформується під час переходу між включеними та виключеними станами.

Ключові слова: зорі; подвійні зорі; джети; методи: числовий; гідродинаміка.

1. Introduction

In the present research we have continued to simulate the ON- and OFF-states generations on the base of microquasar Cyg X-1 by the methods of 3-D numerical hydrodynamics (Nazarenko & Nazarenko, 2014, 2015, 2016, 2017). The present work is devoted to low and high mass accretion rates (low and high mass transfer rates via one-point respectively) in accretion disk simulations on the base of classical microquasar Cyg X-1. The goal of the present research is to compute the donor's wind, one-point-stream formation, its motion in Roche lobe of accretor, accretion disk formation and it's slaved precession for two cases: low accretion rate in disk (order of 10^{-10} solar mass per year) and high mass accretion rate (order of 10^{-9} solar mass per year).

2. The numerical algorithm

The description of the numerical algorithm in use in details is given in our previous works (Nazarenko & Nazarenko, 2014, 2015, 2016, 2017). Shortly, this algorithm is as follows: to resolve the non-stationary Euler's hydrodynamical equations we have used the astrophysical variant of "large-particles" code by Belotserkovsky and Davydov (Belotserkovskii & Davydov, 1982); to simulate one-point-stream we use the donor's atmosphere model that in turn is constructed on the base Kurucz's grid (Kurucz, 1979) with the donor's parameters; we use the free-flow boundary conditions allowing to a gas to flow freely via the calculation area boundaries; to calculate mass flow real temperature we use the radiation cooling explicitly (Cox & Daltabuit, 1971). In the present calculation we use the rectangular coordinate system centred on the donor's centre. We have adopted the donor's mass to be equal to 40 solar mass and the accretor's mass to be equal to 10 solar mass. The precession period in the present simulations is about of 4 orbital periods. Hereafter all the distances will be given in units of the orbital separations; the average volume disk specific viscosity and the average volume disk specific angular momentum will be given in units of $V_0 A$, where V_0 is the orbital speed and A – the orbital separation.

3. The results

Before a starting precession we run our simulations over 5 precession periods to show a stationary state in disk over long time. The precession starting is on time equal to zero. After a precession starting we run our simulation over $5 \div 6$ precession periods. This time interval is containing two ON-states and two

OFF-states. The essential parameters of a disk before a starting of precession are as follows: the number density in one-point is equal to $3.0 \cdot 10^{10} \text{ cm}^{-3}$, the average volume number density in a disk is order of $2.0 \cdot 10^{12} \text{ cm}^{-3}$, the mass accretion rate and mass transfer rate via one-point are equal to $2.5 \cdot 10^{-10}$ solar mass per year for low mass accretion rate case; the number density in one-point is equal to $3.0 \cdot 10^{11} \text{ cm}^{-3}$, the average volume number density in a disk is order of $2.0 \cdot 10^{13} \text{ cm}^{-3}$, the mass accretion rate and mass transfer rate via one-point are equal to $2.5 \cdot 10^{-9}$ solar mass per year for high mass accretion rate case. The key parameter in our present simulations is the time behaviour of the disk mass accretion rate. This behaviour is showing for low and high mass accretion rate cases in Fig. 1 and Fig. 2. As it is seen from these figures ON-states are about of 2,0 and 5,0 precession periods and OFF-states are in the time intervals from 0 to 2 and from 2 to 4 precession periods. The comparison of both Fig.1 and Fig. 2 shows that in the low mass accretion rate case the time intervals of ON-states are more short relatively the high mass accretion rate case. It show that Fig. 1 more corresponds to observational data of Cyg X-1 (Lachowicz et al., 2006). To illustrate the present computations in more details we are plotted in Fig. 3 and Fig. 4 the time dependencies of the averaged volume disk specific viscosity and the averaged volume disk specific angular momentum for low mass accretion rate case. As it is led from these figures, the disk have the high specific viscosity and low specific angular momentum over ON-states and on contrary, the disk have the low specific viscosity and high specific angular momentum over OFF-states. By the other words, the disk is very rapidly rotating with small viscosity over OFF-states and the situation is contrary over ON-states. To show the geometrical disk structure over ON- and OFF-states we are plotted the cross-sections of the calculation area by the disk plane and by the z-x plane for ON- state (Fig. 5 and Fig. 6) and for OFF-state (Fig. 7 and Fig. 8) for high mass accretion rate case. In these Figures the numbers 1 and 2 are marking the disk and the vicinity of one-point and one-point-stream respectively. As it is easy seen from these figures in the case of ON-state the disk have very small radius (by the other words is very compact), is very dense and is having the very power and dense one-point-stream. In the case of OFF-state the disk is very large with the radius of 0.35 approximately, is having relatively small density and is having the very small size in the vertical direction.

4. Summary and conclusions

The present calculations show that over OFF-state our numerical disk model have relatively large radius

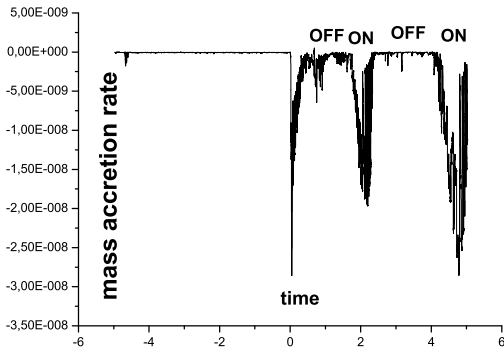


Figure 1: The mass accretion rate versus time for low mass accretion rate.

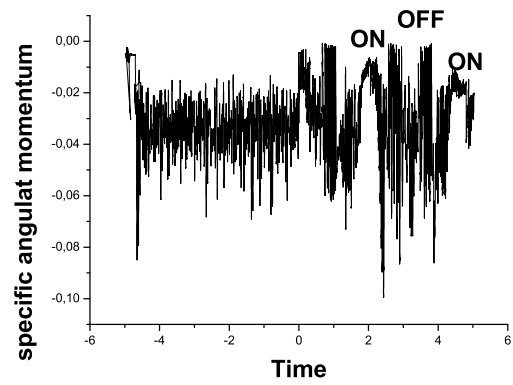


Figure 4: The disk average volume specific angular momentum versus time for low mass accretion rate.

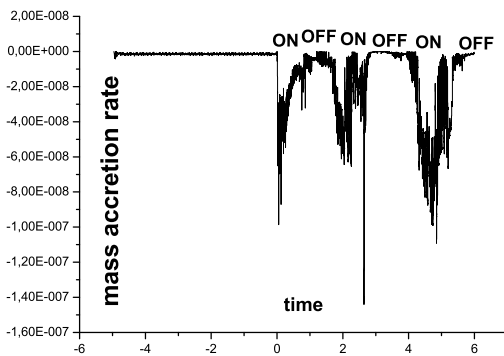


Figure 2: The mass accretion rate versus time for high mass accretion rate.

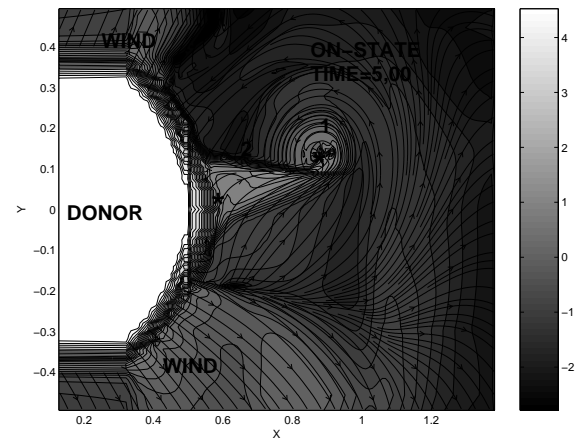


Figure 5: The cross-section of the disk by disk-plane for on-state.

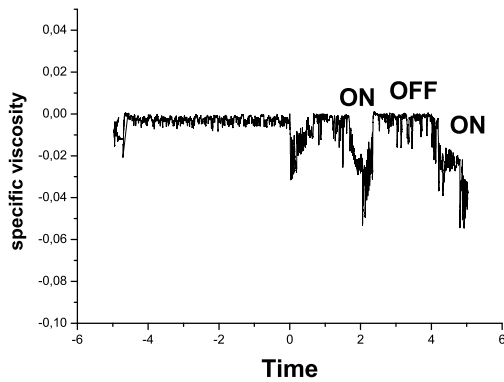


Figure 3: The disk average volume specific viscosity versus time for low mass accretion rate.

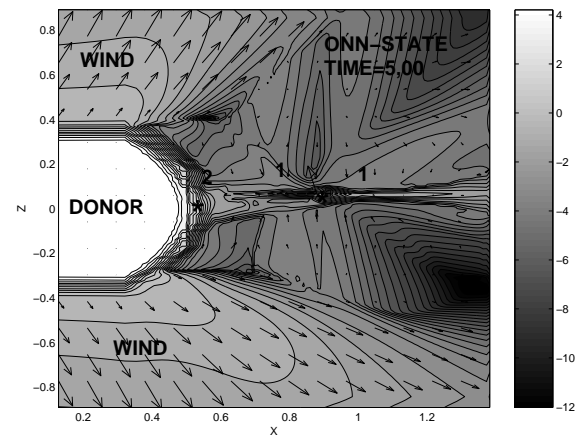


Figure 6: The cross-section of the disk by the z-x plane for on-state.

(about of 0.35) and is rotating very rapidly. On contrary over On-state the disk is very dense, have the very dense one-point stream, have the very small radius (about of 0.09) and have also the high specific viscosity. The main conclusion of the present research

is that the low accretion rate case is in the very good accordance with observational data of Cyg X-1 (X-ray observations - Lachowicz et al., 2006).

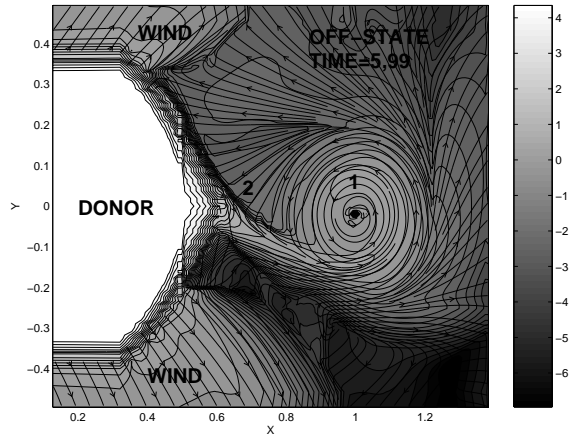


Figure 7: The cross-section of the disk by disk-plane for off-state.

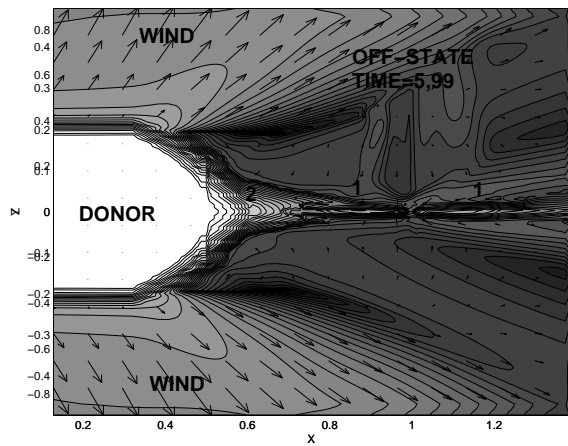


Figure 8: The cross-section of the disk by the z-x plane for off-state.

References

- Belotserkovskii O.M., Davydov Yu.M.: 1982, "The large particles code in gas dynamics", Moscow, Nauka, 391.
- Cox D. P., Daltabuit E.: 1971, *ApJ*, **167**, 113.
- Fabrika, S.: 2004, *Astrophysics and Space Physics Reviews*, **12**, 1.
- Kurucz, R.L.: 1979, *ApJ.Suppl.Ser.*, **40**, 1
- Lachowicz P. et al.: 2006, *MNRAS*, **368**, 1025.
- Nazarenko V.V., Nazarenko S.V.: 2014, *Odessa Astron. Publ.*, **27**, 137.
- Nazarenko V.V., Nazarenko S.V.: 2015, *Odessa Astron. Publ.*, **28**, 171.
- Nazarenko V.V., Nazarenko S.V.: 2016, *Odessa Astron. Publ.*, **29**, 82.
- Nazarenko V.V., Nazarenko S.V.: 2017, *Odessa Astron. Publ.*, **30**, 113.

DOI: <http://dx.doi.org/10.18524/1810-4215.2018.31.144622>

ADDITIONAL SUPPORT FOR RELATIVE WAVELENGTH INDEPENDENCE OF IR LAGS IN NGC 4151 OVER THE PAST DECADE

V. L. Oknyansky¹, V. I. Shenavrin¹, N. V. Metlova¹,
C. M. Gaskell²

¹ M. V. Lomonosov Moscow State University, Sternberg Astronomical Institute, 119234, Moscow, Universitetsky pr-t, 13, Russian Federation

² Department of Astronomy and Astrophysics, University of California, Santa Cruz, USA

ABSTRACT. We present results of a study of the correlation between the infrared (*JHKL*) and optical (*B*) fluxes of the nucleus of the Seyfert galaxy NGC 4151 for the years 2010–2015 using our own data (partially published) in combination with published data [1, 2, 3, 4]. We find similar lags for each of the *HKL* passbands relative to the optical of 37 ± 3 days. The lags are the same to within the accuracy of measurement. We do not confirm a significant decrease in the lag for *HKL* in 2013–2014 previously reported by Schnülle et al. [4], but we find that the lag of the short-lag component of *J* increased. We discuss our results within the framework of the standard model, where the variable infrared radiation is mainly due to the thermal re-emission of short-wave radiation by dust clouds close to a variable central source. There is also some contribution to the IR emission from the accretion disk, and this contribution increases with decreasing wavelength. The variability in *J* and *K* is not entirely simultaneous, which may be due to the differing contributions of the radiation from the accretion disk in these bands. The absence of strong wavelength-dependent changes in infrared lag across the *HKL* passbands can be explained by having the dust clouds during 2010–2015 be located beyond the sublimation radius. The relative wavelength independence of the infrared lags is also consistent with the hollow bi-conical outflow model of Oknyansky et al. [5].

Key words: Galsxies – active galaxies: individual: NGC 4151

АБСТРАКТ. Дана робота є продовженням серії наших досліджень кореляції інфрачервоної і оптичної змінності в NGC4151, а також змінності величин ІЧ-запізнювання і їх залежності від довжини хвилі. У цих роботах було знайдено, що величина запізнювання у фільтрі *K* різна в різних станах активного ядра, а також що відношення величин запізнювань у фільтрах *L* і *K* значно міняється в межах 1-3. Докладний історичний огляд і обговорення отриманих результатів представлені в наших попередніх публікаціях. У даній роботі ми на повнішому наглядовому матеріалі, застосовуючи два незалежні методи аналізу, підтвердили відносну незалежність ІЧ-запізнювань від довжини хвилі протягом 2010-2015 рр.

Досліджено кореляцію між інфрачервоним (*JHKL*) і оптичним (*B*) потоками змінного ядра сейфертівської галактики NGC 4151, використовуючи наші дані (частково опубліковані), а також опубліковані дані [1, 2, 3, 4] за 2010–2015 рр. Знайдені запізнювання змінності потоку в *HKL* щодо оптичних варіацій збігаються в межах точності вимірювань і рівні приблизно 37 ± 3 дням. Ми не підтвердили значне зменшення запізнення для *HKL* в 2013–2014 рр., яке виявили Шнулле і ін. [4], але помітили, що компонент з коротким запізненням в *J* посилюється.

Ми обговорюємо наші результати в рамках стандартної моделі, де змінна інфрачервоного випромінювання пов'язана головним чином з тепловим перевипромінюванням короткохвильового випромінювання пиловими хмарами, близькими до змінного центрального джерела. Існує також певний внесок в ІЧ-емісію від аккреційного диска, причому цей внесок збільшується із зменшенням довжини хвилі. Змінність в *J* і *K* відбувається не зовсім синхронно, що, можливо, пов'язано з різним внеском випромінювання аккреційного диска в цих фільтрах. Відсутність змін ІЧ-запізнення з довжиною хвилі (*HKL*) можна пояснити тим, що пилові хмари протягом 2010–2015 рр. були локалізовані далі, ніж радіус області можливої сублімації. Відносна незалежність ІЧ-запізнення від довжини хвилі також узгоджується з моделлю порожнинного біконічного витоку пилових хмар [5]. Створення самоузгодженої моделі ІЧ-випромінювання поблизу активного ядра виходить за рамки даної статті.

Key words: Galsxies – active galaxies: individual: NGC 4151

1. Introduction

The nucleus of NGC 4151 is one of the most studied active galactic nuclei (AGNs), due to its brightness and significant variability at all frequencies, with the exception of radio frequencies. It has been intensively studied since the discovery of variability in 1967 [6]. The historical optical light curves from photographic plates dating back to 1906 [7, 8, 9, 10] and subsequent photoelectric observations (in particular observations by V. M. Lyutyi) are among the longest for any AGN.

There are a number of IR and optical photoelectric observations dating back before 1967 (see references in [11, 12, 9]). The variability of NGC 4151 was discovered back in 1958 from photoelectric observations, but these results were published only 10 years later [13], when the variability of the object was already established. NGC 4151, had changed its type from Sy1 to Sy2 [14, 15, 16]. It then returned, after a while, to being a Sy1 [17]. That was one of the first discovered so-called "changing look" cases with AGNs. At present, several dozen such cases of "changing-look" AGNs (CL AGNs) have been recognized, which allows us to conclude that this is not just a one-time phenomenon, but is relatively common. Obviously, the orientation of the object cannot change so quickly and thus CL AGNs are a serious problem for the simple orientation-unification model (e.g. [18]). The unification model is based on the concept of the existence of a so-called "dusty torus", which, for viewing angles far from the axis of symmetry, obscures the broad line region (BLR) from the observer. The IR radiation of AGNs is dominated by thermal emission of dust heated by radiation from the inner regions of the accretion disc – emission that is energetically dominated by the extreme UV. The shape and structure of the torus is uncertain. Although it is commonly depicted in cartoons as being like a doughnut. Spatially-resolution IR observations of a number of AGNs show that dust clouds predominantly emitting in the mid-IR and far-IR range are not concentrated in the plane of the galaxy or of the accretion disc, as expected, but in polar regions [19, 20, 21, 22]. The main method for studying the unresolved structure of the emission from warm dust is reverberation mapping using IR and optical (UV) variability data. NGC 4151 was the first AGN for which such a lag was assumed on the basis of a visual analysis of light curves [23]. This lag was interpreted as a consequence of the spatial remoteness of the dust heated by the variable radiation from the central source. The lag was later measured using the standard cross-correlation analysis of series of observations [11, 24]. The first measurement of the lag in variability in the K band with respect to the optical in NGC 4151 gave a lag of about 18 days [11]. The lag was longer, about 26 days, for the L band from the same data Oknyansky2001. The IR lag for NGC 4151 varies with the level of luminosity of the central source, but with a delay of some years [25, 26]. The change in the lag can occur as a result of sublimation and dust recovery processes with changes in the level of the UV radiation of the nucleus. At present, such studies have been carried out for several dozen AGNs. Of great interest is the study of the dependence of the magnitude of the lag on the wavelength in the infrared range. For NGC 4151, in our first IR reverberation papers [24, 27, 28] it was noted that the lag in the

longer-wavelength L band was significantly greater than the lag in the shorter wavelength K band. After the outburst of the nucleus in 1996, the IR lag significantly increased and, interestingly, the lags in the K and L bands were identical to within the limits of measurement accuracy [29]. In our more recent papers [30, 31] we again found that the lags in all IR bands of *JHKL* were the same to within the accuracy of the measurements. Our analysis of the published photometric data for a number of other AGNs has shown that this relative independence of lags with IR wavelength is more the rule than the exception [30, 31]. We suggested that a significant increase in IR lag with wavelength can be observed during a period of significant growth of the luminosity of the central source, when dust sublimation occurs and the lag value increases. Because of the delay of several years in changes of the size of the lags, an increase in the magnitude of infrared lags with a wavelength can be observed after a few years after a major outburst. A straight-forward explanation would be that the dust clouds are located beyond the region of possible dust sublimation at the current luminosity level. Obviously, for most objects this situation is realized, when a major outburst occurred in the past and not in the time interval being studied. The possibility of determining cosmological constants based on the lag of infrared variability was first mentioned by [32] and was independently proposed and first implemented by [33, 27]. In recent publications of [34, 35, 36, 37], this method is considered in detail and practically applied (see also the discussion in [31]). Our discovery of the relative independence of the infrared lag from the wavelength for most AGNs is important in the practical application of this method, since it reduces the problem of a change in lag because of the shift in the rest-frame wavelengths of AGNs as a function of the redshift (for small $z \leq 0.2$). The application of this method to determine the distance to NGC 4151 has shown that this AGN is located at a significantly larger distance than previously thought [35]. The present paper is a continuation of our study of the lags of the IR passbands with respect to the optical in NGC 4151. We present results based on new monitoring in the *JHKL* bands combined with optical photoelectric and CCD photometry for the period 2010–2015. For a detailed review of the research and a description of the observational methods and data analysis the reader is referred to [30]. In addition to our own observations we make use of IR and optical data published of [4]. The combination of the data sets helps to make the light curves more complete and hence gives a more reliable determination of the infrared lags. Lags are determined for the time series using our MCCF code as discussed in previous papers in this series. We also use the JAVELIN - Monte Carlo Markov Chain method of [38].

2. Observational data

The method of IR observations in *JHKL* bands has been described in detail in our previous papers (see, for example, [39]). In the present study, we use our observations only for the 2010–2015 interval. Observations up to 2011 have been published in tabular form in Taranova and Shenavrin (2013), and observations up to 2015 are available on-line in an open access archive at [http : http : //www.sai.msu.ru/basa/inf.html](http://www.sai.msu.ru/basa/inf.html). We have already analyzed data from 2008–2013 in an earlier papers [30, 31]. Similarly we add here our new observations for 2013–2015, and also combined them with the published IR and optical data of Schnülle et al. [3, 4]. Most of the infrared observations have an accuracy of not worse than 1–2%. Compared to our earlier papers, the accuracy of our IR measurements improved during the interval being studied because of a number of upgrades of the equipment. In rare cases, the measurement errors were greater, but for further analysis we use only measurements with errors of no worse than 7%. In total, for the period 2010–2015, the average numbers of measurements per night in the *J*, *H*, *K* and *L* bands were 66, 54, 54, 66 respectively. Our data in *JHK* bands were supplemented by measurements of Schnülle et al. for 29 dates for 2010–2014. We reduced their data to our system. The method of optical photoelectric observations remained the same as that used by V.M. Lyutyi up to 2008 (see [24], but additional CCD measurements were used from a 60-cm telescope at the Southern Station of the SAI (see description in [40]). Since there are no *U* band CCD measurements, we used the data in the band *B* to construct a composite optical light curve. The CCD observations were reduced to a system of photoelectric measurements with a 27 arcsec aperture. As in our previous papers (see [5, 30, 31]) *B*-band data were supplemented with published CCD *B*-band measurements of Roberts and Rumstey [1] and 17 nights from Guo et al.[2]. In addition, we used 29 nights of optical measurements of Schnülle et al. [3, 4] in the red *z* band (29 dates) which were also reduced to our system *B*. Thus, all optical and infrared data are combined into one system. The formal accuracy of photoelectric measurements is generally not worse than 1–2%, but systematic differences between the measurements obtained on different instruments are possible. According to our estimates, these errors do not exceed 10% in the combined *B*-band light curve constructed for the 197 dates of the *B* value. The combined light curves NGC 4151 for 2010–2015 for *JHKL* and *B* are presented in Fig.1. As it can be seen in Fig.1, variations in the brightness in the *JHKL* bands occurred almost synchronously, without any noticeable differences or shifts. There are fewer

points in the *L* band, since Schnülle et al. have no observations in this band. In the changes there are rapid variations (with a characteristic time of tens of days) and a long-term trend (with a characteristic time of several years or more) with a maximum at the beginning of the time period. The optical light curve also exhibits rapid and slow changes with the same characteristic times, and the slow trend is more noticeable than in the IR light curves. In addition, rapid changes of a small amplitude with a characteristic time on the order of several days are noticeable in the optical variability.

3. Methodology of cross-correlation analysis

Cross-correlation analysis of astronomical time series presents difficulties because the time series are often unevenly sampled. To analyze the series, we applied our MCCF code, which is an upgrade of the method of Gaskell and Sparke [41]. The methodology of our analysis has not changed, and is described in detail in previous papers (see e.g. [30, 31, 42]). In the MCCF method, we strive to introduce a minimum number of arbitrary parameters, and also significantly reduce the contribution made by interpolation errors. A detailed discussion of other methods of cross-correlation analysis of non-uniform series, and their comparison with the MCCF method, was carried out in our previous papers [30, 31, 42].

We also carried out an analysis of the time series using the JAVELIN Monte Carlo Markov chain code of Zu et al. [43, 38]. Further details and links can be found in [42]. The JAVELIN method is not a very common method of cross-correlation analysis. In this method, the light curves are simulated 10,000 times on the basis of assumptions about the properties of the AGN variability which is assumed to be a damped random walk (see [44], and then lags are found for each pair of these simulated light curves. A histogram is constructed of the lags thus found, which is used to find the optimal lag and its error (see, for example, [45, 43, 38]. Of course, this method has similar problems as any method using interpolation and extrapolation of the time series. Nevertheless, this method has been used recently in some studies and it usually yields similar results as other methods. We decided to use this method as an additional check of our results given by the MCCF method, and without any changes in the author's code.

To estimate the errors in the lags derived by the MCCF, we applied the same Monte Carlo procedure as before [24, 30, 31]. Our estimates of the errors in the lags gave a value of about 3 days. The histograms obtained in the JAVELIN method can be used to estimate the optimal lags (JAVELIN) and their mean-square errors (see details, e.g., [45, 38]).

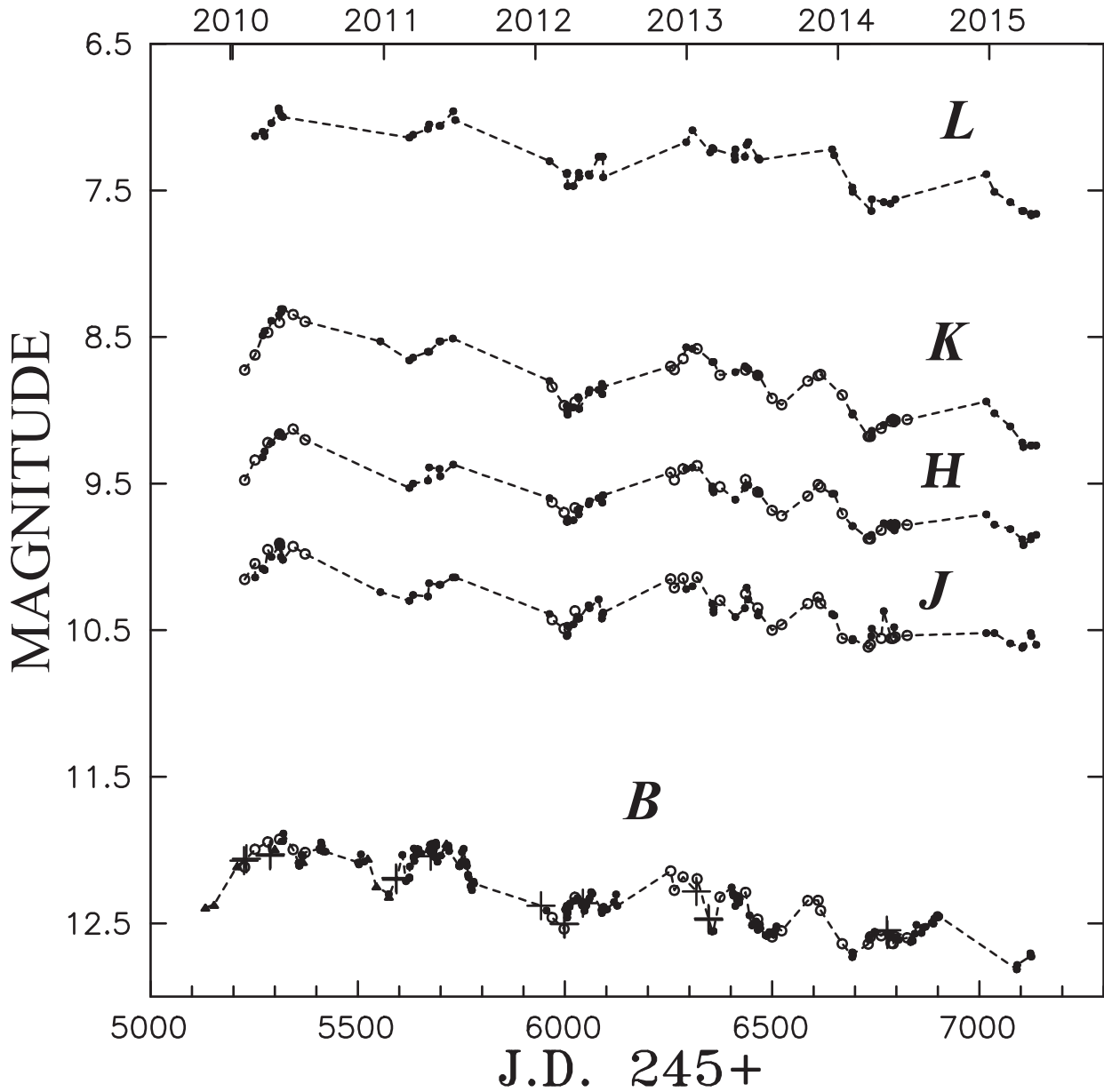


Figure 1: Combined light curves in IR bands $JHKL$ and optical B in 2010–2015. In IR light curves: filled circles - our data, open circles - data of Schnülle et al. ([3, 4]). In the light curve B : the points are our Crimean photoelectric and CCD measurements, the triangles are the reduced data of Roberts and Rumstey [1], the crosses are the reduced dots by Guo et al. [2], and the open circles are the reduced data of Schnülle et al.

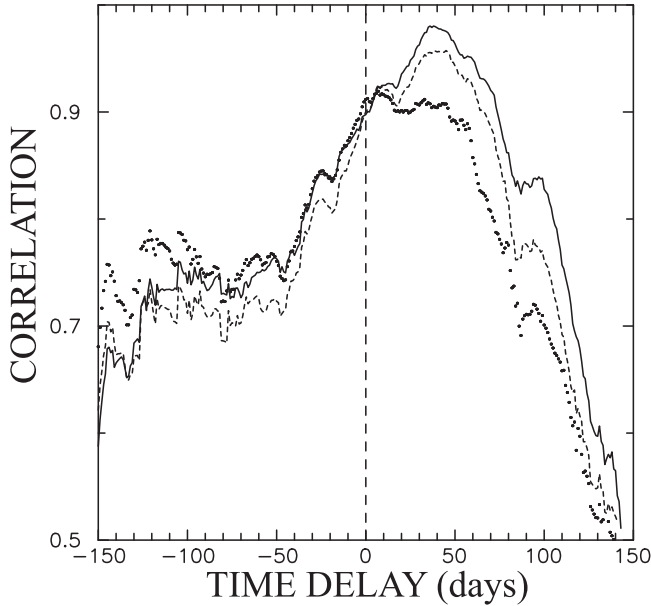


Figure 2: Cross-correlation functions for K (solid line), H (dashed lines), J (points) and B in the interval 2010–2015. The vertical dashed line indicates zero lag.

4. Cross-correlation of light curves

We have got cross-correlation functions of MCCF for the combined light curve in B and the variability in the $JHKL$ bands in the periods 2010–2015 and for 2013–2014 (Fig.2). Also we have made reverberation mapping with the JAVELIN method for the same data (not shown). Both methods give approximately the same results. For all IR pathbands most probable delay relative to B was found 37 ± 3 days. The magnitude of the lag of the variability at K relative to the optical remained almost the same as we found for the interval 2008–2013. Also, as in our earlier paper, the lag, within a measurement accuracy of ± 3 days is practically independent of the wavelength. But at the same time, the form of cross-correlation functions in the region near zero lag is noticeably different. One can notice that the secondary maximum and its significance fall as one goes to increasingly longer wavelength bands from J to L . For J , this maximum is about 4–6 days. This maximum is possibly associated with the variability of the accretion disc in the infrared. The delay for K and L (which are less depend for the AD radiation) were found about the same (see Fig.3). Our analysis did not confirm the result of Schnülle et al. [4] that there was decrease in the lag in 2012–2014 interval for the bands K and H , but for the band J the lag became noticeably smaller.

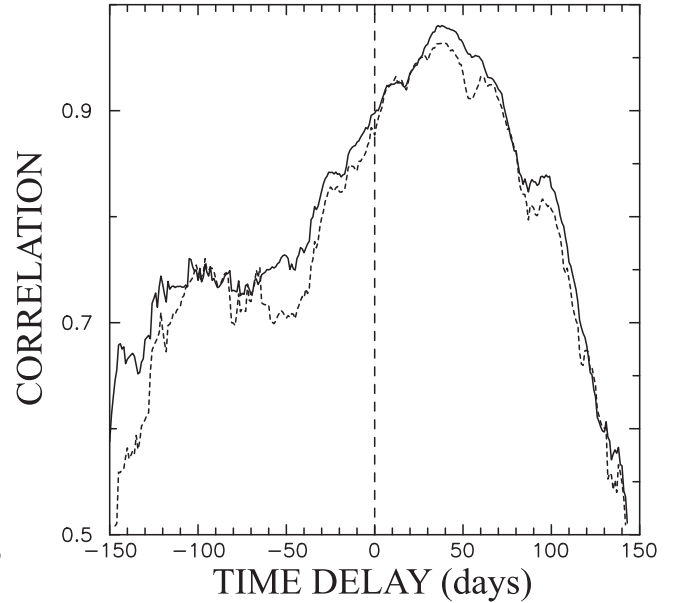


Figure 3: Cross-correlation functions for L (dashed lines), K (solid line) and B in the interval 2010–2015. The vertical dashed line indicates zero lag.

5. Conclusion

This paper is a continuation of our series of studies on the correlation between infrared and optical variability in NGC 4151, as well as the variability of the IR lag values and their dependence on the wavelength [11, 24, 29, 25, 30, 31]. In these studies we found that the delay in the K band is different in different activity states of the AGN, and also that the ratio of the lag values in the bands L and K varies considerably in the range 1–3. The results obtained in these studies were independently partially confirmed in other investigations [46, 26, 3, 47]. A detailed historical review and discussion of the obtained results was carried out in our previous paper [30]. In the present paper, using more complete observational material and using two independent methods of analysis, we confirmed the relative independence of infrared lags from the wavelength during 2010–2015. Taking into account our past investigations we can say that the IR time delays relative to the optical variations were wavelengths independent at list during past decade.

Acknowledgements. We are grateful to S. Hönig for useful discussions, and also to D.-F. Guo for providing optical photometric data.

This work is devoted to the memory of Olga Taranova (1938–2017), our co-author in many studies of the IR variability of NGC 4151 over the decades.

References

- [1] Roberts C. A. and Rumstay K. R.: 2012, *Journal of the Southeastern Association for Research in Astronomy*, **6**, 47
- [2] Guo D.-F., Hu S.-M., Tao J. et al.: 2014, *Research in Astronomy and Astrophysics*, **14**, 923
- [3] Schnülle K., Pott J.-U., Rix H.-W. et al.: 2013, *A&A*, **557**, L13
- [4] Schnülle K., Pott J.-U., Rix H.-W. et al.: 2015, *A&A*, **578**, A57
- [5] Oknyansky V. L., Gaskell C. M. and Shimanovskaya E. V.: 2015, *Odessa Astron. Publ.*, **28**, 175
- [6] Fitch W. S., Pacholczyk A. G. and Weymann R. J.: 1967, *ApJ*, **150**, L67
- [7] Oknyanskij V. L.: 1978, *Peremennye Zvezdy*, **21**, 71
- [8] Oknyanskij V. L.: 1983, *Astronomicheskij Tsirkulyar*, **1300**, 1
- [9] Oknyanskij V. L., Metlova N. V., Huseynov N. A. et al.: 2016, *Odessa Astron. Publ.*, **29**, 95
- [10] Pacholczyk A. G.: 1971, *ApJ*, **163**, 449
- [11] Oknyanskii V. L.: 1993, *Astronomy Letters*, **19**, 416
- [12] Oknyanskij V. L. and Lyuty V. M.: 2007, *Odessa Astron. Publ.*, **20**, 160
- [13] de Vaucouleurs G. and de Vaucouleurs A.: 1968, *Basic data on Seyfert galaxies*, Publications University of Texas, Series II, Vol. 7, 1
- [14] Lyutyj V. M., Oknyanskij V. L. and Chuvaev K. K.: 1984, *Soviet Astronomy Letters*, **10**, 335
- [15] Penston M. V. and Perez E.: 1984, *MNRAS*, **211**, 33P
- [16] Chuvaev K. K. and Oknyanskii V. L.: 1989, *Soviet Ast.*, **33**, 1
- [17] Oknyansky V. L., Lyuty V. M. and Chuvaev K. K.: 1991, *Pisma v Astronomicheskii Zhurnal*, **17**, 238
- [18] Antonucci R.: 1993, *ARA&A*, **31**, 473
- [19] Braatz J. A., Wilson A. S., Gezari D. Y. et al.: 1993, *ApJ*, **409**, L5
- [20] Cameron M., Storey J. W. V., Rotaciuc V. et al.: 1993, *ApJ*, **419**, 136
- [21] Bock J. J., Neugebauer G., Matthews K. et al.: 2000, *AJ*, **120**, 2904
- [22] Hönig S. F., Kishimoto M., Antonucci R. et al.: 2012, *ApJ*, **755**, 149
- [23] Penston M. V., Penston M. J., Neugebauer G. et al.: 1971, *MNRAS*, **153**, 29
- [24] Oknyanskij V. L., Lyuty V. M., Taranova O. G. et al.: 1999, *Astronomy Letters*, **25**, 483
- [25] Oknyanskij V. L., Lyuty V. M., Taranova O. G. et al.: 2008, *Odessa Astron. Publ.*, **21**, 79
- [26] Kishimoto M., Hönig S. F., Antonucci R. et al.: 2013, *ApJ*, **775**, L36
- [27] Oknyanskij V. L.: 2002, in *Galaxies: the Third Dimension* (Rosada M., Binette L. and Arias L., eds.), vol. 282 of *ASP Conf. Ser.*, p 330
- [28] Oknyanskij V. L. and Horne K. : 2001, in *Probing the Physics of Active Galactic Nuclei* (Peterson B. M., Pogge R. W. and Polidan R. S., eds.), vol. 224 of *ASP Conf. Ser.*, p 149
- [29] Oknyanskij V. L., Lyuty V. M., Taranova O. G. et al. : 2006, in *AGN Variability from X-Rays to Radio Waves* (Gaskell C. M., McHardy I. M., Peterson B. M. et al., eds.), vol. 360 of *ASP Conf. Ser.*, p 75
- [30] Oknyansky V. L., Metlova N. V., Taranova O. G. et al.: 2014, *Astronomy Letters*, **40**, 527
- [31] Oknyansky V. L., Metlova N. V., Taranova O. G. et al.: 2014, *Odessa Astron. Publ.*, **27**, 47
- [32] Kobayashi Y., Yoshii Y., Peterson B. A. et al.: 1998, *Proceedings of SPIE*, **3352**, 120
- [33] Oknyanskij V. L.: 1999, *Odessa Astron. Publ.*, **12**, 99
- [34] Yoshii Y., Kobayashi Y., Minezaki T. et al.: 2014, *ApJ*, **784**, L11
- [35] Hönig S. F.: 2014, *ApJ*, **784**, L4
- [36] Hönig S. F., Watson D., Kishimoto M. et al.: 2014, *Nature*, **515**, 528
- [37] Koshida S., Yoshii Y., Kobayashi Y. et al.: 2017, *ApJ*, **842**, L13
- [38] Zu Y., Kochanek C. S., Kozłowski S. et al.: 2013, *ApJ*, **765**, 106
- [39] Taranova O. G. and Shenavrin V. I.: 2013, *Astronomy Reports*, **57**, 71
- [40] Oknyanskij V., Metlova N., Artamonov B. et al.: 2012, *Odessa Astron. Publ.*, **25**, 179
- [41] Gaskell C. M. and Sparke L. S.: 1986, *ApJ*, **305**, 175.
- [42] Oknyansky V. L., Gaskell C. M., Huseynov N. A. et al.: 2017, *MNRAS*, **467**, 1496
- [43] Zu Y., Kochanek C. S. and Peterson B. M.: 2011, *ApJ*, **735**, 80
- [44] Gaskell C. M. and Peterson B. M.: 1987, *ApJS*, **65**, 1
- [45] Shappee B. J., Prieto J. L., Grupe D. et al.: 2014, *ApJ*, **788**, 48
- [46] Koshida S., Yoshii Y., Kobayashi Y. et al.: 2009, *ApJ*, **700**, L109
- [47] Hönig S. F. and Kishimoto M.: 2011, *A&A*, **534**, A121

DOI: <http://dx.doi.org/10.18524/1810-4215.2018.31.144691>

MOLYBDENUM ABUNDANCE IN SOME OPEN CLUSTERS

Shereta E.¹, Carraro G.^{2,3}, Gorbaneva T.¹, Mishenina T.¹

¹ Astronomical Observatory, Odessa National University, Shevchenko Park, 65014 Odessa, Ukraine

² European Southern Observatory, Alonso de Cordova 3107, 19001 Santiago de Chile, Chile

³ Dipartimento di Fisica e Astronomia, Universita di Padova, Italy

ABSTRACT. This paper presents the results of determination of the molybdenum abundances in 13 G, K type stars in the open clusters NGC 2477 and NGC 2506. The abundances of molybdenum were determined using stellar atmosphere models by Castelli & Kurucz (2004), as well as a modified STARSP LTE spectral synthesis code (Tsymbal, 1996). For the used Mo I lines 5506 and 5533 Å the oscillator strengths $\log g_f$ were adopted from the latest version of the VALD database dated 2016 (Kupka *et al.*, 1999). The high resolution spectra were obtained with a VLT telescope at the European Southern observatory (ESO, Chile).

We used atmospheric parameters of the investigated stars which we had obtained earlier. We have found out that the molybdenum abundances depend on metallicity [Fe/H] in giants of NGC 2506 and NGC 2477. For the stars in NGC 2506, molybdenum is slightly overabundant as compared to the solar abundance; such an overabundance is slightly higher in the stars of the second investigated cluster NGC 2477. Further investigation of the Mo abundance in larger number of open clusters is required to draw reliable conclusions.

Keywords: stars: abundances – stars: late-type – Galaxy: disc – Galaxy: evolution.

АБСТРАКТ. Наведено результати визначення вмісту молібдену в 13 зорях спектральних класів G, K, розсіяних скупчень NGC 2477 та NGC 2506. Вміст молібдену визначається за моделями атмосфери Кастеллі і Куруц (2004) та модифікованим кодом спектрального синтезу STARSP LTE. Для використовуваних ліній Мо I 5506 та 5533 Å сили осциляторів $\log g_f$ були взяті з останньої версії (2016) бази даних VALD (Купка *та ін.*, 1999). Спектри високої роздільної здатності були отримані за використання телескопу VLT Європейської південної обсерваторії (ESO, Чилі).

Атмосферні параметри досліджуваних зір були отримані нами раніше. Ми виявили залежність величини вмісту молібдену від металичності [Fe/H] у гігантів скупчень NGC 2506 та NGC 2477. Для зір скупчення NGC 2506 ми отримали малі надлишки вмісту молібдену від сонячного значення і дещо більші для другого досліджуваного скупчення - NGC 2477. Необхідно додатково досліджувати вміст Мо в багатьох РС для отримання більш надійних висновків.

1. Introduction

Stellar clusters are groups of loosely gravitationally bound stars which were formed from one and the same gas-and-dust cloud and have similar kinematics and chemical composition.

Open clusters (OC) belong to the plane of the Galactic disc. The age of OCs vary from few Myr to several Gyr. The stellar density in OCs is lower than in globular clusters (GCs) and is decreasing towards the cluster centre. The metallicity [Fe/H] of the OC stars is close to that of the Sun and may differ by a factor of 5. For older clusters, [Fe/H] decreases with increasing distance from the centre of the Galaxy, and on average, it is lower than metallicities of the clusters formed later.

This paper presents the molybdenum abundances estimated for two open clusters, namely NGC 2477 and NGC 2506. The target stars in this study are the G and K type red giants.

It is known that molybdenum is produced in several different processes, such as slow neutron-capture (s-process), rapid neutron-capture (r-process) and proton-capture (p-process) processes.

Mo is a highly convolved element that receives contributions from both the s-process and the p-process and less from the main and weak r-processes (see, e.g. Hansen *et al.*, 2014).

The study of molybdenum is of interest for several reasons: there is limited number of determinations of the molybdenum abundance in the open cluster stars; and virtually, there have been no observations of the field stars with the solar metallicities. At the same time, an important feature of molybdenum is that current model calculations of nucleosynthesis do not describe its contribution to the relevant solar abundance. The data which we obtained make it possible to investigate the ways of production of molybdenum and its enrichment in both individual components of the Galaxy and the entire Galaxy itself.

2. Observation data. Basic parameters of the investigated clusters and constituent stars

The spectra used in this study had been obtained earlier by G. Carraro with the multi-object fibre-fed FLAMES facility mounted at the VLT/UT2 telescope at the Paranal Observatory operated by the European Southern Observatory (ESO) in Chile. Either two or three exposures (depending on the cluster; Table 1) were taken with the red arm of

the UVES high-resolution cross-dispersed echelle spectrograph. The UVES spectrograph was set up at the central wavelength 5800 Å thereby covering the 4760–6840 Å wavelength range and providing a resolution $R=47000$.

The following basic parameters of the investigated clusters are listed in Table 1: Galactic coordinates (for J2000.0); Galactocentric distance R_{GC} and age. More detailed information on the data sources can be found in (Mishenina *et al.*, 2015).

Table 1: Basic parameters of the investigated clusters

| Name of cluster | l , (deg) | b , (deg) | R_{GC} , (kpc) | age, (Gyr) | V_r , (mag) |
|-----------------|-------------|-------------|------------------|------------|---------------|
| NGC 2477 | 253.563 | –05.838 | 8.9 | 0.6 | +5.8 |
| NGC 2506 | 230.564 | 9.935 | 10.9 | 1.9 | +7,6 |

As can be seen in Table 1, the cluster NGC 2506 is older and more distant from the Galactic centre than the NGC 2477 cluster.

Earlier, we have determined the atmospheric parameters and chemical abundances of the stars in the clusters NGC 2477 and NGC 2506 (Mishenina *et al.*, 2015).

The following basic and atmospheric parameters are given in Table 2: the ICRS coordinates; photometric data (V , $B-V$); effective temperatures T_{eff} ; gravity factor $\log g$; microturbulent velocity V_t ; metallicity [Fe/H] and radial velocity V_r .

Table 2: Basic data and atmospheric parameters of the investigated stars

| Star number | RA(2000.0), (deg) | Dec(2000.0), (deg) | V , (mag) | $B-V$, (mag) | T_{eff} , (K) | $\log g$ | V_t , (km/s) | [Fe/H] | V_r , (km/s) |
|-------------|-------------------|--------------------|-------------|---------------|-----------------|----------|----------------|--------|------------------|
| NGC 2477 | | | | | | | | | |
| 4027 | 118.087 917 | –38.577 194 | 12.153 | 1.198 | 4966 | 2.7 | 1.4 | 0.1 | 7.03 ± 0.13 |
| 4221 | 118.152 083 | –38.631 750 | 12.27 | 1.171 | 4975 | 2.8 | 1.2 | 0.19 | 8.80 ± 0.23 |
| 5043 | 118.040 417 | –38.598 306 | 12.165 | 1.17 | 5001 | 2.8 | 1.2 | 0.08 | 13.22 ± 0.27 |
| 5076 | 118.061 667 | –38.629 194 | 12.41 | 1.22 | 4954 | 2.7 | 1.2 | 0.18 | 9.22 ± 0.33 |
| 7266 | 117.955 000 | –38.535 694 | 12.252 | 1.193 | 4966 | 2.8 | 1.2 | 0.19 | 9.30 ± 0.14 |
| 7273 | 117.947 917 | –38.543 389 | 12.39 | 1.174 | 4985 | 2.8 | 1.2 | 0.2 | 8.77 ± 0.51 |
| 8216 | 118.064 583 | –38.457 306 | 12.334 | 1.272 | 4945 | 2.7 | 1.2 | 0.14 | 3.99 ± 0.50 |
| NGC 2506 | | | | | | | | | |
| 1112 | 120.013 750 | –10.762 250 | 12.961 | 0.958 | 4969 | 2.6 | 1.2 | –0.22 | 83.99 ± 0.27 |
| 1229 | 120.030 833 | –10.740 722 | 13.118 | 1.011 | 4728 | 2.4 | 1 | –0.22 | 82.54 ± 0.58 |
| 2109 | 120.029 583 | –10.779 000 | 13.146 | 0.89 | 5040 | 2.6 | 0.9 | –0.22 | 89.31 ± 0.05 |
| 2380 | 120.038 750 | –10.818 806 | 13.187 | 0.927 | 4992 | 2.6 | 1 | –0.19 | 83.64 ± 0.53 |
| 3231 | 119.982 917 | –10.805 944 | 13.105 | 0.952 | 4974 | 2.6 | 1.2 | –0.22 | 84.36 ± 0.51 |
| 5271 | 120.028 750 | –10.752 000 | 13.204 | 0.923 | 4993 | 2.6 | 1.1 | –0.24 | 83.52 ± 0.15 |

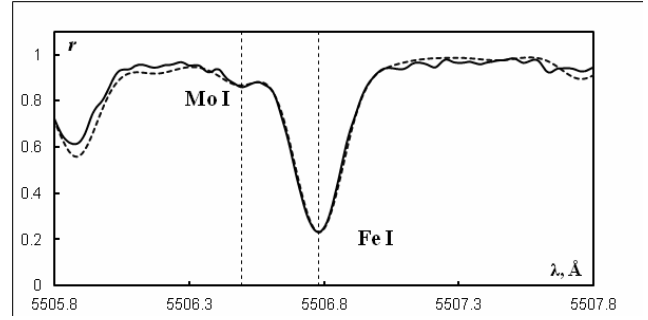


Figure 1: An example of the observed and synthetic spectra in the region near the Mo I 5506.493 Å line for the star 5271 in the NGC 2506 cluster.

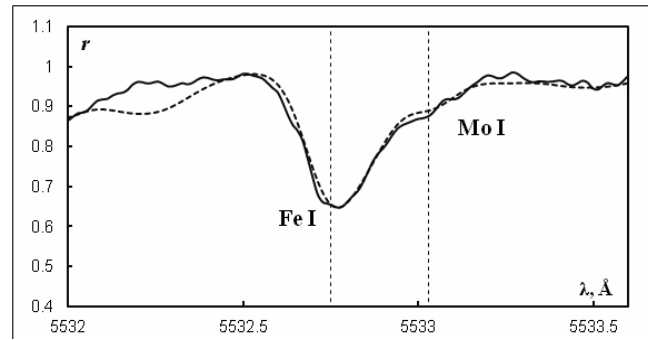


Figure 2: An example of the observed and synthetic spectra in the region near the Mo I 5533.031 Å line for the star 5271 in the NGC 2506 cluster.

Table 3: The resulting Mo abundance determinations, rms deviations σ and metallicities $[\text{Fe}/\text{H}]$ (Mishenina *et al.*, 2015) for 13 giants in NGC 2477 and NGC 2506.

| NGC 2477 | | | | |
|-------------|------------------------|-------------|------------------------|-------------|
| Star number | $[\text{Fe}/\text{H}]$ | $\pm\sigma$ | $[\text{Mo}/\text{H}]$ | $\pm\sigma$ |
| 4027 | 0.1 | 0.12 | -0.12 | 0.14 |
| 4221 | 0.19 | 0.09 | -0.19 | 0.06 |
| 5043 | 0.08 | 0.12 | -0.23 | 0.14 |
| 5076 | 0.18 | 0.12 | -0.14 | 0.12 |
| 7266 | 0.19 | 0.12 | -0.08 | 0.08 |
| 7273 | 0.2 | 0.1 | -0.11 | 0.07 |
| 8216 | 0.14 | 0.12 | -0.24 | 0.06 |
| NGC 2506 | | | | |
| Star number | $[\text{Fe}/\text{H}]$ | $\pm\sigma$ | $[\text{Mo}/\text{H}]$ | $\pm\sigma$ |
| 1112 | -0.22 | 0.1 | -0.12 | 0.19 |
| 1229 | -0.22 | 0.11 | -0.4 | 0.12 |
| 2109 | -0.21 | 0.17 | -0.09 | 0.07 |
| 2380 | -0.19 | 0.13 | -0.23 | 0.35 |
| 5271 | -0.22 | 0.13 | -0.22 | 0.09 |
| 3231 | -0.24 | 0.12 | -0.11 | 0.11 |

3. Analysis of the abundance determinations and the results obtained

The molybdenum abundances were determined for 13 giants in two OCs using stellar atmosphere models by Castelli & Kurucz (2004), as well as a modified STARSP LTE spectral synthesis code (Tsymbal, 1996). For the used Mo I lines 5506 and 5533 Å the oscillator strengths $\log g_f$ were adopted from the latest version of the VALD database dated 2016 (Kupka *et al.*, 1999).

The processing of observed spectra (continuum definition, smoothing at three points etc.) was carried out using the DECH20 software package (Galazutdinov, 1992).

The examples of fitting the calculated spectra to the observed spectra of the star 5271 in the NGC 2506 cluster are shown in Figs. 1 and 2.

As can be seen from Figs. 1 and 2, the molybdenum line is in the wing of the iron line at 5506.493 Å and 5533.031 Å lines, respectively, i.e. it is blended by the iron line. This means that correct determination of the molybdenum abundance requires fitting the synthetic spectrum to the observed spectrum at the regions near the Fe lines 5506.440 Å and 5532.870 Å, respectively; hence, we carried out such a fitting in this study.

Table 3 summarizes the resulting determinations of the molybdenum abundance, the root-mean-square (rms) deviations σ and metallicities $[\text{Fe}/\text{H}]$ (Mishenina *et al.*, 2015) for 13 giants in NGC 2477 and NGC 2506.

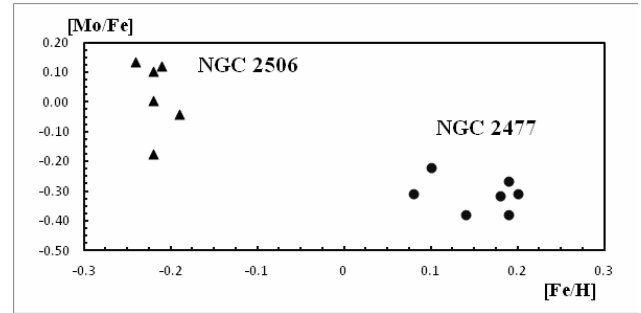


Figure 3: The dependence of the molybdenum abundance on the metallicity $[\text{Fe}/\text{H}]$ for all stars in the OCs NGC 2506 and NGC 2477.

The dependence of the molybdenum abundance on the metallicity $[\text{Fe}/\text{H}]$ in the investigated stars in NGC 2506 and NGC 2477 is shown in Fig. 3.

To determine the ratio between the Mo abundance and the solar $[\text{Mo}/\text{Fe}]$, the following data of the Fe and Mo abundances in the solar atmosphere were adopted from the study (Asplund *et al.*, 2009): Mo = 1.88, Fe = 7.50.

4. Conclusions

The molybdenum abundances in NGC 2477 and NGC 2506 are close to the solar ones.

For the stars in NGC 2506, molybdenum is slightly overabundant as compared to its solar abundance; such an overabundance is slightly higher in the stars of the second investigated cluster NGC 2477.

In future in order to provide a detailed picture of the enrichment of open clusters in molybdenum, we are to determine the molybdenum abundances for a larger number of clusters and compare these data with those reported in the literature.

References

- Asplund M., Grevesse N., Sauval, J. A., Scott P.: 2009, *ARA&A*, **47**, 481.
 Castelli F., Kurucz R.: 2004, *preprint (ArXiv:0405087)*.
 Galazutdinov G.A. Echelle spectra processing program package: 1992, *Preprint SAO*, N92.
 Hansen C. J., Andersen A. C., Christlieb N.: 2014, *A&A*, **568**, A47.
 Kupka F., Piskunov N., Ryabchikova T. A., et al., 1999, *A&AS*, **138**, 119.
 Mishenina T., Pignatari M., Carraro G., Korotin S., Shereta E., Yegorova I. and Herwig F.: 2015, *MNRAS*, **446**, 3651.
 Tsymbal V.: 1996, *ASP Conf. Ser.*, **108**, 198.

DOI: <http://dx.doi.org/10.18524/1810-4215.2018.31.145280>

PERIOD VARIATIONS AND POSSIBLE THIRD COMPONENTS IN THE ECLIPSING BINARIES AH TAURI AND ZZ CASSIOPEIAE

D.E. Tvardovskyi^{1,2}, V.I. Marsakova^{1,2}, I.L. Andronov², L.S. Shakun³¹ Odessa I. I. Mechnikov National University, Odessa, Ukraine, dmytro.tvardovskyi@gmail.com
vmarsakova@onu.edu.ua² Department “Mathematics, Physics and Astronomy”, Odessa National Maritime University
Odessa, Ukraine, tt_ari@ukr.net³ Astronomical Observatory, Odessa I. I. Mechnikov National University, Odessa, Ukraine,
leomspace@gmail.com

ABSTRACT. In our research, we investigated two variable stars: AH Tau and ZZ Cas. They are eclipsing binary stars of W Ursae Majoris and β Lyrae types. The period between eclipses of these stars changes with time. The reason for steady changes of the period could be the mass transfer (the flow of matter) between components of these stellar systems. For ZZ Cas the changes of the period are cyclic. That is why we assume the cyclic changes could be caused by the presence of the hypothetical third component (either a small star or a large planet). The cyclic changes of the period for AH Tau superimpose on steady ones (the period decrease). Thus we assume the third component and mass transfer are present. We also assume that the third components do not take part in the eclipses. However, due to their gravity, they make the visible close binary systems rotate and become closer or further to an observer. This explanation is called Light-Time Effect (LTE). Generally, an orbit of a third component is not a circle, but an ellipse and it is inclined relatively to the observer's line of sight. Using special plot called O-C curve we estimated the parameters of a third component's orbit such as a semi-major axis, an eccentricity, angles of orientation and a period of a third component's rotation. The O-C curve is the plot which shows how the difference between an observed and calculated moment of minimal brightness changes during a long period of time (usually it is several decades). To do this we created a modeling computer program using the computer language Python. In addition, we can calculate errors of third component's orbit parameters and even estimate its mass. The values of masses of the third components within errors of calculations show that the third components are probably stars. All these calculations were made using all available data from international database BRNO (Brno Regional Network for Observers). Moreover, we used moments of minima which we calculated as the result of observation processing from AAVSO database (American Association of Variable Stars Observers). These results are provided in the tables and plots.

АБСТРАКТ. У нашій роботі було досліджено дві змінні зорі: AH Tau та ZZ Cas. Вони є затемнювано-подвійними зорями типів W Великої Ведмедиці та β Ліри. Період між затемненнями цих зір змінюється з

часом. Причиною постійних змін періоду може бути перетікання речовини (потік речовини) між зорями. У ZZ Cas зміни періоду є циклічними. Тому ми припускаємо, що вони можуть бути викликані наявністю гіпотетичного третього компонента (малої зорі або великої планети). У AH Tau циклічні зміни періоду накладаються на постійні (період зменшується). Отже ми припускаємо, що присутні й перетікання речовини, й третій компонент. Ми також припускаємо, що треті компоненти не беруть участі в затемненнях, але завдяки своїй силі тяжіння вони змушують видимі тісні подвійні системи наближатися або віддалятися від спостерігача. Це пояснення називається ефектом затримки світлового сигналу (LTE). У загальному випадку орбіта третього компонента не є колом, а еліпсом і нахилена відносно променю зору спостерігача. Використовуючи спеціальний графік, який називається кривою O-C, ми оцінюємо такі параметри орбіти третього компонента, як велику піввісь, ексцентриситет, кути орієнтації та період обертання третього компонента. Крива O-C – це графік, який показує, як різниця між спостережуваним і розрахованим моментами мінімальної яскравості змінюється протягом тривалого проміжку часу (як правило, це кілька десятиліть). Для цього ми створили комп'ютерну програму для моделювання, використовуючи мову програмування Python. Крім того, ми можемо обчислити похибки параметрів орбіти третього компонента і навіть оцінити його масу. Маса третіх компонентів в межах похибок розрахунків показує, що треті компоненти, напевно, є зорями. Всі ці розрахунки були зроблені з використанням усіх наявних даних з міжнародної бази даних BRNO (Brno Regional Network for Observers) та моментів мінімумів, які ми розраховували з використанням спостережень з бази даних AAVSO (American Association of Variable Stars Observers). Ці результати наводяться у таблицях та на графіках.

Key words: general: O-C curve, phase curve, β Lyrae type, W Ursae Majoris type, ephemerid, eclipsing binaries, semi-detached system; **individual:** AH Tau, ZZ Cas.

1. Introduction

For this research, we chose two eclipsing variable stars with period changes that are cyclic, but not sinusoidal: AH Tau and ZZ Cas. The analysis for the several eclipsing variables with cyclic period changes we discussed in our previous papers (Tvardovskyi; Marsakova & Andronov (2017) and Tvardovskyi & Marsakova (2015)). The main observational parameters of the variables were taken from General Catalogue of Variable Stars (GCVS) and listed in Table 1. Some fundamental parameters were published in articles Xiang et al. (2015) and Liao & Qian (2009). Geometrical and physical parameters of the stellar systems were computed there. In the current article we compare parameters of the third components such as masses and orbital elements with ones published in the previous articles of other researchers.

Moreover, there is some additional information about these stars as the result of previous researches made by other astronomers. For both stellar systems, the presence of the third components was suspected by other authors, but for ZZ Cas even presence of the fourth component was supposed. Mass transfer/loss was supposed for AH Tau. For both stars, geometrical and physical parameters were computed.

This study was carried out in a frame of the projects “Inter-Longitude Astronomy” (Andronov et al., 2017) and “AstroInformatics” (Vavilova et al., 2017) projects.

Table 1: Observational parameters provided in General Catalogue of Variable Stars (GCVS, Samus et al., 2018) and by Xiang et al. (2015) and Liao & Qian (2009).

| Parameter | AH Tau | ZZ Cas |
|---------------------|--|--|
| RA | 03 ^h 47 ^m 11.98 ^s | 00 ^h 33 ^m 30.38 ^s |
| DEC | 25°06'59.5" | 62°30'40.2" |
| Type of variability | EW/KW | EB |
| Initial epoch (JD) | 31062.5081 | 33437.5 |
| Period (days) | 0.3326754 | 1.243527 |
| Spectral type | G1p | B3 |
| M_1, M_{\odot} | 1.04 | 7.6 |
| M_2, M_{\odot} | 0.52 | 5.32 |
| Article | Xiang et al. (2015) | Liao & Qian (2009) |

Table 2: Articles of other authors where different types of results were provided. The first column identifies the types of information, which is necessary for the current research. Next two columns are the lists of references for articles where these kinds of calculations were published.

| | AH Tau | ZZ Cas |
|---|---|---|
| Ephemerid correction | - | Taylor (1941); Frieboes-Conde & Herczeg, (1971); Kreiner & Tremko, (1991). |
| Spectral observations | - | Struve (1947); Taylor (1941). |
| Presence of a third component | Xiang et al. (2015); Yang et al (2010); Zasche et al (2008); Lee et al (2004). | Frieboes-Conde & Herczeg (1971); Kreiner & Tremko (1991); Liao & Qian (2009). |
| Presence of a 4 th component | - | Liao & Qian (2009). |
| Mass transfer/loss | Xiang et al. (2015); Yang et al (2010); Zasche et al (2008); Lee et al (2004); Yulan Yang & Qingyao Liu (2002). | - |
| Parameters of the system | Xiang et al. (2015); El-Sadek et al (2009); Yang et al (2010); Byboth et al (2004); Liu et al (1991). | Struve (1947); Liao & Qian (2009). |

2. O-C analysis

To build O-C curves we used observations from different sources. Most of them were taken from Brno Regional Network of Observers (BRNO). In addition, we computed moments of minima for all available data from American Association of Variable Stars Observers database (AAVSO) using the software MAVKA (Andrych et al., 2017). For all available moments of minima, we calculated the values of O-C and built the O-C curve. In our research, we investigated stellar systems, which have one of two different types of O-C curves:

- cyclic period changes (they correspond to possible presence of the third component);
- superposition of cyclic period changes and parabolic trend (they correspond to both presence of the third component and mass transfer).

More details about possible explanations of different types of period changes are provided in Tvardovskyi, Marsakova & Andronov (2017) and Tvardovskyi & Marsakova (2015).

3. Orbital elements of the third body

In both stars we detected that cyclic period changes on O-C curve are similar to sinusoidal, but they have clear asymmetry. We suppose that this asymmetry is caused by the elliptical shape and inclination of the third bodies' orbits. We assume that the visible components of the stellar systems are close to each other and the third one has a lot wider elliptical orbit. Each orbit we can describe by its seven parameters, such as:

- semi-major axis (a);
- eccentricity (e);
- three angles of inclination (argument of the pericenter (Ω), inclination (i) and longitude of pericenter (ω));
- orbital period (T);
- moment of the pericenter transit (t_0).

We decided to calculate these parameters and create a model O-C curve in the case of the presence of the third body in the system. To make the calculations we wrote a computer program on the computer language Python 3.5. This program uses the Levenberg-Marquard algorithm (Marquardt, 1963, Moré, 1977), which represents the least squares method for the non-linear model. This algorithm builds the model O-C curve for initial parameters (this is our own function), then corrects them and repeats the procedure until the squares of the differences will be as little as possible.

Using the Kepler's equation and formulas of the coordinate system turn, we can easily write the equation which describes the shape of O-C curve for different orbital elements:

$$\Delta t = \frac{a}{c} \sin i \left((\cos E - e) \sin \omega + \sin E \cos \omega \sqrt{1 - e^2} \right) \quad (1)$$

As we can see from this formula, we cannot calculate all the orbital elements. Particularly, we cannot compute the argument of the pericenter or the major semi-axis and inclination angle separately. We can calculate only the projection of the semi-major axis on the line of sight. Moreover, AH Tau has a superposition of a parabolic trend and cyclic period changes. For this star, we modified Eq. (1) to consider the parabolic trend:

$$\Delta t = \alpha t^2 + \beta t + \gamma + \frac{a}{c} \sin i \cdot \left((\cos E - e) \sin \omega + \sin E \cos \omega \sqrt{1 - e^2} \right) \quad (2)$$

Here α , β and γ are the coefficients of the parabolic trend.

Before making calculations, our program needs the list of initial values of the parameters (Table 4). We estimated the amplitude and period of the O-C cyclic changes 'by eye'. We set the argument of the pericenter as π radians or 180 degrees, as the average of the least and the largest possible. Eccentricity was set as 0.1. Coefficients α , β , γ and t_0 are set as equal to zero.

After calculations, the program returns the list of corrected elements with their errors (Table 2) and the picture (Fig. 2-5).

This is the table with parameters of the binary system orbit about the common barycenter. However, most of them will be the same for the third component's orbit. These ones are eccentricity, pericenter argument, initial moment of minima and rotation period. Semi-major axis of the third body's orbit will be the same number times bigger than one in the binary system, than relation of the masses of the binary system and of the third component.

4. Taking into consideration the weights

In the investigated systems, we detected some systematic deviations between model O-C and observations. Some of them are caused by the large scatter of old visual observations. It happens if we assume that all observations have the same "importance" for approximation. Thus, we decided to analyze which types of observations exist on O-C curves. There are 4 main types of observations: visual ("vis"), photometric ("ccd"), photoelectric ("pe") and ones which were made using photographic plates ("pg", that are similar to visual observations).

Using this information, we created the system of weights. Weight of the point is a multiplier of the deviation between observations and model value of O-C for this point in the sum of the squares of deviations. It allows to take in consideration different accuracies of the minimum brightness determination. The better is the accuracy of the O-C value determination – the larger is the weight of the point. For "vis" and "pg" observations we set the weight equal to 1. For all other types of observations ("ccd", "pe") we set the weight equal to 10. This ratio (1 to 10) is equivalent to difference by one order in the accuracies of moments of minimal brightness determination according to the number of significant digits given in BRNO database. The visual observations were provided there with 3 digits after comma, and the photometric ones – with 4 digits, that corresponds the difference in accuracy of 10 times.

5. Ephemerid correction

Ephemerid is the special formula for calculation the moment of minima:

$$T_c = T_0 + P \cdot E \quad (3)$$

The third summand appears in the case of parabolic trend presence:

$$T_c = T_0 + P \cdot E + P' \cdot E^2 = T_0 + P \cdot E + \dot{P} \cdot P \cdot E^2 \quad (4)$$

Here P is a period; E is a cycle number; T_0 is a moment of minima, which we set as the zero point and called the initial epoch; $P' = P \cdot \dot{P}$ is the rate of the period changes (days per cycle).

We used coefficients of approximation (α , β , γ) for correction.

- Coefficient α is the error of the value of the initial epoch;
- Coefficient β is the error of the value of a period;
- Coefficient γ is the quadratic addition, which describes the rate of the period changes (see section "Rate of the mass transfer").

Such correction was done for the stellar system AH Tau. The corrected ephemerid is:

$$T_c = (31062.7754 \pm 0.010) + (0.33266942 \pm 0.00000014) \cdot E + (-9.28 \pm 0.15) \cdot 10^{-11} \cdot E^2$$

6. Masses of the third bodies

To estimate the masses of the third components, we suppose that in both researched systems the distance between the third component and two visible ones is much larger than the distance between visible components. In this case we used third Kepler law and the formula for the barycenter position. We derived the minimal possible mass of the third component after simplifications:

$$M_3 = \frac{c \Delta t}{\sqrt[3]{G}} \left[\frac{2\pi}{T} \cdot (M_1 + M_2 + M_3) \right]^{\frac{2}{3}} \quad (5)$$

Here:

- G is the gravitational constant;
- T is the orbital period of the third body (and the period of O-C changes);
- M_1, M_2, M_3 are the masses of the components;
- c is the speed of light;
- Δt is semi-amplitude of O-C cyclic changes.

After several iterations we got mass of the third component. In addition, we estimated errors of calculations using formula (6):

$$\sigma M_3 = \left(\frac{1}{M_3} - \frac{2}{3M} \right)^{-1} \cdot \sqrt{\frac{\sigma_{\Delta t}^2}{\Delta t^2} + \frac{4}{9} \left[\frac{\sigma_{M_1}^2}{M_1^2} + \frac{\sigma_{M_2}^2}{M_2^2} + \frac{\sigma_T^2}{T^2} \right]} \quad (6)$$

Here:

- $M = M_1 + M_2 + M_3$ – total mass of a triple system (visible components and a third one);
- $\sigma_{\Delta t}$ – error of semi-amplitude of O-C cyclic changes;
- σ_{M_1} and σ_{M_2} – errors of masses (they were not provided in the articles, so for both stars we estimated them as 5% of the masses);
- σ_T – error of a period of cyclic changes.

More details about calculation of minimal mass of the third component are provided in Tvardovskyi, Marsakova & Andronov (2017).

7. Rate of the mass transfer

If a star has a parabolic O–C curve or a cyclic one with parabolic trend, its period changes steadily. As the result of the O–C analysis, we detected that AH Tau has steady

period changes, which we interpreted as the mass transfer from one of the components to another. To calculate the rate of the mass transfer, we used the formula (Andronov, 1991):

$$\dot{M} = \frac{1}{3} \frac{\dot{P}}{P} \frac{M_1 M_2}{(M_1 - M_2)} = \frac{1}{3} \frac{P'}{P^2} \frac{M_1 M_2}{(M_1 - M_2)} \quad (7)$$

In this formula: \dot{M} is a rate of the mass transfer, M_1, M_2 are masses of the components in a close binary system, P is a period of variability, \dot{P} is a derivative of the period with the time, $P' = 2\gamma$ is the derivative of the period with cycle number (Andronov, 1991). To obtain \dot{M} in the standard units used in astronomy (solar masses per year) we must multiply it by the average quantity of days in the year (365.25).

Classical monographs on study of eclipsing binaries are e.g. by Tsesevich (1973) and Hofmeister et al. (1980).

8. Conclusions and discussions

We studied two eclipsing binary stars with period changes: AH Tau and ZZ Cas. For both of these stars we calculated minimal possible mass of the third components. The mass of the third component for AH Tau equals to $0.37 M_{\odot}$, that corresponds to the parameters of an M-type star.

Our value is approximately 50% larger than value obtained by Dong Joo Lee et al (2004). For ZZ Cas the third component was supposed for the first time.

According to its mass of about $3.9 M_{\odot}$ (that is 20% smaller than the value published in Liao & Qian (2009)) the third component is rather a B-type star. Unfortunately, errors in these two articles were not published, so it is hard to say whose results are correct. For both stars we calculated parameters of the third bodies orbits. For AH Tau they are generally close to the ones published in Lee et al (2004). However, there are some deviations, especially in the value of the longitude of pericenter. In addition, we calculated the rate of the mass transfer for AH Tau. The similar calculation was done in Lee et al (2004). Nevertheless, there is 17 times difference between our and their results. Such a huge deviation could be explained by a small amount of observations and shorter time interval that is crucial for the accurate calculations.

Acknowledgments: We sincerely thank the AAVSO (Kavka, 2018) and BRNO associations of variable stars observers for their work that has made this research possible.

Table 3: Initial values of orbital elements of researched stars.

| Parameter | Units of measurement | I Boo | ZZ Cas |
|-----------|--------------------------------|-----------|--------|
| α | $10^{-12} \text{ days}^{-1}$ | 0 | - |
| β | 10^{-7} | 0 | - |
| γ | days | 0 | - |
| $\sin i$ | 10^6 km | 2000 | 2000 |
| e | 1 | 0.1 | 0.1 |
| ω | degrees | 180 | 180 |
| t0 | JD-240000, 10^3 days | 5000 | 0 |
| T | 10^3 days | 20000 | 7000 |
| Trend | | parabolic | none |

Table 4. Corrected values of orbital elements of researched stars.

| Parameter | Units of measurement | AH Tau | | ZZ Cas |
|-----------|-----------------------------------|---------------|--------------------------|---------------|
| α | $10^{-12} \text{ days}^{-1}$ | -276±4 | -164 | - |
| β | 10^{-7} | 178±4 | - | - |
| γ | 10^{-3} days | -266±10 | - | - |
| $\sin i$ | 10^6 km | 440±5 | 426 | 624±4 |
| e | 1 | 0.330±0.014 | 0.52 | 0.582±0.005 |
| ω | degrees | 112.8±3.0 | 164.4 | 192.9±0.2 |
| t_0 | JD-240000, 10^3 days | 12.204±0.020 | 45.452 | 2.28±0.08 |
| T | 10^3 days | 15.53±0.09 | 12.93 | 6.79±0.01 |
| σ | days | 0.00544 | - | 0.00312 |
| Source | | This research | Dong Joo Lee et al, 2004 | This research |

Table 5. Minimal possible masses of the third components and rate of the mass transfer.

| | Rate of the mass transfer (Solar masses per year) | | Minimal mass of the third component (Solar masses) | |
|--------|---|---|--|----------------------------------|
| | | | | |
| AH Tau | $(6.3 \pm 0.7) \cdot 10^{-7}$ | $3.8 \cdot 10^{-8}$ [Dong Joo Lee et al (2004)] | 0.37±0.02 | 0.24 [Dong Joo Lee et al (2004)] |
| ZZ Cas | - | - | 3.90±0.22 | 5.00 [Liao & Qian (2009)] |
| Source | This article | Other authors | This article | Other authors |

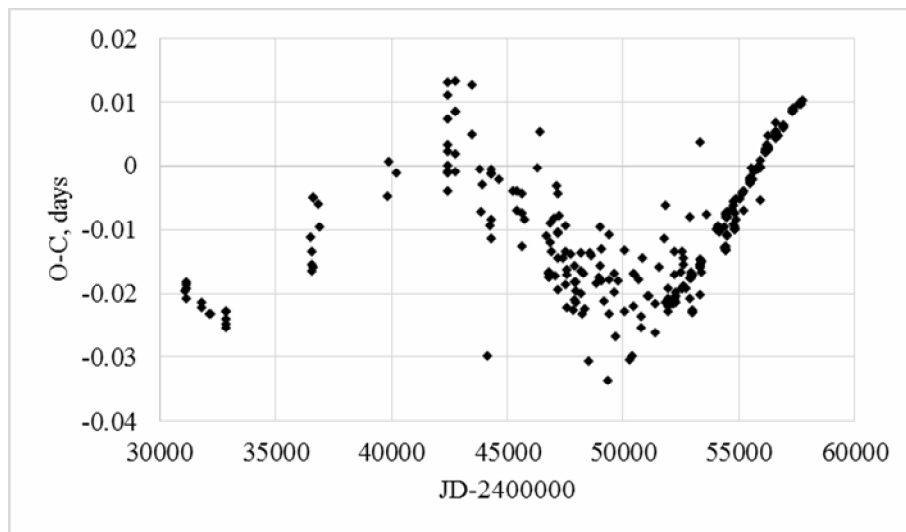


Figure 1: O-C curve of AH Tau with subtracted parabolic trend

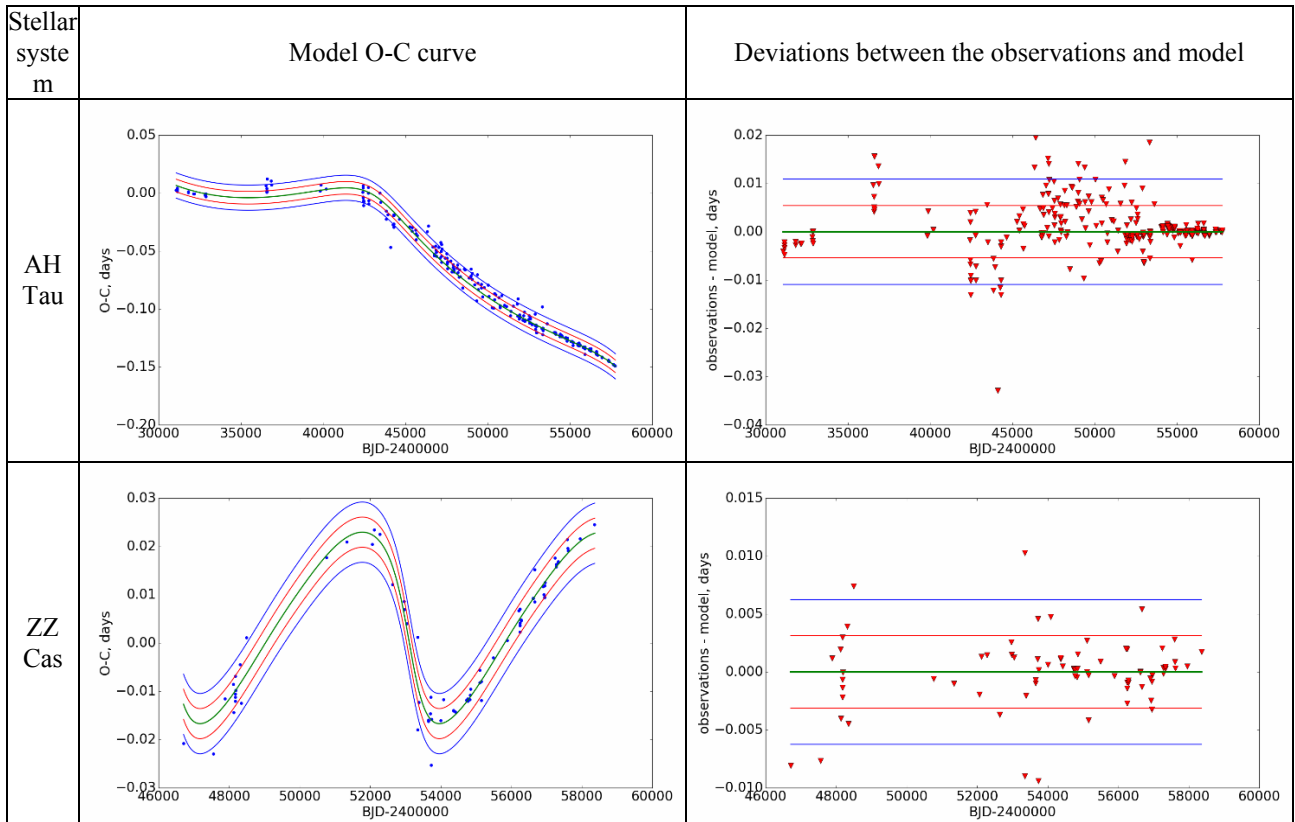


Figure 2-5: Plots of approximation of O-C curve by model of the elliptical orbit and deviations between observational data and model O-C curve. In the second column, the dots are observations, the solid green line is the model O-C for corrected values of the orbital elements, red and blue lines correspond to 1σ and 2σ intervals.

Table 6: Obtained moments of minima using the time series observations from the AAVSO database

| Observer code | Filter | BJD of the minimum | Error | Degree of polynomial |
|---------------|--------|--------------------|---------|----------------------|
| <i>ZZ Cas</i> | | | | |
| BM | Vis. | 56620.57802 | 0.00014 | 8 |
| SAH | V | 57279.65393 | 0.00016 | 8 |
| SNE | V | 57330.63960 | 0.00023 | 8 |
| SAH | V | 57611.67947 | 0.00027 | 8 |
| SAH | V | 58367.74877 | 0.00042 | 8 |
| <i>AH Tau</i> | | | | |
| DKS | V | 54399.89762 | 0.00011 | 8 |
| DKS | V | 54402.72580 | 0.00009 | 8 |
| DKS | V | 54402.89155 | 0.00008 | 8 |
| DKS | V | 54429.67196 | 0.00011 | 8 |
| GKA | V | 54475.58074 | 0.00009 | 6 |
| GKA | V | 54429.83824 | 0.00009 | 8 |
| GKA | V | 54512.67332 | 0.00015 | 8 |
| GKA | V | 54736.89537 | 0.00008 | 8 |
| GKA | V | 54829.54492 | 0.00013 | 8 |
| WAB | V | 54830.54276 | 0.00008 | 8 |
| WAB | V | 54837.52885 | 0.00009 | 8 |
| WAB | V | 54848.67374 | 0.00014 | 8 |
| WAB | V | 54399.89762 | 0.00011 | 8 |
| WAB | V | 54402.72580 | 0.00009 | 8 |

References:

- AAVSO: 2018, <http://www.aavso.org/>
- Andronov I. L.; Baklanov A. V.: 2004, *Astronomical School's Report*, 5, 264
- Andronov I.L. et al.: 2017, *ASP Conf. Ser.*, 511, 43
- Andronov I.L.: 2003, *ASP Conf. Ser.*, 292, 391
- Andronov I.L. Structure and evolution of variable stars. Odessa, p. 48 (1991) (in Russian)
- Andrych K.D., Andronov I.L., Chinarova L.L.: 2017, *Odessa Astronomical Publications*, 30, 57
- Bakulin P.I., Kononovich E.V., Moroz V.I. "Course of general astronomy". Nauka, Moscow, USSR., pp. 79–84. (1977) (in Russian)
- Bessel M.S.: 2005, *Annual Review of Astronomy & Astrophysics*, 43, 293
- Brno Regional Network of Observers (BRNO). <http://var.astro.cz/ocgate/>;
- Byboth K. N. et al.: 2004, *Information Bulletin on Variable Stars*, 5554, 1
- Chrastina M., Hroch F.: 2008, *Open European Journal on Variable Stars*, 95, 21
- Dong Joo Lee et al.: 2004, *J. Astron. Space Sci.* 21(4), 283
- El-Saldek et al.: 2008, *NRIAG Journal of Astronomy and Astrophysics*, Special Issue, 57
- Frieboes-Conde H., Herczeg T.: 1973, *Astron. Astrophys. Suppl.*, 12, 1
- Samus N.N. et al.: 2017, *Astronomy Reports*, 61, 80, <http://www.sai.msu.su/gcvs/cgi-bin/search.htm>;
- Kreiner J. M., Tremko J.: 1991, *Publishing House of the Czechoslovak Academy of Sciences*, 42, 345;
- Hofmeister C., Richter G., Wenzel W. *Variable Stars*. Springer-Verlag, Berlin, Heidelberg, New York, Tokyo. The original 1st edition, 182 p. (1980)
- Liao Wen-Ping, Qian Sheng-Bang.: 2009, *Publ. Astronomical Society of Japan*, 61, 777
- Liu Qing-Yao et al.: 1991, *Chinese Astronomy and Astrophysics*, 15, 2, 143
- Marquardt D.: 1963, *SIAM Journal on Applied Mathematics*. 11 (2): 431
- Moré J.J.: 1977, *Proceedings of the Biennial Conference*, 630, 105. DOI:10.1007/bfb0067700
- Physics of Space. Small Encyclopedia. Ed.: R.A. Sunyaev et al. *Soviet Encyclopedia*, 783 p. (1986) (in Russian);
- Pinskii A.A., Kabardin O.F., Orlov V.A., Evenchik E.E. *Physics grade 10. Prosveschenie, Moskow*, pp. 364–372 (1999) (in Russian);
- Python: <http://www.python.org>;
- Russo G., Sollazzo C.: 1981, *Astrophysics and Space Science*, 78, 141;
- Scipy library: <https://www.scipy.org/>;
- Struve O.: 1947, *Astrophysical Journal*, 106, 92
- Tatum J.B. *Physics topics. Celestial Mechanics*: <http://astrowww.phys.uvic.ca/~tatum/celmechs/>;
- Taylor P.H.: 1941, *Astronomical Society of the Pacific*, 53, 117
- Tvardovskyi D.E., Marsakova V.I., Andronov I.L.: 2017, *OAP*, 30, 135
- Tvardovskyi D. E.; Marsakova V.I.: 2015, *AASP*, 5, 75
- Tsesevich V.P.: 1973, *Eclipsing variable stars*. New York, J.Wiley, 1973evs..book.....T
- Vavilova I. B., et al.: 2017, *IAUS*, 325, 361
- Wolf M.: 2014 *Contributions of the Astronomical Observatory Skalnaté Pleso*, 43, 493
- Xiang Fu-Yuan, Xiao Ting-Yu, Yu Yun-Xia: 2015, *The Astronomical Journal*, 150, 25
- Yang Y.-G., et al.: 2010, *The Astronomical Journal*, 139, 195
- Yang Yulan, Qingyao Liu: 2002, *Astronomy and Astrophysics*, 390, 555
- Zasche P., et al.: 2009, *New Astronomy*, 14, 121

DOI: <http://dx.doi.org/10.18524/1810-4215.2018.31.145374>

ON THE IRREGULAR VARIATIONS IN THE LIGHT CURVES OF RY Vul

S.N.Udovichenko, L.E.Keir

Astronomical Observatory, Odessa National University,
Odessa, Ukraine, udovich222@ukr.net

ABSTRACT. In the Astronomical observatory of the Odesa National University traditionally study variable stars of different types: pulsating, double, irregular et al. By photometric observations it is possible to set the type of variable star, period of the brightness changes, spectral class, to estimate the temperature of surface. For observations variable stars there was the chosen area of star sky from by two stars Y Vul and RY Vul in the distance not more than 15 angular minutes (angular size of one frame). For these stars was got more than 5900 images during 56 nights during observant seasons 2011-2017. For all observations were got the curves of light variations. Results are for variable star Y Vul (type RR Lyr) published separately, and in this publication we bring results over of observation for star RY Vul. The star RY Vul according General Catalogue of Variable Star (GCVS) is RR Lyr variable, but period and initial epoch are unknown. To determine these parameters the photometric observations during several seasons in 2011-2017 of the variable star RY Vul on the Astronomical station near Odessa have been carried out. The 48-cm telescope reflector AZT-3 equipped with CCD photometer was used. The light curves in V and R band were obtained and analyzed. It turned out that the light curves of the star is fully irregular. Therefore, the variable star RY Vul should be attribute to type "irregular variables".

Keywords: Stars: oscillations – stars; variables: stars: individual: RY Vul.

АБСТРАКТ. В Астрономічній обсерваторії Одеського Національного університету традиційно вивчають змінні зорі різних типів: пульсуючі, подвійні, нерегулярні та інші. Шляхом фотометричних спостережень можна встановити тип змінної зорі, період зміни блиску, спектральний клас, оцінити температуру поверхні. Для спостережень змінних зір була вибрана ділянка зоряного неба з двома зорями Y Vul та RY Vul на відстані не більше 15 кутових хвилин (кутовий розмір одного кадру). Для цих зір було отримано більше ніж 5900 експозицій протягом 56

ночей впродовж спостережних сезонів 2011-2017 років. Для всіх спостережень були отримані криві блиску. Результати для змінної зорі Y Vul (тип RR Lyr) опубліковані окремо, а в цій публікації ми приводимо результати спостережень блиску для зорі RY Vul. Зоря RY Vul згідно Загального Каталогу Змінних Зір (ЗКЗЗ) є змінною типу RR Lyr, але її період та початкова епоха невідомі. Щоб визначити ці параметри були проведені фотометричні спостереження змінної зорі RY Vul на астрономічній станції біля Одеси протягом декількох сезонів. Всі спостереження були проведені за допомогою 48-см телескопа-рефлектора AZT-3, оснащеного ПЗЗ фотометром з охолодженням елементом Пельтьє та стабілізацією температури. Криві блиску були отримані та проаналізовані в смугах V і R. Обробка зоряних зображень була виконана за допомогою програми MUNIPACK (Motl, 2009-17). В цій програмі для калібрування зоряних ПЗЗ кадрів використовуються зображення темного кадру та плоского поля. Виявилось, що криві блиску зорі повністю нерегулярні протягом всіх років спостережень. Приводяться криві блиску, частотний аналіз фотометричних спостережень. Висновок: змінну зорю RY Vul необхідно віднести до типу «нерегулярні змінні зорі».

Ключові слова: Зорі: осциляції – зорі; змінні: зорі: індивідуально: RY Vul.

1. Introduction

RY Vul (AN 1907.0025, GSC 2126.00973), ($\alpha_{J2000.0} = 19^h04^m33.8^s$; $\delta_{J2000.0} = +24^\circ46'25.0''$) according GCVS is RR Lyr variable. The variability of the star was found by Parenago (1934). The finding chart for this star was published by Tsesevich and Kazanasmas, (1971). The star has been poorly investigated, only Steinbach H.M. reported that RY Vul was observed in August-September 2009 in 4 nights with a total amount of nearly 10 hours in Johnson V-Band. During that time the star showed no variability at all

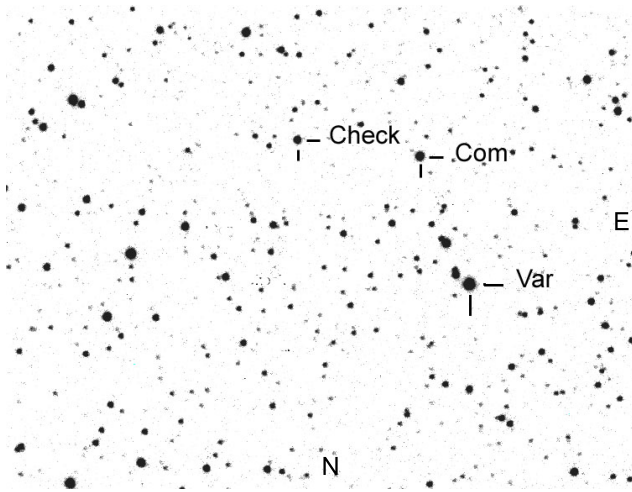


Figure 1: The finding chart RY Vul with the comparison and check stars marked.

but remained constant at 11.60^m in accordance with the value mentioned in the GSC. He drawn a conclusion that RY Vul obviously is not a variable star and should be discarded from the GCVS (Steinbach, 2010).

2. Observations

To study this phenomenon, we have to realize as much as possible observations of this star. The photometric CCD observations of RY Vul in Astronomical station near Odessa in observation season 2011, 2012, 2014, 2017 years have been carried out.

Two stars were chosen as comparison and check stars (comp=UCAC4 1125-11260150, Vcomp= $13.^m10$ (APASS, 2010), check=UCAC4 1125-11251433). The 48 cm reflector AZT-3 with the f/4.5 Newtonian focus and CCD photometer with chip Sony ICX429ALL (600x800 pixels), equipped with V and R filters, Peltier cooler were used (Udovichenko, 2012). The hermetic housing and thermoelectric (Peltier) cooler provide a temperature difference between the sensor CCD and the environment of about -40°C , and the temperature was supported by a constant. The exposure time for variable and comparison stars for the most part were chosen to exclude a saturation of frame. More than 5900 CCD frames were gathered during 56 nights.

The standard reductions of the CCD frames were carried out using the MUNIPACK (Motl, 2009-17) software. The procedures for the aperture photometry is composed of the dark-level and flat field corrections and determination of the instrumental magnitude and precision. The finding chart with comparison and check stars are shown in Fig. 1. The errors on individual data points vary between 0.005 mag to 0.015 mag.

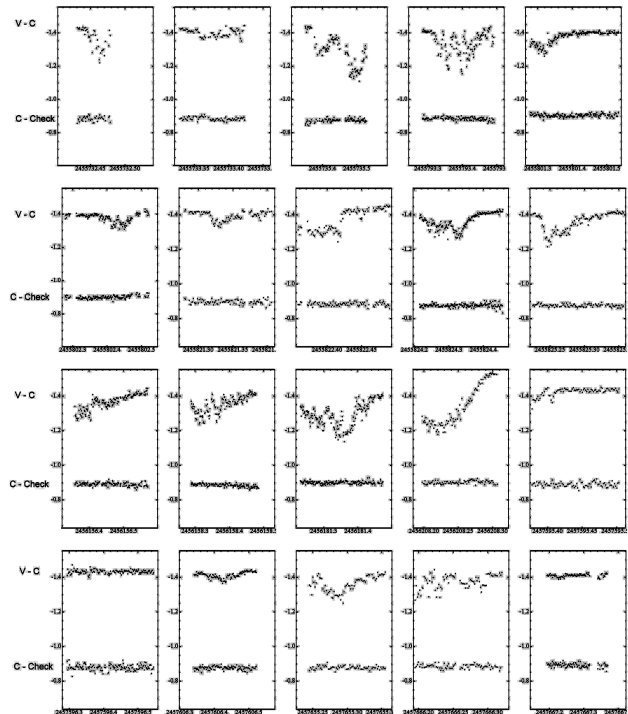


Figure 2: The differences V-C and C-Check vs HJD for the several nights observations.

3. Analysis of data

For all our observations of RY Vul were determined the difference magnitudes comparatively of variable-comparison star (V-C), and comparison-check star (C-Check). These differences for several nights are presented in Fig. 2.

These curves testify and show, that light of a star from night by the night changes nonperiodic, irregularity. Also the frequency analyses were performed using a package of computer programs with single-frequency and multiple-frequency techniques by using utilize Fourier as well as multiple-least-squares algorithms (program Period04, Lenz and Breger, 2004). The frequency analyses for our observations and ASAS data (Pojmanski G., 2002) have not shown some the significant periods (Fig. 3). It is not considered the alliance peaks connected with periodicity of observations (multiple one days).

From catalogs XPM(Fedorov), NOMAD the star RY Vul has $B-V = 1.2-1.44$, $T_{\text{eff}} = 3831.8\text{K}$ (Gaia) and concerns to late spectral classes K-M (VizieR, 2018).

Thus, the variable star RY Vul should not be discarded from the GCVS catalogue and should be ranked as type **ISB: Rapid irregular variables of the intermediate and late spectral types F-M.**

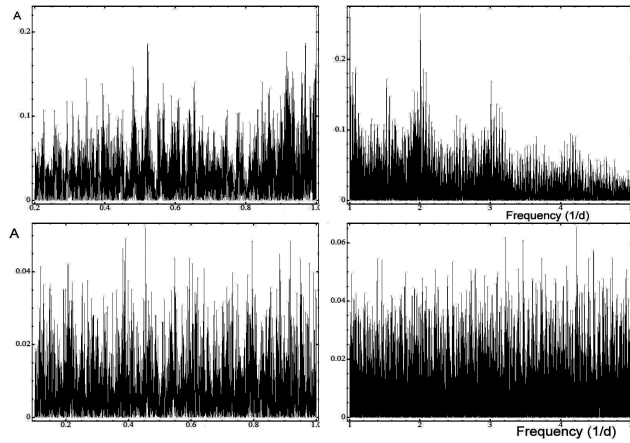


Figure 3: The Fourier amplitude spectrum for our observations (top) and ASAS data (bottom).

References

- APASS, Star catalog: 2010, <http://www.aavso.org>
- Lenz P., Breger M.: 2004, *Comm.in Asteroseismology* **144**, 41.
- Motl D.: 2009-17 <http://sourceforge.net/projects/c-munipack>
- Parenago P.: 1934, *Perem. Zvezdy* **4**, 301.
- Pojmanski G.: 2002, *Acta Astronomica*, **52**, 397.
- Samus N.N., Durlevich O.V., Kazarovets E.V., Kireeva N.N., Pastukhova E.N., Zharova A.V. et al.: 2011, *General Catalogue of Variable Stars* (GCVS database, Version 2011Jan).
- Tsesevich V.P., Kazanasmas M.S.: 1971, Atlas of Finding Charts of Variable Stars, Moscow.
- Steinbach H.M.: 2010, *BAVSR* **59**, 5.
- Udovichenko S.N.: 2012, *Odessa Astron. Publ.*, **25**, 32.
- VizieR: 2018, Online Data Catalog. — <http://vizier.u-strasbg.fr>

DOI: <http://dx.doi.org/10.18524/1810-4215.2018.31.145379>

SPECTROSCOPIC INVESTIGATIONS OF GALACTIC CLUSTERS WITH ASSOCIATED CEPHEID VARIABLES.

I. POLARIS CLUSTER AND α UMI.

I. A. Usenko^{1,2}, A. S. Miroshnichenko³, S. Danford³, V. V. Kovtyukh¹, D. G. Turner⁴,
A. V. Shul'ga², Yu. I. Protsyuk²

¹ Astronomical Observatory, Odessa National University, Shevchenko Park, Odessa 65014, Ukraine, vkovtyukh@ukr.net

² Mykolaiv Astronomical Observatory, Obsevatorna 1, Mykolaiv 54030, Ukraine, igus99@ukr.net; shulga-av@ukr.net; procsys@gmail.com

³ Dept. of Physics and Astronomy, University of North Carolina at Greensboro, P.O. Box 26170, Greensboro, NC 27402, USA, a_mirosh@uncg.edu; danford@uncg.edu

⁴ Dept. of Physics and Astronomy, Saint Mary's University, 923 Robie Street, Halifax B3H3C3, Nova Scotia, Canada, turner@ap.smu.ca

ABSTRACT. We present the results of an analysis of the spectra of nine so called Polaris cluster $A-FV$ stars obtained during 2016-2018. Radial velocities (RV) and GAIA DR 18 parallaxes-distances for these stars allow us to determine their membership in the cluster and to construct its 3D kinematic model. However T_{eff} for four stars determined spectroscopically give cause for doubts about the GAIA DR 18 parallaxes accuracy. The comparison between their M_V and distances with the those from Pecaut & Mamajek (2013) calibrations shows significant differences for the objects with parallaxes less than 8 mas. The differences in distances increase exponentially with decreasing parallax. These facts indicate an unreliability of the GAIA DR2 parallax measurements of less than 10 mas. We estimated the distance to Polaris B to be 104.2 pc.

АБСТРАКТ. Ми надаємо результати аналізу спектрів дев'яти зір спектрального класу $A-FV$ з так званого "скупчення Полярної", що були отримані на протязі 2016-2018 років. Радіальні швидкості та відстані, що отримані по паралаксах GAIA DR 18 для цих зір дозволяють нам встановити їх належність до скупчення за збудувати їх кінематичну 3D-модель. Але оцінки T_{eff} , що отримані спектроскопічно для чотирьох зір надають причину для сумніву у точності значень паралаксів GAIA DR 18. Порівняння з їх M_V та відстанями з подібними, взятими з калібровок Pecaut & Mamajek (2013) показують значні розбіжності для об'єктів з паралаксами менше ніж 8 мас. Ці розбіжності у відстанях зростають експоненційно зі зменшенням паралаксу. Ці факти викривають ненадійність оцінок паралаксів GAIA DR 18 менше ніж 10 мас.

Ми оцінили відстань до Полярної В у 104.2 парсека.

Key words: Open clusters; Stars; radial velocities; GAIA parallaxes; Cepheids and main-sequence stars; effective temperatures; distances; Cepheids; α UMi

1. Introduction

In a recent paper of Engle et al. (2018) the authors determined the distance to the Polaris AB system of 137.1 ± 0.53 pc based on an estimate of the GAIA DR2 parallax for Polaris B of 7.292 ± 0.03 mas. This distance assumes the Cepheid's radius near $47-50 R_{\odot}$, although the "canonical" $P-R$ (period versus radius) relationship (Gieren et al. 1998) gives nearly $33 R_{\odot}$. Such a parallax measurement is close to 132 ± 9 ps determined by HIPPARCOS (ESA 1997). It is known that the HIPPARCOS parallax data for Cepheids have been repeatedly questioned, and the GAIA project was aimed at resolving these doubts. On the other hand, based on HIPPARCOS photometric data Turner (2009) established that field stars in the Polaris region belong to a poorly-populated star cluster. Most of these stars have parallaxes that correspond to a distance of 99 ± 2 pc. A colour-magnitude diagramme for possible Polaris cluster stars constructed from 2MASS data suggests a distance of 106 ± 7 pc for a colour-excess of $E_{B-V} = 0.02$ mag (Turner 2009). Usenko & Klochkova (2008) determined spectroscopically $T_{\text{eff}} = 6900 \pm 50$ K for Polaris B and assuming an $F3V$ main-sequence star radius of $1.4 R_{\odot}$ derived its $M_V = +3.30$ mag and a distance of 109.5 pc. This result is an ideal agreement with 110 pc derived by Kamper (1996) using astrometric methods. Such a significant discrepancy in the estimates

and the radius of Polaris create grounds for a speculation about its evolutionary status and pulsational mode. In addition, Polaris is the nearest Cepheid to the Sun and determining the exact distance to it and its radius, respectively, is an important step in establishing the "P – L" relationship for Cepheids.

To resolve this problem we performed spectroscopic observations of the Polaris cluster main-sequence stars in order to determine their RV (to establish their membership in the cluster) and effective temperatures (to determine the radii and distances from known spectral types). These objects were taken from Turner et al. (2005). In addition to our RV measurements, combination with their GAIA DR2 parallaxes makes it possible to construct a kinematic 3D cluster model.

2. Observations

Nine spectra were taken during 2016 – 2018 with the 0.81 m telescope of the Three College Observatory (TCO), located in central North Carolina, USA. They were obtained with an échelle spectrograph manufactured by Shelyak Instruments¹ in a spectral range from 4250 to 7800 Å with a spectral resolving power of $R \sim 12000$ and no gaps between the spectral orders. The data were reduced using the *échelle* package in IRAF.

The DECH30 package (Galazutdinov, 2007) was used to measure the line depths and radial velocities using spectra in FITS format. Lines depths were used to determine the effective temperature (a method based on the spectroscopic criteria – Kovtyukh, 2007). Objects, their magnitudes, color-indices, and derived RVs for each spectrum are given in Table 1. V , $B - V$ and spectral types are taken from SIMBAD database, RV were measured using the metals (RV (met)) and hydrogen (H_α , H_β) absorptional lines.

3. Results and Analysis

Since the investigated objects are A-F main sequence stars, the radii and luminosities of which show an almost linear relation on the effective temperatures (intrinsic colors), we can compare our values of $(B - V)$ and T_{eff} with the ones calculated by Pecaut & Mamajek (2013) for a specific spectral type. This paper allows us to move from $(B - V)$ and T_{eff} to the radii of the stars, and hence to the distances to them. In Table 2 we represent the $(B - V)$ estimates from Turner et al. (2005). For the intrinsic color-indices $(B - V)_0$ we used the $(B - V)$ data for from Pecaut & Mamajek (2013). This way the color-excesses and reddenings were determined for each star. In addition, in Table 2 we included the reddening and distance for each object, defined taking into account the color-excess $E_{B-V} =$

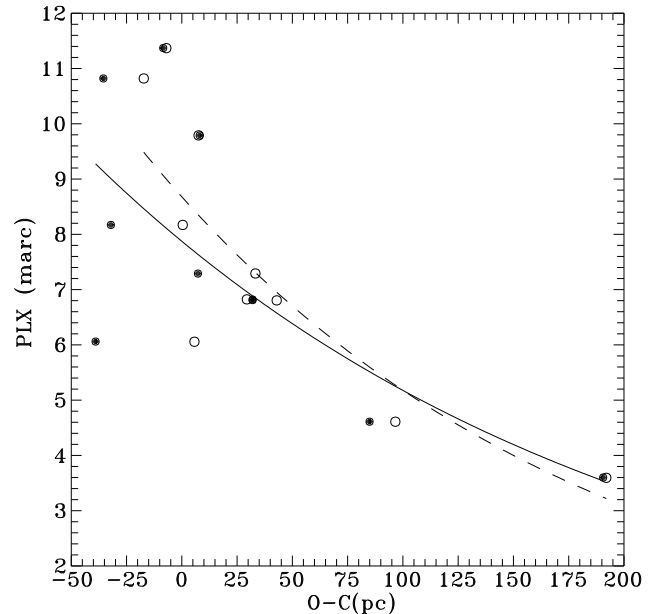


Figure 1: (O-C) distances - GAIA DR2 parallaxes relationship for the Polaris cluster stars. Open circles – calculated with E_{B-V} and A_V according to the intrinsic color-indices from Pecaut & Mamajek (2013), filled circles – calculated with $E_{B-V} = 0.04$ according to Turner (2009).

0.04 from Turner (2009). As can be seen from Table 2, for 6 stars from the list the difference in distance estimates varies from 11 to 45 pc. This indicates that the color-excesses for most of the cluster stars need to be refined.

For four stars from the list, there are estimates of T_{eff} , determined spectroscopically: HD 5914 - $T_{\text{eff}} = 8800 \pm 50$ K (Usenko et al., 2008) and Polaris B - $T_{\text{eff}} = 6900 \pm 50$ K (Usenko & Klochkova, 2008) from hydrogen line profiles; HD 209556 - $T_{\text{eff}} = 6301 \pm 17$ K and HD 163988 - $T_{\text{eff}} = 6369 \pm 20$ K from the ratio of the metal absorption line depths (Kovtyukh, 2007). Unfortunately, the latter method works only for stars of the spectral types later than F4 V. Nevertheless, according to Table 2, the difference between the radii determined from the spectroscopic estimates of T_{eff} and the values of Pecaut & Mamajek (2013) for this spectral type is approximately $\sim 0.1 R_\odot$. In this case, the difference in the value of T_{eff} of 250 K gives an error in the distance is about 5.4 pc. Thus, the data from Pecaut & Mamajek (2013) can be used for calibration of the distances to the cluster stars.

Table 3 shows the GAIA DR2 parallaxes (except for HD 66368) for stars from the list and the absolute magnitudes and distances determined from them, as well as the data according to Pecaut & Mamajek (2013) for comparison. As can be seen from this Table, the smallest discrepancies in distances are found for the stars with parallaxes larger 8 mas. Figure 1 shows the rela-

¹<http://www.shelyak.com>

Table 1: Polaris cluster objects. Observational list and RV.

| Object | V | $B - V$ | SpT | RV, km s^{-1} | | | | |
|-----------|------|---------|-----|------------------------|-----|------------|-----------|-----------|
| | | | | RV (met) | NL | H_α | H_β | Reference |
| HD 5914 | 6.46 | 0.10 | A3V | +0.1±3.3 | 110 | +1.7 | -2.1 | |
| HD 66368 | 7.13 | 0.14 | A0V | -7.9±2.8 | 86 | -4.4 | -2.0 | |
| HD 11696 | 8.13 | 0.27 | A3V | +8.3±0.6 | 56 | -5.0 | - | |
| HD 224687 | 6.74 | 0.06 | A0V | -16.3±2.1 | 30 | -13.6 | -8.4 | |
| HD 224991 | 7.84 | 0.30 | F0V | +3.1±2.4 | 57 | -1.9 | +3.0 | 1 |
| | | | | -5.7±4.1 | 88 | - | - | |
| HD 16335 | 7.84 | 0.36 | F0V | -22.8±2.9 | 57 | -30.1 | -28.4 | 1 |
| | | | | -31.6±3.2 | 104 | - | - | |
| Polaris B | 8.20 | 0.57 | F3V | -18.9±3.6 | 63 | -16.6 | - | 2 |
| HD 14369 | 8.11 | 0.35 | F0V | -8.5±2.1 | 157 | -7.8 | -6.4 | |
| HD 209556 | 8.37 | 0.45 | F5V | -8.7±2.4 | 51 | -13.5 | -14.4 | |
| HD 163988 | 8.11 | 0.47 | F5V | -12.2±2.2 | 33 | -1.0 | -4.8 | |

NL - number of lines

[1] - two groups of absorption lines of metals, probably a spectroscopic binary star.

[2] - RV data according to Usenko & Klochkova (2008).

Table 2: Intrinsic colors, reddenings, effective temperatures, absolute magnitudes, distances, and radii are determined using data from Pecaut & Mamajek (2013).

| Star | $B - V$ | SpT | $(B - V)_0$ | E_{B-V} | A_V | A_V (T) | T_{eff} | M_V | d | d (T) | R | $R(T_{\text{eff}})$ |
|-----------|---------|-----|-------------|-----------|-------|-----------|------------------|-------|-------|---------|------|---------------------|
| HD 5914 | 0.10 | A3V | 0.090 | 0.010 | 0.057 | 0.067 | 8550 | 1.55 | 93.5 | 93.0 | 2.01 | 1.90 |
| HD 66368 | 0.14 | A0V | 0.000 | 0.140 | 0.585 | 0.067 | 9700 | 1.11 | 120.5 | 153.0 | 2.09 | - |
| HD 11696 | 0.27 | A3V | 0.090 | 0.180 | 0.609 | 0.067 | 8550 | 1.55 | 157.8 | 202.5 | 2.01 | - |
| HD 224687 | 0.06 | A0V | 0.000 | 0.060 | 0.272 | 0.067 | 9700 | 1.11 | 118.5 | 130.2 | 2.09 | - |
| HD 224991 | 0.30 | F0V | 0.300 | 0.000 | 0.020 | 0.068 | 7220 | 2.51 | 115.9 | 113.3 | 1.79 | - |
| HD 16335 | 0.36 | F0V | 0.294 | 0.066 | 0.288 | 0.068 | 7220 | 2.51 | 102.4 | 113.3 | 1.79 | - |
| Polaris B | 0.57 | F3V | 0.389 | 0.181 | 0.570 | 0.067 | 6720 | 2.99 | 104.2 | 128.4 | 1.60 | 1.52 |
| HD 14369 | 0.35 | F0V | 0.294 | 0.056 | 0.404 | 0.068 | 7220 | 2.51 | 108.9 | 127.2 | 1.79 | - |
| HD 209556 | 0.45 | F5V | 0.438 | 0.012 | 0.101 | 0.067 | 6510 | 3.40 | 94.2 | 95.6 | 1.46 | 1.57 |
| HD 163988 | 0.47 | F5V | 0.438 | 0.032 | 0.124 | 0.067 | 6510 | 3.40 | 83.8 | 85.2 | 1.46 | 1.53 |

 A_V (T) and d (T) - reddening and distance from $E_{B-V} = 0.04$ (Turner, 2009)

Table 3: Comparison between absolute magnitudes and distances determined using GAIA DR2 parallaxes and Pecaut & Mamajek (2013) data.

| Object | PLX (GAIA DR2) | | | P & M | |
|-----------|-------------------------|-----------|-----------|-------|----------|
| | π (mac) | M_V | d (pc) | M_V | d (pc) |
| HD 5914 | 9.7893±0.0418 | 1.37±0.01 | 101.1±0.4 | 1.55 | 93.5 |
| HD 66368 | 8.17 ¹ ±0.55 | 1.62±0.15 | 120.9±8.0 | 1.11 | 120.5 |
| HD 11696 | 6.0574±0.0319 | 2.02±0.01 | 163.5±1.1 | 1.55 | 157.8 |
| HD 224687 | 4.6108±0.0363 | 0.02±0.03 | 215.1±2.5 | 1.11 | 118.5 |
| HD 224991 | 6.8234±0.0305 | 1.97±0.03 | 145.3±2.0 | 2.51 | 115.9 |
| HD 16335 | 6.8055±0.0259 | 1.97±0.01 | 145.3±0.6 | 2.51 | 102.4 |
| Polaris B | 7.2920±0.0280 | 2.87±0.01 | 135.7±0.6 | 2.99 | 104.2 |
| HD 14369 | 10.8196±0.0291 | 3.22±0.01 | 91.7±0.4 | 2.51 | 108.9 |
| HD 209556 | 11.3687±0.0869 | 3.60±0.02 | 87.2±0.2 | 3.40 | 94.2 |
| HD 163988 | 3.5955±0.0321 | 0.85±0.02 | 275.8±2.5 | 3.40 | 83.8 |

[1] - value from van Leeuwen (2007)

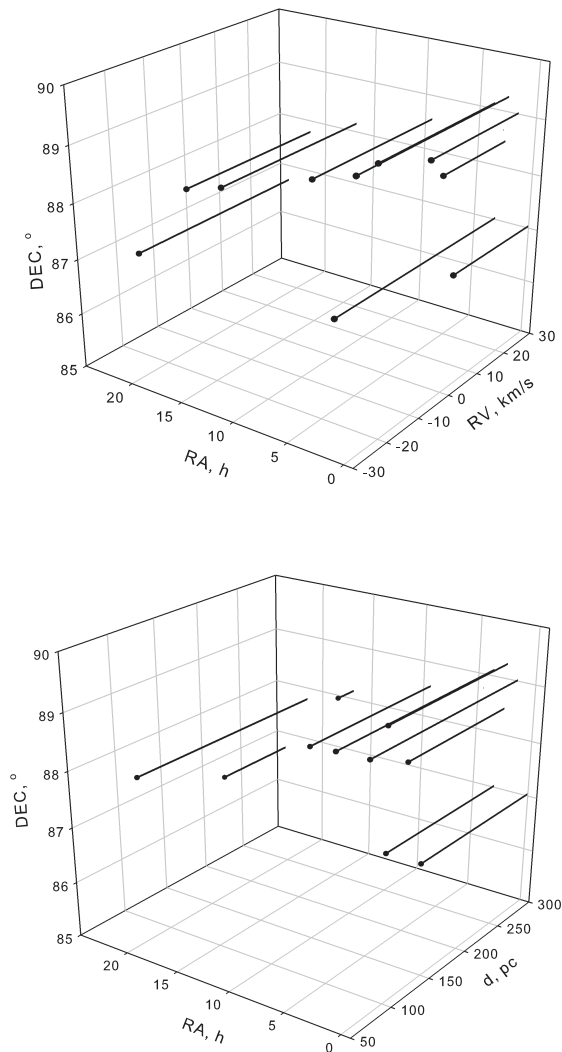


Figure 2: Polaris cluster 3D view by distance (bottom) and RV (top).

tionships of (O-C) in distances - GAIA DR2 parallaxes for two different cases of estimates of the color-excess of cluster stars. To construct this relationship calculated distances (C) were derived using data from Pecaut & Mamajek (2013), while the observed (O) ones came from the GAIA DR2 parallaxes. As can be seen from the Figure, both dependences are close to one another and are of exponential character, indicating that the errors in the distance determination to the cluster stars increase with decreasing parallaxes. This fact means that the GAIA DR2 parallaxes of less than 8 mas are unreliable. This is especially true for the assessment of Polaris B which is used to calibrate the distance for the Cepheid Polaris.

Nevertheless as seen from Figure 2, a 3D view of the Polaris cluster composed from our RV measurements and GAIA DR2 distances show the membership of our objects to the cluster.

4. Summary

1. According to RV values all these stars belong to the same moving group.
2. The distances of these stars determined from Pecaut & Mamajek (2013) calibrations and GAIA DR2 parallaxes indicate that these objects belong to the same cluster.
3. This fact is also evidenced by the distances determined for four stars (HD 5914, Polaris B, HD 163988, HD 209556) by means of their radii and T_{eff} .
4. The distances determined from GAIA DR2 parallaxes show significant differences - the smaller the parallax, the greater the distance to the star.
5. (O-C) - Parallax relation, there O, - distance in Pecaut & Mamajek (2013) calibration, and C - on parallaxes, has an exponential character.
6. The greatest differences between O and C begin after parallax estimates in 8 mas.
7. These facts indicate the unreliability of the estimates of GAIA DR2 parallaxes of less than 10 mas.
8. Estimating the distance to Polaris B in 137 pc should be revised. Its realistic value within the bounds of 100-110 pc (Usenko & Klochkona, 2008; Turner, 2009).

References

- Cutri R.M. et al.: 2003, *2MASS All-Sky Catalog of Point Sources*. Univ. Massachusetts and Infrared Processing and Analysis Center (IPAC)/ California Institute of Technology
- Engle S.G., Guinan E.F. & Harmanec P.: 2018, *RNAAS*, **2**, 126.
- ESA 1997, ESA-SP 1200 The Hipparcos and Tycho catalogues. ESA Publications Division, Noordwijk
- GAIA DR2 2018, *CDS/ADS Collection of Electronic Catalogues* **1345**, 0
- Galazutdinov G.A.: 2007, <http://gazinur.com/DECH-software.html>
- Gieren W.P., Fouqué P., Gómez H.: 1998, *ApJ*, **496**, 17.
- Kamper K.W.: 1996, *JRASC*, **90**, 140.
- Kovtuykh V.V.: 2007, *MNRAS*, **378**, 617.
- Pecaut M.J., Mamajek E.E.: 2013, *ApJS*, **208**, 9.
- Turner D.G., Savoy J., Derrah J., Abdel-Sabour Abdel-Latif M., Berdnikov L.N.: 2005, *PASP*, **117**, 207.
- Turner D.G.: 2009, *AIPC*, **1170**, 59.
- Usenko I.A., Klochkova V.G.: 2008, *MNRAS*, **387**, L1.
- Usenko I.A., Miroshnichemnko A.S., Klochkova V.G., Panchuk V.E.: 2008, *Odessa Astron. Publ.*, **21**, 127.
- van Leeuwen F.: 2007, *A&A*, **474**, 653.

DOI: <http://dx.doi.org/10.18524/1810-4215.2018.31.145381>

SPECTROSCOPIC INVESTIGATIONS OF GALACTIC CLUSTERS WITH ASSOCIATED CEPHEID VARIABLES.

II. NGC 5662 AND V CEN

I. A. Usenko^{1,2}, A. Yu. Kniazev^{3,4}, V. V. Kovtyukh¹, T. V. Mishenina¹,
A. S. Miroshnichenko⁵, D. G. Turner⁶, Yu. I. Protsyuk²

¹ Astronomical Observatory, Odessa National University, Shevchenko Park, Odessa 65014, Ukraine, vkovtyukh@ukr.net

² Mykolaiv Astronomical Observatory, Obsevatorna 1, Mykolaiv 54030, Ukraine, igus99@ukr.net; procsys@gmail.com

³ South African Astronomical Observatory, P.O. 7925, Cape Town, South Africa akniazev@saaao.ac.za

⁴ Southern African Large Telescope Foundation, P.O. 7925, Cape Town, South Africa

⁵ Dept. of Physics and Astronomy, University of North Carolina at Greensboro, P.O.Box 261170, Greensboro, NC 27402, USA, a_mirosh@uncg.edu

⁶ Dept. of Physics and Astronomy, Saint Mary's University, 923 Robie Street, Halifax B3H3C3, Nova Scotia, Canada, turner@ap.smu.ca

ABSTRACT. We present the results of a spectroscopic and photometric investigation of 15 objects from the open cluster NGC 5662, which contains the Cepheid V Cen. Besides the Cepheid, we studied one G-supergiant, two K-giants, four B-giants, and seven main sequence stars. Radial velocities (RV), $v \sin i$, T_{eff} , $\log g$, and $[\text{Fe}/\text{H}]$ were determined using model fitting. We have derived the color-excesses, reddenings, and intrinsic colors for these stars to determine their true T_{eff} and $\log g$ from comparison to the atmosphere models, especially for hot stars, and to determine their absolute magnitudes. RV and GAIA DR2 2018 parallax/distance values for these stars allowed us to determine their membership in the cluster and to construct its 3D kinematic models. These parallaxes and reddenings led to the distances in a range of 700–875 pc, while photometric M_V gave the distances of 550–660 pc. Two objects from our list were found to be non-members of the cluster, and two other objects to be background stars. All members have $[\text{Fe}/\text{H}] = -0.1 \pm 0.04$ dex. The main sequence stars and B-giants have abundances of C, N, and Na close to the solar one, while the cool supergiants and giants show a deficit of carbon, an overabundance of nitrogen, and a small overabundance or close to the solar sodium content. Two Li-rich K-giants, HD 127733 and HD 127753, were discovered in the cluster.

АБСТРАКТ. Ми презентуємо результати спектроскопічних та фотометричних дослідів 15 об'єктів розсіяного скупчення NGC 5662 з цефеїдою V Cen. Окрім цефеїди ми дослідили один G-надгігант, два K-гіганти, чотири B-гіганти та сім зір головної послідовності. За

допомогою модельного фітінгу були отримані оцінки радіальних швидкостей (RV), $v \sin i$, T_{eff} , $\log g$, та $[\text{Fe}/\text{H}]$. Ми розрахували надлишки кольору, почервоніння та справжні кольори для цих зір, щоб знайти їх справжні T_{eff} та $\log g$ шляхом порівняння з моделями атмосфер, особливо для гарячих зір, та абсолютні магнітуди. Оцінки RV та паралакс/відстань з каталогу GAIA DR2 2018 для цих зір дозволяють виявити їх належність до скупчення та збудувати його кінематичні 3D-моделі. Ці паралакси та почервоніння дають оцінки відстаней у межах 700–850 пс, тоді як фотометричні M_V давали оцінки у 550–660 пс. Два об'єкти з нашого списку виявилися не членами скупчення, та ще два - біля меж скупчення. Усі члени мають $[\text{Fe}/\text{H}] = -0.1 \pm 0.04$ dex. Зорі головної послідовності та B-гіганти мають вміст C, N, та Na близьким до сонячного, тоді як холодні надгіганти та гіганти показують дефіцит вуглецю, надлишок азоту, та маленький надлишок, або сонячний вміст натрію. У скупченні були відкриті два багатих літієм K-гіганта - HD 127733 та HD 127753.

Key words: Open clusters: radial velocities; Stars: abundance; GAIA parallaxes; Cepheids; Lithium giants; individual: NGC 5662, V Cen, HD 127733, HD 127753.

1. Introduction

The open cluster NGC 5662 belongs to the Centaurus section of the Milky Way. Being the Trumpler class II3m, it consists of a central grouping in the northern part and a southern one with the Cepheid V

Cen and a loose concentration of *B*- and *A*-type stars (Turner, 1982). According to Claria et al. (1991), the earliest spectral type stars in it is B7, $E(B - V) = 0.31$, $V - M_V = 9.80$, $d = 790 \pm 5$ pc, $[Fe/H] = -0.03$, and an age near 7.9×10^7 yr. Kharchenko et al. (2016) give a $[Fe/H] = 0.03$ for this cluster. NGC 5662 has not been carefully studied spectroscopically except for V Cen. Therefore, the main goals of our investigation are as follows: 1) to measure the radial and rotational velocities of the cluster's stars, 2) to determine the atmosphere parameters, metallicities, CNO, and Na abundances and compare the abundances between the objects of different spectral types, and 3) to determine the distances using GAIA DR2 parallaxes and RV data and to construct a 3D cluster's kinematic model.

2. Observations

All observations were taken using the 11m SALT (Southern African Large Telescope) equipped with HRS (High Resolution Spectrograph). HRS is a dual-beam (3700-5500 & 5500-8900 Å) fiber-fed, white-pupil, échelle spectrograph, which uses VHP gratings as cross dispersers. We obtained one spectrum for each object using the *medium mode* with the spectral resolving power $R = 40000$, an average S/N of over 100, which is enough to reach our observational goals. These spectra will be used to derive the atmosphere parameters and chemical abundances for some elements of the open cluster members. The data were reduced using the *échelle* context in *MIDAS*. Also, the *feros* package developed for échelle data reduction from the Fiber-fed Extended Range Optical Spectrograph (FEROS) was used. Both FEROS and HRS provide very similar échelle data.

We used the DECH30 package (Galazutdinov, 2007) designed to use the spectra in FITS format to measure the line depths and their equivalent widths. The radial and rotational velocities were measured by fitting of the observed spectrum with a model from Coelho (2014). The object IDs, their magnitudes, spectral types, and measured radial and rotational velocities for each spectrum are given in Table 1. It should be noted that our results are consistent with those from other sources: $RV = -21.74$ km s^{-1} (Mermillod et al., 2008) and -20.89 km s^{-1} (GAIA DR2, 2018) for HD 127427; -21.02 km s^{-1} (Mermillod et al., 2008), and -21.31 km s^{-1} (GAIA DR2 2018) for HD 127753, respectively.

3. Results and Analysis

3.1. Color-indices, color-excesses, reddenings, and atmosphere parameters

Since the objects of NGC 5662 from our list have

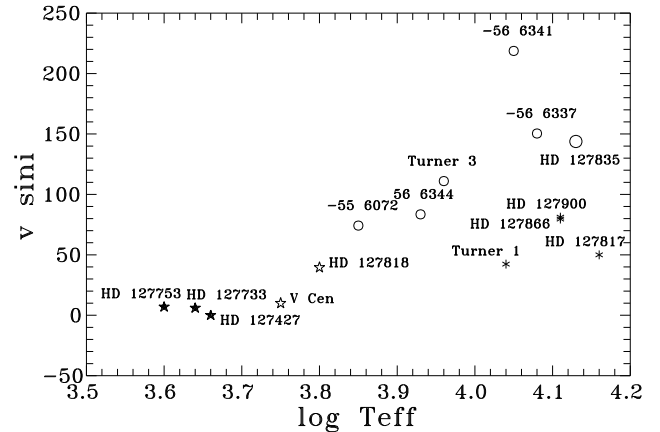


Figure 1: Relation between the rotation velocity and T_{eff} for the NGC 5662 open clusters' objects. Open circles show the main sequence stars, filled five-point stars show K-supergiants, open five-point stars show FG-supergiants, and six-point stars show B-giants.

different spectral types, masses, and evolutionary status, we have used different methods to determine their atmosphere parameters. First, for the T_{eff} , $\log g$, and $[Fe/H]$ determination, as mentioned above, model fitting was performed. Next, the T_{eff} estimates were verified using the Gray (1992) calibrations for color-indices. A final determination of the atmosphere parameters was performed in the following way. We have used the $U - B$ and $B - V$ intrinsic color-indices for luminosity types and metallicity based on the Kurucz (1993) models from Bessel et al. (1998) to determine T_{eff} and $\log g$ for the B- and A-type stars. For more evolved stars of *FGK* spectral types with a large number of narrow metallic absorption lines we have used the lines depth relation to derive T_{eff} (Kovtuykh, 2007), a Fe ionization balance to derive $\log g$, and the absence of an Fe abundance dependence upon the equivalent width to derive V_t . It is obvious that we needed correct $(U - B)_0$ and $(B - V)_0$ not only for T_{eff} and $\log g$, but also M_V data for our stars distance and radius determination. Therefore in Table 2 we show color-excess, intrinsic color, reddening, and extinction data that we have determined. As seen from Table 2, the majority of stars have close values of the color-excesses and reddenings, except for HD 127818 and HD 127733. Table 3 presents the results of the atmosphere parameters determination. As seen from this Table, the best agreement is achieved between all the methods of the T_{eff} determination for all stars as a whole, although there are discrepancies for some cool stars. The same can be said about the $\log g$ determinations.

Figure 1 represents a relation between the rotational velocity and T_{eff} . It shows that all main-sequence stars as well as cool giants and supergiants found the

Table 1: General data for the observed objects in NGC 5662 and derived RVs.

| Object | V | Sp.type | $RV, \text{km s}^{-1}$ | $v \sin i, \text{km s}^{-1}$ |
|----------------------|--------|-----------|------------------------|------------------------------|
| V Cen | 6.930 | F5 Ib-II | -23.50 ± 0.50^1 | 10.4 ± 0.1 |
| HD 127427 | 7.744 | G8 II-III | -21.86 ± 0.02 | 0.0 ± 0.0 |
| HD 127866 | 8.287 | B7 III | -22.25 ± 0.14 | 79.6 ± 0.3 |
| CPD $-56^\circ 6337$ | 10.659 | A1 V | -58.16 ± 0.21 | 150.4 ± 0.5 |
| HD 127817 | 9.157 | A0 V | -18.57 ± 0.09 | 50.0 ± 0.2 |
| HD 127753 | 7.043 | K5 III | -22.53 ± 0.03 | 6.9 ± 0.1 |
| HD 127835 | 9.375 | B8 V | -15.37 ± 0.12 | 143.8 ± 0.4 |
| HD 127900 | 8.817 | B8 II-III | -20.82 ± 0.10 | 81.2 ± 0.2 |
| CPD $-56^\circ 6341$ | 10.787 | B9 V | -14.97 ± 0.22 | 218.7 ± 0.7 |
| CPD $-55^\circ 6072$ | 11.296 | | -37.55 ± 0.08 | 74.2 ± 0.2 |
| CPD $-56^\circ 6344$ | 11.347 | | -24.83 ± 0.15 | 83.5 ± 0.2 |
| HD 127818 | 9.485 | F6/8 IV-V | -10.62 ± 0.06 | 40.0 ± 0.1 |
| HD 127733 | 8.599 | K2/3 III | $+7.35 \pm 0.03$ | 6.0 ± 0.1 |
| HD 127199 (Turner 1) | 10.620 | B5/7 III | -27.84 ± 0.09 | 42.3 ± 0.2 |
| Turner 3 | 12.030 | | -46.99 ± 0.17 | 111.0 ± 0.4 |

1 - Phase $0.P575$ according to GCVS (1985)

Table 2: Observed colors, color-excesses, intrinsic colors, reddenings, and extinctions for the NGC 5662 objects.

| Star | B-V | U-B | $(B-V)_0$ | E_{B-V} | $(U-B)_0$ | E_{U-B} | A_V | V_0 | R |
|----------------------|------|-------|-----------|-----------|-----------|-----------|-------|-------|------|
| V Cen | 0.91 | 0.60 | 0.60 | 0.31 | 0.36 | 0.24 | 1.18 | 5.75 | 3.80 |
| HD 127427 | 1.45 | 1.30 | 1.04 | 0.45 | 1.03 | 0.37 | 1.11 | 6.39 | 3.00 |
| HD 127866 | 0.16 | -0.24 | -0.12 | 0.28 | -0.45 | 0.22 | 0.92 | 7.45 | 2.97 |
| CPD $-56^\circ 6337$ | 0.25 | -0.02 | -0.08 | 0.33 | -0.26 | 0.22 | 0.99 | 9.68 | 3.00 |
| HD 127817 | 0.20 | -0.25 | -0.14 | 0.54 | -0.49 | 0.24 | 0.99 | 8.13 | 2.99 |
| HD 127753 | 1.86 | 2.04 | 1.33 | 0.60 | 1.75 | 0.27 | 1.11 | 5.23 | 3.00 |
| HD 127835 | 0.13 | -0.29 | -0.13 | 0.26 | -0.48 | 0.20 | 0.81 | 8.60 | 3.00 |
| HD 127900 | 0.14 | -0.26 | -0.14 | 0.28 | -0.46 | 0.20 | 0.87 | 7.98 | 3.00 |
| CPD $-56^\circ 6341$ | 0.33 | 0.10 | -0.06 | 0.40 | -0.18 | 0.27 | 1.14 | 9.61 | 3.80 |
| CPD $-55^\circ 6072$ | 0.57 | 0.24 | 0.29 | 0.29 | - | - | 0.88 | 10.42 | 3.00 |
| CPD $-56^\circ 6344$ | 0.42 | 0.26 | 0.19 | 0.24 | 0.01 | 0.21 | 0.71 | 10.64 | 3.02 |
| HD 127818 | 0.57 | 0.16 | 0.36 | 0.22 | - | - | 0.65 | 8.84 | 3.02 |
| HD 127733 | 1.70 | 1.85 | 1.29 | 0.47 | 1.56 | - | 1.94 | 7.20 | 3.46 |
| HD 127199 (Turner 1) | 0.26 | 0.06 | -0.07 | 0.34 | -0.18 | 0.24 | 0.96 | 9.61 | 3.10 |
| Turner 3 | 0.61 | 0.29 | 0.38 | 0.35 | 0.05 | 0.24 | 0.99 | 11.00 | 3.20 |

Table 3: Atmosphere parameters for the NGC 5662 objects.

| Star | T_{eff} | | | | | log g | | | | V_t |
|----------------------|------------------|-------|-------|------|---------|-------|------|------|---------|-------|
| | Gray | Fit | Phot | AMod | Adopted | Fit | Phot | AMod | Adopted | |
| V Cen | | 5824 | | 5596 | 5596 | 0.70 | | 1.80 | 1.80 | 3.10 |
| HD 127427 | 4771 | 4937 | | 4610 | 4620 | 2.24 | | 1.40 | 1.40 | 2.00 |
| HD 127866 | 13537 | 12912 | 12891 | | 12891 | 3.57 | 3.22 | | 3.22 | 3.80 |
| CPD $-56^\circ 6337$ | 11863 | 11712 | 12000 | | 12000 | 4.22 | 4.25 | | 4.25 | 2.70 |
| HD 127817 | 14607 | 14000 | 14230 | | 14230 | 3.89 | 3.90 | | 3.90 | 3.50 |
| HD 127753 | 4229 | 4134 | | 3840 | 3840 | 1.27 | | 0.40 | 0.40 | 2.20 |
| HD 127835 | 14049 | 13347 | 13400 | | 13400 | 3.75 | 3.75 | | 3.75 | 3.80 |
| HD 127900 | 14049 | 13000 | 13000 | | 13000 | 3.74 | 3.50 | | 3.50 | 3.50 |
| CPD $-56^\circ 6341$ | 11205 | 14416 | 11300 | | 11300 | 4.33 | 4.30 | | 4.30 | 3.50 |
| CPD $-55^\circ 6072$ | 6994 | 7000 | | | 7000 | 3.48 | | | 3.48 | |
| CPD $-56^\circ 6344$ | 7534 | 8415 | 8375 | | 8375 | 4.35 | 4.00 | | 4.00 | 5.50 |
| HD 127818 | 6704 | 6600 | | 6355 | 6355 | 3.92 | | 3.40 | 3.40 | 2.00 |
| HD 127733 | 4296 | 4472 | | 4350 | 4350 | 2.75 | | 2.00 | 2.00 | 1.80 |
| HD 127199 (Turner 1) | 11521 | 14000 | 10467 | | 10467 | 4.13 | 4.10 | | 4.10 | 2.50 |
| Turner 3 | 7040 | 9556 | 9050 | | 9050 | 3.30 | 4.00 | | 4.00 | 3.50 |

Gray - according to Gray (1992); Fit - using fitting;
 Phot - from photometry; AMod - using atmosphere models.

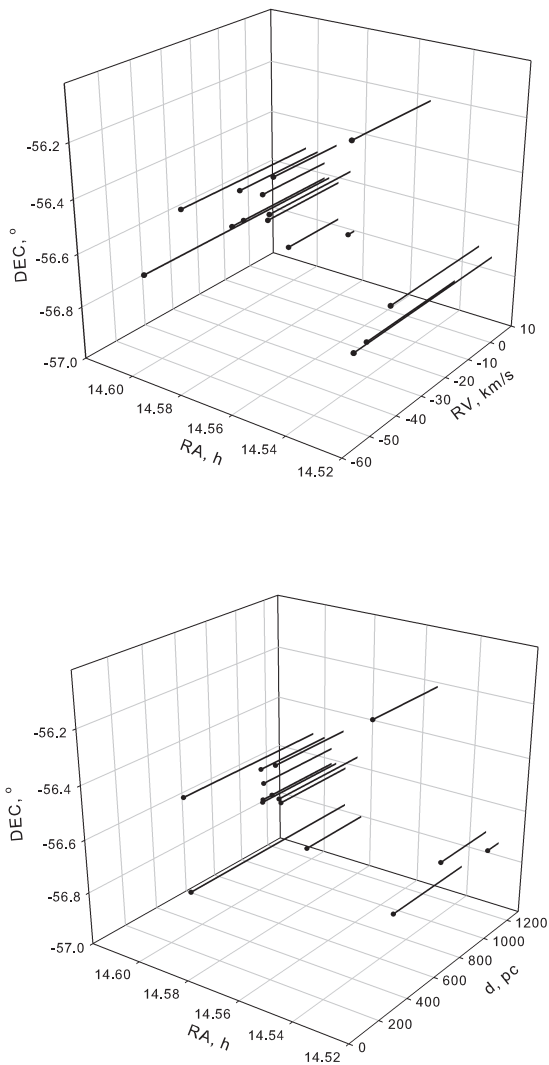


Figure 2: A 3D view of the NGC 5663 cluster by distance and radial velocities.

clear dependence, while blue giants form a separate region.

3.2. Parallaxes, absolute magnitudes, distances, and radii

Table 4 contains the GAIA DR2 parallaxes for our stars as well as absolute magnitudes and distances determined from them, and next to compare, - data from photometric observations. As can be seen from the Table, the parallax-based distances for 12 objects lie in a range of 700–875 pc, and they are close to the 790 ± 5 pc value from Claria et al. (1991). According

to these authors, CPD $-55^{\circ}6072$ and HD 127818 are non-members of the cluster, and this fact is confirmed in this Table. Similar to V Cen, HD 127199 (Turner 1) and Turner 3 are located in the cluster's background. However the distance to the Cepheid is close to the average one for the cluster, while the hot stars are much more distant. At the same time, the distance problem for Turner 1 and Turner 3 is eliminated by using the distances of 550–660 pc derived from the absolute magnitudes, although there are still uncertainties with M_V for two cool giants and supergiant. The results for the stellar radii differ slightly for the main-sequence stars (except for Turner 1 and Turner 3), but for K-giants these discrepancies are significant.

Figure 2 represents kinematic 3D models of NGC 5662. The majority of our list stars are the cluster members, while CPD $-55^{\circ}6072$ and HD 127818 are definitely non-members and Turner 1 and Turner 3 are the clusters' background stars.

3.3 Chemical abundances

When the atmospheric parameters were derived, we used the VALD oscillator strengths (Kupka et al., 1999) and LTE model atmospheres from Castelli & Kurucz (2004) for determination of the element abundances. Table 5 presents the iron content, which was determined using fitting of the entire spectrum to a model spectrum and the atmosphere models method, and abundances for the "key"-elements of yellow supergiants stellar evolution - carbon, nitrogen, oxygen, and sodium. It shows that the $[\text{Fe}/\text{H}]$ abundances determined using atmosphere models lie in a range from -0.1 to $+0.04$ dex for all the stars (except for HD 127818) that is in good agreement with the results from Claria et al. (1991) and Kharchenko et al. (2016). The carbon abundance is close to than of the Sun or a little higher for the main-sequence stars and hot giants and shows a moderate deficit for the cool giants and supergiants, except for HD 127753 with the lowest value. The nitrogen abundance is close to solar one or little higher for the main-sequence and hot giant stars except for HD 127818, but all the cool giants and supergiants have a typical overabundance. The oxygen content varies from a small deficit to the solar one. A very interesting situation is seen with sodium: a noticeable overabundance has only HD 127733, while the Cepheid and other cool stars as well as two main-sequence stars have a content close to the solar, again except for HD 127818.

3.4 Lithium rich giants

Two K-giants, HD 127733 and HD 127753, were found as the lithium-rich stars. Using the synth approximation with the atmosphere parameters

Table 4: Comparison between absolute magnitudes, distances, and radii determined using GAIA DR2 parallaxes and photometric data.

| Object | PLX (GAIA DR2) | | | | Photometry | | |
|----------------------|----------------|------------|---------|-------------------|--------------------|--------|-------------------|
| | π (mac) | M_V | d (pc) | R (R_\odot) | M_V | d (pc) | R (R_\odot) |
| V Cen | 1.340±0.045 | -3.60±0.08 | 740±27 | 50.2±1.9 | -3.24 | 628 | 43 ¹ |
| HD 127427 | 1.244±0.039 | -2.86±0.08 | 796±27 | 52.6±1.8 | -2.85 ² | 787 | 52 |
| HD 127866 | 1.271±0.054 | -2.06±0.08 | 780±28 | 4.7±0.1 | -1.70 | 652 | 4.0 |
| CPD -56°6337 | 1.334±0.046 | +0.37±0.05 | 738±17 | 1.8±0.0 | +0.85 | 581 | 1.4 |
| HD 127817 | 1.231±0.042 | -1.33±0.07 | 809±26 | 2.7±0.1 | -0.85 | 637 | 2.2 |
| HD 127753 | 1.402±0.044 | -3.28±0.07 | 704±23 | 87.6±2.1 | -2.00 ³ | 385 | 51 |
| | | | | | -4.27 ² | 1096 | 146 |
| HD 127835 | 1.256±0.042 | -0.86±0.05 | 776±17 | 2.5±0.1 | -0.30 | 594 | 1.9 |
| HD 127900 | 1.207±0.038 | -1.61±0.08 | 828±30 | 3.7±0.2 | -1.20 | 676 | 3.1 |
| CPD -56°6341 | 1.258±0.041 | +0.12±0.08 | 802±29 | 2.2±0.1 | +0.56 | 658 | 1.8 |
| CPD -55°6072 | 2.573±0.345 | +2.49±0.28 | 386±46 | 2.0±0.3 | +1.37 | 646 | 3.3 |
| CPD -56°6344 | 1.133±0.088 | +0.93±0.16 | 875±8 | 2.8±0.2 | +1.68 | 619 | 2.1 |
| HD 127818 | 4.910±0.034 | +2.32±0.01 | 201±1 | 2.6±0.0 | +3.26 | 131 | 1.7 |
| HD 127733 | 1.143±0.040 | -2.98±0.05 | 863±20 | 62.6±1.5 | +0.80 ³ | 149 | 11 |
| | | | | | -2.30 ² | 619 | 46 |
| HD 127199 (Turner 1) | 1.077±0.042 | -0.16±0.10 | 920±41 | 2.7±0.1 | +0.95 | 552 | 1.8 |
| Turner 3 | 0.832±0.042 | +0.72±0.10 | 1197±54 | 2.7±0.1 | +2.07 | 622 | 1.4 |

1 - Phase 0.^P575 according to GCVS (1985)

2 - M_V according to Claria et al. (1991)

3 - M_V according to FitzGerald et al. (1979)

Table 5: Chemical abundances for NGC 5662 objects

| Object | [Fe/H] | | [C/H] | [N/H] | [O/H] | [Na/H] |
|----------------------|--------|-------|-------|-------|-------|--------|
| | Fit | AtMod | | | | |
| V Cen | -0.24 | -0.04 | -0.30 | 0.37 | -0.10 | 0.10 |
| HD 127427 | -0.11 | -0.06 | -0.43 | 0.56 | -0.27 | -0.02 |
| HD 127866 | -0.33 | -0.05 | 0.18 | 0.05 | -0.39 | - |
| CPD -56°6337 | -0.63 | -0.03 | - | - | -0.31 | - |
| HD 127817 | -0.36 | -0.05 | 0.22 | -0.12 | -0.26 | - |
| HD 127753 | -0.27 | 0.04 | -0.93 | 0.73 | -0.52 | -0.09 |
| HD 127835 | -0.28 | 0.00 | 0.02 | -0.12 | -0.26 | 0.00 |
| HD 127900 | -0.50 | -0.07 | - | 0.22 | -0.03 | - |
| CPD -56°6341 | -0.17 | -0.03 | - | - | 0.08 | - |
| CPD -55°6072 | -0.28 | - | - | - | - | - |
| CPD -56°6344 | -0.18 | -0.10 | - | -0.12 | -0.36 | 0.00 |
| HD 127818 | -0.20 | -0.12 | -0.43 | -0.30 | 0.03 | 0.17 |
| HD 127733 | -0.20 | -0.02 | -0.16 | 0.18 | -0.01 | 0.42 |
| HD 127199 (Turner 1) | -0.18 | 0.03 | 0.02 | 0.15 | 0.00 | - |
| Turner 3 | -0.41 | -0.04 | - | - | -0.27 | - |

from Table 3, we obtained $\log A(\text{Li}) = 1.27$ dex and $\log A(\text{Li}) = 0.72$ dex, respectively (see Figures 3 and 4).

4. Summary

1. According to the derived RV, color-indices, and distances only 13 of the 15 objects we investigated are confidently members of NGC 5662.
2. The fitting method used to determine radial and rotational velocities of the cluster stars yields results with an accuracy of 0.5 km s^{-1} in RV and

0.7 km s^{-1} for $v \sin i$.

3. We have revised color-excesses and reddenings for these objects, and it allowed us to refine their intrinsic colors, especially for the hot stars.
4. The atmosphere parameters of the hot stars were determined initially by fitting and finally refined using the atmosphere models based on the intrinsic colors. A good agreement is found for T_{eff} and $\log g$ determined by both methods.
5. The atmosphere parameters of the cool supergiants and giants were determined exclusively by

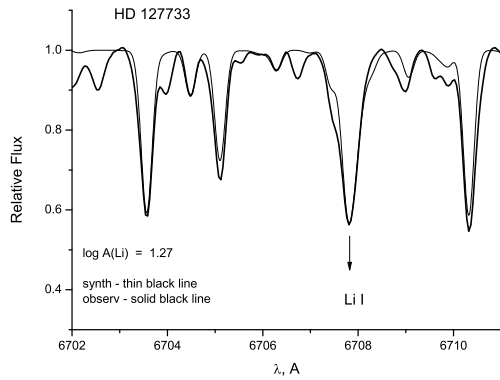


Figure 3: Li sc I 6707 Å absorption line in the atmosphere of HD 127733 and its approximation by synth.

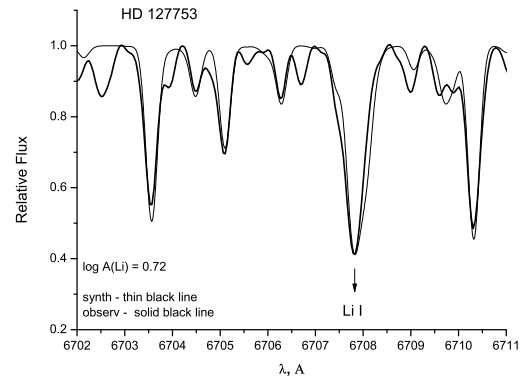


Figure 4: Li I 6707 Å absorption line in HD 127753 atmosphere and its approximation by synth.

the method of atmosphere models. Their final results differ significantly from those derived by fitting.

6. The distances of the most cluster stars determined from the GAIA DR2 2018 parallaxes lie in a range of 700–875 pc that roughly correspond to the mean cluster distance determined by Claria et al. (1991) using photometry, 790 ± 5 pc, with problematic results for Turner 1 and Turner 3. However, the distances found using the visual absolute magnitudes M_V lie in a range of 550–660 pc and are problematic for the cool supergiant and giants.
7. The radii determined from our T_{eff} and the distances found by the two methods differ slightly for the hot stars and significantly for the cool giants.
8. According to kinematic 3D cluster models, 11 objects are the cluster members, Turner 1 and Turner 3 are cluster background stars, and CPD –55°6072 and HD 127818 are non-members of the cluster.
9. The [Fe/H] estimates determined by fitting differ significantly from those determined using atmosphere models.
10. All the cluster members have [Fe/H] from –0.1 to +0.03 dex that is close to the photometrically estimated ones.
11. The contents of carbon and nitrogen in the hot stars turned out to be close to the solar one, while for the cool supergiants and giants there is a deficit of C and an overabundance of N. This fact indicates that the FGK-type objects have already passed through the "first dredge-up" stage. The sodium content is determined only for two main-sequence stars, and it is close to the solar one.

The cool supergiants and giants have either a near-solar content or a small overabundance.

12. Two K-giants from the cluster are lithium-rich stars.
13. Distances to NGC 5662 objects should be further revised.

References

- Bessell, M.S., Castelli, F. & Pelz, B.: 1998 *A&A* **333**, 231.
- Castelli F., Kurucz R.L.: 2004 *arXiv: astro-ph/0405087*
- Claria J.J., Lapasset E. & Bosio M.A.: 1991, *MNRAS*, **249**, 193.
- Coelho P.R.T.: 2014, *MNRAS*, **440**, 1027.
- FitzGerald M.P., Luiken M., Maitzen H.M., Hoffat A.F.J.: 1979, *A&AS*, **37**, 345.
- GAIA DR2 2018, *CDS/ADS Collection of Electronic Catalogues* **1345**, 0.
- Galazutdinov G.A.: 2007, <http://gazinur.com/DECH-software.html>
- General Catalog of Variable Stars (GCVS), 1985, 4nd Edition, Moscow, Nauka.
- Gray, D.: 1992, *Observation and Analysis of Stellar Atmospheres*, 2nd edn. Cambridge Univ. Press, Cambridge.
- Kharchenko N.V., Piskunov A.E., Schilbach E., Röser S., Scholz R.-D.: 2018, *A&A*, **585**, 101.
- Kovtuykh V.V.: 2007, *MNRAS*, **378**, 617.
- Kupka F., Piskunov N.E., Ryabchikova T.A., Stempels H.S., Weiss W.W.: 1999, *A&A*, **138**, 119.
- Kurucz R.L.: 1993, *CD-ROM No. 23*.
- Mermilliod J.C., Mayor M. & Udry S.: 2008, *A&A*, **485**, 303.
- Turner D.G.: 1982, *PASP*, **94**, 1003.

DOI: <http://dx.doi.org/10.18524/1810-4215.2018.31.144742>

KINEMATICS OF THE MILKY WAY FROM VELOCITIES OF YOUNG RED CLUMP GIANTS USING THE PMA AND GAIA DR2 DATA

A. B. Velichko, P. N. Fedorov

Institute of astronomy of V.N. Karazin Kharkiv national university,
Kharkiv, Ukraine, velichko.anna.b@gmail.com

ABSTRACT. Subsample of 19,600 young red clump giants with distances up to 1200 pc was selected from 7.2 mln Gaia DR2 data with radial velocities using the M_G vs. $G - K_S$ diagram. Ages of these stars do not exceed 2 bln years. For this stellar subsample kinematic parameters of the Ogorodnikov-Milne model as well as the K_{xy} -term, Solar apex coordinates L_\odot, B_\odot were derived from the 3D and 2D Gaia DR2 data as well as from the PMA proper motions. It was found that values of the OMM parameters derived from the 3D and 2D Gaia DR2 data are different. Removing stars with heliocentric distances 0-500 pc make the results consistent. For the 500-1200 pc stellar subsample value of the rotation velocity of the Galaxy at the Solar distance V_{rot} derived from the PMA proper motions is $205.2 \pm 0.5 \text{ km s}^{-1}$ while the values derived from the Gaia DR2 data are noticeably higher: $V_{\text{rot}}(2D \text{ Gaia DR2}) = 217.8 \pm 0.3 \text{ km s}^{-1}$ and $V_{\text{rot}}(2D \text{ Gaia DR2}) = 218.6 \pm 0.3 \text{ km s}^{-1}$. The K_{xy} -term is negative and equal to $-0.80 \pm 0.03 \text{ mas yr}^{-1}$ when using 3D Gaia DR2 data while it diminishes significantly in case of usage of Gaia DR2 and PMA proper motions.

Keywords: Astrometric catalogues, Galactic kinematics, stellar proper motions, stellar radial velocities, Hertzsprung-Russel diagram.

АБСТРАКТ. Використовуючи діаграму $M_G - (G - K_S)$ з 7.2 мільйонів об'єктів Gaia DR2 з відомими променевими швидкостями була виділена підвбірка 19,600 молодих гігантів червоного згущення з відстанями до 1200 пк. Для того, щоб виправити дані за почервоніння і поглинання, використовувалася тривимірна карта поглинань Гончарова. Згідно з теоретичними розрахунками Жірдді, ці зірки мають маси не менше $2-2.5M_\odot$, а значить їх віки не перевищують 2 мільярдів років. Для цієї підвбірки зірок за 2D (з використанням тільки власних рухів) і 3D (власні рухи плюс променеві швидкості) даними Gaia DR2, а також за власними рухам каталогу PMA були отримані кінематичні параметри моделі Огороднікова-Мілна, а також параметр розширення-стиснення

в галактичній площини $(x, y) - K_{xy}$, і координати апека Сонця L_\odot, B_\odot . Було виявлено, що значення деяких параметрів моделі, отриманих за 2D і 3D даними Gaia DR2, помітно різняться між собою. Так, наприклад, значення параметра M_{12}^+ , отриманого шляхом спільного рішення трьох рівнянь моделі Огороднікова-Мілна методом найменших квадратів, на 0.2 мсд г^{-1} менше, ніж значення, яке було отримане за допомогою спільного рішення рівнянь тільки для власних рухів Gaia DR2. Видалення з вибірки зірок з відстанями 0-500 пк робить результати більш узгодженими. Для підвбірки 500-1200 пк параметри ω_3 і M_{12}^+ , отримані за даними Gaia DR2, відповідно рівні $-2.54 \pm 0.04 \text{ мсд г}^{-1}$ і $3.22 \pm 0.04 \text{ мсд г}^{-1}$, тоді як за даними каталогу PMA їх значення становлять $-2.59 \pm 0.06 \text{ мсд г}^{-1}$ і $2.83 \pm 0.08 \text{ мсд г}^{-1}$. В результаті значення лінійної швидкості обертання Галактики на відстані Сонця V_{rot} , яке було отримано за власними рухами PMA, становить $205.2 \pm 0.5 \text{ км с}^{-1}$, тоді як значення, отримане за даними Gaia DR2, на 13 км с^{-1} вище: $V_{\text{rot}}(\text{Gaia DR2}) = 218.2 \pm 0.3 \text{ км с}^{-1}$. За даними 3D Gaia DR2 параметр K_{xy} є негативним і рівним $-0.80 \pm 0.03 \text{ мсд г}^{-1}$. Його величина по модулю значно зменшується в разі використання власних рухів Gaia DR2 і PMA, і в межах 3σ є незначущою. Значення компоненти швидкості Сонця уздовж галактичної осі y, V_\odot , відносно центроїда зірок має значення $11.59 \pm 0.30 \text{ км с}^{-1}$ за даними PMA і $13.0 \pm 0.20 \text{ км с}^{-1}$ за даними Gaia DR2. Цей факт є непрямим свідченням того, що зірки з нашої вибірки дійсно мають віки не більше 2 мільярдів років (Gontcharov, 2012b).

Ключові слова: Астрометричні каталоги, кінематика Галактики, власні рухи зірок, променеві швидкості зірок, діаграма Герцшпрунга-Рассела.

1. Introduction

On April 25, 2018 the second release of the Gaia mission (*Gaia* DR2) has come out (Gaia collaboration *et al.*, 2016; Gaia collaboration *et al.*, 2018b). Based on 22 month observational time baseline, it provides coordinates, proper motions and parallaxes for more than 1.3 bln stars distributed uniformly through the celestial sphere. Among them, there is a ~ 7.2 mln stellar subsample with magnitudes $G < 15$ for which median radial velocities (RV) were provided as well. This subsample includes stars that have effective temperatures T_{eff} within the range 3550-6900 K corresponding to FGK spectral types. These data give us a full information about how do stars move in the space.

It is well known that the Galaxy has a complex structure: there are at least four components such as thin, thick disks, halo and buldge. They differ from each other by kinematics, ages, metallicity, α -element abundances, and maybe some others. In this study we select stars with ages do not exceeding 2 bln years and therefore belonging to the Galactic thin disk. Stellar ages of the *Gaia* DR2 RV subsample used are not known but we have took advantage of the known property of the secondary clump of red giants in the colour-magnitude diagram (CMD). Since the works by Girardi *et al.* (1998) and Girardi (1999), the clump of stars located in the slightly bluer and fainter part of the CMD than the ordinary (main) clump of red giants is recognized as being formed by stars with initial masses $M \geq M_{\text{Hef}} \sim 2 - 2.5 M_{\odot}$ in the stage of central helium burning (CHeB). The main difference between giants belonging to the main and secondary clumps is that in the latter case stars reach the CHeB stage skipping the electron-degenerate core phase after the central hydrogen exhaustion, i.e. helium ignition begins under non-degenerate conditions (Girardi, 1999). Lifetimes of stars with masses $M > 2 - 2.5 M_{\odot}$ do not exceed 2 Gyr. Therefore, following Gontcharov (2012) we refer red giants belonging to the secondary clump to as young red clump giants (YRCG).

The paper is organized as follows. Section 2 presents description of some properties of input data used for analysis of the stellar velocity field. In section 3 the procedure of selection of the young red clump giants is given. Details of usage of the Ogorodnikov-Milne model are presented in section 4. Kinematic analysis and conclusions are given in sections 5 and 6 respectively.

2. Input data

For kinematic analysis the *Gaia* DR2 RV and PMA catalogues data were used. As was noticed in Introduction, the *Gaia* DR2 RV subsample contains only FGK-type stars. Positions and parallaxes of these stars were derived with typical uncertainty 0.02 - 0.04 mas. Their proper motions are evaluated to be

better than 0.07 mas yr^{-1} while the RV precision varies from 0.3 km s^{-1} at $G_{\text{RVs}} < 8$ and 1.8 km s^{-1} at $G_{\text{RVs}} = 11.75$. Systematic RV errors are expected to be from less than 0.1 km s^{-1} at $G_{\text{RVs}} < 9$ to 0.5 km s^{-1} at $G_{\text{RVs}} = 11.75$. According to Gaia collaboration *et al.* (2018b), the second realisation of the *Gaia* celestial reference frame (*Gaia*-CRF2) at the faint end ($G \sim 19$) is aligned with the ICRF to about 0.02 mas at epoch J2015.5 and non-rotating with respect to the ICRF to within 0.02 mas yr^{-1} .

The PMA (Proper Motion Absolute) catalogue was derived in the laboratory of astrometry of Institute of astronomy of V.N. Karazin Kharkiv national university (Akhmetov *et al.*, 2017) from combination of *Gaia* DR1 and 2MASS catalogues. It contains positions, proper motions, and G, J, H, K_S photometry for more than 420 mln objects covered the whole celestial sphere including the Galactic plane. From this stellar sample ~ 6.9 mln stars that are common with the *Gaia* DR2 RV subsample were selected. Typical uncertainty of stellar positions is 10 mas. Proper motions are estimated to have errors of the order of 2-5 mas yr^{-1} at $10 < G < 17$. The zero-point of the proper motions was established using 1.6 mln extragalactic sources. It has been shown (Akhmetov *et al.*, 2017) that the PMA coordinate axes are non-rotating with respect to extragalactic sources from the LQAC3 and ICRF catalogues.

3. Selection of young red clump giants

All YRCG are in the Galactic plane. Therefore it is necessary to take into account interstellar extinction. To do this, the Gontcharov's 3D extinction map (Gontcharov, 2017) was used. This map is limited by distance to 1200 pc and by Galactic coordinate $Z \pm 600$ pc. It is organized as follows. At every point of space with galactic coordinates x, y, z (or l, b, r) values of $E(J - K_S)$, $E(B - V)$, R_V and A_V are provided. The resolution of the map is $50 \times 50 \times 50$ pc. To compute extinction and reddening at a given point (x^*, y^*, z^*) the trilinear interpolation formula 1 was used.

$$f(x^*, y^*, z^*) \simeq a [f(x_1, y_1, z_1)(x_2 - x^*)(y_2 - y^*)(z_2 - z^*) + f(x_1, y_1, z_2)(x_2 - x^*)(y_2 - y^*)(z^* - z_1) + f(x_1, y_2, z_1)(x_2 - x^*)(y^* - y_1)(z_2 - z^*) + f(x_1, y_2, z_2)(x_2 - x^*)(y^* - y_1)(z^* - z_1) + f(x_2, y_1, z_1)(x^* - x_1)(y_2 - y^*)(z_2 - z^*) + f(x_2, y_1, z_2)(x^* - x_1)(y_2 - y^*)(z^* - z_1) + f(x_2, y_2, z_1)(x^* - x_1)(y^* - y_1)(z_2 - z^*) + f(x_2, y_2, z_2)(x^* - x_1)(y^* - y_1)(z^* - z_1)] (1)$$

where

$$a = \frac{1}{(x_2 - x_1)(y_2 - y_1)(z_2 - z_1)}$$

YRCG can be identified using the colour-magnitude diagram in the $M_G - (G - K_S)$ coordinates. The red clump region in the CMD for stars with low extinction $E(J - K_S) < 0.05$ is shown in Fig. 1. It can be seen that there is a weak concentration of stars inside the ellipse shown by black solid line. These are the YRCG. We suggested that a star belongs to the secondary clump if it falls inside the ellipse centered at $(M_G, G - K_S) = (0.6, 1.9)$ with semiaxes $(\Delta M_G, \Delta(G - K_S)) = (0.5, 0.13)$. All bad quality objects with $\sigma_\varpi/\varpi > 0.2$ were removed from the sample. As a result 19,600 YRCG with distances up to 1200 pc and $Z \pm 600$ pc were selected.

The Gontcharov's map does not provide reddening for colour $G - K_S$, so we have found empirical relation between $E(J - K_S)$ and $E(G - K_S)$:

$$E(G - K_S) = -904.2 E(J - K_S)^4 + 271.5 E(J - K_S)^3 - 12.1 E(J - K_S)^2 + 1.1 E(J - K_S) \quad (2)$$

4. Usage of the Ogorodnikov-Milne model

All calculations were made in the rectangular heliocentric Galactic coordinate system the main plane of which coincides with the Galactic plane. The x axis is directed towards the Galactic centre ($l = 0^\circ, b = 0^\circ$), hereafter it will be referred to as the x or 1 axis. The y or 2 axis is directed towards direction of Galactic rotation ($l = 90^\circ, b = 0^\circ$) while z axis towards the direction parallel to one from centre of the Galaxy to its North pole ($b = 0^\circ$).

To analyse the stellar velocity field the Ogorodnikov-Milne model (OMM) was used (Ogorodnikov, 1965).

$$\mathbf{V} = \mathbf{V}_0 + \boldsymbol{\Omega} \times \mathbf{r} + \mathbf{M}^+ \times \mathbf{r} \quad (3)$$

The OMM model contains 12 kinematic parameters:

$X_\odot, Y_\odot, Z_\odot$ are the Solar motion components relative to the centroid; $\omega_1, \omega_2, \omega_3$, are components of the rigid-body rotation vector $\boldsymbol{\Omega}$; $M_{12}^+, M_{13}^+, M_{23}^+$ are components of the tensor \mathbf{M}^+ characterizing velocities of deformations in the (x,y), (x,z) and (y,z) Galactic planes; $M_{11}^+, M_{22}^+, M_{33}^+$ are components of the tensor \mathbf{M}^+ responsible for velocities of contraction-expansion of the stellar sample used.

Projecting the equation 3 onto the unit vectors of the Galactic coordinate system yields the following system of equations

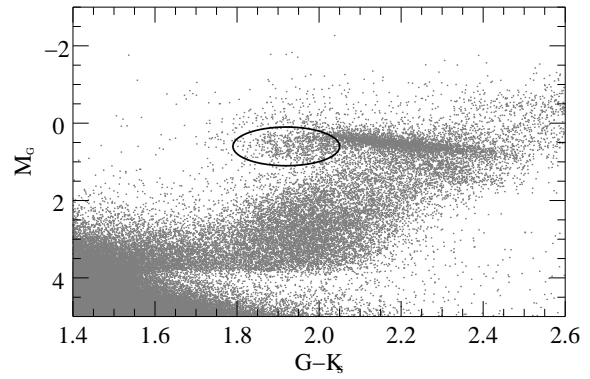


Figure 1: Zoom of the CMD $M_G - (G - K_S)$. YRCG are inside the ellipse.

$$\begin{aligned} \eta \mu_l \cos b &= X_\odot/r \sin l - Y_\odot/r \cos l - \omega_1 \sin b \cos l - \\ &\quad - \omega_2 \sin b \sin l + \omega_3 \cos b + M_{12}^+ \cos b \cos 2l - \\ &\quad - M_{13}^+ \sin b \sin l + M_{23}^+ \sin b \cos l - \\ &\quad - 0.5 M_{11}^+ \cos b \sin 2l + 0.5 M_{22}^+ \cos b \sin 2l \quad (4) \end{aligned}$$

$$\begin{aligned} \eta \mu_b &= X_\odot/r \cos l \sin b + Y_\odot/r \sin l \sin b - Z_\odot/r \cos b + \\ &\quad + \omega_1 \sin l - \omega_2 \cos l - 0.5 M_{12}^+ \sin 2b \sin 2l - \\ &\quad - M_{13}^+ \cos 2b \cos l + M_{23}^+ \cos 2b \sin l - \\ &\quad - 0.5 M_{11}^+ \sin 2b \cos^2 l - 0.5 M_{22}^+ \sin 2b \sin^2 l + \\ &\quad + 0.5 M_{33}^+ \sin 2b \quad (5) \end{aligned}$$

$$\begin{aligned} V_r/r &= -X_\odot/r \cos l \cos b - Y_\odot/r \sin l \cos b - \\ &\quad - Z_\odot/r \sin b + M_{13}^+ \sin 2b \cos l + M_{23}^+ \sin 2b \sin l + \\ &\quad + M_{12}^+ \cos^2 b \sin 2l + M_{11}^+ \cos^2 b \cos^2 l + \\ &\quad + M_{22}^+ \cos^2 b \sin^2 l + M_{33}^+ \sin^2 b \quad (6) \end{aligned}$$

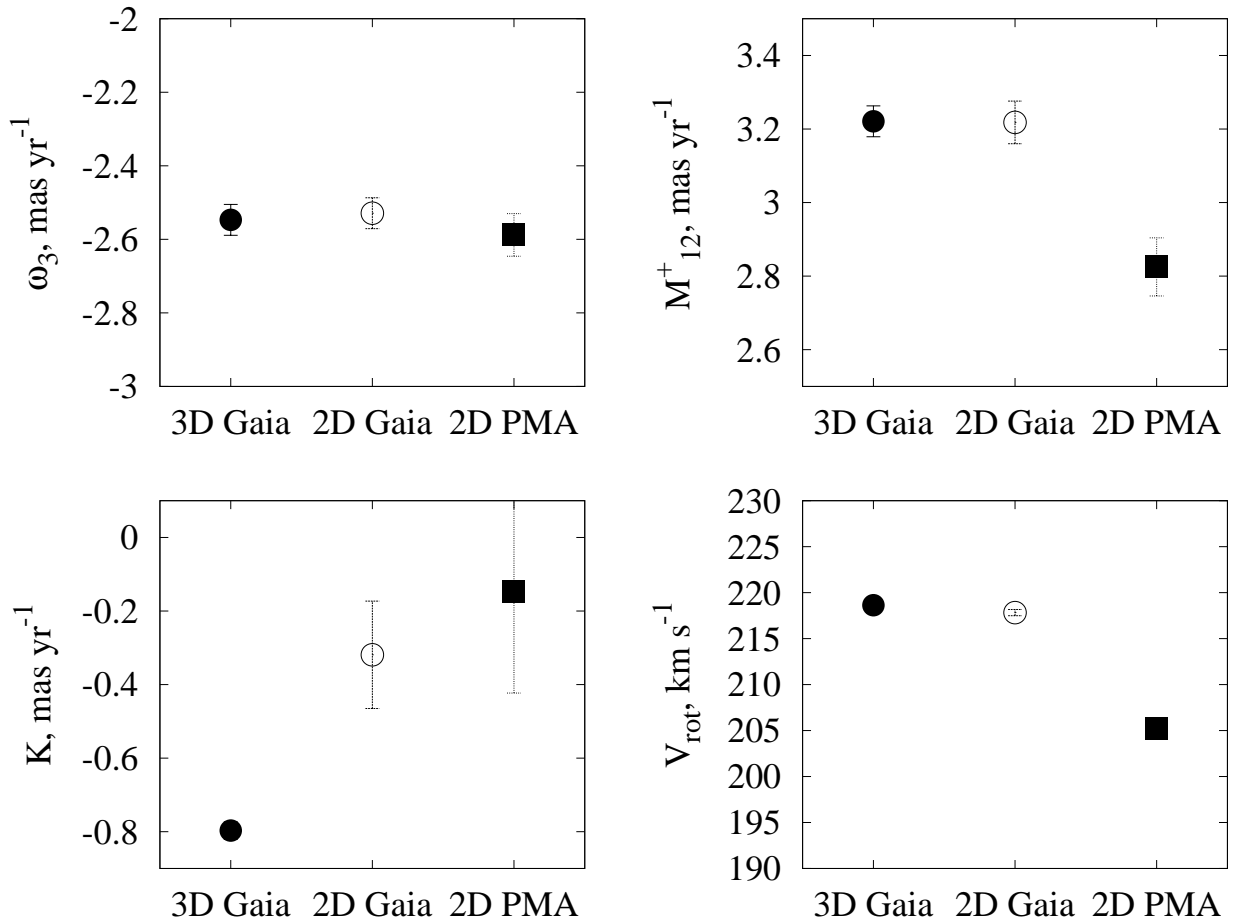
Where $\eta = 4.74$ is the conversion factor from mas yr^{-1} to $\text{kms}^{-1} \text{kpc}^{-1}$, μ_l, μ_b are proper motions in mas yr^{-1} , V_r are radial velocities in km s^{-1} .

When proper motions only are used, one of diagonal elements of the deformation matrix \mathbf{M}^+ remains undetermined. Therefore, only differences $M_{11}^* = M_{11}^+ - M_{22}^+$ and $M_{33}^* = M_{33}^+ - M_{22}^+$ can be derived suggesting that $M_{22}^+ = 0$. Values of the K_{xy} -term characterizing contraction-expansion of the stellar sample in the x, y Galactic plane were derived as well: $K = 0.5(M_{11}^+ + M_{22}^+)$. In the case of usage of proper motions only the K -term can be evaluated using the following equation: $K = 0.5(M_{11}^* - 2M_{33}^*)$. The M_{12}^+ and ω_3 parameters are analogues of the Oort constants A and B from the simplified Oort-Lindblad kinematic model. The linear rotation velocity of the Galaxy V_{rot} at the Solar distance R_\odot can be derived from combination of these two parameters by the following relation: $V_{\text{rot}} = (M_{12}^+ - \omega_3) \eta R_\odot$. The value of R_\odot is assumed to be equal to 8.0 ± 0.2 kpc (Vallée, 2017).

In addition, the Solar apex coordinates L_\odot, B_\odot were estimated.

Table 1: The OMM kinematic parameters derived in this work.

| Parameter | Unit | 0-1200 pc | | | 500-1200 pc | | |
|----------------------|----------------------|------------|------------|------------|-------------|------------|------------|
| | | Gaia, 3D | Gaia, 2D | PMA, 2D | Gaia, 3D | Gaia, 2D | PMA, 2D |
| X_{\odot} | km s ⁻¹ | 9.83±0.13 | 9.32±0.17 | 9.89±0.19 | 10.89±0.15 | 10.83±0.19 | 11.62±0.26 |
| Y_{\odot} | km s ⁻¹ | 11.64±0.13 | 11.71±0.18 | 10.6±0.21 | 12.63±0.15 | 13.40±0.22 | 11.59±0.30 |
| Z_{\odot} | km s ⁻¹ | 7.80±0.13 | 7.72±0.15 | 7.66±0.17 | 7.29±0.15 | 7.26±0.16 | 7.46±0.21 |
| ω_1 | mas yr ⁻¹ | 0.37±0.10 | 0.44±0.11 | 0.50±0.13 | 0.09±0.08 | 0.05±0.09 | 0.12±0.12 |
| ω_2 | mas yr ⁻¹ | -0.73±0.10 | -0.72±0.11 | -0.92±0.13 | -0.55±0.08 | -0.45±0.09 | -0.68±0.12 |
| ω_3 | mas yr ⁻¹ | -2.54±0.10 | -2.58±0.06 | -2.62±0.07 | -2.55±0.04 | -2.53±0.04 | -2.59±0.06 |
| M_{23}^+ | mas yr ⁻¹ | -0.26±0.10 | -0.35±0.13 | -0.43±0.15 | 0.03±0.08 | 0.10±0.10 | -0.02±0.14 |
| M_{13}^+ | mas yr ⁻¹ | -0.55±0.10 | -0.55±0.13 | -0.95±0.15 | -0.41±0.08 | -0.27±0.10 | -0.67±0.13 |
| M_{12}^+ | mas yr ⁻¹ | 3.24±0.06 | 3.04±0.09 | 2.70±0.10 | 3.22±0.04 | 3.22±0.06 | 2.83±0.08 |
| $M_{11}^+(M_{11}^*)$ | mas yr ⁻¹ | -1.86±0.09 | -2.19±0.24 | -2.05±0.19 | -1.76±0.06 | -2.00±0.11 | -2.11±0.16 |
| M_{22}^+ | mas yr ⁻¹ | 0.19±0.08 | - | - | 0.16±0.16 | - | - |
| $M_{33}^+(M_{33}^*)$ | mas yr ⁻¹ | -0.06±0.08 | -0.63±0.23 | -0.82±0.27 | -0.23±0.14 | -0.68±0.17 | -2.11±0.23 |
| V_{rot} | km s ⁻¹ | 219.1±0.4 | 213.1±0.5 | 201.65±0.6 | 218.6±0.3 | 217.8±0.3 | 205.2±0.5 |
| K | mas yr ⁻¹ | -0.84±0.05 | -0.09±0.04 | -0.02±0.04 | -0.80±0.03 | -0.32±0.14 | -0.14±0.27 |
| L_{\odot} | degree | 49.8±3.8 | 51.5±0.1 | 47.0±0.2 | 49.3±4.6 | 51.0±0.1 | 44.9±0.3 |
| B_{\odot} | degree | 27.1±1.6 | 27.3±0.1 | 27.1±0.1 | 23.6±1.8 | 22.9±0.1 | 24.5±0.1 |

Figure 2: The ω_3 , M_{12}^+ , V_{rot} OMM parameters and K_{xy} -term derived from the 3D (filled circles), 2D Gaia DR2 (open circles) and PMA (filled squares) data for the 500-1200 pc YRCG subsample.

5. Kinematic analysis

All calculations were performed for the YRCG subsample described in section 3. The OMM equations 4, 5, 6 were solved by the least square method (LSR) using the Gaia DR2 RV data. This case we refer to as 3D one, because both proper motions and radial velocities were used. For comparison, the OMM parameters were derived from the Gaia DR2 proper motions only, i.e. by joint solving the equations 4, 5 (2D case). The results are given in columns 2, 3 of Table 1 as well as in Fig. 2. It can be seen that values of the ω_3 parameter derived from 3D and 2D Gaia DR2 data are very close while values of the M_{12}^+ parameter have difference $M_{12}^+(3D) - M_{12}^+(2D) = 0.2 \text{ mas yr}^{-1}$ leading to difference between values of linear Galactic rotation velocity: $V_{\text{rot}}(3D) = 219.1 \pm 0.4 \text{ mas yr}^{-1}$ versus $V_{\text{rot}}(2D) = 213.1 \pm 0.5 \text{ mas yr}^{-1}$. Proximity of the ω_3 values in 3D and 2D cases can be explained by the fact that rotational components of the OMM ω_1 , ω_2 , ω_3 do not have projections onto radial direction. However, there are small differences of order of $0.02\text{--}0.06 \text{ mas yr}^{-1}$ caused by redistribution of the OMM parameter values when using the LSM.

It is well known that the stellar velocity field in the Solar neighborhood can be disturbed by influence of the Gould Belt stars the characteristic radius of which is estimated to be $\sim 500 \text{ pc}$. We removed stars with distances up to 500 pc from the YRCG subsample resulting in $15,600$ stars within a distance range $500 - 1200 \text{ pc}$. The OMM parameters were recalculated for the second YRCG subsample using the 3D and 2D Gaia DR2 data. The results are shown in columns 5,6 of Table 1. It can be seen that values of the OMM parameters derived from the 3D and 2D Gaia DR2 data have become much more consistent. So, one can make a conclusion that a probable cause of the discrepancy between 3D and 2D calculations can be peculiarities of motions of the Gould Belt stars.

As for the K_{xy} -term, it has a negative values when using radial velocities: $K = -0.84 \pm 0.05 \text{ mas yr}^{-1}$ and $-0.80 \pm 0.03 \text{ mas yr}^{-1}$ for $0\text{--}1200 \text{ pc}$ and $500\text{--}1200 \text{ pc}$ stellar subsamples respectively. It means that the stellar subsample contracts. The K_{xy} -term becomes insignificant within 3σ when using proper motions only.

In columns 4 and 7 of Table 1 values of the OMM parameters derived from the PMA proper motions are presented. Note a quite large difference between values of the M_{12}^+ parameter derived from the Gaia DR2 and PMA data leading to a lower estimation of V_{rot} $205.2 \pm 0.5 \text{ km s}^{-1}$ from the PMA proper motions versus $217.8 \pm 0.3 \text{ km s}^{-1}$ from the Gaia DR2 proper motions. Values of the K_{xy} term derived from the PMA data is insignificant within 3σ .

The mean age of the YRCG subsample can be estimated from values of the Solar motion component along the y Galactic axis Y_{\odot} . According to Gontcharov (2012b), the older stars the higher Y_{\odot} . It can be seen from our calculations that values of

the Y_{\odot} parameter vary from $10.6 \pm 0.21 \text{ km s}^{-1}$ to $13.40 \pm 0.22 \text{ km s}^{-1}$ depending on data used. This fact means that ages of stars belonging to the selected YRCG subsample do not exceed 2 bln years , as we expected.

Values of the Solar apex coordinate L_{\odot} vary from $44^{\circ}.9 \pm 0^{\circ}.3$ to $51^{\circ}.5 \pm 0^{\circ}.1$ depending on data used. Values of the B_{\odot} are systematically shifted when using different stellar subsamples. B_{\odot} in average is equal to $27^{\circ}.2$ for the $0\text{--}1200 \text{ pc}$ stellar subsample while $23^{\circ}.7$ for the $500\text{--}1200 \text{ pc}$ one.

6. Conclusions

Kinematic analysis of the stellar velocity field of the YRCG with distances up to 1200 pc using the OMM was carried out. The kinematic parameters from the 3D, 2D Gaia DR2 and PMA data were derived. It was concluded that the stellar velocity field within 500 pc around the Sun is probably disturbed by influence of the Gould Belt stars. When removing stars with distances $0\text{--}500 \text{ pc}$ from the YRCG subsample the results derived from the 3D and 2D Gaia DR2 data become consistent.

Value of the rotation velocity of the Galaxy at the Solar distance V_{rot} derived from the PMA data for the $500\text{--}1200 \text{ pc}$ subsample is lower by 13.4 km s^{-1} and 12.6 km s^{-1} than values derived from the 3D and 2D Gaia DR data respectively. $V_{\text{rot}}(\text{PMA}) = 205.2 \pm 0.5 \text{ km s}^{-1}$, $V_{\text{rot}}(2D \text{ Gaia DR2}) = 217.8 \pm 0.3 \text{ km s}^{-1}$, $V_{\text{rot}}(3D \text{ Gaia DR2}) = 218.6 \pm 0.3 \text{ km s}^{-1}$.

The K_{xy} -term is negative and equal to $-0.80 \pm 0.03 \text{ mas yr}^{-1}$ when using 3D Gaia DR2 data while it diminishes in case of usage of Gaia DR2 and PMA proper motions.

Acknowledgements. This work has made use of data from the European Space Agency (ESA) mission *Gaia* (<https://www.cosmos.esa.int/gaia>), processed by the *Gaia* Data Processing and Analysis Consortium (DPAC, <https://www.cosmos.esa.int/web/gaia/dpac/consortium>). Funding for the DPAC has been provided by national institutions, in particular the institutions participating in the *Gaia* Multilateral Agreement.

References

- Akhmetov V.S., Fedorov P.N., Velichko A.B., Shulga V.M.: 2017, *MNRAS*, **469**, 1.
 Gaia collaboration et al.: 2016, *A&A*, **595**, A1.
 Gaia collaboration et al.: 2018b, *A&A*, **616**, A1.
 Girardi L.: 1999, *MNRAS*, **308**, 818-832.
 Girardi L. Groenewegen M.A.T., Weiss A., Salaris M.: 1998, *MNRAS*, **301**, 149.
 Gontcharov G.A.: 2012, *Spatial distribution of stars, their kinematics and interstellar absorption in the nearest kiloparsec* (PhD thesis)
 Gontcharov G.A.: 2012b, *Astron. Lett.*, **38**, 12.
 Gontcharov G.A.: 2017, *Astron. Lett.*, **43**, 7, 472-488.
 Vallée G. A.: 2017, *Ap&SS*, **362**, 79V.
 Ogorodnikov K. F.: 1965, *Dynamics of stellar systems*, Fizmatgiz, Moscow [in russian]

RADIOASTRONOMY

DOI: <http://dx.doi.org/10.18524/1810-4215.2018.31.144460>

RADIO TELESCOPE URAN-4 AND THE PROBLEM OF RADIO INTERFERENCE

V.V. Galanin, O.A. Lytvynenko, V.G. Derevyagin, R.O. Kravetz

URAN-4 Observatory of IRA NASU, Odessa, Ukraine, uran4@te.net.ua

ABSTRACT. The URAN-4 decameter radio telescope, which is located in the village of Mayaki of the Odessa region, is an element of system of the URAN radio telescopes (Ukrainian Radiointerferometer of the Academy of Sciences). The radio telescope is used according to the following scientific programs: measurements in the composition of the Interferometer with the Super Large Base (VLBI), to study the angular structure of discrete radio sources; the study of the nonstationarity of the flux of cosmic radio sources and the study of the influence of the space environment on the characteristics of the received signals.

RT URAN-4 operates at frequencies of 10-30 MHz and consists of an antenna and an equipment complex. A telescope antenna is an electrically controlled phased array of 128 turnstile vibrators. It identifies two linear signal components and is endowed with the possibility of changing the position of the antenna pattern in space (2048 discrete positions of the beam). The geometric dimensions of the array 238 meters (West-East direction) and 28 meters (North-South direction). The size of the antenna pattern in the modulation mode of signal reception at a frequency of 25 MHz is 2.7 x 22 degrees. In the VLBI interferometer mode, a resolution of about 2 seconds of arc is realized. The instrumental complex of the RT URAN-4 is represented by two types of modulation radiometers, which make it possible to measure the flux densities of radio sources and apparatus intended for VLBB measurements.

The working frequency range in which RT URAN-4 operates has a high level of radio interference. The work gives definitions of interference acting in the decameter range. Considered methods of dealing with them. One of the methods to combat interference is the work of the radio telescope on the frequencies permitted and legally protected from interference, the list of which is given in the article. The paper deals with issues related to the organization of the security zone around the radio telescope. On its territory, the maximum allowable power for existing nearby transmitting radio facilities and interfering industrial facilities should be legitimized, in the designated working lanes. At the same time, a monitoring service for the radio spectrum should be organized. The paper deals with the developed and manufactured portable direction finder. Its characteristics are given, recommendations on its use are given.

Keywords: radio telescope, interference, frequency band, radiometer, direction finder.

АБСТРАКТ. Декаметровий радіотелескоп УРАН-4, що розташований в селі Маяки Одеської області, є елементом системи радіотелескопів УРАН (Український радіоінтерферометр Академії наук). Радіотелескоп використовується по наступних наукових програмах: проведення вимірів у складі Інтерферометра з Понад Великою Базою (РПВБ), для вивчення кутової структури радіоджерел; дослідження нестационарності потоків космічних радіоджерел і вивчення впливу середовища на характеристики прийнятих сигналів.

РТ УРАН-4 працює на частотах 10-30 МГц і складається з антени й апаратурного комплексу. Антена телескопа – це електрично керована фазована решітка з 128 турнікетних вібраторів. Вона виділяє дві лінійні складові сигналів й наділена можливістю зміни положення діаграми спрямованості в просторі (2048 дискретних положень променя). Геометричні розміри її – 238 метрів (напрямок Захід-Схід) і 28 метрів (напрямок Південь-Північ). Розміри діаграми спрямованості в модуляційному режимі прийому сигналу на частоті 25 МГц становить 2.7 x 22 градуса. У режимі РПВБ інтерферометра реалізується просторова роздільна здатність близько 2 секунд дуги. Апаратурний комплекс РТ представлений двома видами модуляційних радіометрів, які дозволяють вимірювати щільності потоків радіоджерел, і апаратурою, яка призначена для РСДБ вимірів.

Робочий діапазон частот, у якому працює РТ УРАН-4, має високий рівень радіозавад. У роботі даються визначення завадам, діючим у декаметровому діапазоні. Розглядаються методи боротьби з ними. Одним з методів боротьби з завадами є робота радіотелескопу на дозволених і юридично захищених від завад частотах, перелік яких наведено в статті. У роботі розглядаються питання, пов'язані з організацією навколо радіотелескопа охоронної зони. На її території повинна бути узаконена у відведених робочих смугах максимально припустима потужність для існуючих поруч передавальних радіозасобів і промислових об'єктів, що заважають. Одночасно із цим, повинна бути організована служба контролю за радіо спектром. У роботі розглядається розроблений і виготовлений переносний пеленгатор. Наводяться його характеристики, даються рекомендації з його використанням.

Ключові слова: радіотелескоп, радіозавади, смуга частот, пеленгатор.

1. Introduction

Radiotelescopes are highly sensitive instruments and therefore the requirements for the cleanliness of the spectrum, in the range in which they operate, are extremely important. The URAN-4 decimeter radio telescope, which is located in the village of Mayaki of the Odessa region, is an element of system of the URAN radio telescopes (Ukrainian Radiointerferometer of the Academy of Sciences). Its main purpose is to work in the mode of the very large base interferometer (VLBI). The RT URAN-4 is used for the following scientific programs: VLBI measurements with the UTR-2 radio telescope to study the angular structure of galactic and extragalactic radio sources; studying the nonstationarity of cosmic radio sources; study of the influence of the space environment on the characteristics of received signals; improvement of methods for receiving and processing signals.

The place for the RT URAN-4 was chosen after lot of research based on the following considerations. The place was located on the edge of the village, with developed engineering networks, and the lack of industrial facilities and, as a result, the absence of industrial interference. Studies of the radio band showed that there are no transmitters of considerable power in the radius of propagation of a direct wave and the range is relatively free from various kinds of interference of artificial origin. The radio telescope began its work in 1985.

Unfortunately, since then, the interference environment has changed dramatically, and the fight against interference has become more urgent.

2. Radio telescope URAN-4

The URAN-4 radio telescope (Galanin, 1989) consists of an antenna and a measuring complex and operates at frequencies of 10-30 MHz. The antenna is an electrically controlled phased array of 128 turnstile vibrators. It is endowed with the ability to separate the two linear components of the signal and change the position of the antenna pattern (AP) in space. In the North-South direction, 16 beam positions were implemented, and in the West-East direction, 128 (a total of 2048 individual beam positions) were implemented. The geometrical dimensions of the array are 238 meters (West-East direction) and 28 meters (North-South direction). The dimensions of the AP in the modulation mode of receiving a signal with a frequency of 25 MHz are 2.7 x 22 degrees. In the VLBI interferometer mode, a resolution of about 2 seconds of arc is implemented. The maximum value of the directivity of the antenna at a frequency of 25 MHz is 618. The efficiency at the same frequency is 0.1.

The measuring complex includes Dicke radiometers, which allow measuring the flux densities of radio sources and apparatus intended for VLBI measurements. During the operation of the RT URAN-4, the measuring complex has undergone several modifications. Initially, narrow-band receivers with a bandwidth of up to 20 kHz were used. Currently, the band has increased from 250 kHz to a single MHz. The expansion of the bandwidth of the receiving equipment, has led to an increase in the sensitivity of the radio telescope. At the same time, digital

registration and digital signal processing allowed the use of various methods of filtering interference. In spite of this, a significant deterioration of the interference environment in recent years in some cases reduces the effectiveness of conducting observations

3. The Decimeter Interference

World Administrative Radiocommunication Conference, (WARC-79) held in 1979, gave the definition of harmful interference. Harmful is considered to be interference, which increases the noise temperature of the radio telescope by more than 10%.

The Interference of decimeter range can be divided into two groups: remote and local.

The remote sources of interference include broadcasting radio stations, communication systems and radar, ionospheric stations. In this case, ionospheric propagation of the interference occurs.

Ways to deal with them: conducting observations at night, when the possible maximum applicable frequencies are below the operating frequency of the radio telescope; use of narrow antenna pattern with narrow side lobes; frequency, temporal and spatial filtering of interference; the dynamic range of signal amplification systems increase; the allocation and use for radioastronomic studies of legally protected frequency bands defined by the International Telecommunication Union.

Of the above methods of dealing with interference, which are widely reported in the literature, let us dwell on the latter. Already during the formation of radio astronomy, much attention was paid to the allocation of frequencies for radio telescopes. So, frequencies: 2.5, 5, 10, 15, 20, 25, 37, 73, 79 MHz for low-frequency radio astronomy observations were recommended by the Radio Frequency Body of the International Telecommunication Union, Geneva, Switzerland. (Kraus, 1973). In 1979, the World Administrative Conference on Radiocommunication allocated a number of legally protected bands for low-frequency radio astronomy: 13.360-13.410 MHz, 25.550-25.570 MHz, 37.5-38.25 MHz, 73.0-74.6 MHz. Allocated bands have different legal protection statuses. The prerequisite for protection is the registration of transmitters and radio telescopes at the State Telecommunications Inspection and the International Registry (Dubinsky, 1985).

The local sources of interference include industrial and domestic interference, including corona discharges on high-voltage power lines, special process equipment, switching power supplies, and high-power fluorescent lighting devices. Most of the interference from local sources have a broadband spectrum, which significantly complicates the fight against them. Therefore, the main method of dealing with local interference is to identify and solve the problem by organizational and administrative methods.

To implement this approach, an important task is to establish a radio telescope security zone (Dolan, 1973). On its territory, the maximum permissible radiation power of transmitting radio equipment, industrial and household object should be legalized, in the designated working bands. At the same time, a radio monitoring service should be organized on the radio telescope, the task of which would be to detect interference and determine their location.

4. The effect of interference on the operation of a radio telescope

Radiometers of URAN radio telescopes are formed according to the interferometer with a small base. The elements of the interferometer are the two halves of the antenna array of the radio telescope, the signals from the halves of the arrays go to the two channels of the radiometer and are subsequently multiplied. This scheme allows you to suppress galactic noise, the intensity of which exceeds the signal intensity of most discrete cosmic sources in the decameter range. This scheme allows the use of correlation and modulation radiometers. Regular for RT URAN-4 are modulation radiometers.

Radio interference penetrating the reception path of the RT URAN-4 and affecting the operation of the modulation radiometer can be divided into three groups:

1. Narrow-band continuous interference.
2. Narrowband impulse interference;
3. Broadband interference.

An example of three types of interference is shown in Fig. 1. The recording of the spectra was made at RT URAN-4 using an SDR receiver with a bandwidth of 1 MHz.

Narrowband continuous interference leads to a zero offset when recording a cosmic source. In the case of moderate intensity of interference, this effect is eliminated by digital data processing, by frequency filtering of interference. Offset of the zero level is not always possible to detect in the output signal of the radiometer. In particular, it is possible to use the tracking mode of a cosmic source, in which the source completely crosses the fixed antenna pattern. In this case, it is possible to apply the technique of inscribing the antenna pattern, which excludes measurement error associated with the offset of the zero recording level (if the interference power during this time remains constant).

Narrow-band impulse interference leads to emissions of the output signal of the radiometer (note that if the pause between pulses is less than the constant integration of the radiometer, then the interference is perceived as continuous). Frequency and temporal filtering can be used to combat such interference. Broadband interference is not amenable to frequency filtering. Continuous broadband interference leads to a zero offset of the cosmic recording. When the above conditions are met, to reduce the measurement error possible to use the technique of inscribing the antenna pattern. With the fluctuating power of broadband interference, the inscribing technique becomes ineffective. Temporal filtering can be applied to combat impulse broadband interference.

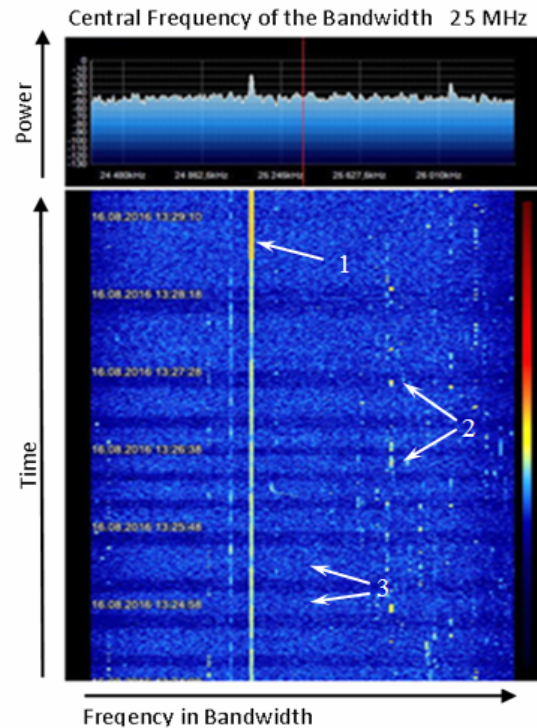


Figure 1: The signal spectrum containing three types of interference. The upper panel is the power spectrum in the time interval of 6 minutes. The bottom panel is a dynamic spectrum on the same time interval. 1 – continuous narrowband interference, 2 – pulsed narrowband interference, 3 – wideband pulsating interference.

5. Direction Finder

To interference combat, a portable direction finder was designed and manufactured with a working range of 10–30 MHz. The device consists of a tunable loop antenna with dimensions less than 0.1 wavelength, a whip antenna, antenna switch and receiver, covering the entire decameter range.

The development of a loop antenna was carried out in two stages. Initially, using a computer program, a future loop antenna was designed. Fig. 2 shows its calculated antenna pattern. Then several experimental samples were made, one of which was adopted as a worker. For field tests, a portable transmitter was used, with which the shape of the beam antenna pattern was checked.

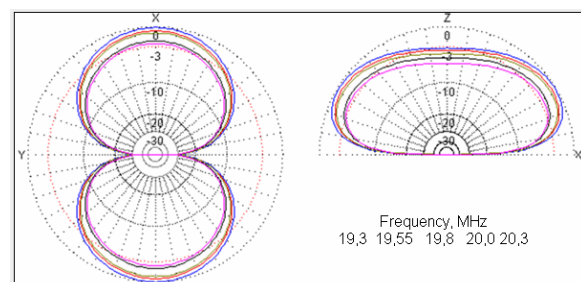


Figure 2: The calculated antenna pattern of the direction finder antenna

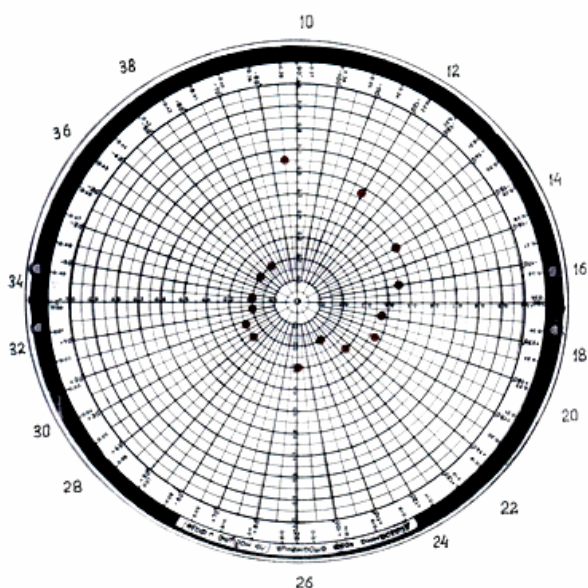


Figure 3: The reflection coefficients of the antenna direction finder, measured at frequencies of 10-38 MHz

The characteristics of the loop antenna of the made direction finder are measured. Fig. 3 shows the reflection coefficients of the loop antenna, measured at frequencies from 10 to 38 MHz. The calculated antenna efficiency at 10 and 38 MHz was 0.6 and 0.96 respectively.

Work with the direction finder includes two modes. The operator using a whip antenna scans the specified frequency band. Upon detecting interference, the operator switches the receiver to a loop antenna, adjusts it to the receiving frequency. To determine the location of the source of interference, it is necessary to take several bearings and plot them on the map of the study area.

6. Conclusion

The characteristics of the URAN-4 radio telescope are given. An analysis of interference affecting the radio telescope was carried out. Made their classification. The main software and hardware methods of dealing with this interference are considered. It is noted that not all interference that occurs can be eliminated in this way. This especially applies to local interference, as a rule, occupying a wide frequency band. In this case, there are two ways: the use of legally protected frequencies and the organization of the radio telescope protection zone, which determines the permissible economic activity, in terms of radio emission levels. For the protection zone to function, the service of monitoring the radio spectrum and identifying sources of interference is necessary. A portable decameter direction finder has been designed and manufactured for solving these tasks.

References

- Galanin V. et al: 1989, *Kinem. and Phys. of Cel. Bod.*, **5**, № 5, 87.
 Dolan J.L.: 1973, *Proc. IEEE*, **61**, № 9, 242.
 Dubinskii B.: 1985, in *Abstracts of the report of the 17th All-Union Conference, Yerevan*, 503.
 John D. Kraus: 1973, *Radio Astronomy*, 427.

DOI: <http://dx.doi.org/10.18524/1810-4215.2018.31.144541>

THE RELATIONSHIP OF THE SCR WITH PARAMETERS OF RADIO BURSTS AND CME

E.A. Isaeva

Institute of Radio astronomy of NAS of Ukraine, isaevaode@gmail.com

ABSTRACT. The relationship the intensity of the proton flux I_p of solar cosmic rays (SCR) with the parameters of continual radio bursts of the IV type, with the speed of coronal mass ejections (CME) of V_{CME} , as well as with the parameters of slowly drifting radio bursts of type II is investigated. Comparative analysis showed that for the vast majority of proton events a strong correlation of the intensity of the proton flux I_p with the integral flux $\int F_{\mu} dt$ of microwave bursts and the CME velocity V_{CME} is observed, where the correlation coefficient r between the investigated parameters is 0.80 and 0.72, respectively. Earlier, the author reported on a strong connection between the integral flux $\int F_{\mu} dt$ of the microwave bursts and the CME velocity V_{CME} , where the correlation coefficient r between the investigated quantities is about 0.80. The strong connection between the intensity of the proton flux I_p and the integral flux $\int F_{\mu} dt$ of microwave bursts and the speed of the CME, as well as the strong connection between the integral flux $\int F_{\mu} dt$ of the microwave bursts and the CME velocity V_{CME} , attests about the common origin of SCRs and CMEs during proton flares. In this paper it is also shown that there is a strong relationship between the intensity of the proton flux I_p and the parameter of type II burst V_{II} , which characterizes the shock front displacement velocity. Moreover, the relationship between the intensity of the proton flux I_p and the parameter V_{II} depends to a large extent on the frequency f_2 of the maximum of the type II radio burst on the second harmonic at a given time t and on the energy of the protons E_p . The maximum correlation between the proton flux I_p and parameter V_{II} is observed for protons with an energy $E_p > 30$ MeV and for the upper frequency f_2 in the range 25-60 MHz.

АБСТРАКТ. Досліджено зв'язок інтенсивності потоку протонів I_p сонячних космічних променів (СКП) з параметрами континуальних радіосплесків IV типу, зі швидкістю корональних викидів маси (КВМ) V_{CME} , а також з параметрами повільно дрейфуючих радіосплесків II типу. Порівняльний аналіз показав, що для переважної більшості протонних подій спостерігається сильний зв'язок інтенсивності потоку протонів I_p з інтегральним потоком $\int F_{\mu} dt$ мікрохвильових сплесків і швидкістю КВМ V_{CME} , де коефіцієнт кореляції r між досліджуваними параметрами дорівнює 0.80 і 0.72, відповідно. Раніше автором повідомлялося про сильний зв'язок між інтегральним потоком $\int F_{\mu} dt$ мікрохвильових сплесків і швидкістю КВМ V_{CME} , де коефіцієнт кореляції r між досліджуваними величинами ≈ 0.80 . Наявність силь-

ного зв'язку інтенсивності потоку протонів I_p з інтегральним потоком $\int F_{\mu} dt$ мікрохвильових сплесків і швидкістю КВМ, а також сильного зв'язку між інтегральним потоком $\int F_{\mu} dt$ мікрохвильових сплесків і швидкістю КВМ V_{CME} свідчить про спільність походження СКП і КВМ під час протонних спалахів. У даній роботі також показано, що існує сильний зв'язок між інтенсивністю потоку протонів I_p і параметром сплесків II типу V_{II} , який характеризує швидкість зсуву фронту ударної хвилі. Причому, зв'язок між інтенсивністю потоку протонів I_p і параметром V_{II} значною мірою залежить від частоти f_2 максимуму радіосплесків II типу на другій гармоніці в даний момент часу t і від енергії протонів E_p . Максимальна кореляція між потоком протонів I_p і параметром V_{II} спостерігається для протонів з енергією $E_p > 30$ MeV і для верхньої частоти f_2 в діапазоні 25-60 МГц.

Keywords: Proton flux, coronal mass ejections, radio bursts.

1. Introduction

The fundamentals of short-term prognosis methods for the flux of solar cosmic ray protons (SCR) were laid in the works of a number of authors. In the work (Chertok, 1982) it was shown that the parameters of microwave radio bursts (μ -bursts) can be used to judge the total number of accelerated particles and their energy spectrum. It was also shown that by the parameters of meter bursts one can judge the conditions for the exit of accelerated particles into interplanetary space. The presence of a sufficiently powerful meter component indicates favorable exit conditions, the absence on the unfavorable exit conditions (Akinian et al., 1977). (Melnikov et al., 1986) showed that the presence of a strong coupling between the flow of subrelativistic electrons of the SCR and the integral flux of μ -bursts indicates that the SCR electrons and the electrons generating the radio burst are accelerated in a single process. On the basis of this, statistical models connecting proton and electron fluxes with parameters of microwave bursts were obtained (Melnikov et al., 1991).

In this paper, the emphasis is on investigating the connection between the SCR proton flux and the parameters of radio bursts of type II and comparing the results with what is obtained from the parameters of microwave bursts. Earlier in the works (Tsap & Isaeva, 2011; 2012; 2013) some questions were considered regarding the relation of

the SCR proton flux with the parameters of type II radio bursts. In the course of studies of the connection between the speed of the frequency drift of meter-decameter type II bursts and the intensity of the proton flux I_p of different energies, two families of events were discovered. This involves the generation of shock waves both in the region of flare energy release and by moving coronal mass ejection (CME) (Isaeva & Tsap, 2011). In the works (Isaeva & Tsap, 2011; Tsap & Isaeva, 2012; 2013), the results of the investigation of the efficiency of the acceleration of SCR by coronal and interplanetary shock waves are given, and arguments are also presented in favor of a two-step acceleration of protons. A comparative analysis showed that acceleration of protons by coronal shock waves is more effective than interplanetary shock waves, and that the main acceleration of protons occurs in the flare region and additional by the shock waves. A study of the fine spectral structure of the meter-decameter radio bursts of type II showed that there is a sufficiently strong connection between the proton flux and the relative distance $b = (f_2 - f_1)/f_1$ between the first and second harmonics at a given time t , where the correlation coefficient r between the parameters ≈ 0.70 , while the connection between the drift velocity and the proton flux turned out to be weak, and the correlation coefficient r between the proton flux and the drift velocity does not exceed ≈ 0.40 (Tsap & Isaeva, 2013).

2. Relationship between the intensity of the proton flux I_p SCR and the integral flux $\int F dt$ of radio bursts in the range 245-15400 MHz

For the analysis, the original records of the radio emission of the Sun were used at 8 fixed frequencies of 245, 410, 610, 1415, 2695, 4995, 8800 and 15400 MHz (<https://www.ngdc.noaa.gov/stp/space-weather/solar-data/solar-features/solar-radio/rstn-1-second/>), original recordings of the proton flux intensity I_p with proton energy $E_p > 0.8-100$ MeV (https://satdat.ngdc.noaa.gov/sem/goes/data/new_avg/), as well as a list of proton events (<ftp://ftp.swpc.noaa.gov/pub/indices/SPE.txt>). The investigated sample contains 147 proton events for the period from 06-02-1986 to 14-10-2014. Protonic events were selected according to generally accepted criteria for protonity. It is known that for events having a U or W type of a frequency radio spectrum with maxima in the meter and centimeter wavelength bands and with a minimum in the decimeter band, the best correlation between the parameters of μ -bursts and the intensity of the flux of the subrelativistic electrons and protons SCR is observed. Confirmation of this fact can be seen in Fig. 1 a), where the connection between the integral flux of continual μ -bursts at a frequency of 8800 MHz and the intensity of the proton flux I_p with an energy $E_p > 30$ MeV is shown. For such events, the correlation coefficient r between $\int F dt$ and $I_p \approx 0.80$. At the same time, the relationship between the intensity of the proton flux I_p and the integral flux of the continual radio bursts depends to a large extent on the frequency f of the radio burst (see Fig. 1 b) and the energy of the

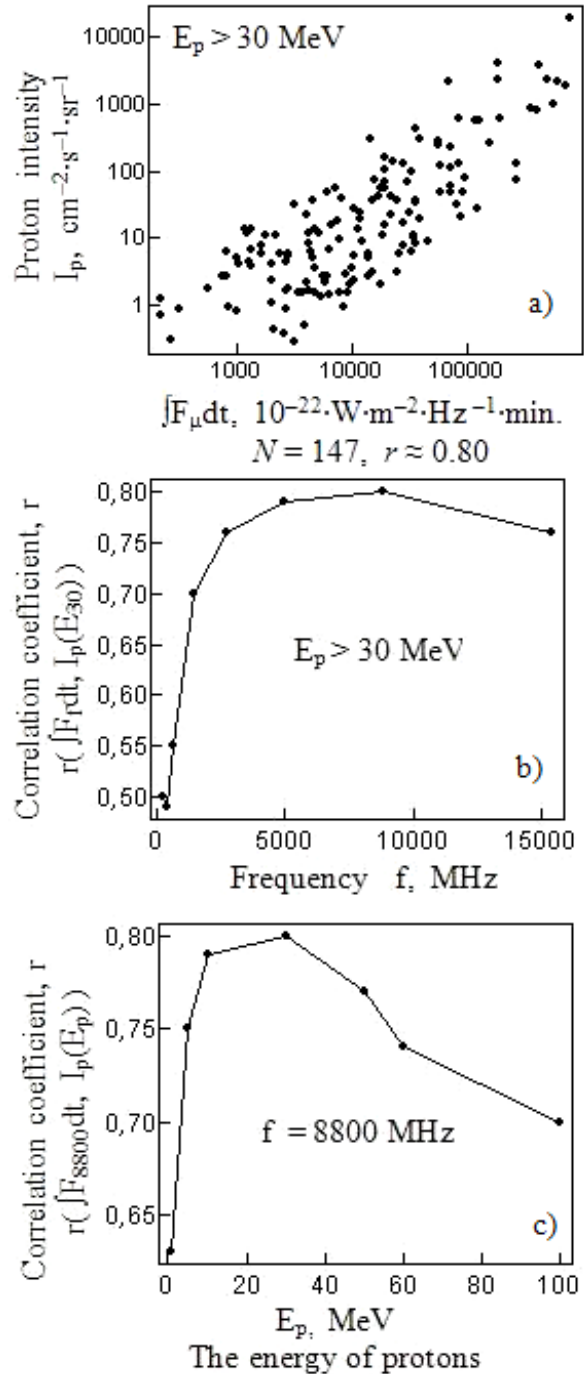


Figure 1 : The connection between the proton flux I_p and the integral flux $\int F dt$ of the continuum radio bursts

protons E_p , see Fig. 1 c). The relationship between I_p and the integral flux of radio bursts $\int F dt$ sharply decreases in the decimeter range and is practically absent in the meter range, see Fig. 1 b). The strongest connection between I_p and $\int F dt$ is observed for the subrelativistic protons with energy $E_p > 30$ MeV and the integral flux of μ -bursts, see Fig. 1 c).

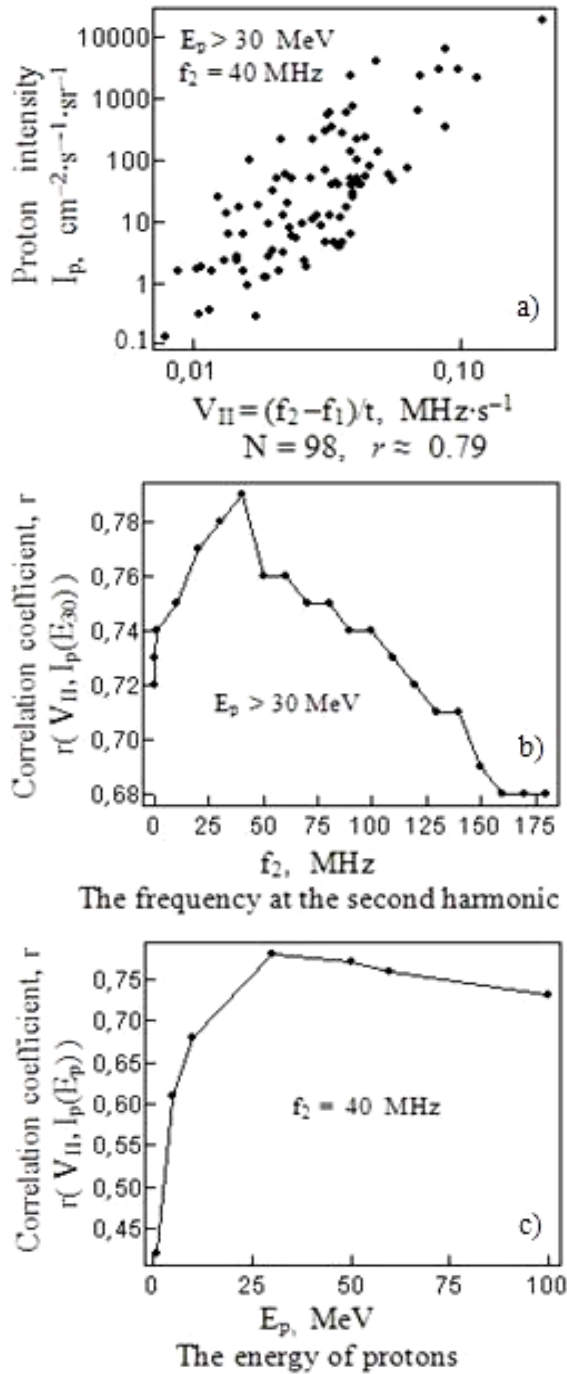


Figure 2 : The connection between the proton flux I_p and the parameter V_{II} of radio bursts of type II

3. Relationship between the intensity of the proton flux I_p SCR and the parameters of radio bursts of type II in the range 25-180 MHz

The relationship between the intensity of the proton flux I_p of SCR and the parameters of radio bursts of type II in the range 25-180 MHz is studied. The sample under study contains 98 proton events for the period from 24-11-2000 to 20-12-2014. For the analysis, original records of dynamic spectra in the range 25-180 MHz from the solar radio spectrograph (SRS) were used (<http://www.ngdc.noaa.gov/stp/space-weather/solar-data/solar-features/solar-radio/rstn-spectral/>).

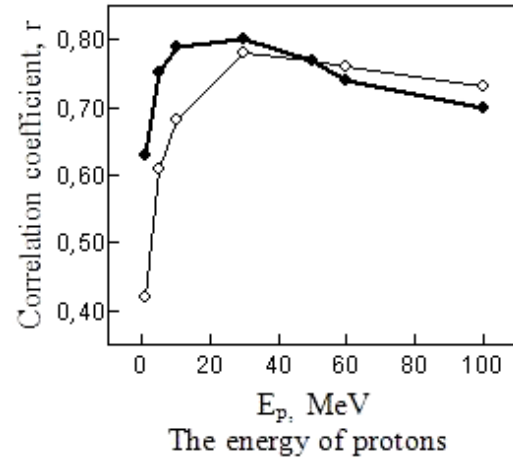


Figure 3 : Dependence of the correlation coefficient r between I_p and V_{II} (a thin line) and between I_p and the integral flux of microwave bursts $\int F dt$ (a bold line) on the proton energy E_p

In this paper, a new regression model was used to approximate the harmonics of the type II burst (1), where $f_{i,j}$ - the frequency of the maximum of the type II burst on the given harmonic at a given time t , i - the count number, and j - the number of the harmonic, a and b - a coefficients of linear regression.

$$\log_{10} f_{i,j} = a \cdot \sqrt{t} + b. \quad (1)$$

This dependence allows us to estimate the rate of frequency drift sufficiently accurately for 95% of type II bursts in the range 25-180 MHz, for which the correlation coefficient r between the observed and calculated values of the frequency $r > 0.98$. The zero point of time for all events corresponded to the beginning of the first harmonic at a frequency of 180 MHz.

Earlier in the work (Tsap & Isaeva, 2013) it was pointed out that there is a sufficiently strong connection between the proton flux I_p and the relative distance between the harmonics of the type II burst at a given instant t , where the correlation coefficient r between the investigated values of ≈ 0.70 , while the relationship between I_p and the drift velocity turned out to be low ($r \approx 0.40$). However, it was noted that if when calculating the frequency drift velocity V_{II} (2), take into account the frequency distance between the harmonics of the type II burst at a given time t , then the relationship between I_p and parameter V_{II} increases sharply.

$$V_{II} = \frac{f_2 - f_1}{t}, \quad (2)$$

where f_1 and f_2 are the frequencies of the maximum of the type II burst at a given time t at the first and second harmonics, respectively. Time t is measured from the beginning of the second harmonic at a frequency of 180 MHz. In Fig. 2 a) shows the relationship between the proton flux I_p and the parameter V_{II} for protons with an energy $E_p > 30 \text{ MeV}$ and an upper frequency $f_2 = 40 \text{ MHz}$. In Fig. 2 b) shows the dependence of the correlation coefficient between I_p and V_{II} , depending on the upper frequency f_2 , and

in Fig. 2 c), depending on the energy of the protons E_p . In Fig. 2 b) and c) it is seen that the maximum correlation between the proton flux I_p and the parameter V_{II} is observed for the upper frequency f_2 in the range 25-60 MHz and for protons with the energy $E_p > 30$ -100 MeV. In Fig. 3 shows the relationship the intensity of the proton flux I_p with the parameter V_{II} (a thin line) and the integral flux $\int F dt$ of microwave bursts (a bold line) as a function of the proton energy E_p . In Fig. 3), it is seen that the relationship of I_p with the parameter V_{II} and with the integral flux $\int F dt$ of microwave bursts is approximately the same for protons with an energy $E_p > 30$ MeV. However, the relationship of I_p with the parameter V_{II} decreases sharply for protons with an energy $E_p < 30$ MeV, while the relationship I_p with the microwave flux $\int F dt$ remains strong enough for protons with an energy $E_p < 30$ MeV. It follows that the contribution of shock waves to proton acceleration is much higher for high-energy protons.

4. Relationship between the intensity of the proton flux I_p and the velocity of coronal mass ejections V_{CME}

Almost all proton events are accompanied by coronal mass ejections (CME). Earlier in the work (Isaeva & Tsap, 2017) it was shown that there is a strong relationship between the speed of the CME V_{CME} and the integral flux of the continuum microwave bursts $\int F_{\mu} dt$. Moreover, the connection between the speed of the CME and the integral flux of the continual radio bursts of the IV type weakens with a decrease in the frequency of the burst of the IV type and is practically absent already in the meter-decameter range. The presence of a high correlation between the speed of the CME and the integral flux of microwave bursts during proton events indicates the flare origin of the CME. Such CMEs are formed in the region of flare energy release and are associated with the exit of high-energy particles into the interplanetary space. And so these CMEs have the strongest influence on space weather.

The sample studied contains 177 coronal mass ejections (CME) associated with proton events for the period from 04-11-1997 to 26-01-2015. For the analysis, tabular data of the CME velocity (https://cdaw.gsfc.nasa.gov/CME_list/UNIVERSAL/text_ver/univ_all.txt) was used. A comparative analysis showed that there is a fairly strong relationship between the intensity of the flux of the subrelativistic protons I_p and the velocity of the CME V_{CME} . In Fig. 4 a) shows the relationship between I_p with the proton energy $E_p > 30$ MeV and the velocity of the CME, where the correlation coefficient r between the investigated quantities is ≈ 0.72 . In Fig. 4 b) shows the dependence of the correlation coefficient r between $\int F dt$ and V_{CME} (thin line), as well as between $\int F dt$ and I_p (bold line) from the frequency f of the continual radio burst type IV. In Fig. 4 c) shows the dependence of the correlation coefficient between I_p and V_{CME} (thin line), and also between I_p and the integral flux of microwave bursts $\int F_{\mu} dt$ at 8800 MHz (bold line) from the energy of protons E_p . It is noteworthy that the connection between V_{CME} and I_p with $\int F_{\mu} dt$ as a function of frequency f is very similar (see Fig. 4 b)). The same tendency is seen in Fig. 4c), where it is seen that the behavior of the relationship of the I_p with V_{CME} and with $\int F_{\mu} dt$ as a function of the proton energy E_p is also very

similar. However, the relationship of I_p with V_{CME} is somewhat lower than I_p with $\int F_{\mu} dt$.

5. Conclusion

In this paper, on the basis of a new independent sample of proton events, the presence of a strong coupling between the intensity of the proton flux SCR I_p and the integral flux of microwave bursts $\int F_{\mu} dt$ was confirmed. Also

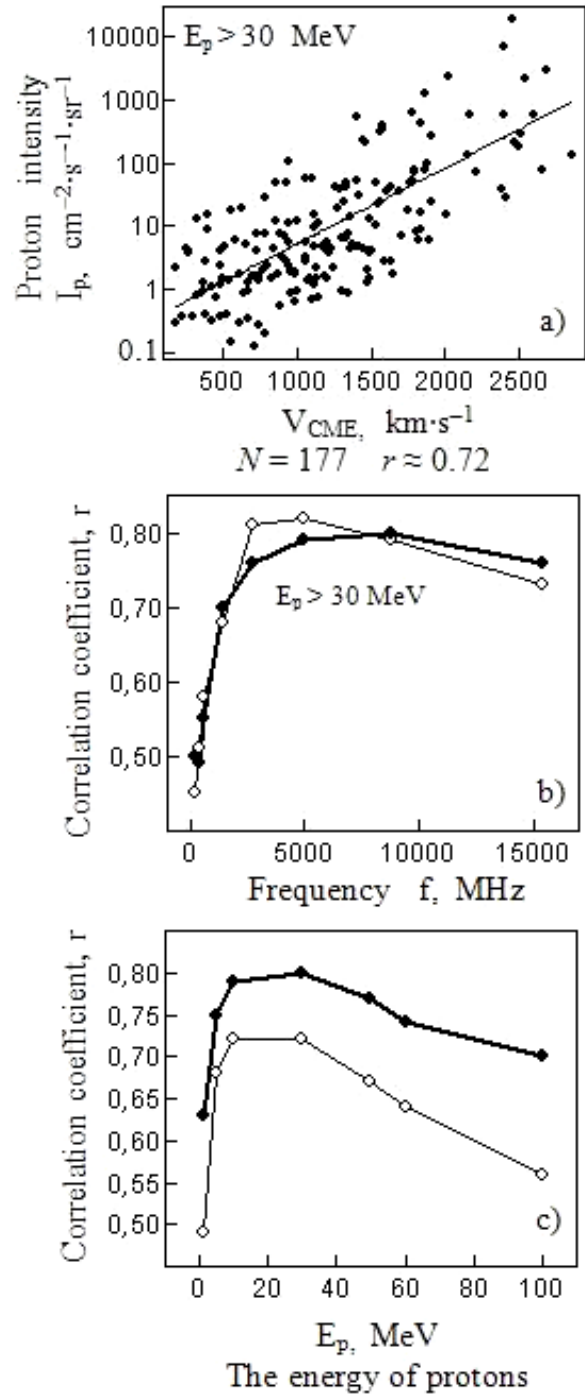


Figure 4 : The relationship between the proton flux and the CME

in this paper, arguments are given indicating the presence of a strong connection between the proton flux I_p and the frequency drift velocity $V_{II} = (f_2 - f_1) / t$, calculated with allowance for the frequency distance between the first and second harmonics of the type II burst at a given time t . It is shown that the relationship between the proton flux I_p and the parameter V_{II} depends to a large extent on the frequency of the maximum of the type II burst at the second harmonic f_2 at a given time t and on the proton energy E_p . The maximum correlation between I_p and V_{II} is observed for protons with an energy $E_p > 30-100$ MeV and in a narrow frequency range of values for the upper frequency f_2 from 25 to 60 MHz. Also, for a large sample of CMEs associated with proton events, it is confirmed that there is a sufficiently strong connection between the proton flux I_p and the velocity of the CME, as previously reported (Grechnev et al., 2015).

References

- Akinian S., Fomichev V., Chertok I.: 1977, *Geomagnetism and Aeronomy*, **17**, 5.
- Chertok I.: 1982, *Geomagnetizm i Aeronomiia*, **22**, 182.
- Grechev V., Kiselev V., Meshalkina N. et al.: 2015, *Solar Physics*, **290**, 2827.
- Isaeva E., Tsap Yu.: 2011, *Bulletin of the Crimean Astrophysical Observatory*, **107**, 78.
- Isaeva E., Tsap Yu.: 2017, *Odessa Astronomical Publications*, **30**, 78.
- Melnikov V., Podstrigach T., Kurt V. et al.: 1986, *Kosmicheskie Issledovaniia*, **24**, 610.
- Mel'nikov V., Podstrigach T., Daibog E. et al.: 1991, *Cosmic Res.*, **29**, № 1, 87.
- Tsap Yu., Isaeva E.: 2012, *Bulletin of the Crimean Astrophysical Observatory*, **108**, 52.
- Tsap Yu., Isaeva E.: 2012, *Geomagnetism and Aeronomy*, **52**, № 7, 921.

DOI: <http://dx.doi.org/10.18524/1810-4215.2018.31.144662>

ALGORITHMS OF MULTI FREQUENCY RADIOMETRY IN THE CONDITIONS OF BROADBAND INTERFERENCE

V.V. Orlov, O.A. Lytvynenko, V.V. Galanin

URAN-4 Observatory of IRA NASU, Odessa, Ukraine, uran4@te.net.ua

ABSTRACT. The development of digital technologies for multi-frequency signal reception in the low-frequency range creates the prerequisites for the application of optimal algorithms for real-time beamforming without changing the aperture of the radio telescope antenna.

In the present paper, a model of the system based on multiplicative processing (MP) is considered and investigated. The system consists of two antenna arrays, the signals from the outputs of which pass through the narrow-band filters of receiving devices. After filtration, they undergo MP and weighted summation. Next, we consider an algorithm for the formation of a narrow beam of the antenna pattern (AP) of a multi-frequency radio interferometer based on the well-known cosinusoid summation method. Its meaning lies in summing up the results of multiplicative processing of signals from the outputs of several spatially separated different scales bases. In work, using MP, a method is proposed for reducing the width of the main lobe of AP on one base by receiving signals at several frequencies. The further development of the method is associated with the optimization of the AP in multi-frequency MP, which leads to the possibility of lowering the side-lobe levels by weighing the signals from the outputs of the MP channels. For this purpose, for the sum of odd cosine waves, it is necessary to determine the weighting factors that ensure the minimum root-mean-square level of side lobes in a given zone of AP suppression. As a result of MP processing, we obtain a decrease in the amplitudes of side lobes with an insignificant increase in the width of the antenna pattern of the antenna system. In work the algorithm of suppression of broadband hindrances is also considered. The synthesis of the optimization algorithm is reduced to the need to determine the weighting coefficients and frequencies that provide the minimum rms level of the side lobes of the AP in a given zone of suppression, with a limited range of frequency separation. These methods are proposed to use in radio astronomy to improve the quality of research.

Keywords: antenna array, multiplicative processing, optimization, antenna pattern.

АБСТРАКТ. Розвиток цифрових технологій для багаточастотного прийому сигналів у низькочастотному діапазоні створює передумови для застосування оптимальних алгоритмів формування діаграми

спрямованості (ДС) в реальному часі без зміни апертури антени радіотелескопа.

У представленій роботі розглядається й досліджується модель системи на основі мультиплікативної обробки (МО). Система складається із двох антенних решіток, сигнали з виходів яких, проходять через вузькосмугові фільтри приймальних пристроїв. Після фільтрації вони піддаються МО й ваговому підсумовуванню. Далі розглядається алгоритм формування вузького променя діаграми спрямованості багаточастотного радіоінтерферометра на основі відомого методу підсумовування косинусоїд. Зміст його полягає в підсумовуванні результатів мультиплікативної обробки сигналів з виходів декількох просторово рознесених двоканальних баз різного масштабу. У роботі, використовуючи МО, пропонується метод зменшення ширини головного пелюстка ДС на одній базі за рахунок прийому сигналів на декількох частотах. Подальший розвиток методу пов'язаний з оптимізацією ДС у багаточастотній МО, що приводить до можливості зниження рівня бічних пелюстків за рахунок зважування сигналів з виходів каналів МО. Для цієї мети, для суми непарних косинусоїд необхідно визначити вагові коефіцієнти, що забезпечують мінімальний середньоквадратичний рівень бічних пелюстків у заданій зоні зниження рівня ДС. У результаті МО обробки одержуємо зменшення амплітуд бічних пелюстків при незначному збільшенні ширини ДС антеної системи. У роботі розглядається так само алгоритм зменшення широкосмугових завад. Синтез алгоритму оптимізації зводиться до необхідності визначення вагових коефіцієнтів і частот, що забезпечують мінімальний середньоквадратичний рівень бічних пелюстків ДС у заданій зоні зниження, при обмеженому діапазоні розносу частот. Перераховані методи пропонується використати в радіоастрономії для поліпшення якості проведених досліджень.

Ключові слова: антена решітка, мультиплікативна обробка, оптимізація, діаграма спрямованості.

1. Introduction

Striving for the effective use of decimeter wavelengths in radio astronomy leads to the need to improve hardware and algorithmic tools to: increase the sample signal size, increase noise immunity, and improve the quality of the

antenna pattern (AP) of the antenna with limited aperture sizes (Men, 1997), (Konovalenko, 2016). An effective way to increase the sample size is to use the properties of the broadband signal, due to which sample accumulation can be performed at several frequencies (Men, 2000), (Shaw, 1965). In this case, it is necessary to take into account the dependence of the AP shape on the carrier frequency, especially the width of the main lobe and side lobes. The development of digital technologies for multi-frequency signal reception in the range of 10–200 MHz also creates prerequisites for the application of optimal AP formation algorithms in real time without changing the aperture of the radio telescope (RT).

This article proposes algorithms for optimizing AP due to signal processing at several frequencies. A system of radiometry based on multiplicative multi-frequency signal processing is being modeled, the possibilities of minimizing the level of side lobes of AP are being investigated.

2. Model of the system under study

The system under study based on multiplicative signal processing (fig.1) consists of 2 sub-arrays AP_1, AP_2 , the signals from whose outputs pass through Φ_{1l}, Φ_{2l} narrow-band filters $l = 1, \dots, L$ of receivers tuned to ω_l frequencies, then subjected to MP and weighted summation with coefficients g_l .

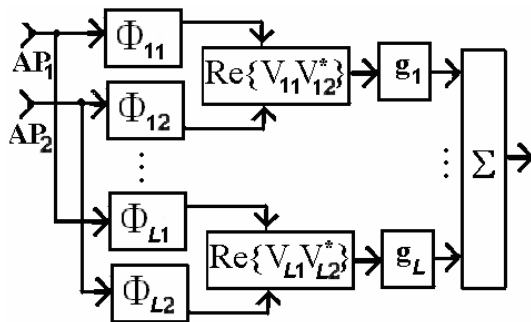


Figure 1: Radiometry system with multi-frequency processing

The model of a monochromatic point source of a signal from the outputs of a pair of filters of the l frequency channel of two omnidirectional antennas can be represented as

$$\begin{aligned} U_{1l}(t) &= U \exp\{j(\omega_l(t+t_0) + \varphi_{0l})\} = U \exp\{j(\omega_l t + \varphi_{0l} + \psi_l)\} \\ U_{2l}(t) &= U \exp\{j(\omega_l(t-t_0) + \varphi_{0l})\} = U \exp\{j(\omega_l t + \varphi_{0l} - \psi_l)\}, \end{aligned} \quad (1)$$

Where t_0 – the delay time of arrival of the wave front along the aperture of MP, the size of which $d = \lambda/2 = \pi v/\omega$ is matched with the wavelength λ , main (first) carrier frequency $\omega = \omega_1$, speed of wave propagation v , $\psi_l = \omega_l t_0 = \pi(\omega_l/\omega) \cos \varphi$ – the phase of spatial delay of the wave front arrival at the frequency ω_l , φ – the angle of the wave front arrival rela-

tive to the normal of AP base, φ_0 – the initial phase. It is assumed that in filters Φ_{1l}, Φ_{2l} , $l = 1, \dots, L$, the amplitude, phase and mutual frequency distortions are eliminated to the accuracy of power leveling in frequency channels $P = P_l = \langle U_{1l} * U_{2l} \rangle$, $l = 1, \dots, L$, where $\langle \rangle$ are the averaging symbols of the process over time.

3. Algorithm for the formation of a narrow beam AP multifrequency radiointerferometer

A known method of forming a narrow beam receiving antenna is the method of summing up sinusoids (Denisov, 2002), which consists in summing the results of multiplicative processing of signals from the outputs of several spatially separated two-channel bases of different scale.

A method is proposed for reducing the width of the main lobe of the AP on one base by receiving signals at several frequencies. The signals U_{1l}, U_{2l} from the outputs of a pair of filters tuned to odd $l = 2i - 1$ frequencies are subjected to MP

$$U_{\text{out}} = \sum_{l=1}^L g_{2l-1} \text{Re}\{U_{1,2l-1} U_{2,2l-1}^*\} = U^2 \sum_{l=1}^L g_{2l-1} \cos\{(2l-1)\psi\}.$$

The output signal, taking into account the AP of the same sub-arrays $Y(\psi)$, determines the AP of multiplicative processing $D(\psi)$

$$U_{\text{out}} = U^2 Y^2(\psi) \sum_{l=1}^L \cos\{(2l-1)\psi\} = U^2 Y^2(\psi) D(\psi) \quad (2)$$

It is easy to show that when using odd frequencies and equal weights ($g_l = 1$), the AP MP is determined by the relation (Gradstein, 1971)

$$D(\psi) = \sum_{l=1}^L \cos\{(2l-1)\psi\} = 0.5 \sin(2L\psi) / \sin(\psi) \quad (3)$$

The level of maximum side lobes of AP (3) is -6.6 dB, while for linear $N = 4L$ -elemental AP with the same beam width is -13.2 dB. The difference between them is explained by the fact that (3) determines the AP of the MP in power, and the AP of the linear AR has a similar form in amplitude.

4. Optimization of AP of multi-frequency MP

A further decrease in the level of side lobes of the AP MP, it is possible to carry out by weighing the signals from the outputs of the MP channels. For the sum of odd sinusoids, it is proposed to perform optimization in the following formulation: it is necessary to determine the weighting coefficients g_l that ensure the minimum root-mean-square level of side lobes in a given zone of AP suppression.

The output signal with regard to (1) and (2) for odd frequencies, taking into account the AP of the same sub-arrays $Y(\psi)$, determines the AP of multiplicative processing $D(\psi)$

$$U_{\text{out}} = U^2 Y^2(\psi) \sum_{l=1}^L \cos\{(2l-1)\psi\} = U^2 Y^2(\psi) D(\psi), \quad (4)$$

Imagine the normalized signal at the output of the L -frequency MP in the form

$$y = U_{\text{out}} / U^2 = G^T X, \quad (5)$$

where $X^T = \{\cos \phi, \cos 2\phi, \dots, \cos(2L-1)\phi\}$ – the vector of signals of the angular direction ϕ from the outputs of MP, $G^T = \{g_1, g_2, \dots, g_L\}$ – the vector of weighting coefficients. Then the function H minimized by the vector, with the signal $S^T = \{1, 1, \dots, 1\}$, with the angular position in the maximum of the AP ($\phi = 0$), is determined by the expression

$$H = \min_G \int_z y^2(\phi) d\phi, \quad \text{npu } G^T S = L \quad (6)$$

Where z – the side lobe suppression zone, $z \in [K\pi/2L, \pi/2]$, K – the coefficient of expansion maxim AP.

In the matrix form (6) has the form (7)

$$H = \inf_{G^T S=L} G^T R_{XX} G, \quad (7)$$

where R_{XX} – the correlation matrix of the input signal with the elements

$$r_{ij} = \int_z \cos[(2i-1)\phi] \cos[(2j-1)\phi] d\phi = \begin{cases} -0,5 \left(\frac{\sin K\pi(i+j-1)/L}{i+j-1} + \frac{\sin K\pi(i-j-1)/L}{i-j-1} \right), & i \neq j \\ \pi/2 - K\pi/2L - \frac{\sin K\pi(2i-1)/L}{4i-2}, & i = j \end{cases} \quad (8)$$

To find the vector G , the method of indeterminate Lagrange multipliers α is used and an auxiliary function (Burakov, 1976) $B = 0,5G^T R_{XX} G + \alpha(S^T G - L)$ is introduced. After equating the derivative to zero $dB/dG = 0$, the solution of the resulting equation is

$$G = R_{XX}^{-1} S (S^T R_{XX}^{-1} S)^{-1} L. \quad (9)$$

On Fig. 2 shows the antenna pattern consisting of two dipoles (line 1), the same antenna, but using MP with the same weights (line 2) and the same antenna, but with optimized weighting coefficients (line 3).

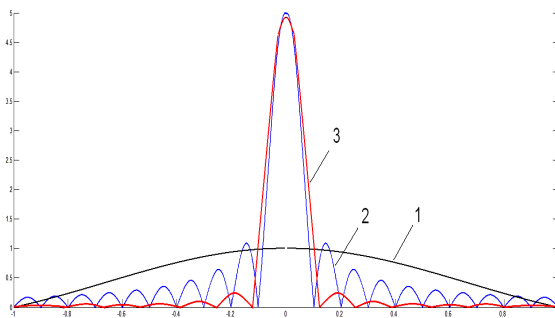


Figure 2: Optimization of the antenna pattern

Analysis of AP MP with weight processing (9) showed that with a given widening of the main lobe $K = 1.1$, the level of the maximum side lobe is -11.2 dB, and for the zone of moderate expansion of the main lobe ($K < 2.5$) the level of the maximum side lobe decreases up to -21 dB.

5. Algorithm for suppressing broadband interference

The possibilities of lowering the side lobes of the AP in a narrow frequency separation range (as compared with the previous algorithm), with a deviation from the reference frequency $\omega = \omega_1$ in the range $(1 \dots 1.5)\omega$ are investigated. The reduction of the root-mean-square level of side lobes of the antenna array antenna pattern can be carried out in a given region, if in the whole region the maximum of the antenna directive gain is provided.

The optimization algorithm is synthesized in the following formulation: it is necessary to determine the weighting coefficients and frequencies that ensure the minimum of the root-mean-square level of side lobes of the AP in a given suppression zone, with a limited frequency separation range.

The output signals of the adjacent equidistant N -element sub-arrays 1 and 2 at an arbitrary carrier frequency ω_l , taking into account (1) and (2), have the form

$$U_{1l}(t) = \sum_{i=1}^N U \exp\{j[\omega_l(t + t_0(i-1)) + \phi_{0l}]\} = \sum_{i=1}^N U \exp\{j(\omega_l t + \phi_{0l} + (i-1)\psi_l)\} = \frac{U \sin(N\psi_l/2)}{\sin(\psi_l/2)} \exp\{j(\omega_l t + \phi_{0l} + (N-1)\psi_l/2)\}$$

$$U_{2l}(t) = \frac{U \sin(N\psi_l/2)}{\sin(\psi_l/2)} \exp\{j(\omega_l t + \phi_{0l} - (N-1)\psi_l/2)\},$$

where $\psi_l = \omega_l t_0 = \pi(\omega_l / \omega) \sin \phi$ – the phase of the spatial delay of the arrival of the wave front at the frequency ω_l , ϕ – the angle of the arrival of the wave front relative to the normal to the array, taking values in the interval $[-\pi/2, \pi/2]$.

Then the output signal after summing the frequency channel responses is determined

$$U_{\text{out}} = \text{Re}\{U_{1l} U_{2l}^*\} = U^2 \sum_{l=1}^L g_l \left(\frac{\sin(N\psi_l/2)}{\sin(\psi_l/2)} \right)^2 \cos\{\psi_l(N-1)\}. \quad (10)$$

Similar to the method of the previous optimization of the AP, we represent the normalized signal (10), as a function of the angle ϕ of arrival of the wave, at the output L -frequency MP as

$$y = U_{\text{out}} / U^2 = \sum_{l=1}^L g_l x_l(\phi) = G^T X, \quad (11)$$

where the elements X of the vector signals from the L outputs of the MP are determined by the expression

$$x_l = \left(\frac{\sin(N\pi(\omega_l/2\omega)\sin\varphi)}{\sin(\pi(\omega_l/2\omega)\sin\varphi)} \right)^2 \cos\{(N-1)\pi(\omega_l/\omega)\sin\varphi\}.$$

Then the function H minimized by the vectors G, Ω , with the signal $S^T = \{1, 1, \dots, 1\}$, with the angular position at the peak of the AP ($\varphi = 0$), is determined by the expression

$$H = \min_{G, \Omega} \int_z y^2(\varphi) d\varphi, \quad \text{npu} \quad G^T S = L \quad (12)$$

where the minimization of the functional is carried out along two vectors G, Ω of variables, z – the side-lobe suppression zone, $z \in [\varphi_1, \varphi_2]$, $\Omega^T = \{\omega_1, \dots, \omega_L\}$ – selected frequencies containing wideband interference. If the set of M frequencies Ω is predetermined and its size $M = L$ coincides with the size of the vector G , then the optimization problem is solved by the previous method. If it is necessary to select L individual channels of multi-channel reception from the full set of all $M > L$ frequencies, optimization (11) is carried out for each combination of the M and L then, after going through all the combinations, the global minimum is determined. Reduction of computational operations can be achieved using a priori information about the number of interference and the zone of possible interference directions. There is a known theorem (Shirman, 1974) that for the complete suppression of M point-like interference, additional M frequency channels of are sufficient. From this it follows that to suppress 1 point interference, 1 additional frequency channel is sufficient. In this case, the choice of the frequency at which the amplitude of the side lobe is equal and opposite in the direction of interference of the main and additional frequency channels is the simplest. The suppression adjustment is implemented by a single multiplier.

The zone of possible interference suppression is determined by the objectives. If it is necessary to suppress the signal of an interfering space radio source that falls into the side lobe of the AP, then the range of angular directions (φ_1, φ_2) is known. In this case, only individual side lobes corresponding to the interfering radio source are minimized. If it is necessary to compensate for interference from terrestrial radio stations (RFI2010, 2010), then side lobes are minimized in a given zone of large angles (φ_1, φ_2) . On Fig. 3 shows the APs of the 64-element antenna sub-arrays, $N = 64$, for two frequency channels with frequency detuning $\omega_2/\omega_1 = 1.1$. The analysis of dependences showed that for two-frequency processing with an angular separation of radio sources of more than 1.4 degrees, side lobes may already have different signs in the frequency channels.

In radio astronomical signal processing systems, various methods of adaptation to changes in the parameters of the ionosphere and to disturbing radio sources began to be introduced (Barnbaum, 1998), (Afroimovich, 2008). The proposed approach allows adaptation by selecting frequencies and already with two-frequency processing $L = 2$, forming zeros in the direction of the interfering radio source.

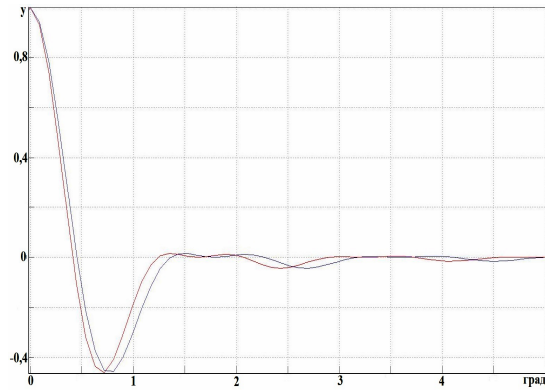


Figure 3: AP of two frequency channels

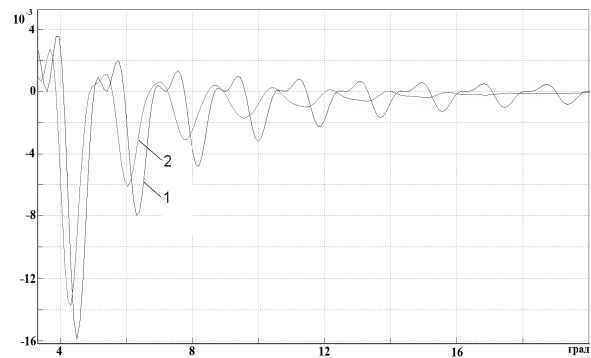


Figure 4: The side lobes of the AP at the same frequency and with averaging over the frequency range

In practice, to reduce the level of side lobes of the AP, a quasi-optimal algorithm is often used, which consists in averaging (10) in the frequency range from to with constant weighting coefficients. In Fig. 4 shows the fragments of the side lobes of the AP at the initial frequency (line 1) and when averaged in a uniform grid of the frequency range $\omega_L/\omega_1 = 1.1$, $L = 100$ (line 2).

It is easy to see that the efficiency of the averaging method is insignificant for angles less than 4 degrees and significantly increases with large angular detuning of the studied and interfering radio sources.

6. Conclusion

The proposed approach expands radiometry capabilities in relation to radio astronomy in the formation of AP due by time processing in frequency channels. Open the way to adapt to interference without the use of auxiliary antennas. Computational methods of adaptive processing are realizable in real time, taking into account the rotation of the Earth, scanning the beam and the angular location of interfering cosmic sources.

In general, the choice of frequency grid and weighted multi-frequency signal processing provide a reduction in the width of the main beam of the beam with limited antenna aperture sizes, an increase in the signal-to-noise ratio, as well as a decrease in side lobe level and interference effects.

References

- Afraimovich E., Smolkov G. et al.: 2008, in *Rep. of the Academy of Sciences Astronomy, Astrophysics, Cosmology*, **419**, No. 5, 618.
- Barnbaum, C., Bradley R. F.: 1998, *Astron. J.*, **116**, 2598.
- Burakov V. et al.: *Foreign Radioelectronics*, **8**, 35.
- Denisov V. et al.: 2002, Phase direction finders. Monograph. (Tomsk: TUSUR), 251.
- Gradstein I., Ryzhik I.: 1971, Tables of integrals, sums, series and products.
- Konovalenko A., Erin S. et al.: 2016, *Radio Physics and Radioastronomy*, **21**, No. 2, 83.
- Megn A., Braude, S. et al.: 1997, *Radio Physics and Radio Astronomy*, **2**, No. 4, 385.
- Megn A., Braude S.: 2000, *Radio Physics and Radio Astronomy*, **5**, № 1, 5.
- RFI2010, 2010.: Overview of RFI mitigation methods in existing and new systems (invited) (RFI mitigation workshop. RFI2010. 29-31 March 2010. Groningen, the Netherlands. <https://pos.sissa.it/107/>. RFI2010_007.pdf).
- Shirman J.: 1974, Resolution and compression of signals. (M.: Soviet Radio), 360.
- Shaw E., Davis D.: 1965, *Foreign Radioelectronics*, **11**, 103.

DOI: <http://dx.doi.org/10.18524/1810-4215.2018.31.144736>

ON THE INFLUENCE OF MHD TURBULENCE ON THE STRUCTURE OF THE RADIOGALAXY LOBES

N.O.Tsvyk

Institute of Radio Astronomy of the NAS of Ukraine, Kharkiv, Ukraine

natalitsv69@gmail.com

ABSTRACT. There is considered the evolution of the shape for the radio galaxy lobes of FRI and FRII types from the point of view on changing the configuration of large-scale structure of magnetic field, and energy transport in the turbulent MHD waves. There have been studied the interaction and transformation of waves in the active regions of the lobes, and so studied the role of MHD waves and vortexes in media-mixing processes and in the amplification of the average magnetic field. The transport of low-energy e-cosmic rays (e-CRs) responsible for the radio emission in the MHz band (recorded at the UTR-2 and GURT telescopes) is analyzed for the sources like the Cygnus A and M87. It is shown that the transport of e-CRs mainly corresponds to the diffusion of CRs on MHD and turbulence scatter, and the entrainment of CRs by quasi-regular post-jet flows inside to the lobe. So, the MHz radio emission that observed emphasizes the peculiarities in the lobe which arising when the magnetic field is in reorganization.

АБСТРАКТ. Розглянуто еволюцію форми пелюстки радіоґалактик FRI і FRII типів з точки зору зміни конфігурації великомасштабної структури магнітного поля, і перенесення енергії у вигляді турбулентних МГД хвиль. Досліджено взаємодію і трансформацію хвиль; роль МГД хвиль та вихорів в процесах змішування середовищ і в посиленні середнього магнітного поля. Проаналізовано перенесення е-космічних променів (е-КП) малих енергій, відповідальних за радіовипромінювання в МГц діапазоні (реєстроване на телескопах УТР-2 і ГУРТ), на прикладі джерел Лебідь А і М87. Показано, що за перенесення е-КП, головним чином, відповідають процеси дифузії КП на МГД турбулентності, і захоплення космічних променів квазірегулярним пост-джетовим потоком всередині пелюстки. В ближній околиці горячої плями FRII радіоґалактики космічні промені виносяться регулярно течією разом з пост-джетовим потоком швидше, ніж дифузійним механізмом. Регулярне перенесення і дифузія на вихоровій турбулентності малих масштабів визначають поширення е-КП малих енергій лише у внутрішній частині пелюсток радіо ґалактики; в той же час, як дифузійне поширення променів, що відбувається за рахунок розсіювання на МГД хвилях, є домінуючим механізмом перенесення КП в зовнішніх шарах пелюсток радіоґалактик. В FRI радіоґалактиках переважно домінує перенесення е-КП з течією. Електронні КП малих енергій дифундують повільніше за енергійні е-космічні про-

мені, і вони щільніше прилягають до ліній магнітного поля; в результаті чого, МГц- випромінювання, що спостерігається, підкреслить всі особливості пелюстки, які виникають при перебудові магнітного поля, і ретельніше промалює структуру переднього краю пелюсток в радіоґалактиках обох типів.

Key words: radio galaxy, lobes, FRII, Cygnus A, FRI, M87, cosmic rays, magnetic field, MHD turbulence, transport of CRs, diffusion.

1. Introduction

The model of radio galaxy (RG) as the Jet-Lobe structure is formed at the second part of the 20th century (see Begelman, et al., 1984), and then it was developed in much works, such as Kino, et al. (2004), Canvin J.R., et al. (2005), Mathews, Guo (2011, 2012), Guidetti et al., (2011), and others. It was shown that the magnetic fields in the RG lobes are approximately in equipartition with the cosmic-ray pressure, so that from the radio observations of synchrotron radiation it is possible to estimate the magnetic field strengths. A more detailed analysis (Pudritz et al., 2012), based on wide-ranging RG observations, has now shown that, for most lobes, the magnetic pressure is much less than the plasma pressure, while the magnetic pressure is approximately comparable to the pressure of the thermal and relativistic plasma only inside the jet. Thus, the condition of smallness of the magnetic field inside the lobe indicates that the law of freezing of the magnetic field in the plasma of the lobe should be interpreted as the entrainment of magnetic fields together with the heat plasma streams, and the thermal medium of the lobe is in the processes of constant mixing the intra cluster matter with the substance of post-jet flow.

The evolution of the lobe is accompanied by a number of physical processes. Jet and post-jet streams entrain magnetic fields into the lobe. In the boundary of flow layers, the Kelvin-Helmholtz instability is excited, which converts the energy of the flows into the energy of MHD and eddy (vortex) turbulence, and they, in turn, accompany the processes of amplification of the large-scale quasi regular (average) magnetic field in the jet and in the lobe. The relativistic jet is effectively supported by viscous forces, and by quasi regular magnetic fields that fro-

zen in the jet. In the lobes, there are also processes of mixing media, and accelerating the cosmic rays on shock gaps of jet and post-jet streams. The presence of e-CRs is detected in observations at the form of synchrotron (radio) and inverse Compton (X-ray) radiations.

In this paper, based on the HD-approximations, the formation of the jet-lobe structure and the structure of quasi regular magnetic fields in FRI-FRII radio galaxies are considered. Furthermore, MHD waves are "superimposed" on these lobe structures, and vortex perturbations that participate in mixing processes of the post-jet flow media with CRs and ICM. Finally, we consider the transport of CRs in the RG-lobes with the characteristic parameters of media in both Cygnus A (FRII type) and M87 (FRI type) radio galaxies, taking into account the propagation of CRs in diffuse-scattering by magnetic field fluctuations from MHD and eddy turbulence, and its quasi regular flows with the matter. Conclusions are made about the features of the shape of the lobes visible in the MHz radio band, and about the correlation of the visible shape of the lobe with the physical processes of mentioned above.

2. Magnetic fields and flow structure in the RG-lobe

The quasi-regular magnetic field of the lobe consists of two components: a poloidal B_p -magnetic field, elongated along the post-jet streams of matter, and a toroidal B_ϕ -magnetic field, wrapping the jet and amplified by the diffusion currents. So, the poloidal component of the field is formed under the influence of dynamic flows in the lobe of radio galaxies, and the toroidal field is formed by the diffusion currents associated with the advance of relativistic plasma with cosmic rays into the lobe.

In the case of FRII-lobes, the B_p -component of the field is formed under the influence of the Hill vortex (Tsvyk, 2015) dynamically sweeping up the ICM, adjacent to the wind-flow from the viscous post-jet relativistic plasma "blown" out from the hot spot (HS: the point where the jet is "reflected" in a collision with ICM). This Hill vortex accompanies the formation of a cavity in the FRII lobes, with a large content of rarefied relativistic plasma and CRs coming from the post-jet substance. The structure of the Jet - HS - Hill vortex is a consequence of the steady advancement of a powerful subrelativistic flow which has the high viscous within the rarefied jet-channel medium ($\eta/\rho = 10^{30} \text{ cm}^2/\text{s}$, see Table 1). So, the B_p -magnetic field lines follow along the jet flow, then they follow along the vortex lines flow near the HS, and they go away the lobe near the lobe surface and bow shock.

At the same time, a lobe-tail is formed in the FRI-RGs, they are the less powerful than FRII-RG sources, which show a viscous dissipation of a jet and a post-jet flow, supported by strong B_ϕ magnetic fields. Here: $\eta/\rho = 10^{25} \text{ cm}^2/\text{s}$ (see Table 1). The evolution of this viscous jet can be described within the framework of a simple hydrodynamic model (see, for example: Landau, Lifshitz, 1986); and only consider the magnetic fields as a small addition to the medium pressure. At the same time, it is the magnetic fields that effectively trap the CRs inside the RG-lobes, and the transport of the CRs, as well as their distri-

bution, are closely related to the structure of the large-scale magnetic fields in the lobe.

3. MHD waves in RG lobes and diffusion of media

The quasi-regularly magnetic fields of the lobes change dynamically and are strongly perturbed by large-scale MHD waves (Alfvén and fast magneto-sonic, with wavelengths of $\lambda_w \sim (0.01 \dots 0.1) r_{HS} > 1 \text{ kpc}$), and small-scale vortex perturbations ($\lambda_{mix, vx} \sim c_s \min(\tau_{ib}, \tau_{ia}) \sim 0.1\text{-}3 \text{ pc}$), accompanying the mixing of post-jet plasma and ICM (with small part of atoms, $\rho_a < 10^{-4} \rho_{ICM}$). Vortex perturbations dissipate when they interacting with relativistic particles from post-jet plasma, and their intensity is maximum in the inner part of the lobe ($B_{vx}/B_0 \sim 0.1\text{-}0.3$), where the rate of dissipation of the perturbations is balanced with the rate of their build-up in the processes of diffusion mixing of media. So, the intensity of the MHD waves is maximal in the vicinity of the hot spot, and at the shock front layers ($B_w/B_0 \sim 0.3$), and they decreases with distance from these places, both inside and outside the lobe (up to $B_w/B_0 \sim 0.003$); while, outside the lobe, the magnetic fields again become chaotic ($B_{vx}/B_0 \sim 0.7$).

Inside the lobe of the RG, the characteristics of the MHD waves also change. Thus, according to the MHD concepts (Akhiezer, 1974), the Alfvén waves ($B_{w,A} \sim 0.3 B_0$) accompanying the jet flow (with Doppler shifted velocity, $v_{g,A} \sim c_A + u_{j0} \sim c_A + c/3$) effectively propagate near the jet, and weakly damped in FRII-RG. These waves are accompanied by a rapid energy transfer along the FRII-jet along with the flux of relativistic low-density ρ_{jet} plasma (with a large content of the electron-positron component). They also participate in focusing the wave energy inside the jet channel when the phase matching conditions for wave perturbations ($B_0^2/\rho_{jet} = \text{const}$) are fulfilled in it, and ensure the formation of a bow shock front in the head of the jet. Reflection of A-waves on fluctuations in the density of the jet flow forms a flux of fast MS waves ($B_{w,MS} \sim 0.1 B_0$), diverging from the jet inside the lobe.

In FRI-radio galaxies A-waves dissipate faster than fast MS waves (see table 1); and the dissipation of A-waves is stronger because of the phase-spreading mechanism in the propagation of waves in an inhomogeneous medium. Thus, in low-power FRI-radio galaxies, the jet accompanies a stream of fast MS waves: with MS-waves, $B_{w,MS} \sim 0.2 B_0$, that propagating along the jet at the velocity of $v_{g,MS} \sim c_s + c_A + u_{j0}$.

Inside the lobe, there is a constant mixing of media on pc-scales, $\lambda_{mix, vx}$. The vortex perturbations, excited in these processes, determine the diffusion of the matter of the post-jet flow and the CRs to come they on the periphery of the lobe; and the mixing-diffusion of the ICM to come it inside the lobe, with a diffusion coefficient: $D_{diff, th, vx} \sim \lambda_{mix, vx} c_s \sim 10^{30} \text{ cm}^2/\text{s}$.

At the same time, the ICM is pushed out the lobe under the pressure of the post-jet substance, which is accompanied in FRII-lobes by the blowing out of the post-jet relativistic plasma from the HS, and the formation the dynamic Hill in the head-end of the jet, which first pushes out the ICM medium from the lobe-bubble, and then diffusively returns it to the inside of the lobe.

Table 1: The model of the parameters of FRII-radio galaxy (Cygnus A) and FRI-radio galaxy (M87) recovered under the assumption of the Jet-HS-Lobe structure with viscous fluxes. The main parameters of the sources give by Mathews, Guo (2012, 2011); the other parameters (see right part of table) are calculated by model approximation, according to this paper, Tsvyk (2015) and Toptygin (2007).

| Main parameters | Cygnus A | M 87 | Model parameters | Cygnus A | M87 |
|---|------------------------|--------------------------|---|-----------|-----------|
| Jet-lobe power: L_{jet} , erg/s | $\sim 5 \cdot 10^{46}$ | $\sim 10^{45}$ | Sound velocity, $\langle c_s \rangle / c$ | 0.0012 | 0.0017 |
| Lobe density: $\langle \rho \rangle / m_p$, cm^{-3} | 0.02 | 0.04 | Alfven velocity, $\langle c_A \rangle / c$ | 0.001 | 0.00013 |
| Magnetic field, B , mkG | 300..20 | 15..5 | Collision time, τ_{ii} , Myr | 0.1..1 | 3..10 |
| Lobe presser, $\langle P \rangle$, dyne/cm ² | $<10^{-8}$ | $<10^{-9}$ | Collision time, τ_{ia} , kyr | 10..100 | 0.1..1 |
| HS position, r_{HS} , kpc | 70 | 13 | Kinematic. visc., $\langle \eta_K / \rho \rangle$, cm ² /s | 10^{26} | 10^{24} |
| Lobe length, R_{Lobe} , kpc | 110 | 90..120 | Magnetic visc., $\langle \eta_B / \rho \rangle$, cm ² /s | 10^{17} | 10^{16} |
| HS velocity, u_{HS}/c | 0.01 | <0.1 c _s /c | Viscosity in HS, $\eta_{K HS} / \rho$, cm ² /s | 10^{30} | 10^{28} |
| Bow shock or flow velocity, $u_{tail (Bow shock)}/c$ | $25 c_{s,ext}/c$ | $\sim c_s/c$ | Dumping length, $\lambda_{dump A}$, kpc | 10..100 | 0.1 |
| RG age, t_{age} , Myr | 10 | 30 | Dumping length, $\lambda_{dump MS}$, kpc | 1..3 | 1 |

4. The transport of the e-CR in the RG-lobes. The features of MHz-radio emission

The evolution of the post-jet flow and the transport of e-CRs in the lobes were considered using the toy-model of radio galaxies: the FRII type, like of Cygnus A (see the characteristic parameters inside the lobe at Mathews, Guo (2011) and Table 1), and the FRI type, like of the M87 (see characteristic parameters inside the lobe at Mathews, Guo (2012) and Table 1).

It was assumed in the model that e-CRs are produced from the jet-HS at these distances from AGNs: $r_{HS} = 70$ kpc (for Cygnus A) and 13 kpc (for M87) (see Table 1). Next, we considered: the regular transport of the e-CRs together with the fluxes of post-jet plasma (which determines the characteristic “radiation” age of the e-CRs, $\Delta t_{age} = |\vec{r} - \vec{r}_{HS}| / u_{flow}$; and diffusion transport of CR due to their scattering by small-scale vortex and large-scale MHD turbulences. In FRII radio galaxies, the post-jet stream is controlled by a dynamic Hill vortex, spinning at a transonic velocity near the HS ($\Delta t_{age} \sim 0..10$ Myr); and in FRI-RG there is an inertial advance of the post-jet flow from the HS with subsonic speed in the form of a viscous expanding jet-tail ($\Delta t_{age} \sim 0..30$ Myr).

The diffusion transport of the e-CRs at each given moment can be characterized by $\gamma = E/(m_e c^2)$, the diffusion-path length for the CRs of a given energy. In these cases, the diffusion of CRs in scattering by small-scale vortex turbulence is characterized by a coefficient that not varies from CR energy ($D_{diff_CR_Vx} \sim D_{diff_th_Vx}$), and the coefficient

for CR-diffusion on MHD fluctuations of the magnetic field depends on the CRs energy as (Toptygin, 1986):

$$D_{diff_MHD}(\gamma, \dots) \sim (\Lambda_{\parallel Be}(\gamma, \dots) \cdot c/3) \cdot fct(B_{\parallel}, B_{\phi});$$

$$\Lambda_{\parallel Be}(\gamma, \dots) \sim (B_w / B_0)^{-2} \left(\frac{L_0}{R_{gB}} \right)^{2/3} R_{gB} \gamma^{1/3},$$

$$L_0 \sim \lambda_{dump,A} + \lambda_{dump,MS} = \rho(\eta_K + \eta_M)^{-1} \cdot c_A^3 \omega_{A0}^{-2} + \frac{1}{2} \rho(\eta_K + \eta_M)^{-1} \cdot c_S^3 \omega_{MS0}^{-2},$$

here $R_{gB}(B_0)$ is gyro radius of low energy e-CR at $\gamma=2$, L_0 is correlation length of the MHD fluctuations, that is proportional to the wave-dumping lengths (at waves frequency of $\omega_{A0} \sim \omega_{MS0} \sim 10^{-5} yr^{-1}$).

The Figures 1 and 2 show the maps of the characteristic diffusion transport lengths for the FRII RG (Cygnus A) and the FRI RG (M87): (a) - for the post-jet flow matter; and (b)- for the e-CRs with energies of $\gamma = 30..300$ (it corresponds to the synchrotron radio emission in the MHz band with a magnetic field strength of $\sim 5..20$ mkG). It was believed that the post-jet relativistic plasma is transported from the jet due to the quasiregular flow, and the diffusion by eddy turbulence:

$$\lambda_{pj_Diff,reg} \sim (D_{diff_rel_Vx} \cdot \Delta t_{age})^{1/2} + (0.1..1)c_s \Delta t_{age},$$

and the e-CRs are transported due to the quasiregular flow, and the diffusion by eddy turbulence and MHD waves:

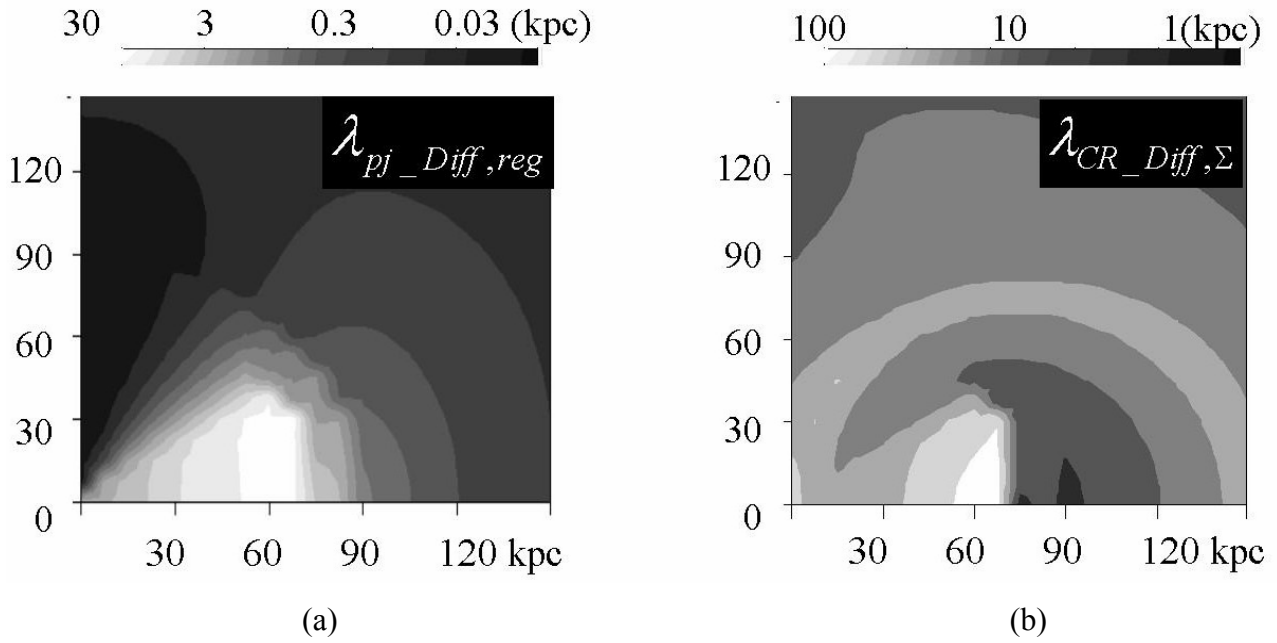


Figure 1: The maps of the characteristic matter transport lengths for the FRII radio galaxy (like Cygnus A): (a) – for the post-jet matter; and (b) – for the e-CRs with energies of $\gamma=30$ (it corresponds to the synchrotron radio emission in the MHz band with a magnetic field strength of 20 mG).

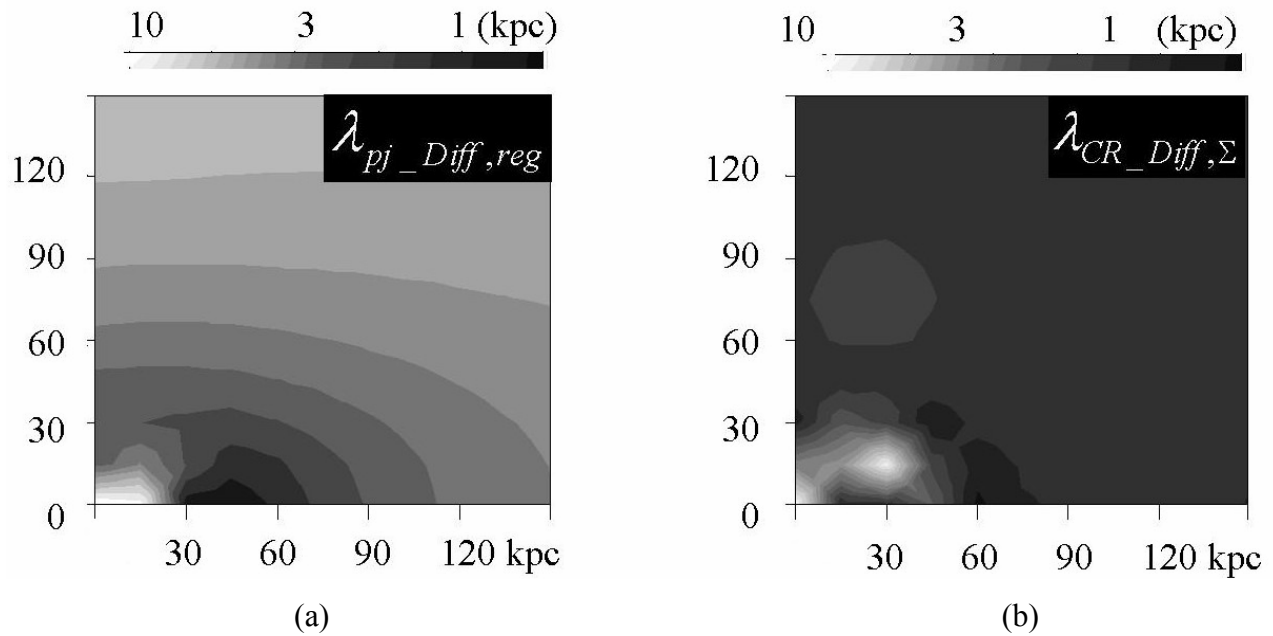


Figure 2: The maps of the characteristic matter transport lengths for the FRI radio galaxy (like M87): (a) – for the post-jet matter; and (b) – for the e-CRs with energies of $\gamma=300$ (it corresponds to the synchrotron radio emission in the MHz band with a magnetic field strength of ~ 5 mG).

$$\lambda_{CR_Diff,\Sigma} \sim \left((D_{diff_MHD} + D_{diff_Vx}) \cdot \Delta t_{age} \right)^{1/2};$$

$$\lambda_{CR,\Sigma} \sim \lambda_{pj_reg} + \lambda_{CR_Diff,\Sigma}.$$

It can be seen from the calculations (Fig. 1) that in FR II RG the transport of CRs is mainly determined by the diffusion of CRs, with vortex turbulence responsible for the transfer within the lobe, and MHD waves in the outer layers of the lobe. So: $\lambda_{pj_Diff,reg} = (1-7)$ kpc; $\lambda_{CR_Diff,\Sigma} = (0.1-10)$ kpc. Only in the near vicinity of HS RG carried out a regular flow along with the post-jet stream a little faster than the diffusion mechanism.

Then, in FRI-radio galaxies (Fig. 2), the diffusion mechanism carries the CRs more slowly than the regular flow: $\lambda_{pj_Diff,reg} \sim \lambda_{pj_reg} = (1-10)$ kpc; $\lambda_{CR_Diff,\Sigma} = (1-3)$ kpc. Although, in the anterior part of the post-jet lobe-tail, the diffusion of CRs at $\gamma \sim 300$ by MHD turbulence overlaps its regular floating of the lobe, and becomes the diffusion as the determining mechanism in the CR-transport.

5. Conclusions

Thus, it was shown that regular transport and diffusion on small-scale eddy turbulence determine the propagation of low-energy e-CR only in the inner part of the RG lobes; while the diffusion propagation due to scattering by MHD waves is the dominant mechanism for the transfer of CR in the outer layers of the RG-lobes. In this case, the radio emission of CRs in the MHz band will emphasize the features of the structure of the magnetic field in the lobes, outlining the areas of locking the CR of low energies, so that observations of the UTR-2 and GURT can monitor the tuning of the quasiregular magnetic field of the lobe, revealing the regions of brightness of the MHz radio emission in the lobes of the radio galaxy.

References

- Begelman M.C., et al.: 1984, *Rev. Mod. Phys.*, **156**, 255.
 Kino M., et al.: 2004, *MNRAS*, **349**, 336.
 Canvin J.R., et.al.: 2005, *MNRAS*, **363**, 1223.
 Guidetti D. et al.: 2011, *MNRAS*, **413**, 2525.
 Pudritz R.E. et al.: 2012, *Space Sci. Rev.*, **169**, 27.
 Tsyk N.O.: 2015: *Odessa Astron. Publ.*, **28**, 248.
 Landau L.D., Lifshitz Y.M.: 1986, *Hydrodynamic/ Theoretical physics* (in Russian), Moscow, **6**, 118.
 Akhiezer A.I.: 1974, *Plasma electrodynamics* (in Russian), Moscow.
 Mathews W.G. et al.: 2012, *ApJ*, **755**, 13.
 Mathews W.G. et al.: 2011, *ApJ*, **736**, 6.
 Bykov A. M. et al.: 2007, *Physics–Uspekhi*, **50**, 141.
 Toptygin I.N.: 1983, *Cosmic rays in intra planetary magnetic fields* (in Russian), Moscow.

SUN, SOLAR ACTIVITY AND ASTROBIOLOGY

DOI: <http://dx.doi.org/10.18524/1810-4215.2018.31.144543>

NEW APPROXIMATION OF THE ENERGY SPECTRUM OF PROTON SCR

E.A. Isaeva

Institute of Radio astronomy of NAS of Ukraine, isaevaode@gmail.com

ABSTRACT. In this paper, we consider a new approximation of the integrated energy spectrum of protons of solar cosmic rays (SCR) in the range $E_p > 1-100$ MeV. The sample studied contains 342 proton events for the period from 03-02-1986 to 23-07-2016. This sample is complete, since it contains very weak and superimposed proton events. The superimposed events were separated and identified according to the criteria of protonity. Out of 342 proton events, 164 events were identified and processed by the author independently. For the analysis, original records of the intensity of the proton flux with energy $E_p > 1-100$ MeV from the spacecraft GOES series were used. As the parameter characterizing the intensity of the proton flux, the maximum intensity of the proton flux I_p in each energy channel during the proton event was chosen. The intensity of the proton flux I_p was calculated from the preflare level. In the case of superposition of proton events, the intensity of the proton flux I_p was calculated from the level of the preceding event. Also, when processing original records of proton events, emissions associated with technical interference and with the of interplanetary shock waves were eliminated. Comparative analysis showed that all events can be conditionally divided into 5 types according to the form of the energy spectrum of protons. It is known that for most proton events, the energy spectrum of SCR protons is described quite accurately by two power-law models. However, there remains a large number of events for which the energy spectrum of protons can not be approximated accurately by two power-law models. In connection with this, another dependence was used in this work, which allows us to approximate the energy spectrum of the protons for all events quite accurately.

АБСТРАКТ. У даній статті розглядається нова апроксимація інтегрального енергетичного спектра протонів сонячних космічних променів (СКП) в діапазоні $E_p > 1-100$ MeV. Досліджувана вибірка містить 342 протонних подій за період з 03-02-1986 по 23-07-2016 року. Дана вибірка є повною, оскільки містить дуже слабкі і накладені протонні події. Накладені події поділялися і ототожнювалися відповідно до критеріїв протонності. З 342 протонних подій 164 події були ототожені і оброблені автором самостійно. Для аналізу були використані оригінальні записи інтенсивності потоку протонів з енергією $E_p > 1-100$ MeV з космічних апаратів серії GOES. Як параметр, що характеризує інтенсивність потоку протонів, було вибрано максимальне значення інтенсивності потоку протонів

I_p в кожному енергетичному каналі під час протонної події. При цьому інтенсивність потоку протонів I_p обчислювалася від рівня перед спалахом. У разі накладення протонних подій інтенсивність потоку протонів I_p обчислювалася від рівня попередньої події. Також при обробки оригінальних записів протонних подій виключалися викиди, пов'язані з технічними перешкодами і з накладенням міжпланетних ударних хвиль.

Порівняльний аналіз показав, що всі події можна розділити умовно на 5 типів за формою енергетичного спектру протонів. Відомо, що для більшості протонних подій енергетичний спектр протонів СКП досить точно описується двоступеневими моделями. Однак залишається велика кількість подій, для яких енергетичний спектр протонів неможливо точно апроксимувати двоступеневими моделями. У зв'язку з цим в цій роботі була використана інша залежність, що дозволяє досить точно апроксимувати енергетичний спектр протонів для всіх подій.

Keywords: Proton events, energy spectrum of protons, intensity of the proton flux.

1. Introduction

The spectrum of solar cosmic rays (SCR) for most solar proton events can overlap 4-5 orders of magnitude in energy from 1 MeV to $\geq 10-100$ GeV. The difference in intensities at the edges of the spectrum, due to the large steepness of the spectrum in the high-energy region, can reach 6-8 orders of magnitude (Miroshnichenko, 2000). And this creates certain difficulties in the approximation and interpretation of the observed energy spectra of proton events. In narrow energy intervals, SCR researchers most often use power-law and exponential functions to approximate the energy spectrum of SCR protons. Sometimes a more complex representation of the spectra is used in the form of a combination of a power-law and exponential function with a cutoff of the energy spectrum (Akin'ian et al., 1983; Ellison et al., 1985), and also a spectrum representation by two power-law functions with a inflection point at a certain energy (Band et al., 1993; Mewaldt et al., 2005; 2006; 2012). The variety of models for approximating the SCR spectra indicates that the formation of a spectrum taking into account the conditions at the source and taking into account transport effects in interplanetary space can not be accurately described by simple relations.

In this connection, attempts are being made to empirically represent the spectrum from the observed values of the proton flux over a wide energy range. In reality, it is very difficult to obtain the true spectrum of accelerated protons in the source (Miroshnichenko, 2014; 2018). The influence of propagation effects of accelerated protons in interplanetary space leads to a large variety of spectra in form and intensity.

2. Initial data and methods for processing proton events

For the analysis, we used the original records of the intensity of the proton flux I_p with the energy E_p in the range $E_p > 0.8-100$ MeV from data from apparatuses of the GOES series (https://satdat.ngdc.noaa.gov/sem/goes/data/new_avg/), and also a list of solar proton events (SPE). The sample studied contains 342 proton events for the period from 03-02-1986 to 23-07-2016. This sample is complete, since it contains almost all events registered for the specified period, including very weak events and superimposed events, which were separated and identified by the author independently. In this connection, errors associated with the separation and identification of proton events are possible. In this sample of 342 SEP 164 events were identified by the author, and the remaining events are present in the SEP directory (<ftp://ftp.swpc.noaa.gov/pub/indices/SPE.txt>). For all these events, an attempt was made to find a single empirical dependence of the proton flux intensity I_p on the proton energy $E_p > 0.8-100$ MeV. To this end, original records of the intensity of the proton flux I_p with the energy E_p in the range $E_p > 0.8-100$ MeV for all 342 proton events were processed. As a parameter characterizing the proton flux, the maximum intensity of the proton flux I_p of a given energy was chosen during the proton event. The value of the I_p parameter was calculated from the preflare level. In the case of superposition of proton events, the value of I_p was calculated from the level of the previous proton event. Emissions associated with interference and with the imposition of shock waves were also eliminated.

3. Types of integral energy spectra of protons SCR in the range $E_p > 1-100$ MeV and their approximation

After calculating the maximum values of the proton flux I_p , the observed integral energy spectra of protons for all proton events were constructed and analyzed in each energy channel. A comparative analysis showed that all proton events can be conditionally divided according to the form of the observed energy spectrum into 5 characteristic types, see Fig. 1 (left). The observed values of the intensity of the proton flux in Fig. 1 (on the left) are indicated by black badges, the fine black line shows the calculated values of I_p calculated using the regression model (1), where a , b , c and d are the coefficients of the regression model (1). The coefficients of the regression model were calculated using the method of least squares. This functional (1) contains three functions (2-4) and allows us to estimate the intensity of the proton flux I_p with the

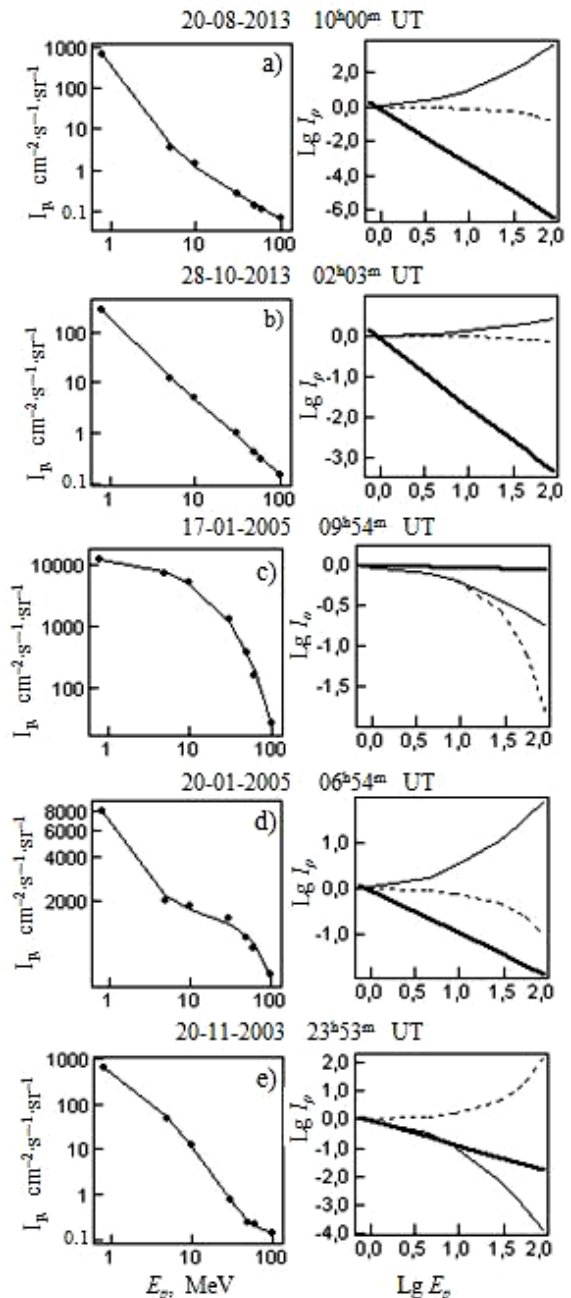


Figure 1: Types of spectra and their approximations

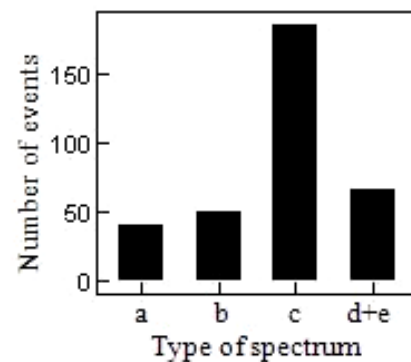


Figure 2: Histogram of the distribution of events with this type of spectrum

$$I_p = 10^d \cdot E_p^a \cdot 10^{bE_p} \cdot 10^{c \cdot (\log_{10} E_p)^2} \quad (1)$$

$$I_p = E_p^a \quad (2)$$

$$I_p = 10^{bE_p} \quad (3)$$

$$I_p = 10^{c \cdot (\log_{10} E_p)^2} \quad (4)$$

$$I_p = 10^d \cdot E_p^a \cdot e^{bE_p} \quad (5)$$

energy E_p in the range $E_p > 0.8-100$ MeV quite accurately. This functional is obtained exclusively empirically and this is its main drawback, since it is impossible to estimate the real contribution of these or those mechanisms to the acceleration of SCR protons. But nevertheless, this functional allows us to estimate the contribution of a parameters (2-4) in the functional (1) to the observed intensity of the proton flux I_p . In Fig. 1 (right) shows the contribution of each parameter to the intensity of the proton flux. For convenience, the values of the logarithms E_p and I_p , respectively, are plotted along the X and Y axes. In Fig. 1 (right) shows that for events having different characteristic types of spectra, a different contribution of the parameters (2-4) in the functional (1) to the intensity of the proton flux is observed.

Thus, in Fig. 1 b) (right), it is clear that the main contribution to the proton flux I_p comes from processes that are described by a power-law function (2) (a thick line), while the contribution of the remaining parameters is insignificant. For events with the characteristic type of the spectrum in Fig. 1 c) (on the right), on the contrary, the main contribution is made by processes described by exponential functions, denoted by a dashed (3) and thin solid line (4). While the contribution from the power-law function (2) is insignificant and constant. For events having a combined type of spectrum, see Fig. 1 d) and e) (right), the processes described by the three parameters (2-4) contribute to the observed proton flux. In Fig. 2 shows a histogram of the distribution of the number of events with a given type of energy spectrum of protons SCR. The X-axis shows the type of the spectrum. On the histogram, events having the type of the spectrum d) and e) in Fig. 2 are summed. Figure 2 shows that more than half of all proton events have the type of spectrum shown in Fig. 1c).

Convinced that the regression model (1) gives a fairly good approximation of the SCR proton flux for 5 events with the characteristic types of observed spectra, proton fluxes for all 342 proton events were calculated. In Fig. 3 shows the scattering diagrams between the observed and calculated values of the proton flux with energy in the range $E_p > 5-100$ MeV. The X and Y axes show the calculated and observed values of the proton flux I_p , respectively. Figure 3 shows that the regression model (1) gives a fairly good approximation for all 342 proton events.

4. Comparison and discussion of the results

It was noted above that the functional (1) is purely empirical and does not allow us to estimate the real contribution of these or other mechanisms (processes) to the acceleration of SCR protons. Therefore, it is advisable to compare

the calculated values of the intensity of the proton flux with the help of the functional (1) and standard functionals, which predict the models of the proton acceleration of SCR. For comparison, a functional containing the power-law and exponential function (5) was chosen.

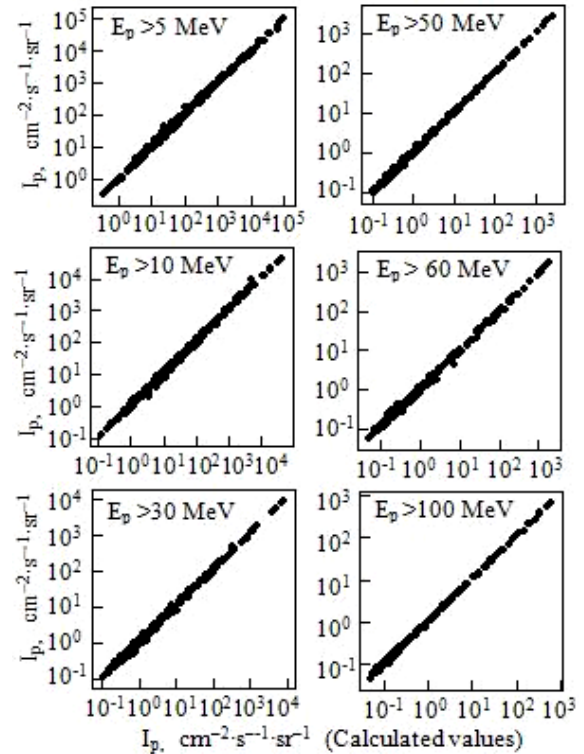


Figure 3: Diagrams of scattering between observed and calculated values of I_p

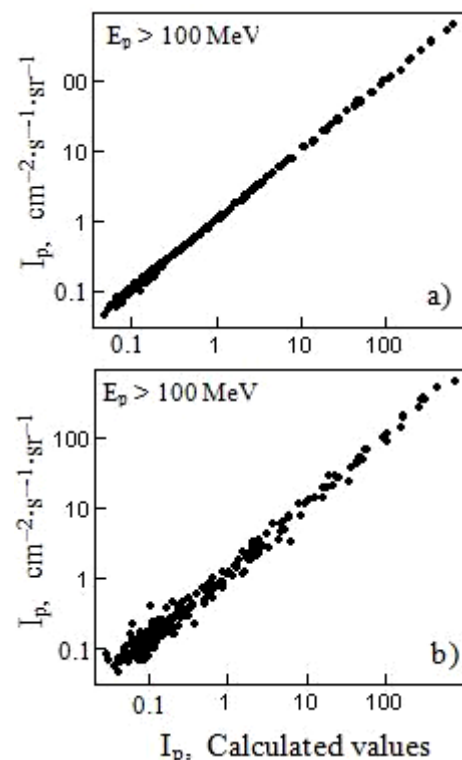


Figure 4: Diagrams of scattering between observed and calculated values of I_p

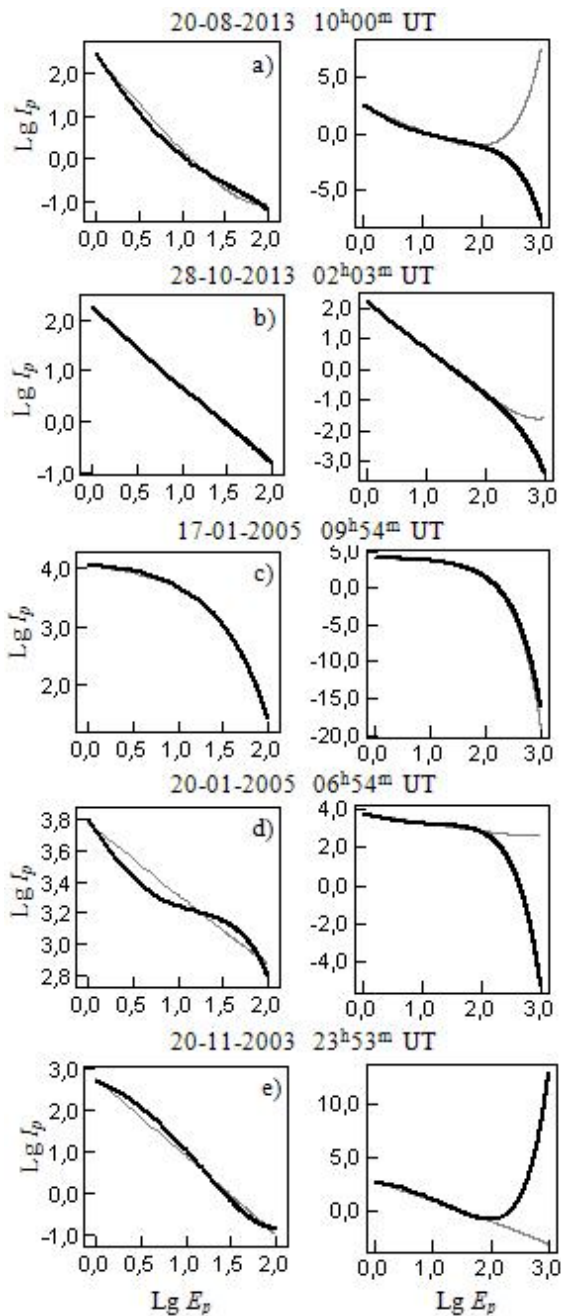


Figure 5: A comparison of the dependences of $Lg I_p$ on $Lg E_p$ in the range $E_p > 1-1000$ MeV obtained with the help of the functionals (1) and (5)

In Fig. 4 a) and b) are diagrams of the scattering between the observed and calculated values of the proton flux with energy $E_p > 100$ MeV, calculated with the help of the functionals (1) and (5). In Fig. 4b), it is seen that for the values of the proton flux calculated with the help of the functional (5), there are quite large deviations between the calculated and observed values of the intensity of the proton flux, while for the values of the proton flux calculated with the help of the functional (1), the calculated and observed values of the proton flux practically coincide.

It is known that the behavior of the limiting integral empirical spectrum (Mirishnichenko et al., 1994; 1996; 2013;) and the limiting physical spectrum (Struminsky, 2015) of SCR protons significantly differs at the spectral

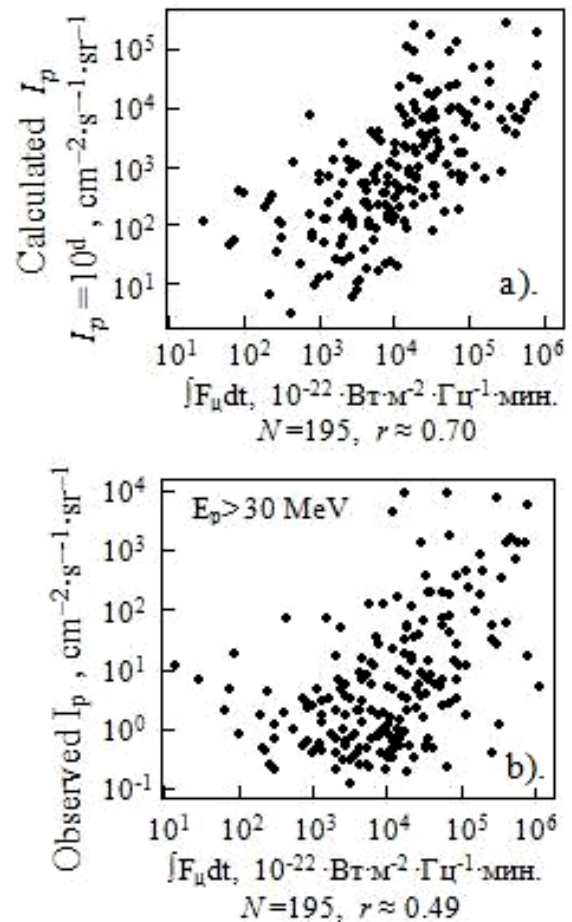


Figure 6: The relationship I_p and parameter 10^u with the integral flux of microwave bursts $[F_p dt]$

edges in the region of low energies and in the region of relativistic energies. In this connection, the behavior of the functionals (1) and (5) for protons with energy in the range $E_p > 1-1000$ MeV was investigated. Comparative analysis showed that for protons with energies in the range $E_p > 1-100$ MeV, both functionals give a fairly good agreement between the calculated values of I_p for the 5 characteristic types of the spectrum, see Fig. 5 (left). However, for protons with energies $E_p > 100-1000$ MeV, considerable deviations are observed between the calculated values of the proton flux calculated with the help of the functionals (1) (black bold line) and (5) (gray thin line), see Fig. 5 (right). In this figure, for proton events with characteristic types of the spectrum a), b) and d), the calculated values of the proton flux I_p increase with increasing proton energy E_p (thin gray line), which is unrealistic. The same situation is observed for the calculated proton fluxes with the help of the functional (1) for events having the characteristic type of the spectrum in Fig. 5 (e) (left). However, for the vast majority of proton events, the functional (1) predicts more or less real values of the computed proton fluxes with an energy $E_p > 100-1000$ MeV. It should be noted that both functional (1) and (5) give a fairly good agreement between the calculated values of the intensity of the proton flux with energy in the range $E_p > 1-1000$ MeV for events having the characteristic type of the spec-

trum in Fig. 5 (c). As noted above, events with this type of spectrum account for more than 50% of the total number of proton events.

5. Relationship between the observed and calculated values of the intensity of the proton flux I_p with the integral flux $\int F_{\mu} dt$ of microwave bursts

Also, the connection between the parameters in the functional (1) and the integral flux $\int F_{\mu} dt$ of microwave bursts at a frequency of 8800 MHz was investigated. The investigated sample contains 195 proton events for the period from 06-02-1986 to 20-12-2014. Comparative analysis showed that there is a sufficiently strong connection between the integral flux $\int F_{\mu} dt$ of microwave bursts and the parameter 10^d in the functional (1), where the correlation coefficient r between the investigated quantities is about 0.70 (see Fig. 6 a)). At the same time, the connection between $\int F_{\mu} dt$ and the observed intensity of the proton flux I_p ($E_p > 30$ MeV) is much worse ($r \approx 0.49$), see Fig. 6 b). Recall that the parameter 10^d in the functional (1) characterizes the initial (total) number of accelerated protons with $E_p > 1-100$ MeV. The presence of a strong connection between the integral flux $\int F_{\mu} dt$ of microwave bursts and the parameter 10^d agrees with the previously obtained results in the work (Chertok, 1982), which states that the parameters of microwave bursts can be used to estimate the total number of accelerated particles and their energy spectrum.

The presence of a sufficiently strong connection between $\int F_{\mu} dt$ and the parameter 10^d , indicates that the main acceleration of protons occurs in the flare region. In Fig. 6 b) there are significant deviations of the observed values of the intensity of the proton flux I_p relative to the values of the integral fluxes $\int F_{\mu} dt$ of microwave bursts. Significantly overestimated observed values of the intensity of the proton flux I_p can probably be explained by the additional acceleration of protons by shock waves, and significantly underestimated values can be explained by the effects of propagation of accelerated protons in the solar corona and in interplanetary space.

6. Conclusion

The results obtained are preliminary, since the final conclusion regarding the accuracy of the approximation of the observed energy spectra of the SCR protons with the help of the functional (1) can be made only after careful studies have been carried out between the calculated and observed values of the proton flux with energy $E_p > 100-1000$ MeV. Which is supposed to be done in the next work.

References

- Akin`ian S., Logachev Iu.: 1983, *Catalogue of Solar Proton Events 1970-1979*, IZMIRAN.
- Band D., Matteson J., Ford L. et al.: 1993, *Astrophys. J.*, **413**, 281.
- Chertok I.: 1982, *Geomagnetizm i Aeronomiia*, **22**, 182.
- Ellison D., Ramaty R.: 1985, *Astrophys. J.*, **298**, 400.
- Mewaldt R., Cohen C., Labrador A. et al.: 2005, *Geophys. Res.*, **110**, A09S18.
- Mewaldt R.: 2006, *Space Sci. Rev.*, **124**, 303.
- Mewaldt R., Looper C., Cohen D. et al.: 2012, *Space Science Reviews*, **171**, Issue 1-4, 97.
- Miroshnichenko L.: 1994, *Geomagnetizm i Aeronomiya*, **34**, 29.
- Miroshnichenko L.: 1996, *Radiation Measurements*, **26**, 421.
- Miroshnichenko L., De Koning C., Perez-Enriquez R.: 2000, *Space Sci. Rev.*, **91**, 615.
- Mirishnichenko L., Vashenyuk E., Perez-Peraza J.: 2013, *Geomagnetism and Aeronomy*, **53**, 541.
- Miroshnichenko L.: 2014, *Solar Cosmic Rays: Fundamentals and Applications 2nd ed.*, (New York: Springer).
- Mirishnichenko L.: 2018, *Phys. Usp.*, **61**, 323.
- Struminskiy A.: 2015, *Solnechnaya i solnechno-zemnaya fizika-2015*, 343.

DOI: <http://dx.doi.org/10.18524/1810-4215.2018.31.144560>

PROBLEM OF SUPER-STRONG MAGNETIC FIELDS ON THE SUN: BRIEF CHRONOLOGY AND NEW OBSERVATIONAL DATA

V.G. Lozitsky¹, V.B. Yurchyshyn², K. Ahn², H. Wang², N.I. Lozitska¹

¹ Astronomical Observatory of the Taras Shevchenko National University
of Kyiv, Kyiv, Ukraine, lozitsky@observ.univ.kiev.ua, nloz@observ.univ.kiev.ua

² Big Bear Solar Observatory, New Jersey Institute of Technology,
Big Bear City, USA, vayur@bbsso.njit.edu

ABSTRACT. In this study we present the old and new observational data concerning the problem of extreme magnetic fields (≥ 5 kG) in the Sun's atmosphere. We emphasize that the upper limit of the intensity of the magnetic field in the solar atmosphere is unknown to date. Severny (1957) heuristically suggested that the magnetic fields in the sunspots could reach 50 kG. As for the observational data, at least three arguments in favor of the magnetic fields of the order of $\leq 10^4$ G can be specified: (1) the dependence of the measured magnetic field on the factor $g_{\text{eff}}\lambda^2$ of magnetosensitive lines (Gopasyuk et al., 1973; Lozitsky, 1980), (2) local extremums in splitting of bisectors in the profiles $I \pm V$ for lines with different Lande factors (Lozitsky, 1980; 2015) and (3) the reliable splitting of emission peaks in Fe I lines with very low Lande factors, about 0.01, in the spectra of powerful solar flares (Lozitsky, 1993; 1998). Theoretically, superstrong fields should have gigantic magnetic pressure and can exist only with a specific topology of field lines, apparently of a force-free type (Soloviev and Lozitsky, 1986). To further develop this problem, we are analyzing new observational data obtained with the NIRIS spectropolarimeter of the largest GST solar telescope of the Big Bear Solar Observatory (BBSO). Our observations relate to the active region NOAA 12673, which was the most flare-productive in the 24th cycle. Stokes-metric measurements are made in the Fe I 15648.5 Å line with a signal-to-noise ratio of about 10^4 . In this active region, superstrong magnetic field of 5.57 kG was discovered recently by Wang et al. (2018). An additional study of about 70 different places in this active region suggested that there were two types of places that can be conventionally called "typical" and "peculiar". In "typical" areas, the magnitude of the magnetic field in general is the greater, the less the intensity in the spectral continuum, and the maximum field here does not exceed 4 kG. All "peculiar" places correspond to positions with the highest intensity in the spectral continuum, and the magnetic field strength is here in the range of 3.0-5.7 kG. Notice, such strong magnetic fields were firstly discovered outside the sunspot umbra. The orientation of the magnetic field vector in "peculiar" places is close to the transversal, which is also atypical for "typical" regions and can reflect strong twisting of field lines.

Keywords: Sun, solar activity, sunspots, solar flares, magnetic fields, spectral lines, the Zeeman effect, superstrong magnetic fields.

АБСТРАКТ. У цьому дослідженні ми представляємо старі й нові спостережні дані, що стосуються проблеми екстремально сильних магнітних полів (≥ 5 кГс) в атмосфері Сонця. Ми наголошуємо, що верхня межа напруженості магнітного поля в атмосфері Сонця є на сьогодні невідомою. Северний (1957) припускав евристично, що магнітні поля у сонячних плямах можуть досягати 50 кГс. Щодо спостережних даних, то можна вказати принаймні три аргументи на користь магнітних полів рівня $\leq 10^4$ Гс: (1) залежність вимірюваного магнітного поля від фактора $g_{\text{eff}}\lambda^2$ магніточутливих ліній (Gopasyuk et al., 1973; Lozitsky, 1980), (2) локальні екстремуми розщеплення бісекторів у профілях $I \pm V$ для ліній з різними факторами Ланде (Lozitsky, 1980; 2015) і (3) достовірне розщеплення емісійних піків в лініях Fe I з дуже низькими факторами Ланде, близько 0.01, у спектрах потужних сонячних спалахів (Lozitsky, 1993; 1998). Теоретично, надсильні поля повинні мати гігантський магнітний тиск і можуть існувати лише при специфічній топології силових ліній, очевидно, безсилового типу (Soloviev and Lozitsky, 1986). Для подальшої розробки цієї проблеми ми аналізуємо нові спостережні дані, отримані на спектрополяриметри NIRIS найбільшого на сьогодні сонячного телескопа GST обсерваторії Біг Бер (BBSO). Наші спостереження стосуються активної області NOAA 12673, яка була найбільш спалахово-продуктивною у 24-му циклі. Стокс-метричні вимірювання виконані в лінії Fe I 15648.5 Å при відношенні сигнал/шум близько 10^4 . Саме в цій області були недавно виявлені магнітні поля з напруженістю 5.57 кГс (Wang et al., 2018). Додаткове дослідження приблизно 70 різних місць цієї активної області показало, що в ній існували ділянки двох типів, які умовно можна назвати «типовими» і «специфічними». В «типових» ділянках величина магнітного поля в цілому тим більша, чим менша інтенсивність в континуумі, причому максимальне поле тут не перевищує 4 кГс. Всі «специфічні»

ділянки відповідали місцям з найбільшою інтенсивністю у спектральному континуумі, причому напруженість магнітного поля тут в межах 3.0-5.7 кГс. Слід зауважити, що такі сильні магнітні поля були вперше виявлені за межами тіней сонячних плям. Орієнтація вектора магнітного поля в «специфічних» ділянках близька до трансверсальної, що також нетипово для «типових» ділянок і може вказувати на сильне скручування силових ліній.

Ключові слова: Сонце, сонячна активність, сонячні плями, сонячні спалахи, магнітні поля, спектральні лінії, ефект Зесмана, надсильні магнітні поля.

1. Introduction

The upper limit of the magnetic field strength in the solar atmosphere is unknown at present. The predominant point of view is that the strongest fields can be found in the darkest parts of the umbra of largest sunspots. According to observations, the field strength in the umbra is, on average, 2100–2900 G, reaching at times 3500–4000 G (Solanki, 2003; Lozitska, 2010). Earliest measurements by Baranovsky and Petrova (1957), and Steshenko (1968) showed that the field strength in sunspot may reach 4900 G and 5350 G, respectively. The record field of 6100 G in a sunspot umbra was reported by Livingston et al (2006).

As far as sunspot penumbra is concerned, Van Noort et al. (2013) found very strong fields ($B = 7\text{--}7.5$ kG) in places with significant plasma downflows of 20 km / s.

We note that while Livingston et al. (2006) directly measured Zeeman splitting in various spectral lines with large Lande factors, Van Noort et al. (2013) analyzed full Stokes vector spectropolarimetry using an indirect Fourier technique to probe smallest spatial scales. It is also worth noting that when magnetic fields reach 7–8 kG and the Doppler velocities reach 20 km/s, the Fe I 6301.5 and 6302.5 Å lines used in Van Noort et al. (2013) should be considered as mutually blended. This, of course, complicates diagnostics of very strong fields (Lozitsky, 2016).

Perhaps, extremely strong magnetic fields can exist in spatially unresolved structures with very small filling factor f ($f \ll 1$). In this case, they may manifest themselves as a very weak Zeeman effects in the spectrum. Lozitsky (2016, 2017) found evidence of presence of 8-kG fields in the sunspot umbra. The filling factor there is thought to be 0.2–0.3 here, and relative Doppler velocities associated with upflowing plasma (excluding Evershed's flows) range from -1.7 to -3.1 km / s.

Solar flares are interesting and violent processes in solar active regions where the strongest fields could exist as well. Each flare is a grandiose explosion occurring in a wide range of heights in the solar atmosphere, with a sharp increase in temperature, gas pressure and ionization of plasma. Hot pressurized flaring plasma outside magnetic flux tubes may press on walls of these tubes thus increasing magnetic strength inside the tubes. In addition, increased of plasma ionization leads to amplification of electric currents and to magnetic field intensification, if the structure of underlying magnetic field is force-free.

There were suggestions that magnetic fields with strength of tens of kilogauss may also exist on the Sun. Thus, Severny (1957) supposed the 50 kG fields in small-scale spatially unresolved magnetic elements of sunspots, which are averaged out when they are measured with insufficient spatial resolution.

Bruce (1966) suggested that during a flare extended wings of H α line (till 8 Å) could intensify due to Zeeman effect in 10–100 kG fields. Really, this is one of possible interpretation: a some account to the line-profile broadening should give also temperature, turbulent velocity and electric fields. For these effects separation, the full Stokes parameters I , Q , U and V of polarized light are needed. On the other hand, if the magnetic field is tangled at sub-telescopic scales (for instance, in a form of mixed polarity structures) the Stokes diagnostics can not be applied since we can have essential broadening of Stokes I profile but practically zero polarization at various distances from line center.

With the advances in solar instrumentation there is renewed interest in superstrong magnetic fields on the Sun as evidence by the most recent publications (Wang et al., 2018, Takenori et al., 2017).

The objective of our work is twofold, namely, we would like to review previous studies devoted to the problem of superstrong field, as well as to present new relevant results. Here we present main arguments in favor of the existence of especially strong magnetic fields.

2. First Argument: Dependence of Measurements on the $g\lambda^2$ Factor

In 1973, an important observational result was obtained, which may be considered as an indirect indication of the existence of extremely strong magnetic fields outside sunspots and flares. Gopasyuk et al. (1973) found an unexpected dependence of relative observed field $R_i = B_{\parallel}(\lambda_i)/B_{\parallel}(6103)$ on magnetic sensitivity factor $g\lambda^2$ using magnetographic data obtained in 13 spectral lines λ_i (Fig. 1). The data were obtained with the solar magnetograph of Crimea Astrophysical observatory. Longitudinal magnetic fields, B_{\parallel} , were measured in range $|B_{\parallel}| \leq 100\text{--}200$ G using Stokes V parameter. In this field range, the weak field approximation is applicable, when $B_{\parallel} \sim V/g\lambda^2$. Due to this reason, measured fields should not be dependent on $g\lambda^2$ factor, assuming that the solar magnetic fields are really weak. Contrary to the above reasoning, a remarkable dependence was found: R_i values were nearly the same for the lines with high magnetic sensitivity, while these values display a rapid grown for the lines with decreasing $g\lambda^2$ factor.

Similar dependence was also observed by Lozitsky (1978) using Stokes I data recorded by the Crimea spectrograph in areas of two weak solar flares, where the measured magnetic field was stronger, ≤ 1000 G (triangles in Fig. 1). The magnetic field were estimated by observed Stokes I intensity gradient, $dr_i/d\lambda$, measured for about ten Fe I lines and compared with theoretical expectations derived from Unno (1956) theory. One can see from Fig. 1 that Stokes V and I measurements are in excellent agreement, which seemingly rules out the instrumental nature of the above mentioned effects and suggests that it has an solar origin.

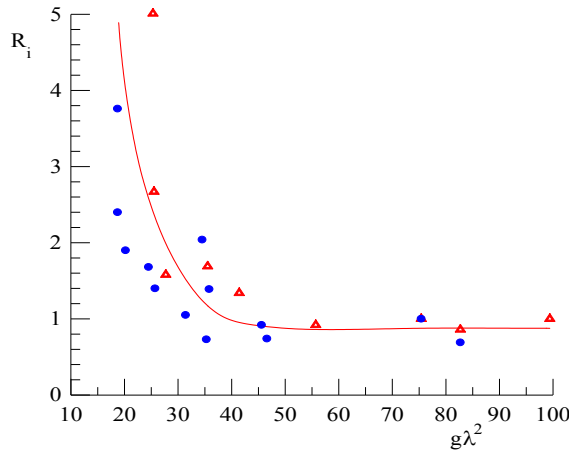


Figure 1: Observed dependence of the relative observed field $R_i = B_{\parallel}(\lambda_i)/B_{\parallel}(6103)$ on the magnetic sensitivity factor $g\lambda^2$ as derived from Stokes V (filled dots) and Stokes I (triangles) parameters.

Lozitsky (1980) further showed that such dependence may arise in case that the underlying magnetic field is two-component consisting of a relatively weak background field and spatially unresolved magnetic elements with strong fields of order of 8-10 kG, depending on the spectral line half-width and Doppler velocities present in these assumed sub-telescopic structures. In this case, the filling factor, f , of such structures should be proportional to magnitude of the background field B_{back} .

3. Second Argument: Local Extrema in the Splitting of Bisectors

Lozitsky (1980) reported another deviation from the weak field approximation found for sub-kilogauss, ≤ 600 G, non-sunspot magnetic fields. The observed data were obtained with the Echelle spectrograph installed on the Horizontal Solar Telescope (HST) of the Astronomical Observatory of Taras Shevchenko National University of Kyiv (Lozitsky, 2016). It was found that the measured splitting, $(\Delta\lambda_{\text{H}})_{\text{obs}}$, of $I \pm V$ profiles changes with the distance, $\Delta\lambda$, from the center of spectral lines with a small Lande factors ($g_{\text{eff}} = 1-1.3$) and a considerable half-widths ($\Delta\lambda_{1/2} = 0.2-0.3 \text{ \AA}$). While some of the analyzed spectral lines exhibited an increase in the magnitude of splitting, other showed a decrease or even a non-monotonic dependence. To reduce influence of possible errors, the measurements were averaged over a solar region of about 36 arc sec length.

In weak-field approximation the value of $(\Delta\lambda_{\text{H}})_{\text{obs}}$ (or splitting of bisectors, BS , of $I \pm V$ profiles) should be the same at all distances, $\Delta\lambda$, from the line center, while observations showed to the contrary.

In Fig. 2 we plot BS as a function of $\Delta\lambda/g\lambda^2$, which shows three distinct maxima. The reason for this is easy to understand, if we recall that the Zeeman splitting $\Delta\lambda_{\text{H}}$ is

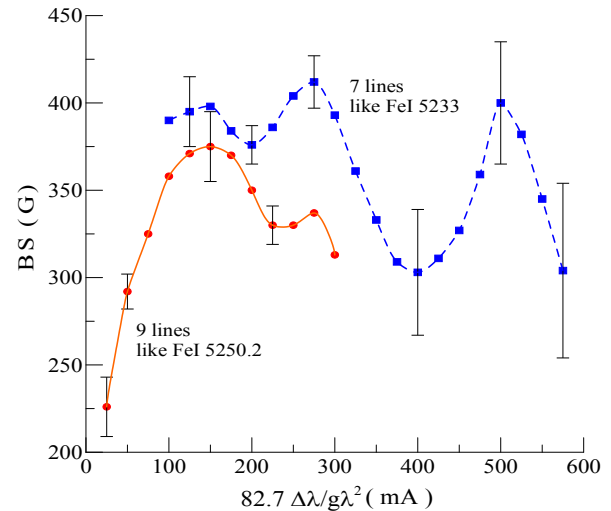


Figure 2: Averaged bisector splitting BS vs. the normalized distance from the line center, $82.7 \Delta\lambda/g\lambda^2$, plotted for 9 narrow lines such as FeI 5250.2 (filled circles and solid line) and for 7 lines such as FeI 5233 (squares and stroke line). The Landé factors of these lines ranges from 1.0 to 3.0. The mean-square errors of measurements are indicated with the vertical intervals. (Lozitsky, 2015).

proportional to the product $g\lambda^2 B$, where B is the magnetic field strength. Thus, when we take the ratio $\Delta\lambda/g\lambda^2$ for any maximum in Fig. 2, we in fact fix the magnitude B of the magnetic field because $B \sim \Delta\lambda_{\text{H}}/g\lambda^2$.

One can see from Fig. 2 that although the narrow spectral lines such as FeI 5250.2 and wider lines such as FeI 5233 exhibit certain discrepancy between the absolute values of the measured BS , the position of the maximums in the coordinates “ $BS - \Delta\lambda/g\lambda^2$ ” coincides well for lines of both types and corresponds to fields strength of 3–4, 7–8 and ≈ 13 kG. This leads to an interesting conclusion that the intensity of the magnetic field in spatially unresolved structures may not only reach 10^4 G, but it may also acquire discrete values. It was latter shown that theoretical interpretation of such superstrong and “quantized” magnetic fields is possible within the framework of a linear force-free model (Soloviev and Lozitsky, 1986). This model is described by Bessel’s functions J_0 and J_1 of zero and first orders and has a multipolar periphery and the magnetic field up to $\sim 10^4$ G with discrete values near the tube axis. For a 10^4 G field, a large number of discrete layers with opposite magnetic polarity is required to be present inside one small-scale structure.

Similar results were later obtained for solar flares as well (Lozitsky, 2015) and they are shown in Fig. 3. Here, the magnitude of splitting of bisectors of $I \pm V$ profiles is shown at different distances from the center of FeI 5233 \AA spectral line averaged over a number of solar flares, ranging from 3 to 12. The dots and solid lines represent observed flare data, and the dashed lines show the noise level in each case. Since both emission and absorption spectral contributions of strong fields are possible during flares, as well as contributions from different magnetic polarities, the $SDFLT$ values in Fig. 3 show the averaged standard deviation of the observed bisector splitting from the linear trend (regardless of the sign) on dependence “ $BS - \Delta\lambda$ ”.

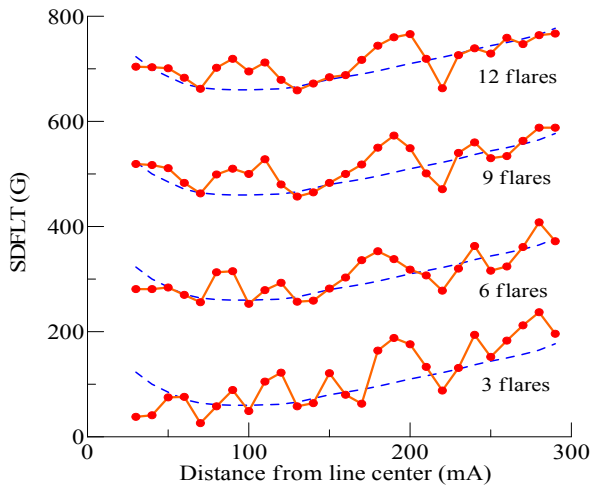


Figure 3: Averaged standard deviation of observed bisector splitting observed during flares from the linear trend (SDFLT) calculated for Fe I 5233 Å line. Dependencies for 6, 9 and 12 flares are shifted along the y-axis by 200, 400 and 600 G, respectively, for the sake of clarity. The dashed lines denote the expected error level.

It can be seen that when averaging over the maximum number of flares, two distinct peaks appear at 80-100 and 170-200 mÅ from the center. If we interpret this effect as an evidence of presence of weak Zeeman sigma components associated with spatially unresolved magnetic structures, then the corresponding magnetic field strengths will approximately be 6 and 12 kG, i.e. close to the 7-8 and ≈ 13 kG, estimates obtained earlier for non-flare regions.

It is interesting to note that similar conclusions were made by Ulrich et al. (2009) using Fe I 5233 line measured in quiet Sun regions. They observed only one maximum at 80 mÅ (see Fig. 7 in Ulrich et al., 2009)). It is possible, the absence of the second maximum at 170-200 mÅ in case of quiet regions reflects a simpler magnetic field structure, as compared to a flaring active region, with fewer types (modes) of flux tubes with different magnetic intensities.

According to simulations (Lozitskii, 1986), the above interpretation of data shown in Figs. 2 and 3 is applicable only if the real half-widths of the spectral lines measured in locations of very strong fields are much smaller than those usually observed in quiet Sun regions. For example, for Fe I 5233 line it is necessary to assume that its width in places with an extremely strong field is reduced by approximately 6-7 times – from 300 mÅ to 40-50 mÅ. However, we will show later, that the width reduction occurs at least in places of bright emission of solar flares.

4. Third Argument: Splitting of Emissive Peaks in Lines with Lande Factors about 0.01

Lozitsky (1993, 1998) presented the most direct evidence for existence of superstrong magnetic fields in solar flares inferred from data collected using Fe I lines with very low Lande factors (Lozitsky, 1993, 1998). The data were obtained with HST Echelle spectrograph. It was found

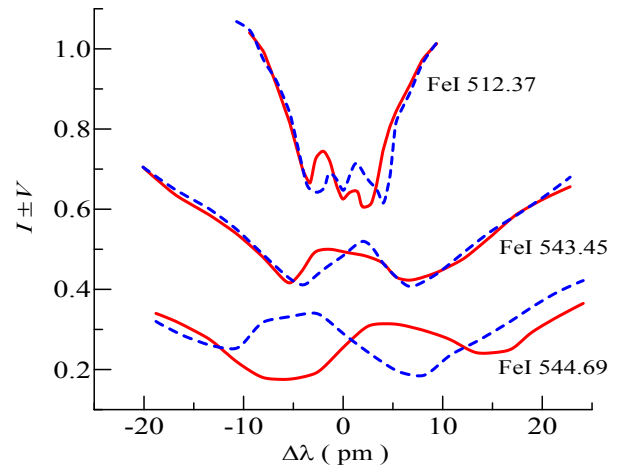


Figure 4: Comparison of $I \pm V$ profiles of Fe I 5123.7, Fe I 5434.5 and Fe I 5446.9 lines observed during a solar flare on 16 June 1989 (Lozitsky, 1998; 2003). Their empirically determined Lande factors are -0.013 , -0.014 and 1.249 , respectively. One can see not only a significant splitting of the emission peaks in the first two lines, but also that the sign of this splitting (i.e., the sign of the Stokes V parameter) is opposite to the sign of similar effect in the third line, which has positive Lande factor.

that Stokes $I \pm V$ profiles of some spectral lines, such as Fe I $^5F_1^5F_1 \lambda = 5123.723$ Å and Fe I $^5F_1^5D_0 \lambda = 5434.527$ Å, exhibit narrow and splitted emission peaks in their cores during flares. Both these lines have a zero theoretical Lande factors for LS coupling, however, their laboratory determined Lande factors, g_{Lab} , are exceptionally small, non-zero, $g_{Lab} = -0.013$ and -0.014 , respectively (Landi Degl'Innocenti, 1982).

The observed splitting of emission peaks in $I \pm V$ profiles was measured to be $\Delta\lambda_V = 10-36$ mÅ, whereas the splitting in $I \pm Q$ profiles was close to zero ($\Delta\lambda_Q \leq 5$ mÅ). Taking into account that the non-flaring profiles did not display similar effects, it was assumed to be manifestation of the Zeeman effect in a field of $B \approx 26-94$ kG.

According to the data, other significant features of superstrong magnetic fields in flares are as follows. The maximum value of the superstrong field (about 90 kG) was observed in the maximum phase of the flare, similar to the peak of kilo-gauss fields (1.1-1.5 kG) according to Fe I 5247.1 and 5250.2 data which was observed also in peak of a flare and not in its flash phase (Lozitska and Lozitsky, 1994).

The observed width of the flare emission in Fe I 5123.7 and 5434.5 lines reached 30 mÅ suggesting that the actual width should only be 10-20 mÅ after the instrumental profile of the spectrograph is taken into account (Lozitsky et al., 1999). As can be seen from Fig. 4, the magnetic field inferred from a spectral line with Lande factor of 1.25 was about 3 kG while the lines with Lande factor of 0.01 produced estimates close to 90 kG. This means that the underlying magnetic field structure was multicomponent and included both 10^3 G and 10^4 G fields.

To date, manifestation of superstrong magnetic fields have been detected in five powerful solar flares. However, it is not yet known whether these superstrong fields are

the prerogative of only powerful flares, or they may exist in other solar structures but their spectral manifestation is too weak to be detected with modern instrumentation.

5. New Observational Data

We studied in detail magnetic fields in an active region NOAA 12673, which was the most flare productive active region (AR) in the solar cycle No. 24. It produced four X-class flares including the X9.3 flare on 2017 September 06 and the X8.2 limb event on September 10. Wang et al (2018) detected extremely strong magnetic fields of 5.57 kG in this AR, which is about 1300 G above what Zirin and Wang (1993) found in flare productive sunspots.

Observations were carried out with the Goode Solar Telescope of Big Bear Solar Observatory (Cao et al., 2010). The GST is the first of a new generation of large aperture solar telescopes that will culminate in the ATST and the EST with 4-m apertures. This telescope has an adaptive optics system and can reach the diffraction limit of angular resolution which is equal of 0.06" at 500 nm and 0.2" at 1565 nm.

Stokes $\{I, Q, U, V\}$ profiles of FeI 15648.5 Å line ($g_{\text{eff}} = 3.0$) were obtained with the Near-Infrared Imaging Spectro-polarimeter (NIRIS) on 6 September 2017, when the AR was located at angular distance of 34 deg from the disk center. This instrument has spectral resolution about 0.1 Å and signal-to-noise ratio about 10^{-4} . Spectral line FeI 15648.5 forms about 200-300 km deeper than well-known visible lines FeI 5250.2, 5247.1, 6301.5 and 6302.5 Å (Khomenko and Collados, 2007) and one can expect that FeI 15648.5 line measurements represent such levels in atmosphere where magnetic fields can be particularly strong.

In comparison with the previously published findings of Wang et al. (2018), we probed the magnetic field at about 70 locations in the AR, which include a large number of anomalous Stokes profiles originating in a non-uniform magnetic field. In this study, we focus our attention only on the most simple effects that can be interpreted within the framework of the transfer theory in a homogeneous magnetic field.

Due to the high magnetic sensitivity of the FeI 15648.5 line and its relatively small spectral range, complete separation of the Zeeman π and σ components could be observed only when the magnetic field exceeds 1500 G. In this case, the modulus of the magnetic field strength is measured, rather than its longitudinal component, as it is customary for magnetographic measurements. In most cases, full component separation was most clearly recorded in Stokes U profile, that is, in linear polarizations (Fig. 5).

Comparison of the measured field strength to the continuum intensity near FeI 15648.5 Å line showed an important feature, namely, i.e., in the "magnetic field versus continuum intensity" diagram (Fig. 6), all measurements are divided into two clusters: consisting of typical and unusual dependencies.

For typical dependencies, a well-known relationship between the magnetic field and intensity is observed, when the greater the magnitude of the magnetic field is, the lower the corresponding intensity in the continuum. The magnetic

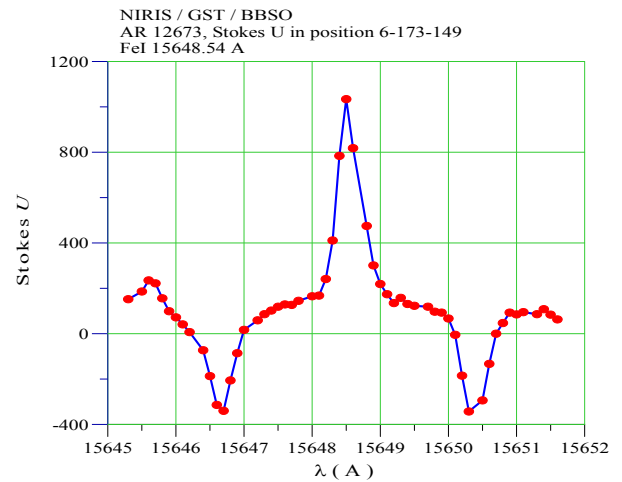


Figure 5: Stokes U of FeI 15648.5 line observed with NIRIS in position # 6 in AR 12673 which corresponds to a light bridge between two umbra of a sunspot. Spectral distance between σ components is equal here 3.7 Å ($\Delta\lambda_H = 1.85$ Å) which corresponds to magnetic field of 5.4 kG.

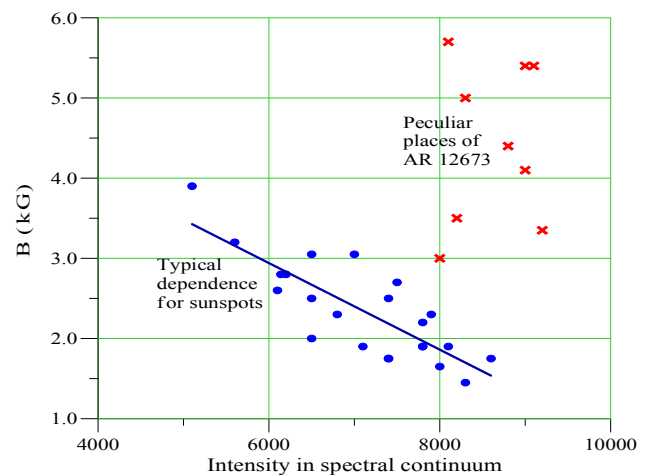


Figure 6: Measured magnetic field B in AR 12673 versus intensity in spectral continuum. One can see that all places in this AR can be divided on two types: "typical" and "peculiar" (see the text).

field here ranges from 1.5 to 3.9 kG, and it may be linearly approximated with decreasing intensity in the continuum. All the unusual locations displayed the highest continuum intensity, and the magnetic field there was found to be between 3.0 and 5.7 kG.

As far as we know, this situation is marked for the first time. Usually the strongest magnetic fields are localized in the dark umbra of sunspots, and not in bright areas outside these spots.

It is well known that the orientation of the magnetic field vector in the center of sunspot umbra is close to radial, i.e. it coincides with the vertical direction at a given location of the solar surface. It is therefore interesting to determine the orientation of the magnetic vector in these peculiar regions. In view of the large number of anomalous Stokes profiles that have been observed, more

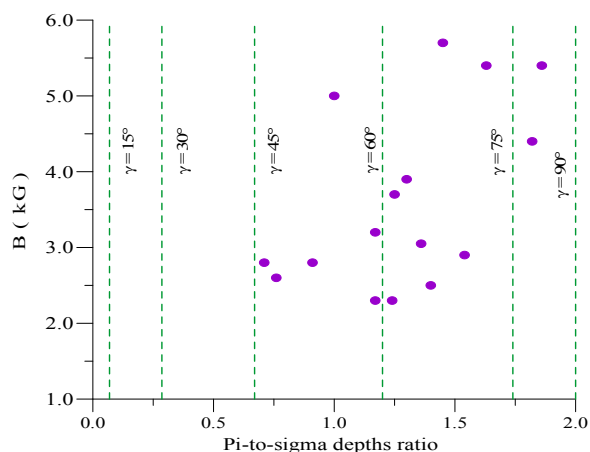


Figure 7: Estimates of the directional angle γ between the magnetic field vector and the line of sight derived from formula (2). Vertical dashed lines show the calculated ratio of the depths of of π and σ components corresponding to a certain angle of inclination of the field.

reliable determinations of the orientation of the vector \mathbf{B} can apparently be made along the profiles of the integral intensity, I . The Fe I 15648.5 Å line is rather weak, and its central depth outside spots is about 0.3. In this case, the approximation of an optically thin line is applicable, which makes it possible to use the Seares (1913) formula

$$d_{\pi}/d_{\sigma} = 0.5 \sin^2 \gamma / 0.25 (1 + \cos^2 \gamma), \quad (1)$$

where d_{π} and d_{σ} are depths of π and σ components, respectively, and γ is an directional angle between the magnetic field vector and the line of sight. If we denote $d_{\pi}/d_{\sigma} = k$, then, we obtain that

$$\cos \gamma = \{(1 - k/2)/(1 + k/2)\}^{1/2}. \quad (2)$$

The directional angle, γ , determined according to formula (2) are shown in Fig. 7. This includes only those cases where the π and σ components are completely spectrally separated and do not affect the depth of the neighboring component of the Zeeman splitting.

Figure 7 shows an interesting feature: all locations with strongest fields in the given AR exhibit the greatest directional angles, γ . In particular, three cases with $B = 5.4 - 5.7$ kG correspond to $67^\circ < \gamma < 79^\circ$.

The heliocentric angle, θ , of the AR was approximately 34 degrees. In this case, depending on the orientation of the field vector in the picture plane, the angles of the lines of force with respect to the vertical should be from $\gamma - \theta$ to $\gamma + \theta$. Based on the data in Figure 7, we find that the actual angles to the vertical direction were between 33-45 degrees and 101-113 degrees.

The large direction angle possibly indicates the extremely strong fields there were nearly horizontal, and not vertical, as in the sunspot umbra. A direct comparison of the obtained measurements of the magnetic field with heliograms in the molecular TiO line showed that all the strongest fields were localized in the bright bridges between the sunspot umbra.

6. Discussion and Conclusion

The Fe I 15648.5 Å line is attractive for measurements not only because it gives the magnetic field module at fields above 1.5 kG, but also because due to its high magnetic sensitivity it allows estimating the dispersion of the field strengths in magnetic elements. Really, Botygina et al. (2016) found that in quiet Sun regions outside sunspots the diameter of the smallest flux tubes is about 15-20 km. The spatial resolution of the GST NIRIS data is about 150 km, that is an order of magnitude less than required to resolve such elementary structures. Thus, it is likely that there is a hidden complex structure within the sampling pixel of NIRIS instrument. If the magnetic fields would significantly differ in intensity, we would observe diffuse σ components in the Zeeman effect. However, the observed blurring of these components, at all is negligible since the observed half-width is about 0.5 Å (Fig. 5), while the observed line width in quiet Sun region is much smaller and is about 0.3 Å. This indicates that the dispersion of the field intensity in neighboring sub-telescopic flux tubes comparison a single NIRIS pixel, is generally negligible.

Let us summarize our findings. The modulus of the magnetic field vector was measured in several locations across AR NOAA 12673 – the most flare-producing sunspot group in the 24th cycle of solar activity. Unlike earlier studies that involved magnetographic measurements and inversion methods our measurements are the most direct and therefore reliable.

We report that a case when extremely strong magnetic fields in the range 5.0-5.7 kG were concentrated not in the dark nuclei of sunspot, but in bright areas of an AR.

Comparison of approximately 70 data points associated with various magnetic structures in the AR showed that there were two types of profiles. In typical areas, the magnetic field was within 1.5-3.9 kG and the more intense fields were associated with lower continuum intensity. In other, unusual locations, the intensity of the magnetic field was ranging from 3.0 to 5.7 kG, all of them were associated with nearly the same underlying continuum intensity. The orientation of the field vector in those unusual locations was determined to be close to transverse, which may indicate a strong twist of magnetic structures.

Acknowledgements. VYu acknowledges support from AFOSR FA9550-15-1-0322 and NSF AST-1614457 grants. BBSO operation is supported by NJIT and US NSF AGS-1821294. GST operation is partly supported by the Korea Astronomy and Space Science Institute (KASI), Seoul National University, and by strategic priority research program of CAS with Grant No. XDB09000000. This study was funded by Kyiv Taras Shevchenko National University project No. 16БФ023-01.

References

- Baranovsky E.A., Petrova N.N.: 1957, *Solnechnyje Dannyje*, № 5, 118.
- Botygina O.O., Gordovskyy M.Yu., Lozitsky V.G.: 2016, *Adv. Astron. Space Phys.*, **6**, 20.
- Bruce C.E.R.: 1966, *Observatory*, **86**, 82.

- Cao W., Gorceix N., Coulter R. et al.: 2010, *Astron. Nachr.*, **331**, 620.
- Gopasyuk S.I., Kotov V.A., Severny A.B. et al.: 1973, *Solar Phys.*, **31**, 307.
- Khomenko E., Collados M.: 2007, *The Astrophys. J.*, **659**, 1726.
- Landi Degl'Innocenti E.L.: 1982, *Solar Phys.*, **77**, 285.
- Livingston, W., Harvey, J.W., Malanushenko O.V.: 2006, *Solar Phys.*, **239**, 41.
- Lozitska N., Lozitsky V.: 1994, *Solar Phys.*, **151**, 319.
- Lozitska N.I.: 2010, *Kosm. Nauka i Tekhnologia*, **16**, 30.
- Lozitskii V.G.: 1986, *Kinem. Fiz. Neb. Tel*, **2**, 28.
- Lozitsky V.G., Lozitska N.I., Gordovskyy M.Yu.: 1999, *Bull. Taras Shevch. Nat. Univ. of Kyiv. Astronomy*, **35**, 17.
- Lozitsky V.G.: 1978, *Solnechnyje Dannyje*, № 8, 74.
- Lozitsky V.G.: 1980, *Physica Solariterr.*, Potsdam, 14, 88.
- Lozitsky V.G.: 1993, *Kinem. Phys. Celest. Bodies*, **9**, 18.
- Lozitsky V.G.: 1998, *Kinem. Phys. Celest. Bodies*, **14**, 401.
- Lozitsky V.G.: 2003, *DrSci Thesis*, Kiev, 299p.
- Lozitsky V.G.: 2015, *Adv. Space Res.*, **55**, 958.
- Lozitsky V.G.: 2016, *Adv. Space Res.* **57**, 398.
- Lozitsky V.G.: 2017, *Adv. Space Res.* **59**, 1416.
- Seares F.H.: 1913, *Astrophys. J.* 38, 99.
- Severny A.B.: 1957, *Astron. Zhurnal*, **34**, 684.
- Solanki S.: 2003, *The Astron. Astrophys. Rev.*, 11, 153.
- Soloviev A.A., Lozitsky V.G.: 1986, *Kinematika i Fizika Nebesn. Tel*, **2**, 80.
- Steshenko N.V.: 1967, *Bull. Crimea Astrophys. Obs.*, **37**, 21.
- Takenori Okamoto, Takashi Sakurai: 2017, *arXiv*: 1712.08700v1[astro-ph.SR] 23 Dec 2017.
- Ulrich, R.K., Bertello, L., Boyden, J.E. et al.: 2009, *Solar Phys.* **255**, 53.
- Unno W.: 1956, *Publs. Astron. Soc. Japan*, **8**, 108.
- Van Noort M., Lagg A., Tiwari S.K. et al.: 2013, *Astron. Astrophys.* **557**, id.A24, 14 pp.
- Wang Y., Yurchyshyn V., Lin C. et al.: 2018, *Res. Notes of the American Astron. Society*, **2**, No. 1.

DOI: <http://dx.doi.org/10.18524/1810-4215.2018.31.144687>

PRELIMINARY RESULTS OF INTERFEROMETRIC OBSERVATIONS OF THE QUIET SUN AT THE FREQUENCIES 8 – 32 MHz

V.A. Shepelev¹, V. N. Melnik¹, R.V. Vashchishin²¹ Institute of Radio Astronomy, Kharkiv, Ukraine² Gravimetric Observatory of IGP, Poltava, Ukraine

ABSTRACT. We studied a radio emission of the quiet Sun at decameter wavelengths to determine its angular dimensions. Observations were conducted using interferometers composed of antenna sections of the UTR-2 radio telescope. A number of interferometers with baselines of 225 to 1400 m, oriented along the meridian, operated at two frequencies of 20 and 25 MHz with a bandwidth 250 kHz. We used them to estimate a shape of a source brightness distribution. To measure the angular size of the Sun in a wide frequency band of 8-32 MHz another set of interferometers was used. It consisted of two pairs of the interferometers with the baselines of 225 and 450 m elongated both along the parallel and the meridian. They used digital wideband receivers operating at the frequencies of 8 to 32 MHz to record received signals. There was some sporadic solar activity during observational campaign in March-April 2015 that complicated determination of parameters of the quiet Sun radiation. A large number of radio frequency interference also noted. To mitigate their influence we applied a few data cleaning algorithms. The use of the algorithms in spectral strips with a low level of interferences in periods free from powerful sporadic solar radiation allowed us to make estimation of the angular size of the quiet Sun in two orthogonal directions at some separate frequencies in the range of 20 to 32 MHz. Calculation of the dimensions was performed in an assumption of Gaussian radio brightness distribution of the source. Our estimates of the quiet Sun sizes agree well with the data of other authors. The simplicity and convenience of determining the angular size using the data obtained with two interferometers with different baselines are noted. Continuation such study will allow to extend the frequency range down to the lowest frequencies where observations from the Earth's surface are possible and give us a possibility to study how the angular size of the quiet Sun depend on a phase of solar activity. This study will allow us to construct a model of solar corona at distances of 1.5-3 solar radii directly from the radio observations and to find out how the effective temperature of the Sun changes with the frequency.

Key words: quiet Sun, angular diameter, interferometer, decameter range.

АБСТРАКТ. Проведено дослідження радіовипромінювання спокійного Сонця на декаметрових хвилях з метою визначення його кутових розмірів. Спостереження проводилися за допомогою інтерферометрів,

що склалися із секцій антени радіотелескопу УТР-2. Одна низка інтерферометрів з базами від 225 до 1400 м, орієнтованими вздовж меридіана, працювала на двох частотах 20 і 25 МГц з шириною смуги 250 кГц. Вона використовувалася для оцінки форми розподілу яскравості джерела. Для вимірювання кутових розмірів у широкому діапазоні частот застосовано іншу групу, що складалася з двох пар інтерферометрів з базами 225 і 450 м, розташованими як уздовж паралелі, так і вздовж меридіана. Для реєстрації випромінювання в них використано цифрові широкосмугові приймачі, що працюють в діапазоні частот від 8 до 32 МГц. У спостереженнях, проведених в березні-квітні 2015 року, спостерігалися прояви спорадичної активності, які ускладнювали визначення параметрів випромінювання спокійного Сонця. Також зазначалася велика кількість радіозавод штучного походження. Для усунення їх впливу використовувалися кілька алгоритмів очищення даних. Застосування цих алгоритмів на ділянках спектра з малою кількістю завод в періоди, вільні від потужного спорадичного випромінювання, дозволило зробити попередні оцінки кутових розмірів спокійного Сонця в двох ортогональних напрямках на низці частот від 20 до 32 МГц. Визначення розмірів проведено у наближенні гаусового розподілу радіояскравості джерела. Отримані оцінки розмірів спокійного Сонця добре збігаються з даними інших авторів. Відзначено простоту і зручність визначення кутового розміру за даними двох інтерферометрів з довільними базами. Продовження подібних досліджень дозволить розширити частотний діапазон до найнижчих частот, на яких можливе проведення спостережень з поверхні Землі, вивчити залежність кутових розмірів спокійного Сонця від фази його активності. Це дозволить також побудувати модель корони на відстанях 1.5-3 радіусу Сонця безпосередньо з радіоспостережень, знайти, як змінюється з частотою ефективна температура Сонця.

Ключові слова: спокійне Сонце, кутовий діаметр, інтерферометр, декаметровий діапазон.

1. Introduction

Radio emission of the quiet Sun was studied in a wide range of wavelengths, from millimeter to decameter ones. However, observations were not very frequent at the long wavelengths and only at some separate frequencies. One

of the reasons is that a flux density of the solar radio emission decrease with wavelength with spectral index $\alpha > 2$ in decameter range and flux value become less than 1000 Jy. At the same time, the radio emission of the galactic background increases with wavelength and exceeds significantly the radiation of the quiet Sun at decameter wavelengths. This requires using of antennas with a large effective area for the observations. It is of particular interest to determine how parameters of the quiet Sun depend on the wavelength, so these antennae and a backend facilities have to be sufficiently broadband. Besides, they must have a high dynamic range because of a significant level of RFI at the decameter wavelengths. The UTR-2 radio telescope (Braude et al., 1978) allows carrying out such investigations. Nowadays this radio telescope is equipped with broadband digital spectral polarimeters DSPZ (Zakharenko et al., 2016) with a capability to conduct observations at frequencies of 8 to 33 MHz simultaneously. Determination of the solar size dependence on frequency is quite important for construction of models of physical processes underlying generation of the coronal radio emission. As it is well known angular sizes of radio Sun do not differ noticeably from its optical size down to short meters. At the same time the first observations (Aubier et al., 1971) showed that the size of the quiet Sun at frequencies of 29 and 36 MHz is noticeably larger than the optical one and increases with decreasing frequency. Some other observations were carried out from time to time and only at some separate frequencies not lower than 19 MHz. We present preliminary results of observations with the UTR-2 radio telescope to determine angular sizes of the quiet Sun in the broadband range of the decameter wavelengths.

2. Observations and results

The angular size of a radio source can be determined by scanning with a beam of a radio telescope. In this case an output signal is a convolution of brightness distribution of the source with an antenna pattern. If the angular size of the source significantly exceeds a beam width, one can easily find the true size of the object from the width of an output response. In the case of comparable sizes it is necessary to take into account the antenna smoothing, which increases the response width in comparison with the true size. For example, width of the UTR-2 radio telescope beam at 25 MHz equals 25' and it is comparable with the angular diameter of the quiet Sun at this frequency, which is approximately equal to 1° as measured by Abranin and Bazelyan (1986). Unfortunately, the UTR-2 as well as other antenna arrays used in low-frequency radio astronomy has antenna pattern with appreciable level of side lobes. Moreover, correlation radiometers, which are used to eliminate an influence of the galactic background, result in alternating-sign view of the side lobes. Hence, two-dimensional pattern of side lobes of such antenna is quite complicated and changes notably with beam orientation that complicates accounting of antenna smoothing.

In the scanning method the size of the source are determined by width of the antenna response. An alternative method is an interferometer one, according to which, an angular size of an object can be calculated based on amplitudes of response of interferometers with different base-

lines. The antenna of the UTR-2 radio telescope has T-shape view and consists of two rectangular arrays oriented in the north-south and the east-west directions. Each array consists of a number of sections with a distance between their centers 225 m. It allows forming a number of interferometers with different lengths and direction of their baselines. Ability of such interferometers to measure the angular size are illustrated in Fig. 1, where the calculated dependence of normalized visibility function γ_n on a length of the baseline L at 25 MHz is shown. Calculations were made for sources with different diameters with Gaussian radio brightness distribution, located at a declination of 22°. It is obvious, that the interferometers with the baseline of 225 m formed by the nearest sections and also with the baselines of 450 and 675 m can be used to determine the angular diameter of the quiet Sun.

Observations of the quiet Sun with such interferometers were made in May, 2014 (Melnik et al., 2018) with multichannel receivers (Rashkovsky et al., 2012), which are usually used in observations with the URAN interferometer network (Megn et al., 1997). Experimental data $\gamma(L)$ were close to calculated dependencies of a source with Gaussian brightness distribution that allowed to determine the angular diameter of the Sun using values of a correlation coefficient γ_1 and γ_2 , determined only at two baselines L_1 and L_2 , according to expression:

$$\theta = \frac{2\lambda\sqrt{\ln(2)}}{\pi} \sqrt{\frac{\ln(\gamma_1/\gamma_2)}{L_2^2 - L_1^2}} \quad (1)$$

Technique of the observations and calibrations of the interferometers for such measurements is described by Shepelev (2015). Basic restriction of the receiver used in the observations is an ability to operate only at two discrete frequencies with a bandwidth 250 kHz that limits a range and sensitivity of the observations.

To study the possibility of determining parameters of the quiet Sun radio emission in a wide frequencies range, we observe this radio source since 31 March to 5 April, 2015. The DSPZ wideband spectral polarimeters operating in the range 8–32 MHz were used as receivers. Each

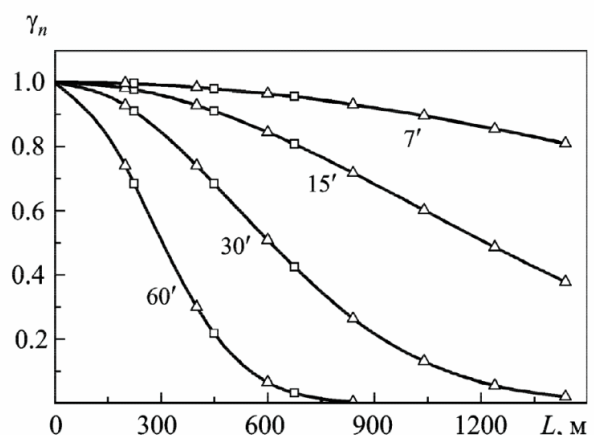


Figure 1: Dependence of normalized visibility function on a baseline and an angular size of a source. Squares mark the baselines shaped by sections of the EW antenna, triangles – by sections of the NS antenna

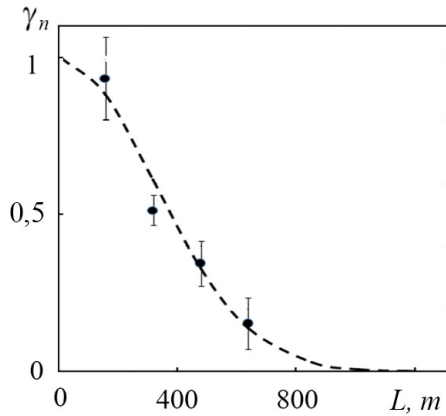


Figure 2: The experimental values of normalized visibility function versus a baseline length at frequency of 20 MHz

receiver forms at its output a complex dynamic cross spectrum that is dependence of a covariance of two input signals on frequency and time. Four receivers were connected to outputs of the sections of the north-south and east-west arrays of the UTR-2 radio telescope, forming two interferometers with the baselines of 225 and 450 m oriented along a meridian, and two similar interferometers oriented along a parallel. This configuration of the equipment allows determining the angular size of the quiet Sun radiation in the equatorial and polar directions in the entire frequency range of the radio telescope using the visibility function, measured on two different baselines. To determine a shape of the dependence using observations on a larger number of baselines we applied two four-channel URAN's receivers with operation frequencies 20 and 25 MHz connected to the sections of the north-south antenna. Observations with these interferometers showed that the experimental dependences $\gamma(L)$ were close to the calculated responses from a source with a Gaussian brightness distribution (see Fig. 2) and reaffirmed admissibility of applying a technique of determination of the size from responses of two broadband interferometers according to (1).

Note that at the beginning of April a declination of the Sun is about 6° , therefore projections of the interferometer baselines are noticeably shorter than distances between the sections of the north-south antenna. For the same reason, the low position of the Sun, there was a significant amount of RFI in the observations. For illustration in Fig.3 we presents dependence of the angular size of the Sun on frequency and time, calculated according with (1) using data obtained during one day of the observation on April 4. Raw output signals of the receivers used for these calculations were processed in no way. Obviously there are a large amount of interferences in the signal, especially at the lowest frequencies, that makes it possible to estimate only the tendency to increase a size with decreasing frequency. To obtain reliable results in such observations, it is necessary to develop algorithms for removal of RFI, for example, those used in URAN's receivers (Rashkovsky et al., 2012). This is especially true for the lowest part of the frequency range.

To process these noisy data, we chose areas with a bandwidth of about 1 MHz and with duration of several

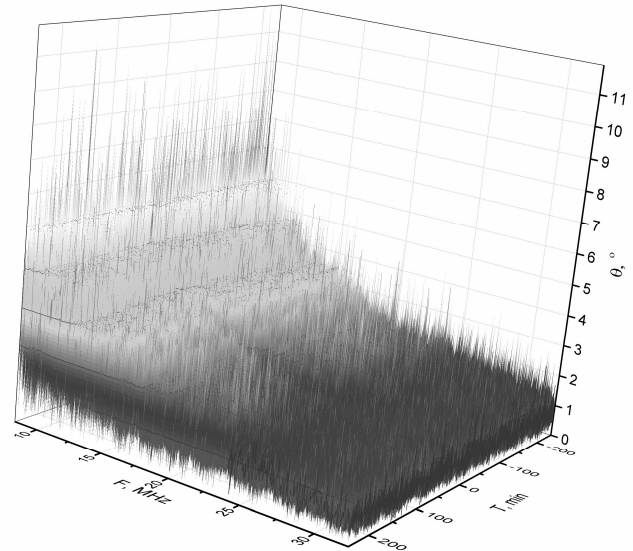


Figure 3: Angular size of the quiet Sun versus frequency and time

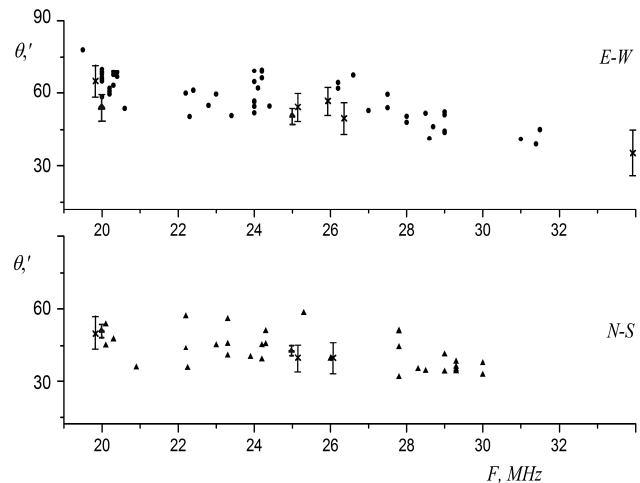


Figure 4: Dependence of angular sizes of the quiet Sun on frequency: a) equatorial diameter; b) polar diameter

minutes with relatively low level of the interferences. In such a frequency bandwidth the size of the quiet Sun can be considered constant and within a few minutes a modulation of a signal by the antenna pattern is rather low. In this time-frequency frame of the signal various methods of interference mitigation such as median filtering, threshold limitation, averaging were tested and their effect on a final result was evaluated. In our opinion, a combination of the median filter, which allows removing short in time or narrow frequency interference, followed by the threshold limitation which removes more extended interference was the most effective. Such an algorithm had a significant amount of manual processing, consisting in the frame selection and threshold finding, however it allowed making preliminary estimates of the angular diameter of the Sun in the equatorial and the polar direction, presented in Fig. 4.

In fig. 4a the dependence of the angular size of the quiet Sun on a frequency found with the east-west interferome-

ters is shown. It represents the equatorial section of the source. In fig. 4b the same dependence for polar section is shown. Mean value of a ratio of the polar diameter to the equatorial one is ~ 0.75 . For comparison, the results obtained by Melnik et al. (2018) at frequencies of 20 and 25 MHz are shown by triangular marks with error bars, and data of Abranin and Bazelian (1986) at 25 MHz, Stanislavsky et al (2013) at 20 and 26 MHz, and Subramanian (2004) at 34.5 MHz are indicated by crosses. Our data at frequencies below 20 MHz obtained in these observations were not reliable enough, so they are not shown in Fig. 4.

3. Conclusions

Observations of radio emission of the quiet Sun with UTR-2 radio telescope in interferometric regime in the continuous frequency band of 8-32 MHz allowed obtaining the first preliminary results on solar sizes dependence on frequency in the east-west and north-south directions. Due to many ionosphere and artificial interferences, reliable results were obtained for frequencies from 20 to 32 MHz. However, the technique of data processing needs significant improvement for obtaining reliable results in all decameter range from 8 to 32 MHz. Using different sections of UTR-2 radio telescope as an interferometer showed good perspectives in finding sizes of the Sun at low frequencies in different periods of solar activity. This will allow to study some physical processes such as elementary processes of radiation, refraction, scattering and radio waves propagation in the solar corona at heights 0.5–2.5 solar radii, which are in the base of radio emission of the quiet Sun. We hope also to determine the frequency dependence of brightness temperature of the Sun and answer the question if the radio emission of the Sun is blackbody or not.

References

- Abranin E.P. and Bazelian L.L.: 1986, Preprint #304, (in Russian), Kharkov, IRE NASU.
- Aubier M., Leblanc Y., Boischot A.: 1971, *Astron. & Astrophys.*, **12**, 435.
- Braude S.Ya., Megn A.V. Sodin L.G.: 1978, *Antenny iss* **26**, (in Russian), Moskow, Sviaz
- Megn A.V., Braude S.Ya., Rashkovsky S.L. et al.: 1997, *Radiophys. and Radioastron.* (in Russian), **2**, 4, 385.
- Melnik V.N., Shepelev V.A., Poedts S. et al.: 2018, *Solar Phys.*, **293**, 97.
- Rashkovsky S.L., Belov A.S., Ivanov et al.: 2012, *Radiophys. and Radioastron.* (in Russian), **17**, 3, 207.
- Stanislavsky A.A., Koval A.A., Konovalenko A.A.: 2013, *Astron. Nachr.*, **334**, 10, 1086.
- Subramanian K.R.: 2004, *Astron. & Astrophys.*, **426**, 329.
- Shepelev V.A.: 2015, *Radiophys. and Radioastron.* (in Russian), **20**, 1, 20.
- Zakharenko V., Konovalenko A.A., Zarka P. et al.: 2016, *Astron. Instrum.*, **5**, 4.

DOI: <http://dx.doi.org/10.18524/1810-4215.2018.31.146662>

THE CATALOG OF MAGNETIC STORMS FOR ODESSA MAGNETIC ANOMALY ZONE

L.I. Sobitnyak¹, M.I. Ryabov¹, A.L. Sukharev¹, M.I. Orlyuk², A.O. Romenets², Yu.P. Sumaruk²¹ URAN-4 Observatory, Radio-astronomical institute of NAS of Ukraine² Institute of geophysics NAS of Ukraine

ABSTRACT. On magnetic observatory "Odessa" since 1948 measurements of a magnetic field of Earth. At the same time measurements of three elements of a magnetic field are registered: horizontal component (H), vertical component (Z) and induction (D). On the basis of these data the catalog of magnetic storms in the 21st century is made. In this release of the catalog during 2000-2009 date and time of the beginning and end of a storm, the storm duration, amplitude on three elements of a magnetic field are specified: H, Z, D, the characteristic of magnetic storms with the indication of the fissile periods. The magnetic station "Odessa" is located near a zone of a magnetic anomaly. For identification of reaction in the nature of the geomagnetic activity arising owing to existence of a magnetic anomaly comparison of geomagnetic disturbances at Odessa and Moscow was carried out.

Keywords: Solar activity, magnetic storms, magnetic storm catalog, magnetic anomaly.

АБСТРАКТ. На магнітній обсерваторії «Одеса» з 1948 року ведуться вимірювання магнітного поля Землі. При цьому реєструються вимірювання трьох елементів магнітного поля: горизонтальної складової (H), вертикальної складової (Z) і схилення (D). На підставі цих даних складено каталог магнітних бур в XXI столітті. У цьому випуску каталогу, за період 2000-2009 роки, вказані дата і час початку і кінця бурі, тривалість бурі, амплітуда по трьох елементах магнітного поля: H, Z, D, характеристика магнітних бур із зазначенням активних періодів.

Моніторинг потоків потужних галактичних і позагалактичних радіоджерел виконується на радіотелескопі «УРАН-4» Одеської обсерваторії Радіоастрономічного інституту НАН України з 1987 р. і до тепер. У програму моніторингу входять радіогалактики 3C274, 3C405 і залишки наднових 3C144, 3C461. Спостереження радіоджерел проводилися окремими сеансами, в межах ± 2 години до і після часу їх кульмінації. Час проходження радіоджерел 3C144, 3C274, 3C405 через діаграму

спрямованості становило 40 хвилин (для кожного часового кута), для 3C461 – 60 хвилин. Загальний час добового моніторингу перевищує 13 годин. Зміни потоків випромінювання радіоджерел на декаметрових хвилях визначаються станом іоносфери під впливом космічної погоди. Цей каталог був складений, щоб визначити причини зміни потоку космічних радіоджерел за даними спостереження на радіотелескопі URAN-4 в Одеській обсерваторії Інституту радіоастрономії Національної академії наук України.

Магнітна обсерваторія «Одеса» розташована поблизу зони магнітної аномалії. Для виявлення ефектів «відгуку» в прояві характеру геомагнітних бур, які виникають внаслідок наявності магнітної аномалії, було проведено порівняння геомагнітних збурень на магнітних обсерваторіях «Одеса» та «Москва» (ІЗМІРАН). Зокрема виявлено що загальна тривалість магнітних бур за період 2000-2009 роки в Одесі довше, ніж в Москві. В більшості випадків тривалість потужних магнітних бур в Одесі більше, ніж в Москві.

Ключові слова: сонячна активність, магнітні бурі, каталог магнітних бур, магнітна аномалія.

The magnetic observatory «Odessa» was founded by the Novorossiysk Imperial University, in the territory of a botanical garden, at the beginning of the XX century. In 1936 it was transferred to the village of Stepanovka (near Odessa) by the Odessa State University. After World War 2th the station became to belong to the Institute of Geophysics. From 1948 to 2010, analog measurements of the Earth's magnetic field were conducted at the «Odessa» Magnetic Observatory. At the same time measurements of three elements of a magnetic field are registered: horizontal component (H), vertical component (Z) and inclination (D) [1]. Figure 1 presents a monthly review of the state of the magnetic field in November 2003.

Table 1: Digital catalog of magnetic storms and their characteristics

| Beginning | | End | | Duration, h | Amplitude | | | Storm class | Active periods | | | | Comment |
|------------|-------|------------|-------|----------------|-----------|-----|----|----------------|----------------|-------|------------|-------|---|
| date | UT | date | UT | | H | D | Z | | begin | | end | | |
| | | | | date | | | | UT | date | UT | | | |
| 03.01.2003 | 12:00 | 04.01.2003 | 0:00 | 36 | 95 | 94 | 36 | minor | | | | | Minor storm with the gradual beginning |
| 18.01.2003 | 6:00 | 20.01.2003 | 6:00 | 48 | 105 | 64 | 39 | minor | | | | | Minor storm with the gradual beginning |
| 20.01.2003 | 10:00 | 23.01.2003 | 4:00 | 66 | 98 | 68 | 38 | minor | | | | | Minor storm with the gradual beginning |
| 29.01.2003 | 9:00 | 30.01.2003 | 20:00 | 35 | 116 | 124 | 42 | moderate | | | | | Moderate storm with the gradual beginning |
| 01.02.2003 | 15:00 | 05.02.2003 | 3:00 | 84 | 176 | 145 | 82 | moderate | 01.02.2003 | 18:00 | 03.02.2003 | 2:00 | Moderate storm with the gradual beginning |
| | | | | | | | | | 03.02.2003 | 12:00 | 04.02.2003 | 12:00 | |
| 08.02.2003 | 7:00 | 09.02.2003 | 3:00 | 20 | 75 | 70 | 26 | minor | | | | | Minor storm with the gradual beginning |
| 12.02.2003 | 8:00 | 13.02.2003 | 1:00 | 17 | 83 | 74 | 26 | minor | | | | | Minor storm with the gradual beginning |
| 13.02.2003 | 21:00 | 15.02.2003 | 21:00 | 48 | 80 | 105 | 35 | minor | 14.02.2003 | 9:00 | 15.02.2003 | 18:00 | Minor storm with the gradual beginning |
| 16.02.2003 | 6:00 | 17.02.2003 | 2:00 | 20 | 86 | 62 | 32 | minor | | | | | Minor storm with the gradual beginning |
| 26.02.2003 | 6:00 | 28.02.2003 | 1:00 | 43 | 106 | 114 | 48 | moderate | | | | | Moderate storm with the gradual beginning |
| 28.02.2003 | 6:00 | 01.03.2003 | 3:00 | 21 | 93 | 85 | 42 | minor | | | | | Minor storm with the gradual beginning |
| 03.03.2003 | 15:00 | 05.03.2003 | 3:00 | 36 | 92 | 131 | 57 | moderate | | | | | Moderate storm with the gradual beginning |
| 05.03.2003 | 9:00 | 07.03.2003 | 12:00 | 51 | 103 | 96 | 46 | minor | | | | | Minor storm with the gradual beginning |
| 20.03.2003 | 6:00 | 22.03.2003 | 2:00 | 44 | 119 | 101 | 50 | moderate | | | | | Moderate storm with the gradual beginning |
| 22.03.2003 | 19:00 | 24.03.2003 | 2:00 | 31 | 106 | 85 | 32 | minor | | | | | Minor storm with the gradual beginning |
| 28.03.2003 | 16:00 | 31.03.2001 | 3:00 | 59 | 98 | 124 | 81 | moderate | | | | | Moderate storm with the gradual beginning |
| 31.03.2003 | 6:00 | 01.04.2003 | 4:00 | 22 | 127 | 111 | 62 | moderate | | | | | Moderate storm with the gradual beginning |

Table 2: Amount of magnetic storms in the catalog for 2000-2009

| Storm class | 2000 | 2001 | 2002 | 2003 | 2004 | 2005 | 2006 | 2007 | 2008 | 2009 |
|-------------|------|------|------|------|------|------|------|------|------|------|
| minor | 25 | 31 | 39 | 38 | 31 | 30 | 32 | 34 | 28 | 11 |
| moderate | 16 | 27 | 21 | 36 | 11 | 16 | 9 | 5 | 4 | 0 |
| strong | 5 | 4 | 4 | 1 | 4 | 5 | 1 | 0 | 0 | 0 |
| extreme | 3 | 6 | 2 | 2 | 2 | 4 | 0 | 0 | 0 | 0 |

Table 3: The duration of the most intense magnetic storms according to the magnetic observatories "Odessa" and IZMIRAN

| 2001 | | | 2002 | | | 2003 | | |
|------------|--------|--------|------------|--------|--------|------------|--------|--------|
| Date | Odessa | Moscow | Date | Odessa | Moscow | Date | Odessa | Moscow |
| 19.03.2001 | 38 | 40 | 10.01.2002 | 89 | 30 | 24.04.2003 | 108 | 41 |
| 28.03.2001 | 35 | 28 | 17.04.2002 | 43 | 21 | 26.06.2003 | 102 | 41 |
| 31.03.2001 | 70 | 9 | 19.04.2002 | 39 | 9 | 15.07.2003 | 52 | 2 |
| 08.04.2001 | 35 | 24 | 11.05.2002 | 30 | 22 | 28.07.2003 | 157 | 40 |
| 11.04.2001 | 29 | 18 | 23.05.2002 | 12 | 9 | 20.08.2003 | 116 | 56 |
| 18.04.2001 | 34 | 10 | 01.08.2002 | 88 | 26 | 15.09.2003 | 127 | 56 |
| 17.08.2001 | 36 | 8 | 01.10.2002 | 45 | 61 | 16.10.2003 | 91 | 40 |
| 21.10.2001 | 48 | 4 | 03.10.2002 | 65 | 50 | 15.11.2003 | 94 | 2 |
| 05.11.2001 | 62 | 40 | 02.11.2002 | 125 | 20 | 20.11.2003 | 43 | 9 |

to identify manifestations of geomagnetic disturbances during radio astronomical observations and their contribution to changes in radio source fluxes on decameter waves.

3. These studies will also be supplemented by a comparative analysis of the manifestation of magnetic storms of the magnetic anomaly zone in Odessa and data from other magnetic observatories in Ukraine.

References

- Orliuk M., Sumaruk Yu., Sumaruk T., Romenets A., Melnychuk I.: 2009, in The IAGA11th Scientific Assembly in Sopron, Hungary, iaga2009sopron.hu/iaga_abstracts.
- Russel, C. T. and McPherron, R. L., 1973. Semiannual Variation of Geomagnetic Activity. *J. Geophys. Res. Space Phys.* vol. 78, is. 1, pp. 92–108. DOI: 10.1029/JA078i001p000922.
- Plasma heliogeophysics. Moscow: Fizmatlit, 2008, 1-2, 560.
- Miroshnichenko L.I., Physics of the Sun and solar-terrestrial connections. M.: University book, 2011, 174 p.
- Obridko V.N., Nagovitsyn Y.A. Solar activity, cyclicity and prediction methods. St. Petersburg: BBM, 2017, 467p.
- BRUZEK, A. and DURRANT, C. J., eds., 1977 Illustrated glossary for solar and solar-terrestrial physics. Dordrecht, Boston: D. Reidel Pub. Co.

SOLAR SYSTEM

DOI: <http://dx.doi.org/10.18524/1810-4215.2018.31.144550>

DOPPLER STATION FOR ORBITAL TRACKING OF LOW-ORBIT SPACECRAFTS BY THEIR RADIO BEACON SIGNALS

F. Bushuev, M. Kaliuzhnyi, M. Khalaley, V. Kryuchkovskiy, M. Kulichenko, O. Shulga

Research Institute "Mykolaiv Astronomical Observatory" (RI "MAO"),
Mykolaiv, Ukraine, dir@mao.nikolaev.ua

ABSTRACT. A ground station of orbital tracking of low-orbit spacecrafts has been developed and tested in the RI "Mykolaiv Astronomical Observatory". The station uses the Doppler shift of frequencies of signals radiated by spacecraft radio beacons for their orbital tracking. The station consists of: 1) 10-section antenna with a circular directional diagram and the operating frequency band 400-450 MHz, 2) electronic unit of connection of the antenna sections to a receiver, 3) the SDR-receiver used USB receiver of terrestrial digital TV and radio ("DVB-T+DAB+FM"), 4) personal computer. Software of the station includes the free program HSDR for SDR-receiver control, as well as an antenna direction control program, a program for determining a frequency of a signal, emitted by satellite radio beacon and received by the station, and a program for clarifying elements of satellite's orbit using the measured values of the frequency.

The NORAD ID of a satellite and a frequency of the signal emitted by its radio beacon should be set to clarify the satellite orbit. The antenna direction control program download current TLE (Two Line Elements) orbital elements of the satellite from the space-track.org site using the satellite's ID. These elements are used by the program to calculate, as functions of time, the values of range, azimuth and elevation angle of the satellite relative to the station. The program determines then the moments of the connections of the necessary antenna sections to the receiver, and performs these connections in the automatic mode, which provides continuous tracking of the satellite during its passage in the zone of direct radio visibility of the station. Simultaneous recording of the received radio signal is performed by the HSDR program in wav-files. The program of determining a frequency of satellite radio beacon signal analyzes the records and automatically detects the radio beacon signal and determines its frequency. The initial orbital elements obtained from the space-track site are clarified according to the measured values of the frequency using the program developed by V.A. Yamnitsky.

The report presents the results of the station test, which include an estimation of internal errors of the orbital elements determining of tracked satellites.

A network of stations similar to the one considered in the report could be used to orbital tracking of low-orbit spacecrafts equipped with radio beacons.

Keywords: Doppler's effect, radio beacon, low orbit spacecraft.

АБСТРАКТ. В НДІ «МАО» розроблена та протестована наземна станція орбітального супроводу низько орбітальних космічних апаратів. Для орбітального супроводу станція використовує доплерівський зсув частоти сигналів, які випромінюються радіомаяками космічних апаратів. До складу станції входить: 1) 10-секційна антена з круговою діаграмою спрямованості в діапазоні частот 400-450 МГц, 2) електронний блок підключення секцій антени до приймача, 3) SDR-приймач, створений з використанням USB-приймача наземного цифрового телебачення і радіо («DVB-T+DAB+FM»), 4) персональний комп'ютер. Програмне забезпечення станції включає безкоштовну програму HSDR управління SDR-приймачем, програму управління діаграмою спрямованості антени, програму визначення частоти сигналу, випроміненого радіомаяком супутника і прийнятого станцією, а також програму уточнення елементів орбіти супутника за вимірними значеннями частоти.

Для уточнення орбіти необхідно задати ідентифікатор NORAD супутника (ID) та частоту сигналу, випромінюваного його радіомаяком. Знаючи ID програма управління діаграмою спрямованості антени завантажує з сайту space-track.org поточні значення елементів орбіти супутника в TLE (Two-Line Elements) форматі. Отримані елементи орбіти використовуються програмою для обчислення змінювання у часі значень відстані до супутника, азимуту та кута місця супутника відносно станції та визначення моментів часу підключення необхідних секцій антени до приймача. Програма виконує ці підключення в автоматичному режимі, що забезпечує безперервний супровід супутника під час проходження ним зони прямої видимості станції. Одночасно програмою HSDR прийнятий радіосигнал записується в wav-файли. Програма визначення частоти сигналу супутникового радіомаяка аналізує записи, автоматично виявляє сигнал радіомаяка та визначає його частоту. За допомогою програми, розробленої В.А. Ямницьким, початкові значення елементів орбіти супутника, отримані з сайту space-track.org, уточнюються за вимірними значеннями частоти.

В статті представлено результати тестування станції, які включають оцінку внутрішньої похибки визначення орбіти контрольованого супутника.

Мережа станцій, подібних розглянутих в статті, може бути використана для орбітального супроводу низько орбітальних супутників, обладнаних радіомаяками.

Ключові слова: Доплерівський ефект, радіомаяк, низькоорбітальний космічний корабель.

1. Introduction

The Doppler's effect is widely used for objects positioning in the past and today. For example, the Doppler systems Transit (in the USA), Tsikada and Parus (in the former USSR) were the first global navigation satellite systems in the world. The Transit system operated in 1967-1991 and its best accuracy was 20 m (Transit (satellite), 2018).

Another example is the Franco-American project ARGOS (ARGOS, 2018). It is a nowadays operating global satellite-based location and data collection system. The system is used to study and protect our planet's environment. Its purpose is locating any mobile objects (which named platforms) equipped with a compatible transmitter. The system uses the Doppler's effect on a transmission frequency ($401.650 \text{ MHz} \pm 30 \text{ kHz}$) to determine positions of the platforms. Herewith the exact value of a frequency transmitted by the platform is an unknown value and is determined together with platform coordinates. The system consist of six polar orbit satellites at an attitude of 859 km, nearly 60 ground receiving stations and two ARGOS processing centers (in the USA and France). The accuracy of the system is 250 m.

Well known also the French radar-based space surveillance system named GRAVES. It is an active Doppler radar which emits the CW (Continuous Wave) signal of 750 kW power at the frequency of 143050 kHz and has the range of 2000 km (Graves (system), 2018). There is a possibility to receive the GRAVES signal reflected by satellites and the Moon using relatively simple equipment even in Ukraine (Bushuev et al., 2013).

The Doppler station developed and tested in the RI "MAO" uses the passive radar principle and is intended to clarify orbits of low-orbit satellites by measuring the Doppler shift of frequencies of their radio beacons. Initial orbits of tracked satellites are taken from (SPACE-TRACK.ORG, 2018). The station uses a compact high-tech receiver of the megahertz frequency range that greatly simplifies and reduces the cost of its hardware.

2. Doppler station hardware and software

Block diagram of the station is shown in Fig. 1. As it follows from the figure, the station consists of the next equipment:

- 10-sections omnidirectional antenna in the upper hemisphere (S1, ..., S10);
- Antenna switches unit;
- Software defined radio (SDR) that includes personal computer (PC) and receiver used microchip Realtek RTL2832U as a demodulator of radio frequency signals (RF) of terrestrial digital television and radio "DVB-T+DAB+FM" (Digital Video Broadcasting-Terrestrial + Digital Audio Broadcasting + Frequency Modulation).

The height of the antenna is 9 m. Each its section is a Yagi-Uda antenna with horizontal polarization. The sections from S1 to S8 have eight (S1 and S5) or seven dipoles. The direction of these sections changes from the north (S1) to the east through 45 degrees. The sections S9 and S10 have only one dipole each and orthogonal directions: the north-south and east-west, respectively. These two sections are used for observations satellites which pass right over the station. The frequency band of the antenna is 430-440 MHz. The appearance of the antenna is shown in Fig. 2.

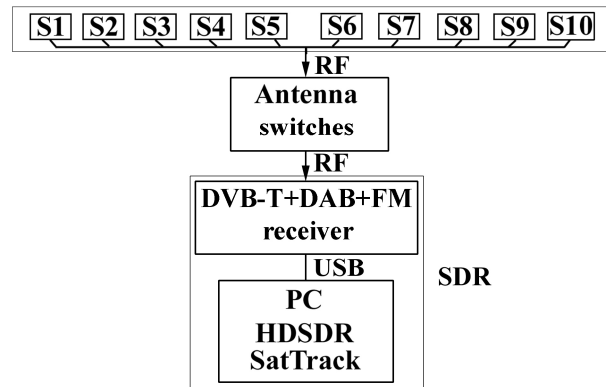


Figure 1: The block diagram of the station



Figure 2: The appearance of the antenna

The antenna switches unit has a microcontroller, transistor switches and reed relays that directly connect the desired antenna section to the receiver. Herewith the RS232 interface is used to exchange data with the PC. It is made on the FT232 chip that allows one to connect the unit to the PC via USB.

The "DVB-T+DAB+FM" receiver has the follow characteristics:

- 24-1766 MHz frequency band;
- 0.22 μV sensitivity;
- 50 dB dynamic range;
- using USB as an interface with the PC and as a power supply.

As the part of the SDR, the receiver provides analog-digital converting and transmitting to the PC the stream of 8-bit quadrature signals with sampling rate up to 3.2 MHz (GNSS-SDR, 2018).

Station software driven by Windows consists of:

- Drivers of the "DVB-T+DAB+FM" receiver with microchip RTL2832U;
- Freeware program HSDR (High Definition Software Defined Radio) is for control the receiver and for recording received signals into wav-files (HSDR, 2018);
- Program SatTrack is for calculating current position of a tracking satellite using its TLE (Two Line Elements) orbital elements from (SPACE-TRACK.ORG, 2018) and for automatically switching the antenna sections according to azimuth and elevation of the satellite;
- Program SatDoppler is for automatically detecting the satellite track on the plane "frequency-time" and determining function $F(t)$, where F – is a radio beacon frequency at a moment t ;

– Program WinMNK is for clarifying of TLE orbital elements using $F(t)$. The program has been developed by V.A.Yamnitsky (Kozelkov, 2012).

There are two stages to clarify orbit elements of the given satellite: real time and post processing. Next steps should be performed in real time:

- Setting the NORAD ID of the given satellite and start tracking the satellite using SatTrack for switching antenna sections;
- Setting (using HSDSR) the receiver’s frequency that corresponds to the satellite radio beacon frequency;
- Recording received signals in wav-files using HSDSR.

Post processing includes:

- Analyzing the wav-files and determining a function $F(t)$ using SatDoppler;
- Taking into account the measured function $F(t)$ clarifying of the satellite orbital elements using WinMNK.

3. Doppler station testing results

Figure 3 shows an HSDSR screenshot and illustrates satellites tracking. In order to improve the screenshot quality, its RGB colors were inverted and converted in grayscale. The screenshot contains so called "waterfall": amplitude distributions of spectral components of a signal received by the station during the given time interval.

On the "waterfall" the amplitude of the signal in the time-frequency domain is displayed using the brightness and color of the corresponding points of the domain - the marks. The "waterfall" shown on Fig. 3 is obtained during a passage of the OSCAR-19 satellite on 19 July 2018. As Fig. 3 shows, the signal duration is about 680 s and its frequency is in the range from 437118 kHz to 437099 kHz. The middle frequency of the given range is equal to $f_n = 437108.5$ kHz. Figure 3 also shows that f_n may be seen as an approximate estimation of a true radio beacon frequency f_0 . But the OSCAR-19 radio beacon has the frequency that is equal to $f_0 = 437125$ kHz (N2YO.COM, 2018). So, there is a difference between the frequency obtained HSDSR and the true radio beacon frequency which is equal to $(f_n - f_0) = -16.5$ kHz. This difference is due to the odds between the valid (f_v) and nominal (f_n) frequencies of a reference generator of the receiver. In this case, however, the ratio between f_v and f_n does not depend from frequency value and is

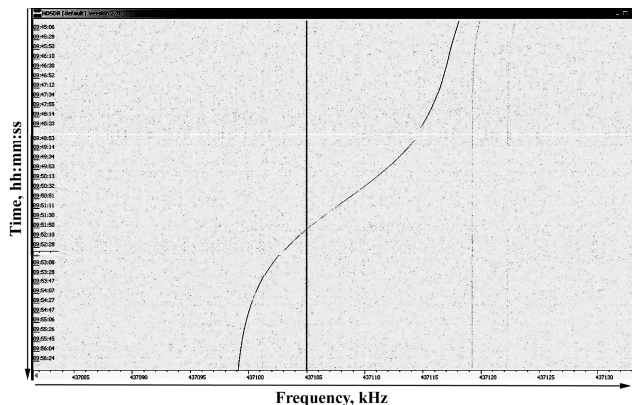


Figure 3: The HSDSR screenshot obtained during the OSCAR-19 passage on 19 July 2018.

determined for each receiver using a rubidium atomic reference generator. This ratio takes into account when the function $F(t)$ is determined.

Let $f_d = F(t) - f_0$ denote the frequency shift due to the Doppler effect. Let f_{dobs} denote the measured value of f_d and f_{dcalc} – the calculated value of f_d obtained using clarified orbital elements. The measured (v_{obs}) and calculated (v_{calc}) values of the radial component of the satellite velocity may be also obtained using the formula $v = -f_d \cdot c/f_0$, where c is speed of light.

Figure 4 illustrates the orbit determination results on the example of CUTE-1 tracked at 20 June 2017. Values of f_{dobs} (bold line) and f_{dcalc} (thin line) as a function of time are shown in Fig. 4(a). In Fig. 4(b) a distribution of residuals ($v_{obs} - v_{calc}$) are shown as the function of amplitude of the received signal. The data shown in Fig. 4(a) and (b) are obtained using the same observation of CUTE-1.

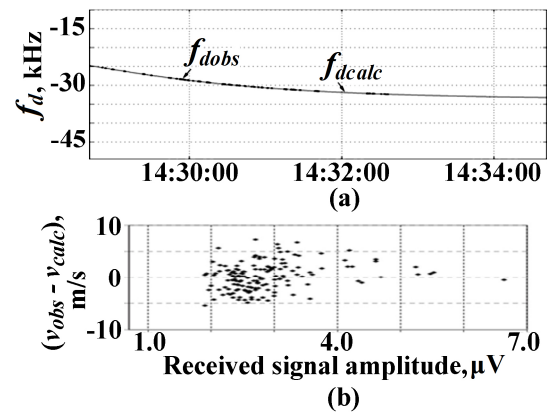


Figure 4: Orbit determination results on the example of CUTE-1 tracked at 20 June 2017.

Table 1: The main information about low-orbit satellites have been tracked by the station

| Sat Name | NORAD ID | f_0 , MHz | Num Tracking |
|-----------------------|----------|-------------|--------------|
| CUTE-1 | 27844 | 436.8375 | 9 |
| CUTE-1.7 | 28941 | 437.382 | 2 |
| KISEKI | 33499 | 437.385 | 2 |
| ITU-pSat1 | 35935 | 437.325 | 2 |
| AAUSAT-4 | 41460 | 437.425 | 2 |
| SwissCube-1 | 35932 | 437.505 | 1 |
| PSat-A/B | 40654 | 435.350 | 1 |
| Somp | 39134 | 437.503 | 1 |
| Studsat1 | 35935 | 437.325 | 1 |
| Techsat ^{*)} | 42829 | 435.959 | 1 |
| Oscar-19 | 20442 | 437.125 | 1 |

^{*)} The satellite has a laser ranging retroreflector.

The standard deviation of residuals ($f_{dobs} - f_{dcalc}$) for the f_{dobs} and f_{dcalc} values shown in Fig. 4(a) had been calculated and equal to 3.8 Hz. Figure 4(b) shows that there is a tendency of decreasing of absolute values of ($v_{obs} - v_{calc}$) when signal amplitude increasing.

Table 1 summarizes the main information about 11 low-orbit satellites tracked by the station up to now. The following information is in the table:

- Satellite's name (Sat Name);
- NORAD ID;
- Frequency of satellite radio beacon (f_0);
- Number of performed tracking of satellite (Num Tracking).

4. Conclusion

The ground station of orbital tracking of low-orbit spacecrafts has been developed and tested in the RI "MAO". The station uses the Doppler shift of frequencies of signals radiated by spacecraft radio beacons for their orbital elements determinations. Eleven satellites with radio beacons have been tracked now.

The following is proposed:

- Searching satellites with radio beacons based on Internet data and next checking by the Doppler station;
- Improvement station hardware and software to achieve full automation of the orbital tracking of satellites independent of radio signal spectrum;
- Comparison the Techsat orbit positions obtained by the station with corresponding the ILRS (International Laser Ranging Service) data.

Acknowledgements. Valeriy Aronovych Yamnitsky gone. Authors mourn the loss. Rest in peace, dear teacher and colleague.

References

- ARGOS. Products & Services. Advanced processing service, [online] Available at: <http://www.argos-system.org/> [Accessed 10 October 2018].
- Bushuev F.I., Vorsin G.V., Grinchenko A.A. et al.: 2013, in The Bulletin of the Ukrainian Centre of determination of the Earth Orientation Parameters, **5**, 48 (in Russian).
- GNSS-SDR operation with a Realtek RTL2832U USB dongle DVB-T receiver, [online] Available at: <http://gnss-sdr.org/node/50> [Accessed 10 October 2018].
- Graves (system), [online] Available at: [https://en.wikipedia.org/wiki/Graves_\(system\)](https://en.wikipedia.org/wiki/Graves_(system)) [Accessed 10 October 2018].
- HDSDR. High Definition Software Defined Radio, [online] Available at: <http://hdsdr.de/> [Accessed 10 October 2018].
- Kozelkov S.V., Makhonin E.I., Morgun A.A. et al.: 2012, Information Processing Systems, **2**, 42 (issue 3 (101)) (in Russian).
- N2YO.COM. Live Real Time Satellite Tracking and Predictions, [online] Available at: <http://www.n2yo.com> [Accessed 10 October 2018].
- SPACE-TRACK.ORG, [online] Available at: <https://www.space-track.org/auth/login> [Accessed 10 October 2018].
- Transit (satellite), [online] Available at: [https://en.wikipedia.org/wiki/Transit_\(satellite\)](https://en.wikipedia.org/wiki/Transit_(satellite)) [Accessed 10 October 2018].

DOI: <http://dx.doi.org/10.18524/1810-4215.2018.31.145360>

EXTERNAL COMPARISON SATELLITE POSITIONS OBTAINED BY THE NETWORK OF PASSIVE CORRELATION RANGING OF GEOSTATIONARY TELECOMMUNICATION SATELLITES

F. Bushuev¹, M. Kaliuzhnyi¹, O. Mazhaev¹, O. Shulga¹, L. Shakun², V. Bezrukovs³,
O. Reznichenko⁴, S. Moskalenko⁵, Ye. Malynovskyi⁶

¹ Research Institute “Mykolaiv Astronomical Observatory” (RI “MAO”), Mykolaiv, Ukraine, dir@mao.nikolaev.ua

² Research Institute “Astronomical Observatory” of the Mechnikov Odesa National University, Odesa, Ukraine, astronomical_observatory@onu.edu.ua

³ Ventspils University College, Ventspils, Latvia, virac@venta.lv

⁴ Institute of Radio Astronomy of the NASU, Kharkiv, Ukraine, rai@ri.kharkov.ua

⁵ Western Center of Radio Engineering Surveillance, Mukacheve, Ukraine, ckako@i.ua

⁶ Rivne Minor Academy of Science of School Age Youth, Rivne, Ukraine, man.rivne@ukr.net

ABSTRACT. Network of passive correlation ranging contains of five stations located in Ukraine and Latvia. It has been created at the initiative of the RI “Mykolaiv Astronomical Observatory” to have independent means to track the future Ukrainian geostationary satellite “Lybid”. Regular observations of the geostationary telecommunication satellite “Eutelsat-13B” has being carried out by the network since February 2015. A catalog of daily orbital elements of the tracked satellite has been created using the network observations. The analytical model SGP4/SDP4 of satellite motion and a numerical model of integration of equations of satellite motion are used to determine the orbital elements. The numerical model takes into account the gravitational attraction of the Sun and Moon, and non-spherical Earth. Software of the orbital elements determinations has been developed by the RI “Astronomical Observatory” of the Mechnikov Odesa National University.

Satellite positions calculated using orbital elements from the catalog were compared with ones obtained using the NORAD space-track.org site and optical observations performed by the Ukrainian Network of Optical Stations. The satellite position comparisons were carried out only for time intervals of unperturbed motion of the satellite. The free motion time intervals were determined using the algorithm that had been tested using satellite owner data about the moments of satellite maneuvers. Herewith values of right ascension and declination were compared. Regular (mean) and random (standard deviation) values of the residuals are given in the report.

Keywords: geostationary satellite, passive correlation ranging, orbital elements.

АБСТРАКТ. До складу мережі пасивного кореляційного дистанціювання входять п'ять станцій розташованих в Україні і в Латвії. Мережа була створена за ініціативою НДІ «Миколаївська астрономічна обсерваторія» як незалежний засіб супроводу майбутнього українського геостационарного супутника «Либідь». Регулярні спостереження геостационарного телекомунікаційного супутника «Eutelsat-13B» проводяться мережею з лютого 2015 року. За результатами спостережень створено каталог щодобових значень елементів орбіти супроводжуваного супутника. Елементи орбіти визначаються з використанням аналітичної моделі SGP4/SDP4 руху супутника та чисельної моделі інтегрування рівнянь руху супутника. Чисельна модель враховує гравітаційне тяжіння Сонця і Місяця, а також несферичної Землі. Програмне забезпечення для визначення елементів орбіти було розроблено в НДІ «Астрономічна обсерваторія» Одеського національного університету імені І.І.Мечникова.

Положення супутника, обчислені з використанням елементів орбіти з каталогу, порівнювалися з положеннями, обчисленими з використанням елементів орбіти з сайту NORAD space-track.org, а також з положеннями, отриманими в результаті оптичних спостережень, виконаних Українською мережею оптичних станцій. Порівняння положень супутника проводилися тільки для інтервалів часу незбуреного руху супутника. Інтервали часу незбуреного руху визначалися за алгоритмом, який був протестований з використанням даних про час виконання маневрів, отриманих від власника супутника. При цьому порівнювалися значення прямого сходження і схилення. В статті наводяться отримані регулярні (середнє) та випадкові

(середньоквадратична похибка) значення різниці положень супутника.

Ключові слова: геостационарний супутник, пасивне супровід, елементи орбіти.

1. Introduction

The development of global satellite navigation and Internet, capable of providing device synchronization and data transfer, regardless of the distance between them, has led to the development of a cheap, fully passive, spatially distributed radio engineering system (network) to determine the position of geostationary satellites. The basic principle of the operation of such a network is the use of correlation analysis to calculate Time Difference Of Arrival (TDOA) of signals emitted by satellites and received by spatially separated network stations. Such a passive correlation ranging (PaCoRa) system has been developed by the SES (Société Européenne des Satellites) in 2010-2013 and is considered by the European Space Agency (ESA) as a highly accurate alternative to conventional radar used two-way ranging method (ESA, 2018).

Network of passive correlation ranging (NetPCR) consisted of two stations has been created and tested by the RI “MAO” in August 2011. Since February 2015 the NetPCR carries out regular observations of the geostationary telecommunication satellite “Eutelsat-13B” first by four and then by five stations located in Ukraine and Latvia (Bushuev et al., 2016; Kaliuzhnyi et al., 2016). Single-measurement error (1 sigma) of the TDOA has been obtained and equal about ± 8.7 ns for the all pairs of the stations. A catalog of daily satellite’s orbital elements has been created using the analytical model SGP4/SDP4 of satellite motion and a numerical model of integration of equations of satellite motion. The internal error of coordinate determination of the tracked satellite has been obtained in a local orbital frame (Package, 2018) and it does not exceed 225 m that approximately equal to the error of the PaCoRa system (Bushuev et al., 2017). Means and standard deviations of the residuals of Eutelsat-13B Cartesian coordinates obtained by the NetPCR and Eutelsat (owner of the satellite) in the ITRF are also given in (Bushuev et al., 2017). The numerical model as more accurate has been used to calculate the coordinates. Here-with the maximum absolute value of the means was less than 900 m and the maximum standard deviation was 1280 m. These values were obtained for the time when Eutelsat-13B orbit was undisturbed. The significant differences in coordinates may be due to the difference of satellite motion models used by Eutelsat and ourselves to calculate coordinates.

2. Optical and radio observations comparison

Optical observations of Eutelsat-13B have been performed in 2015 and 2016 by an automatic telescope KT-50 which is a part of a complex of mobile telescopes (MOBITEL) of the RI “MAO” (Shulga, 2010). MOBITEL is also a part of the Ukrainian Network of Optical Stations (UMOS, 2018).

Right ascensions (α_o) and declinations (δ_o) measured by the telescope are compared with α_r and δ_r computed using daily orbital elements (the numerical model) from the NetPCR catalogue (Geostationary satellites, 2018). Here-with an inertial coordinate system was EME2000 (Earth’s Mean Equator and Equinox) or J2000 and the space dynamic library OREKIT was used for astronomical computations (Orekit, 2018). Light-time correction was also taken into account to compute α_r and δ_r at the moment of optical measurements.

Totally the 24 different sets of α_o and δ_o were obtained but only 7 of them were taken into consideration. The reasons for the rejection of observations were as follows:

- Maneuver could take place during the day of the observation;
- Another satellite was observed in the same geostationary cell;
- Sample size of measured values of α_o and δ_o (N) was less than 4.

Satellite Cartesian coordinates in the ITRF were computed on the day ends (at 23:59 and 00:00) using orbit elements from the catalogue for three consecutive days: at a day of optical observations and at days before and after it. It is assumed that a maneuver may take place at the day if jumps of the coordinates on the ends were greater than 200 m. The coordinate jump threshold (200 m) was determined using information about Eutelsat-13B maneuvers which was obtained from the satellite owner (Bushuev et al., 2017).

Another satellite (Eutelsat-13C or 13E instead of 13B) was observed if the residuals (Δ) between measured (α_o and δ_o) and calculated (α_c and δ_c) right ascensions and destinations were greater for Eutelsat-13B than for Eutelsat-13C or Eutelsat-13E. The NORAD data or TLE (Two Line Elements) orbital elements from the space-track.org site are used to calculate α_c and δ_c .

Average values (Mean) and standard deviations (SD) of the optic-radio residuals ($\Delta_{\alpha o} = \alpha_o - \alpha_r$ and $\Delta_{\delta o} = \delta_o - \delta_r$) are estimated for the 7 observations are shown in Table 1 in arc seconds.

Table 1: Means and standard deviations of the optic-radio residuals, arc seconds.

| Date | N | Mean of $\Delta_{\alpha o}$ | SD of $\Delta_{\alpha o}$ | Mean of $\Delta_{\delta o}$ | SD of $\Delta_{\delta o}$ |
|----------|-----|-----------------------------|---------------------------|-----------------------------|---------------------------|
| 31.10.15 | 12 | -10.0 | 2.3 | -10.2 | 0.5 |
| 20.05.16 | 18 | -12.5 | 5.7 | 4.1 | 0.9 |
| 09.06.16 | 15 | -15.1 | 3.0 | 0.7 | 0.7 |
| 30.06.16 | 12 | -16.4 | 1.5 | -2.8 | 0.7 |
| 03.09.16 | 9 | 36.5 | 2.3 | -7.2 | 0.3 |
| 06.09.16 | 8 | 36.7 | 1.8 | -6.7 | 0.4 |
| 30.09.16 | 12 | 26.5 | 2.5 | -11.1 | 0.2 |

Table 1 shows that the mean (absolute value) and SD of Δ_{α} are less than 37” and 6”, respectively. The corresponding values for Δ_{δ} are equal 12” and 1”.

Table 2: Mean and SD intervals of the optic-radio and radio-NORAD residuals, arc seconds

| Residuals | Mean of Δ_α | SD of Δ_α | Mean of Δ_δ | SD of Δ_δ |
|-------------|-------------------------|-----------------------|-------------------------|-----------------------|
| Optic-radio | -15.4 \div 36.7 | 1.5 \div 5.7 | -11.1 \div 4.1 | 0.2 \div 0.9 |
| Radio-NORAD | -11.4 \div -2.7 | 2.4 \div 4.5 | -0.8 \div 0.4 | 1.0 \div 4.9 |

3. Comparison radio observations with NORAD data

The values of α_r and δ_r are also compared with α_c and δ_c computed using NORAD data from the space-track.org site for the 7 days from Table 1. The intervals of changing means and SD of the radio-NORAD residuals $\Delta_{\alpha c} = \alpha_r - \alpha_c$ and $\Delta_{\delta c} = \delta_r - \delta_c$ are given in Table 2. The corresponding intervals for $\Delta_{\alpha o}$ and $\Delta_{\delta o}$ are also shown in the table for comparison.

Table 2 shows that the means of the residuals are less for the radio-NORAD residuals than the optic-radio ones. Herewith the standard deviations of the residuals are greater especially for δ .

4. Conclusion

Eutelsat13-B positions obtained by the network of passive correlation ranging and gathered in the catalogue were compared with optical measurements and with the data from the space-track.org site (the NORAD data).

The comparisons were performed for 7 days in 2015 and 2016 when Eutelsat-13B positions were measured by the optical telescope KT-50 MOBITEL (RI "MAO") and the probability of satellite maneuver was minimum.

The means and standard deviations of α and δ residuals (optic-radio) are in the next intervals (arc seconds):

- Means of $\Delta\alpha$: -15.4" \div +36.7", SD of $\Delta\alpha$: 1.5" \div 5.7";
- Means of $\Delta\delta$: -11.1" \div +4.1", SD of $\Delta\delta$: 0.2" \div 0.9";

The regular components of the residuals (means) between the NetPCR and NORAD α and δ were less than the similar values for the optic and NetPCR measurements. Herewith the random components (SD) were greater especially for δ .

The following is proposed to improve the NetPCR accuracy:

- Eliminate hardware errors (including inaccuracy of antennae phase centers positions);

– Taking into account tropospheric delays and light-time corrections during orbital elements computations using the numerical model of satellite motion.

References

- Bushuev F., Kaliuzhnyi M., Sybiryakova Ye. et al.: 2016, *Latvian Journal of Physics and Technical Sciences*, **53**, No. 5, 5.
- Bushuev F. Kaliuzhnyi V., Shulga O. et al.: 2017, in *Proceedings of the 9th IAASS Conference Session 11: Space Traffic Control – I*, Toulouse (France), 18-20 October 2017, 213.
- ESA. BUSINESS APPLICATIONS. ARTES. PASSIVE CORRELATION RANGING (PACORA), [online]. Available at: <https://artes.esa.int/projects/passive-correlation-ranging-pacora> [Accessed 10 October 2018].
- Geostationary satellites. Radio interferometric network for tracking of geostationary telecommunication satellites, [online]. Available at: http://www.nao.nikolaev.ua/index.php?catalog_id=459 [Accessed 10 October 2018].
- Kaliuzhnyi M., Bushuev F., Shulga O. et al.: 2016, *Odessa astronomical publications*, **29**, 203.
- Orekit. An accurate and efficient core layer for space flight dynamics applications, [online]. Available at: <http://orekit.org/> [Accessed 10 October 2018]
- Package org.orekit.frames Class LocalOrbitalFrame, [online]. Available at: <https://www.orekit.org/static/apidocs/org/orekit/frames/LocalOrbitalFrame.html> [Accessed 10 October 2018].
- Shulga O., Kozyryev Y., Sybiryakova Y.: 2010, *Proc. of Gaia follow-up network for Solar system objects workshop held at IMCCE-Paris observatory*, November 29 – December 1, 2010, France, 97.
- UMOS. Ukraine Network of Optical Stations, [online]. Available at: <http://umos.mao.kiev.ua/eng/> [Accessed 10 October 2018].

DOI: <http://dx.doi.org/10.18524/1810-4215.2018.31.145083>

THE EXISTENCE OF GROUPS OF METEORITE-PRODUCING FIREBALLS AND METEORITES IN COMET-LIKE ORBITS

N.A. Konovalova¹, Yu.M. Gorbanev², N.H. Davruqov³

¹ Institute of Astrophysics of the Academy of Sciences of the Republic of Tajikistan, lnakonovalova@mail.ru

² Astronomical Observatory of Odessa National University, Ukraine, skydust@ukr.net

³ Institute of Astrophysics of the Academy of Sciences of the Republic of Tajikistan, Naqqosh89@mail.ru

ABSTRACT. This paper discusses the existence of groups of meteorite-producing fireballs and ordinary chondrites in the Earth-crossing Jupiter-family comet-like (JFC) orbits. The similarity of the orbits of meteorite-producing fireballs and those of meteorites in the groups was established by applying three criteria of orbital similarity – namely, the DSH criterion introduced by Southworth and Hawkins, the DDR criterion suggested by Drummond, and DN criterion reported by Jopek. We have detected six groups of meteorite-producing meteoroids and ordinary chondrites of L3.5-H5 types observed over the determined periods of increased fireball activity. Carrying out systematic and well-targeted observations, especially during the determined periods of increased fireball activity, enables to obtain reliable statistics from the collected observational data on the meteorite-producing meteoroids in order to determine their orbits, as well as their physical characteristics. The six target groups in this study, which contain 89 meteorite-producing meteoroids and six ordinary chondrites, may be groups of dynamically connected bodies. The genetic relationship between the investigated bodies within groups needs to be considered on the basis of the analysis of orbital evolution of the members of each group over the past several thousand years. The data on the mean heliocentric orbit of the group of meteorite-producing meteoroids enable us to link the group with its likely source, which may be either an asteroid, a family of asteroids or a comet, thereby making it possible to obtain information about the source itself. The search for potential parent bodies of the investigated groups of meteorite-producing fireballs and meteorites was carried out among new near-Earth asteroids. Consequently, several asteroids were selected in each group with the following criteria of the similarity between the asteroid orbit and mean orbit of the respective group: $DD \leq 0.06$, DSH and $DN \leq 0.12$.

Keywords: group – fireball – meteorite – ordinary chondrite – orbit – comet – Jupiter family.

АБСТРАКТ. У статті розглянуто існування груп метеоритоутворюючих болідів і метеоритів із класу звичайних хондритів на кометоподібних орбітах типу JFCs, які перетинають земну орбіту. Близькість орбіт болідів і метеоритів в групах встановлювалася на основі трьох динамічних критеріїв близькості DSH-

критерію Саутворт і Хокінса, DD-критерію Друммонда і DN-критерію Йопека. Виявлено шість груп метеоритоутворюючих метеороїдів та метеоритів з класу звичайних хондритів типу L3.5 – H5, що спостерігалися в знайдених періодах підвищення болідної активності.

Проведення систематичних і цілеспрямованих спостережень, особливо у зазначені інтервали часу підвищення болідної активності дозволяє отримати добре забезпечену статистику спостережних даних про метеоритоутворюючі метеороїди для визначення їх орбіт, а також їх фізичних характеристик. Досліджені групи, що включають 89 метеоритоутворюючих метеороїдів та 6 метеоритів з класу звичайних хондритів типу L3.5 – H5, можуть бути групами динамічно пов'язаних небесних тіл. Питання про генетичний зв'язок досліджених тіл в групі необхідно розглядати на основі аналізу еволюції орбіт членів групи на інтервалі в декілька тисяч років в минулому.

Дані про середню геліоцентричної орбіті групи метеоритоутворюючих болідів дозволяють зв'язати групу з її ймовірним джерелом – астероїдом, астероїдним сімейством або кометою, і таким чином отримати інформацію про джерело. Серед астероїдів проведено пошук можливих батьківських тіл досліджених груп метеоритоутворюючих болідів і метеоритів. В результаті відібрано по кілька астероїдів для кожної групи з критеріями близькості орбіти астероїда і середньої орбіти групи: $DD \leq 0.06$, DSH і $DN \leq 0.12$.

Ключові слова: група – болід – метеорит – звичайний хондрит – орбіта – комета – сімейство Юпітера.

1. Introduction

The problem of asteroid and comet impact hazard (ACIH) has been becoming progressively more acute nowadays, especially considering the increasing number of nuclear power stations, chemical plants and hydroelectric power station dams, as well as the expansion of densely populated areas, and addressing this problem requires raising funds from different sources. To this end, national and international sky survey programmes employing various observation tools for the detection of potentially hazardous space objects have been developed to work out countermeasures against the threat these objects

pose to our planet. Earlier, the Earth-crossing objects larger than 100 m were assumed to be potentially hazardous objects (PHO). However, this approach has been modified upon the Chelyabinsk meteor event took place on 15 February, 2013, in Russia [1]; hence now even objects smaller in decametric size ($>10 \div 20$ m) should be considered hazardous, especially due to their numerousness in the near-Earth space. The surveillance of fireballs using various observation tools enable to obtain more precise data on their atmospheric paths, orbits in the near-Earth space and coordinates of the predicted meteorite impact sites.

The importance of meteorite studies is also justified by the fact that chondrites, which comprise the most numerous group of meteorites, are similar in chemical composition to the Sun and represent the unprocessed primary matter from which the Solar System had emerged. The estimated daily mass influx of extra-terrestrial material to the Earth is within the range from 100 to 1,000 tons. Relatively large objects, i.e. meteorites, make up just about 1% of the above indicated total quantity. Three quarters of this quantity falls into the oceans while the majority of the remaining portion fall onto inaccessible or uninhabited and sparsely populated regions where meteorites are unlikely to be found. Most small meteorites, having fallen onto the ground, get lost among the terrestrial rocks. Obtaining data from fireball observations and finding meteorites, i.e. extra-terrestrial samples, are of great scientific importance with regard to understanding their origin and search for their sources in the Solar System.

2. Observations of meteorite-producing fireballs carried out by meteor stations and fireball networks

Observations of meteors and fireballs have been performed by meteor stations and fireball networks, which allow us to obtain data on the fireball passage through the atmosphere, its orbit in the near-Earth space, as well as coordinates of the meteorite impact site for sufficiently large bodies. With increasing statistics on the instrumentally observed meteorites, it has become possible to separate groups of meteorite-producing meteoroids from the sporadic meteoroid background in the near-Earth space.

The existence of meteoroid groups consisting of bodies producing meteorites was discussed in [2, 3] on the basis of well-determined fireball orbits obtained in the Canadian Meteorite Observation and Recovery Project (MORP) and by the U.S. Prairie Meteorite Network.

The current statistics on meteorite-producing sporadic bright fireballs and superbolides show that such events occur rather frequently – approximately once a week or fortnight [4]. Within the framework of the asteroid and comet impact hazard (ACIH) problem, it is crucial to carry out systematic observations of meteorite-producing fireballs, for which the data on the periods of activity are needed. To identify such periods of fireball activity, the distribution of quantity N of the observed sporadic bright fireballs and meteorites with known fall dates along the solar longitude L_{\odot} throughout the year was investigated using meteor observation data published in catalogues and academic journals [5]. As a result, we plotted a bar chart of annual distribution of quantity N of sporadic fireballs and superbolides with asteroid and comet-like orbits, as well as meteorites with known fall dates, including those with instrumentally determined atmospheric trajectory and orbits, in the solar longitude L_{\odot} with a time step of 2° . The resulting bar chart is shown in Fig. 1 wherein arrows indicate the dates of instrumentally recorded sporadic fireballs, after which the falls of known meteorites, i.e. chondrites of L3.5-H5 types with Jupiter-family comet-like orbits (namely Benešov, Neuschwanstein, Příbram, Park Forest, Košice and Mason Gully meteorites), took place. The obtained profile of annual activity of sporadic meteorite-producing fireballs and meteorites shows six major (1-6 Maj) and two minor (1-2 Min) periods of increased fireball activity throughout the year.

A potentially hazardous object in the Earth-crossing orbit can be detected while it is still in the near-Earth space and has not yet entered the Earth's atmosphere. There are already several on-going projects, e.g. the ATLAS project, developed for the early detection and monitoring of the short-period objects (with an orbital period of less than 20 years) approaching the Earth (with the perihelion distance $q < 1.3$ AU), which can be either near-Earth Jupiter-family comets (NEJFCs) or near-Earth asteroids well before their

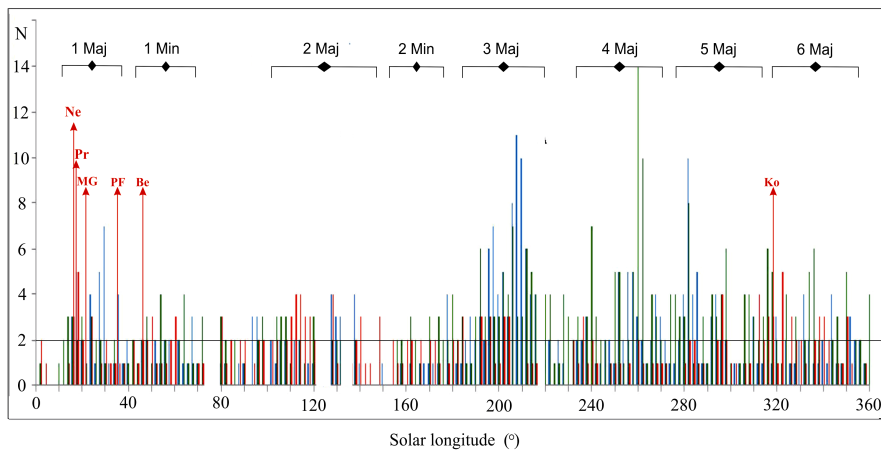


Figure 1: A bar chart representing the annual distribution of the quantity N of meteorite-producing sporadic fireballs and meteorites in the solar longitude L_{\odot} .

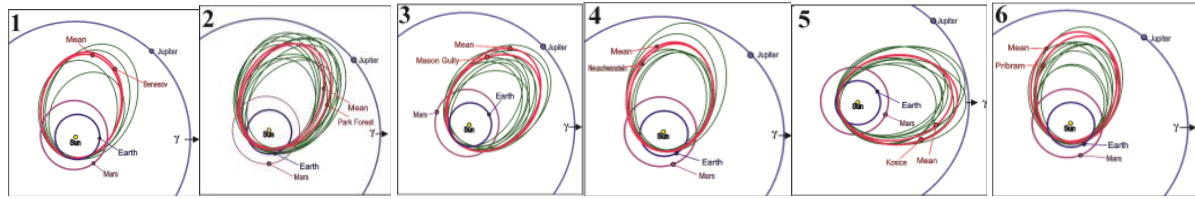


Figure 2: Meteorite and fireball orbits, as well as mean orbits of the six groups of meteorite-producing meteoroids, projected onto the ecliptic.

(NEAs). It is likely that in the nearest future it will be feasible to detect such objects as the Chelyabinsk meteorite entering the Earth's atmosphere, as well as to predict the likelihood of their fall onto the Earth's surface in the computationally predicted area. There have been two cases of the early detection of the objects approaching the Earth reported so far, whose fall was predicted well in advance, namely the Almahata Sitta meteorite (2008 TC3) [6] and the second object 2014 AA, which fell into the Atlantic ocean [7]. These cases have proved a clear need for systematic and well-targeted observations, especially during periods of increased fireball activity, in order to obtain reliable statistics on the meteoroids expected to produce meteorites which will enable to determine their orbits and physical characteristics. The collected observational statistic data will allow us to separate potential groups which may consist of potentially hazardous meteoroids based on the results of the analysis of orbital elements of the meteorite-producing meteoroids.

3. The origin of groups of meteorite-producing meteoroids and their sources

There are observational evidences of the existence of rubble-pile asteroids, such as Itokawa and NEA 1950 DA [8]. Many of such asteroids could be formed from collisions between the Main-belt asteroids. According to their structure, rubble-pile asteroids are heterogeneous asteroids in the form of an aggregate of components held together by relatively weak gravity. Such asteroids can undergo tidal disruption during their close fly-bys around the planet within the Roche limit [9]. There are several other mechanisms that may cause the disintegration of an asteroid body, such as gravitational perturbations of Jupiter and other Solar System planets; the Yarkovsky – O'Keefe – Radzievskii – Paddack (YORP) effect spin-up; thermal stress in the object may also result in its partial or complete break-up into a host of fragments of different size – from decametric to metric sized ones and smaller. The resulting fragments form a group of asteroidal fragments, including meteorite-producing ones with identical heliocentric orbits, which being evolving gradually move to the Earth-crossing orbits due to the resonance effect primarily with Jupiter. Another possible mechanism of the formation of asteroidal fragments may be the collision between the asteroid and another space body, i.e. large meteoroid or small asteroid. Disintegration of asteroids, as well as of comets [10], results in the formation of groups of fragments, i.e. meteoroids of different size, in the near-Earth space in the orbits similar to those of their parent bodies.

4. Groups of meteorite-producing fireballs and ordinary chondrites in the Jupiter-family comet-like orbits

This study is aimed to investigate the possibility of the existence of groups of meteorite-producing meteoroids with Jupiter-family comet-like orbits in the near-Earth space, as well as the correlation between such groups of meteoroids and six known ordinary chondrites of L3.5-H5 type, which have been observed so far. The target groups of meteorite-producing meteoroids were named after the known meteorites comprising the respective groups. Scientific publications and meteor catalogues were used to search for meteorite-producing fireballs with orbits similar to the Jupiter-family comet-like (JFC) orbits of the six chondrites. The similarity of meteorite-producing meteoroid orbits with those of the six ordinary chondrites was established by applying commonly used criteria of orbital similarity (D-criteria), such as the DSH criterion introduced by Southworth and Hawkins [11], the DDR criterion suggested by Drummond [12] and DN criterion reported by Jopek et al. [13].

We determined whether the meteorite-producing fireball orbits are comet-like or not using the Tisserand parameter T_J calculated by formula (1):

$$T_j = \frac{a_j}{a} + 2 \cos i \times \left[\left(\frac{a}{a_j} \right) (1 - e^2) \right]^{0.5}, \quad (1)$$

where a and a_j are the semi-major axes of a fireball and Jupiter, respectively; e and i are the eccentricity and inclination of the fireball orbit to the ecliptic, respectively. For the comet-like orbits the value of the Tisserand parameter was $T_j < 3.1$. Fig. 2 illustrates the orbits of meteorites and fireballs, as well as mean orbits of the six groups of meteorite-producing fireballs, projected onto the ecliptic.

The following data on the mean radiant and orbits of the groups, as well as meteorites comprising the respective groups, are given in Table 1: the right ascension α_R ($^\circ$) and declination δ_R ($^\circ$) of the radiant; out-of-atmosphere velocity V_∞ (km/sec); perihelion distance q (AU); semi-major axis a (AU); eccentricity e ; orbital inclination i ($^\circ$); argument of periapsis ω ($^\circ$); and the longitude of the ascending node Ω ($^\circ$). The values of DSH, DDR and DN criteria of the similarity between the meteorite orbit and mean orbit of the group are presented in the last three columns of the table.

Table 1: Groups of meteorites and meteorite-producing fireballs with similar orbits (J2000.0)

| Name | α_R ($^\circ$) | δ_R ($^\circ$) | V_∞ km/s | q a.e. | a a.e. | e | i ($^\circ$) | ω ($^\circ$) | Ω ($^\circ$) | Ddr | Dsh | D_N |
|-----------------------------------|----------------------------|----------------------------|--------------------|-----------|-----------|-------|-------------------|--------------------------|--------------------------|-------|-------|-------|
| Group of meteorite Benesov | | | | | | | | | | | | |
| Mean | 224.0 | 40.6 | 19.3 | 0.948 | 2.360 | 0.588 | 20.4 | 211.6 | 53.4 | 0.00 | 0.00 | 0.00 |
| Benesov | 227.6 | 39.9 | 21.1 | 0.925 | 2.483 | 0.627 | 23.7 | 218.4 | 47.0 | 0.04 | 0.08 | 0.08 |
| (2000JF5) | | | | 0.911 | 2.065 | 0.559 | 13.8 | 216.8 | 58.1 | 0.060 | 0.162 | 0.160 |
| (2010JH3) | | | | 1.054 | 2.706 | 0.611 | 21.0 | 228.0 | 42.8 | 0.070 | 0.141 | 0.139 |
| Group of meteorite Neuschwanstein | | | | | | | | | | | | |
| Mean | 183.6 | -6.9 | 19.9 | 0.798 | 2.430 | 0.665 | 4.5 | 240.2 | 21.0 | 0.00 | 0.00 | 0.00 |
| Neuschwanstein | 192.3 | 19.5 | 21.0 | 0.793 | 2.401 | 0.671 | 11.4 | 241.2 | 16.8 | 0.04 | 0.13 | 0.10 |
| (2005 RW3) ? | | | | 0.749 | 2.105 | 0.644 | 2.70 | 219.6 | 48.9 | 0.051 | 0.108 | 0.106 |
| (2010 GE35) | | | | 0.850 | 2.226 | 0.618 | 5.41 | 233.1 | 34.3 | 0.054 | 0.103 | 0.103 |
| Group of meteorite Park Forest | | | | | | | | | | | | |
| Mean | 173.6 | 10.8 | 19.3 | 0.830 | 2.486 | 0.663 | 5.1 | 233.6 | 6.5 | 0.00 | 0.00 | 0.00 |
| Park Forest. | 171.8 | 11.2 | 19.5 | 0.811 | 2.530 | 0.680 | 3.2 | 237.5 | 6.1 | 0.03 | 0.09 | 0.09 |
| (2011 CY46) | | | | 0.836 | 2.150 | 0.611 | 11.5 | 221.1 | 11.1 | 0.063 | 0.152 | 0.150 |
| (2013 EV108) | | | | 0.877 | 2.397 | 0.634 | 8.42 | 215.2 | 33.4 | 0.053 | 0.136 | 0.134 |
| Group of meteorite Pribram | | | | | | | | | | | | |
| Mean | 184.4 | -4.5 | 19.8 | 0.795 | 2.495 | 0.664 | 3.8 | 238.3 | 25.9 | 0.00 | 0.00 | 0.00 |
| Pribram | 192.3 | 17.5 | 20.9 | 0.790 | 2.401 | 0.671 | 10.5 | 241.8 | 17.8 | 0.06 | 0.13 | 0.13 |
| (2013 GT79) | | | | 0.842 | 2.213 | 0.619 | 1.57 | 224.6 | 44.4 | 0.053 | 0.097 | 0.096 |
| (2001OK153) | | | | 0.756 | 2.439 | 0.690 | 7.57 | 260.6 | 2.6 | 0.052 | 0.119 | 0.117 |
| Group of meteorite Mason Gully | | | | | | | | | | | | |
| Mean | 151.9 | 10.9 | 16.8 | 0.905 | 2.455 | 0.624 | 5.3 | 41.1 | 176.8 | 0.00 | 0.00 | 0.00 |
| Mason Gully | 148.4 | 9.0 | 14.6 | 0.982 | 2.556 | 0.616 | 0.9 | 19.0 | 203.2 | 0.05 | 0.12 | 0.10 |
| (2009 FS) | | | | 0.929 | 2.447 | 0.620 | 4.73 | 44.2 | 173.7 | 0.014 | 0.026 | 0.026 |
| (2011 KK15) | | | | 0.948 | 2.436 | 0.611 | 1.25 | 342.8 | 230.7 | 0.042 | 0.105 | 0.101 |
| Group of meteorite Kosice | | | | | | | | | | | | |
| Mean | 113.0 | 23.1 | 17.0 | 0.884 | 2.564 | 0.652 | 3.4 | 219.9 | 327.3 | 0.00 | 0.00 | 0.00 |
| Kosice | 114.3 | 29.0 | 15.0 | 0.957 | 2.710 | 0.647 | 2.0 | 204.2 | 340.1 | 0.04 | 0.08 | 0.06 |
| (2008 BE15) | | | | 0.848 | 2.504 | 0.662 | 2.52 | 64.7 | 122.5 | 0.040 | 0.108 | 0.106 |
| (2011 KG13) | | | | 0.876 | 2.298 | 0.619 | 2.56 | 121.4 | 71.2 | 0.049 | 0.109 | 0.108 |

5. Physical characteristics of fireballs from the six meteorite-producing meteoroid groups

One of the important physical characteristics of a meteoroid is its structural strength that counteracts the disruptive effect of the aerodynamic pressure P_{dyn} of the incoming atmospheric air flow during its plunging. The meteoroid disruption, which is usually accompanied by a bright flare, occurs when the aerodynamic pressure of the incoming air flow exceeds the meteoroid's threshold compressive strength. The aerodynamic break-up pressure P_{dyn} , at which the meteoroid disintegration occurs, can be calculated by formula (2) [14]:

$$P_{dyn} = \Gamma \cdot \rho a \cdot V^2, \tag{2}$$

where ρa is the atmospheric density at the height H_{max} of the maximum brightness where the break-up occurred; V is the fireball velocity at the disruption point; Γ is the drag factor ($\Gamma=1$). Adopting graph (1) from the study [15], the meteoroid bulk density ρ_m was calculated using the aerodynamic break-up pressure P_{dyn} . The resulting bulk den-

sity ρ_m of the meteoroids of the six groups are given in Table 2.

The following causes may explain the observed differences between the bulk densities of fireballs calculated using the aerodynamic break-up pressure P_{dyn} and densities of meteorites δ_m resulted from the laboratory measurements:

1) When a fireball is plunging through the atmosphere, due to the atmospheric thermal effect (i.e. heating) the loss of volatile material occurs, which results in the fireball break-up into smaller, sturdier and denser fragments that are able to survive the fall through the Earth's atmosphere and land on the surface as meteorites.

2) The estimated fireball bulk densities ρ_m calculated using the aerodynamic break-up pressure P_{dyn} contain inaccuracies in the fireball height H_{max} and velocity V measurements at the point of its breaking up into fragments, as well as in the applied value of the drag factor Γ .

Table 2: Bulk densities of meteoroids of the six meteorite-producing groups

| Name of the group | Bulk density ρ_m (kg/m ³) |
|--------------------------------|--|
| Pribram meteorite group | 900 ÷ 1750 |
| Benešov meteorite group | 700 ÷ 1400 |
| Neuschwanstein meteorite group | 1150 ÷ 2050 |
| Park Forest meteorite group | 750 ÷ 1900 |
| Košice meteorite group | 1050 ÷ 1250 |
| Mason Gully meteorite group | 1050 ÷ 2000 |

6. Results and conclusion

We have detected six groups of meteorite-producing meteoroids and ordinary chondrites observed over the determined periods of increased fireball activity. The data on the mean heliocentric orbit of the group of meteorite-producing meteoroids enables to link the group with its likely source, such as an asteroid, a family of asteroids or a comet, thereby making it possible to obtain information about the source itself. The obtained results in the context of the existence of groups of meteorite-producing meteoroids in the Jupiter-family comet-like Earth-crossing orbits indicate that large and strong fragments with comet-like orbits may overcome the disruptive effect of the Earth's atmosphere and reach the surface as meteorites. The six target groups, which contain 89 meteorite-producing meteoroids and six meteorites, may be groups of dynamically connected bodies. These groups may still comprise meteorite-producing meteoroids which can fall onto the Earth's surface as meteorites nowadays. It may serve as a good incentive for monitoring fireballs in these groups in the regions of their radiants over the determined periods of the fireballs activity. The investigation of the possibility of the existence of groups of meteorite-producing meteoroids and their sources is of practical value with regard to carrying out monitoring aimed at detection of potentially hazardous objects in the near-Earth orbits well before their entering the atmosphere.

In summary, we can conclude that meteorite-producing groups in the Earth-crossing comet-like orbits may contain large meteorite-producing meteoroids. The detailed study of physical and structural properties of this component of interplanetary bodies provides very important information about the sources of meteorites and meteorite-producing meteoroids from which they originated.

References

- [1] Popova O.P., Jenniskens P., Emel'yanenko V., Kartashova A., et al.: 2013, *Science*, **342**, Is. 6162, 1069.
- [2] Halliday I., Blackwell A.T., Griffin A.A.: 1990, *Meteoritics*, **25**, 93.
- [3] Beech M.: 2006, *WGN, the Journal of IMO*, **34**, 104.
- [4] Spurny P., Borovicka: 2015, *IAU General Assembly – Meeting 29* – id.2253907.
- [5] Konovalova N.A.: 2015, *DAH PT*, **58**, No.7, 577.
- [6] Jenniskens P., Shaddad M. H., Numan D., et al.: 2009, *Nature*, **458**, 485.
- [7] Farnocchia D., Chesley S.R., Brown P., Chodas P.W.: 2016, *Icarus*, **274**, 327.
- [8] Fujiwara A., et al.: 2006, *Science*, **312**, 1330.
- [9] Toth J., Veres P., Kornos L.: 2011, *Mon. Not. R. Astron. Soc.*, **312**, 1527.
- [10] Ibadinov Kh.I., Buriev A.M., Safarov A.G., Rahmonov A.A.: 2015, *Adv. in Space Res.*, **56**, 187.
- [11] Southworth R.B., Hawkins G.S.: 1963, *Smiths. Contrib. Astrophys.*, **7**, 261.
- [12] Drummond J.D.: 1981, *Icarus*, **45**, 545.
- [13] Jopek T.J., Farinella P., Froeschle Ch., Gonczi R.: 1995, *A&A*, **302**, 290.
- [14] Bronsthen V.A.: 1981, *Geophys. and Astrophys. Mon.*, Reidel, Dordrecht, 124 p.
- [15] ReVelle D.O.: 2002, in *Proc. of Asteroids, Comets, Meteors*, Technical University Berlin, Germany (ESA-SP-500), 127.

DOI: <http://dx.doi.org/10.18524/1810-4215.2018.31.147807>

MONITORING OF SPACE DEBRIS ROTATION BASED ON PHOTOMETRY

N.Koshkin, L.Shakun, E.Korobeinikova, S.Melikyants, S.Strakhova, V.Dragomiretsky, A.Ryabov, T.Golubovskaya, S.Terpan

Astronomical Observatory of Odessa I.I.Mechnikov University
Nikkoshkin(a)yahoo.com

ABSTRACT. The number of spacecraft and space debris (SD) in orbit has become so great that there is a real threat to flight safety. The task of precision calculation of the upcoming positions of any space objects (SO) in orbit in order to predict dangerous mutual approaches and to solve practical tasks has become topical. For the development of a modern orbit propagation model and the associated unified forecast of the evolution of orientation and rotation of an uncontrolled satellite, it is necessary to rely on long-term series of high-quality measurements and their analysis. At present, the direction of research on determining the state of SO rotation around a center of mass has become more and more developed. In our work, we analyze the results of photometric observations of several large objects of space debris obtained at the Astronomical Observatory of Odessa University using the KT-50 telescope during the last six years or more. The results of the evolution of the rotation rate and orientation of the Topex/Poseidon, Envisat, Oicets, Cosmos-2487 (Kondor-E) and Sich-2 satellites are presented.

Keywords: Space debris; Photometry; Period of rotation; Orientation of rotation axis.

АБСТРАКТ. Кількість космічних апаратів (КА) і тіл космічного сміття (КС) на орбіті сьогодні стала настільки великою, що виникла реальна загроза безпеці польотів. Зробилась актуальною задача прецизійного розрахунку майбутніх положень будь-яких космічних об'єктів (КО) на орбіті з метою прогнозування небезпечних взаємних зближень та для вирішення інших практичних завдань. Для розвитку сучасної моделі орбітального поширення і пов'язаного з ним прогнозу еволюції орієнтації та обертання неконтрольованого супутника необхідно спиратися на тривалі ряди високоякісних вимірювань та їхній аналіз. На початковому етапі освоєння космосу головним завданням спостережень КА було вимірювання їхніх положень серед зірок з метою забезпечення прогнозу наступного циклу спостережень. Але коли кількість КА і тіл космічного брухту на орбіті зростає настільки, що виникла реальна загроза безпеці польотів, актуалізувалося завдання прецизійного розрахунку майбутніх положень будь-яких космічних об'єктів на орбіті з метою прогнозування небезпечних взаємних зближень. На нинішньому етапі боротьби із засміченням навколосемного космосу і появи реальної технологіч-

ної можливості активного видалення КС з орбіти, зростає роль фотометричних і інших некоординатних вимірювань КО для вирішення завдання по визначенню параметрів власного обертання великих космічних тіл навколо центру маси. В даний час спостерігається помітне зростання числа досліджень, що націлені на визначення параметрів обертання КО. Це продемонструвала і остання 7-ма Європейська конференція з космічного брухту, що пройшла в квітні 2017 року. У даній роботі ми аналізуємо результати фотометричних спостережень декількох великих об'єктів космічного брухту, що були отримані в Астрономічній обсерваторії Одеського національного університету ім. І.І.Мечникова з використанням телескопа КТ-50 протягом останніх шести або більше років. Наведено результати по еволюції швидкості обертання і орієнтації КА Topex/Poseidon, Envisat, Oicets, Cosmos-2487 (Kondor-E) та Sich-2.

Ключові слова: Космічний брухт (сміття); Фотометрія; Період обертання; Орієнтація вісі обертання.

1. Introduction

As the number of tasks solved using spacecraft (SC) orbiting the Earth and the corresponding increase in the number of existing and planned space constellation, as well as the quality and quantity of observations of these bodies improves, the objectives of the space awareness has change. At the first stage of space exploration, the main task of spacecraft observation was to measure their position on the stars background to ensure the prediction of the subsequent observation cycle. When the number of spacecraft and space debris (SD) in orbit became so large that there was a real threat to flight safety, the task of precise calculation of the upcoming positions of any space objects (SO) in orbit was actualized in order to predict of dangerous mutual approaches. At the present stage of striving for clearing of near-Earth space and the emergence of a real technological possibility of active debris removal (ADR) out of orbit, the role of photometric and other non-coordinate measurements of SO has increased to solve the problem of determining the parameters of proper spin of large bodies in orbit. This data should be used both when planning ADR missions and to provide highly accurate prediction of the movement and SO's approaches, since the upper atmosphere drag significantly depends on the cross-sectional area, i.e. on body orientation.

Currently, there is a noticeable increase in the number of researches aimed at determining the parameters of the SO's spin. This was demonstrated by the last 7th European Conference on Space Debris, held in April 2017. Many reports were devoted to determining the orientation and monitoring the spacecraft rotation about center of mass, developing the optical observational networks, analyzing the situation in low-Earth orbits (LEO), of methods for reducing the risk of space flight and discuss of the ADR relevance. According to L. Anselmo and C. Pardini (Anselmo, 2017, see Fig. 1), for average solar activity level, for a spacecraft having the mass to area ratio equal 85 kg/m^2 and circular orbit with initial height of $\sim 740 \text{ km}$, his lifetime is 100 years, and for another with initial height of 985 km – about 1000 years.

Boer (2017) describes the international network TAROT, operating since 1999 under the authority of CNES. The network consists of 4 high-speed robotic optical telescopes, three of which are located in the southern hemisphere. The largest of them (Zadko 1m telescope) is located in Australia at the Gingin observatory and has a sensitivity of up to 20^m in the R-band. Fiedler (2017) and colleagues described the first results of the SMARTnet network. This network, which is German-Swiss at the first stage, declares openness to membership with a free exchange of primary measurement results. The network consists of two 20 cm and one 50 cm automated optical telescopes located in Europe. It is planned to expand the network points in Australia and South America. The Spanish Space Surveillance and Tracking System (S3T) is described in the report of Gómez (2017). The system consists of a national operating center and a set of ground-based sensors, which include five optical telescopes (including one active), as well one radar. The system began work in mid-2016, but the autonomous catalogue has already been created, based on observations from a network of sensors. In the Flohrer (2017) report outlined the ESA concept of development of SSA as consisting of three areas, including space surveillance and tracking (SST). At the same time, at this stage (2017-2020), the main initiative is given to the national SST resources.

In the work of Alives (2017) the automatic assessment of the orientation and rotation of the spacecraft based on ISAR-images (using the example of Envisat observations) by building chains of consecutive fitted images of model is considered. The work of Sommer (2017) and other German researchers is also devoted to the spin of Envisat. Based on the set of 19 ISAR-images, they clarify the kind of the change in the inertial spin rate of the satellite over time, covering the period from August 2011 to March 2017. Silha (2017) analyzes the rotational motion and orientation of SD using simulations of various observation methods, including passive photometric measurements, SLR and radar images. In this paper, the ESA project "Debris Attitude Motion Measurements and Modeling" aimed at short-term (days) and long-term (months and years) prediction of the rotation of large SD objects as part of the ADR task is considered. Kirchner (2017) with colleagues who had previously developed a method for determining the attitude of satellites equipped with a laser reflectors unit based on range (distance) measurements by a high-frequency laser, in the new work complement laser

data too measurements of target brightness using a highly sensitive photometer. The targets used are Envisat, Oicets, as well as many inactive Glonass satellites. In particular, variations in the rotation period of the Glonass-41 over almost 3 years are noted.

In the work of Šilha, Schildknecht (2017) the Data Base of light curves of almost 500 SOs obtained in AIUB for 10 years using the 1-m ZIMLAT telescope is presented. Rotational rates were estimated for 397 objects and the classification of light curves by their complexity was proposed, which are reflecting the state of body rotation. The orientation and rotation of the SWISSCUBE CUBESAT small satellite is described in Pittet (2017). To obtain the data, satellite lightcurves are used, as well as satellite radio reception data and gyroscopes measurements on board. Benson (2017) with colleagues analyzed the GSS light curves of GOES series. The data were obtained at the Lowell Observatory in Flagstaff in 2016 using 1.8 m and 1.1 m optical telescopes. They try to explain the complex and non-periodic kind of the light curve by the presence of two fundamental periods for tumbling motion of satellite. One period corresponds to spin around either of the satellite's extremal axes and the second period to precession and nutation of that axis about the rotational angular momentum vector.

2. Equipment and method of observation

The KT-50 high-speed telescope (Shakun, 2016) is equipped with a GPS-receiver for accurate time measurements and digital angle encoders on the telescope's axes. Location of telescope – longitude 30.755667 , latitude 46.477778 , height 56 m. Alt-azimuth mount, D/F = 500/2000; the receiver TV-CCD WAT 902H2 Sup, frame size of 768×576 pixels, FOV is 12×9 arcmin, resolution scale about 1 asec/px (Shakun, 2014).

The mount allows track of LEO satellites in the altitude range of $350 \div 5000 \text{ km}$, in orbits with an inclination $i > 45^\circ$; the maximum tracking rate is $\sim 4 \text{ deg/sec}$; the mean standard deviation of the astrometric measurements is $\sim 1 \text{ asec}$ (Shakun, 2014). The photometry is currently carried out without light filters (in integral light) with the time resolution of $\Delta T = 0.02 \text{ s}$; the limiting stellar magnitude value for TV-CCD mode on frequency equal of 25 fps is 9-10m. Requires re-equipment of executive engines to automate tracking at high speeds.

3. Topex and Envisat spacecrafts rotation monitoring

The photometric monitoring of space debris for several years allows detecting unexpected trends in the change of their rotation parameters. The analysis of the light curves makes it possible, first of all, to notice a change in the visible period of rotation of the body. In Figure 1 shows the change in the synodic (that is, not inertial, visible) rotation period of the Topex/Poseidon satellite (due to technical problem was decommissioned at the end of 2005), obtained from our measurements during June 2009 – June 2018. During this time span, the rotation period of the satellite decreased from 18.9 seconds to 10.3 seconds. This satellite orbits with an inclination of 66° , remaining at an altitude of about 1340 km above the Earth's surface,

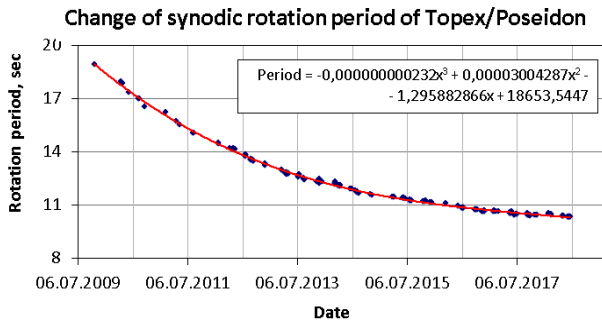


Figure 1: The change in the visible rotation period of the Topex/Poseidon satellite, obtained from photometric measurements using the KT-50 telescope during 2009-2018. In this cubic fit, the argument is counted from 01-01-2014 in days.

has an asymmetric shape because of one large solar panel. As shown in Kucharski (2017) in this case, the pressure of direct solar radiation leads to acceleration of satellite rotation. At present, the rate of spin period change has slowed, but has not yet fallen to zero, that is, Topex continues to slowly accelerate its rotation, reducing time of full revolution as about a quarter of second per year, or 2.6%. Note that the rate of the decrease in the visible period is fluctuating on different time scales. In particular, two fluctuations are clearly observed during half a year.

Another important characteristic of satellite rotation in orbit is the orientation of the vector of the spin axis in space (we assume that it coincides with the vector of angular

momentum) and its movement with time. In the work of Kucharsky (2017) the orientation of the spin axis at 401 positions during time was determined on the basis of data from Satellite Laser Ranging (SLR) of Topex over two years (June 2014 – June 2016). In Figure 2 shows the movement of the pole of rotation of Topex in the equatorial (left) and orbital (right) coordinate system, which is calculated according to the theory given in this work. We see that an oscillatory motion of the spin axis occurs near the orbital plane with an amplitude of about 12 degrees around a point close to the perigee of the Topex orbit.

In order to test this solution for the orientation of the spin axis of Topex, we consider the light curves of this satellite, obtained at the same time in Odessa using KT-50 telescope. Figure 3 shows a fragment of the observed light curve of June 23, 2014 (below) and the corresponding fragment of the theoretical light curve of the optical-geometric model of Topex (above) calculated for the same conditions of lighting and observation and for the above indicated orientation of its spin axis in space. It is necessary to state a good qualitative correspondence between the theoretical and the observed light curves during the five rotation cycles shown. This can be regarded as an independent confirmation of the spin axis solution obtained on the basis of SLR data only.

The synchronous basic (baseline) photometric measurements of the Topex during a short time interval were obtained on July 28, 2014 in Odessa and in Kazan, MMT (see Fig. 4). The pattern of satellite brightness variation is

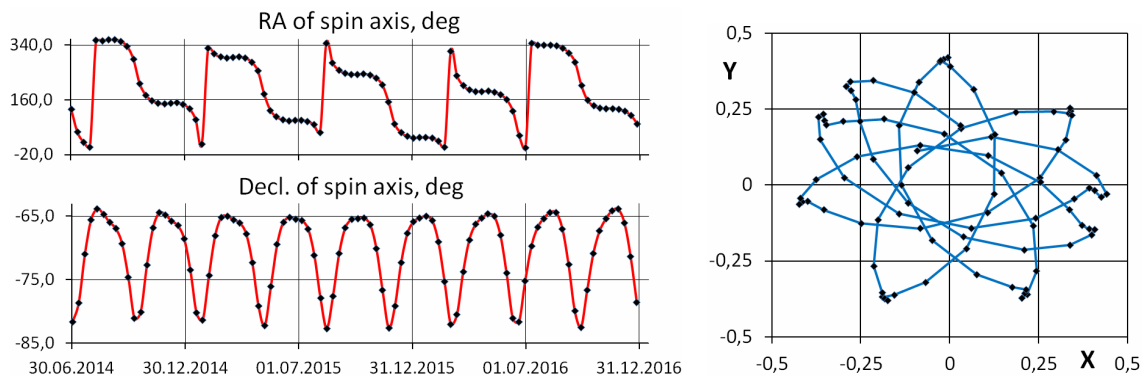


Figure 2: The Topex/Poseidon orientations of spin axes in equatorial coordinate system (left). The projection of the Topex spin axes on the XY-plane, which is perpendicular to the orbit perigee direction (right).

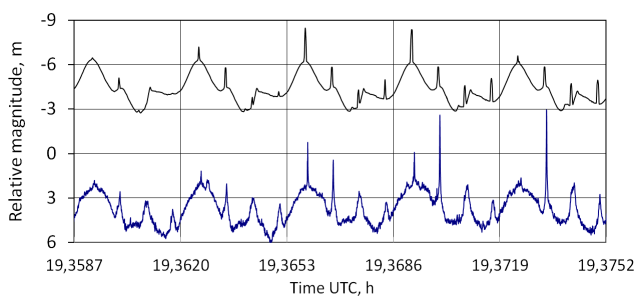


Figure 3: Fragment of the observed light curve dated June 23, 2014 (below) and the theoretical light curve of the Topex model (above) calculated for its rotation axis orientation in space $RA_{rot} = 174^\circ$, $Decl_{rot} = -77^\circ$.

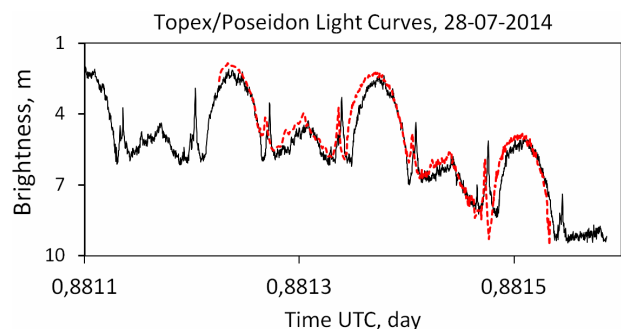


Figure 4: Fragment of the Topex/Poseidon light curve dated July 28, 2014, observed simultaneously from two points. The solid black curve – Odessa, KT-50; red dotted curve – Kazan, MMT (Katkova, 2017; <http://astroguard.ru/satellites>).

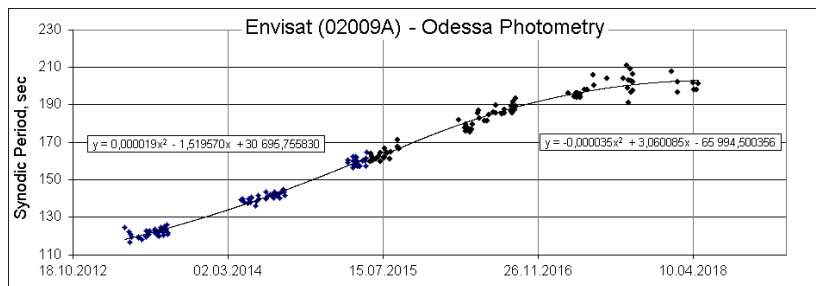


Figure 5: Change in the visible period of Envisat rotation, obtained from the observed light curves, Odessa, KT-50. From April 2013 to May 2015, the rotation period increased with acceleration (Koshkin, 2016); from May 2015 to April 2018 – it is increased with a slowdown.

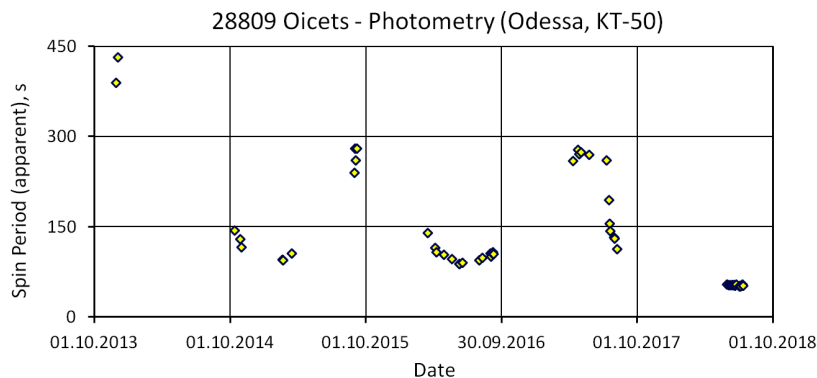


Figure 6: The change of the apparent rotation period of the Oicets satellite, obtained from the observed light curves, Odessa, KT-50.

almost completely repeated on both light curves, but with a small but significant time shift, which is probably explained by the parallactic delay for spaced observation stations and depends on the direction and rotation speed of the satellite.

In paper Koshkin (2016) on the basis of photometry in 2013–2015, we estimated the rate of rotation period change of another large space debris object – the inactive European satellite Envisat orbiting on altitude of 760 km with inclination of 98° . This object also has a very asymmetrical shape, but unlike the case described above, the Envisat's rotation period increases with time, that is, the satellite's rotation slows down. While (at the same time), according to measurements of the visible period of 2013–2015, as well as according to estimates of the inertial period, it was possible to conclude that the rotation period does not grow linearly, but with a slight “acceleration” (weak quadratic dependence on time). Pittet (2018) and colleagues during a similar interval of measurements using the technology of satellite laser range (SLR) estimate the slowdown of the rotation period of Envisat. They have developed a method for determining the rotational motion of a satellite (the period and orientation of the rotation axis) during a single pass.

In the more late work of Sommer (2017) based on their own data on the Envisat rotation period, obtained using an inverse synthetic aperture radar (ISAR) during the period 2013–2017, and analyzing our and other available data of colleagues, they clarify the nature of the inertial period change of the satellite evaluating it as linear. A theoretical analysis of Envisat's long-term rotational motion and a

comparison with estimates of its orientation and rotation period from observational data is given in Sagnières, 2018. A distinct nutation of the satellite angular momentum vector relative to the orbit normal is predicted, and its period evaluated of the order of several days. Over time, it is expected that the nutation of the rotation axis will become more and faster simultaneously with a decrease of the angular velocity. Our new photometric measurements from June 2015 to April 2018 showed that in 2015 the nature of Envisat deceleration changed and in the last two years the growth of the rotation period almost stopped (Fig. 5). We also note that the scatter of the values of the visible period in 2017–2018 has increased markedly, which may indicate an increase in the nutation amplitude of the rotation axis in accordance with the Sagnières (2018) forecast.

4. Different rotational behavior of LEO inactive spacecraft

Other large objects of space debris demonstrate the complex nature of the change in rotational speed. In Figure 6 shows the change in the apparent spin period of the Oicets satellite, obtained according to photometry data on the KT-50 telescope from the end of 2013 to the middle of 2018. This spacecraft is in an almost circular orbit with altitude of about 570 km and inclination of 98° , and has been inactive since September 2009. As you can see, several intervals of acceleration and deceleration of the satellite rotation were observed. The cyclicity was about 600–640 days.

The photometric observations during almost 1000 days of the Russian spacecraft COSMOS-2487 (Kondor-E) show an almost linear increase in the visible rotation period against time (Fig. 7). This spacecraft is in orbit with altitude of only 450 km and inclination of 74.7° and carries a large SAR antenna measuring 6×7 square meters. Slow deceleration of rotation indicates the passive status of this spacecraft, although we do not know the official confirmation of this fact.

The communication with the Ukrainian remote sensing satellite Sich-2 was discontinued on December 12, 2012 due to battery failure. It remains in orbit at altitude of 690 km and inclination of 98° . Photometric monitoring of this inactive satellite is conducted by us from April 2013 to July 2018. Figure 8 presents data on the change of the photometric visible rotation period of this spacecraft obtained in Odessa and in Evpatoria (Ukrainian SSA Center). A few months after the failure, at the beginning of April 2013, the satellite rotated with frequency of 4.4 revolutions per minute (apparent rotation period was 13.6 seconds), but over time the rotation speed grew rapidly. By the middle of August 2013, Sich-2 was rotating with frequency of 9.2 revolutions per minute ($P_{app} = 6.52$ s).

After that, there was a long period of slow growth of the rotational speed and in July 2018 the apparent period is 3.64 seconds.

This spacecraft has a symmetrical cube shape and four solar panels parallel to one face. Therefore, it can be assumed that the rotation axis in the satellite body coincides with the longitudinal axis of symmetry or with one of the normals to the side faces (Lopachenko, 2013). The light curve of this spacecraft usually shows a weak-specular reflection of light by the satellite planes. Figure 9 shows the Sich-2 light curve obtained on May 11, 2018 in Odessa. At beginning of the passage, acute but wide maxima of brightness are observed (see Figure10, the top composite curve is obtained by folde the first 10 cycles), at the end of the passage the phase angle has increased to 120° and the maxima changed to rounded quasi-sinusoidal shape (Fig.10, the lower composite curve is obtained by folde the last 10 cycles of brightness fluctuations).

But in both areas we see that two diametrically opposite faces give a brighter shine and show the amplitude of the oscillation of about $4 \div 5$ stellar magnitudes, while the intermediate ones are 2-4 times smaller than the amplitude. This can be explained if it is assumed that brighter

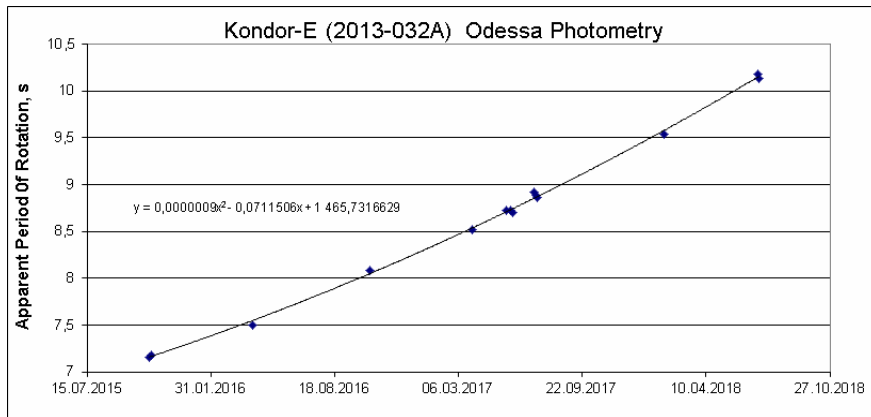


Figure 7: Change of the apparent rotation period of the COSMOS-2487 (Kondor-E) satellite, obtained from the observed light curves, Odessa, KT-50.

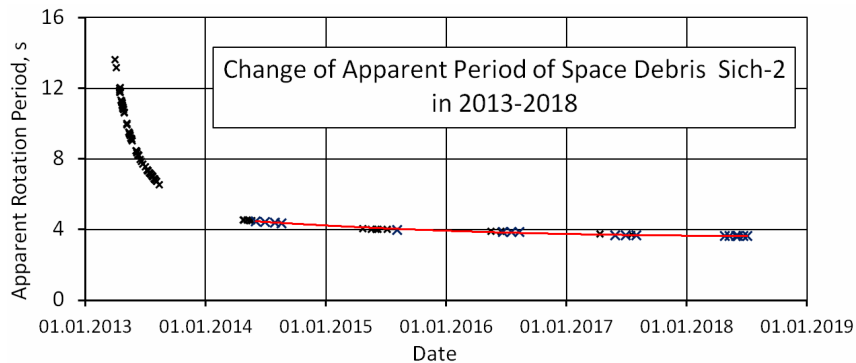


Figure 8: The change of the apparent rotation period of the Sich-2 satellite obtained from the observed light curves in Odessa on the KT-50 telescope and in Evpatoria, KOS "Sazhen" (AZT-28).

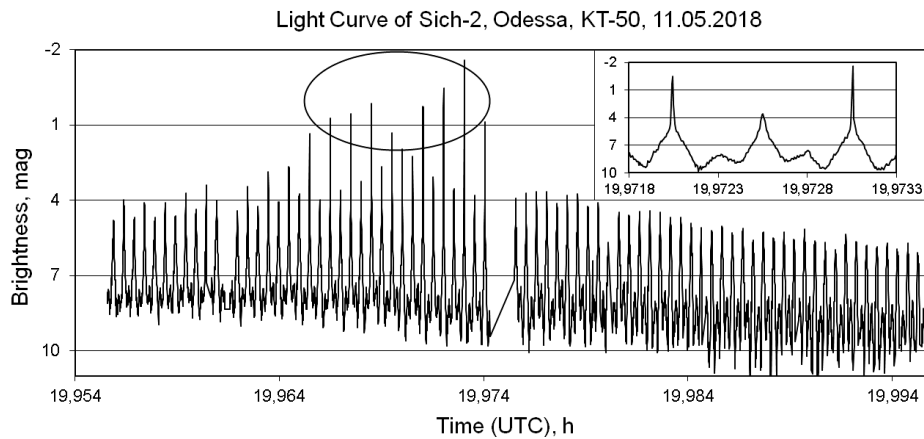


Figure 9: The light curve of the Sich-2 satellite dated May 11, 2018, obtained in Odessa using the KT-50 telescope. The oval marked the time interval when the specular reflection of light are observed. A fragment of the same light curve on a large scale is shown in the inset to demonstrate the mirror nature of the reflection of light during flashes.

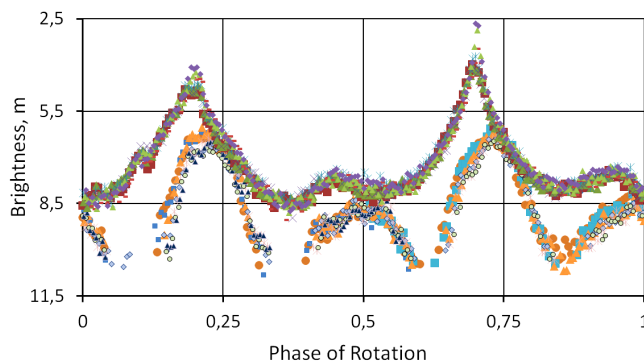


Figure 10: The convolution of the Sich-2 light curve dated May 11, 2018 with a period of 3.633 seconds. Two fragments of the folded light curve are shown. The upper composite curve includes the first 10 cycles of Sich-2 rotation; the lower composite curve includes the last 10 cycles.

flashes of shine are formed with the participation of flat solar panels. In this case, the rotation axis in the satellite body is parallel to the plane of these panels (or makes a small angle, that is, not strictly perpendicular to one of the side faces). This kind of Sich-2 light curves have in most passages, when the maximum satellite brightness does not exceed about 4m. But in rare passages (approximately in a quarter of cases), bright specular flashes appear on the light curve, during which the brightness increases by 3-5 mag (to 1m and even to $-1 \div -2$ m). The like area is indicated on the light curve of May 11, 2018 (Figure 9) and on the insert we can clearly see the mirror nature of the flashes in this area of light curve. For such time intervals with bright specular flashes, we calculated the direction of the phase-angle bisectors (PAB). All of them fall into a limited area in space: $RA_{bis} = -3 \div 89^\circ$, $Decl_{bis} = -41 \div +15^\circ$ (with a midpoint of $RA_{bis} = 56^\circ$, $Decl_{bis} = -14.3^\circ$).

Taking into account the symmetry of the satellite shape and the fact that the angles between the actual normal to the orbit and the corresponding PAB remains on average close to 100° , it can be assumed that the rotation axis makes an angle close to 90° with the normal of the 'reflecting' planes. Then the vector of the Sich-2 rotation axis over the entire time interval considered may experience oscillations near the mean pole $RA_{rot} = 56^\circ$, $Decl_{rot} = 75.7^\circ$ (Fig.11).

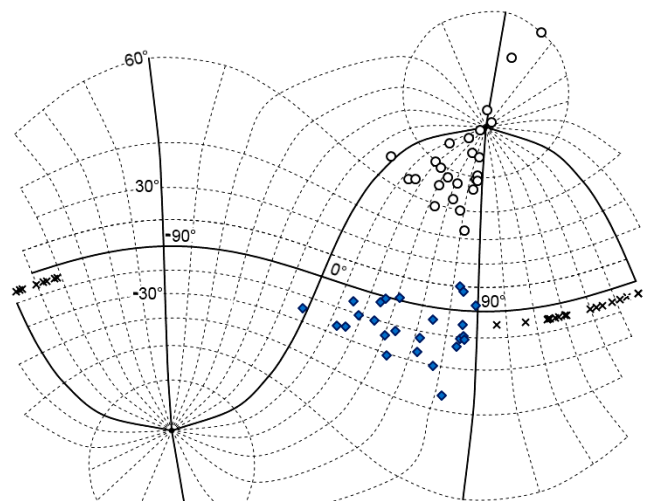


Figure 11: The location of PAB directions on the celestial sphere (shown by diamondes. Calculated for the middle of intervals when are appear bright specular flashes of brightness) for 25 light curves of the Sich-2 obtained from 16-05-2013 through 01-08-2018. Open circles indicate the estimated corresponding positions of the spacecraft rotation axis for these passages. The crosses indicate the directions of the normals to the plane of the satellite orbit during of these observations.

Figure 12 shows a fragment of the same light curve of the Sich-2 spacecraft obtained on May 11, 2018 (the lower curve) and the theoretical light curve of the satellite's optical-geometric model (upper curve) is given for comparison. The theoretical curve was obtained under the same lighting and observation conditions as the real one, and the rotation axis in the model body is perpendicular to one of the side faces of the cube (parallel to the solar panel plane), and in the inertial equatorial coordinate system it is directed to the pole $RA_{rot} = 56^\circ$, $Decl_{rot} = 75.7^\circ$. Despite the imperfection of the parameters characterizing the light scattering by this model, nevertheless, for the indicated orientation of the rotation axis in space, a similar pattern of changes in the brightness of the real Sich-2 satellite and its model was obtained. In order to independ

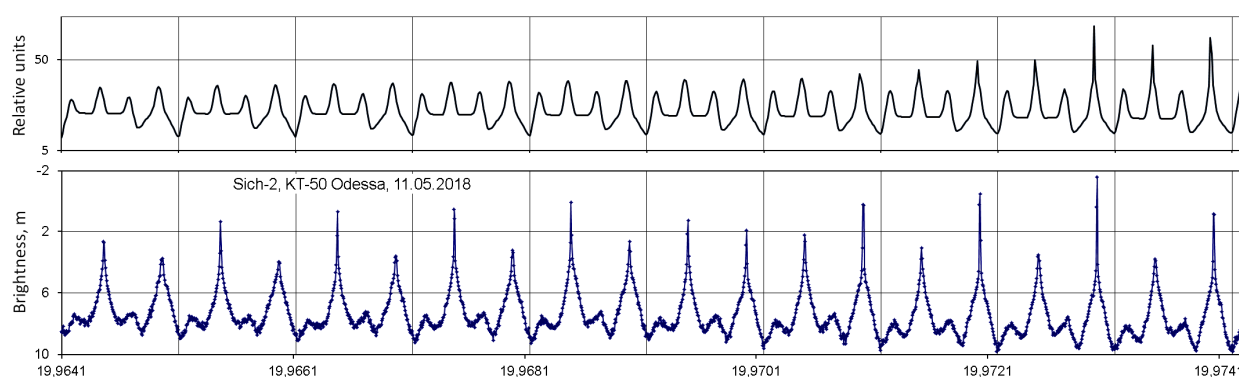


Figure 12: The fragment of the light curve of the Sich-2 spacecraft dated May 11, 2018, obtained in Odessa using the KT-50 telescope (below) and the theoretical light curve of the satellite model (above) calculated for the same conditions and orientation of its rotation axis in the equatorial system: $RA_rot = 56^\circ$, $Decl_rot = 75.7^\circ$.

ently confirm the results of our analysis, it is advisable to obtain synchronous basis photometric observations of the Sich-2 satellite with a high measurement frequency and impeccable timing.

5. Conclusion

The development of a modern orbital propagation model and a closely related unified forecast of the evolution of attitude and rotation of an uncontrolled satellite should be based on long-term series of high-quality measurements and their analysis. In our work, we analyze the results of photometric observations of several large objects of space debris obtained at the Astronomical Observatory of Odessa University using the KT-50 telescope over the past six years. Different conditions and factors of near-Earth space influence the rotation of these spacecraft around the center of mass in different ways. First of all, we can estimate the rotation speed of the satellites and its change over time. Some inactive satellites demonstrate a slowing down of rotation under the action of moments of gravitational forces, a magnetic field, and the pressure of sunlight and a rarefied upper atmosphere, while others, on the contrary, experience an acceleration of rotation at a certain time interval. Still others show the cyclical nature of these processes.

The analysis of the geometric conditions in which the brightness of a satellite is measured (especially the presence of specular reflection of light by its surface) makes it possible in some cases to estimate the orientation of its axis of rotation in the inertial and orbital coordinate system. As a rule, at the first stage, this is the rough average position of the rotation axis in the body and in space; however, this allows you to continue the analysis of the available photometric data by simulating and comparing the real and theoretical light curves of the satellite. This implies the importance of the adequacy of such optical-geometrical models to real prototypes in orbit. A preflight measurement of the main optical parameters and characteristics of the spacecraft is strongly required. It is also obvious that it is necessary to include in the model analysis the complex nature of the satellite rotation, including nutational motion with variable amplitude, which will make full use of the high information potential contained in high-frequency measurements of the brightness of artificial bodies in orbit.

References

- Anselmo L. and Pardini C.: 2017, in *Proc. of 7th Europ. Conf. on Space Debris, Sect. P-Modeling* (17-21 Apr., Darmstadt, Germany) <https://conference.sdo.esoc.esa.int/>.
- Avilés M., et al.: 2017, in *Proc. of 7th Europ. Conf. on Space Debris, Sect. MEAS-3* (17-21 Apr., Darmstadt, Germany).
- Benson C., et al.: 2017, in *Proc. of 7th Europ. Conf. on Space Debris, Sect. P-OBS* (17-21 Apr., Darmstadt, Germany).
- Boër M., et al.: 2017, in *Proc. of 7th Europ. Conf. on Space Debris, Sect. SST-1* (17-21 Apr., Darmstadt, Germany).
- Fiedler H., et al.: 2017, in *Proc. of 7th Europ. Conf. on Space Debris, Sect. SST-1* (17-21 Apr., Darmstadt, Germany).
- Flohrer T., Krag H.: 2017, in *Proc. of 7th Europ. Conf. on Space Debris, SST-1* (17-21 Apr., Darmstadt, Germany).
- Gómez I. A., et al.: 2017, in *Proc. of 7th Europ. Conf. on Space Debris, SST-1* (17-21 Apr., Darmstadt, Germany).
- Katkova E., et al.: 2017, "Photometry of the satellite at MMT-9 for three years", (http://astroguard.ru/data/data_open/2017/articles/articles_2017_1.pdf, <http://astroguard.ru/satellites>)
- Kirchner G., et al.: 2017, in *Proc. of 7th Europ. Conf. on Space Debris, MEAS-3* (17-21 Apr., Darmstadt, Germany).
- Koshkin N., et al.: 2016, *Adv. in Space Res.*, **58**, 358. (<https://doi.org/10.1016/j.asr.2016.04.024>)
- Kucharski D., et al.: 2017, *Earth and Space Science*, **4**, 661. (<https://doi.org/10.1002/2017EA000329>)
- Lopachenko V., et al.: 2013, *Bull. of Ukrainian EOP Laboratory*, **8**, 79. (<http://cdsads.u-strasbg.fr/abs/2013BUEOP...8...79L>)
- Pittet J.-N., et al.: 2017, in *Proc. of 7th Europ. Conf. on Space Debris, MEAS-3* (17-21 Apr., Darmstadt, Germany).
- Pittet J.-N., Silha J. and Schildknecht T.: 2018, *Adv. in Space Res.*, **61**, 1121. ([doi:10.1016/j.asr.2017.11.035](https://doi.org/10.1016/j.asr.2017.11.035))
- Sagnières L. and Sharf I.: 2018, *J. of Guidance, Control and Dyn.*, 1-13. *In print.* (<https://doi.org/10.2514/1.G003647>)
- Shakun L.S., Koshkin N.I.: 2014, *Adv. Space Res.*, **53** (12), 1834.
- Shakun L., et al.: 2016, *Odessa Astron. Publ.*, **29**, 217. (<http://oap.onu.edu.ua/article/view/85234>)
- Silha J., et al.: 2017, in *Proc. of 7th Europ. Conf. on Space Debris, Sect. MEAS-3* (17-21 Apr., Darmstadt, Germany).
- Silha J., Schildknecht T., et al.: 2017, in *Proc. of 7th Europ. Conf. on Space Debris, Sect. MEAS-1* (17-21 Apr., Darmstadt, Germany).
- Sommer S., et al.: 2017, in *Proc. of 7th Europ. Conf. on Space Debris, MEAS-3* (17-21 Apr., Darmstadt, Germany).

DOI: <http://dx.doi.org/10.18524/1810-4215.2018.31.145340>

RADIANTS AND ORBITAL DISTRIBUTION OF TV FAINT SPORADIC METEORS

M.O.Kulichenko, O.V.Shulga

Research Institute "Mykolaiv Astronomical Observatory"

niiko4kulichenko@gmail.com, shulga-av@ukr.net

ABSTRACT. Double station meteor observation using TV CCD unintensified techniques was started in 2013 in Nikolaev astronomical observatory (RI NAO). During observational campaign in 2013-2016 catalog containing 1055 meteoroid orbits has been obtained. Registered meteoroid photometric masses (Kruchinenko, 2012) are between 10^{-7} and 10^{-2} kg. Distribution of radiants, velocities and elements of heliocentric orbits with accent on meteoroids with low masses are analyzed in the work. Comparison with data from meteoroid orbit catalogs SonotaCo, EDMOND and NFC networks is also given. Two kinds of databases/catalogs are distinguished: "narrow field" and "wide field" depending on which type of camera system were used in observations. For analysis of the different catalogs only sporadic meteors were selected. Comparison of sporadic meteoroid radiants and orbital elements for different databases has shown that "narrow field" observations have next typical characteristics:

1) more relative number of low-mass meteoroids (about 30%) than large databases obtained by wide-angle observations;

2) significant increasing of number of low-velocity ($V_g < 20$ km/s) meteors.

Meteoroids with $m < 0.01$ g has some specific characteristics different for wide- and narrow-angle observations:

1) "narrow-field" databases have more orbits with $e < 0.8$ than "wide-field" ones;

2) aphelion distances in "narrow-field" databases are mostly less than 4.6 au but inclination for such orbits mostly more than 75° , "wide-field" databases show only retrograde with aphelion distances $Q > 4.6$ predominantly;

3) low-mass meteoroids in "wide-field" databases caused Apex contribution only, notable part of this objects from "narrow-field" data has radiants close to Antihelion source.

Keywords: meteors, meteoroid orbits, video observation.

АБСТРАКТ. У 2013 році в Миколаївській астрономічній обсерваторії (НДІ "МАО") розпочато базисні спостереження метеорів із застосуванням телевізійної ПЗЗ-техніки. В ході спостережної кампанії 2013-2016 рр. було отримано каталог, в якому містяться 1055 орбіт метеороїдів. Зареєстровані фотометричні маси метеороїдів (Kruchinenko, 2012) знаходяться у діапазоні 10^{-7} - 10^{-2} кг. В роботі проаналізовано розподіл радіантів, швидкостей та елементів геліоцентричних орбіт з акцентом на метеорні тіла з малими масами. Також наведено порівняння з даними каталогів метеороїдних орбіт

SonotaCo, EDMOND та NFC. Розрізняються два типи баз даних/каталогів: "малого поля" та "широкого поля" в залежності від того, який тип оптичної системи використовувався в спостереженнях. Для аналізу різних каталогів були відібрані лише спорадичні метеори. Порівняння спорадичних метеорних радіантів та елементів орбіт для різних баз даних показало, що спостереження "малого поля" мають наступні характерні ознаки:

1) більш відносно число маломасивних метеороїдів (близько 30%), порівняно з великими базами даних, отриманими з ширококутних спостережень;

2) істотне збільшення кількості метеорів з малою швидкістю ($V_g < 20$ км/с).

Метеороїди з $m < 0.01$ г мають деякі характерні ознаки, що відрізняються також у випадках спостережень різними оптичними системами:

1) бази даних "малого поля" мають більше орбіт з $e < 0.8$, ніж дані "широкого поля";

2) афелійні відстані в даних "малого поля" в основному менші за 4.6 а.о., але нахили таких орбіт більші за 75° , дані ширококутних спостережень мають лише ретроградні орбіти з афелійними відстанями, що переважно більші ніж 4.6 а.о.;

3) маломасивні метеороїди в "ширококутних" даних зумовлені лише радіантами апексної групи, помітна частина таких же метеороїдів за даними спостережень малими полями зору мають радіанти близькі до групи протисонячного джерела (Antihelion source).

Ключові слова: метеори, орбіти метеороїдів, телевізійні спостереження.

1. Introduction

Study of faint meteors caused by low mass (10^{-6} - 10^{-2} g) meteoroids does a significant refinement of small bodies distribution in Solar System (Koukal et al. 2015). Most part of information about these objects came from radar observation of meteors (Voloshchuk & Kasheev, 1981; Janches et al, 2003) and satellite researches (Carrillo-Sanchez et al., 2015). Another way of detecting small particles is using intensified CCD technique (Vitek et al., 2016; Ohsawa et al., 2018). Recent works (Koukal et al., 2015; Kulichenko et al., 2015, Kulichenko & Shulga, 2017) have shown that unintensified TV CCD cameras with narrow fields of view ($<10^\circ$) can also be used as efficient instrument for faint meteors investigation.

2. Meteoroid orbital data from TV observations

At the end of the twentieth century, there were just a few video systems around, which were operated occasionally during major showers or exceptional events. With the availability of automated meteor detection software, not only the number of video observers steadily increased, but they also organized in observing networks to join forces in creating large meteor and meteoroid orbit databases. In this work some of the largest databases of these networks were used for comparing with results obtained in RI “MAO”.

2.1. “Wide field” catalogs

The largest databases obtained by both amateur and professional video meteor networks are SonotaCo (Japan) and EDMOND (Europe).

SonotaCo started operation in August 2004 and by January 2008 had grown to 31 stations with more than 130 cameras (Rentdel & Arlt, 2017). These cameras are almost exclusively non-intensified monochrome video cameras with fields of view between 30° and 90° ($f=3.8-12$ mm, $f/0.8$). Software for meteor detecting, processing and meteoroid orbit calculation is calling UFO Tool Suite developed by SonotaCo group. The orbital data are published every year on website (<http://sonotaco.jp/doc/SNM/index.html>). By the end of 2017 more than 220 000 orbits were obtained by the network.

EDMOND (European viDeo MeteOr Network Database) is a database of orbits based and computed from video meteor data – observed and analysed with UFO and other (e.g. MetRec) software. It is not another camera network but it is a result of cooperation of several European networks including IMO and national observing groups from 14 countries (Rentdel & Arlt 2017). Fields of view of used cameras are between (40-90)°. UFO Orbit is main software for computation meteoroid orbits. Database contains more than 322 000 orbits for 2001-2016 and stored on website MeteorNews (<https://www.meteornews.net>).

2.2. “Narrow field” catalogs

NFC (Narrow Field Camera) network was created in 2014 on the base of CEMeNt (Central European MEteor NeTwork) and uses cameras with fields of view 5.4°×6.8° ($f=50$ mm, $f/1.0$). Such system allows detecting fainter meteors than in networks described above. Software for observation and calculating orbits is UFO Tools (Koukal et al. 2015). Database stored on MeteorNews website contains 1234 meteoroid orbits.

In 2013-2016 in Research Institute “Mykolaiv astronomical observatory” 1055 meteoroid orbits were obtained by double station observation. Cameras have fields of view less than 5° (4 lens: $f=85$ mm, $f/1.8$, 2 lens: $f=100$ mm, $f/2.0$). Observational system, method and results described in works Kulichenko et al. (2015), Kulichenko & Shulga (2017). For more strict comparison catalog of orbital data was calculated in format of UFO Tools software.

3. Analysis

To estimate the contribution of faint meteors in all databases the simplified model of meteoroid photometric mass m_0 (Kruchinenko, 2012) was used:

$$m_0 = \frac{1.62 \cdot 10^5 \cdot 2.512^{-M}}{V_0^4 \cdot \cos(z_R)},$$

whereas M – absolute magnitude of meteor, V_0 – preatmospheric geocentric velocity, km/s, z_R – zenithal distance of meteor radiant, radians. This parameter was used rather in statistical sense than as real meteoroid mass value. On Fig. 1, meteoroid photometric mass distributions are shown for all described databases. Catalogs based on narrow field observations show shifts of their distributions maxima towards the lower masses. Relative contribution of faint meteors in these catalogs is about 30% (Table 1).

For further analysis of the catalogs only sporadic meteors were selected. Due to low population index of shower meteors (Rentdel & Arlt, 2017) their contribution to narrow field observations cannot be compared with large catalogs. Percentage of sporadic meteors is given in the table 1.

Also group of sporadic meteoroids with photometric masses < 0.01 g were analyzed.

On Fig. 2 (a, b) solar elongation and geocentric velocity distributions of sporadic meteors for all databases are shown. Comparing with large catalogs “narrow-field” catalogs have more meteors with $V_g < 20$ km/s which is one of the advantages of narrow-field camera systems (Koseki, 2018). This fact can be explain rather by observational conditions than by low-mass meteoroids contribution (Fig. 2, c, d). One more typical maximum with $V_g = 65$ is so called Apex contribution km/s or meteors which observed in early morning observations when observer is located in the front of the Earth with respect to the Earth’s direction of movement (Drolshagen et al., 2014; Kulichenko & Shulga, 2017).

Solar elongation and geocentric velocity distributions of sporadic meteors with $m < 0.01$ g (Fig.2, c, d) show that low mass component of sporadic background in EDMOND and SonotaCo databeses entirely caused by Apex

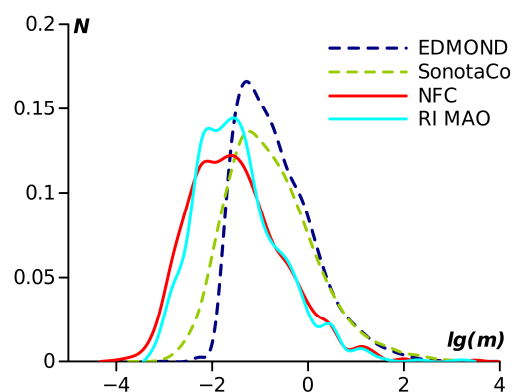


Figure 1: Meteoroid photometric mass distribution standardized by the total number of meteors (see table 1).

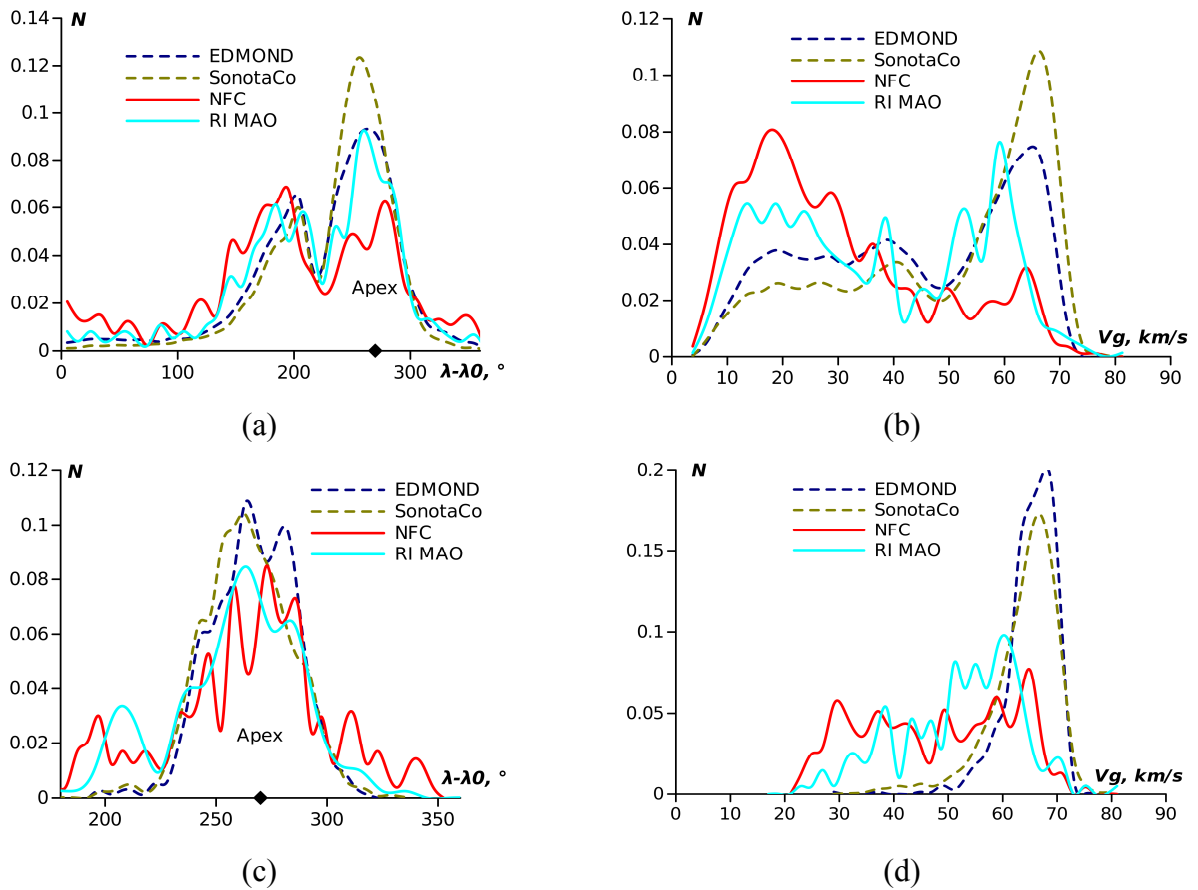


Figure 2: Solar elongation (a, c) and velocity (b, d) distributions of sporadic meteors (a, b) and sporadic meteors with $m < 0.01$ g (c, d)

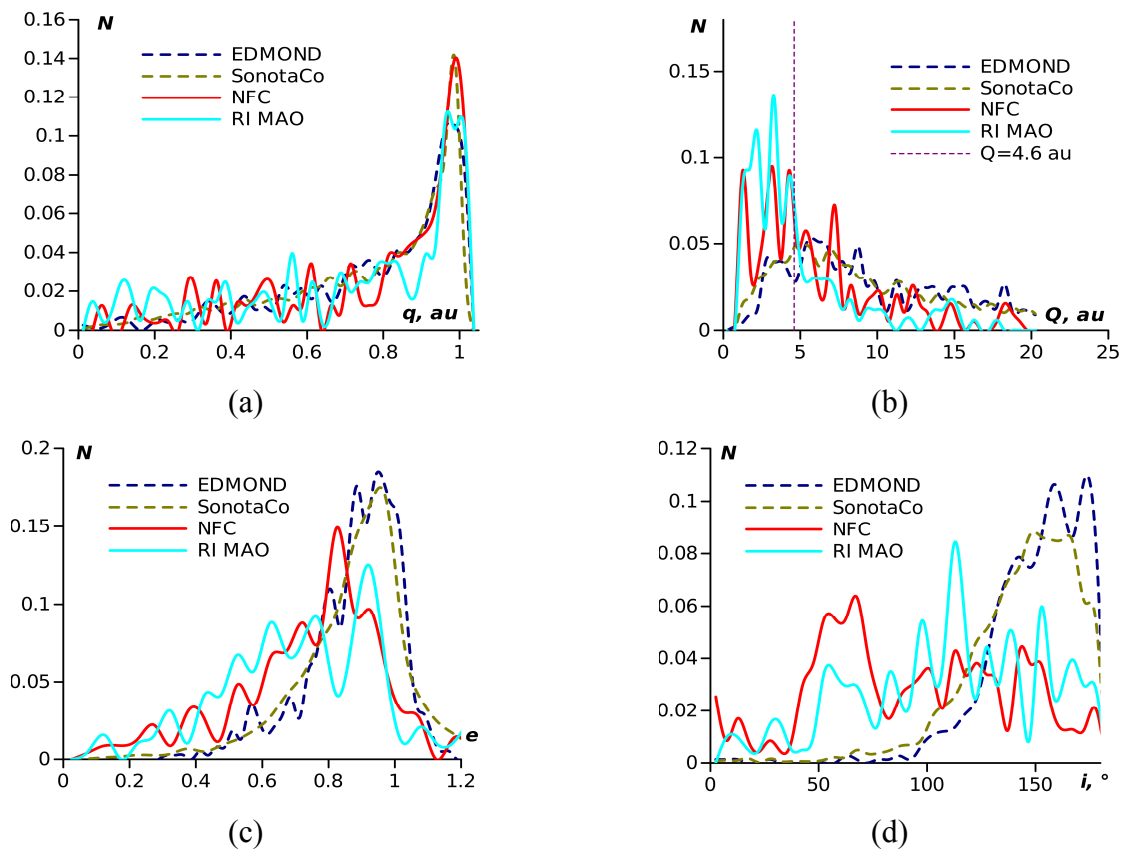


Figure 3: Perihelion distance (a), aphelion distance (b), eccentricity (c) and inclination (d) distributions for sporadic meteors with $m < 0.01$ g (c, d)

Table 1: Databases of meteoroid orbits obtained from video observations

| Network | SonotaCo | EDMOND | NFC | RI “MAO” |
|---|---------------------------------|------------------------------------|-------------------------------|--|
| Countries participants | Japan | Western and Central Europe | Czech Republic, Slovakia | Ukraine |
| Number of cameras (stations) | >130 (30) | (155) | 6 (6) | 6 (2) |
| Camera systems (lens focal length and aperture, field of view) | 3.8–12 mm; f/0.8; 30°–90° | 3–8 mm; f/0.8–f/1.4; 40°–90° | 50 mm; f/1.0; 6.8°x5.4° | 85-mm, 100-mm; f/1.8, f/2.0; 3.2°x4.2°; 2.7°x3.6° |
| Number of orbits 2013-2016 | 89465 | 209702 | 1244 | 1055 |
| Meteoroid minimal mass, g | $\sim 10^{-2}$ | $\sim 10^{-2}$ | $\sim 10^{-4}$ | $\sim 10^{-4}$ |
| Average absolute magnitude | -0.8 | -1.2 | 3.0 | 1.9 |
| Limiting absolute magnitude | 3.0 | 1.7 | 6.2 | 5.4 |
| Number of sporadic orbits | 54673 (61.1%) | 97810 (46.6%) | 824 (65.5%) | 737 (69.9%) |
| Number of orbits with $m < 0.01$ g | 5130 (7%) | 750 (1%) | 236 (34%) | 203 (30%) |
| Sporadic orbits with $Q < 4.6$ au | 21791 (24%) | 40581 (19%) | 557 (44%) | 568 (54%) |
| Sporadic orbits with $Q < 4.6$ au and $i < 75^\circ$ | 11770 (13%) | 26529 (13%) | 473 (38%) | 349 (33%) |
| Sporadic orbits with $Q < 4.6$ au and $m < 0.01$ g | 1696 (1.9%) | 210 (0.1%) | 117 (9.3%) | 138 (13.1%) |
| Sporadic orbits with $Q < 4.6$ au and $i < 75^\circ$ and $m < 0.01$ g | 34 (0.04%) | 7 (0.003%) | 53 (4.2%) | 27 (2.5%) |

contribution. In NFC and RI MAO databases most part of low mass meteoroids belongs to Apex group but also there are meteoroids close to Antihelion source of sporadic meteors ($\lambda - \lambda_0 = 180^\circ$).

Potential parents of low mass meteoroids can be searched by comparison of the distributions of the orbital elements of low mass sporadic meteors with distributions of NEA, short and long periodic comets (Jaksova et al., 2015). On Fig. 3 some of the orbital elements distributions for low mass meteoroids are shown. Comparing different databases it is clear that meteoroids from narrow-field catalogs have more relative numbers of low-eccentricity orbits ($e < 0.8$) which is typical for NEA and short periodic comets. Q-criterion of C-A (cometary or asteroid type of orbit) classification (Williams & Jopek, 2013) (Fig. 3, b) shows that catalogs NFC and RI MAO contain about 50% meteoroids with asteroid orbits but if the orbits with $i > 75^\circ$ are omitted it is clear that vast majority of meteoroids (Table 1) has cometary origin. As Williams & Jopek (2013) supposed such large influx of pseudo-asteroid orbits can be caused by Poynting-Robertson drag which decrease aphelion distances of comet type orbits especially for low-mass bodies.

4. Conclusion

Comparison of sporadic meteoroid radiants and orbital elements for different databases has shown that “narrow field” observations have next typical characteristics:

- 1) more relative number of low-mass meteoroids (about 30%) than large databases obtained by wide-angle observations;
- 2) significant increasing of number of low-velocity ($V_g < 20$ km/s) meteors.

Meteoroids with $m < 0.01$ g has some specific characteristics different for wide- and narrow-angle observations:

- 1) “narrow-field” databases have more orbits with $e < 0.8$ than “wide-field” ones;
- 2) aphelion distances in “narrow-field” databases are mostly less than 4.6 au but inclination for such orbits mostly more than 75° , “wide-field” databases show only retrograde with aphelion distances $Q > 4.6$ predominantly;
- 3) low-mass meteoroids in “wide-field” databases caused Apex contribution only, notable part of this objects from “narrow-field” data has radiants close to Antihelion source.

Low-mass meteoroids research needs more observational data and narrow-angle cameras are efficient and

relatively low-cost instrument for obtaining these kind of observations.

References

- Carillo-Sanchez J.D., Plane J.M.C., Feng W. et al.: 2015, *Geophys. Res. Lett.*, **42**, 6518.
- Drolshagen E., Ott T., Koschny D. et al.: 2014, in Rault J.-L., Roggemans P., eds, IMC, 16.
- Jaksova I., Porubcan V., Klacka J.: 2015, *Publ. Astron. Soc. Japan*, **67**, 99.
- Janches D., Nolan M.C., Meisel D.D. et al.: 2003, *Journal Of Geophysical Research*, **108**, A6, 1222.
- Koseki M.: 2018, *WGN, the Journal of the IMO*, **46**, 119.
- Koukal J., Srba J., Gorkova S.: 2015, in Rault J.-L., Roggemans P., eds, IMC, 1.
- Kruchinenko V.G.: 2012, *Math.-phys. analysis of meteor phenomenon* (Kyiv: Naukova dumka)
- Kulichenko N., Shulga O., Kozyryev Y., et al.: 2015, *WGN, Journal of the International Meteor Organization*, **43**, 81.
- Kulichenko N., Shulga O.: 2017, *Odessa Astron. Publ.*, **30**, 230.
- Ohsawa R., Sako S., Sarugaku Y., et al.: 2018, preprint (arXiv:1809.08816).
- Rendtel J., Arlt R. (Eds.): 2017, *Handbook for meteor observers*. (International Meteor Organization, Potsdam)
- Vitek S., Pata P., Koten P., et al.: 2016, *Sensors*, **16**, 1493.
- Voloshchuk I.I., Kashcheev B.L.: 1981, *The distribution of meteoroids near the earth's orbit* (Izdatel'stvo Nauka, Moscow).
- Williams I.P., Jopek T.J.: 2013, in Jopek T.J., Rietmeijer F.J.M., Watanabe J., Williams I.P., eds, *Meteoroids 2013*, 179.

DOI: <http://dx.doi.org/10.18524/1810-4215.2018.31.145962>

FEATURES OF KOTLIN ORBIT ESTIMATION LIBRARY

L.S.Shakun

Astronomical Observatory of Odessa I.I.Mechnikov National University,
Odessa, Ukraine, leomspace@gmail.com

ABSTRACT. Since the launch of Sputnik 1, the number of objects in near-earth orbit has been constantly increasing. The growth of number of these objects increases the risk of their collisions with existing satellites and ones which will be launched, that can be accompanied by their failure or even destruction. Most space agencies and many countries have their own space surveillance networks. These networks continually measure the positions of known objects, find new ones and predict their future positions. It is necessary to know the position of the objects with an accuracy of up to the characteristic size of the operating satellites (about 10 cm or more) to prevent collisions. Today, this task can be solved only for a small number of reference satellites and only for the past.

The calculation of the objects positions in near-Earth space requires the implementation of complex models of the Earth motion and a space object using many factors affecting the final result. Some of these factors, for example, the atmospheric density and the attitude of the satellite in the space, are not well predicted by modern models and require constant refinement from observations. Ukrainian Optical Facilities for Near-Earth Space Surveillance Network (UMOS) is used to surveillance and study near-Earth space in Ukraine.

There are many practical tasks that require knowledge of the positions of the space objects. The different software solutions are being applied to solve them. All of them must implement motion models of near-Earth space objects, the Earth and the main bodies of the Solar System for their needs. Space dynamics libraries are developed to implement these models. Orekit is one of these libraries. The Kotlin Orbit Estimation Library (KOrbEstLib) is built on the features of Orekit and extends them. KOrbEstLib expands the set of input and output data types, implementing the support of a number of Ukrainian and international data formats, in particular, the formats used in the UMOS network. In addition, KOrbEstLib offers an alternative implementation for estimating the parameters of the motion model of space objects in comparison with Orekit. This paper discusses a number of implementation features of the KOrbEstLib.

Keywords: artificial satellite, optical observation, space dynamic software, orbit estimation, Orekit.

АБСТРАКТ. З моменту запуску першого космічного супутника кількість об'єктів на навколоземній орбіті неухильно зростає. Збільшення кількості цих об'єктів підвищує ризик їх зіткнень з діючими супутниками і тими, що тільки виводяться, це може супроводжуватися виходом їх з ладу або навіть руйнуванням. Для

запобігання зіткнень необхідно знати положення всіх великих космічних об'єктів. Більшість космічних агентств і багато країн мають свої мережі спостереження за космічним простором. Ці мережі постійно вимірюють положення відомих об'єктів, займаються пошуком нових і прогнозують їхнє майбутнє положення. Для запобігання зіткнень необхідно знати розташування об'єктів з точністю до характерних розмірів діючих супутників (від 10 см до декількох метрів). На сьогоднішній день така задача може бути вирішена тільки для невеликої кількості еталонних супутників і тільки для минулого часу.

Обчислення положень об'єктів в навколоземному просторі вимагає реалізації складних моделей руху Землі та космічного об'єкта з урахуванням великої кількості факторів, що впливають на кінцевий результат. Ряд цих факторів, наприклад густина атмосфери і орієнтація супутника в просторі, недостатньо добре передбачаються сучасними моделями і вимагають постійного уточнення з спостережень. Українська мережа оптичних станцій для дослідження навколоземного простору (УМОС) використовується для цілей контролю та його вивчення.

Існує безліч практичних завдань, що вимагають знання положення космічних об'єктів. Для їх вирішення застосовуються різноманітні програмні рішення. Всі вони повинні для своїх потреб реалізувати моделі руху навколоземних космічних об'єктів, Землі і основних тіл Сонячної системи. Для реалізації цих моделей розробляються бібліотеки для космічної динаміки. Однією з таких бібліотек є Orekit. Kotlin Orbit Estimation Library (KOrbEstLib) спирається на можливості Orekit та розширює їх. KOrbEstLib впроваджує додатковий набір вхідних і вихідних типів даних, реалізуючи підтримку ряду українських і міжнародних форматів даних, зокрема форматів прийнятих в мережі УМОС. Крім цього, KOrbEstLib пропонує альтернативну в порівнянні з Orekit реалізацію для оцінки параметрів моделі руху космічних об'єктів. У роботі розглядаються ряд особливостей реалізації бібліотеки Kotlin Orbit Estimation Library.

Ключові слова: штучні супутники, оптичні спостереження, програмне забезпечення, визначення орбіт, Orekit.

1. Introduction

Since the launch of Sputnik 1 on October 4, 1957, the number of objects in near-earth orbit has been constantly increasing. The launch of artificial satellites of Earth and results of the destruction of objects in orbit is the main

sources of these objects. Only 8% of cataloged objects are active satellites and the rest are space debris (ESA, 2018). According the NASA forecast the number of the objects will grow on in the future (Liou et al., 2004; 2018; NASA, 2006; 2014; Liou, 2010). Retrospective comparison of past forecast with the current object number shows that now the object number is growing faster than in optimistic forecasts (Radtke & Stoll, 2016). Thus the risk of collisions of the operating objects with the space debris that can lead their breakdown will increase. The most famous collision occurred on February 10, 2009, when the non-operational satellite Kosmos-2251 and the active satellite Iridium-33 collided. Today, an active satellite can avoid the collision only by performing a debris avoidance manoeuvre. It is necessary to foresee possible collisions for this. Many space agencies and countries create and maintain surveillance space networks for this purpose. The responsibilities of these networks include cataloging of objects and predicting the object positions in orbits.

The typical size of most of the currently operating satellites are in the range from 10 cm to 10 m for low orbits, and from 1 m to 10 m for high orbits (ESA, 2018). To predict a collision, it is necessary to be able to estimate the position of space objects (including space debris) in near-Earth space with an accuracy up to the characteristic sizes of operating satellites over an interval of several days. We need to perform observations and obtain measurements of the position of the satellite for this. There are many different methods to measure the position of a satellite. We usually need our own coordinate system in which measurements are made for each method. Many effects that cause a distortion in measurement results are conveniently described in their own coordinate systems. Simulation of satellite motion usually performed in one of the pseudo-inertial geocentric coordinate systems. In addition to the explicitly required coordinate systems, it usually makes sense to introduce a number of intermediate coordinate systems. As one can see, the process of measuring and modeling of satellite motion requires the determination of many different coordinate systems. Thus, we need

1. To provide the possibility of free determination of various coordinate systems and to provide transformations between them in accordance with modern recommendations for using Earth rotation information (for example IERS2010);
2. To develop the satellite motion model that propagates the satellite position over a period of several days with an accuracy 1 m or better.
3. To obtain a sufficient set of observations for estimation of the parameters of the satellite's motion model with an accuracy better than 1 m.
4. To develop algorithms for estimation of the model parameters based on the obtained observations with an accuracy better than 1 m.

At the present time, there are no open observations and software solutions that satisfy all of the listed requirements. Items from the first to the second related to the forward problem of the calculating the satellite position in any moment of time when the parameters of the motion model are known. Items 3 to 4 are related to the inverse problem. It is well known that the forward problems are easier to solve than inverse ones. Nevertheless, finding

free software that solves only items 1-2 without any additional restrictions is a difficult task. It is even more difficult to find well-documented software with a free commercial use license. Many scientists develop their own software for this purpose or buy one.

We chose the Orbit Extrapolation Kit (Orekit) (Maisonobe et al., 2008), a low level space dynamics library written in Java. Orekit fully satisfies the requirements of item 1 and satisfies item 2 with a number of limitations. Orekit is open source software. It is distributed under the Apache License version 2.0, a well-known business-friendly license. This means anybody can use it to build any application, free or not.

Ukrainian Optical Facilities for Near-Earth Space Surveillance Network (UMOS – Ukrainian acronym) is used for purposes of space surveillance in Ukraine (Shulga et al., 2015). It is a voluntary association of academic observatories mainly. This network has been operating since 2011. It has obtained 14,401 tracks for 1,832 objects for all type of near-earth orbits from 2011 to 2017. This number of observations is certainly not enough to fulfill the requirements of paragraph 4. However, they are sufficient for the development and debugging of algorithms for estimating the parameters of the orbit of objects in near-earth space using optical observations.

2. Comparison of the implementation features of the measurements representation and optimization of orbit parameters in Orekit and KOrbEstLib

The Kotlin Orbit Estimation Library (KOrbEstLib) aims to provide access to all observations of the UMOS network and provide algorithms for estimating the parameters of the Orekit satellites motion models based on the optical observations. Figure 1 illustrates the KOrbEstLib architecture.

Orekit includes the ability to estimate the motion parameters of a space object based on observations beginning from version 8.0. KOrbEstLib introduces an alternative way to estimate the parameters of the satellite motion model.

In Orekit, any type of measurement is represented as an array of real numbers with an appropriate weight for each array element of measurement (tab. 1). A model estimation is a real array with size equal to the size of measurement array. The physical sense of array elements of estimation and measurement is the same. The code of the residuals is hidden from a user and is implemented as the weighted differences of measurements and their estimates. Optimization of the motion model parameters is minimizing the squares of the residuals. In fact, Orekit implements the least squares method, where the realization form of measurements defines the optimization form of the parameters of the satellite motion model. This approach provides the right implementation of the least squares method in the case of non-correlated measurements. However, it will not be the optimal solution in the case of correlated measurements or if we have some a priori information about the motion model of a space object.

KOrbEstLib offers a different measurement model. Each measurement type can have own form that describes measurement. The user can define this form by his prefer-

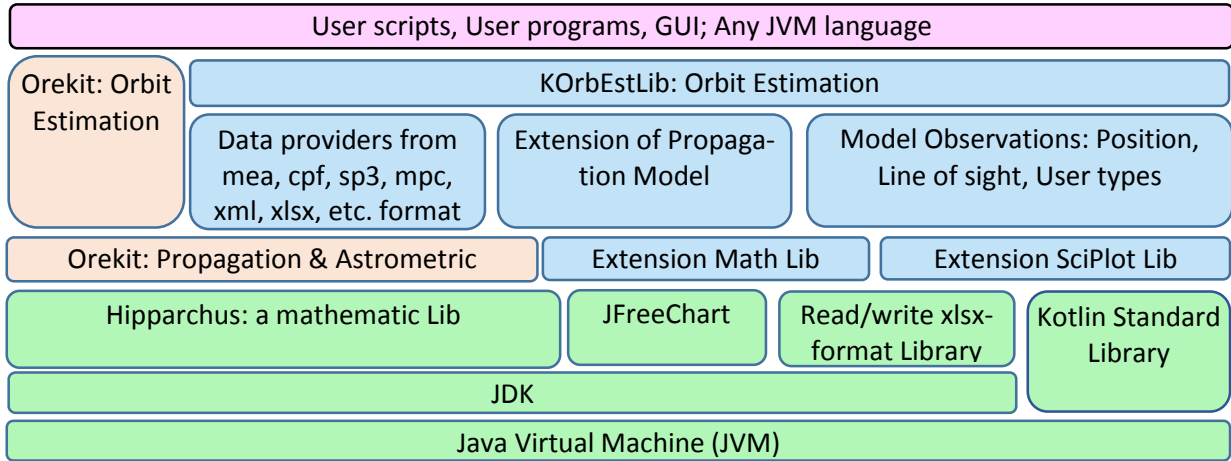


Figure 1: the architecture of the Kotlin Orbit Estimation Library. Blue is the KOrbEstLib components; brown is Orekit components; green is free libraries and JVM; pink is user capabilities to develop their own software using KOrbEstLib.

Table 1: the comparison of the most important differences in the approaches for estimating the parameters of the motion model.

| Feature | Orekit | KOrbEstLib |
|--------------------|--|----------------------------------|
| measurement | public x_1, x_2, \dots, x_n | user defined |
| weights | public w_1, w_2, \dots, w_n the same size that in the measurement | user defined |
| estimation | x'_1, x'_2, \dots, x'_n the same size that in the measurement | user defined |
| residuals | private $w_1 \cdot (x_1 - x'_1),$ $w_2 \cdot (x_2 - x'_2),$ $\dots,$ $w_n \cdot (x_n - x'_n)$ the same size that in the measurement | required interface; user defined |
| Optimized function | private $f = \sum_{i=1,n} r_i^2$ r_i – residuals | parameter user defined |

nce. The estimation type that corresponds to measurement type can have the form that describes estimation, not same with measurement form. The only one requirement that KOrbEstLib imposes is the ability to calculate the residuals between the measurement and its estimation. Moreover, this requirement is important only when we optimizing the model for an observations set consisted of several measurement types (for example, optical and radio observations). The free form of the optimize function allows defining the problems wider than least squares problem.

In order to illustrate the difficulties that arise when the measurements implemented in the Orekit form, let us consider ordinary angular measurements that obtained in optical observations. Usually, such measurements are represented

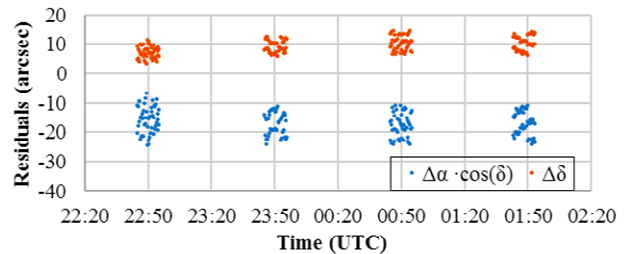


Figure 2: the residuals between observations and estimations in right ascension and declination.

in the form of angle coordinate pair (α – right ascension and δ – declination) of an object in the star catalog frame. The residuals between the model and the measurements are represented as $\Delta\alpha \cdot \cos\delta$ and $\Delta\delta$ respectively. Already at this stage, we are enforced to correct the nonlinearity of right ascension via using the weighting factor $\cos\delta$. This approach has application limits. $\Delta\alpha \cdot \cos\delta$ incorrectly describes the residuals in right ascension since nonlinear terms in $\Delta\alpha$ cannot be neglected in the polar regions. Since that the magnitude of residuals is usually very small, of the order of the arcseconds, such the polar region is small and the researchers simply avoid use measurements in it. Figure 2 shows an example of the residuals in terms of $\Delta\alpha \cdot \cos\delta$ и $\Delta\delta$. Considering Figure 2, it is easy to make the following conclusion. Random errors for each of the coordinates measurements are approximately equal. But the cause of the observed systematic bias is difficult to determine immediately.

One of the main features of satellites optical observations is related to the high mobility of satellites compared with stars. Important, this property is characteristic of satellites at all altitudes. If this is obvious for objects on low orbits, then for high objects it is necessary to take note the exposure time for the image. It reaches several seconds and the satellite displacement during this time is much larger than satellite size on the image. Hence such objects are highly mobile. Thus, regardless of the orbit type of a

near-Earth space object in optical measurements, there is a special direction along the visible direction of satellite motion.

Figure 3 shows the same differences between measurements and their estimates as in Figure 2, but already along and across the visible satellite track. Such representation of residuals becomes possible only after calculating the model satellite positions and velocities, and, therefore, does not agree with the representation form of measurements in Orekit. It should be noted that Orekit allows defining the similar measurement type if the measurement itself encapsulates the a priori information about the satellite orbit. But this is not always achievable. KOrbEstLib does not impose any restrictions on the software implementation of the measurements and does not require the correspondences of the measurements and estimations implementation. Hence, there are no obstacles to implement measurements in the form of right ascension and declination and the minimize objective function in the least square problem in the form of the differences along and across the visible satellite track. Thus, the form of the measurement implementation in KOrbEstLib can be easily matched with the representation of the measurement residuals along and across the trajectory. The residuals along and across the visible trajectory have another useful property, the nonlinear terms are small at any point of the celestial sphere, and all the residuals do not require re-normalization from measurement to measurement. We do not need to avoid near-polar regions as in the case of the residuals in right ascension and declination.

In Figure 3, we clearly see that the systematic differences between measurements and estimates are related with the direction along visible satellite track. Moreover, the random error of measurement is significantly larger in the direction along track than across it. In the overwhelming number of cases and in the example we are considering, this is due to the errors in the moment registration of measurement. Such errors are usually hardly revealed since they cannot be detected within the scheme of the measurements themselves. It is necessary to compare observations with a priori high-precision orbits that to reveal them, which is not always easy to perform at the site of observation. Physically correct choice of directions of decomposition of residuals allow to introduce weights for measurements easily, and often more correctly.

The values that describe the measurement can be implemented in KOrbEstLib “measurement” class as private. The consequence of this is the possibility of implementati-

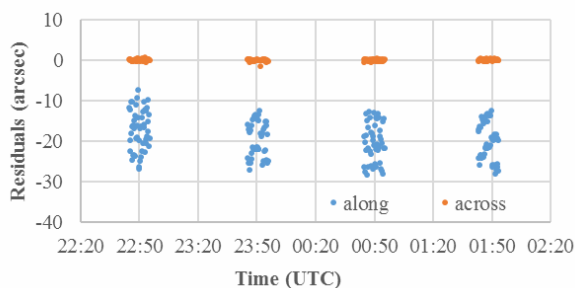


Figure 3: the residuals between observations and estimations in the along and across directions relatively the visible satellite track.

on of immutable objects of measurement, that under certain conditions allows you to write more high-performance code.

3. Additional features for support input and output data formats in KOrbEstLib

KOrbEstLib extends the set of ephemeris formats that supported Orekit by adding consolidated prediction format (CPF). KOrbEstLib allows you to combine several ephemeris with time gaps between them, which allows you just to make comparisons of observations and ephemeris for the large time intervals when there are difficulties with obtaining continuous ephemeris.

KOrbEstLib supports reading observations from the minor planet center (MPC) format and reading and writing in the MEA format. The MEA format is used to exchange observations by members of the UMOS network. The MPC format was designed to represent astronomical observations, where the duration of exposure is usually in seconds, and the measurement accuracy of the observation time moment rarely exceeds 0.1 seconds. The MPC format does not allow to specify moments in time with an accuracy of more than 0.001 seconds. The measurement accuracy of the time moments should be not worse than 0.0001 sec when measuring of the coordinates of low-orbit objects with an accuracy of the order of 0.1 arcseconds. The time moments of the measurements have to be aligned to the moments of the seconds beginning, to overcome complications in representing the time in the MPC format. The MEA-format avoids these complexities by allowing you to transfer moments with an accuracy of 0.0001 sec and can be extended in a compatible way to support greater accuracy in the time presentation.

KOrbEstLib supports the ability to describe models of satellite motion in the XML-format, which simplifies the writing of scripts for processing observations. The results of the calculation of the orbits or residuals can be saved in Excel files, which simplifies their further analysis.

4. Conclusion

KOrbEstLib extends the Orekit. All the features of the source library are available for use.

KOrbEstLib is written in Kotlin language, which is very well compatible with the Java language. This makes it easy to use KOrbEstLib and Orekit everywhere and at the same time, where JVM compatible languages can be used.

KOrbEstLib offers a more flexible model for the implementing measurements and the objective functions, which makes it possible to expand the orbit optimization scenarios. KOrbEstLib was used to processing of real observations in paper Shakun L., 2017, where the general considerations from this article were applied in practice.

KOrbEstLib supports international data exchange formats and formats used in the UMOS network. It provides data conversion tools. These features make it quite simple to use KOrbEstLib and Orekit to analyze the observations of the UMOS network.

References

- ESA's Annual Space Environment Report, [online] Available at: (https://www.sdo.esoc.esa.int/environment_report/Space_Environment_Report_latest.pdf) [Accessed 10 October 2018].
- Liou J.-C., Hall D., Krisko P. et al.: 2004, *Adv. Sp. Res.*, **34(5)**, 981.
- Liou J.-C.: 2010, *Orbital Debris Quarterly News*, **14(1)**, 7 [online] Available at: (<https://orbitaldebris.jsc.nasa.gov/quarterly-news/pdfs/odqnv14i1.pdf>)
- Liou J.-C., Matney M., a. Vavrin A. et al.: 2018, *Orbital Debris Quarterly News*, **22(3)**, [online] Available at: (<https://orbitaldebris.jsc.nasa.gov/quarterly-news/pdfs/odqnv22i3.pdf>)
- Maisonobe, L., Pommier V., Parraud P.: 2008, Orekit, An accurate and efficient core layer for space flight dynamics applications, Available at: (<https://orekit.org/>).
- NASA: 2006, 10(2), 1 *Orbital Debris Quarterly News*, [online] Available at: (<https://orbitaldebris.jsc.nasa.gov/quarterly-news/pdfs/odqnv10i2.pdf>).
- NASA: 2010, *Orbital Debris Quarterly News*, **14(1)**, 1, [online] Available at: (<https://orbitaldebris.jsc.nasa.gov/quarterly-news/pdfs/odqnv14i1.pdf>)
- Radtke J., Stoll E.: 2016, *Acta Astroautical*, **127**, 482.
- Shakun, L., Koshkin, N., Korobeynikova E. et al.: 2017, *Odessa Astron. Publ.*, **30**, 242.
- Shulga A., Kravchuk, S., Sybiryakova Ye. et al.: 2015, *KNIT*, **21(3)**, 74.

DOI: <http://dx.doi.org/10.18524/1810-4215.2018.31.144748>

PHOTOMETRY OF COMET C/2009 P1 (GARRADD) BEFORE AND AFTER PERIHELION

S.F. Velichko¹, M.V. Andreev²

¹Institute of Astronomy of V.N. Karazin Kharkiv National University, Sumska 35, 61022 Kharkiv, Ukraine, sergvelichko.sv@gmail.com

²International Center for Astronomical, Medical and Ecological Research of the National Academy of Sciences of Ukraine

ABSTRACT. During the period from September 2011 to February 2012, photometric observations of comet C/2009 P1 (Garradd) were performed on the 0.6-m telescope MC AMED at the peak Terskol (North-Caucasus).

The paper presents an analysis of photometric observations of Comet C/2009 P1 (Garradd) obtained for heliocentric distances of 2.0-2.1 au before and 1.7-1.8 au after perihelion passage. The measurements of the comet were performed using a CCD camera SiTe003AB with narrow-band comet filters BC ($\lambda 4450/67\text{\AA}$), GC($\lambda 5260/56\text{\AA}$), RC($\lambda 7128/58\text{\AA}$) and C₂($\lambda 5141/118\text{\AA}$), CN($\lambda 3870/62\text{\AA}$) HB-set (Farnham T., 2000). Observation data were obtained during 11 nights.

According to the results of observations, the dust production A_{fp} (A'Hearn M.F. et al., 1984) of comet, the gas production of comet for molecules C₂, CN using the Hazer model (Haser L., 1957), dust-to-gas ratio and color were calculated.

The obtained results showed that the physical parameters of the comet are close to the average characteristics typical for dynamically new comets.

Key words: comet, photometry, dust production, gas production, colour, dust-to-gas ratio.

АБСТРАКТ. В період з вересня 2011 року по лютий 2012 року були проведені фотометричні спостереження комети C/2009 P1 (Garradd) на 0,6-м телескопі Цейс-600 на піку Терскол (Північний Кавказ).

В статті представлені результати фотометричних досліджень комети C/2009 P1 (Garradd), отриманих на геліоцентричних відстанях 2,0-2,1 а.о. до перигелію та на відстанях 1,7-1,8 а.о. після. Спостереження комети виконані з використанням ПЗЗ-камери SiTe003AB, яка була споряджена інтерференційними кометними фільтрами набору HB: BC($\lambda 4450/67\text{\AA}$), GC ($\lambda 5260/56\text{\AA}$), RC($\lambda 7128/58\text{\AA}$), C₂ ($\lambda 5141/118\text{\AA}$) та CN ($\lambda 3870 / 62\text{\AA}$). Дані спостереження були отримані протягом 11 ночей.

Отримані спостереження дозволили розрахувати пилопродукування A_{fp} комети для трьох смуг континууму, газопродукування молекул C₂, CN комети, використовуючи модель Хазера, співвідношення пил-газ та колір пилу.

Отримані результати показали, що фізичні параметри комети близькі до середніх значень, характерних для динамічно нових комет та добре узгоджуються з результатами, отриманими іншими дослідниками.

Comet C/2009 P1 (Garradd) was discovered by Gordon J. Garradd (Siding Spring Observatory, Australia) in August 2009 at a heliocentric distance of 8.7 au. The comet passed through perihelion on December 23, 2011 ($r=1.55$ au) and was at closest approach to Earth on March 5, 2012 ($\Delta=1.27$ au).

According to the orbit's parameters, such as eccentricity e , orbit inclination, semimajor axis, the comet refers to long-periodic ones which came to us from the Oort's cloud.

Observations of the comet by numerous researchers during 2011-2012 years showed high degree of CO abundance. Moreover, existence of main volatile components such as H₂O, CO, CH₄, C₂H₂, C₂H₆, HCN, NH₃, H₂CO, CH₃OH (Mumma et al. 2012) was established. High abundance of CO was confirmed by space observations produced by the Deep Impact spacecraft (Feaga et al. 2012), and the Hubble space telescope (Feldman et al. 2012).

The comet C/2009 P1 Garradd was observed in the period from 17 of September to 19 of September 2011 before passing through perihelion as well as from 13 of February to 22 of February 2012 during ten nights.

The observations were carried out using the 60 cm telescope Zeiss-600 at the mountain observatory on Peak Terskol. As a radiation receiver the CCD camera Pixel-Vision Vienna was used. The camera was equipped by a narrow-band filters HB-set in blue, green and red continuum spectrum ranges as well as CN and C₂ emission lines. The receiver's field of view was 11 by 11 minutes with resolution of 0.63 seconds per pixel.

Reduction of images was carried out using standard method including bias and dark current subtracting, dividing by flat field as well as cleaning the images from cosmic particle tracks. As photometric standards the stars 96 Hercules and HD 120086 were used. Absolute fluxes in continuum ranges and emissions were derived using the method described in Farnham's work (Farnham T., 2000).

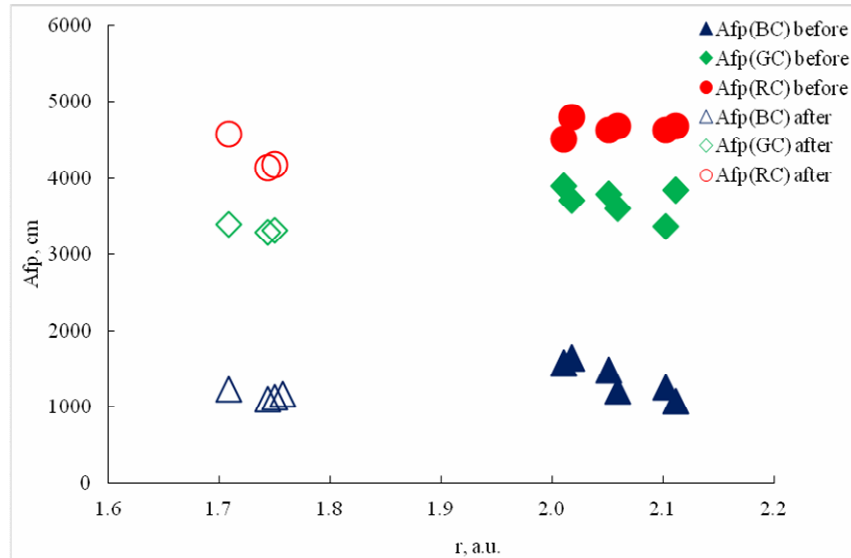


Figure 1: In the figure dependence of the Afp parameter on heliocentric distance is shown. Filled symbols are values before passing of perihelion while open symbols – after passing of perihelion in different continuum narrow band.

Table 1: Result of photometric measurements of comet C/2009 P1 (Garradd).

| Date | UT, h | Airmass | r, a.u. | Δ , a.u. | CN(3870/62Å) | BC(4450/67Å) | C ₂ (5141/118Å) | GC(5260/56Å) | RC(7128/58Å) |
|------------|-------|---------|---------|-----------------|--------------|--------------|----------------------------|--------------|--------------|
| 2011-09-07 | 19.5 | 1.245 | 2.111 | 1.456 | 11.34±0.03 | 11.74±0.02 | 9.84±0.04 | 10.34±0.03 | 10.13±0.04 |
| 2011-09-08 | 19.8 | 1.330 | 2.102 | 1.464 | 10.50±0.02 | 11.55±0.02 | 10.53±0.04 | 10.49±0.02 | 10.14±0.03 |
| 2011-09-13 | 21.4 | 2.352 | 2.059 | 1.509 | 9.78±0.10 | 11.59±0.12 | 10.35±0.13 | 10.40±0.06 | 10.12±0.04 |
| 2011-09-14 | 21.2 | 2.276 | 2.051 | 1.518 | 9.63±0.12 | 11.36±0.11 | 10.44±0.08 | 10.34±0.10 | 10.13±0.11 |
| 2011-09-18 | 19.7 | 1.652 | 2.018 | 1.559 | 9.69±0.03 | 11.24±0.03 | 9.60±0.04 | 10.36±0.02 | 10.08±0.02 |
| 2011-09-19 | 19.9 | 1.774 | 2.010 | 1.570 | 9.75±0.05 | 11.29±0.03 | 9.74±0.02 | 10.31±0.06 | 10.15±0.06 |
| 2012-02-13 | 23.9 | 1.429 | 1.708 | 1.387 | ----/---- | 11.07±0.02 | 9.84±0.03 | 10.35±0.02 | 9.64±0.09 |
| 2012-02-20 | 2.5 | 1.053 | 1.744 | 1.329 | 10.03±0.07 | 11.20±0.05 | 10.40±0.03 | 10.39±0.03 | 9.75±0.06 |
| 2012-02-21 | 2.4 | 1.052 | 1.750 | 1.320 | 9.96±0.06 | 11.17±0.04 | 10.42±0.03 | 10.39±0.03 | 9.74±0.06 |
| 2012-02-22 | 2.2 | 1.059 | 1.757 | 1.313 | 10.14±0.07 | 11.13±0.06 | ----/---- | ----/---- | ----/---- |

The results of the photometric measurements of comet are presented in the *Table 1*. The *Table 1* contains date of observations, air mass, helio – and geo-centric distances of the comet, its magnitudes for different filters with errors. For aperture photometry of the comet 20'' – aperture was used.

Analysis of flux of solar radiation dispersed by the comet gives an opportunity to evaluate such characteristics of dust as dust production, colour, spectral gradient of reflectivity, gas-to-dust ratio.

To evaluate the rate of dust production in the comet from flux of its radiation in continuum the Afp value is used. This value was introduced by A'Hearn et al. (A'Hearn M.F. et al., 1984) and is effective scattering cross-section of all particles falling into the field of view divided by projection of its field of view to the celestial sphere. The common equation present:

$$Afp = (4r^2 * \Delta^2 * 10^{0.4(m_{sun} - m_{comet})}) / \rho, \quad (1)$$

where the Afp itself is expressed in centimeters, Δ is geo-centric distance expressed in centimeters as well, r is heliocentric distance, in astronomical units, ρ is the aperture

radius used to integrate signal came from a comet and projected to the celestial sphere. The latter is expressed in centimeters.

In the *Figure 1* dependence of the Afp parameter on heliocentric distance is shown. Filled symbols are values before passing of perihelion while open symbols – after passing of perihelion. As can be seen, dust production increases with approaching to the Sun and decreases with receding from the Sun. Also growth of dust production with wavelength length is seen. The latter indicates that redder particles prevail in the comet which corresponds to bigger sizes particles.

In the *Table 2* results of calculations of dust production, gas-to-dust ratio and colours are presented. To characterize quantitatively the gas-to-dust ratio in comets ratio of flux measured in C₂ band to flux measured in continuum $WC_2 = F_{C_2} / F_{BC}$ is commonly used. In case of comets with strong continuum equivalent width of the C₂ band is in a range up to 500 Å.

Equivalent widths of the comet C/2009 P1 (Garradd) indicates that the comet refers to dust-reach ones.

Table 2: Dust production, colours and gas-to-dust ratio of comet C/2009 P1 (Garradd).

| Date | UT, h | Airmass | r, a.u. | Δ , a.u. | Afp(BC) | Afp(GC) | Afp(RC) | BC-GC | GC-RC | BC-RC | W(Fc ₂ /Fbc) |
|------------|-------|---------|---------|-----------------|---------|---------|---------|-------|-------|-------|-------------------------|
| 2011-09-07 | 19.5 | 1.245 | 2.111 | 1.456 | 1068.94 | 3849.64 | 4680.46 | 1.39 | 0.21 | 1.6 | 5.72 |
| 2011-09-08 | 19.8 | 1.330 | 2.102 | 1.464 | 1266.43 | 3371.47 | 4622.53 | 1.06 | 0.34 | 1.41 | 2.55 |
| 2011-09-13 | 21.4 | 2.352 | 2.059 | 1.509 | 1210.09 | 3608.29 | 4674.04 | 1.19 | 0.28 | 1.47 | 3.13 |
| 2011-09-14 | 21.2 | 2.276 | 2.051 | 1.518 | 1488.75 | 3793.42 | 4631.38 | 1.02 | 0.22 | 1.23 | 2.33 |
| 2011-09-18 | 19.7 | 1.652 | 2.018 | 1.559 | 1645.51 | 3707.8 | 4795.36 | 0.88 | 0.28 | 1.16 | 4.56 |
| 2011-09-19 | 19.9 | 1.774 | 2.010 | 1.570 | 1576.07 | 3894.72 | 4501.23 | 0.98 | 0.16 | 1.14 | 4.18 |
| 2012-02-13 | 23.9 | 1.429 | 1.708 | 1.387 | 1228.03 | 3397.75 | 4577.99 | 0.73 | 0.7 | 1.43 | 3.1 |
| 2012-02-20 | 2.5 | 1.053 | 1.744 | 1.329 | 1095.67 | 3290.35 | 4140.68 | 0.8 | 0.64 | 1.44 | 2.09 |
| 2012-02-21 | 2.4 | 1.052 | 1.750 | 1.320 | 1126.07 | 3307.97 | 4173.77 | 0.78 | 0.64 | 1.42 | 1.98 |
| 2012-02-22 | 2.2 | 1.059 | 1.757 | 1.313 | 1164.11 | ----- | ----- | ----- | ----- | ----- | ----- |

Table 3: The gas production and column density of the comet C/2009 P1 (Garradd).

| Date | r, a.u. | Δ , a.u. | C ₂ (5141/118Å) | | CN(3870/62Å) | |
|------------|---------|-----------------|----------------------------|--------------|--------------|--------------|
| | | | lg(N), cm-2 | lg(Q), mol/s | lg(N), cm-2 | lg(Q), mol/s |
| 2011-09-07 | 2.111 | 1.456 | 28.42 | 24.84 | 28.22 | 24.46 |
| 2011-09-08 | 2.102 | 1.464 | 28.15 | 24.56 | 28.56 | 24.79 |
| 2011-09-13 | 2.059 | 1.509 | 28.23 | 24.61 | 28.85 | 25.05 |
| 2011-09-14 | 2.051 | 1.518 | 28.20 | 24.57 | 28.92 | 25.11 |
| 2011-09-18 | 2.018 | 1.559 | 28.54 | 24.89 | 28.90 | 25.07 |
| 2011-09-19 | 2.010 | 1.570 | 28.49 | 24.83 | 28.88 | 25.04 |
| 2012-02-13 | 1.708 | 1.387 | 28.20 | 24.56 | ----- | ----- |
| 2012-02-20 | 1.744 | 1.329 | 27.96 | 24.56 | 28.50 | 24.72 |
| 2012-02-21 | 1.750 | 1.320 | 27.94 | 24.35 | 28.53 | 24.76 |
| 2012-02-22 | 1.757 | 1.313 | ----- | ----- | 28.45 | 24.69 |

In the *Table 3* values of gas production and column density of the comet derived using the Haser model (Haser L., 1957) are presented. The derived values of gas molecules production are typically for long-period comets and for dynamical new ones.

Conclusions

In this work the results of photometric observations of the comet C/2009 P1 (Garradd) before and after crossing of perihelion carried out from 17 of September 2011 to 22 of February 2012 during ten nights are presented.

Analysis of the photometric data has shown that the comet's continuum is redder than the solar one, colour excess in average is from 0.2 to 0.5 magnitude for different filters. As for steepness of spectral gradient of reflectivity, during the whole period of observations its value was equal 10 percent per 1000 Å which is typical for majority of comets.

Evaluations of *Afp*, characterizing degree of dust production in the comet C/2009 P1 (Garradd), amounted from 1000 to 5500 centimeters in narrow-band filters cutting

continuum. According to evaluations of colour and dust production, the comet C/2009 P1 (Garradd) refers to dust-reach comets.

The values of gas molecules production derived are typical for long-period comets as well as for dynamical new ones.

Dynamical new, long-period comet C/2009 P1 (Garradd) refers to dust-reach comets.

References

- Farnham T.: 2000, *Icarus* 147, 180–204.
 Feaga L., et. al.: 2011, *Proc. Conf. Baltimore, Maryland, USA*, 30 July–3 August, 2011. ASP Conference Series. V. 457. P. 233.
 Feldman P.D., et. al.: 2012, *Proc. Conf. 2012. LPI Contribution № 1667*. id. 6165.
 Haser L.: 1957, *Bull. Acad. Roy. Belgique, Classe des Sciences*. V. 43. P. 740–750.
 A'Hearn M.F. et al.: 1984, *Astron. J.* V. 89. P. 579–591.
 Mumma M.J., et al.: 2012, *Amer. Astron. Soc. DPS Meeting* 44, 506.07.

ASTROINFORMATICS

DOI: <http://dx.doi.org/10.18524/1810-4215.2018.31.144734>

THE CATALOGUES ANALYSIS OF STARS EQUATORIAL COORDINATES AND B-MAGNITUDE OF THE FON PROJECT

V. S. Akhmetov¹, S. V. Khlamov¹, V. M. Andruk², Yu. I. Protsyuk³¹ Institute of Astronomy, V. N. Karazin Kharkiv National University, Kharkiv, Ukraine, akhmetovvs@gmail.com, sergii.khlamov@gmail.com² Main Astronomical Observatory, National Academy of Sciences of Ukraine, Kiev, Ukraine, andruk@mao.kiev.ua³ Research Institute: Mykolaiv Astronomical Observatory, Mykolaiv, Ukraine, yuri@nao.nikolaev.ua

ABSTRACT. FON project was expected a catalogue of stellar positions and B magnitude of Northern sky from combination six astronomical observatories of the former USSR were equipped with the same wide-angle astrographs: Goloseevo (Ukraine), Zvenigorod, Zelenchuk (Russia), Abastumani (Georgia), Kitab (Uzbekistan) and HisorAO (Tajikistan). This paper has been presented the comparison results of three catalogues (FON-KIEV, FON-KITAB and FON-DUSHANBE) were received as result of scanning and astrometric reduction of photographic plates in the coordinate system of Tycho-2 catalogue. The data of zero zone (from -2 to 2 degrees of declination) from the mentioned catalogues was used during the research.

The number of common objects after cross-match of catalogues with a circular search window equals to 1.5 arc seconds was more than 500 thousands. The estimation of random accuracy of stars positions from the mentioned catalogues was performed by the Wielen method. Final dispersions were calculated for every sub-range of magnitudes. The stars with individual differences of position and magnitude that exceed three standard deviations were rejected.

The data from catalogues PMA was used for estimation of the systematic errors. It is obvious that the internal estimates of position accuracy of stars in the compared catalogues are low in one or all catalogues, and additional research is required. Analysis of the behavior of the systematic differences and standard deviations of the stellar positions of these catalogues have shown that there are a big values reaching 1 arcsec only in small sky regions. However, the internal estimation of accuracy that presented in catalogues is well matched with the systematic differences and standard deviations in the other sky regions.

Keywords: Astrometry, astrometry-catalogue, photographic plates, data analysis.

АБСТРАКТ. Проект FON передбачав створення каталогу положень та B зоряних величин північного неба шляхом об'єднання фотографічних спостережень отриманих на ширококутних астрографах 6 різних обсерваторій СРСР: Київ (Україна), Звенигород, Зеленецьк (Росія), Абастумані (Грузія), Китаб (Узбекистан)

та Гіссар АО (Таджикистан). В роботі представлені основні результати порівняння трьох фотографічних каталогів (FON-KIEV, FON-KITAB та FON-DUSHANBE), що отримані в результаті сканування та астрометричної редукції фотографічних пластинок в систему положень каталогу Tycho2. Для дослідження вище наведених каталогів були використані дані нульової зони (від -2 до 2 градусів схилення).

Кількість спільних об'єктів після проведення координатного ототожнення даних каталогів, з круговим вікном пошуку рівним 1,5 секунд дуги, становить більше ніж 500 тисяч. Оцінка випадкової точності позицій зірок згаданих каталогів була виконана методом Вільєна. Остаточні оцінки випадкових похибок положень зірок були розраховані для кожного діапазону зоряних величин. Об'єкти з індивідуальними різницями положень, які перевищують три стандартні відхилення, не використовувались в обчисленні.

Дані з каталогів PMA були використані для оцінки системних помилок. Очевидно, що внутрішні оцінки точності позицій зірок у порівнюваних каталогах є заниженими в одному або всіх каталогах, і необхідні додаткові дослідження. Аналіз поведінки систематичних відмінностей та стандартних відхилень положень зірок цих каталогів показав, що є великі значення, що досягають 1 секунди дуги, тільки в малих ділянках небесної сфери. Проте внутрішня оцінка точності, представлена в каталогах, добре узгоджується з систематичними відмінностями та стандартними відхиленнями для більшої частини досліджуваної небесної сфери.

Ключові слова: астрометрія, астрометричні каталоги, фотопластинки, аналіз даних.

1. Introduction

In 1976, the researchers of MAO AS USSR have proposed a FON project of photographic survey of the Northern sky. This project was aimed at clarifying and extending of the existing system of proper motions of stars to the region of weak stellar magnitudes. As a result, it was ex-

pected to obtain a highly accurate uniform coordinate system, which will be used for solving the modern problems of astrometry, celestial mechanics, astrophysics and other directions in the astronomy.

One of the favorable factors in the development of the project was a fact that in the 70s of the last century many astronomical observatories of the former USSR were equipped with the same wide-angle astrographs of the Karl Zeiss (Jena) company with an aperture of 40 cm and a focal length of 2 or 3 meters. The following observatories took a place in the FON project: Goloseevo (Ukraine), Zvenigorod, Zelenchuk (Russia), Abastumani (Georgia), Kitab (Uzbekistan) and GisAO (Tajikistan). All of them were divided into four groups. The Northern sky was supposed to be photographed four times with overlapping. The observations were carried out with an exposure whose duration ensured usable for measuring images of stars up to 16-17 magnitude. This work distribution among observatories gave an advantage to the FON project compared to the zone observations such as NPM and SPM. Namely, each star will be photographed at least four times by different telescopes from different places, which is very important for eliminating systematic errors in the future catalogue.

Unfortunately, due to the well-known situation of the 90s of the last century, the observations and work on the FON project were terminated. However, with help of the efforts of institutes' staff the photographic plates, records and files of the FON project have been kept in a good condition. A few years ago, in MAO NASU, the work on the FON project was restored by supporting of the Ukraine Virtual Observatory (Vavilova et al., 2012). The first catalogue, which was digitized and processed is the FON-KIEV catalogue. The approbation of technique for scanning and processing of the photographic plates was performed with this catalogue. Professional scanners and original scanning methods were used for scanning (Andruk et al., 2015). Processing of the received images was carried out by a unique algorithm developed by the MAO NASU researcher V. M. Andruk using the MIDAS/ROMAFOT environment (Andruk, 2016a; Andruk, 2016b; Andruk, 2017). Astrometric reduction of all objects in the equatorial coordinate system (α , δ) of the Tycho-2 catalogue at the epoch of observation was done. Photometric reduction of instrumental values magnitude into the system of photoelectric B-magnitudes was done (Andruk et al., 2015). The data of zero zone (from -2 to 2 degrees of declination) from the FON-KIEV, FON-KITAB and FON-DUSHANBE catalogues was used in this research.

2. Estimation of external accuracy of the star positions

The method used for estimation of external accuracy of the star positions was described by Wielen in 1995 (Wielen, 1995). It is very robust under condition of independence of the compared data. In such case the dispersion of the differences of positions or photometry is equal to the sum of their dispersions because their correlation coefficient is zero. With three or more independent catalogues it is easy to estimate the external accuracy of each of them:

$$\sigma_1 = \sqrt{\frac{D_{12} + D_{13} - D_{23}}{2}}$$

$$\sigma_2 = \sqrt{\frac{D_{12} + D_{23} - D_{13}}{2}}$$

$$\sigma_3 = \sqrt{\frac{D_{13} + D_{23} - D_{12}}{2}}$$

where D_{12} , D_{13} and D_{23} are the dispersions of differences of positions or magnitudes for three compared catalogues.

Before the calculation of dispersions one should test that the correct values are obtained. The possible source of the incorrectness is an assumption that the means of initial values are zero in the case when catalogues with systematic errors have some non-zero means. Therefore it is important to determine the behavior of the systematic differences. Fortunately, in most cases the systematic differences of researched values are some smooth functions that can be calculated and excluded. Finally, in our case the dispersions are calculated by iteration method for every small range of magnitude with rejection of the stars with individual difference less than 3 standard deviations.

For analysis by mean of Wielen method the FON-KIEV, FON-KITAB, FON-DUSHANBE catalogues have been used. We also used data from PMA and GaiaDR2 (Gaia collaboration, 2018) catalogues for the comparison and cross-identification of objects.

3. Catalogues

3.1. FON-KIEV catalogue

The FON-KIEV is a catalogue of star positions and B-magnitudes of stars from the Northern Sky Survey project (from -4° to $+90^\circ$), which was created by V. Andruk, L. Pakuliak, V. Golovnia, G. Ivanov, A. Yatsenko, S. Shatokhina, O. Yizhakevych (Andruk et al., 2015; 2016a; 2016b). It has been created under the motto of rational use of the resources accumulated in UkrVO JDA (Joint Digital Archive) in MAO NASU. The catalogue contains 19 451 751 stars and galaxies with $B = 16.5^m$ for the epoch of 1988.1 year. The coordinates of stars and galaxies were obtained in the Tycho-2 reference system, and B-value in the system of photoelectric standards. The internal accuracy of the catalogue for all objects is $\sigma_{\alpha\delta} = 0.23''$ and $\sigma_B = 0.14^m$ (for stars in the range of $B = 7^m - 14^m$ errors are $\sigma_{\alpha\delta} = 0.10''$ and $\sigma_B = 0.07^m$).

3.2. FON-KITAB catalogue

The FON-KITAB is a catalogue of equatorial coordinates and B-magnitudes of the Kitab's part of the FON project, which was created by Q. Yuldoshev, Yu. Protshuk, H. Relke, Sh. Ehgamberdiev, M. Muminov, V. Andruk (Yuldoshev et al., 2018).

The photographic plates of the FON project were exposed on the double telescope DAZ (Double Zeiss Astrograph, $D/F = 40/300$, $69''/\text{mm}$) at the Kitab observatory of the Republic of Uzbekistan. The number of the photographic plates used for the catalogue is 1963. The catalogue contains near 13.4 million stars and galaxies in the

sky from 0° to -20° according to declination down to $B = 17.5^m$ at the middle epoch of observation as 1985.0 year. The mean internal errors of the new catalogue for all objects are $\sigma_{\alpha\delta} = 0.23''$ and $\sigma_B = 0.15^m$ (for the stars in the range of $B = 5^m - 14^m$ the errors are $\sigma_{\alpha\delta} = 0.085''$ and $\sigma_B = 0.054^m$) (Yuldoshev et al., 2017a; 2017b).

3.3. FON-DUSHANBE catalogue

The FON-DUSHANBE is a small equatorial realization of the project "FON-DUSHANBE catalogue" created by A. Mullo-Abdolov, H. Relke, G. Kokhirova, Q. Yuldoshev, Yu. Protsyuk, V. Andruk (Mullo-Abdolov et al., 2017).

Since May 2018 the process of the scanning and processing of photographic plates from the archive of Institute of Astrophysics Academy of Sciences of Tajikistan has begun. It is a matter of approximately 1560 photographic plates in the sky regions from -8° to $+90^\circ$ that were exposed for the FON project in the Hissar observatory (HissAO) during 1985-1992 years. The size of the photographic plates is $8^\circ \times 8^\circ$ or 30×30 cm, the size of the digitized images is 13000×13000 px. So far the first results of the processing of the 71 plates of zero zone and the 58 plates of 64, 68 and 72 zones were obtained. The errors in the definition of 29 equatorial coordinates and B-magnitudes for the stars in the range of $5^m - 17^m$ are the following: $\sigma_{\alpha\delta} = \pm 0.33''$ and $\sigma_B = \pm 0.12^m$. The differences between the calculated positions and B-magnitudes and the reference one from the Tycho-2 catalogue are $\sigma_{\alpha\delta} = \pm 0.12''$ and $\sigma_{BT} = \pm 0.19^m$ respectively. The difference between the calculated and the photoelectric B-magnitudes equals to $\sigma_B = \pm 0.15^m$.

3.4. PMA catalogue

The PMA catalogue (Akhmetov et al., 2017) contains about 421 million absolute proper motions of stars. It was derived from the combination of positions from Gaia DR1 and 2MASS, with a mean difference of epochs of about 15 years. Most of the systematic zonal errors inherent in the 2MASS catalogue were eliminated before deriving the absolute proper motions. The absolute calibration procedure was carried out using about 1.6 million positions of extragalactic sources. The mean formal error of the absolute calibration is less than 0.35 mas/yr. The RMS error of proper motions depends on the stellar magnitude and ranges from 2-5 mas/yr for stars with $10 \text{ mag} < G < 17$ mag to 5-10 mas/yr for faint ones.

4. Cross-identification of objects

In this paper the star magnitudes of all described catalogues were not used for cross-identification because of a significant difference in their band-pass, significant random and systematic errors of photometry. The cross-identification was carried out using only coordinates of objects. It should be noted that such cross-identification is usually named positional association and is not necessarily an exact identification.

At the first step all positions of each object in PMA catalogue was calculated to the means epoch of FON-KIEV, FON-KITAB, FON-DUSHANBE catalogues respectively.

The second step of cross-identification was a simple cross-match: each object of the PMA catalogue was compared with the object of the FON-KIEV, FON-KITAB, FON-DUSHANBE catalogues with circular window size of 1.5 arcsec by means of special software (Akhmetov et al., 2018). Then corresponded proper motion of PMA objects was compared with the objects from FON catalogues. This procedure was needed because of existing of large difference between the mean epoch of FON-KITAB (about 1983.7 year) and FON-KIEV or FON-DUSHANBE (about 1990.4 year) and also the significant scatter of epochs in each catalogues in range 4-12 years. The base epoch we used is equal to 1990.37 year as a mean epoch of FON-KIEV. All data from FON-KITAB and FON-DUSHANBE were reduced to this epoch by means of proper motion of PMA catalogue. The next step of cross-identification was a search of the common objects for pairs FON-KIEV and FON-DUSHANBE. We used the following rule: if an angular distance is less than 1.0 arcsec it is a common object. The results of this cross-identification procedure of FON-KIEV and FON-DUSHANBE catalogues we compared with stellar position of FON-KITAB catalogue with circular window size of 1.0 arcsec. This cross-identification procedure made it possible to obtain lists of pairs of stars from all three catalogues. As a result of the FON-KIEV-DUSHANBE-KITAB data more than 500 thousands common stars have been obtained in declination zone -2° to 2° and then inserted to database for analysis. The position difference between FONs catalogues produced mainly only by the difference between random and systematic errors of objects in catalogues.

5. The estimation results of external accuracy and systematic errors data of catalogues

For the quality analysis of stellar equatorial coordinates of FON project catalogues the different tests have been made. Some results of this investigation of the FON-KIEV, FON-KITAB and FON-DUSHANBE catalogues are presented below. The comparison of the stellar positions of FON project catalogues is shown in figure 1. It represents the systematic differences of positions in the sense of FON-KIEV minus FON-DUSHANBE, FON-KIEV minus FON-KITAB and FON-DUSHANBE minus FON-KITAB catalogues.

The mean values of systematic differences of positions in right ascension are less than 15 mas in the both coordinates and are increasing for faintest stars up to 50-75 mas for right ascension and up to 25-40 mas for declination. As showed in figure 1, the stars position of all FON project catalogues are good agreement in magnitude range of Tycho-2 stars that were used for astrometric reduction. This behavior of differences in the stars positions is associated with a significant brightness equation on photographic plates. Therefore, to eliminate the brightness equation, it is necessary to use during the reduction a reference catalogue, which covers the entire range of magnitudes.

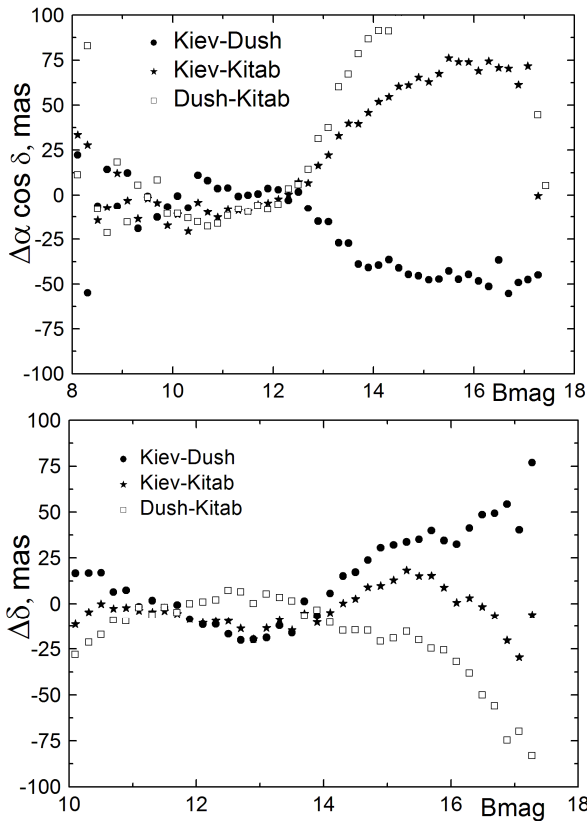


Figure 1: The systematic differences of stellar position of FON project catalogues: KIEV-DUSHANBE (black dots), KIEV-KITAB (asterisks) and DUSHANBE-KITAB (open rectangle) depending on the B-magnitude of FON-KIEV.

The estimations of external accuracy of stellar positions of FON project catalogues are some functions of stellar magnitude and equal to about 50 mas for brightest stars in the range of reference Tycho-2 stars for FON-KIEV and FON-KITAB data and about 120 mas for FON-DUSHANBE data. After 12 stellar magnitudes we can see the significant increasing up to 250 mas for FON-KIEV and FON-KITAB data and up to 350 mas for FON-DUSHANBE data (Figure 2).

These external estimations of positional precision of FON project catalogues are in a very good agreement with their internal accuracy at the mean epoch of observation. The systematic differences of internal accuracy minus external estimations of positional precision as function of stellar magnitude are presented in the figure 3. The mean values of these systematic differences are not more than 30 mas for brightest stars.

From the figure 3 we can see clearly that the internal accuracy of stellar position is systematically overestimated for the faintest stars of FON-KIEV and FON-DUSHANBE catalogues. On the other hand it is underestimated in this magnitude range for the stellar position of FON-KITAB catalogue. The noted facts should be taking into account in course that to creating of all catalogues of FON project the only data from plates of digitized astronegatives was used without any CCD-observations. For example, the positional precision of 2MASS (Skrutskie et al., 2006) stars catalogue obtained from CCD-observations with the same pixel resolution is about 50-150 mas.

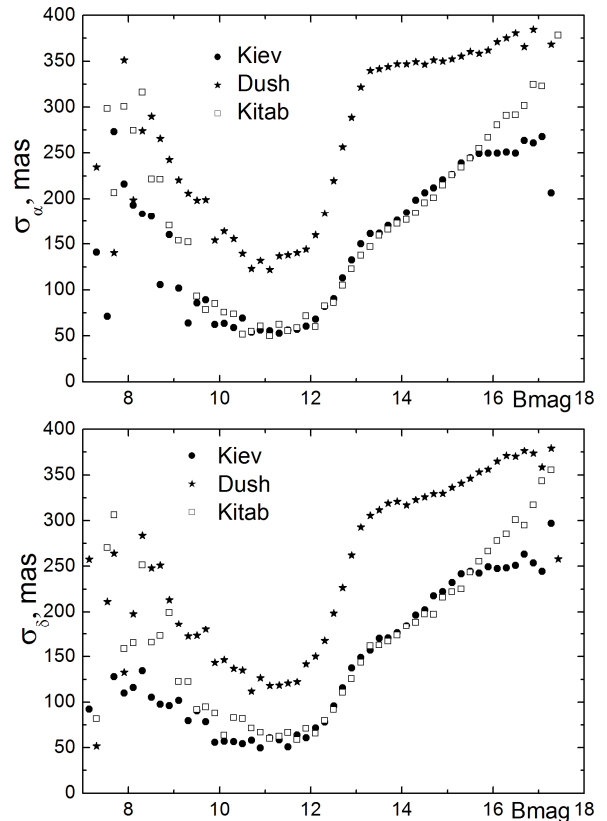


Figure 2: The standard deviations of stellar position of FON project catalogues: KIEV (black dots), DUSHANBE (asterisks) and KITAB (open rectangle) obtained by Wielen method depending on the B-magnitude of KIEV

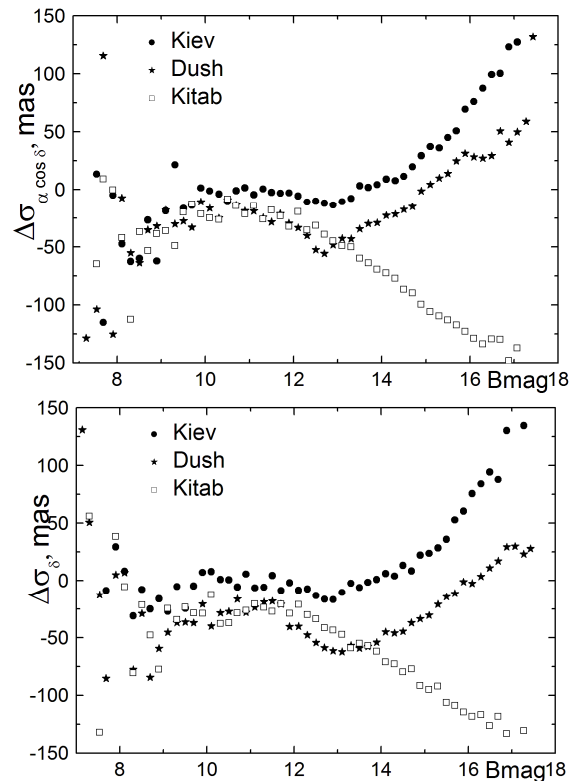


Figure 3: The systematic differences of external estimations and internal accuracy of the positional precision as function of stellar magnitude of FON project catalogues: KIEV (black dots), KIEV-KITAB (asterisks) and DUSHANBE-KITAB (open rectangle) depending on the B-magnitude of KIEV

6. Conclusion

The external accuracy of stars position of catalogues FON project are good agreement with their internal accuracy and equal from 50 and 350 mas for brightest and faintest stars correspondingly.

Random error of the objects positions is within 50 to 250 mas for the FON-KIEV and FON-KITAB catalogues, and in two times more for the positions in the FON-DUSHANBE catalogue – within 150 to 400 mas. This is due to the quality of scanned material.

The usage of high-precision reference catalogue in the whole range of magnitudes (for example, PMA or GaiaDR2) for the reduction will eliminate the brightness equation and improve the stars position both systematically and randomly.

The research results of astrometric and photometric characteristics of the FON project catalogues allow making the following conclusion. The positions and photometric measurements of objects in the FON project catalogues are obtained and they correspond to the accuracy for ground based photographic observations. The obtained observational data makes it possible to create a catalogue of positions and proper motions of the Northern Sky.

References

- Akhmetov V.S. Fedorov P.N., Velichko A.B., Shulga V.M.: 2017, *MNRAS*, **469**, 763.
- Akhmetov V., Dmytrenko A., Khlamov S.: 2018, *IEEE CSIT*, **13**, 266.
- Andruk V.M., Pakuliak L.K., Golovnia V.V. et al.: 2015, *Odessa Astron. Publ.*, **28**, 192.
- Andruk V.M., Golovnia V.V., Ivanov G.A. et al.: 2016a, *Kinem. Phys. Cel. Bodies*, **32**, N1, 38.
- Andruk V.M., Pakuliak L.K., Golovnia V.V. et al.: 2016b, *Kinem. Phys. Cel. Bodies*, **32**, N5, 260.
- Andruk V.M. et al.: 2017, *Odessa Astron Publ.*, **30**, 159.
- Gaia Collaboration et al.: 2018, *A&A* **616**, A1.
- Mullo-Abdolov A., Kokhirova A., Relke H. et al.: 2017, *Odessa Astron Publ.*, **30**, 186.
- Skrutskie M.F. et al.: 2006, *ApJ*, **131**, 1163.
- Vavilova I.B. et al.: 2012, *Kinemat. Physics Celest. Bodies*, **28**, N2, 85.
- Yuldoshev Q.X., Muminov M.M., Ehgamberdiev Sh.A. et al.: 2017a, *Odessa Astron Publ.*, **30**, 205.
- Yuldoshev Q.X., Ehgamberdiev Sh.A., Muminov M.M. et al.: 2017b, *Kinem. Phys. Cel. Bodies*, **33**, N5, 250.
- Yuldoshev Q., Protsyuk Yu., Relke H. et al.: 2019, *Astron. Nakh.*, 58, In press.
- Wielen R.: 1995, *A&A*, **302**, 613.

DOI: <http://dx.doi.org/10.18524/1810-4215.2018.31.144438>

ASTEROIDS EXPLORATION WITH BALDONE SCHMIDT TELESCOPE

I.Eglitis

Institute of Astronomy of the University of Latvia,
Riga, Latvia, ilgmars.eglitis@lu.lv

ABSTRACT. CCD observations of asteroids were obtained in 2008 with the Baldone Schmidt telescope (aperture/diameter/focal length = 80/120/240 cm) at the Baldone Astrophysical observatory (code 069) of the Institute of Astronomy of the University of Latvia. The methodology of monitoring of asteroids and orbit calculations are described. In the Minor Planet Circulars and the Minor Planet Electronic Circulars 5434 astrometric positions of 1488 asteroids were published. Among them, 76 asteroids of different type were newly discovered at Baldone Observatory. Twelve asteroids were named.

Baldone Schmidt telescope optical system was improved by inserting an additional optical system in the telescope, forming a flat telescope focal surface that coincides with the surface of the flat beam receiver. Two large (4096 x 4096 pixels) CCD cameras are now installed on the plate holder of the telescope. They cover two square degrees of the sky.

The digitizing of the Baldone Schmidt archive began in 2012. The processing results of 152 plates obtained in U, B, V, R bands in 1967-1996 were used to search for images of small bodies of the Solar system. Images were processed using advanced complex LINUX / MIDAS / ROMAPHOT programs updated in the Main Observatory of National Academy of Sciences of Ukraine. 57 asteroids and 2 comets (31P/Schwassmann-Wachmann 2, C/1969 T1 (Tago-Sato-Kosaka)) were identified on these plates. Overall 87 positions of asteroids of different types and 2 positions of comets were measured. These objects cover magnitude range from 9.8 to 17.1.

Keywords: Asteroids, Schmidt camera, plates archive

АБСТРАКТ. ПЗЗ-спостереження астероїдів були отримані в 2008 році за допомогою телескопа системи Шмідта в Балдоне (діафрагма/діаметр/фокусна відстань = 80/120/240 см) на Астрофізичній обсерваторії Балдоне (код 069) Інституту астрономії Латвійського університету. Описано методологію моніторингу астероїдів та обчислень їх орбіт. В циркулярах "Малі планети" та в електронних циркулярах "Малі планети" опубліковано 5434 астрометричних позицій для 1488 астероїдів. Серед них в обсерваторії Балдоне було відкрито 76 астероїдів різного типу. Дванадцять астероїдів отримали назви.

Оптична система телескопа Шмідта в Балдоне була вдосконалена введенням додаткової оптичної системи для створення плоскої фокальної поверхні, яка

збігається з плоскою поверхнею приймача. Дві великі (4096x4096 пікселів) ПЗЗ-камери встановлені на тримачі телескопа. Вони покривають поле неба у два квадратні градуси.

Оцифрування архіву телескопа Шмідта в Балдоне розпочалося в 2012 році. Результати обробки 152 фотоплатівок, отриманих в смугах U, B, V, R в 1967-1996 роках, були використані для пошуку зображень малих тіл Сонячної системи. Зображення були оброблені за допомогою сучасних програм LINUX/MIDAS/ ROMAPHOT, вдосконалених в Головній астрономічній обсерваторії Національної академії наук України. На цих платівках було знайдено 57 астероїдів та 2 комети (31P/Schwassmann-Wachmann 2, C/1969 T1 (Tago-Sato-Kosaka)). Всього було проміряно 87 позицій для астероїдів різних типів і 2 позиції комет. Ці об'єкти покривають діапазон від 9,8 до 17,1 зоряної величини.

Ключові слова: астероїди, камера Шмідта, архів фотоплатівок

1. Introduction

The surfaces of smallest planets and moons of the Solar system are covered with large number of craters created by asteroids. Every day, Earth is bombarded with more than 100 tons of dust and millimeter-sized particles from space. About once a year, a two meter sized asteroid hits Earth's atmosphere, often creating a bolide event as the friction of Earth's atmosphere causes disintegration of it – sometimes explosively. Chelyabinsk type event takes part about every five years. The largest impact during the last 20-year interval was the recent daytime Chelyabinsk event (440,000 – 500,000 tons of TNT) recorded over central Russia on February 15, 2013. This small asteroid that exploded in the atmosphere near Chelyabinsk, Russia was about 16 meters in size before it hit the Earth. While that impact focused public attention on the potential hazards of NEO impacts with Earth, space scientists have long known that such events are just a part of Earth's geologic history. The larger trails of asteroid falls still can be found on the Earth, e.g. 4 000 year-old Kali crater in Estonia on Saaremaa island, 50 000 year old Arizona crater near Winslow in the USA, etc. Many of small impacts similar to Chelyabinsk are unknown because they happened in regions with no inhabitants – Siberia, Amazon jungles, oceans and deserts. The radar observations reveal that asteroids similar to Chelyabinsk event hit the Earth on

average every 5 years. With radar observations it is possible to detect small asteroids that are disintegrated in the Earth's atmosphere (Planetary Science). Scientific assessments of the risk, as well as the hazards posed by future asteroid impacts with Earth vary. In an article published in "Nature" Brown (2013) and his colleagues reported that "telescopic surveys have only discovered about 500 near-Earth asteroids that are 10-20 meters in diameter (comparable to the Chelyabinsk asteroid) of an estimated near-Earth asteroid population of around 20 million, implying that a significant impactor population at these sizes could be present but not yet cataloged in the discovered near-Earth asteroid population". The importance of such research of asteroids is proved by the fact, that the largest known celestial threat to the Earth within the period after Christ was the 320 m large asteroid Apophis which was discovered only in June 2004. This fact and the yearly discoveries of a large number of new NEO type asteroids show how little attention has been given to the studies of the small bodies in the Solar system so far. The importance of the small body studies in the Solar system can be properly evaluated if we recall the volcanic eruption effects in Iceland, comparable to the effect caused by the fall of a small asteroid. The fall of an asteroid larger than 50 m will be a disaster that can stop the progress in the world for several years, but the fall of a 300 m and larger body can terminate the development of civilization on the Earth for several decades, or even destroy the humanity at all. At the 5th meeting of the PECS Committee on 27th of May 2009 in Esrin (Italy), the total number of NEO and hazard asteroids, measures to 66 000 (Bobrinsky, 2009). Successful results were achieved on monitoring systems such as Pan-STARRS, Catalina Sky Survey, Mt. Lemmon Survey, Kitt Peak-Spacewatch, LINEAR, and some space missions such as WISE monitoring asteroids. Despite that, the current progress is not fast enough. Catalogue of NEO listed 17791 hazard objects on February 2018 (Minor Planet Center, 2018) or 27% of all hazard objects. NASA congress on 5th of March 2007 provided an assessment of the problem in Near-Earth Object Survey and Deflection Analysis of Alternatives. It concluded that only a wide ground base plus space sensor observations of Venus, like the orbit, can allow a more prompt solution of the problem, i.e. to discover the NEO asteroids in the nearest future (Milani et al., 2013).

Finally, the research of asteroids manages to draw vast attention of mass media, thus promoting an awareness of the importance of science, including astronomy, among public at large, young people in particular. From the other point of view the investigation of asteroids properties are important for development of evolution theory of the Solar system and classification of small objects in the Solar system. From photometric study of light curves an additional information can be obtained about size, rotation period, structure of objects, existence of craters and ice fields on the surface, which is very important data for space missions and for fantastic ideas about mineral mining on asteroids. The spectral observations can give information about chemical composition of asteroids and comets.

2. Asteroid observations

The Baldone Schmidt system telescope was launched in 1966 at Riekstukalns observation site of the Institute of Astronomy, the University of Latvia (the Radio Astrophysical observatory of Latvian Acad. Sci. until 2001) near Baldone. The diameter of the correction plate of the telescope is 800 mm, the diameter of the main mirror – 1200 mm. The main mirror is mounted at a distance of 4780 mm from the correction plate. The reflecting surface of the mirror was restored in 2005. The image, which covers 4046' of sky diameter, appears on the spherical surface of the main focus with a bend radius of 2400 mm.

The asteroid project of the Baldone Observatory (IAU code 069, longitude 24.4041 E, latitude 56.7734 N, altitude 103 m) includes astrometric and photometric observations of asteroids and the newly discovered Near Earth Objects (NEOs), including their monitoring. Astrometric CCD observations of asteroids at the Baldone Observatory were started in January of 2008, using the Schmidt telescope with a ST-10XME CCD camera (field of view $21' \times 14'$). The first three new asteroids were discovered in January of 2008 (2008AL86, 2008AU101 and 2008AV101). Two exceptional objects have been discovered: the Apollo-type NEO 2008OS9 (Cernis & Eglitis, 2008), a Centaur-type asteroid 2009HW77 (Cernis & Eglitis, 2009) and two Trojan group asteroids (2011 QA50 with $a=5.27$ au and 2013 RO26 with $a=5.12$ au). The limiting R magnitude for the Baldone Schmidt telescope is about 21 for unfiltered CCD images with an exposure time of about 8 minutes. All astrometric measurements and reductions were done using Astrometrica software (Raab, 2003) and pipeline program SkySift (Holvercem, 2018). SkySift was intensely used for research in fields with high density of stars. Reference stars were selected from the catalogs USNO-A2.0, USNO-B1.0, UCAC-2 and UCAC-4. Most of asteroids were discovered in the morning sky about 15-20 days before their opposition time at 150-160 deg elongations. The sky survey has been done close to the ecliptic (mostly no more than 10 deg from the ecliptic line), taking three (or sometimes four) CCD images from the same field, with 20-30 min time spans between exposures. The Baldone Schmidt telescope is very useful for searching new asteroids and doing follow-up astrometry of poorly observed NEOs and unusual objects. During 2008-2013, 2117 CCD images (using 116 observing nights) for astrometry of asteroids and comets were obtained by I. Eglitis. K. Cernis (Institute of Astronomy, Vilnius University) have processed CCD images for new objects and measured positions of all asteroids appearing in the CCD frames. 3511 astrometric observations of 826 asteroids, including at least 5 NEOs, were published in the Minor Planet Circulars (MPC) and Minor Planet Electronic Circulars (MPEC). But during 2016-2018, 12587 CCD images (using 68 observing nights) for astrometry of asteroids and comets were obtained. 4395 astrometric observations of 1465 asteroids were published in the MPC. Till now, 2018 October, the credits for discovery of 34 asteroids have been received by the Baldone Observatory from the Minor Planet Center. 12 of them have been named (see Table 1). Our contribution is about 0.012 % of all of the 55.7×10^6 observations of asteroids done during

this period in the world. The newly discovered (76) compose a similar part, 0.015%, of all 523800 asteroids discovered. In this period a great numbers of asteroids was discovered by the specialized projects: LONEOS, LINEAR, Spacewatch, Catalina and Panstarrs.

3. Baldone Schmidt telescope optical system development

Schmidt telescopes are used to produce high quality large field star images, which in many ways outweigh all other telescopes with similar aperture diameters. These telescopes are no longer used in world, due to the technological transition to electronic sensors for the purpose of capturing the space images. Schmidt cameras have very strongly curved focal planes, thus requiring for detector to be correspondingly curved. When transitioning to a new type of image object acquisition – from photography to the use of video sensors, we encounter an unresolved problem, – how to match the curved large scale telescope's focal surface with the surface of a flat light imaging sensor.

The team of the Institute of the Astronomy has succeeded in designing a small optical circuitry that would improve the Baldone Schmidt optical system. Small lens combination is inserted in the telescope forming a flat telescope focal surface which coincides with the surface of the flat-beam receiver. This lens combination is positioned before two SBIG CCD cameras STX-16803. This optical system upgrade makes it possible to use the existing large-field flat-panel video sensors without loss of quality, at relatively low cost and without the expensive Schmidt telescope reconstruction. SBIG STX-16803 CCD camera has KAF-16803 4096x4096 pixels Monochrome Sensor with size 36 x 36 mm. The size of one pixel is 9 x 9 micron.

We have created Schmidt telescope with an upgraded optical system. To establish how they work together, basic technological components are integrated into the main focal plane of Baldone Schmidt telescope. There are two STX -16803 cameras that are positioned on cassette holder position. Both cameras cover two square degrees of the sky.

3. Digitizing of Baldone Schmidt telescope archive

The regular digitization and processing of photographic astroplates was started in Baldone observatory from 2013. The photos were digitized using Epson Expression 10000XL and 11000XL commercial scanners with 1200 dpi (or 2400 dpi) resolution. For processing purposes all images were transformed from TIFF format to the FITS format with an original program created at the Institute of Astronomy. Till this moment more than 18000 (from 22000) direct photos have been digitized. Scans are stored on the server of the University of Latvia

The digitizing of the UV-part of Baldone collection started in June 2016 with two EPSON EXPRESSION 10000XL and three 11000XL flatbed scanners. Its photometric and astrometric characteristics were previously tested, and the optimum mode of scanning was found (Protsyuk et al., 2014). Images were processed using ad-

vanced LINUX / MIDAS / ROMAPHOT programs (Andruk, 2015). The software was developed and implemented in Main Astronomical Observatory of the National Academy Science of Ukraine to process the digitized astronomic photos as well as to obtain astrometric coordinates and photometric magnitudes of stars and compact galaxies.

In order to investigate variability of stars within time span from 1967 to 2005, many of the sky regions have been photographed tens and some of them even hundreds of times.

In addition to the main tasks, digitized photos of star fields allows to carry out a massive search for images of small bodies of the solar system and to determine their coordinates. From the observations of earlier epoch it is possible to extract information about the locations of these bodies (Eglitis et al., 2016).

4. Results

During the sky survey of the ecliptic, 76 new asteroids were discovered in 2008–2018: 43 of them have multiple-apparition orbits, 9 are one opposition objects from which 7 have no orbit.

The first successful observations with upgraded Baldone Schmidt telescope were made in August-September 2017. The quality of the images is high. Four plates obtained at different declinations (from 2 degrees till 60 degrees) with 60 sec exposures were measured. The results of diameter measurements of different magnitude stars show that diameters of 17th magnitude stars do not exceed six pixels in the center and four pixels in corners of the images.

The processing results of 152 observations of clusters and Pluto in UBV bands from 1967 to 1996 were used for broad search for images of small bodies of the Solar system. As a result, 57 asteroids and 2 comets (31P/Schwassmann-Wachmann 2, C/1969 T1 (Tago-Satoko-Kosaka)) were identified on these plates. From them 87 positions of asteroids and 2 positions of comets were received. These objects cover a magnitude range of 9.8 to 17.1. Their orbit types are: Main Belts, Apollo, Centaur, Trojan, Hungarias and Mars-crosser.

5. Conclusion

The project, together with other observatories and space missions, will contribute to plan cataloging of NEO-type and Earth-hazard objects of at least 90% till 2021. The project will complement observations of asteroid positions that are missing to accurately determine orbital elements. The research results will be sent to the Minor Planet Center, which operates at the Smithsonian Observatory and are published in Minor Planet Circulars. The results of calculations of orbital elements were compiled in 3 papers, which are included in the Web of Science database. It is important to analyze the chemical composition of asteroids from the point of view of evolution and practical applications. The planned multicolor photometric and low-resolution spectral observations will allow classification of asteroids – the division of C-type (carbonaceous), S-type (silicate) and M-type (metallic). The resulting light

curves will allow not only to determine the rotation period of small bodies, but also to design an asteroid model by shape. On the other hand, the rapid changes in light curves over the main change in the brightness make it possible to predict the existence of large deep craters on the surface (in the case of a sharp drop in brightness) or the areas of ice fields on the surface (in the case of rapid increase of brightness). All of these asteroid characteristics are important for evaluating the albedo, modelling the form and detecting the sizes of objects. Asteroid rotation calculations are important for planning space missions for their direct exploration and also for mining them in the future.

The efficiency of the new optical system is obvious. In August-September 2017 after improvement of the optical system, 21 new asteroids were discovered. In the previous years (2008 – 2015), using one small (10 x 15 mm) SBIG CCD ST-10XME, only 49 new asteroids were discovered (Cernis et al., 2015). In the Autumn 2018 seven new discoveries were added.

Asteroids with high accuracy of up to 16-17 magnitudes can be detected on the photographic plates of Baldone Observatory. Among those may be objects which are discovered much later than observed. The presence of the archive of all observations in time scale 1966-2002 will give the possibility to sort and analyze the asteroids of interest, including the bright Kuiper Belt objects.

According to data analysis, the rms-error of measurements of coordinates increases from 0.10 to 0.25 arcsec by increasing asteroid's magnitude from 13 to 16. (Eglitis et al., 2016).

Acknowledgements. This investigation is supported by project Nr. Izp-2018/1-0401 „Complex investigations of Solar System small bodies”.

References

- Andruk V.M., Pakuliak L.K., Golovnya V.V. et al.: 2015, arxiv.org/abs/1512.05535.
- Bobrinsky N.: 2009, *The European SSA Preparatory Programme. 5th meeting of the PECS committee*, ESRIN, Italy. [online]: http://esamultimedia.esa.int/multimedia/esoc/opsg/opsg_forum_ssa_05122008.ppt
- Brown P.G., Assink J.D., Astiz L. et al.: 2013, *Nature*, **503**, 238.
- Cernis K., Eglitis I.: 2008, *Minor Planet Electronic Circular*, 2008-O66.
- Cernis K., Eglitis I.: 2009, *Minor Planet Electronic Circular*, 2009-U68.
- Cernis K., Wlodarczyk I., Eglitis I.: 2015, *Baltic Astronomy*, **24**, 251.
- Eglitis I., Eglite M., Shatokhina S.V. et al.: 2016, *Odessa Astron. Publ.*, **29**, 123.
- Holvercem P.: 2018, *SkySift* [online]: <http://sites.mpc.com.br/holvercem/>
- Milani A., un c.: 2013, *International BELISSIMA conference*, Belgrade, Romania [online]: https://www.researchgate.net/profile/Ivana_Milic_Zitnik/publication/308969745_CCD_OBSERVATIONS_OF_ERS_WITH_THE_60_cm_TELESCOPE_AT_ASV/links/57fb9c9608ae8da3ce60fd5f/CCD-OBSERVATIONS-OF-ERS-WITH-THE-60-cm-TELESCOPE-AT-ASV.pdf
- Minor Planet Center: 2018 [online]: https://www.minorplanetcenter.net/db_search/show_by_neo_type?utf8=%E2%9C%93&neo_type=neo
- Protsyuk Yu.I., Andruk V.N., Muminov M.M. et al.: 2014, *Odessa Astron. Publ.*, **27**, 59.
- Planetary Science [online]: <https://www.nasa.gov/jpl/bolide-events-1994-2013>
- Raab H.: 2003, *Astrometrica* [online]: <http://www.astrometrica.at/> (electronic version)

Table 1: Named asteroids discovered in Baldone observatory

| Number | Label | Name | Named year | Diameter |
|--------|------------|-----------|------------|----------|
| 274084 | 2008 AU101 | Baldone | 2011 | 1,5 |
| 284984 | 2010 GC158 | Ikaunieks | 2012 | 1,5 |
| 294664 | 2008 AL86 | Trakai | 2012 | 3,5 |
| 321324 | 2009 HJ68 | Vytautas | 2012 | 3 |
| 330836 | 2009 HW77 | Orius | 2013 | 35 |
| 343157 | 2009 HH68 | Mindaugas | 2013 | 3,5 |
| 392142 | 2009 HV19 | Solheim | 2014 | 3 |
| 332530 | 2008 OS18 | Canders | 2015 | 2 |
| 352646 | 2008 OZ1 | Blumbahs | 2015 | 1,5 |
| 418220 | 2008 CL177 | Kestutis | 2016 | 1 |
| 428694 | 2008 OS9 | Saule | 2016 | 0.7 |
| 457743 | 2009 HW20 | Balklavs | 2017 | 1 |

DOI: <http://dx.doi.org/10.18524/1810-4215.2018.31.146194>

BALDONE 1.2M TELESCOPE PLATE ARCHIVE – HIDDEN RESERVES OF THE FON PROJECT

I. Eglitis¹, V. Eglite¹, V. Andruk², Yu. Protsyuk³, S. Protsyuk³, O. Kovylianska³

¹Institute of Astronomy, University of Latvia, Riga, Latvia, ilgmars@latnet.lv

²Main Astronomical Observatory NASU, Ukraine, andruk@mao.kiev.ua

³Research Institute “Mykolaiv Astronomical Observatory”, Ukraine, yuri@nao.nikolaev.ua

ABSTRACT. The plate archive of the 1.2 m Baldone telescope (Latvia) has approximately 780 and 4660 astronegatives exposed in 1967-1993 in the U (ZU21 + UG1 filter plates) and V (A600N + ZS17 filter films) closed to Johnson system U and V passbands. Digitization of astronegatives is carried out using the Epson Expression 10000XL scanner, the scanning mode is 1200 or 2400 dpi, each field covers 19 square degrees of sky. The plates and films are scanned at the Baldone Observatory, processing of digitized scans is carried out by the observers in Baldone, at the Research Institute "Mykolaiv Astronomical Observatory" and at the Main Astronomical Observatory of the National Academy of Sciences of Ukraine. The Epson Expression 10000XL Scanner, along with the software developed, allows us to digitize and process the plates and receive coordinates and magnitudes of registered objects (with high, moderate and low brightness) with an internal error of no worse than 0.05 seconds of arc and 0.03 magnitude. The astrometric and photometric reduction of digitized astronegatives is done in the Tycho-2 reference system and U, V photoelectric system. At this report, we present first results of reduction of more than 2000 astronegatives. Data of U and V magnitudes of stars and galaxies will be used as the photometric addition to the FON project, without, the long-term series of U, V observations have an independent value for studying the variability of stars. Also, many plates included open clusters and will be used for investigation of their population and photometric parallaxes.

Keywords: scanning, processing of digitized plates, FON project, astrometry, photometry, data analysis

АБСТРАКТ. Архів склотеки 1.2м телескопу в Балдоне (Латвія) нараховує близько 780 та 4660 астронегативів, експонованих в 1967-1993 роках в U (платівки ZU21 + фільтр UG1) та V (плівки A600N + фільтр ZS17) смугах системи Джонсона. Оцифрування астронегативів здійснюється за допомогою сканера Epson Expression 10000XL, режим сканування — 1200 або 2400 dpi, робоче поле — 19 кв. градусів. Платівки та плівки скануються в обсерваторії Балдоне, обробка

оцифрованих сканів здійснюється співробітниками обсерваторії в Балдоне, в НДІ “Миколаївська астрономічна обсерваторія” та в Головній астрономічній обсерваторії НАН України. Планшетний сканер Epson Expression 10000XL разом з розробленим програмним забезпеченням дозволяє оцифрувати і обробляти платівки та отримувати координати та зоряні величини зареєстрованих об'єктів (високої, помірної та слабкої яскравості) з внутрішньою похибкою не гірше 0.05 секунди дуги та 0.03 зоряної величини. Астрометрична та фотометрична редукція оцифрованих астронегативів здійснюється в системі опорного каталога Tycho-2 та U,V фотоелектричних вимірів зір відповідно. В цій роботі ми представляємо перші результати обробки для понад 2000 астронегативів. Дані про U та V величини зір і галактик будуть використані для фотометричного доповнення проекту ФОН, а багаторічні ряди U,V спостережень мають самостійне значення для дослідження змінності зір. Крім того, багато платівок включають розсіяні зоряні скупчення і будуть використані для дослідження їх населення та визначення фотометричних паралаксів.

Ключові слова: сканування, обробка оцифрованих платівок, програма ФОН, астрометрія, фотометрія, аналіз даних

1. Introduction

Baldone Observatory of Institute of Astronomy of Latvian University has the photographic collection more than 22000 plates obtained using 1.2 m Schmidt telescope. (Eglite et al, 2016; Eglitis et al., 2017a). Photographic observation began at the end of 1966 and lasted for 39 years. Each image of Baldone Schmidt telescope covers about 19 square degree of the sky and contains from 10 to 50 thousand images of celestial objects. Scale is 72 "/mm. As a result, photographic observational archive of Baldone observatory has about 780 U-plates, 5000 V-plates, 4600 V-films and more than 10000 R-plates (Eglitis et al, 2016a; 2016b). Regarding the astronegatives

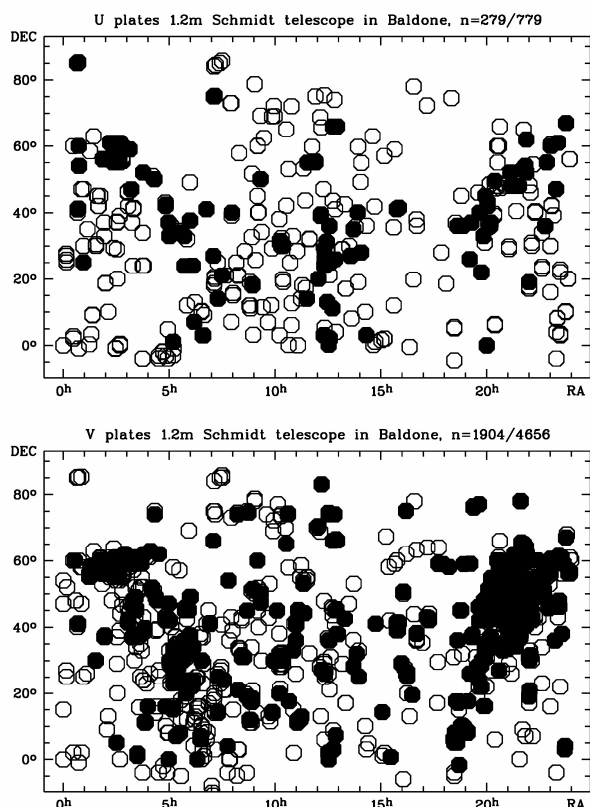


Figure 1: The current state of U and V bands of plate archive digitizing and processing.

exposed in the U (ZU21 plates + UG1 filter) and V (A600N films + ZS17 filters) Johnson system bands, the plate archive, respectively, has about 780 plates and 4660 films, exposed in 1967-1993 (Figure 1). The astronegative U and V collections are scanned on an EPSON EXPRESSION 10000XL scanner with a spatial resolution of 1200 dpi with pixel size near 1.81".

In figure 1 the sections of the starry sky exposed on the 1.2m Schmidt telescope in Baldone in the U (upper part) and V (lower part) bands are presented. Blackened circles correspond to the processed scans of the plates. The astrometric and photometric reduction of digitized astronegatives is done in the Tycho-2 and U, V photoelectric system respectively. The first results of scan processing show that limit of B and V magnitude on plates with 20 minute exposure is about 19 and 17 magnitude respectively.

Random errors of the scanner for the astronegatives of the Schmidt telescope were investigated (Eglitis et al., 2017b). Studies have shown that for rectangular coordinates, the errors of one determination of the values of coordinate differences are $\sigma_{xy} = 0.021-0.027$ px, the errors in the determination of instrumental stellar magnitudes do not exceed the values $\sigma_m = 0.014^m-0.016^m$. Considering the scale factor (the value of which is close to two due to the scale and technical characteristics of scanning for astrometry and photoemulsion contrast), the practical errors for the system of equatorial coordinates and U-values will be twice as large. And the following conclusion was made: the Epson Expression 10000XL flatbed scanner together with the developed software

allows digitizing and processing the plates and obtaining the characteristics of objects (with high, moderate and low brightness) with an internal error of no worse than 0.05 arc seconds and 0.03 magnitude. For boundary faint objects (U = 16m-17m), our studies gave a result about two times worse. This conclusion concerns scan modes 1200 dpi for astronegatives of 240x240 mm.

2. The photometric part of the project FON

The plan for a photographic survey of the northern sky (FON in russian) was proposed in 1976 by the staff of the Main Astronomical Observatory of Academy of Sciences of USSR I.G. Kolchinsky and A.B. Onegina (Kolchinsky, 1977; Pakuliak, 2016). Earlier, in 2016 within the framework of the UkrVO project (Vavilova, 2012; Vavilova, 2016; Vavilova, 2017) implemented the Kiev part of the FON project (Andruk, 2015; Andruk, 2016a; Andruk, 2016b) and in 2017 - the Kitab part of the FON project (Yuldoshev, 2017a; Yuldoshev, 2017b). Data of U and V magnitudes of stars and galaxies from Baldone archive will be used as the useful photometric addition to the FON project.

The photometry of stars and galaxies for the U and V astroplates of the 1.2m telescope in Baldone is made on the basis of the principles implemented in processing the plates of the FON project (Andruk, 2017a) using photoelectric measurements of stars to construct the characteristic curves of plates (Relke, 2015). Future plans include the creation of a consolidated catalogue of the FON project (Andruk, 2017b), including U and V values based on the results of processing digitized plates of the 1.2-m telescope in Baldone (Eglitis, 2016a; Eglitis, 2016b). Regarding the accuracy of processing of digitized U plates, the studies gave the following result. The internal accuracy for all objects is $\sigma_{\alpha\delta} = 0.28''$ and $\sigma_U = 0.20^m$ (for stars in the interval U = 8^m-14^m, the errors are $\sigma_{\alpha\delta} = 0.11''$ and $\sigma_U = 0.09^m$) for equatorial coordinates and star magnitudes, respectively. The convergence of the coordinates with the Tycho-2 reference system is $\sigma_{\alpha\delta} = 0.06''$. The convergence with photoelectric stellar U_{pe} values is $\sigma_B = 0.13^m$. The results of processing photographic observations of the 1.2 m telescope in Baldone can be used to improve the photometric parameters of the summary FON catalogue, to study variable stars and open clusters. The coordinate part in the U band can also be used to refine the proper motions of stars. To use the coordinate part in the V band, it is necessary to carry out studies of films deformation during scanning and improve processing techniques.

3. Conclusion

Baldone Schmidt archive in some area of sky contain 20 – 30 years regular observations, that will be a good source for investigation of variable stars of different type and for detection of proper motion of stars.

The traditional field of research in Baldone observatory is an investigation of carbon stars. Some of this late objects are situated close to clusters. One of the unclear characteristics of C stars in the Milky Way galaxy is their absolute magnitude. Therefore Baldone archive contains

multicolour wide-field observations of open clusters which are near carbon stars. These digitized plates will be an exclusive source for investigation of their population and photometric parallaxes.

At present, according to the accepted methodology (as part of the FON project), more than two thousand astronegatives exposed at the 1.2 m Schmidt telescope in Baldone in the U and V bands are being processed. The coordinates of stars and galaxies are reduced to the Tycho-2 catalogue system, U and V values to the photoelectric standards system. Work on the processing of astronegatives continues.

References

- Andruk V.M., Pakuliak L.K., Golovnia V.V. et al.: 2015, *Odessa Astron. Publ.*, **28**, 192.
- Andruk V.M., Golovnia V.V., Ivanov G.A. et al.: 2016, *Kinem. Phys. Cel. Bodies*, **32**, N1, 38.
- Andruk V.M., Pakuliak L.K., Golovnia V.V. et al.: 2016, *Kinem. Phys. Cel. Bodies*, **32**, N5, 260.
- Andruk V.M., Pakuliak L.K., Golovnia V.V. et al.: 2017, *Science and Innovation*, **13a**, 17.
- Andruk V., Yuldoshev Q., Eglitis I. et al.: 2017, *Odessa Astron Publ.*, **30**, 159.
- Eglite M., Eglitis I.: 2016, *Odessa Astron Publ.*, **29**, 120.
- Eglitis I., Eglite M., Pakuliak L.K., Andruk V.M.: 2016, *Odessa Astron Publ.*, **29**, 126.
- Eglitis I., Eglite M., Andruk V. et al.: 2016, *BTSNU*, **54**, 21.
- Eglitis I., Eglite M.: 2017, *Science and Innovation*, **13a**, 55.
- Eglitis I., Andruk V.: 2017, *Open Astronomy*, **26**, 7.
- Kolchinsky I.G., Onegina A.B.: 1977, *Astrometry and Astrophysics*, **33**, 11.
- Pakuliak L.K., Andruk V.M., Golovnia V.V. et al.: 2016, *Odessa Astron. Publ.*, **29**, 132.
- Relke E., Protsyuk Yu.I., Andruk V.M.: 2015, *Odessa Astron. Publ.*, **28**, 211.
- Vavilova I.B., Pakulyak L.K., Shlyapnikov A.A. et al.: 2012, *Kinem. Phys. Cel. Bodies*, **28**, N4, 85.
- Vavilova I.B.: 2016, *Odessa Astron. Publ.*, **29**, 109.
- Vavilova I.B., Yatskiv Ya.S., Pakuliak L.K.: 2017, *IAUS*, **325**, 361.
- Yuldoshev Q.X., Muminov M.M., Ehgamberdiev Sh.A. et al.: 2017, *Odessa Astron Publ.*, **30**, 205.
- Yuldoshev Q.X., Ehgamberdiev Sh.A., Muminov M.M. et al.: 2017, *Kinem. Phys. Cel. Bodies*, **33**, N5, 250.

DOI: <http://dx.doi.org/10.18524/1810-4215.2018.31.144076>

DEVELOPMENT AND IMPROVEMENTS OF COMPUTATIONAL METHODS IMPLEMENTED TO THE COLITEC SOFTWARE

S. V. Khlamov^{1,2}, V. E. Savanevych³, O. B. Briukhovetskyi³, E. N. Dikov⁴, I. B. Vavilova²¹ Institute of Astronomy, V. N. Karazin Kharkiv National University, Kharkiv, Ukraine, sergii.khlamov@gmail.com² Main Astronomical Observatory, National Academy of Sciences of Ukraine, Kyiv, Ukraine, irivav@mao.kiev.ua³ Western Radio Technical Surveillance Center, National Space Agency of Ukraine, Mukachevo, Ukraine, vadym@savanevych.com, izumsasha@gmail.com⁴ Scientific Research, Design and Technology Institute of Micrographs, Kharkiv, Ukraine, endikov@gmail.com

ABSTRACT. The CoLiTec software is a large complex of processing modules that implements computational methods for the different purposes: brightness equalization of CCD-frames; automated calibration of the frames by bias-frame, dark-frame, and flat-field for reducing the dynamic range of brightness of the image background; frames track & stack; automated rejection of the anomaly pixels; automated excluding of the objects with anomaly errors; determining the equatorial coordinates of the Solar System small bodies; accurate parameter's estimation of objects in frames; star's identification in the frames; astronegative plate's processing; ensemble differential photometry using comparison stars; determining the instrumental brightness of stars in CCD-frames; automated light curve creation; detection of very slow and very fast objects in series of CCD-frames; detection of objects with a near-zero apparent motion in series of CCD-frames.

The described methods work with the different forms of object images (point, long) and during the different observational conditions (with daily telescope guidance and without it). These methods lead to the increasing of astrometry and photometry accuracy indicators as well as the quality indicators for detection of the Solar System small bodies in series of CCD-frames.

The CoLiTec software is installed at several observatories of the world. In total, it was used for about 700 000 observations and discovery of more than 1560 asteroids, including five NEO, four comets (C/2011 X1 (Elenin), P/2011 NO1 (Elenin), C/2012 S1 (ISON), and P/2013 V3 (Nevski)), 21 Trojan asteroids of Jupiter, and one Centaur.

The paper deals with the CoLiTec software 1) to process the different types of astrometry information, which can be fed on-line in different forms, for example, files stream and video stream, astroplates; 2) to decide the data saving problem at various servers and virtual observatories sites; 3) to improve computational methods and algorithms for automated detection of Solar System small objects; 4) to improve the accuracy of astrometry/photometry reduction.

Keywords: CCD, series of frames, observations, astrometry, photometry, computational methods, CoLiTec.

АБСТРАКТ. Програмне забезпечення CoLiTec – це потужний комплекс модулів обробки астрономічних даних, що реалізують обчислювальні методи вирівнювання яскравості ПЗЗ-кадрів; автоматичного калібрування кадрів за допомогою bias, dark та flat кадрів для зменшення динамічного діапазону яскравості фону зображення; складання кадрів; автоматичного виявлення аномальних пікселів; автоматичного виключення вимірювань положення об'єктів з аномальними помилками; точної оцінки положення об'єктів на кадрах; визначення екваторіальних координат малих об'єктів Сонячної системи; ототожнення зірок на кадрах та у каталогах, що застосовуються; обробка астронегативних платівок; високоточної фотометрії зір з використанням зір порівняння; визначення інструментальної яскравості зір на ПЗЗ-кадрах; автоматичної побудови кривих блиску зір; виявлення рухомих об'єктів з малою контрастністю зображень; виявлення дуже повільних і дуже швидких об'єктів на серії ПЗЗ-кадрів; виявлення об'єктів з близьконульовим видимим рухом.

Обчислювальні методи працюють з різними формами зображень об'єктів (круговими, протяжними) і в різних умовах спостереження (з добовим веденням телескопа та без нього). Запропоновані та впроваджені методи призвели до покращення показників точності астрометрії та фотометрії, а також показників якості для виявлення малих тіл Сонячної системи на серії ПЗЗ-кадрів.

Програмне забезпечення CoLiTec широко використовується у різних обсерваторіях світу. Всього було виконано близько 700 000 спостережень та відкрито більше 1560 астероїдів, у тому числі п'ять NEO, чотири комети (C/2011 X1 (Сленін), P/2011 NO1 (Сленін), C/2012 S1 (ISON) і P/2013 V3 (Невський)), 21 троянський астероїд Юпітера та один Кентавр.

У роботі розглядаються окремі аспекти програмного забезпечення CoLiTec, а саме 1) для обробки різних типів астроінформаційних даних; 2) для вирішення задачі збереження даних на різних серверах та сайтах віртуальних обсерваторій; 3) для вдосконалення об-

числювальних методів та алгоритмів автоматичного виявлення малих об'єктів Сонячної системи; 4) для покращення астрометричної і фотометричної точності даних зображень на серії ПЗЗ-кадрів.

Ключові слова: ПЗЗ, серія кадрів, спостереження, астрометрія, фотометрія, обчислювальні методи, CoLiTec.

1. Introduction

At the present time the fast technological progress provokes creation of a big amount of the scientific information. There are a lot of different research fields in astronomy that use the high dimensional data sets for analysis. Some of them are as follows: variables stars, asteroids, comets, near-Earth objects, satellites and others.

What can we do with such a big data amount? We should develop and propose the automated software, likely the CoLiTec (Collection Light Technology) software, which is able to: 1) process this big amount of astro-information; 2) discovery the new Solar System small objects in series of CCD-frames, including those that are the potential hazard near-Earth objects; 3) create the light curves of investigated variable stars, satellites, asteroids, etc. We have also the Data Mining problems with these big astronomical data sets. How can we solve them? We should develop the data pre-processing methods and data reduction models to simplify input data sets by reducing unnecessary information.

In this paper we describe the CoLiTec software accentuating on the following tasks: 1) to process the different types of astronomical information in automated mode, which can be fed on-line in various forms, for example, files stream and video stream, astroplates, 2) to decide the data saving problem at the different servers, virtual observatories sites. All these data can be obtained from the networks of automated ground-based and space-born observation systems or from the old astronomical plate's archives.

Authors have developed new and improved already existed methods for the full frames processing, including intraframe processing (parameter's estimation of all objects in the frames) and interframe processing such as parameters estimation of trajectories of all moving objects in the series of frames.

2. CoLiTec software

Software for automated processing of series of frames is necessary for the most effective astronomical observations. This possibility is provided by the CoLiTec software, <http://www.neoastrosoft.com> (Savanevych et al., 2012) that includes the following features:

- Automatic detection of faint moving objects (SNR>2.5);
- Working with a very wide field of view (up to 10 degrees²);
- FrameSmooth software for brightness equalization;
- Auto calibration and cosmetic correction;
- Fully automatic robust algorithm of astrometric reduction;
- Automatic rejection of the worst observations;

- Detection of very slow and very fast objects (from 0.7 to 40.0 pix./frame);
- LookSky – processing results viewer with user-friendly GUI;
- Multi-threaded support for multi-cores systems and local network;
- Processing pipeline managed by OLDAS (On-line Data Analysis System);
- CoLiTec Control Center (3C) with processing monitoring and logging.

These features allow effective using of CoLiTec software at the different observatories in the world.

The very brief sequence of the online processing is presented in Figure 1.

Images that are saved from the input telescopic devices are processed by the CoLiTec software in different modes. As a result, we can get necessary data such as light curves and appropriate reports. The more detailed process workflow of CoLiTec software is presented in Figure 2. The data control during processing is performed with using of the improved method, which is based on the subject mediator according to the UML-diagram (see Figure 3). The main advantage of this approach is the scalability of both the input and output interfaces of program modules in CoLiTec software.

The data mining is performed in OLDAS mode, which is especially significant. It allows us to conduct near real-time data processing and to assign confirmation of the most interesting objects at the night of their preliminary discovery (see Figure 4).

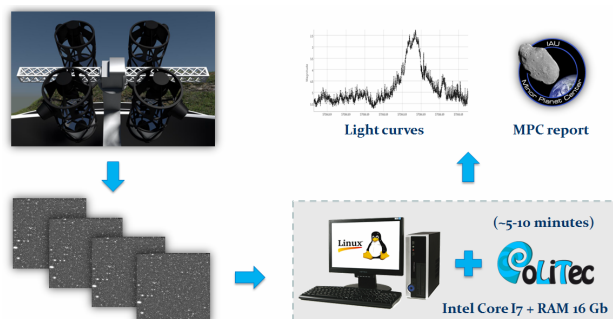


Figure 1: Brief sequence of the online processing by CoLiTec software

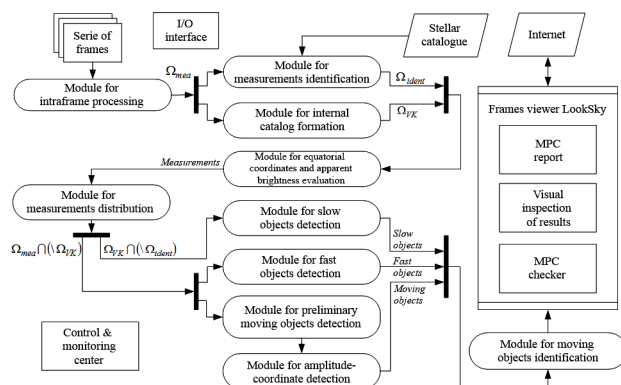


Figure 2: CoLiTec software process workflow

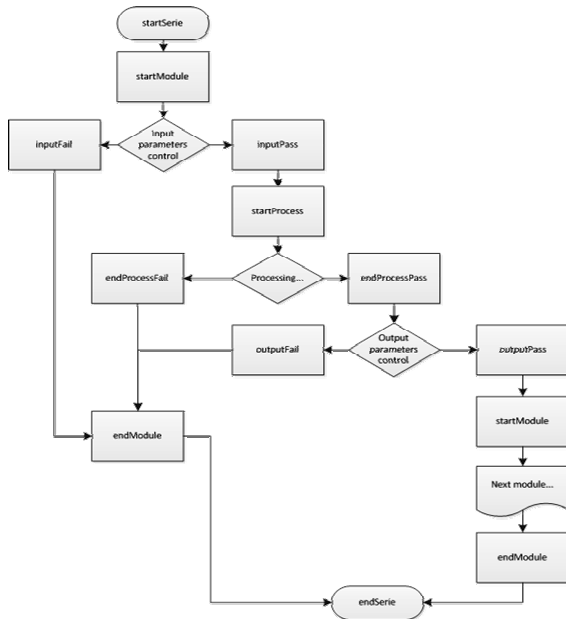


Figure 3: UML-diagram of the subject mediator

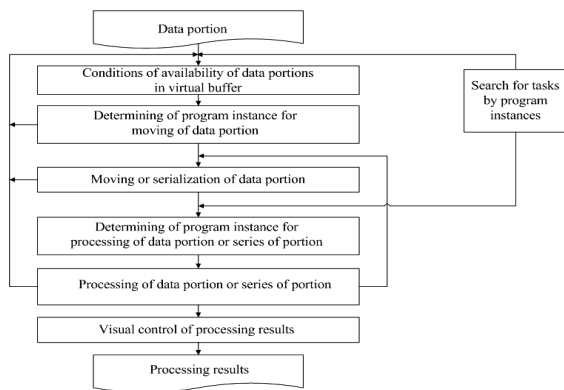


Figure 4: UML-diagram of OLDAS: determining the program instance for moving/processing of data portion

During the pre-processing step of CoLiTec software in OLDAS mode the all unsupported and corrupted frames will be rejected. The remaining useful information in the data set will be categorized into clusters with help of specified attributes. While processing pipeline starts receiving the classified FITS files, it identifies types of them (raw, master-frames, service raw frames – dark, flat, bias). And only after these actions the data is prepared for processing.

3. Intraframe processing methods

There are a lot of different types of telescope's aberration that can cause the corrupted astronomical data, for example, diffraction rays, motion blur, vignetting, flare light, coma and others.

The data with some aberrations is unnecessary information. So, the removing of it on the pre-processing stage allows increasing the quality of processing and reducing the execution time.

Also the pre-processing stage includes analysis of the input data and can make the decision about its quality.

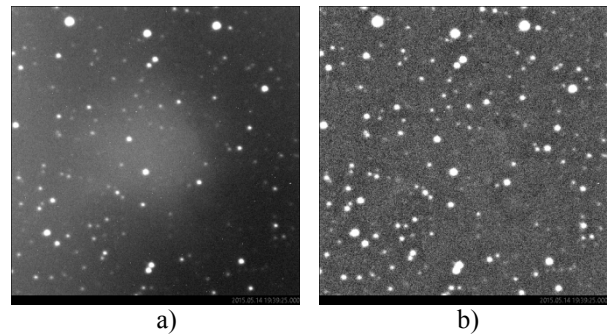


Figure 5: a) raw image with flash, b) processing result

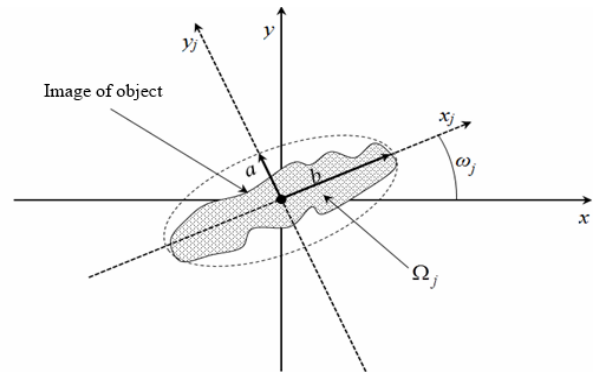


Figure 6: Selective signs for extended image of object

Some aberrations can be removed by developed special mathematical methods for frames filtration, brightness equalization and background alignment.

These methods allow processing the frames in the different frequency range. The real objects in frame are formed by high-frequency spectral components of the image. However, the frame background is the low-frequency component. The subtraction of the low-frequency background variations allows leaving the unchanged high-frequency components of the image.

The inverse median alignment is used in conjunction with calibration frames. It is especially important to use a master-dark frame. All master-frames are formed pixel by pixel. 10% of the largest and 10% of the smallest values of brightness of the each pixel is tentatively discarded (Dubovský et al., 2017).

In contrast to the flat-calibration of frames, inverse median filter removes coarse-grained components that are caused by the illumination from the Moon, the Sun, and illuminations of anthropogenic origin (Figure 5).

These methods lead to increasing of astrometry accuracy indicators and stars photometry quality as well as the quality indicators of asteroids and comets detection.

Also the CoLiTec software contains the improved matched filter, which is used for extended images of objects for CCD-frames taken without the diurnal tracking. It allows reconstructing the real images of extended objects. It is very helpful for working with frames with images of satellites, or for a malfunction of the diurnal tracking.

If all the objects in the frame are circular, and the object under investigation has an extended image, the detection method is based on the selective signs such as the eccentricity and the inclination (Figure 6).

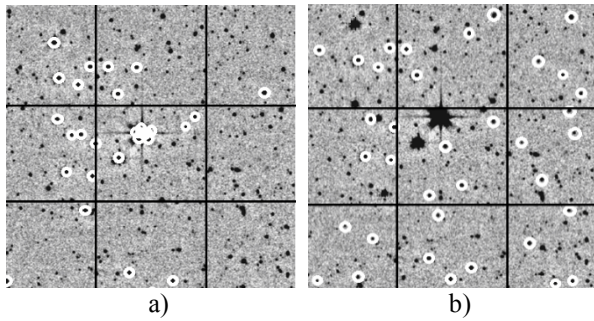


Figure 7: a) positions of the brightest measurements in frame, b) uniform distribution of reference stars in frame

CoLiTec software allows performing of the astrometric and photometric reduction and detecting moving objects such as comets, asteroids or satellites in real time with the visual confirmation of processing results.

The full processing sequence of CoLiTec software includes intraframe and interframe processing stages.

During the astrometric reduction the recognizing of pixels that are related only to the real object's signal is performed. Then software removes all unnecessary pixels from the input data set to reduce amount of the measurements for processing.

After the estimation of the object's position the software starts the frames identification with the stellar catalogs (Akhmetov et al., 2017). This is a very difficult procedure because these catalogs contain more than billions objects with appropriate information about them including astrometric and photometric measurements. The main goal of this stage is to understand to what part of sky these frames are related.

With help of the improved method for the related frames identification the accuracy of astrometric reduction was increased in the CoLiTec software. The main purpose of this method is the special rule (uniform distribution) for the selection of reference stars in the frame (Figure 7).

Also, the accuracy of astrometric reduction as well as accuracy of moving objects detection was increased after using the newest stellar catalogs such as UCAC5 (Fedorov et al., 2018) and GAIA DR2 (Gaia Collaboration, 2016).

The photometric reduction includes the estimation of object's apparent brightness after its signal's amplitude. This stage is performed for all real objects in series of frames.

4. Interframe processing methods

Interframe processing is used to detect and estimate objects trajectories. The core of CoLiTec software consists of preliminary objects detection based on the accumulation of statistics that is proportional to the signals energy along possible object motion paths. Such accumulation is performed by multivalued transformation of the objects coordinates that is equivalent to the Hough space-time transformation (Savanevych et al., 2012).

CoLiTec software has abilities for detecting very slow, very fast objects, and objects with the near-zero apparent motion. Range of visible velocities of detected asteroids by CoLiTec software is from 0.7 to 40.0 pixels per frame. For example, the faster discovered NEO was K12C29D

asteroid (40.0 pix./frame) as well as the slowest discovered object was ISON C/2012 S1 comet (0.8 pix./frame).

These possibilities are provided by the different computational methods that developed by authors and implemented in the CoLiTec software. One of them is a new iteration method for accurate estimation of asteroid coordinates, which is based on the subpixel Gaussian model of a discrete object image (Savanevych et al., 2015). This model of the object image takes into account a prior form of the object image and consequently it is adapted more easily to any forms of real image. The method operates by continuous parameters (asteroid coordinates) in a discrete observational space (the set of pixels potentials) of the CCD-frame.

Full reliability of the detection of moving objects is retained up to the lower limit of SNR equal to 3 units in case of a minimum series consisting of four frames, with no stars covering of asteroid (Savanevych et al., 2015).

The detection of objects with the near-zero apparent motion is performed by the method, which is based on the significance verification of the speed factor of object (Khlamov et al., 2016). Fisher F-criterion is used as significance criterion in this method. It allows detection of objects that have a shift between frames, which isn't exceeded the object's image size by 3 RMS (Savanevych et al., 2018). For example, at the time of discovery, the image size of the comet C 2012 S1 (ISON) was five pixels and it has been shifted by three pixels for the four frames (Khlamov et al., 2017). The Centaur 2013 UL10 has been shifted by ten pixels with the image size of four pixels at the time of discovery.

The another method, which implemented in CoLiTec software, is the method for determining equatorial coordinates of celestial objects based on an assessment of their position in the digital frame (Pohorelov et al., 2016). Different reduction polynomial models (cubic and fifth-power) were implemented in this method. Also it allows assessing the significance of the reduction model coefficients and determining the influence of the polynomial model power on the accuracy of object's position assessment. This method also takes into account the peculiarities of astronomical reduction in long-focus and short-focus optical systems.

CoLiTec software equipped with the modern viewer of obtained results with a user-friendly GUI. LookSky runs independently of the main program and it can be used for independent review of CoLiTec processing results while the main program is processing data.

Also the system for monitoring processing messages with a detailed logging of handling process is implemented into CoLiTec software (Pohorelov et al., 2016). Enhanced control of input and output data is held at the each stage of processing. It allows detecting damaged data from the existed one.

5. Conclusion

The CoLiTec software is widely used in the different observatories in the world. It has been used in about 700 000 observations, during which four comets C/2011 X1 (Elenin), P/2011 NO1 (Elenin), C/2012 S1 (ISON) and P/2013 V3 (Nevski) out of seven discovered in the CIS

and the Baltic States over the past 20 years were identified using CoLiTec. In total, the CoLiTec software was used for discovery more than 1560 asteroids, including 5 NEO, 21 Trojan asteroids of Jupiter and 1 Centaur (see, also, Savanevych et al., 2012, 2015, 2018; Khlamov et al., 2016, 2017; Vavilova et al., 2012, 2017; Vavilova, 2016).

In 2014, the CoLiTec software was recommended to all members of the Gaia-FUN-SSO network for analyzing observations as a tool for detecting faint moving objects on CCD-frames (<https://gaiafunssso.imcce.fr>). Now we are working on the implementation of CoLiTec software into the GOTO project tasks.

References

- Akhmetov V.S., Fedorov P.N., Velichko A.B., Shulga V.M.: 2017, *MNRAS*, **469**, 763-773.
- Dubovský P.A., Briukhovetskyi O.B., Khlamov S.V. et al.: 2017, *OEJV*, **180**, 16.
- Khlamov S.V. et al.: 2016. *Eastern-European Journal of Enterprise Technologies*, **80**, 41-48.
- Khlamov S., Savanevych V., Briukhovetskyi O., Pohorelov A.: 2017, *Proceedings of the International Astronomical Union*, **325**, 349-352.
- Gaia Collaboration: 2016, *A&A*, **595**, A1, 36.
- Fedorov P.N., Akhmetov V.S., Velichko A.B.: 2018, *MNRAS*, **476**, 2743-2750.
- Pohorelov A.V. et al.: 2016, *Eastern-European Journal of Enterprise Technologies*, **82**, 42-49.
- Pohorelov A.V., Khlamov S.V. et al.: 2016, *Odessa Astron. Publ.*, **29**, 136-140.
- Savanevych V.E. et al.: 2012, *Kosm. nauka tehnol.*, **18**, 39-46.
- Savanevych V.E., Briukhovetskyi O.B., Sokovikova N.S. et al.: 2015, *MNRAS*, **451**, 3287-3298.
- Savanevych V.E., Briukhovetskyi A.B., Ivashchenko Yu.N. et al.: 2015, *Kinemat. Phys. Celest. Bodies*, **31**, 302-313.
- Savanevych V.E., Khlamov S.V., Vavilova I.B. et al.: 2018, *Astron. Astrophys.*, **609**, A54, 11.
- Vavilova I.B. et al.: 2012, *Kinemat. Physics Celest. Bodies*, **28**, 85-102.
- Vavilova I.B.: 2016, *Odessa Astron. Publ.*, **29**, 109-115.
- Vavilova I.B. et al.: 2017, *Proceedings of the International Astronomical Union*, **325**, 361-366.

DOI: <http://dx.doi.org/10.18524/1810-4215.2018.31.144562>

HIGH-PRECISION FOLLOW-UP OBSERVATIONS OF NEAR-EARTH OBJECTS

N.V. Maigurova, A.V. Pomazan, A.V. Shulga

Research Institute “Mykolaiv Astronomical Observatory”, Mykolaiv, Ukraine
nadija@mao.nikolaev.ua

ABSTRACT. Main objective of the study is orbit refinement of Near-Earth Objects (NEOs) as part of the global task of asteroid-cometary hazard. We present the latest results of ongoing high-precision astrometric follow-up observations of NEOs using the Mykolaiv Observatory KT-50 telescope of Mobitel Complex that equipped Alta U9000 CCD camera. Main feature of the objects of this study is the fast moving in the field of view. That circumstance makes impossible to observe NEOs as point images and to obtain their precise coordinates by the classical methods of observation. We used modified Rotating-drift-scan CCD mode for obtaining NEOs images and classical mode – for obtaining fields with reference stars to carry out astrometric reductions. The combination of classical and modified observational modes allows us to recover objects having $V < 17$ with high astrometric precision. The comparative statistics of Mykolaiv observations of NEOs for the period 2015-2018 and analysis of positional accuracy are presented. The results of the effect of new observational data on the residual differences (O-C) in both coordinates with respect to HORIZONS JPL ephemerides are shown on examples two potentially-hazard asteroids (2001KB67 and 2017YE5) during their close approaching to Earth in 2018. It is shown that adding new observations can significantly improve the accuracy of determining the orbital elements of such objects.

Keywords: CCD observations, asteroid-cometary hazard, NEOs (near-earth asteroids), PHAs (potentially hazard asteroids), ephemerids of small Solar system bodies.

АБСТРАКТ. Основною метою дослідження є уточнення орбіти об'єктів, що зближуються з Землею (АЗЗ) в рамках глобальної задачі астероїдно-кометної небезпеки. Ми представляємо останні результати алертних високоточних астрометричних спостережень АЗЗ, що отримані за допомогою телескопу КТ-50 комплексу Мобітел Миколаївської обсерваторії, обладнаного ПЗЗ-камерою Alta U9000. Основна особливість об'єктів цього дослідження – це швидке переміщення в полі зору, що робить неможливим отримання точкових зображень та точних координат таких АЗЗ класичними методами спостереження. Ми використовували комбінований режим синхронного переносу заряду з поворотною платформою для отримання зображень АЗЗ та класичний режим – для отримання полів з опорними зірками для подальшого виконання астрометричних редукцій. Поєднання

класичного та комбінованого режимів спостережень дозволяє нам спостерігати об'єкти до 17 зоряної величини (у фільтрі V) з високою астрометричною точністю. Наведено порівняльну статистику Миколаївських спостережень АЗЗ за період 2015-2018 рр. та аналіз позиційної точності. Результати впливу нових даних спостережень на остаточні різниці (O-C) за обома координатами по відношенню до HORIZONS JPL ефемериди показані на прикладах двох потенційно-небезпечних астероїдів (2001KB67 і 2017YE5) під час їх зближення з Землею у 2018 році. Показано, що додавання нових спостережень може значно підвищити точність визначення елементів орбіт таких об'єктів.

Ключові слова: ПЗЗ-спостереження, астероїдно-кометна небезпека, АЗЗ (астероїди, що зближуються з Землею), ПОА (потенційно-небезпечні астероїди) ефемериди руху малих тіл Сонячної системи.

1. Introduction

Ground-based optical position observations of the solar system bodies are the basis for creation of the motion theories, defining and clarifying of the orbits elements and dynamic parameters. Regular observations of near Earth objects (NEOs) are also one of the most important aspects of studying the problem of asteroid-cometary hazard and allow us to do refinement of the orbits, which makes it possible to predict a collision of a quite large body with the Earth in future and to take appropriate measures in advance. The maximum close approach period with the Earth is most favorable for the search of small-scale NEOs because at another time they have rather weak magnitudes and inaccessible to observations even at large telescopes. Much of them belong to the class of potentially-hazard asteroids (PHAs). Fig. 1 shows the distribution of the all known PHAs apparent magnitudes at discovery data (Asteroid list was taken from <https://www.minorplanetcenter.net/iau/lists/PHAs.html> at the beginning of 2018). Apparent magnitudes were calculated with on-line service HORIZONS JPL ephemeris (<https://ssd.jpl.nasa.gov/horizons.cgi>).

The problem of asteroid-cometary hazard is one of the priority tasks around the world. NEOs can pose a threat to existing spacecraft, as well as to the population of the Earth as a whole. Nowadays, many scientific projects, which are allocated significant funding, are engaged in monitoring of known NEOs and the search for new ones.

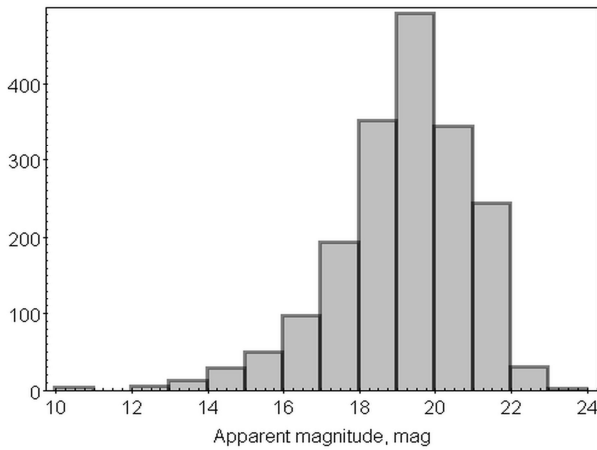


Figure 1: NEOs apparent magnitude on discovery data

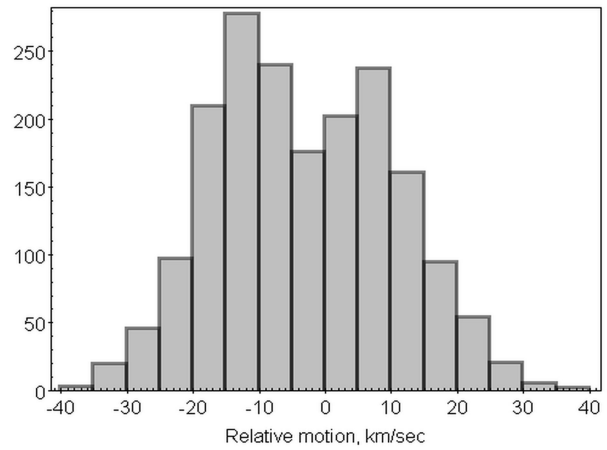


Figure 2: NEOs relative motion on discovery data

The most active project in the field of the search and observations NEOs in the optical range are Pan-Starrs (Wainscoat et al., 2018) and Catalina sky survey (CSS) (Leonard et al., 2017). But despite the efforts being made in this direction, this task cannot be considered solved. Fig. 2 shows the histogram of the distribution of the NEOs versus the relative motion of approaching the Earth on the discovery date of these bodies. The range-rate ("delta-dot") parameter from JPL's HORIZONS ephemeris is used as relative motion. A positive "del-dot" means the NEO is moving away from the Earth, a negative "del-dot" means the NEO is moving toward the Earth. As you can see from Fig. 2 more than 40% of known NEOs were discovered after they had approached to a minimum distance to the Earth. This proves the importance of regular monitoring of the hazardous celestial objects on the approach way to the Earth.

The observations of NEOs on the close distances from the Earth with classic methods is becomes complicated, since their apparent velocity in the field of view may be in the range of 0.2" to 120" per minute and even more. An original combined observation method, the main feature of which is the separate obtaining of images of reference stars by classical drift-scan mode and fast moving bodies with using Rotating-drift-scan CCD is realized in the Mykolaiv Observatory for the positional observations of celestial bodies with high apparent motions. Using Combined observation method allows to get all the images as a point, that in turn to determine the coordinates of the center of the image with maximum accuracy.

2. NEOs Asteroid Observations and Reductions

The array of NEOs CCD observations obtained on the telescope KT-50 of the Mobitel complex RI "MAO" was used to perform astrometric reductions by combine scheme with one of the modern astrometric catalogues (Maigurova et al., 2017). We used UCAC3, 4 catalogues previous to GAIA data release catalogues become available. Mobitel complex is operated for observations since 2011. The telescope KT-50 (F = 3000mm, D = 500mm) is equipped with Alta U9000 camera (3Kx3K, 12x12mkm, 42.5'x42.5' FOV, 0.83"/pixel) in photometric band OG-14 (near standard Rc band). Since 2017 telescope was equipped by standard V filter in Johnson system. The more detailed description of the complex is given in (Shulga et al., 2012). As mentioned above, images with reference stars and NEOs obtain separately. The time exposure for star images is 10 sec. It depends from the expected stellar magnitude for NEOs images and typically exposure time ranges from 60 to 150 seconds. The processing of the stars images was carried out by the package "Astrometrica" (<http://www.astrometrica.at>) in automatic mode. The detailed description of the reduction pipeline is given in (Sibiryakova et al., 2015). Statistics of the NEOs Mykolaiv observations with MPC code 089 during 2015–2018 are shown in Table 1, where N1, N2 – number of obtained positions and asteroids, correspondingly; n1, n2 – number of the positions and asteroids for new objects, which were discovered in the current year. Table column "residuals" are given (O–C) differences with NEODYs-2 ephemeris (<http://newton.dm.unipi.it/neodysl/>) and their RMS.

Table 1: NEOs observations of the RI "MAO" (MPC code 089)

| Year | N1 | N2 | Current year | | Residuals, mas | | | |
|-------|------|-----|--------------|----|----------------|-----|-----|-----|
| | | | n1 | n2 | RA | RMS | DE | RMS |
| 2015 | 742 | 50 | 286 | 21 | 16 | 323 | 74 | 368 |
| 2016 | 172 | 19 | 39 | 6 | -2 | 258 | 135 | 379 |
| 2017 | 695 | 32 | 246 | 12 | -20 | 214 | 71 | 258 |
| 2018* | 633 | 28 | 36 | 3 | 30 | 217 | 42 | 288 |
| All | 2242 | 123 | 607 | 42 | 7 | 260 | 68 | 317 |

*As of beginning of October

It should be noted that despite the fact that the technical capabilities and weather conditions of our observatory are much worse than those of large survey projects, for some objects our observations make up a significant proportion of all available observations. Usage the combined method gives us the opportunity to observe the approaching object among the first on the current orbit turn. Statistics of the selected PHAs is given in Table 2, where N, % mean number of Mykolaiv observations and their part from all MPC observations for these objects, Mag – mean apparent magnitude. As can be seen from the Table 2 some potentially hazardous asteroids have only a few dozen observations and our share is over 10%.

Table 2: Statistics of the selected PHAs

| NEO | N | % | Residuals \pm RMS, mas | | Mag |
|-----------|----|----|--------------------------|---------------|------|
| | | | RA | DE | |
| 1999KW4 | 78 | 20 | 45 \pm 148 | 116 \pm 138 | 14.0 |
| 2015LG2 | 24 | 16 | 47 \pm 275 | 207 \pm 302 | 17.5 |
| 2001KB67 | 46 | 14 | 155 \pm 115 | 146 \pm 212 | 15.2 |
| 2017NS5 | 20 | 12 | 370 \pm 153 | -93 \pm 271 | 16.2 |
| 2017MB1 | 41 | 9 | -190 \pm 193 | -27 \pm 265 | 15.6 |
| 2010NY65 | 32 | 7 | 23 \pm 198 | 213 \pm 211 | 16.8 |
| 2017YE5 | 19 | 6 | 131 \pm 178 | 11 \pm 242 | 15.6 |
| 2011UW158 | 52 | 6 | -6 \pm 321 | 110 \pm 347 | 16.0 |
| 2015DP155 | 38 | 6 | -33 \pm 174 | 5 \pm 378 | 15.3 |
| 2018EJ4 | 19 | 4 | -2 \pm 138 | 176 \pm 225 | 15.6 |

3. Accuracy Analysis

As can be seen from Table 1 during 2015–2018 we have obtained 2242 positions for 123 NEOs. This number is less than sum for column 2 because we observed some asteroids during several periods of visibility, which belong to different years. The duration of a series of frames of one object usually didn't exceed 30 minutes, so the positions of the object in a series of frames were calculated with fixed set of reference stars on a small arc of the orbit. These circumstances make possible to use the mean square error (RMS) of the residual differences (O–C), where (O) is the position obtained from the observations, (C) – the ephemeris position at the time of observation, as an estimate of the intrinsic precision of our measured positions. Fig. 3 shows these errors in both right ascension and declination for a single observation plotted against apparent magnitude.

As can be seen from Fig. 3 and Table 1, precisions of NEOs Mykolaiv observations is high enough for this kind of objects. The rotation-drift-scan CCD mode allows us to observe NEOs with large velocity, when they have maximum brightness. Part of our observations 2017 have index "h – high accuracy" according MPC statistics (<http://www.minorplanetcenter.net/iau/special/residuals.txt>).

It is worth noting, that much of NEOs are potentially-hazardous objects that approach the Earth at a distance of less than 0.05 AU and have an absolute stellar magnitude of less than 22^{mag}. A detailed analysis of the 2018 observations for two of them is given below.

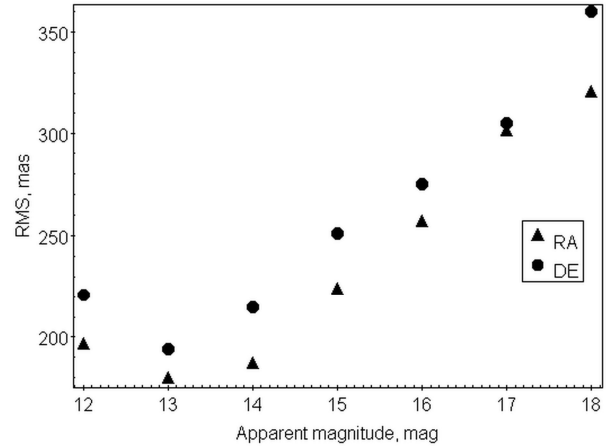


Figure 3: RMS on right ascension (up) and on declination (down) versus asteroid apparent magnitude

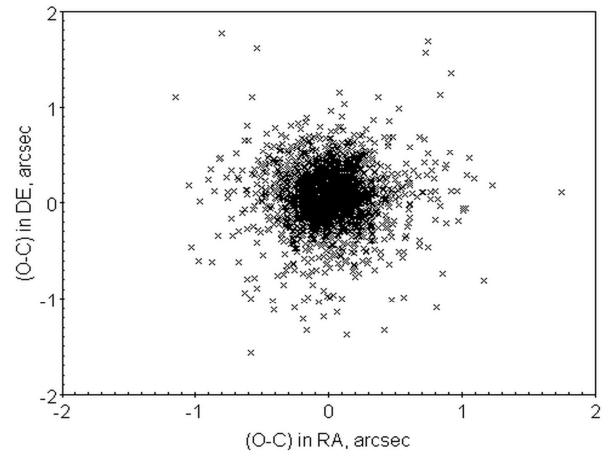


Figure 4: The mutual distribution of residual differences (O–C) in right ascension and declination

The mutual distribution of residual differences (O–C) in right ascension and declination are shown in Fig. 4. Only 2% residuals exceeded the value 1".

3.1. 2001 KB67 (68347)

Asteroid was discovered by LINEAR project on 2001, May 30. Close approach to Earth to 0.024 AU was at 2018, May 29. There were 228 observations with not good accuracy obtained for 2001–2017 period before 2018 observation campaign. The mean residuals differences (O–C)_{ra,de} were (0.01 \pm 0.74)" and (0.13 \pm 0.58)". 309 positions were obtained by 24 observatories during 2018 visibility period. The mean residuals differences (O–C)_{ra,de} for them are (-0.01 \pm 0.33)" and (-0.02 \pm 0.33)".

The Table 3 gives results of comparison 2 series of the Mykolaiv observations (MPC code 089) with JPL ephemeris on date observation (1) and after adding new 2018 observations (2).

3.2. 2017 YE5

Asteroid 2017 YE5 was discovered on 2017, December and approached Earth within 0.04 au on 2018, June 21. The orbit of 2017 YE5 has a Tisserand parameter of 2.875, which is possibly point the object could be an extinct Jupiter-family comet. Only 95 observations were available until 2017 YE5 was approached Earth. Tab. 4 is shown values of the residuals differences (O–C) for the Mykolaiv observations (code 089) with JPL ephemeris, which calculated on June 21(1) and after this date (2), when new observations were added.

Table 3: 2001 KB67 (O–C) differences (MPC code 089)

| Date 2018.05 | (O-C) (1) | | (O-C) (2) | |
|-----------------|--------------|-------------|-------------|--------------|
| | RA | DE | RA | DE |
| 29.028813 | 3.08 | 0.99 | 0.67 | -0.23 |
| 29.031136 | 2.81 | 0.9 | 0.40 | -0.33 |
| 29.033463 | 2.74 | 1.27 | 0.34 | 0.04 |
| 29.035789 | 2.71 | 1.04 | 0.30 | -0.19 |
| Mean | 2.83 | 1.05 | 0.43 | -0.18 |
| RMS | 0.17 | 0.16 | 0.17 | 0.16 |
| 31.003218 | -0.19 | 1.82 | 0.23 | 0.12 |
| 31.005547 | -0.31 | 1.71 | 0.12 | 0.00 |
| 31.007874 | -0.21 | 1.57 | 0.21 | -0.14 |
| 31.010201 | -0.05 | 1.50 | 0.37 | -0.20 |
| 31.012539 | 0.10 | 1.59 | 0.53 | -0.11 |
| 31.014866 | -0.10 | 1.57 | 0.34 | -0.13 |
| 31.017216 | -0.08 | 1.69 | 0.36 | -0.02 |
| 31.019554 | -0.10 | 1.59 | 0.34 | -0.10 |
| Mean | -0.12 | 1.63 | 0.31 | -0.07 |
| RMS | 0.12 | 0.10 | 0.13 | 0.10 |

Total were received new 241 positions for 2017YE5, which made it possible to significantly improve the accuracy of the orbit and successfully conduct radar observations of this asteroid. The mean residuals differences (O–C)_{ra,de} for them are (-0.08±0.39)'' and (-0.04±0.48)''.

Table 4: 2017YE5 (O–C) differences (MPC code 089)

| Date 2018.06 | (O-C) (1) | | (O-C) (2) | |
|-----------------|---------------|--------------|-------------|-------------|
| | RA | DE | RA | DE |
| 20.966624 | -10.67 | -7.23 | -0.14 | 0.01 |
| 20.971275 | -10.57 | -7.07 | -0.04 | 0.17 |
| 20.981830 | -10.33 | -7.52 | 0.20 | -0.27 |
| 20.987260 | -10.43 | -6.84 | 0.09 | 0.43 |
| 20.989585 | -10.29 | -6.99 | 0.22 | 0.28 |
| Mean | -10.43 | -7.21 | 0.09 | 0.04 |
| RMS | 0.15 | 0.31 | 0.15 | 0.31 |

4. Conclusions

In this paper, the results of ongoing observations of NEOs using the Mykolaiv Observatory KT-50 telescope of Mobitel Complex are presented. 2242 positions of 123 NEOs were obtained during last 4 years. The using rotation -drift -scan CCD mode allows us to observe the fast moving asteroids with high accuracy. It was shown also that adding new observations can significantly improve the accuracy of determining the orbital elements of potentially hazard asteroids.

Acknowledgements. This research has made use of the on-line services JPL HORIZONS, NEODYs-2 MPC database. The authors are grateful to colleagues form RI"MAO" who have taken part in observations of NEOs: M. Kulichenko, M. Kaliuzhnyi, V. Kryuchkovskiy, D. Bodryagin, F. Bushuev.

References

Astromerica, [on-line]: <http://www.astromerica.at>
 HORIZONS System, [on-line]: <https://ssd.jpl.nasa.gov/?horizons>
 Leonard G.J., Christensen E.J., Fuls C. et.al.: 2017, *American Astronomical Society*, DPS meeting #49, id.117.07.
 Maigurova N. V., Pomazan A. V., Bodryagin D. V. et al.: 2017, *Odessa Astron. Publ.*, **30**, 182.
 Minor Planet Center, [online]: <https://www.minorplanetcenter.net/iau/lists/PHAs.html>
 Minor Planet Center, [online]: <http://www.minorplanetcenter.net/iau/special/residuals.txt>
 NEODYs-2 Near Earth Objects – Dynamic Site [on-line]: <http://newton.dm.unipi.it/neodys/>
 Shulga A.V., Kozyrev E.S., Sibiryakova E.S. et al.: 2012, *Space science and technology*, **18(4)**, 70 [in Russian]
 Wainscoat R.J., Weryk R.C.: 2018, *American Astronomical Society*, AAS Meeting #231, id.#115.05.

DOI: <http://dx.doi.org/10.18524/1810-4215.2018.31.146198>

ASTROMETRIC CCD OBSERVATIONS OF SELECTED WDS MULTIPLE STAR SYSTEMS

N.V. Maigurova, Yu.I. Protsyuk, L.E. Bondarchuk

Research Institute "Mykolaiv Astronomical Observatory", Mykolaiv, Ukraine
nadija@nao.nikolaev.ua, yuri@nao.nikolaev.ua

ABSTRACT. Main objective of the study is getting information about multiple and double stars that allow us to determine whether this pair is physically link system. Physically bounded star systems are source of unique information such as the ratio of the periods of pairs in one system, the relative orientation of the orbital planes, the distribution of components by mass which is extremely important for determining the parameters of star formation models and for testing stellar models evolution. The results of selected multiple star systems CCD observations, which were carried out at the KT-50 telescope of the Research Institute "Mykolaiv Astronomical Observatory" during the 2016-2018 years are presented. The Washington catalog of double stars (WDS) was used for observational list. There were presented detailed study of 14 multiple star systems. Astrometric reductions of the CCD frames with multiple system components at the current epoch were performed using "Astrometrica" software with Gaia DR2 reference catalog. The combination of the CCD received data with other Strasbourg base catalogs allowed to determine the new values of stars proper motions. Parameters of mutual component configuration (position angle and separation) were also measured for the components of the multiple star systems using REDUC software. The measures standard errors were 0.05" for separations and 0.2° for position angles. Combination ground based original observations with accurate astrometric catalogs available due to Strasbourg astronomical Data Center allowed us obtain new knowledge about investigated objects.

Keywords: Double and multiple stars, binary stars, CCD observations, astrometric positions, common proper motions

АБСТРАКТ. Основною метою дослідження є отримання інформації про системи кратних та подвійних зірок, які дозволяють нам визначити, чи є вони фізично-зв'язаною системою. Кратні та подвійні системи зірок є джерелом унікальної інформації, такої як співвідношення періодів пар в одній системі, відносна орієнтація орбітальних площин, розподіл компонентів за масою та інш., що надзвичайно важливо для визначення параметрів моделей утворення та еволюції зірок. Представлені результати ПЗЗ спостережень вибраних кратних зоряних систем, що проводилися на телескопі КТ-50 НДІ "Миколаївська астрономічна обсерваторія" протягом

2016-2018 років. У якості вхідного списку для спостережень використовувався Вашингтонський каталог подвійних зірок (WDS). Дана робота представляє детальне дослідження 14 кратних зоряних систем. Астрометричні редуції ПЗЗ – кадрів на момент спостережень, що містять компоненти досліджуваних кратних систем, були виконані за допомогою програми "Astrometrica" у системі опорного каталогу GAIA DR2. Комбінація положень, що отримано з наших спостережень та положень з інших каталогів із Страсбурзької бази даних дозволила визначити нові значення власних рухів компонентів цих зоряних систем. Параметри взаємної конфігурації компонентів (позиційний кут та кутове розділення) також були виміряні для компонентів вибраних зоряних систем за допомогою програми REDUC. Стандартні похибки вимірювань склали 0.05" для кутового розділення та 0.2° для позиційного кута. Комбінація даних наших астрометричних спостережень з даними високоточних астрометричних каталогів, що є доступними через Страсбурзький астрономічний центр даних, дозволили нам отримати нові знання про досліджувані об'єкти.

Ключові слова: подвійні та кратні зоряні системи, фізично зв'язані подвійні зорі, ПЗЗ-спостереження, астрометричні положення, власні рухи.

1. Introduction

The Washington Double Star Catalog (WDS) (Mason et al., 2001) lists 142,785 (on the summer 2018) of resolved stellar systems with two and more components. Number of WDS systems with more than 3 components is 59%. Hierarchical systems with known orbits are of special interest objects. Compared to binaries, hierarchical multiples with three or more components contain additional information such as period ratios, mass ratios, and relative orbit orientation. Study (Tokovinin et al., 2014) has shown that 46% of solar-type stars (F-G spectral type) in the vicinity of 67 pc from Sun are non-single and the ratio of stellar systems with a multiplicity of 1: 2:3:4:5 is 54: 33: 8: 4: 1. However, a substantial fraction of the WDS entries are random combinations of background stars. Despite to almost any bright star has faint optical components in the WDS typically their secondary components are faint and often located in crowded regions of the sky. Proper motions are absent for

32% secondary component in WDS catalog, which makes it impossible to understand the true nature of these objects. The appearance Gaia DR2 catalog, that contains highly accurate positions, parallaxes, and proper-motions for more than 1 billion sources brighter than magnitude 20.7 in the white-light photometric G band, significantly will improve the situation on this issue. At the same time, ground-based observations do not lose their value due to the specifics of these objects and space observations.

2. Observations and Reductions

The regular observations of binary and multiple stars at RI «MAO» have been carried out since 2013 at two telescopes: Axial Meridian Circle and KT-50 of Mobitel complex (Shulga A.V. et al., 2012; Bodryagin et al, 2015; Bodryagin et al, 2016; Bodryagin et al, 2017). For this study we used observations that obtained at KT-50 telescope (Mobitel complex) during 2016 -2018. 14 multiple systems were checked from WDS catalog. Some information about these systems is presented in Tab.1. The Tab.1 are given stellar magnitudes of primary component (Mag1) and magnitudes for faintest component (Mag 2), information about proper motions availability for primary (Pm1) and secondary (Pm2). If at least one of system component has no proper motion there is “-” in column Pm2.

Table 1: Selected WDS systems

| WDS | N | Mag1 | Mag2 (min) | Pm1 | Pm2 |
|------------|---|------|------------|-----|-----|
| 09587+1058 | 3 | 7.5 | 11.7 | + | + |
| 10097+0310 | 3 | 8.5 | 12.0 | + | + |
| 11537+7345 | 4 | 7.2 | 16.5 | + | - |
| 12056+6848 | 6 | 7.5 | 12.7 | + | - |
| 12082+6030 | 4 | 10.5 | 15.2 | + | + |
| 12187+1148 | 3 | 9.5 | 11.8 | + | + |
| 12339+2603 | 3 | 11.5 | 14.1 | + | + |
| 12396+1956 | 3 | 8.5 | 15.2 | + | - |
| 12418+0953 | 5 | 7.0 | 14.4 | + | - |
| 12429-0215 | 3 | 9.2 | 13.8 | + | + |
| 12497+0111 | 4 | 8.2 | 14.0 | + | - |
| 12525+0712 | 4 | 9.6 | 15.1 | + | - |
| 12550+5810 | 3 | 8.6 | 9.8 | + | + |
| 17479+3417 | 4 | 6.6 | 13.3 | + | - |

2.1. Astrometric Reductions

The CCD observations of fields with selected WDS systems were obtained in drift scan mode at near R photometric band (OC-14 filter) and at V band (Johnson system) starting from 2018. The numbers of the images for each objects is given in Tab.2. The astrometric reductions of observations were carried out by the package "Astrometrica" (<http://www.astrometrica.at>), version 4.11.1.442. Reference catalogs Gaia DR2 (Gaia Collaboration, 2018) and UCAC4 (Zacharias N. et al., 2013) were used for calculations of equatorial coordinates of stars in the fields. The comparison of mutual distributions of residuals differences (O - C), with

different catalogs are shown in Fig. 1. The differences (O - C) are used in mean O - positions obtained from observations, C - catalog positions.

As can be seen from Fig.1, the usage of GAIA DR2 catalog as reference allows improving accuracy of obtained positions up to 20%. Mean errors in both right ascension and declination for a single observation depends from stellar magnitude and are in range (20 -30) mas for (12-15)^{mag}, and up to 100 mas for 17^{mag}.

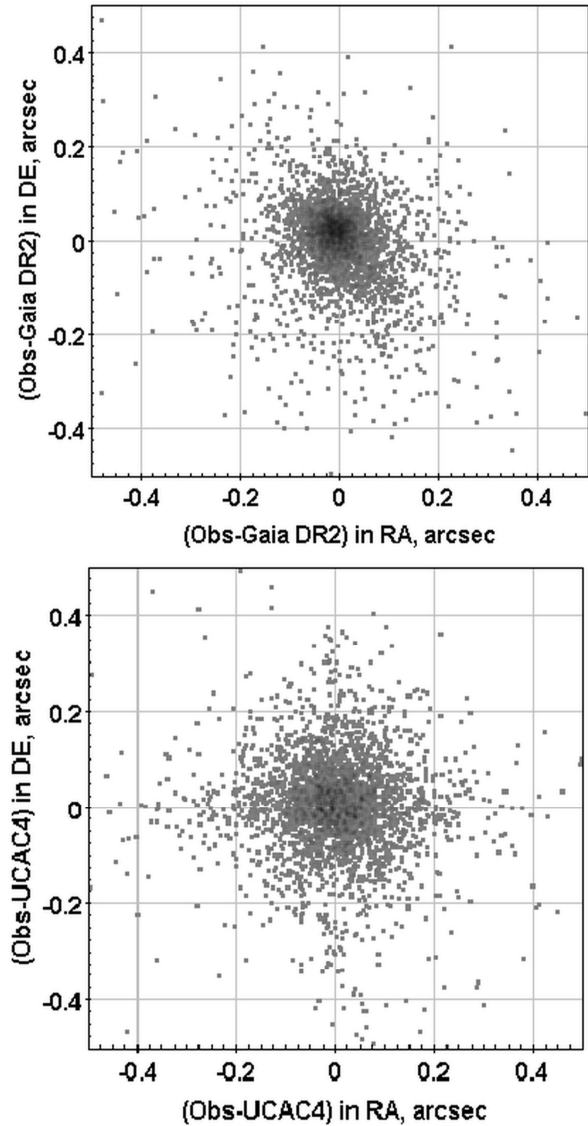


Figure1: Distributions of residuals differences (O - C) in right ascension and declination (up - GAIA DR2 reference catalog, down - UCAC4 reference catalog).

2.2 Measurements

The measurements of doubles were made with REDUC software (<http://www.astrosurf.com/hfosaf/reduc>).

To determine frame orientation, we used previously obtained exact values of orientation angle and image inclination regarding the celestial equator from astrometric reductions. Position angles, separations, and their standard deviations were measured for each component of selected WDS systems. A more detailed

description of the processing procedure is given in (Bodryagin et al, 2016). The results of measurements of A, B mutual configuration (with exception of WDS 11537+7345) are shown in Tab.2. (For WDS 11537+7345 A and B component form a spectroscopic binary system and has separation only 0.5 ".)

Table 2: Result of measurements of AB component for selected WDS systems

| WDS | PA,deg | RMS PA | Sep | RMS | N |
|-------------|--------|--------|--------|------|----|
| 09587+1058 | 347.73 | 0.09 | 49.08 | 0.11 | 16 |
| 10097+0310 | 52.57 | 0.06 | 89.62 | 0.07 | 16 |
| 11537+7345* | 59.45 | 0.17 | 36.90 | 0.13 | 11 |
| 12056+6848 | 166.80 | 0.50 | 10.20 | 0.11 | 10 |
| 12082+6030 | 23.73 | 0.01 | 30.80 | 0.04 | 5 |
| 12187+1148 | 239.89 | 0.36 | 9.53 | 0.08 | 10 |
| 12339+2603 | 337.65 | 0.36 | 15.84 | 0.12 | 10 |
| 12396+1956 | 148.22 | 0.07 | 413.99 | 0.11 | 5 |
| 12418+0953 | 101.83 | 0.04 | 112.75 | 0.03 | 5 |
| 12429-0215 | 92.42 | 0.11 | 53.77 | 0.11 | 10 |
| 12497+0111 | 336.71 | 0.03 | 197.87 | 0.08 | 12 |
| 12525+0712 | 87.39 | 0.20 | 32.66 | 0.06 | 10 |
| 12550+5810 | 274.19 | 0.36 | 18.65 | 0.07 | 10 |
| 17479+3417 | 348.44 | 0.20 | 30.34 | 0.08 | 4 |

*Measurements for A, D component

Mean RMS errors of the measurements for all pair components in the selected systems were 0.18° in positional angle and 0.1" in separation.

3. Results

The astrometric positions on observational epoch of all measurable components of the selected WDS systems were obtained from astrometric reductions. The results of cross-identification of the resulting array of star positions with the main modern catalogs, which can be an additional source of information about the components of selected systems, are presented in Tab. 3.

Table 3: Results of Cross-ID Mobitel KT-50 data with CDS data catalogs

| Catalog | N | Mean Epoch |
|----------------|----|------------|
| Mobitel KT50 | 45 | 2017.19 |
| Gaia DR2 | 44 | 2015.50 |
| GSS 2.3 | 43 | 1996.20 |
| Pan-STARRS DR1 | 45 | 2010.17 |
| SDSS DR12 | 41 | 2003.86 |
| UCAC5 | 44 | 2001.77 |
| AC2000 | 33 | 1907.00 |

The cross-ID procedure was made with using Vizier service by TOPCAT software (Taylor M. B., 2005). The usage of original positions on catalog observation epoch can find out stars with common proper motions and

compare the shot-term measured Gaia DR2 proper motions with the long-term averaged. It should be noted the lock of the components in AC2000 catalog makes it impossible to obtain reliable differences with Gaia data.

Below the more detailed study results for 2 WDS systems are presented with using positional information from different CDS catalogs and data about distances from Bailer-Jones et.al (2018).

The table 4 provides estimates and confidence intervals of distances for the components of WDS 12056+6848 and WDS 12082+6030.

Table 4: Distances for selected components from Bailer-Jones et.al (2018)

| WDS | D, pc | Δ , pc |
|------------|--------------|--------------------|
| 12056+6848 | | |
| A | 217.8 | 215.8-219.8 |
| B | 209.0 | 207.9-210.0 |
| C | 476.3 | 471.1-484.5 |
| D | 426.2 | 421.2-431.2 |
| E | 355.4 | 350.6-360.3 |
| F | 469.6 | 464.1-475.3 |
| 12082+6030 | | |
| A | 789.7 | 773.1-789.7 |
| B | 228.3 | 226.7-230.0 |
| C | 232.9 | 231.3-234.5 |
| D | 1064.1 | 1033.2-1096.8 |

3.1 WDS 12056+6848

This WDS system from the list of the objects studied has the largest (6) number of entries in the WDS catalog. «Notes» column information says that the A, B components form non-physical pair, as A and E components have physical link. KT-50 positions were added to the positions checked from different catalogues and long-term proper motions were calculated from linear interpolation function. As can be seen from Fig.2 only A, B components have common proper motions and can be physical pair. These data are in good agreement with Gaia DR2 proper motions and distances from Bailer-Jones et.al (2018).

3.1 WDS 12082+6030

There are 4 entries for this system in WDS catalog and in «Notes» column contains information that these pairs are non-physical. The Tab.4 distance data allow us to suggest that this is not true and the components B, C form a binary system. The positions of the B, C components obtained from KT-50 and CDS catalogs at different epoch are presented in Fig.3. The proper motions in right ascension and declination that calculated from these data are: -3/-14 mas/year for B and -2/-17 mas/year for C component. These values are in good agreement with GAIA DR2 (-2/-14mas/year and -1/-14mas/year) proper motions. All of the above point that component B and C likely physical pair.

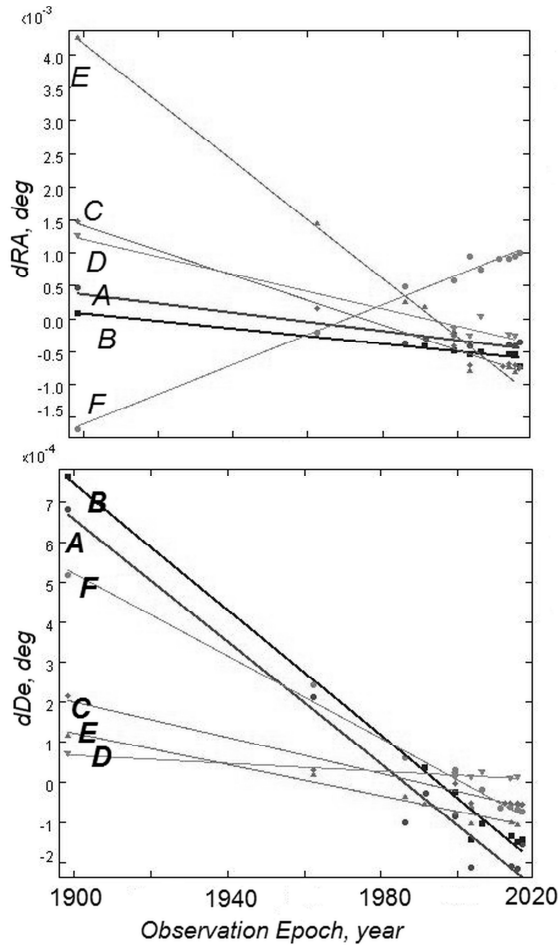


Figure 2: Component positions of the WDS12056+6848 on different catalog epochs, up – right ascension, down – declination.

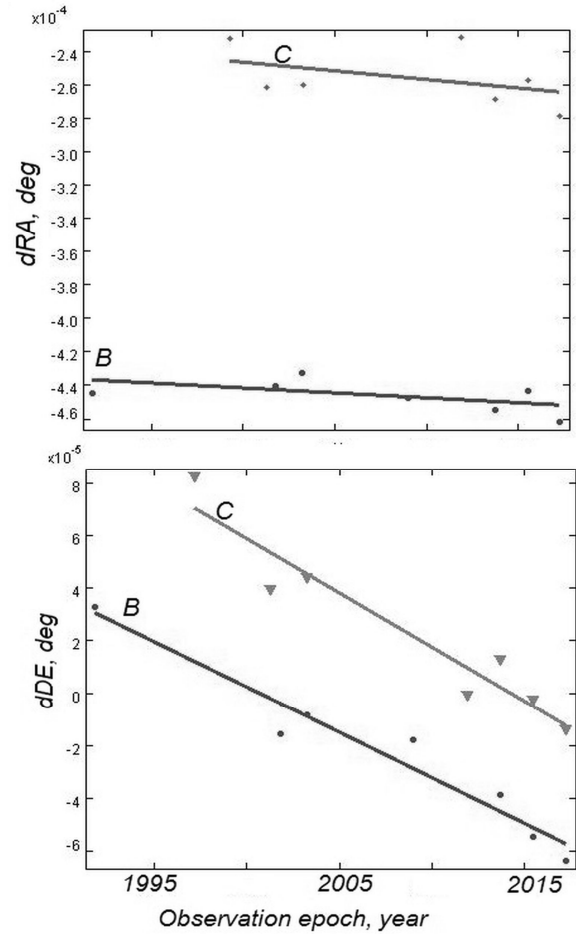


Figure3: Positions of the B, C WDS12082+6030 component on different catalog epochs, up – right ascension, down – declination.

4. Conclusion

Positional data obtained for physically connected components are valuable information for the catalog of orbital elements (Orb6) of binary and multiple stars. New observations of the components of multiple systems on the KT-50 telescope of the Mobitel RI "MAO" complex are obtained. Astrometric reductions and measurements of the parameters of the mutual configuration of the selected WDS multiple systems are performed. Combination new original observations with accurate catalogs available at Strasbourg astronomical Data Center allows not only to obtain new knowledge about investigated objects but also to estimate the accuracy of so-called "instantaneous" parallaxes and proper motions from Gaia catalog.

Observation data and analysis of the results will be sent to the coordinators of the WDS catalog database. We are also planning to continue use resources of MAO to future analysis and refinement of the results.

Acknowledgements. The authors are grateful to colleagues from RI "MAO" who have taken part in observations of WDS stars: M. Kulichenko, M. Kaliuzhnyi, V. Kryuchkovskiy, D. Bodryagin, F. Bushuev, A. Pomazan.

References

Astromerica, [online]. Available at: <http://www.astromerica.at>
 Bailer-Jones C.A.L., Rybizki J., Fouesneau M. et al: 2018, *AJ*, **156**, 58.
 Bodryagin D., Maigurova, N.: 2015, *OAP*, **28**, 163.
 Bodryagin, D. V.; Bondarchuk, L. Ye.; Maigurova, N. V.: 2016, *JDSO*, **320**.
 Bodragin D. V., Bondarchuk, L. Ye.; Maigurova, N. V.: 2017, *Sci. innov.*, **13(1)**, 46.
 Gaia Collaboration: 2018, *A&A*, **616**, A14
 Mason B. D., Wycoff G. L., Hartkopf W. I.: 2001, *AJ*, **122**, 3466.
 Mason B.D. et al: 2001, *Astron. J.*, **122**, 3466.
 REDUC software, [online]. Available at: <http://www.astrosurf.com/hfosaf/reduc>
 Shulga O.V., Kozyryev Ye.S., Sybiryakova Ye.S. et al.: 2012, *Space science and technology (KNiT)*, **18(4)**, 52 [in Russian]
 Taylor M.B.: 2005, *ASPC*, **347**, 29.
 Tokovinin A.: 2014, *AJ*, **147**, 87.
 Zacharias, N., Finch, C. T., Girard, T. M. et al.: 2013, *AJ*, **145**, 44.

DOI: <http://dx.doi.org/10.18524/1810-4215.2018.31.144606>

PROGRESS IN THE REALIZATION OF THE PROJECT FON-DUSHANBE CATALOGUE

A.Mullo-Abdolov¹, H.Relke², G.Kokhirova¹, Q.Yuldoshev³, Yu.Protsyuk⁴, V. Andruk⁵¹Institute of Astrophysics of AS of Republic of Tajikistan, Dushanbe, Tajikistan, aziz.sherzod@gmail.com²Walter Hohmann Observatory, Essen, Germany, helena_relke@yahoo.com³Ulugh Beg Astronomical Institute UAS, Tashkent, Uzbekistan, qudratillo@astrin.uz⁴Research Institute “Mykolaiv Astronomical Observatory”, Mykolaiv, Ukraine, yuri@nao.nikolaev.ua⁵Main Astronomical Observatory NASU, Kiev, Ukraine, andruk@mao.kiev.ua

ABSTRACT. Since May 2018 the process of the scanning and processing of photographic plates from the archive of the Institute of Astrophysics Academy of Sciences of Tajikistan has begun. It is a matter of approximately 1560 photographic plates in the sky zones from -8 to $+90$ degrees that were exposed for the FON project in the Hissar observatory (HisAO) during 1985-1992. The plates are digitized by using of the scanner Microtek ScanMaker 1000XL Plus with the resolution of 1200 dpi. The size of the photographic plates is $8^{\circ} \times 8^{\circ}$ or 30×30 cm, the size of the digitized images is 13000×13000 px. So far the first results of the processing of the 71 plates of zero zone and the 58 plates of 64, 68 and 72 zones were obtained. The errors in the definition of equatorial coordinates and B-magnitudes for the stars in the range of $5^m - 17^m$ are the following: $\sigma_{\alpha\delta} = \pm 0.33''$ and $\sigma_B = \pm 0.12^m$. The differences between the calculated positions and B-magnitudes and the reference one from the Tycho2 catalogue are $\sigma_{\alpha\delta} = \pm 0.12''$ and $\sigma_{BT} = \pm 0.19^m$ respectively. The difference between the calculated and the photoelectric B-magnitudes equals $\sigma_B = \pm 0.15^m$. In the realization of the “FON-Dushanbe catalogue” project five astronomical institutions are involved: Institute of Astrophysics of AS of Republic of Tajikistan; Walter Hohmann Observatory, Essen, Germany; Ulugh Beg Astronomical Institute UAS, Uzbekistan; Research Institute “Mykolaiv Astronomical Observatory”, Ukraine and Main Astronomical Observatory NASU, Ukraine.

Keywords: scanning, processing of digitized plates, FON project, astrometry, photometry, data analysis

АБСТРАКТ. В травні 2018 року за програмою FON розпочато процес масового сканування та обробки фотографічних платівок із колекції Інституту астрофізики АН Республіки Таджикистан. За період 1985-1992 рр. в зонах від -8° до $+90^{\circ}$ експоновано близько 1560 платівок розміром $8^{\circ} \times 8^{\circ}$. Платівки оцифровуються за допомогою сканера Microtek ScanMaker 1000XL Plus, режим сканування — 1200 dpi, розмір платівок – 30×30 см або 13000×13000 px. Отримано перші результати із обробки 71 платівки

нульової зони та 58 платівок 64, 68 і 72 зон. Для фотометричного інтервалу В-зоряних величин від 5^m до 17^m значення похибок визначення екваторіальних координат та В-зоряних величин такі: $\sigma_{\alpha\delta} = 0.33''$ и $\sigma_B = 0.12^m$. Сходимість між обчисленими нами та опорними положеннями із каталогу Tycho2 є такою: $\sigma_{\alpha\delta} = 0.12''$, $\sigma_{BT} = 0.19^m$, а сходимість з фотоелектричними зоряними В-величинами дорівнює $\sigma_B = 0.14^m$. В обробці платівок та створенні каталога ФОН-Душанбе приймають участь п'ять астрономічних закладів: Інститут астрофізики АН Республіки Таджикистан, Обсерваторія ім. Вальтера Хоманна в Ессені (Німеччина), Астрономічний інститут ім. Улугбека АН Республіки Узбекистан, НДІ “Миколаївська астрономічна обсерваторія (Україна) та Головна астрономічна обсерваторія НАН України.

Ключові слова: сканування, обробка оцифрованих платівок, програма ФОН, астрометрія, фотометрія, аналіз даних

1. Introduction

The plan of the photographic survey of the Northern Sky (FON) was proposed in 1976 by the scientists of GAO of USSR G. Kolchinski and A.B. Onegina (Kolchinsky, 1977; Pakuliak, 2016). The idea of the project arose after the acquisition by several observatories of the USSR of identical wide-angle astrographs of the company Karl Zeiss (Jena) with the aperture of 40 cm and the focal lengths of 2 or 3 meters. The project FON was attended by six observatories: Main Astronomical observatory of Ukraine (Goloseevo), Zvenigorod observatory of Russia, Hissar observatory of Tadjikistan, Abastumani observatory of Georgia, Zelenchuk observatory of Russia and Kitab observatory of Uzbekistan. The northern sky should be photographed four times with an overlapping. The Hissar astronomical observatory (HisAO) of the Institute of Astrophysics of AS of Tajikistan also participated in the realisation of the project FON. Regular observations began in 1985 and lasted until 1992. Hamburg O.E., Relke

E.V., Tsygankova M.I., Mullo-Abdolov A. S., Kiselev N.N. took part in the observations. In total, 1578 photographic plates were exposed. The 1560 of which were suitable for the processing. Thanks to the support of the Academy of Sciences of RT the Institute acquired a professional scanner, which allows the scanning of the photoplates with the size of 30 x 30 cm (Mullo-Abdolov, 2017, Rahimi, 2018). In 2017 the scanner was placed on a specially built platform. With the help of the scanner it is planned to digitize the photographic plates exposed for the project FON. The digitized images will be processed with the goal to create a FON-Dushanbe catalogue with exact positions and B-magnitudes of stars, galaxies and other objects. The task is solved together with colleagues from Walter Hohmann Observatory, Essen, Germany; Ulugh Beg Astronomical Institute UAS, Uzbekistan; Research Institute “Mykolaiv Astronomical Observatory”, Ukraine and Main Astronomical Observatory NASU, Ukraine. Earlier, in 2016, within the framework of the UkrVO project (Vavilova, 2012; Vavilova, 2016; Vavilova, 2017) the Kiev part of the program FON was performed (Andruk, 2015b; Andruk, 2016a; Andruk, 2016b) and in 2017 the Kitab part of the project FON was done (Yuldoshev, 2017a; Yuldoshev, 2017b). For the future the creation of the common catalogue of the FON project is planned (Andruk, 2017b). This future FON-catalogue will contain also the U, V values, which will be obtained after processing of digitized photographic plates of 1.2-m telescope in Baldone (Eglitis, 2016; Eglitis, 2017; Eglitis, 2018).

2. First results of processing of the FON-Dushanbe zones

In May 2018 the 71 photographic plates of zero zone and 58 plates of the 64, 68 and 72 zones were digitized and processed. The size of one plate is 8 degrees along the declination and $8\cos\delta$ degrees along the right ascension. So the 90 plates are necessary for the full filling of zero zone with two overlapping. The filling of the sky by the stars of $B = 10^m$ magnitude for zero and near polar zones is showed in the Figure 1 in the form of sky maps. The sequence and principles of the processing of wide-angle digitized plates with the purpose of the obtaining of equatorial coordinates and visual B-magnitudes of registered objects were published in the following works (Andruk, 2015a; Andruk, 2017a).

2.1. Astrometry

Astrometric reduction of the digitized photographic plates with the size of 8×8 degrees is carried out in two steps: the investigation of the systematic errors of the scanner $\Delta\alpha$ and $\Delta\delta$ and then the reduction of rectangular coordinates X, Y of all objects in the system of equatorial coordinates α, δ of Tycho-2 catalogue. At the both steps of data processing the tangential coordinates ξ, η are calculated by the method of the smallest squares using the formula:

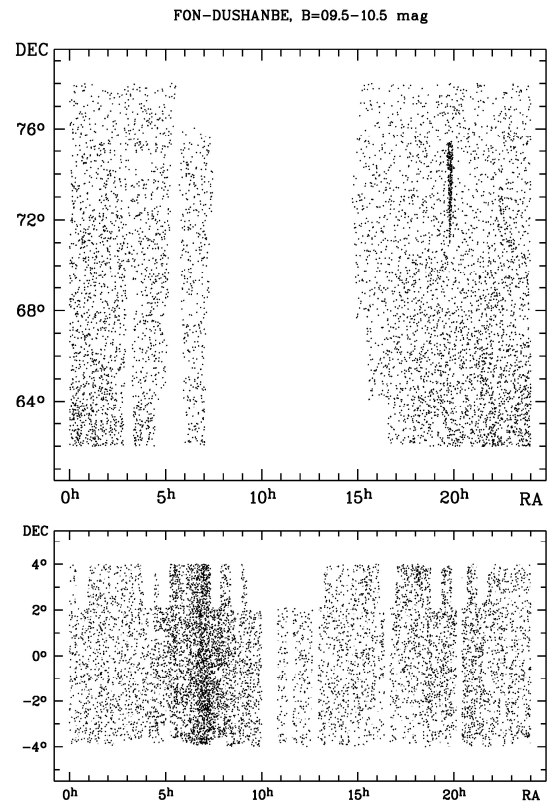


Figure 1: Sky maps. The filling of the sky areas of zero (bottom) and near polar (top) zones of the FON-Dushanbe project with the stars of $B = 10^m$ magnitude

$$\begin{aligned} \xi_i &= a_1 + a_2 X_i f_i + a_3 Y_i f_i + a_4 R_i m_i + a_5 f_i + \sum b_{lm} X_i^l Y_i^m, \\ &\quad (l=0\div 6, m=0\div 6, l+m=n, n=1\div 6) \\ \eta_i &= c_1 + c_2 X_i f_i + c_3 Y_i f_i + c_4 R_i m_i + c_5 f_i + \sum d_{lm} X_i^l Y_i^m, \\ &\quad (l=0\div 6, m=0\div 6, l+m=n, n=1\div 6) \end{aligned}$$

where $i = 1, 2, \dots, N$ – number of stars from the TYCHO-2 catalogue on the digitized plate; X_i, Y_i и R_i – coordinates and distances of star images relative to the center of the plate; m_i – instrumental photometric star values; f_i – diameters of star images; coefficients a_2, a_3, a_4 and c_2, c_3, c_4 are responsible for the coma; coefficients a_5, c_5 – take into account the influence of the brightness equation (these coefficients are calculated separately); the b_{lm} и d_{lm} are the coefficients of the full polynomial of degree six (altogether 27 members), which describe in a general case optical aberrations of the telescope complicated by systematic errors of the scanner. The first results of the processing of 58 plates near polar zones and 71 plates of zero zone of the FON-Dushanbe project are show in the Figure 2.

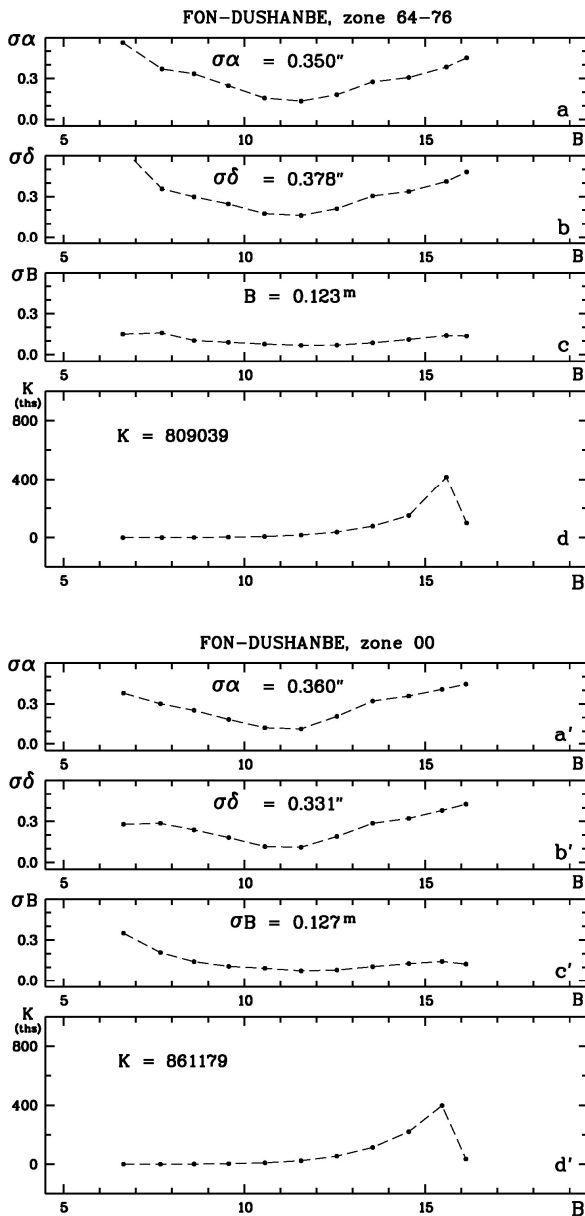


Figure 2: The trend of internal errors for equatorial coordinates and B-magnitudes as well as the number of stars relative to the intervals of the B-magnitudes of the FON-Dushanbe catalogue. The error information for the near polar (64, 68, 72) zones is presented on the upper panels a, b, c and d; for the zero zone - on the lower panels a', b', c' and d'.

The coordinates of the stars and galaxies are obtained in the system of the Tycho-2 catalogue, the B-magnitudes – in the system of photoelectric standards. The mean observation epoch of the FON-Dushanbe catalogue is 1990.5. The values of the internal errors of equatorial coordinates and B-magnitudes of stars and galaxies are equal: $\sigma\alpha\delta = 0.33''$ - $0.36''$ and $\sigma B = 0.13^m$ respectively. The distribution of errors of equatorial coordinates of the FON-Dushanbe catalogue relative to the reference Tycho-2 catalogue for near polar zones and zero zone are presented in the Figure 3.

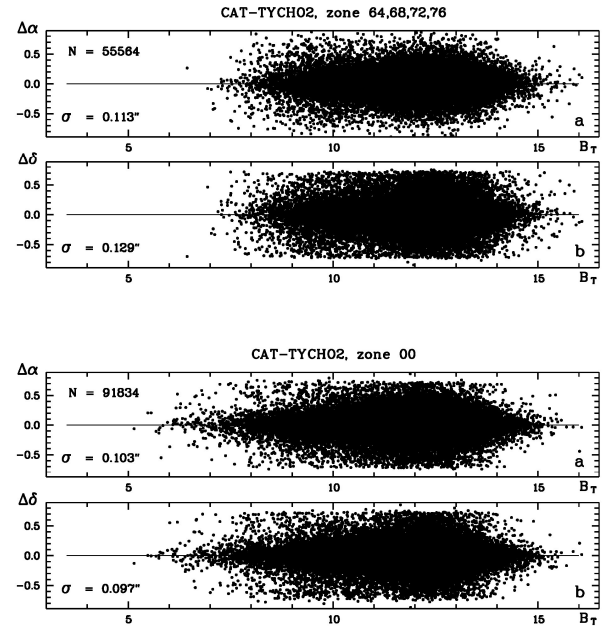


Figure 3: The distribution of mean squared errors of equatorial coordinates of the FON-Dushanbe catalogue relative to the reference Tycho-2 catalogue for the near polar zones (panels a, b) and the zero zone (panels a', b').

2.2. Photometry

The photoelectric B_{pe} values of stars from a specially created catalogue were used as photometric standards for the construction of characteristic curves for each digitized photographic plate (Relke, 2015; Andruk, 2017a). The errors of differences ΔB between the calculated by us B-magnitudes and photoelectric B_{pe} values of stars for more than 2370 stars are equal to $\sigma_B = 0.14^m$. The Figure 4 illustrates the trend of differences ΔB relative to photoelectric values B and B-V.

2.3. Comparison with other catalogues

A separated independent study of astrometric and photometric properties of the zero zone for three catalogues of the FON project (FON-Kiev, FON-Kitab and FON-Dushanbe) were made by special method (Akhmetov, 2016) in the work, which was also presented on the Gamov conference 2018 and was published in the same conference proceeding (Akhmetov, 2018).

3. Conclusion

At the end of June 2018 about 150 photographic plates of zero (00) and polar (64, 68, 72 and 76) zones of the FON-Dushanbe photographic archive were digitized and processed. In parallel these digitized plates are used for the searching of asteroids and comets (Yizhakevych, 2018; Shatokhina, 2017; Shatokhina, 2018). In the Astrophysics Institute of the Academy of Sciences of Tajikistan the work on scanning of plates continues. By the end of 2019 using the results of the processing of all digitized photographic plates (about 1560) it is planned to obtain the FON-Dushanbe catalogue.

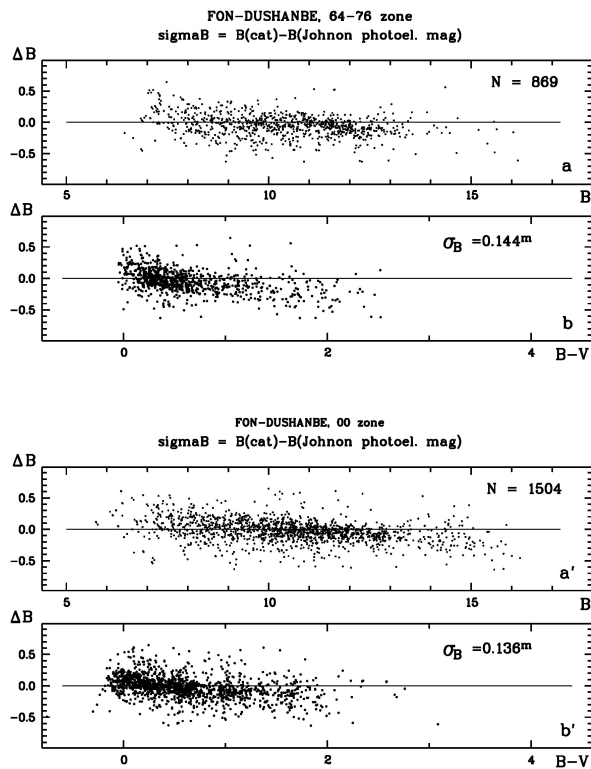


Figure 4: The error distribution of photometry of the FON-Dushanbe catalogue relative to the reference system of the photoelectric B and B-V measurements of stars for the near polar zones (top panels a, b) and zero zone (panels a', b').

Acknowledgements. The authors are thankful to academician Farhod Rahimi, the President of Academy of Sciences of the Republic of Tajikistan, for the supporting of the project “FON-Dushanbe catalogue”.

References

- Akhmetov V.S.: 2016, *Odessa Astron. Publ.*, **29**, 116.
 Akhmetov V.S. Khlamov S.V., Andruk V.M., Protsyuk Yu.I.: 2018, *Odessa Astron. Publ.*, **31**, .
 Andruk V.M., Pakuliak L.K., Golovnya V.V. et al.: 2015, *arxiv.org/abs/1512.05535*.
 Andruk V.M., Pakuliak L.K., Golovnia V.V. et al.: 2015, *Odessa Astron. Publ.*, **28**, 192.
 Andruk V.M., Golovnia V.V., Ivanov G.A. et al.: 2016, *Kinem. Phys. Cel. Bodies*, **32**, N1, 38.
 Andruk V.M., Pakuliak L.K., Golovnia V.V. et al.: 2016, *Kinem. Phys. Cel. Bodies*, **32**, N5, 260.
 Andruk V.M., Pakuliak L.K., Golovnia V.V. et al.: 2017, *Science and Innovation*, **13a**, 17.
 Andruk V., Yuldoshev Q., Eglitis I. et al.: 2017, *Odessa Astron Publ.*, **30**, 159.
 Eglitis I., Eglite M., Pakuliak L.K., Andruk V.M.: 2016, *Odessa Astron Publ.*, **29**, 126.
 Eglitis I., Andruk V.: 2017, *Open Astronomy*, **26**, 7.
 Eglitis I., Eglite V., Andruk V., Protsyuk Yu. et al.: 2018, *Odessa Astron Publ.*, **31**, .
 Kolchinsky I.G., Onegina A.B.: 1977, *Astrometry and Astrophysics*, **33**, 11.
 Mullo-Abdolov A., Kokhirova A., Relke H. et al.: 2017, *Odessa Astron Publ.*, **30**, 186.
 Pakuliak L.K., Andruk V.M., Golovnia V.V. et al.: 2016, *Odessa Astron. Publ.*, **29**, 132.
 Rahimi F., Mullo-Abdolov A.Sh., Kokhirova G.I. et al.: 2018, *Reports AS RT*, **60**, №2, 144.
 Relke E., Protsyuk Yu.I., Andruk V.M.: 2015, *Odessa Astron. Publ.*, **28**, 211.
 Shatokhina S.V., Kazantseva L.V., Yizhakevych O.M. et al.: 2017, *Odessa Astron. Publ.*, **30**, 198.
 Shatokhina S.V., Kazantseva L.V., Yizhakevych O.M., Andruk V.M.: 2018, *Kinem. Phys. Cel. Bodies*, **34**, N5, 70.
 Vavilova I.B., Pakulyak L.K., Shlyapnikov A.A. et al.: 2012, *Kinem. Phys. Cel. Bodies*, **28**, N4, 85.
 Vavilova I.B.: 2016, *Odessa Astron. Publ.*, **29**, 109.
 Vavilova I.B., Yatskiv Ya.S., Pakuliak L.K.: 2017, *IAUS*, **325**, 361.
 Yizhakevych O.M., Mullo-Abdolov A.Sh., Relke H.V. et al.: 2018, *Odessa Astron. Publ.*, **31**, .
 Yuldoshev Q.X., Muminov M.M., Ehgamberdiev Sh.A. et al.: 2017, *Odessa Astron Publ.*, **30**, 205.
 Yuldoshev Q.X., Ehgamberdiev Sh.A., Muminov M.M. et al.: 2017, *Kinem. Phys. Cel. Bodies*, **33**, N5, 250.

DOI: <http://dx.doi.org/10.18524/1810-4215.2018.31.146193>

ANALYSIS OF MASS CCD OBSERVATIONS TO IMPROVE THE ACCURACY OF ASTROMETRIC PROCESSING

Yu. Protsyuk, O. Kovalchuk

Research Institute: Mykolaiv Astronomical Observatory, Mykolaiv, Ukraine

yuri@nao.nikolaev.ua

ABSTRACT. In Research Institute: Mykolaiv Astronomical Observatory (RI MAO) regularly observations of fields with open clusters on the KT50 telescope ($D = 500$ mm, $F = 3000$ mm) with an Alta U9000 CCD camera ($3k \times 3k$, FOV $42.6' \times 42.6'$) in drift scan mode are carried out. For this observation mode, we investigated the dependence of the differences between observed minus calculated (O–C) angular coordinates of reference stars in depending on X coordinate (direction perpendicular to the direction of charge transfer) in the CCD coordinate system. The data of observations of open clusters obtained in the RI MAO in 2011–2017 were used for the study. The data array used to obtain the distribution (O–C) for right ascension (RA) and declination (DEC), depending on X, contains 62 million single observations of stars. The processing of the original data was carried out using the Astrometrica program with the reference catalogue UCAC4. The distribution of the (O–C) value as a function of X according to RA and DEC was obtained by the method of least squares. For the solution is a 10th-degree polynomial of X and a third degree from the integral intensity of the object in the image was used. The study showed the presence of significant (0.01–0.02)" systematic errors in the field of the matrix for bright stars (10–12)^m. For faint stars, the amplitude of the constant part decreases significantly while maintaining the periodic component. Similar studies have also been carried out for a lot of CCD frames obtained from astronomical databases for other instruments. The results will be used to improve the accuracy of astrometric catalogues obtained with the KT50 telescope and to improve the accuracy of the proper motions of stars in the vicinity of open clusters.

Keywords: Astrometry – Data analysis – Astronomical data bases – Catalogues.

АБСТРАКТ. В науково-дослідному інституті "Миколаївська астрономічна обсерваторія" (НДІ МАО) проводяться регулярні спостереження площадок з розсіяними скупченнями на телескопі KT50 ($D = 500$ мм, $F = 3000$ мм) з ПЗЗ камерою Alta U9000 ($3k \times 3k$, FOV $42,6' \times 42,6'$) в режимі синхронного переносу заряду. Для цього режиму спостереження ми досліджували залежність різниці (O–C) кутових координат опорних зірок залежно від координати X (напрямку, перпендикулярного напрямку переносу заряду) в системі координат ПЗЗ матриці. Для дослідження використовувались дані спостережень російських скупчень, отримані в НДІ МАО в 2011–2017 роках. Масив даних, який вико-

ристовувався для отримання розподілу (O–C) для прямого піднесення (RA) та схилення (DEC), залежно від X, містить 62 мільйони одиничних спостережень зірок. Обробка вихідних даних здійснювалася за допомогою програми Astrometrica з опорним каталогом UCAC4. Розподіл значень (O–C) як функції X відповідно до RA та DEC був отриманий методом найменших квадратів. Для рішення використовувались поліноми 10-го ступеня від X та третього ступеня від інтегральної інтенсивності об'єкта на зображенні. Дослідження показало наявність значних (0,01–0,02)" систематичних помилок по полю матриці для яскравих зірок (10–12)^m. Для слабких зірок амплітуда постійної частини значно зменшується при збереженні періодичної складової. Дослідження були також проведені для багатьох ПЗЗ-кадрів, отриманих з астрономічних баз даних для інших інструментів. Результати роботи будуть використовуватися для підвищення точності астрометричних каталогів, отриманих за допомогою телескопа KT50, та для підвищення точності власних рухів зірок в розсіяних скупченнях та їх околицях.

Ключові слова: Астрометрія – Аналіз даних – Астрономічні бази даних – Каталоги.

1. Introduction

During the period from 2011 to 2017 at the KT-50 telescope ($D = 500$ mm, $F = 3000$ mm) of the RI MAO (Shulga et al., 2012), equipped with a U-9000 CCD camera ($3k \times 3k$, FOV $42.6' \times 42.6'$) (Apogee, 2018), a regular observations of open star clusters was performed in the framework of several scientific topics (Protsyuk et al., 2014; 2017). The U-9000 camera was used in synchronous charge transfer (drift scan) mode. The orientation of the camera along the X-axis (row) coincides with the axis of declination on the celestial sphere, Y (column), respectively, with the axis of right ascension. For the entire period, about 62,000,000 single observations of stars up to 17th magnitude were obtained. Thus, for each line element (overall 3000 elements for the U-9000 camera), there is an array of more than 20,000 stars (on average). Processing of observations up to the (O–C) was performed using the Astrometrica program (Raab, 2018) in the UCAC4 reference system (Zacharias et al., 2013). Thus, we have a fairly well-statistically provided material for analyzing the distribution of the values (O–C) as a function of X (the direction is

perpendicular to the direction of transfer of charge packets during the observation process).

2. Investigations

To study the behaviour of the value (O-C) depending on X, we made samples (O-C) for each X and intensity interval, and then we calculated the average value (O-C) for each specific X and the interval of stellar magnitudes. We performed the calculation in several iterations, discarding the samples with too large values (O - C) by the criterion of 3σ . Thus, we obtained the table values of the average value (O-C) for each X of the CCD matrix in a given interval of stellar magnitudes. For example, consider several graphs that display the resulting table data. In Fig. 1 shows a graph of the distribution of (O - C) values depending on declination for stars of the 12th stellar magnitude. As you can see (O-C) has a certain constant component at the level of 0.01 mas, and a variable reaching 0.02 mas at the peak, which is a very significant value. In Fig. 2 shows smoothed dependences for different stellar magnitudes, where dependence on intensity is clearly visible. For stars with 15^m (O-C) values oscillate around zero, for 11^m goes above 0.02 mas.

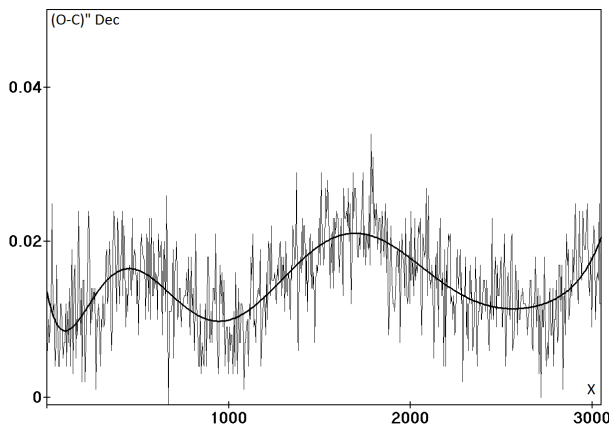


Figure 1: The distribution of (O-C) of the declination from X for stars of the 12th magnitude

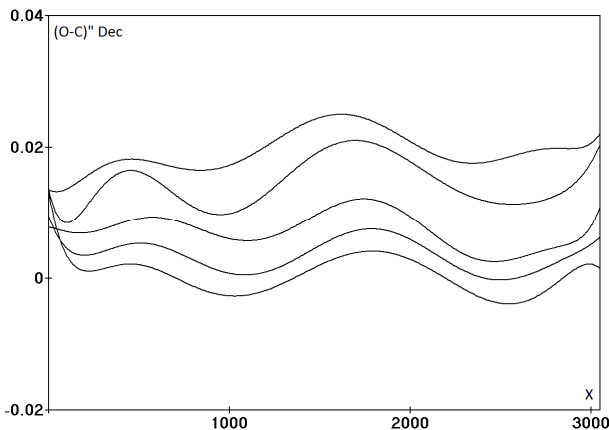


Figure 2: Smoothed distributions of (O-C) of the declination from X, the stars from the 11th to 15th magnitude (from top to bottom)

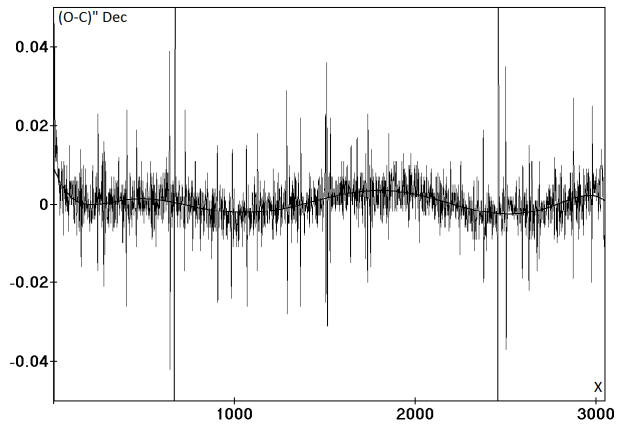


Figure 3: The distribution (O-C) of the declination from X for stars of 15^m and fainter

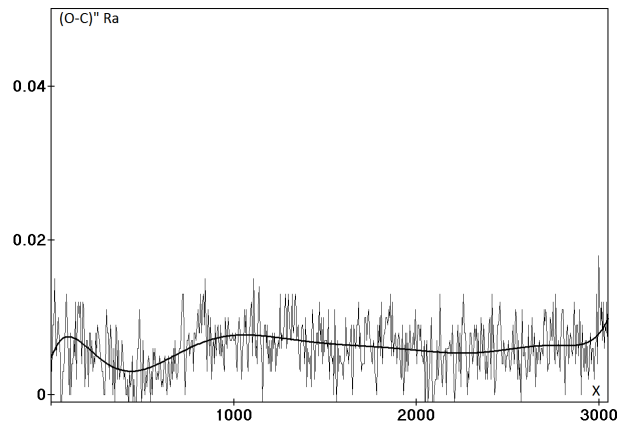


Figure 4: The distribution (O-C) of the right ascension from X for stars of 12^m

An interesting graph of the distribution (O-C) for low intensities (stars of 15^m and fainter) is presented in Fig. 3.

As you can see, the average value (O-C) is small, but on the graph, there is a certain amount of emissions reaching 0.05 mas and more. Such anomalous behaviour (O-C) is explained by the presence of CCD matrix defects, the most significant of them are visible on the images in the form of light or dark columns. Others are not visible with the eye, but if the image of the star gets on them in the process of observations, it adduce to a significant increase of coordinate errors.

Similar data were obtained for (O-C) of right ascension and presented in Fig. 4 and 5.

As can be seen from the graphs, the nature of the error behaviour is different than for the declination axis. This is explained by the mode of operation of the CCD camera, namely, the synchronous charge transfer which adduces to averaging errors across the field exactly on the axis of right ascension. Also, there are practically no abnormal jumps in the values of (O-C) on CCD defects; this is also the effect of synchronous charge transfer.

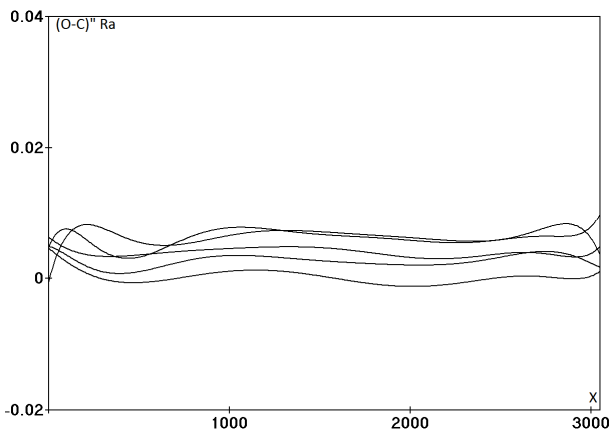


Figure 5: Smoothed distributions of $(O - C)$ of the RA from X, the stars from the 11^m to 15^m (from top to bottom)

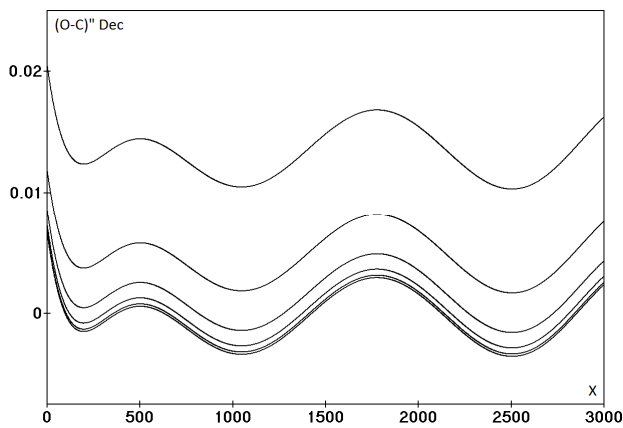


Figure 6: Analytical dependence of distributions of $(O - C)$ of the declination from X, the stars from the 11th to 15th magnitude (from top to bottom)

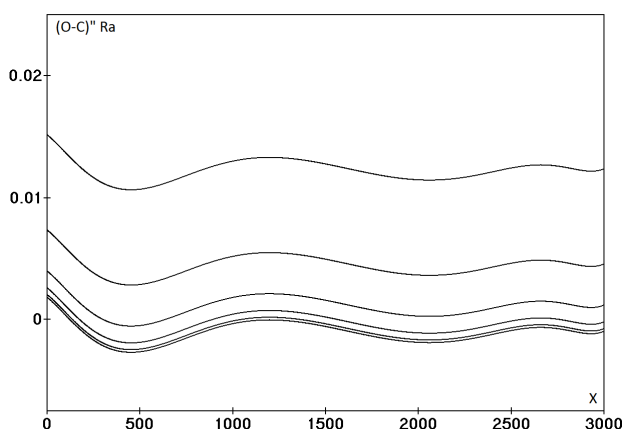


Figure 7: Analytical dependence of distributions of $(O - C)$ of the right ascension from X, the stars from the 11th to 15th magnitude (from top to bottom)

To construct an analytical dependence, we used the method of least squares, which is based on the 10th degree polynomial from the X, and the 3rd degree from the integral intensity. The coefficients of polynomial were calculated in three iterations and we discarding the samples with too large values $(O - C)$ by the criterion of 3σ . The result is in the form of graphs below.

3. Conclusion

As can be seen from the graphs obtained, the system of $(O - C)$ has a significant value for objects with high intensity, namely for stars brighter than the 13th magnitude. Also, an abrupt increase of $(O - C)$ values are observed for images gets on the CCD columns containing defects.

Similar studies have also been carried out for a lot of CCD frames obtained from astronomical databases for other instruments (Protsyuk et al., 2015). They showed similar results for some telescopes.

The results of the investigation will be used to improve the accuracy of astrometric catalogues obtained with the KT50 telescope and to improve the accuracy of the proper motions of stars in the vicinity of open clusters.

References

- Apogee Alta CCD Camera, [online] Available at: (<https://optcorp.com/products/apogee-alta-f9000-d07-monochrome-ccd-camera>) [Accessed 19 September 2018].
- Protsyuk Yu.I., Martynov M.V., Mazhaev A.E.: 2014, *Kinem. Phys. Cel. Bodies.*, **30**, **N6**, 296.
- Protsyuk Yu.I., Kovalchuk O.M.: 2015, *Odessa Astron. Publ.*, **28**, 207.
- Protsyuk Yu.I., Kovalchuk O.M., Mazhaev O.E.: 2017, *Sci.Innov.*, **13**, **N1**, 54.
- Raab H., Astrometrica, [online] Available at: (<http://www.astrometrica.at/>) [Accessed 19 September 2018].
- Shulga O.V., Kozyryev Y.S., Sybiryakova Y.S. et al.: 2012, *KosNT.*, **18**, **N4**, 52.
- Zacharias N., Finch C.T., Girard T.M. et al.: 2013, *Astron. J.* **145**, 44.

DOI: <http://dx.doi.org/10.18524/1810-4215.2018.31.146275>

RESULTS OF PROCESSING OF CCD OBSERVATIONS OF SELECTED OPEN CLUSTERS ON MAIDANAK

Yu.I. Protsyuk¹, Sh.Sh. Shukhratov², O.M. Kovalchuk¹, M.M. Muminov³, Q.H. Yuldoshev²,
R.R. Abdurakhimov³, V.M. Andruk⁴

¹Research Institute "Mykolaiv Astronomical Observatory", Mykolaiv, Ukraine,
yuri@nao.nikolaev.ua

²Ulugh Beg Astronomical Institute UAS, Tashkent, Uzbekistan, *qudratillo@astrin.uz*

³Andijan State University, Andijan, Uzbekistan, *muminov1951@gmail.com*

⁴Main Astronomical Observatory NASU, Kyiv, Ukraine, *andruk@mao.kiev.ua*

ABSTRACT. Observations of 20 open clusters at the Maidanak Observatory were performed using the Zeiss-1000 telescope in the winter of 2018. As the light receiver, a CCD camera Apogee Alta U9000 (3K x 3K, FOV 19.5'x19.5') was used. All observations were performed using BVRI light filters. The exposure time, depending on the filter was from 60 to 150 seconds. Due to the instability of the telescope, images of the stars are slightly elongated. For each observation night, calibration images were obtained. Astrometric processing was carried out after filtering hot pixels. For testing purposes, we used two methods of reduction: by the Astrometrica program and the author's set of programs with primary processing in the MIDAS environment. The reduction of 280 frames was performed using a polynomial of the third degree. As reference stars in different processing options, the Tycho2, UCAC4 and Gaia DR2 catalogs were used. Due to the small field and the small number of reference stars, the processing in Tycho2 showed the worst result. The results obtained by author programs with reference catalogs UCAC4 and Gaia, showed good convergence. Integrated catalog of 18 thousand stars upto 18.5^m was obtained. The accuracy of the catalog is $\sigma_{RA}=0.011''$ and $\sigma_{DEC}=0.013''$, the accuracy of single observation on RA (0.030 - 0.032)'' and DEC (0.035 - 0.037)'' . At the same time, the accuracy of intraframe processing with the Gaia reference catalog turned out to be 2-3 times better than the analogous one with the UCAC4 catalog. The accuracy of processing elongated star images by the Astrometrica program is on the average 3-4 times worse than by the author's programs. Also a systematic dependence of the pixel scale on the using filter was found. Based on the results of the test photometric processing of NGC869 cluster a photometric estimate of the accuracy of the observations was obtained. The internal errors of one measurement of the stellar magnitude in the instrumental system bvr have the values $\sigma_{bvr} = (0.03-0.05)^m$. After the reduction of instrumental stellar magnitudes to the Johnson BVR system, the errors of one measurement are $\sigma_{BVR} = (0.05-0.08)^m$. The processing of observations showed the possibility of carrying out differential observations on the telescope Zeiss-1000 with an

accuracy of one observation, not worse than 0.04'', and near 0.02'' after improving telescope management.

Keywords: Astrometry – Photometry – Open clusters – Data analysis – Catalogues

АБСТРАКТ. Спостереження 20 розсіяних зоряних скупчень на Майданаській обсерваторії виконані на метровому телескопі Zeiss -1000 взимку 2018 року. Як приймач випромінювання використовувалася ПЗЗ камера Apogee Alta U9000 (3K x 3K, FOV 19,5'x19,5 '). Всі спостереження виконані з використанням світлових фільтрів BVRI в системі Бесселя. Тривалість експозиції в залежності від фільтра становила від 60 до 150 секунд. Через нестабільність ведення телескопа зображення зірок трохи витягнуті. Для кожної спостережної ночі отримані калібрувальні зображення. Астрометрична обробка проводилася після фільтрації гарячих пікселів за двома методиками: програмою Astrometrica і авторським набором програм з первинною обробкою в середовищі MIDAS. Редукція виконувалася з використанням полінома 3-го ступеня. В якості опорних зірок в різних варіантах обробки були використані каталоги Tycho2, UCAC4 і Gaia DR2. Через малий розмір поля і малу кількість опорних зірок обробка в Tycho2 показала найгірший результат. Результати, отримані авторськими програмами з опорними каталогами UCAC4 і Gaia, показали хорошу збіжність. Точність інтегрального каталогу 18 тисяч зірок до 18.5^m, отриманого з 280 кадрів, склала по RA - 0.011'' і DEC - 0.013''. Точність одиничного спостереження склала по RA (0.030 - 0.032)'' і DEC (0.035 - 0.037)'' . При цьому точність внутрішньої кадрової обробки з опорним каталогом Gaia виявилася в 2-3 рази краще аналогічної з каталогом UCAC4. Точність обробки витягнутих зображень програмою Astrometrica в середньому в 3-4 рази гірше, ніж авторськими програмами. Також в процесі обробки виявлена систематична залежність величини масштабу пікселя від застосовуваного світлофільтру. За результатами тестової обробки спостережень від 21 січня 2018 р скупчення NGC869 отримана фотометрична оцінка

точності спостережень. Внутрішні помилки одного виміру зоряної величини в інструментальній системі b_{vri} мають значення $\sigma_{b_{\text{vri}}} = (0.03-0.05)^{\text{m}}$. Після редукції інструментальних зоряних величин в систему BVR Джонсона помилки одного виміру рівні $\sigma_{\text{BVR}} = (0.05-0.08)^{\text{m}}$. Обробка спостережень показала можливість проводити диференціальні спостереження на телескопі Zeiss-1000 з точністю одного спостереження не гірше 0."04, а при поліпшенні ведення телескопа, то і 0.02".

Ключові слова: Астрометрія – Фотометрія – Розсіянні скупчення – Аналіз даних – Каталоги

1. Introduction

Observations of 20 open clusters (NGC869, NGC884, NGC957, NGC1039, NGC1245, NGC1444, NGC1496, NGC1528, NGC1545, NGC1907, NGC2099, NGC2168, NGC2281, NGC2331, NGC2335, NGC2420, NGC2632, NGC2682, Berkeley10, Berkeley67) at the Maidanak Observatory (<http://www.academy.uz/en/site/slideview/20>) were performed using the Zeiss-1000 telescope in the winter of 2018. As the light receiver, a CCD camera Apogee Alta U9000 was used. New CCD Camera was installed at 2017 after repairing of the telescope. Camera has 3K x 3K size with FOV 19.5'x19.5' and pixel size 12 x 12 microns or 0.388"/pixel. All observations were performed using BVR light filters with three exposures each. The exposure time, depending on the filter was from 60 to 150 seconds with CCD chip temperature near -20°C. Due to the instability of the telescope, images of the stars are slightly elongated. For each observation night, calibration images were obtained. Astrometric processing was carried out after filtering hot pixels. For testing purposes, we used two methods of reduction: by the Astrometrica program (Raab, 2018) and the author's set of programs with primary processing in the MIDAS environment (Andruk et al., 2005; 2017; Protsyuk et al., 2014a, 2014b). This software was created to process images that are part of the Ukrainian Virtual Observatory (Vavilova et al., 2012; 2017).

2. Astrometric investigations

The reduction of 280 frames was performed using a polynomial of the third degree. As reference stars in different processing options, the Tycho2, UCAC4 (Zacharias et al., 2013) and Gaia DR2 (Gaia Collaboration, 2018) catalogs were used. Due to the small field and the small number of reference stars, the processing in Tycho2 showed the worst result. The results obtained by author programs with reference catalogs UCAC4 and Gaia DR2, showed good convergence (Fig.1). Integrated catalog of 18 thousand stars upto 18.5^m was obtained. The accuracy of the catalog is $\sigma_{\text{RA}}=0.011''$ and $\sigma_{\text{DEC}}=0.013''$, the accuracy of single observation on RA (0.030 - 0.032)" and DEC (0.035 – 0.037)" (Fig. 2).

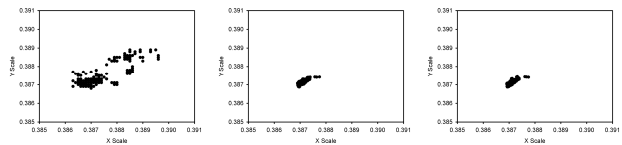


Figure 1: Scale values distribution for all CCD frames depending on the reference catalog Tycho2, UCAC4, Gaia

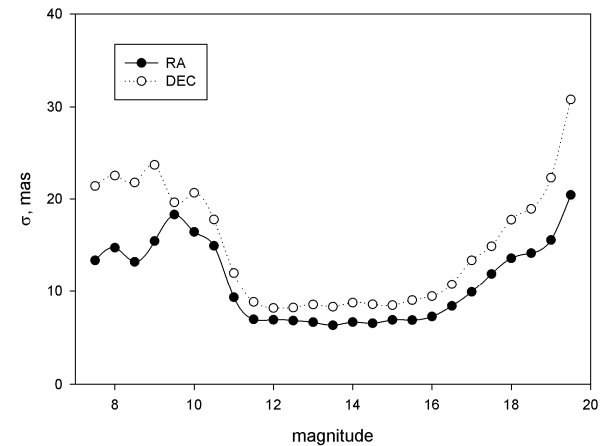


Figure 2: Distribution of catalog accuracy from magnitude, reference catalog Gaia

At the same time, the accuracy of intraframe processing with the Gaia DR2 reference catalog turned out to be 2-3 times better than the analogous one with the UCAC4 catalog (Fig. 3). The accuracy of processing elongated star images by the Astrometrica program is on the average 3-4 times worse than by the author's programs (Table 1). Also a systematic dependence of the pixel scale on the using filter was found (Fig. 4).

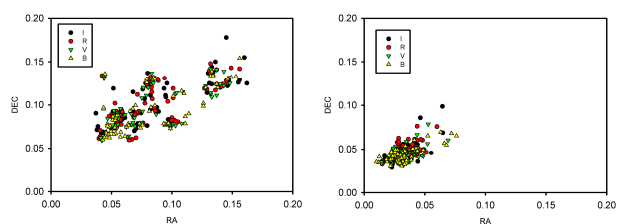


Figure 3: Distribution of RA/DEC accuracy in arcsec of intraframe processing with the reference catalogs UCAC4 (left) and Gaia DR2 (right)

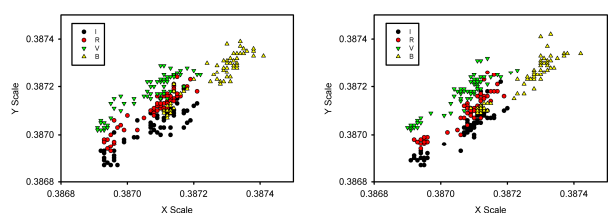


Figure 4: Systematic dependence of the pixel scale on the using filters BVR for the reference catalogs UCAC4 (left) and Gaia DR2 (right)

Table 1: Comparison of the accuracy of single observation with different reductions

| Software | Ref.cat | N ref. stars | N stars | RA, mas | DEC, mas |
|--------------|---------|--------------|---------|---------|----------|
| Astrometrica | UCAC4 | 15516 | 28293 | 96.7 | 164.9 |
| Author's | UCAC4 | 12771 | 18288 | 31.2 | 37.0 |
| Author's | Gaia | 13295 | 18192 | 29.8 | 34.8 |

Table 1 show the number of reference stars, number of stars in received catalogs and accuracy of single observation for this catalogs. Astrometrica finded more objects but overall accuracy worse. Despite the greater accuracy of intraframe processing with Gaia reference catalog (Fig. 3) we received approximate equality of the accuracy of the resulting catalogs for both reference catalogs. This is associated with the worsening of the final result due to the instability of the telescope from frame to frame and a rather large random error.

3. Photometric investigations

CCD observations of open clusters are made by consecutive exposures in each of the Johnson BVRI filters. The duration of one exposure are 60, 90, 120 and 150 seconds for I, R, V and B filters respectively. The processing of raw CCD frames with B, V, R filters was made according to the method of processing digitized images of star fields, which is described by Andruk et al.(2005; 2017). The demonstration of the evaluation of the photometric accuracy of processing CCD frames is considered on the example of observations from January 21, 2018 of the NGC 869 cluster. Figure 5 shows the distribution over the stellar magnitudes of the internal errors of a single measurement of the magnitude in the bvr instrumental system. The figure shows that the internal errors of one measurement of the magnitude in the bvr instrumental system have the values $\sigma_{bvr} = (0.03-0.05)^m$.

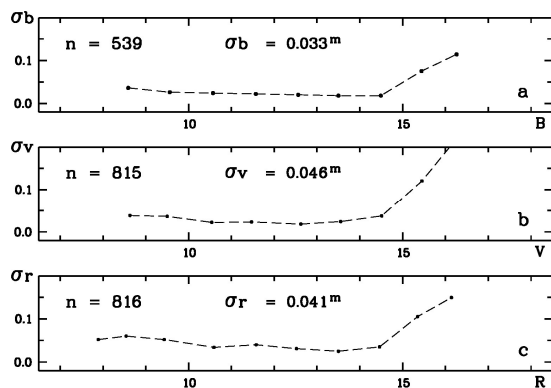


Figure 5: The distributions over the stellar magnitudes of the internal errors of a single measurement of the magnitude in the bvr instrumental system

Also in the figure for each band b, v, r show the number of stars n on frames. The procedure for reducing the instrumental stellar b, v, r to the Johnson system B, V, R is shown in Fig. 6. For searching an functional connection of Johnson's B, V, and R values with instrumental photometric values of b, v, and r we used photoelectric measurements of stars from the Relke et al. (2015) catalog. After the reduction of instrumental stellar influences in the Johnson BVR system, the errors of one dimension are $\sigma_{BVR} = (0.05-0.08)^m$. These results are presented in Fig. 7.

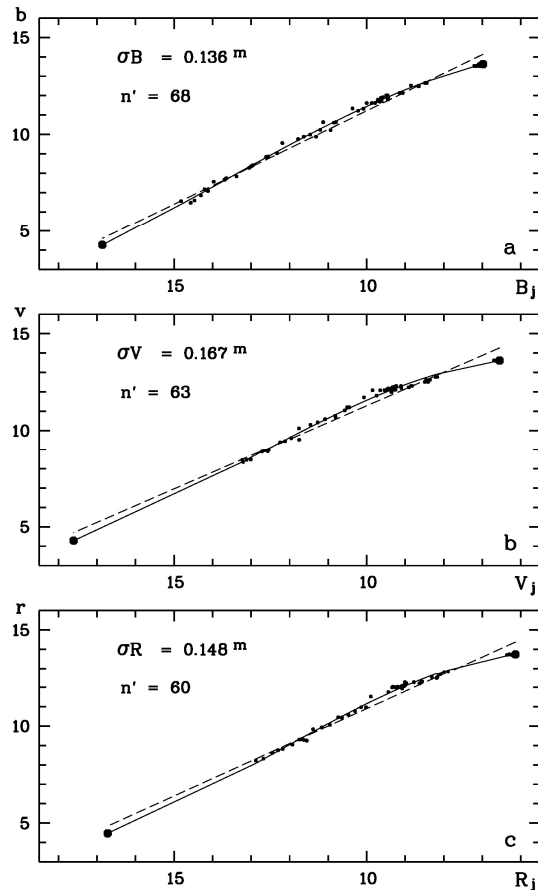


Figure 6: Connection of instrumental stellar magnitudes bvr with a system of stellar magnitudes BVR Johnson

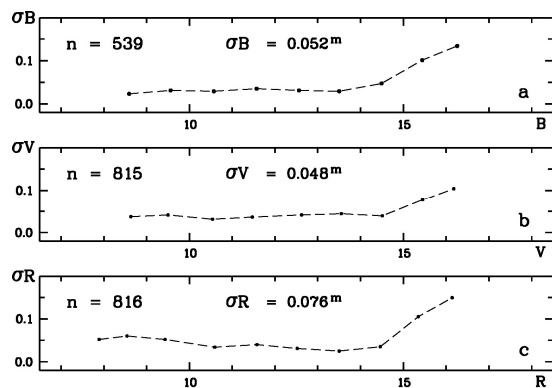


Figure 7: The distributions over the stellar magnitudes of the internal errors of a single measurement of the stellar magnitude after reduction into the Johnson BVR system

4. Conclusion

The processing of observations showed the possibility of carrying out differential observations on the telescope Zeiss-1000 with an accuracy of one observation, not worse than 0.04", and near 0.02" after improving telescope management.

Photometric estimate of the accuracy of the observations was obtained. The internal errors of one measurement of the stellar magnitude in the instrumental system bvr have the values $\sigma_{\text{bvr}} = (0.03-0.05)^m$. After the reduction of instrumental stellar magnitudes to the Johnson BVR system, the errors of one measurement are $\sigma_{\text{BVR}} = (0.05-0.08)^m$.

Astrometric and photometric studies of CCD observation of clusters on Maidanak observatory continue.

References

- Andruk V.M., Pakuliak L.K., Golovnia V.V. et al.: 2017, *Science and Innovation*, **13(1)**, 17.
- Andruk V.M., Vidmachenko A.P., Ivashchenko Yu.M.: 2005, *Kinem. Phys. Cel. Bodies., Suppl.* **5**, 544.
- Apogee Alta CCD Camera, [online] Available at: (<https://optcorp.com/products/apogee-alta-f9000-d07-mono-chrome-ccd-camera>)
- Gaia Collaboration: 2018, *A&A*, **616**, A14.
- Protsyuk Yu.I., Martynov M.V., Mazhaev A.E. et al.: 2014, *Kinem. Phys. Cel. Bodies.*, **30**, **N6**, 296.
- Protsyuk Yu.I., Andruk V.M., Kazantseva L.V.: 2014, *Odessa Astron. Publ.*, **27**, 59.
- Raab H., Astrometrica, [online] Available at: (<http://www.astrometrica.at/>)
- Relke E., Protsyuk Yu.I., Andruk V.M.: 2015, *Odessa Astron. Publ.*, **28**, 211.
- Vavilova I.B., Pakulyak L.K., Shlyapnikov A.A. et al.: 2012, *Kinem. Phys. Cel. Bodies.*, **28**, **N4**, 85.
- Vavilova I.B., Yatskiv Ya.S., Pakuliak L.K. et al: 2017, *IAUS*, **325**, 36.
- Zacharias N., Finch C.T., Girard T.M. et al.: 2013, *Astron. J.* **145**, 44.

DOI: <http://dx.doi.org/10.18524/1810-4215.2018.31.144679>

ASTEROIDS SEARCH RESULTS IN DIGITIZED OBSERVATIONS OF THE NORTHERN SKY SURVEY PROJECT (KITAB PART)

S.V. Shatokhina¹, H. Relke², Q.Yuldoshev³, V.M. Andruk¹, Yu. I. Protsyuk⁴, M. Muminov⁵

¹Main Astronomical Observatory of National Academy of Sciences, 27 Akad. Zabolotno St., 03680, Kyiv, Ukraine, svetash@mao.kiev.ua

²Walter Hohmann Observatory, Essen, Germany, helena_relke@yahoo.com

³Ulugh Beg Astronomical Institute UAS, Tashkent, Uzbekistan

⁴Research Institute Mykolaiv Astronomical Observatory, Mykolaiv, Ukraine

⁵Andijan State University, Andijan, Uzbekistan

ABSTRACT. Photographic observations of XX century contained numerous and varied information about all objects and events of the Universe fixed on the astronegatives. The original and interesting observations of small bodies of the Solar system in previous years can be selected and used for various scientific tasks. Existing databases and online services can help make such selection easily and quickly.

The observations of chronologically earlier oppositions, photometric evaluation of brightness for long periods of time allow refining the orbits of asteroids and identifying various non-stationarities.

Photographic observations of the Northern Sky Survey project (FON project) were used for global search for small bodies of Solar system. About 2,000 photographic plates of Kitab part of the FON project were made using Double Wide Angle Astrograph at the Kitab observatory (Uzbekistan) during 1981-1989. Early, using that digitized observations the catalogue of equatorial coordinates and stellar magnitudes for more than 13 million stars and galaxies up to $B=17.5^m$ was compiled. At present, we analyzed all processing results for the search of asteroids and compiled the catalogue of equatorial coordinates and stellar magnitudes of them.

As a result more than 4,500 asteroids and comets with visual magnitude from $7^m.7$ to $17^m.5$ were identified now. All positions of asteroids were compared with ephemeris. A preliminary analysis of O-C differences was carried out.

New and interesting are that the moments of official discovery of some identified asteroids much later than their moments of Kitab's observation. In addition, some of them are the earliest observations of these asteroids in the world among all known observations. More than 915 observations of such asteroids have been found on the plates of Kitab part of the FON project.

Keywords: catalogue, asteroids positions, FON project

АБСТРАКТ. Фотографічні спостереження ХХ століття містять численну та різноманітну інформацію про всі об'єкти та події Всесвіту, зафіксовані на астронегативах. Оригінальні та цікаві спостереження малих тіл Сонячної системи в попередні роки можна вибрати та використовувати для різних наукових завдань. Існуючі бази даних та онлайн-сервіси можуть допомогти зробити такий вибір легко і швидко.

Спостереження хронологічно більш ранніх опозицій, фотометрична оцінка блиску протягом довгих періодів часу дозволяють уточнювати орбіти астероїдів і виявляти різні нестационарності.

Фотографічні спостереження Фотографічного огляду північного неба (проект ФОН) були використані для глобального пошуку малих тіл Сонячної системи. Близько 2000 фотографічних платівок Кітабської частини проекту ФОН отримані за допомогою подвійного ширококутного астрографа обсерваторії Кітаб, Узбекистан у період з 1981 по 1989 роки. Спочатку, використовуючи ці оцифровані спостереження, був складений каталог екваторіальних координат і зоряних величин для більш ніж 13 млн зірок і галактик до $B=17.5^m$. На даний час ми проаналізували усі результати з метою пошуку астероїдів та склали каталог їх екваторіальних координат та зоряних величин.

В результаті було ідентифіковано більше 4500 зображень астероїдів і комет із візуальною зоряною величиною від $7^m.7$ до $17^m.5$. Всі положення астероїдів порівнювалися з ефемеридами. Проведено попередній аналіз різниць O-C.

Новим і цікавим є те, що моменти спостереження деяких ідентифікованих астероїдів є значно ранішими, ніж моменти їх відкриття. Крім того, деякі з них є найпершими спостереженнями цих астероїдів у світі серед усіх відомих спостережень. Більше 915 спостережень таких астероїдів були знайдені на платівках Кітабської частини проекту ФОН.

Ключові слова: каталог, положення астероїдів, проект ФОН

1. Introduction

In the implementation of the Photographic Survey of the Northern Sky (the FON project) took part six observatories: Main Astronomical Observatory of Ukraine (Goloseevo), Zvenigorod Observatory of Russia, Hissar Observatory of Tadjikistan, Abastumani Observatory of Georgia, Zelenchuk Observatory of Russia and Kitab Observatory of Uzbekistan. (Pakuliak et al., 2016; Andruk et al., 2017a)

The Kyiv part of the project has been successfully completed. The final result of this part was the catalogue of positions and B-magnitudes for more than 19 million stars and galaxies with $B < 16.^m5$ (Andruk et al, 2016b). In addition, a catalogue of 2293 positions of asteroids was compiled based on these observations (Shatokhina et al, 2018).

The Kitab part of the project finished by compilation of the catalogue of equatorial coordinates α , δ , and B-magnitudes for more than 13 million stars and galaxies up to $B \leq 17.^m5$ for the epoch 1984.97 (Yuldoshev et al, 2017). Similar to the previous one, now we used the processing results of digitized astronegatives for a global search for small bodies of the Solar system.

The techniques of astroplate digitization and further processing and determination of coordinates and magnitudes of stars are described in the series of publications (Andruk et al., 2014; 2015; 2016a; 2016b; Protsyuk et al., 2014a; 2014b). The results of the determination of Solar system bodies positions are described in others one (Kazantseva et al., 2015; Yizhakevych et al., 2014; 2015; 2016; 2017; Protsyuk et al., 2014a; 2014b; Eglitis et al., 2016a; 2016b; Shatokhina et al., 2016; 2017; 2018). Notice, that digitizing of astroplates has been performed using Epson Expression 10000XL commercial scanner, with the resolution 1200 dpi. All scans of plates accumulated in Joint Digital Archive of Ukrainian Virtual Observatory (UkrVO). Standard images were processed using advanced software complex for MIDAS / ROMAFOT programs in LINUX environment. The software was developed and implemented in MAO NASU to process the digitized astronomic negative plates as well as to obtain the final product in the form of a catalogue of positions and stellar magnitudes for all registered objects on the plates.

The equatorial coordinates α , δ and stellar B-magnitudes of all objects on the plates were obtained in the reference system of Tycho-2 at the epoch of exposition of each plate. The photometry of stars for astroplates was made on the basis of the principles implemented in processing the plates of the FON project (Andruk et al., 2017b) using photoelectric measurements of stars to construct the characteristic curves of plates (Relke et al., 2015). Photographic B-magnitudes of objects were calibrated with photoelectric standards (Andruk et al., 2016b).

2. Results

We analyzed the results of digital processing 1963 photographic plates of the Kitab part of the FON project. Generally, 4529 images of asteroids and 4 images of comets with 8-17.5 magnitudes were found on these plates.

The positions and magnitudes of identified asteroids and comets were compiled into a catalogue.

The quantitative and qualitative characteristics of the received catalog are analyzed. Most of identified asteroids attributed to the Main Belt. Only several of them attributed to the Hilda and Mars crosser families, potentially dangerous and unnumbered ones.

The Fig. 1 shows the distribution on equatorial coordinates RA, DEC of all 4533 identified asteroids for all used plates. Notice, that the plates from Kitab part of the FON project cover the strip on celestial sphere from 0 to 24 hours in right ascension and from -20° to $+02^\circ$ in declination. For a comparison, the similar distribution of asteroids coordinates identified from Kyiv part observations of the FON project shows on the Fig.1 too.

Analogically the Fig.2 shows the distribution of visual magnitudes for all identified asteroids for Kitab part and Kyiv part observations. Generally, in comparison with asteroids of the Kyiv part of the project, asteroids of the Kitab part are identified fainter ones up to 17.5 magnitudes. The number of identified Kitabian asteroids is significantly greater compared to asteroids of the Kyiv part of the project. It was achieved by simultaneous exposure of each pair of plates on two telescope tubes in Kitab.

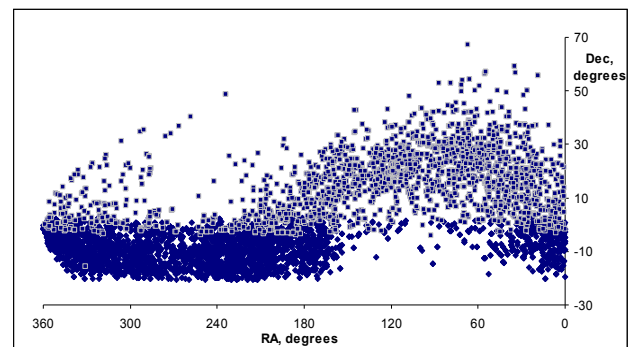


Figure 1: Distribution of coordinates RA, DEC for 4533 identified asteroids of the Kitab part (dark points) and for 2293 asteroids in the Kyiv part (light points) of the FON project.

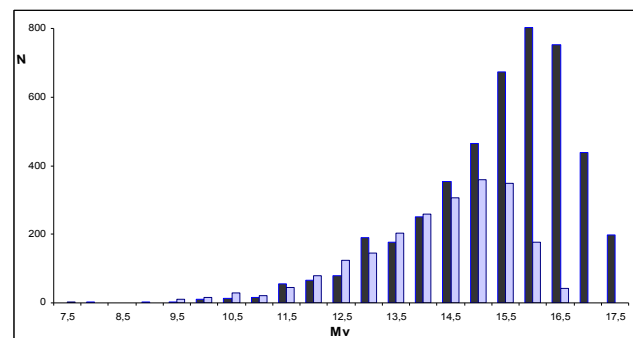


Figure 2: Distribution of visual magnitudes M_v (ephemeris) of asteroids from Kitab part observations (dark bars) and Kyiv part (light bars) of the FON project.

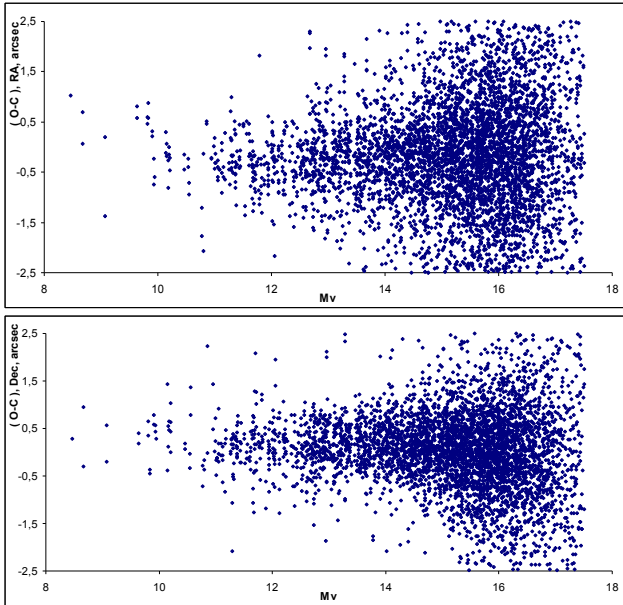


Figure 3: The scatter of individual values O-C for all asteroids in coordinate RA (from above) and coordinate DEC (bottom).

All positions of asteroids were compared with the ephemeris JPL DE431 (<http://ssd.jpl.nasa.gov/horizons>). Identification of asteroids was performed using JPL resources too. The values of O-C differences on both coordinates for all asteroids are presented on Fig.3. The scatter of these values is greater in right ascension than in declination for asteroids with different magnitudes. But it increases in both coordinates for asteroids fainter than 15 magnitudes. The possible reason for this may be the absence of faint reference stars in Tycho-2 catalogue or small exposures for reliable determination of positions of faint objects.

The brightness of asteroids depends on its geocentric and heliocentric distances and from the angle of phase. In addition, all asteroids exhibit short-period fluctuations in brightness due to their own rotation with periods from several hours to one day, in most cases. Therefore, the obtained stellar B-magnitudes of asteroids contain the results of the influence of all these factors. The amplitude of short-period fluctuations in brightness for different asteroids is different and varies from a few hundredths of a stellar magnitude to two stellar magnitudes. For each asteroid we calculated the difference $B-M_v$, where M_v is the visual magnitude calculated by the ephemeris JPL (taking into account the geocentric and heliocentric distances of the asteroid and the phase angle functions). This difference includes the residual short-period variations in brightness. Fig. 4 presented a scatter of such differences $B-M_v$ for all identified asteroids.

The accuracy of determination of coordinates and B-values of asteroids was investigated for the selected 411 pairs of observations performed on both telescope tubes simultaneously. The standard deviations σ from the mean values in both coordinates and the B values for all positions of asteroids from these pairs of observations are shown in Fig. 5.

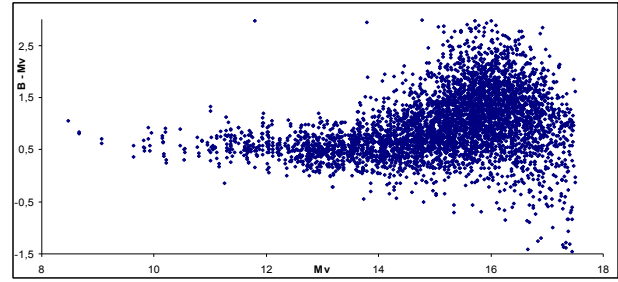


Figure 4: The scatter of differences $B-M_v$ for all asteroids.

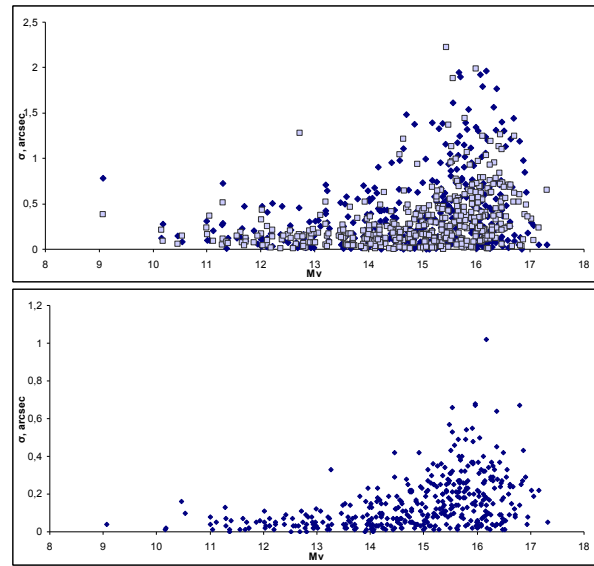


Figure 5: The scatter of values of standard deviations σ in coordinates RA (dark points), DEC (light points) (from above) and B-values (bottom) for asteroids of various stellar magnitudes.

From the preliminary analysis of the catalog data, it was found that 915 asteroids positions have moments of observation preceding their discoveries. Besides, these observations from Kitab part of the FON project are the earliest observations of corresponding asteroids in the world among all known observations (according to MPC data (http://www.minorplanetcenter.net/db_search)). As a rule, this is small faint asteroids discovered by CCD and satellites observations from 1990–2005. Most of them belong to such early oppositions of asteroids, which because of the lack of data are not involved in the calculation of ephemerides. Therefore, their differences in O-C values can be large. Such asteroids are difficult to identify. Some of these asteroids with O-C less than 2.5 arcsec are included into a present catalog now. Another part of such asteroids with large O-C will be included after a critical analysis. The catalog will be presented on UkrVO web-page.

The global search of observations of similar asteroids in the databases of the UkrVO (Vavilova et al., 2012; 2016; 2017) followed by the processing of plates, will increase their number.

3. Conclusion

Large photographic sky surveys can become a basis not only for creating a catalogues of stars and galaxies, but also for compiling a catalogue of the positions of small bodies of the Solar System. Digital processing of photographic plates allows to determine with high accuracy the coordinates and stellar magnitudes for all objects.

From observations of Kitab part of the FON project more than 4,500 asteroids and comets with visual magnitudes from $7^m.7$ to $17^m.5$ were compiled into the catalogue. A significant part of asteroids from that catalog belongs to such early oppositions of asteroids, which because of the lack of observational data are not involved in the calculation of ephemerides.

Using data from such catalogues of the positions and magnitudes of asteroids, the following tasks can be solved, such as refining ephemeris, studying changes in asteroid orbits over time, non-gravitational effects in the evolution of asteroid's orbits, constructing asteroid light curves and phase dependencies.

Intensive work on the creation of catalogues of stars and galaxies and small bodies of the Solar System based on digitized observations of Kiev and Kitab parts of the FON project were successfully carried out with the active support of UkrVO.

References

- Andruk V.N., Golovnya V.V., Ivanov G.A. et al.: 2014, *Odessa Astron. Publ.*, **27**, N1, 53.
- Andruk V.N., Pakuliak L.K., Golovnya V.V. et al.: 2015, *arXiv151205535*.
- Andruk V.M. Golovnia V.V., Ivanov G.A et al.: 2016, *Kinem. Phys. Cel. Bodies*, **32**, N1, 38.
- Andruk V.M., Pakuliak L.K., Golovnia V.V. et al.: 2016, *Kinem. Phys. Cel. Bodies*, **32**, N5, 260.
- Andruk V., Yuldoshev Q., Eglitis I. et al.: 2017, *Odessa Astron. Publ.*, **30**, 159.
- Andruk V.M., Pakuliak L.K., Golovnia V.V. et al.: 2017, *Science and Innovation*, **13a**, 17.
- Eglitis I., Eglite M., Andruk V.M. et al.: 2016, *Odessa Astron. Publ.*, **29**, 126.
- Eglitis I., Eglite M., Andruk V.M.: 2016, *Bull. T. Shevchenko Nat.Univ. Kyiv.Astron.*, **54**, 21 (in Ukrainian)
- Eglitis I., Eglite M., Shatokhina S.V. et al.: 2016, *Odessa Astron. Publ.*, **29**, 123.
- Kazantseva L.V., Shatokhina S.V., Protsyuk Yu.I. et al.: 2015, *Kinem. Phys. Cel. Bodies*, **31**, N1, 37.
- Pakuliak L., Andruk V., Golovnia V. et al.: 2016, *Odessa Astron. Publ.*, **29**, 132.
- Protsyuk Yu.I., Andruk V.N., Muminov M.M. et al.: 2014, *Odessa Astron. Publ.*, **27**, N1, 61.
- Protsyuk Yu.I. Andruk V.N., Kazantseva L.V.: 2014, *Odessa Astron. Publ.*, **27**, N1, 59.
- Relke E., Protsyuk Yu.I., Andruk V.M.: 2015, *Odessa Astron. Publ.*, **28**, 211.
- Shatokhina S., Kazantseva L., Kazantsev A. et al.: 2016, *Odessa Astron. Publ.*, **29**, 151.
- Shatokhina S.V., Andruk V.N., Golovnya V.V.: 2017, *Bull. T. Shevchenko Nat.Univ. Kyiv.Astron.*, **55**, 6 (in Ukrainian).
- Shatokhina S.V., Kazantseva L.V., Yizhakevych O.M. et al.: 2018, *Kinem. Phys. Cel. Bodies*, **34**, N5, 70.
- Vavilova I.B., Pakulyak L.K., Shlyapnikov A.A. et al.: 2012, *Kinem. Phys. Cel. Bodies*, **28**, N4, 85.
- Vavilova I.B.: 2016, *Odessa Astron. Publ.*, **29**, 109.
- Vavilova I.B., Yatskiv Ya.S., Pakuliak L.K.: 2017, *IAUS*, **325**, 361.
- Yizhakevych O., Andruk V., Pakuliak L. et al.: 2014, *Odessa Astron. Publ.*, **27**, N1, 67.
- Yizhakevych O., Andruk V.M., Pakuliak L.K.: 2015, *Odessa Astron. Publ.*, **28**, N2.
- Yizhakevych O.M., Andruk V.M., Pakuliak L.K.: 2016, *Odessa Astron. Publ.*, **29**, 155.
- Yizhakevych O. M., Andruk V.M., Pakuliak L.K.: 2017, *Kinem. Phys. Cel. Bodies*, **33**, N 3, 70.
- Yuldoshev Q.X., Ehgamberdiev Sh.A., Muminov M.M. et al.: 2017, *Kinem. Phys. Cel. Bodies*, **33**, N5, 250.

DOI: <http://dx.doi.org/10.18524/1810-4215.2018.31.146678>

NEW APPROACH FOR ANALYSIS OF THE X-RAY DATA IN CORES OF GALAXY CLUSTERS: BINNING ON THE CONCENTRATION RINGS, CONTOUR BINNING, AND WAVELET TRANSFORMS

I. B. Vavilova & Iu. V. Babyk

Main Astronomical Observatory of the National Academy of Sciences of Ukraine,
27 Zabolotnogo str., Kyiv 03143, Ukraine, irivav@mao.kiev.ua

ABSTRACT. We discuss mathematical methods for analysis of the X-ray observational data to obtain a distribution of the main physical parameters of X-ray galaxy clusters. First of all, this is the binning of galaxy cluster imagery on the concentration rings around the central parts. It allows us to calculate the integrated amount of pixels, which contain the information on temperature and other parameters of hot diffuse gas, cooling flows etc., as well as to detach the central engine of galaxy cluster. The another approach is the so-called “contour binning algorithm”, which allows us to select contours on an adaptively smoothed map in such a manner that the generated bins closely fit the surface brightness. This method is mostly informative when the spectral properties follow surface brightness and/or their distribution is not smooth. We compare these methods using the Chandra observational data for A2029, A2107, and A2151 galaxy clusters. We consider a wavelet analysis likely the “Mexican Hat” as an additional and important approach for the X-ray image processing to determine not only the regions of cores in clusters but also substructures occupied by galaxies and ICM regions while processing their X-ray image contour binning. We confirm that the detachment of substructures should precede further research because of the existence of subclustering imposes doubt in the validity of the hydrostatic equilibrium hypothesis of the X-ray gas when the dynamical matter distribution and the profiles of various physical parameters along radii are considered. A combined application of these three techniques can significantly complement our understanding of the physical processes that occur in X-ray galaxy clusters.

Key words: X-ray astronomy, contour binning algorithm, wavelet analysis – galaxy clusters: individual: A2029, A2107, A2151

АБСТРАКТ. Ми обговорюємо математичні методи аналізу спостережних даних для одержання розподілу основних фізичних параметрів рентгенівських скупчень галактик. Перш за все, це розбиття зображення скупчення галактик на концентричні кільця навколо його центру. Це дозволяє розрахувати інтегровану кількість пікселів, що містять інформацію про температуру та інші параметри гарячого дифузного газу, потоки охолодження тощо, а також виокремити центральну, найяскравішу частину скупчення галактик. Інший підхід - це так званий “алгоритм контурного розбиття”, який дозволяє окреслити контури на адаптивно згладженому зображенні у такий спосіб, що згенеровані області відповідають поверхневій яскравості всього зображення скупчення, і є найбільш інформативним, якщо спектральні властивості узгоджуються з розподілом поверхневої яскравості і/або цей розподіл не є згладженим. Ми порівнюємо ці методи з використанням даних космічної обсерваторії “Чандра” для скупчень галактик A2029, A2107 та A2151. Як додатковий і важливий підхід обробки зображень ми розглядаємо застосування хвилькового аналізу, типу перетворення “Мексиканський капелюх”, щоб визначити не тільки центральну частину скупчення галактик, але й підструктури, зайняті галактиками або областями міжгалактичного середовища, під час обробки їхнього контуру рентгенівського зображення. Ми підтверджуємо, що виокремлення підструктур має передувати подальшому дослідженню, оскільки їхня присутність не дозволяє застосовувати гіпотезу

гідростатичної рівноваги рентгенівського газу при розгляді розподілу динамічної матерії та профілів різних фізичних параметрів вздовж радіуса скупчення галактик. Комбіноване застосування цих трьох методик може суттєво доповнити наше розуміння фізичних процесів, що відбуваються в X-скупченнях галактик.

Ключові слова: рентгенівська астрономія, алгоритм контурного розбиття, хвильковий аналіз – скупчення галактик: A2029, A2107, A2151.

1. Introduction

The success of high-energy astrophysics is rapid and mostly connected with space-born X-ray and gamma-ray telescopes. For example, the first space-born fully imaging X-ray telescope *Einstein* was launched by the NASA in 1978. This observatory with an angular resolution of 3-5 arcsec has resolved over 7000 X-ray sources. Over the next 20 years, with the launch of X-ray observatories of the third generation likely *Chandra* and *XMM – Newton*, the sensitivity of X-ray instruments have been increasing over 10 billion times. This increasing will continue with forth generation of space telescopes such as *XARM (Hitomi – II)*; Toshiro et al., 2018).

In the X-ray astronomy the amount of light available to compose an image is limited. This leads to what you need to assume image processing routines for translating X-ray light, which is beyond human vision, into imagery in a scientifically accurate way. There is no an immediate answer of describing how the observatory are able to see the X-ray photons. The most care in X-ray astronomy is taken to portray X-ray objects truthfully. We note that our sky is not bright in X-ray light. Thus, the X-ray observations with exposure time of 5000 seconds might provide less than a 1000 individual X-ray photons for a celestial object in dependence on its intensity. X-ray detectors are the photon-counting instruments and the basic X-ray data usually comprise lists of events and object's properties. The basic data file includes information about the time-tagged events, each with a position (in detector and celestial coordinates) and an energy. Thus, each event can be thought of as occupying a position in a 4D space. The event may have other attributes of interest, for example, the pattern of pixels on CCDs from which the charge for this event was accumulated. It is often possible to increase signal-to-noise by selecting on these secondary attributes. After filtering the events as required we project them onto 1D or 2D subspaces and bin them up to give images, energy spectra, or lightcurves. X-ray data files are usually photon-limited and sometimes the images, spectra, and lightcurves created from the event lists may have a few or even no photons in many bins.

Each of described above binned datasets requires its

own calibration products. For example, an image analysis uses exposure maps, which accounts the mirror and detector sensitivity across the field-of-view (taking into account any changes in pointing direction), point spread function (PSF) which accounts the probability that a photon of given energy and position is registered in a given image pixel. Energy spectral analysis uses response matrices, which account the probability that a photon of given energy is registered in a given channel. And many others instrumental calibrations, including a systematic error that affects the data analysis accuracy. If we have the misfortune to have a very high signal-to-noise then this systematic error may dominate. We cannot add the systematic to the statistical uncertainties because the systematic uncertainties are usually correlated.

It is significant to note that the data analysis techniques developed in other wavebands may not transfer to X-ray astronomy (see, for example, recent papers by Konovalenko et al., 2016; Laporte et al., 2017; Mommert et al., 2016; Poole et al., 2008; Savanevych et al., 2015, 2018; as well as data analysis tool kits of the ground-based and space-born projects in various spectral ranges). Assuming both imaging and spectroscopic data, we are able to select the required “events” corresponding to a specific region of interested objects using a “region filter”. From these events we are able to build spectra and fit them in a spectral package such as, for example, XSPEC for X-ray data image analysis. Simple geometric shapes, such as annuli, boxes, sectors, ellipses, etc. can be used to assign a region filter. Assuming spherical symmetry and using annuli we can account for projection in galaxy clusters. However, we should note that the most extended sources are not symmetric.

In this paper we provide a brief overview of the *Chandra* X-ray data processing, including specific challenges of X-ray image and spectra processing. Here, we explore image and spectra processing techniques of three galaxy clusters A2029, A2107, A2151 observed by the *Chandra* to study their morphological diversity by different methods.

2. Sample

Our sample includes three galaxy clusters observed by *Chandra* X-ray Observatory. The list of objects and their coordinates, number of observations, exposure, redshift, etc. are presented in Tab. 1. We select X-ray observations with at least 10 ks exposure time to investigate different methods of X-ray image analysis. The multiple observations for one object were combined. The information for these selected objects was taken from NED¹, Simbad², and HyperLEDA³ databases.

¹<https://ned.ipac.caltech.edu/>

²<http://simbad.u-strasbg.fr/>

³Lyon-Meudon Extragalactic Database

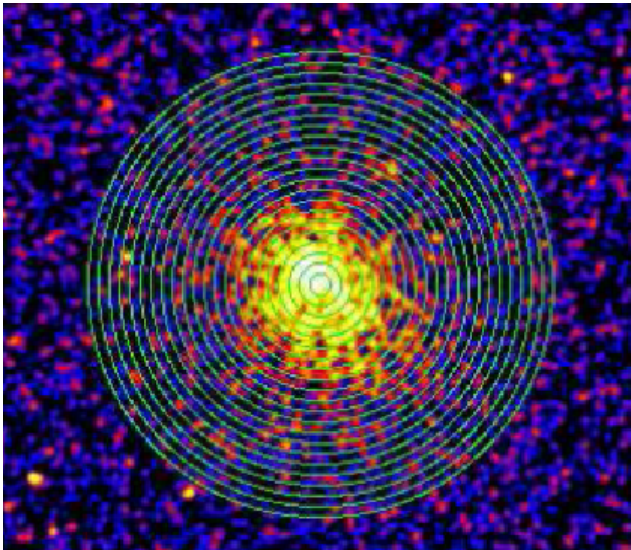


Рис. 1: The 0.5-7.0 keV X-ray image of galaxy cluster A2029 splitted on concentric annular regions.

Angular and luminosity distances were calculated using redshifts and a Λ CDM cosmology with following parameters: $H_0 = 70$ km/s/Mpc, $\Omega_m = 0.3$, and $\Omega_\Lambda = 0.7$. All the studied galaxy clusters were observed with ACIS instrument using chips 3 and 7.

3. Data analysis

The *Chandra* data were reduced following our previous analysis presented in papers by Babyk et al., 2012a,b,c,d,e; Babyk & Vavilova, 2013, 2014a,b; and Babyk et al., 2014, 2018a,b,c; Pulatova et al., 2015; Vavilova et al., 2015. Here we summarize this analysis briefly: we used CIAO v.4.1-4.8 software packages with the latest calibration files; we applied `chandra_repro` tool to extract the level-2 cleaned event files; we also operated with `wavdetect` tool to identify and delete point sources; the background flares and time-dependent gains were removed as well.

3.1. Radial profiles

In this section we describe how we built the spatially resolved radial profiles of X-ray data for these galaxy clusters. Using the cleaned event files we constructed the X-ray images in the 0.5-7.0 keV energy band. These images were splitted on concentric annular regions how it is shown in Fig. 1. We note that there are two conventional methods to split images on concentric rings. In the first case, the X-ray image can be divided on the annuli with the same number of X-ray counts/photons in each annulus. In the second case, the X-ray images can be divided with increased number of X-ray photons in each annuli starting from central annulus. This latter case is used to decrease the accuracy of spectral parameters obtained from the X-ray spectra of each an-

gular region. We note that both methods are generally accepted for an accurate spectral analysis.

The next step is the extraction of the X-ray spectra from each annuli. We used `dmextract` tool to get the *Chandra* spectra and we also apply this tool to obtain `arf` and `rmf` files. The spectra were extracted from annuli, avoiding the point sources and other asymmetric features. One of these spectra for galaxy cluster A2029 within 0.4-7.0 keV energy range is shown in Fig. 2 and was composed with a spectral software package Xspec v.11-12. This package consists of different models to describe thermal and non-thermal components of X-ray spectra. In the case of galaxy clusters, we have deals with thermal emission from the hot diffuse plasma with a temperature of millions Kelvin. Here we use `phabs*apec` model to fit each spectrum. The `apec` model fits the thermal emission from the hot atmosphere, while `phabs` models is component to account the photoelectric absorption and usually is fixed. Here we use column densities given in the last column of Tab. 1. These values were taken from Dickey & Lockman (1990). The `apec` model includes a few parameters, both free and fixed. In our case we left the temperature and metallicity as the free parameters, and the column density and redshift as the fixed parameters. The fitting was verified using two statistics applied in Xspec, χ^2 and Poisson statistics. Here we used χ^2 . The result of such a fitting as well as the quality of fit are given in Fig. 2. All the spectra were well fitted by the above described model with an average χ^2 around 1.

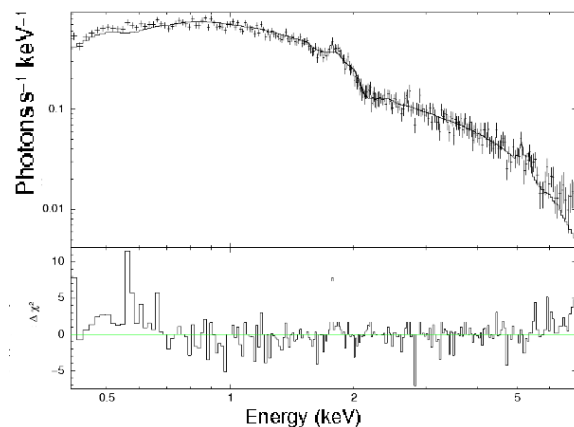


Рис. 2: The X-ray spectrum of annular region of galaxy cluster A2029 fitted by thermal model within 0.4-7.0 keV energy range.

The best-fit temperatures and metallicities of all the spectra are shown in Fig. 3 for all three galaxy clusters. We note that these profiles were obtained from the 2-dimensional images by projected spectra. These spectra are the model dependent, producing unphysical and large uncertainties of temperature, metallicity, density, and, as a result, gas and total mass profiles.

Табл. 1: The list of galaxy clusters with their physical characteristics.

| Name | α J2000 | δ J2000 | ObsID | Exposure ks | z | N_H 10^{20} cm^{-2} |
|-------|-------------------|-------------------|------------|----------------|-------|------------------------------------|
| A2029 | 6.505 | 50.54 | 4977, 6101 | 78.9, 10.0 | 0.077 | 3.07 |
| A2107 | 34.39 | 51.48 | 4960 | 36.0 | 0.041 | 4.53 |
| A2151 | 31.58 | 44.52 | 4996 | 22.1 | 0.036 | 3.49 |

In this case, the deprojection, an approach to get “real” physical parameters from the 3D-image, is required. There are a few different techniques to do this.

Here we apply a Direct Spectral Deprojection (**DSDeproj**) routine (see, Russell et al., 2008) to deproject our projected spectra. **DSDeproj** is a model-independent method, which assumes only spherical symmetry. This approach works as follows. **DSDeproj** takes projected spectra obtained from a series of annuli and suitable backgrounds. Then, **DSDeproj** 1) subtracts the equivalent background spectrum from each spectra, 2) divides the count rate in each spectral energy bin by the volume, 3) scales the spectrum per unit volume from the outer annular region by the volume projected on to the neighbouring inner annular region, 4) subtracts this from the count rate in each spectral energy bin of that annular region, 5) calculates a new count rate per unit volume in each spectral energy bin for this annular region, and 6) subtracts off the projected of each outer annulus from the inner annuli to produce a number of deprojected spectra. Russell et al. (2008) used a Monte Carlo approach, repeating 6000 times, to calculate the uncertainties in the count rate of each spectral bin in each spectrum. They also assumed Gaussian errors due to the binning of input foreground cluster and background spectra with 200 counts per spectral bin.

The resulting spectra can then be modeled in **Xspec** to produce the deprojected temperature and metallicity profiles. These profiles are presented in Fig. 3 as the red points. We found that our deprojected profiles are stable for any choice of radial binning. Any instability is visible, when a particular radial bin contains dramatically different hot gas properties, for example, cold fronts or shocks. The deprojected spectra produce smoother profiles compared to those produced by projected spectra.

3.2. Contour binning

Local instabilities or variations in the temperature and metallicity profiles of galaxy cluster can be traced using the maps of their image created with different approaches. One of these approaches is called as a “contour binning” and is an algorithm for binning X-ray data using contours on an adaptively smoothed map.

The detailed description of **contbin**⁴ technique is presented by Sanders (2006). Here we summarize it briefly.

Physical characteristics (for example, temperature, metallicity, and density) usually vary in the direction of surface brightness varies. “Contour binning” routine uses the surface brightness to identify bins that cover areas of similar brightness. Such technique provides a great opportunity to measure easily the significance of individual spatial features. To apply this method we firstly need to get an estimate of the surface brightness in the image, avoiding of noise and counting statistics. Simple Gaussian smoothing cannot define the small brightness variations. Currently, there are a few methods to get an adaptively smoothed image using surface brightness, namely **asmooth** (Ebeling et al., 2006), **csmooth** (used in **CIAO** and based on **asmooth**), etc. To smooth the image with a top-hat kernel is a simple routine. The size of this kernel varies as a function of position and contains a minimum signal-to-noise ratio. It is also needed the color maps to apply the “contour binning” method. Color maps show the ratio of counts in two different bands. These maps are very useful in X-ray analysis, because the trends in X-ray color map follow physical parameter’s trends such as temperature and metallicity. To generate the color maps the accumulative smoothing described above can also be used. All steps above as well as an adaptive smoothing routine is summarized in **contbin**. This algorithm works in the following way. The algorithm adds neighbouring pixels to a bin, starting at the highest flux pixel on a smoothed image. The algorithm stops to add those pixels when the signal-to-noise ratio exceeds an input threshold. As a result, a new bin is then created.

We need then to extract spectra from those bins and fit them to get the physical parameters. All the programming codes to perform such fitting can be found in the link presented above. In the case of our sample, we performed all the steps described above and built the galaxy cluster emission maps, which were grouped into bins that closely follow their surface brightness. The minimal signal-to-noise (S/N) ratio was selected of 60 for temperature maps to get maps with a high spatial resolution. This ratio corresponds to 3600 net

⁴C++ programming codes of the **contbin** routine can be downloaded from <https://www.xray.ast.cam.ac.uk/papers/contbin/>

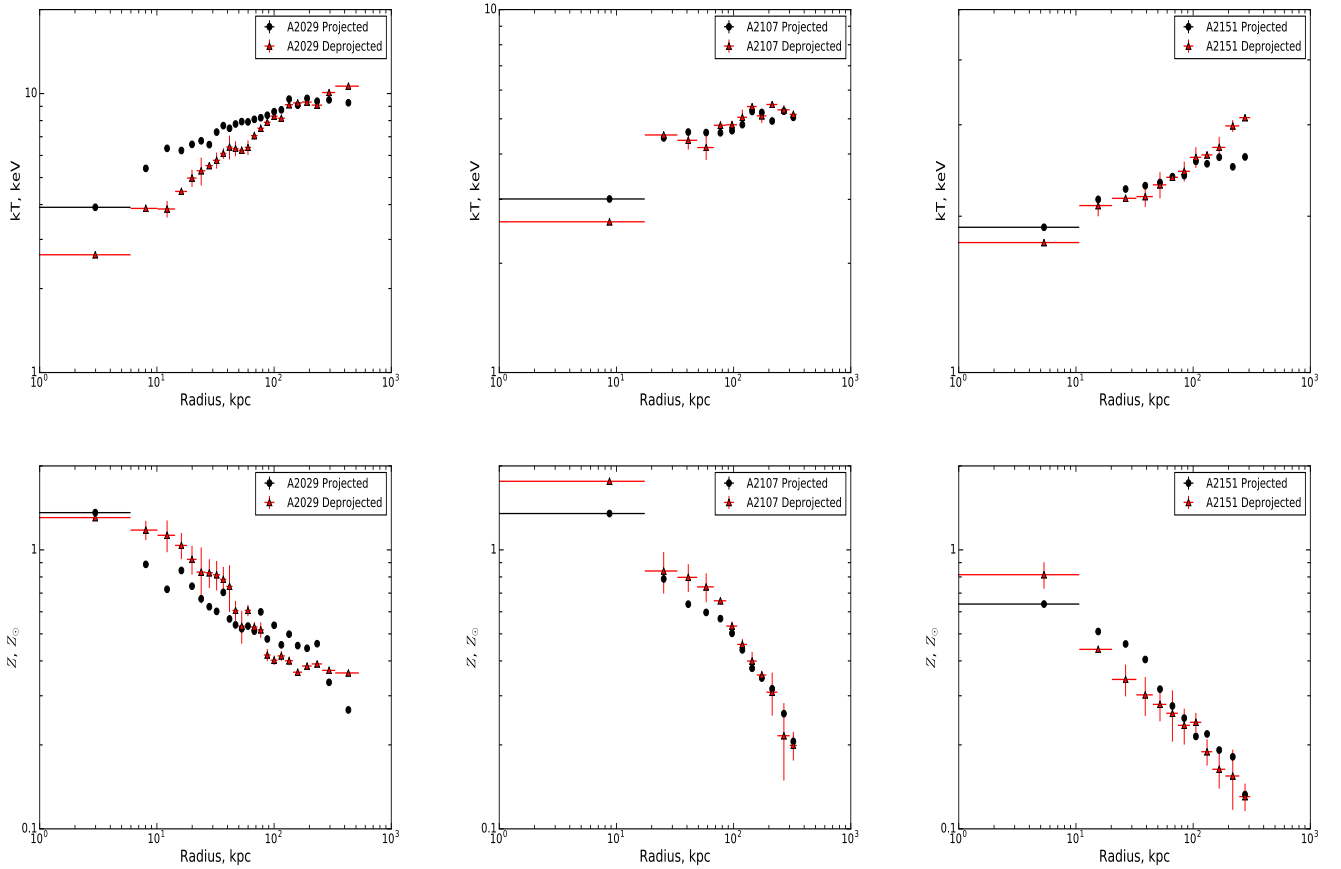


Рис. 3: The projected (black) and deprojected (red) temperature (top row) and metallicity (bottom row) profiles of galaxy clusters A2029, A2107, A2151 .

counts. In case of the metallicity maps, we choose 80 (3600 net counts) as the S/N ratio since accurate metallicity measurements require more counts. The X-ray spectra were extracted from each bin and were fit using the thermal model described above for the radial projected and deprojected spectra. The resulting maps (Fig. 4) are in agreement with radial profiles.

All the three temperature maps as well as the metal abundance maps clearly demonstrate how is important the count rate (statistics) and exposure time of X-ray observations to build such a type of map. The total exposure time of X-ray image of A2029 is about 90 ks, while for other clusters they are about 30 and 20 ks. As a result, the temperature and metallicity maps of A2029 consist of bigger number of temperature and metal abundance sectors (see top-left and top-bottom plots in Fig. 4) as compared to those with less exposure time (central and right plots in the same figure). Bigger number of sectors helps to understand a spatial distribution of different thermodynamic properties. A2107 and A2151 galaxy clusters maps show narrow temperature and metallicity distributions. However, the temperature map of A2029 shows an evidence of

shock at the cluster core. Looking into this map, we conclude that A2029 is a cooling flow cluster, showing clear drop of temperature into the cluster center. We see an obvious temperature jump between the pre- and post-shock bins along the full shock front. The central metal abundance of A2029 is about $1.0Z_{\odot}$ and decreases with radius until $0.3-0.4Z_{\odot}$. We assume that a clear distribution of metallicity in the direction south-west to north-east is seen towards the radio jet. The obtained maps are consistent with recent work of Hogan et al. (2017), where the similar distribution of metallicity was obtained for A2151 galaxy cluster. Hogan et al. (2017) argued that such distribution is a result of cavity moves, namely, the X-ray cavities may lift metals to larger radii during their rise inside the cluster.

3.3. Wavelet analysis

The two-dimensional radial wavelet analysis is very informative for detecting the substructures in the galaxy cluster structure. One of this method, the Mexican Hat as a basic platform for the programming code, was introduced by Slezak et al. (1990), Escalera & Mazure

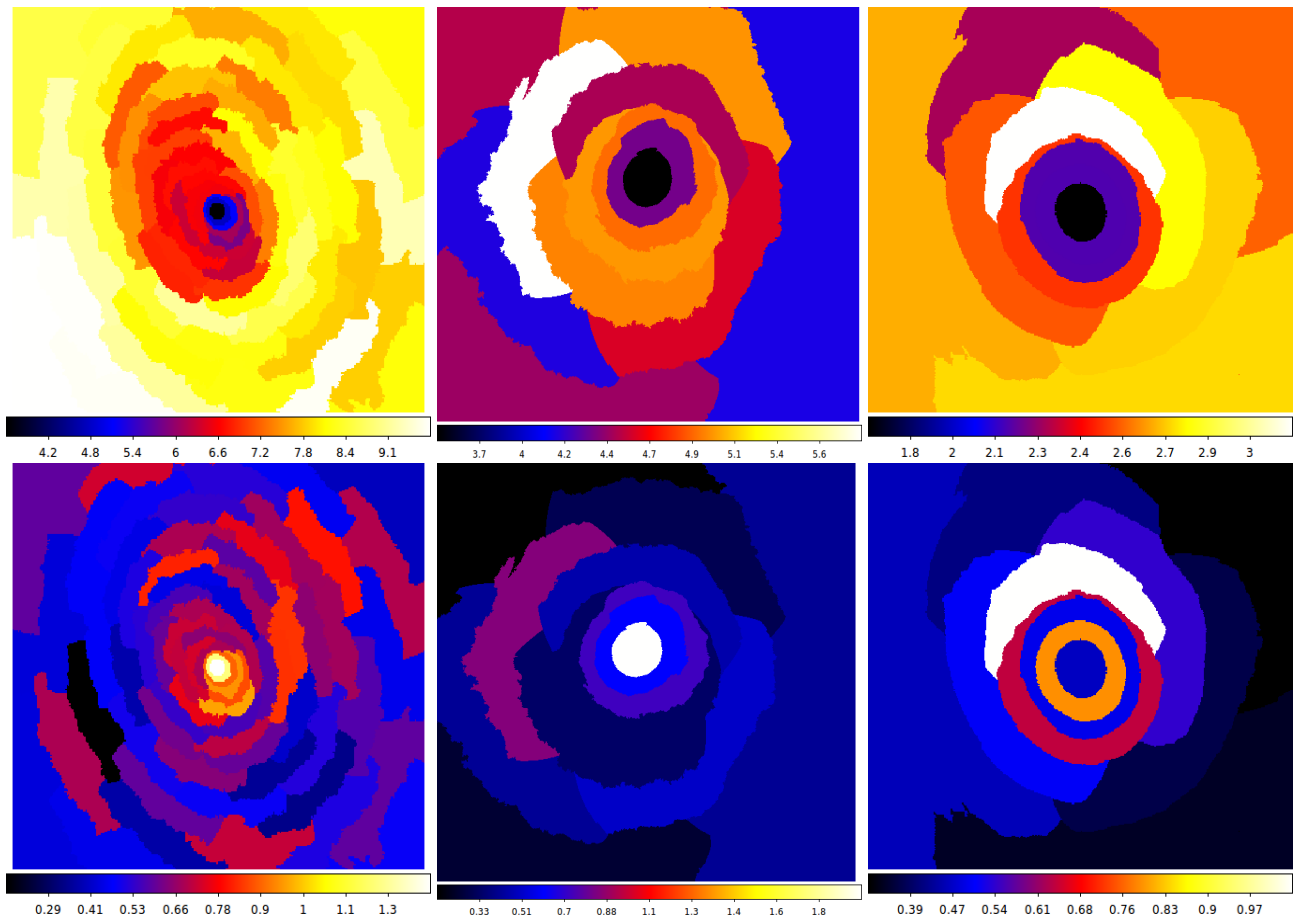


Рис. 4: The temperature (top) and metallicity (bottom) maps of A2029, A2107, and A2151 galaxy clusters (from left to right) obtained by `contbin` algorithm.

(1992) to detach galaxies in the cluster while analyzing its imagery. The dominant condition that the imagery field has covered the size of galaxy cluster (Escalera et al., 1994; Flin & Vavilova, 1995, 1997; Vavilova & Flin, 1997) was adopted for imageries in visible spectral bands but this is an exact case for X-ray images of clusters. The wavelet algorithms process the data at different scales. In case of substructure search, the task is to convolute the two-dimensional object distribution (signal function $s(r)$) on a grid $N \times N$ pixels by the *analyzing wavelet* $F(r, a)$, where a denotes a scale of the wavelet. This parameter determines the extent of spreading the object distribution in the *space of wavelet coefficients* WC and allows to make a further analysis operating only with these coefficients. It is interesting that the Mexican Hat has a radial shape but it's able to detect non-circular substructures (Vavilova, 1997). Among the papers, where different platforms of wavelet analysis were used for detection of subclustering, mainly in the Abell clusters, or for analysis of turbulent processed in the ICM, we note as follows by Flin & Vavilova, 1997; Gambera et al.; Bardelli et al., 1998; Shao Zheng-yi & Zhao Jun-liang, 1999; Flin & Kry-

wult, 2006; Rostagni, 2012; Schwinn et al., 2018; Shi et al., 2018. The algorithm of substructure detection can be described briefly as follows:

- 1) determination of the center on the cluster's image;
- 2) normalization of the data through linear transformation into the range $[-1, 1]$ yielding the radius of analyzed field $R_f=1$;
- 3) search for scale of wavelet using the Mexican Hat formula: $F(r, a) = (2 - r^2/a^2)exp(-r^2/a^2)$, where a is the wavelet's scale, r is the distance between the center and point (x, y) , where the Mexican Hat is calculated;
- 4) analysis of superpositions of the Mexican Hats on the $N \times N$ pixel grid, which substituted the distribution of coordinates of galaxy cluster's components from which the X-ray radiation has been emitting;
- 5) the choice of wavelet scale a is due to condition that the smallest scale $a=0.01R_f$ can correspond to the individual galaxies or the regions of intracluster gas, while the scale $a=0.25R_f$ could correspond to the central part of cluster, especially in case of the rich Abell clusters;
- 6) to verify results using, for example, the Monte-Carlo simulations.

So, we are able to detect the denser regions and the smallest substructures in cluster's components in relation to their coordinates using the Mexican Hat as the wavelet analysis approach. By other words, if the standard methods and contour binning methods allow us to construct profiles of the physical parameters with radii, then the wavelet analysis likely the Mexican Hat or a true algorithm allow to select regions at the smallest scales in the distribution of these parameters and to get the coordinates of relevant components of galaxy cluster.

4. Discussion and conclusions

The X-ray Chandra Observatory is an unprecedented telescope with high-quality imaging and spectra capabilities that provides an extraordinary window into the high-energy Universe. Here we applied different approaches to three galaxy clusters A2029, A2107, and A2151 observed by *Chandra* to present the current possibilities of the X-ray data analysis. Our clusters have a component of cooler gas and/or complex of different substructures in their cores. We built a spatially resolved temperature and metallicity profiles for both cases (projected and deprojected). We applied `DSDeproj` routine to produce the deprojected spectra of our sample.

We also applied the "contour binning" method and showed that this method reliably creates the bins, which follow the surface brightness. We applied `contbin` algorithm to *Chandra* observations of these galaxy clusters. `contbin` algorithm is an ideal, where spectral changes are associated with changes in surface brightness, as is often the case in X-ray astronomy. Using `contbin` algorithm it has been found many important scientific results. For example, Fabian et al. (2005) defined a complex structure of the Centaurus cluster, Sanders et al. (2005) detected the non-thermal emission of a high metal shell associated with a radio bubble in the Perseus cluster, Fabian et al. (2006) found an evidence of temperature changes associated with shock features, Vantyghem et al. (2014) found X-ray cavities associated with an elliptical shock front.

The application of various wavelets transforms is commonly used in astronomical tasks. Mostly the wavelet analysis is applied for search of quasi-periodicities or the characteristics timescales as compare with traditional Fourier-based methods. For example, Hovatta et al. (2008) confirmed the efficiency of the Morlet wavelet transform for analysis of flux curves of 80 active galactic nuclei (AGNs) in their time series at high radio frequencies, when different time scales in their activity were registered. We note that search for such quasi-periodicities is important in relation to constraints on the masses of black holes in galactic X-ray binaries. Another appropriate example of the informativeness of wavelets, namely the Continuous wavelet

transform and the Cross wavelet transform, has been demonstrated by Espaillat et al. (2008) in their analysis of AGN X-ray time variability data obtained with the XMM-Newton and detection of a quasi-period for 3C 273. Because of this period affected the estimation of the black hole mass (the estimate was lower than that by reverberation-mapping methods), the authors concluded that X-ray quasi periodicities would be caused by a higher order oscillatory mode of the accretion disk. Such approach could be useful while the multi-wavelength properties from gamma to radio spectral bands have to be considering in frame of AGN's long-year monitoring programs (see, Breedt et al., 2010; Volvach et al., 2011; Chesnok et al., 2009; Ryabov et al., 2016; and others works) or for analysis of web structure of the Universe (Einasto et al., 2011; Arnalte-Mur et al., 2012).

Since the end of 1990ies the application of wavelet transforms to the detachment of substructures in the X-ray galaxy clusters has activated with the use of the ROSAT and other space-born X-ray observatories data (see, for, example, early works by Slezak et al., 1994; Starck & Pierre, 1998) and has followed till now (see, for example, Finoguenov et al., 2007; Bozkurt, 2009; Akamatsu et al., 2016). Such approach allows to consider also the cores of cluster (mostly virialized) as deeply as to the presence of cD galaxy as well as to find small-scale inhomogeneities related to the intracluster media and cooling flows. In our opinion, the detachment of subclustering in X-ray galaxy clusters should precede further research because of its existence imposes doubt in the validity of the hydrostatic equilibrium hypothesis of the X-ray gas when the dynamical matter distribution and the profiles of various physical parameters along radii are considered. In respect to this, we described the algorithm of applying the wavelet analysis based on the Mexican Hat programming code, which is successfully used to distinguish substructures in the distribution of X-ray emission parameters while analyzing the X-ray imagery of galaxy clusters. Its application altogether with the standard methods of processing the X-ray image and contour binning methods can significantly complement our understanding of the physical processes that occur in X-ray galaxy clusters.

Acknowledgements This research has made use of the data obtained from the Chandra Data Archive and the Chandra Source Catalog, and software provided by the Chandra X-ray Center (CXC) in the application packages CIAO, ChIPS, and Sherpa. We thank all the staff members involved in the Chandra project. Additionally we have used NED, Simbad, HyperLEDA, and ADS facilities. This work was partially supported in frame of the Target Complex Program of the NAS of Ukraine for Space Scientific Research (2018-2022).

References

- Arnalte-Mur P., Labatie A., Clerc N. et al.: 2012, *A&A*, **542**, id.A34, 11 pp.
- Arnaud K. A.: 1996, *ADASS V, ASP Confer. Ser.*, **101**, 17
- Akamatsu H., Gu L., Shimwell T.W. et al.: 2016, *A&A*, **593**, id.L7, 5 pp.
- Babyk Iu. V., Vavilova I. B.: 2012a, *Odessa Astron. Publ.*, **25**, 119
- Babyk Iu., Melnyk O., Elyiv A.: 2012b, *AASP*, **2**, 56
- Babyk Iu. V.: 2012c, *Bull. CrAO*, **108**, 87
- Babyk Iu. V., Elyiv A., Melnyk O., Krivodubskij V. N.: 2012d, *Kinemat. Physics Celest. Bodies*, **28**, 69
- Babyk Iu.V.: 2012e, *J. Physical Studies*, **16**, 1904
- Babyk Iu.V., Vavilova I.B.: 2013, *Odessa Astron. Publ.*, **26**, 175
- Babyk Yu V., Del Popolo A., Vavilova I.B.: 2014, *Astron. Reports*, **58**, 587
- Babyk Iu.V., Vavilova I. B.: 2014a, *Astrophys. & Space Sci.*, **349**, 415
- Babyk Iu.V., Vavilova I.B.: 2014b, *Astrophys. & Space Sci.*, **353**, 613
- Babyk Iu.V., McNamara B.R., Nulsen P.E.J. et al.: 2018a, *ApJ*, **857**, 32
- Babyk Iu.V., McNamara B.R., Nulsen P.E.J. et al.: 2018b, *ApJ*, **862**, 39
- Babyk Iu.V., McNamara B.R., Tamhane P.D. et al.: 2018c, *submitted to ApJ*, arXiv:1810:11465
- Bardelli S., Pisani A., Ramella M. et al.: 1998, *MNRAS*, **300**, 2, 589
- Bozkurt M., Hudaverdi M., Ercan E.N.: 2009, *Publ. Astron. Obs. Belgrade*, **86**, 301
- Breedt E., McHardy I.M., Arvalo P. et al.: 2010, *MNRAS*, **403**, 2, 605
- Chesnok N.G., Sergeev S.G., Vavilova I.B.: 2009, *Kinemat. Physics Celest. Bodies*, **25**, 2, 107
- Dickey J.M., Lockman F.J.: 1990, *ARAA*, **28**, 215
- Ebeling H., White D.A., Rangarajan F.V.N.: 2006, *MNRAS*, **368**, 65
- Einasto J., HIjtsi G., Saar E. et al.: 2011, *A&A*, **531**, id.A75, 11 pp.
- Escalera E., Mazure A.: 1992, *ApJ*, **288**, 23
- Escalera E. et al.: 1994, *ApJ*, **423**, 539
- Espaillat C. et al.: 2008, *ApJ*, **679**, 182
- Fabian A.C., Sanders J.S., Taylor G.B., Allen S.W.: 2005, *MNRAS*, **360**, 20
- Fabian A.C., Sanders J.S., Taylor G.B. et al.: 2006, *MNRAS*, **366**, 417
- Finoguenov A., Guzzo L., Hasinger G. et al.: 2007, *ApJ SS*, **172**, 1, 182
- Flin P., Vavilova I.B.: 1995, *SISSA Ref. 65/95/A*, World Scientific Press, p. 117-122
- Flin P., Vavilova I.B.: 1997, *Astrophys. Letters & Communications*, **36**, 113
- Flin P., Krywult J.: 2006, *A&A*, **450**, 1, 9
- Gambera M., Pagliaro A., Antonuccio-Delogu V., Becciani, U.: 1997, *ApJ*, **488**, 1, 136
- Hogan M.T., McNamara B. R., Pulido F. A. et al.: 2017, *ApJ*, **851**, 66
- Hovatta T. et al.: 2008, *A&A*, **488**, 3, 897
- Laporte N., Bauer F.E., Troncoso-Iribarren P. et al.: 2017, *A&A*, **604**, id.A132, 16 pp.
- Konovalenko A., Sodin L., Zakharenko V. et al.: 2016, *Experimental Astronomy*, **42**, 1, 11
- Mommert M., Moskovitz N., Trilling D.E.: 2016, *AAS DPS meeting*, **48**, id.123.42
- Poole T.S., Breeveld A.A., Page M.J. et al: 2008, *MNRAS*, **383**, 2, 627
- Pulatova N.G., Vavilova I.B., Sawangwit U. et al.: 2015, *MNRAS*, **447**, 2209
- Pulido F.A., McNamara B.R., Edge A.C. et al.: 2018, *ApJ*, **853**, 177
- Rostagni F., Benoist C., Maurogordato S.: 2012, *SFA-2012*, 477
- Russell H.R., Sanders J.S., Fabian A.C.: 2008, *MNRAS*, **390**, 1207
- Ryabov M.I., Sukharev A.L., Donskykh H.I.: 2016, *Radio Physics & Radio Astronomy*, **21**, 161
- Sanders J.S., Fabian A.C., Dunn R.J.H.: 2005, *MNRAS*, **360**, 133
- Sanders J.S.: 2006, *MNRAS*, **371**, 829
- Sanders J.S., Fabian A.C., Allen S.W.: 2000, *MNRAS*, **318**, 733
- Savanevych V.E., Briukhovetskyi O.B., Sokovikova N.S. et al.: 2015, *MNRAS*, **451**, 3, 3287
- Savanevych V.E., Khlamov S.V., Vavilova I.B. et al.: 2018, *A&A*, **609**, id.A54, 11 pp.
- Schwinn J., Baugh C. M., Jauzac M. et al.: 2018, *MNRAS*, bf 481, 4, 4300
- Shao Zheng-yi, Zhao Jun-liang: 1999, *Chinese Astron. Astrophys.*, **23**, 2, 159
- Shi Xun, Nagai D., Lau E.T.: 2018, *MNRAS*. **481**, 1, 1075
- Slezak E., Bijaoui M., Mars G.: 1990, *A&A*, **227**, 301
- Slezak E., Durret F., Gerbal D.: 1994, *AJ*, **108**, 6, 1996
- Starck J.-L., Pierre M.: 1998, *ADASS VII, ASP Confer. Ser.*, **145**, 501
- Tashiro M., Maejima H., Toda K. et al.: 2018b, *Proc. SPIE*, **10699**, id.1069922
- Vantygghem A.N., McNamara B.R., Russell H.R. et al.: 2014, *MNRAS*, **442**, 3192
- Vavilova I.B., Flin P.: 1997, In *ADASS VI, ASP Confer. Ser.*, **125**, 186
- Vavilova I.B.: 1997, *Data Analysis in Astronomy, Proc. 5th Workshop*, World Scientific Press, 297
- Vavilova I.B.: 2000, *Kinemat. Fiz. Nebesn. Tel*, Suppl. no. 3, 155
- Vavilova I. B., Vasylenko A.A., Babyk Iu.V., Pulatova N. G.: 2015, *Odessa Astron. Publ.*, **28**, 150
- Vol'Vach A.E., Vol'Vach L.N., Kut'kin A.M. et al.: 2011, *Astron. Reports*, **55**, 7, 608

DOI: <http://dx.doi.org/10.18524/1810-4215.2018.31.144758>

FIRST RESULTS OF THE SEARCHING OF ASTEROIDS BASED ON THE DATA OF FON-DUSHANBE PROCESSED PLATES

O. M. Yizhakevych¹, A. Sh. Mullo-Abdolv², H. V. Relke³,
G. I. Kokhirova², L. K. Pakuliak¹, V. M. Andruk¹

¹ Main Astronomical Observatory of NASU, Kyiv, Ukraine, izhak@mao.kiev.ua

² Institute of Astrophysics of AS of Republic of Tajikistan, Dushanbe,
Tajikistan, aziz.sherzod@gmail.com

³ Walter Hohmann Observatory, Essen, Germany, helena_relke@yahoo.com

ABSTRACT. We have initiated the search of asteroids and comets on the basis of the processing digital images of plates obtained in the framework of FON project (the photographic survey of the northern hemisphere), Dushanbe section of the observational program. The result is the catalog of positions of the Solar System minor bodies. Observations were obtained in 1985-1992 at the Hissar Astronomical observatory of TajikINASTR (Institute of Astrophysics of the Academy of Sciences of Republic of Tajikistan) on the Zeiss-400 astrograph (Marsden's code 190, D/F=400/2000 mm). The plate collection includes around 1570 negatives covered the northern hemisphere from -8° to $+90^\circ$. The plate digitization has started in 2017 after the commercial scanner Microtek ScanMaker 1000XL Plus was provided. The scanner was previously tested for systematic errors and proved for suitability for digitizing photographic plates. The joint research of MAO NAS of Ukraine and Hissar observatory on Dushanbe glass collection reduction has started in 2017. The astrometric reduction of digitized plates is conducted using the software developed in MAO NAS of Ukraine running in the LINUX/MIDAS/ROMAPHOT complex. To the current moment, 10% of the collection (171 plates) has been processed. For each fixed object we obtain positions in the TYCHO2 reference system. For stars in the magnitude range 5^m - 17^m positional errors were estimated as ± 0.36 arcsec, and B-magnitudes' errors were found $\pm 0.12^m$. Stars and galaxies are not the only objects registered on the plates. During the observations, such objects as comets and asteroid could occasionally get on the picture. Here, we present the first results of the search for such objects on the FON photographic plates. The search and the evaluation of the convergence of minor bodies' observed positions with the theoretic predictions are carried out online by jpl ephemerid service (<https://ssd.jpl.nasa.gov/sbfind>).

Keywords: FON project, digital plate processing, astrometry of asteroids and comets.

АБСТРАКТ. Робота присвячена пошуку та визначенню положень малих тіл Сонячної системи на базі спостережного матеріалу програми ФОН-Душанбе. У 1985-1992 роках Гіссарська Астрономічна обсерваторія Інституту астрофізики Академії наук Республіки Таджикистан приймала участь у проекті ФОН. За допомогою астрографа Ц-400 (Marsden's code 190, D/F=400/2000mm) було отримано майже 1570 фотографічних платівок зоряного неба в межах від -8° до $+90^\circ$ град. До опрацювання цих платівок впритул підійшли тільки у 2017 році, коли було придбано професійний сканер Microtek ScanMaker 1000XL Plus та виконано його дослідження. У цьому ж році започатковано спільну з ГАО НАН України роботу з подальшої редукції цих спостережень за допомогою комплексу програм в операційному середовищі LINUX/MIDAS/ROMAPHOT. Ці програми були спеціально розроблені та запроваджені для здійснення усього проекту ФОН. На даний момент опрацьовано близько 10% фотографічних спостережень, що були отримані у Гіссарській Астрономічній обсерваторії. Визначено екваторіальні координати всіх об'єктів на кожній з 171 пластинки по відношенню до опорної системи каталогу TYCHO2. Похибки екваторіальних координат $\sigma_{\alpha\delta}$ становлять ± 0.36 arcsec, а похибки B-величин σ_B дорівнюють $\pm 0,12$ mg в межах діапазону зоряних величин від 05 до 17 mg. Астронегативи фотопластинок, отримані за програмою ФОН, зберігають в собі неоціненну інформацію про динамічний стан Космосу у певний момент часу. У роботі досліджуються результати позапланових спостережень малих планет Сонячної системи (МП). Після обробки фотографічних пластинок за програмою ФОН-Душанбе розпочато роботу з отожднення зображень астероїдів і комет (МП) на цих астронегативах. Пошук МП та оцінка узгодженості між спостережними та їх теоретичними положеннями здійснюється у режимі online за допомогою jpl-ефемерид інтернет-сервісу (<https://ssd.jpl.nasa.gov/sbfind>).

Ключові слова: проект ФОН, опрацювання оцифрованих пластинок, астрометрія астероїдів та комет.

1. Introduction

The plan of the four-fold covering of the northern sky with the photographic plates of the set of the same wide-angle astrographs was developed and firstly presented in 70th of last century by scientists of MAO NAS of Ukraine I.G. Kolchinsky and A.B. Onegina. (Kolchinsky, 1977; Pakuliak, 2016). 6 observatories of the former USSR equipped with the same Carl Zeiss Jena astrographs (apertures 400 mm and phocal lengths 2000 or 3000 mm) were involved in the realization of this project. Observational periods and periods of plate processing for each observatory were different. Thus, in the framework of UkrVO project (Vavilova, 2012a; Vavilova, 2012b; Vavilova, 2014; Vavilova, 2016; Vavilova, 2017) the Golosiiv part of the FON program was completed (Andruk, 2015; Andruk, 2016a; Andruk, 2016b; Andruk, 2017a), in 2017 r. the Kitab part of the FON program was presented (Yuldoshev, 2016; Andruk, 2017b; Yuldoshev, 2017a; Yuldoshev, 2017b). At the Hissar Astronomical observatory of TajAPHI (Institute of Astrophysics of the Academy of Sciences of Tajikistan), the efforts on the FON-Dushanbe photographic collection processing have been undertaken in 2017 (Mullo-Abdolov, 2017; Mullo-Abdolov, 2018; Rahimi, 2018). The total number of plates is around 1570. Years of observation cover 1985-1992. Plates were obtained on the Carl Zeiss Jena astrograph (Marsden's code 190, D/F=400/2000 mm). Each plate was shot with two exposures of different duration with the shift between expositions by certain distance on both coordinates (Andruk, 2012). The short exposition was 40–60 sec, the second, the main, lasting 18–27 min. Linear dimensions of plates are 30x30 cm (13000 x 13000 pixels) covering the star field 8°x8°. Full descriptions of observational conditions for each plate from the original observational logs were compiled into digital logbook file. The processing of the observational material started after the commercial flat-bed scanner Microtek ScanMaker 1000XL Plus was provided in the TajAPHI. The tests of the scanner, performed on the test plates with the Pleiades cluster, showed that the scanner could provide the astrometric precision of $\sigma_{\alpha\delta} = 0.13''$. The astrometric reduction of digital images was carried out using the software proposed and developed in MAO NAS of Ukraine. The whole process runs in LINUX/MIDAS/ROMAPHOT with TYCHO2 as reference [Andruk, 2015]. The result of proceeding of a small part of FON glass collection (10%) has shown that stars in the range of magnitudes 5^m ... 17^m have positional errors $\sigma_{\alpha\delta} = 0.36$ arcsec, errors of B-magnitudes are $\sigma_B = 0,12^m$. B-magnitudes were obtained in the reference system of photoelectric B_{pe} standards used for the restoration of characteristic curves of separate negatives. Reference stars with photoelectric magnitudes were taken from the catalog by [Relke, 2015]. The final aim of the whole collection treatment is the catalog of positions and magnitudes of all objects down to 17^m registered on the plates. Occasionally, during the observations, some asteroids and comets passing by the observed area at the moment of the shooting were registered on the photographic plates. The identification of asteroids can be performed using internet-service (<https://ssd.jpl.nasa.gov>). From the service, we obtained the list of ephemeris

positions of minor planets in observed sky area at the moment of observations $UT \pm 1$ min.

2. The scheme of minor planet identification

So, for the moment of observation, there are two files for each plate. One of them contains the results of digitized plate reduction. The next one includes ephemeris positions of asteroids and comets in the area of the processed plate. The comparison of data in two files gives the catalog of topocentric positions of all minor planets, got onto the photographic plate. The step-by-step process of the determination of astrometric positions of minor planets from the plates of FON-Dushanbe is as follows:

1. On the first step, for the plate of interest we select the information of observational conditions from the digital log file, namely the moment of its exposure in the units of sidereal time “Mean Sidereal Time in the middle of a long exposure”. Then, the sidereal moment is transformed into the universal time scale UT.

2. On the web-page “Solar System Dynamics on-line Tools” of the service <https://ssd.jpl.nasa.gov> in the section “The small-body identification” we insert the main search parameters for minor planets: date/moment ($UT \pm 1$ min) of observation, location of the observer, coordinates of the plate center, and borders of the sky area covered with the plate taking into account the plate corners declinations.

The output contains the nominal list of ephemeris positions of all minor planets got into the outlined area.

3. On the next step, the search script of the software compares data of two files in order to detect the intended asteroids and comets among the objects registered on the plate. The output file contains the comparison results of observed and theoretical values: $(O-C)\alpha$, $(O-C)\delta$, $(B-V)mg$.

4. The link “Web-Interface” in the “JPL's HORIZONS System” allows deriving the improved ephemeris data for the moment of observation ($UT \pm 1$ sec).

3. Discussion of the search results

To the moment, 71 plates of the zero zone ($\alpha = 0^h \dots 24^h$, $\delta = 0^\circ \pm 4^\circ$) and 100 plates of the circumpolar zone ($\delta = 64^\circ \dots 84^\circ$) have been processed. With the help of the jpl-ephemeris (<https://www.jpl.nasa.gov>), 104 asteroids were identified on 42 plates, and the list of 117 their topocentric positions was obtained. The comparison of these positions with the ephemeris data has shown that the essential part of minor planets' observations in the Hissar observatory has the significant discrepancies with the theory. Yet, the results of observations of the same objects at MAO NAS of Ukraine show the good agreement when comparing to the ephemerid (Shatokhina, 2017; Shatokhina, 2018a). The above-said technique is now applied for completion of the search of asteroids and comets in the photographic collection of FON-Kitab part of the project (Shatokhina, 2018b). Earlier, this technique was tested for the search of satellites of major planets of the Solar System (Yizhakevych, 2014; Yizhakevych, 2015; Yizhakevych, 2016; Yizhakevych, 2017a; Yizhakevych, 2017b).

Table 1. Comparison of asteroid search results on the plates in the declination zone 00 obtained in Gissar observatory (190) and MAO NAS of Ukraine (083)

| Name | code | Npl. | Date, UT | | | OCal'' | OCdl'' | Bph | Vmg | B-V |
|----------|----------|----------|----------|----------|-----------|----------|----------|----------|-----------|-----------|
| <i>1</i> | <i>2</i> | <i>3</i> | <i>4</i> | <i>5</i> | <i>6</i> | <i>7</i> | <i>8</i> | <i>9</i> | <i>10</i> | <i>11</i> |
| 24 | 190 | 1058 | 1989 | 09 | 1.885364 | -2.25 | -0.04 | 12.60 | 12.36 | 0.24 |
| 24 | 190 | 1196 | 1992 | 04 | 7.797387 | -0.60 | 0.56 | 11.17 | 10.96 | 0.21 |
| 24 | 083 | 1504 | 1989 | 09 | 21.930227 | -0.20 | -0.27 | 12.54 | 11.95 | 0.59 |
| 24 | 083 | 1515 | 1989 | 10 | 25.800329 | -0.04 | 0.02 | 13.29 | 12.31 | -0.98 |
| | | | | | | | | | | |
| 47 | 190 | 1058 | 1989 | 09 | 01.885364 | 2.25 | -0.53 | 12.25 | 11.59 | 0.66 |
| 47 | 083 | 821 | 1986 | 02 | 26.700712 | 0.66 | -0.26 | 14.96 | 13.48 | 1.48 |
| 47 | 083 | 822 | 1986 | 02 | 26.718141 | 0.28 | -0.39 | 13.62 | 13.48 | 0.14 |
| 47 | 083 | 1504 | 1989 | 09 | 21.930227 | 0.07 | -0.06 | 11.26 | 11.08 | 0.18 |
| 47 | 083 | 1510 | 1989 | 10 | 19.817000 | -0.23 | 0.16 | 12.69 | 11.45 | 1.24 |
| 47 | 083 | 1957 | 1992 | 02 | 26.951613 | -0.50 | -0.02 | 13.08 | 12.39 | 0.69 |
| | | | | | | | | | | |
| 1142 | 190 | 1058 | 1989 | 09 | 1.885364 | -1.65 | -0.70 | 15.91 | 15.23 | 0.68 |
| 1142 | 083 | 1964 | 1992 | 02 | 28.845964 | -0.12 | 0.76 | 16.19 | 15.21 | 0.98 |
| | | | | | | | | | | |
| 1381 | 190 | 1058 | 1989 | 09 | 01.885364 | -3.15 | -0.98 | 14.95 | 14.90 | 0.05 |
| 1381 | 083 | 1510 | 1989 | 10 | 19.817000 | -0.27 | 0.42 | 15.41 | 14.87 | 0.54 |
| | | | | | | | | | | |
| 1408 | 190 | 1281 | 1990 | 10 | 14.731300 | -1.50 | -0.64 | 15.73 | 15.49 | 0.24 |
| 1408 | 083 | 1718 | 1990 | 10 | 11.842910 | -0.03 | -0.34 | 16.10 | 15.42 | 0.68 |
| | | | | | | | | | | |
| 1425 | 190 | 1423 | 1992 | 05 | 04.771185 | -0.60 | 0.01 | 14.86 | 14.58 | 0.28 |
| 1425 | 083 | 1735 | 1990 | 10 | 14.086536 | -0.74 | -1.20 | 17.00 | 15.94 | 1.06 |
| 1425 | 083 | 1978 | 1992 | 04 | 23.920175 | 0.34 | 0.12 | 14.70 | 14.37 | 0.33 |
| | | | | | | | | | | |
| 1691 | 190 | 1281 | 1990 | 10 | 14.731300 | -2.55 | -0.80 | 15.48 | 15.06 | 0.42 |
| 1691 | 083 | 1920 | 1992 | 01 | 08.929235 | -0.60 | 0.15 | 15.24 | 14.84 | 0.40 |

Below Table 1 shows results of comparing the observations of seven asteroids obtained at two observatories, Hissar observatory and MAO NAS of Ukraine. Columns in Table 1 contain the following data: *1* – asteroid number, *2* – Marsden's code, *3* – plate number, *4-5-6* – year, month, day + UT in fractions of day, *7* – (O-C)'' R.A., *8* – (O-C)'' Dec., *9* – photometric value Bph, *10* – visual magnitude Vmg, *11* – (Bph-V). The possible reason for discrepancies in observed and theoretical positions of minor planets could be the errors of moments' registration in Hissar observatory, namely the underestimation of chronometer corrections. This is primarily evidenced by discrepancies in (O-C) on right ascension. For example, by the previous estimations, the error in the moment registration for the plate number 1058 containing the images of 5 minor planets could reach 4.5 min.

4. Some conclusions

Using the JPL-ephemerids and the search program of MAO NAS of Ukraine software for digital plate processing the identification of minor bodies was made for 171 plates of FON-Dushanbe plate collection. The research on asteroids and comets identification follows the original FON-Dushanbe project astrometric treatment of observations. The most effective is the zero declination zone where 117 topocentric positions for 104 asteroids were derived by the processing of 42 plates. For the determination of dynamic characteristics of minor planets besides positions, it is necessary to have the precise data of registration moment. In our case, additional efforts are required to resolve the problem with determining the exact moments of observations.

After completion of processing all the plates for the FON project, the number of plates with images of minor planets obtained during the same night may increase. Perhaps this will allow, if not to determine the time of exposure of the plate, then at least to estimate the magnitude of its error, which is important in the study of the dynamic processes in the Universe.

Acknowledgements. The authors are thankful to academician Farhod Rahimi, the President of Academy of Sciences of the Republic of Tajikistan, for the supporting of the project “FON-Dushanbe catalogue”.

Reference

- Andruk V.M., Ivanov G.A., Yatsenko A.I. et al.: 2012, *BTSNU*, **48**, 11.
- Andruk V.M., Pakuliak L.K., Golovnia V.V. et al.: 2015, *Odessa Astron. Publ.*, **28**, 192.
- Andruk V.M., Golovnia V.V., Ivanov G.A. et al.: 2016, *Kinem. Phys. Cel. Bodies*, **32**, N1, 38.
- Andruk V.M., Pakuliak L.K., Golovnia V.V. et al.: 2016, *Kinem. Phys. Cel. Bodies*, **32**, N5, 260.
- Andruk V.M., Pakuliak L.K., Golovnia V.V. et al.: 2017, *Science and Innovation*, **13a**, 17.
- Andruk V., Yuldoshev Q., Eglitis I. et al.: 2017, *Odessa Astron. Publ.*, **30**, 159.
- Eglitis I., Eglite M., Shatkhina S.V. et al.: 2016, *Odessa Astron. Publ.*, **29**, 123.
- Kolchinsky I.G., Onegina A.B.: 1977, *Astrometry and Astrophysics*, **33**, 11.
- Mullo-Abdolov A., Kokhirova A., Relke H. et al.: 2017, *Odessa Astron Publ.*, **30**, 186.
- Mullo-Abdolov A., Relke H., Kokhirova A. et al.: 2018, *Odessa Astron Publ.*, **31**, .
- Pakuliak L.K., Andruk V.M., Golovnia V.V. et al.: 2016, *Odessa Astron. Publ.*, **29**, 132.
- Rahimi F., Mullo-Abdolov A.Sh., Kokhirova G.I. et al.: *RpAST*, 2018, **61**, N2, 144.
- Relke E., Protsyuk Yu.I., Andruk V.M.: 2015, *Odessa Astron. Publ.*, **28**, 211.
- Shatkhina S.V., Kazantseva L.V., Yizhakevych O.M. et al.: 2017, *Odessa Astron. Publ.*, **30**, 198.
- Shatkhina S.V., Kazantseva L.V., Yizhakevych O.M. et al.: 2018, *Kinem. Phys. Cel. Bodies*, **34**, N5, 70.
- Shatkhina S.V., Relke H., Yuldoshev Q. et al.: 2018, *Odessa Astron. Publ.*, **31**, .
- Vavilova I.B., Pakulyak L.K., Shlyapnikov A.A. et al.: 2012, *Kinem. Phys. Cel. Bodies*, **28**, N2, 85.
- Vavilova I.B., Pakuliak L.K., Protsyuk Yu.I. et al.: 2012, *Baltic Ast.*, **21**, N3, 356.
- Vavilova, I.B., Golovnya, V.V., Andruk, V.M. et al.: 2014., *Odessa Astron. Publ.*, **27**, 132.
- Vavilova I.B.: 2016, *Odessa Astron. Publ.*, **29**, 109.
- Vavilova I.B., Yatskiv Ya.S., Pakuliak L.K. et al.: 2017, *IAUS*, **325**, 361.
- Yizhakevych O.M., Andruk V.M., Pakuliak L.K. et al.: 2014, *Odessa Astron Publ.*, **27**, 67.
- Yizhakevych O.M., Andruk V.M., Pakuliak L.K. 2015, *Odessa Astron Publ.*, **28**, 213.
- Yizhakevych O.M., Andruk V.M., Pakuliak L.K. 2016, *Odessa Astron Publ.*, **29**, 155.
- Yizhakevych O.M., Andruk V.M., Pakuliak L.K. 2017, *Odessa Astron Publ.*, **30**, 201.
- Yizhakevych O.M., Andruk V.M., Pakuliak L.K. 2017, *Kinem. Phys. Cel. Bodies*, **33**, N3, 142.
- Yuldoshev Q.X., Muminov M.M., Ehgamberdiev Sh.A. et al.: 2016, *Odessa Astron Publ.*, **29**, 160.
- Yuldoshev Q.X., Muminov M.M., Ehgamberdiev Sh.A. et al.: 2017, *Odessa Astron Publ.*, **30**, 205.
- Yuldoshev Q.X., Ehgamberdiev Sh.A., Muminov M.M. et al.: 2017, *Kinem. Phys. Cel. Bodies*, **33**, N5, 250.

DOI: <http://dx.doi.org/10.18524/1810-4215.2018.31.145078>

THE FIRST RESULTS OF PROCESSING OBSERVATIONS OF SS BODIES FROM UBAl PHOTOGRAPHIC PLATE COLLECTION USING THE NEW TECHNIQUE

O.M. Yizhakevych¹, V.M. Andruk¹, Q. Yuldoshev², L.K. Pakuliak¹, M.M. Muminov³¹Main Astronomical Observatory NASU, Kyiv, Ukraine, izhak@mao.kiev.ua²Ulugh Beg Astronomical Institute UzAS, Tashkent, Uzbekistan, qudratillo@astrin.uz³Andijan State University, Uzbekistan, Andijan, muminov1951@gmail.com

ABSTRACT. The paper presents the first results of processing of photographic observations of SS bodies based on materials from the collection of plates of the Ulugh Beg Astronomical Institute of the Academy of Sciences of the Republic of Uzbekistan (UBAI). The glass archive of the UBAI has about 15 thousand photographic plates with images of various space objects. In this paper, we discuss the first results of processing of major planets' photographic observations in Uzbekistan using the new technique. The observations were carried out on two astrographs – Tashkent normal astrograph (TNA, D/F=330/3438) and Kitab Double Zeiss astrograph (DAZ, D/F=400/3000) in 1895-2004. Currently, in AI the work runs to streamline the archive and create a database of observations in a single xls-format. The number of photographic plates with images of major planets obtained on two telescopes is more than 300 negatives. In 2017, together with MAO NAS of Ukraine, the processing of these photographic observations using the new methodology was started. By this time, in the framework of the UkrVO project (Vavilova, 2012a; Vavilova, 2012b; Vavilova, 2014; Vavilova, 2016; Vavilova, 2017) the method of reducing digitized plates was developed for the FON program. The plate digitization is performed on the flat-bed 10000XL in 1200dpi mode. Positions and photometric estimations in B-color of all registered on the plate objects are obtained using the software proposed and developed in MAO NAS of Ukraine running in the LINUX/MIDAS/ROMAPHOT complex.. The search for major planets and their satellites among the whole set of plate objects and the comparison of their observed and predicted positions is carried out online with the help of internet-service (<http://lnfm1.sai.msu.ru/neb/nss/nssephmr.htm>). Up to date, the small part of the plate collection was treated, namely 23 negatives with images of Uranus, Neptune, Pluto and Saturn's satellites, obtained on the Kitab DAZ astrograph. 16 negatives with 19 exposures gave the best results with (O–C) in the range $\pm 1.5''$. In total, we obtained 47 astrometric positions of the objects of interest in the wide interval of brightness's ($8^m \pm 16^m$). The internal positional accuracy of the catalog in the Tycho-2

reference system is $\sigma_{\text{ad}} = 0.08''\text{--}0.13''$, the photometric error of B-magnitudes is estimated as $\sigma_B = 0.2^m$.

Keywords: digital plate processing – astrometry of Major planets – satellites – catalogues.

АБСТРАКТ. Архів склотеки Астрономічного інституту Академії Наук Республіки Узбекистан (UBAI) нараховує майже 15 тисяч фотопластинок із зображеннями різних об'єктів Космосу. В роботі йдеться про перші результати опрацювання спостережень Великих планет та їхніх супутників, зображення яких було отримано за допомогою двох астрографів – Ташкентського нормального астрографа (TNA) та Кітабського Подвійного астрографа Цейса (DAZ) в Узбекистані у подовж 1895-2004 років. На даний час в AI виконуються роботи з упорядкування архіву платівок та створення Банку даних фотографічних спостережень у єдиному xls-форматі. Кількість фотопластинок із зображеннями Великих Планет становить понад 300 негативів. У 2017 році в AI спільно з ГАО НАНУ розпочато опрацювання цих спостережень за новою методою. На той час, у рамках проекту УкрВО (Vavilova, 2012a; Vavilova, 2012b; Vavilova, 2014; Vavilova, 2016; Vavilova, 2017) був розроблений та запропонований метод редукції оцифрованих пластинок для програми ФОН. Оцифрування негативів здійснюється за допомогою планшетного сканера Epson Expression 10000XL в режимі 1200dpi. Подальша редукція оцифрованих платівок відбувається завдяки комплексу програм, спеціально розроблених в ГАО в операційному середовищі LINUX/MIDAS/ROMAFOT. За допомогою інтернет-сайта (<http://lnfm1.sai.msu.ru/neb/nss/nssephmr.htm>) в режимі online відшукуємо зображення Планет серед усіх об'єктів платівки та визначаємо розбіжності (O–C) між обчисленими та їх теоретичними положеннями. На даний момент опрацьовано невелику частку спостережного матеріалу (23 негатива) із зображеннями Урана, Нептуна, Плутона та супутників Сатурна, що були отримані на астрографі DAZ в Кітабі. Успішними виявилися 16 фотопластинок (19 знімків), для яких значення (O–C) не перевищує $\pm 1.5''$. Загалом, ми отримали 47 астрометричних положень Планет в

широкому діапазоні їх яскравості ($8^m \div 16^m$). Внутрішня точність редукції RMS по обох координатах знаходиться в межах $\sigma_{\text{об}} = 0.08'' \div 0.13''$, а похибка визначення зоряної величини становить $\sigma_B = 0.2^m$.

Ключові слова: Опрацювання оцифрованих пластинок – астрометрія – великі планети – супутники – каталоги.

1. Introduction

The glass archive of UBAI possesses a vast collection of photographic observations having been obtained since 1895. The total number of direct plates with selected sky areas is 15 thousand. Observations on the Tashkent normal astrograph (TNA) were successfully performed until 1986. Later, the main observational activity was moved to the Kitab observational site. Here, in 1975 the Zeiss Double Wide-Angle astrograph DAZ (Yuldoshev, 2016; Yuldoshev, 2017a; Yuldoshev, 2017b) was installed for the observations on the FON project (Photographic survey of the northern sky) (Kolchinskiy, 1977; Pakuliak, 2016; Andruk, 2017b). Below, Table 1 gives the parameters of both telescopes. The archive of photographic plates got on DAZ in 2015 was moved from Kitab to Tashkent. Later, the works run to create the data bank of all observations in the single xls-format. In 2017, the photographic plate processing has been initiated together with MAO NAS of Ukraine. The archive of photographic plates got on DAZ in 2015 was moved from Kitab to Tashkent. Later, the works run to create the data bank of all observations in the single xls-format.

Table 1. Parameters of TNA and DAZ telescopes

| Parameter | ТАШКЕНТ, TNA | Kitab, DAZ |
|------------------------|-----------------|--------------------|
| ID | TAS033 | TAS040A TAS040B |
| Marsden's Code | 192 | 186 |
| Longitude | 69°17.'0 | 66° 53.'0 |
| Latitude | 41°19.'5 | 39° 08.'0 |
| Altitude | 482 m | 690 m |
| Aperture | 0.33 m | 0.40 m |
| Focal length | 3.43 m | 3 m |
| Scale | 60"/mm | 69"/mm |
| Field | 2°÷2.5° | 5.5°÷6.0° |
| Glass plate size (max) | 16x16cm | 30x30cm |

In 2017, the photographic plate processing has been initiated together with MAO NAS of Ukraine. The objects of interest were plates with images of major planets obtained in Uzbekistan on two telescopes. The renovation of the Institute building has temporarily complicated the access to the observational material. So, only 23 plates with Kitab DAZ observations were available and had been processed up to date.

2. The procedure of major planets' observation processing

The plate digitization was made using flat-bed commercial scanner Epson Expression 10000XL in grey color range 16-bits with a spatial resolution 1200 dpi (Protsyuk, 2014; Eglitis, 2017). The flat-bed scanner accompanied with the proper software allows digitizing and processing of plates containing objects of any brightnesses. The astrometric reduction of digitized data was made using the software proposed and developed in MAO NAS of Ukraine for the FON project (Relke, 2015; Andruk, 2015; Andruk, 2016a; Andruk, 2016b; Andruk, 2017a). The total package runs in LINUX/MIDAS/ROMAFOT operational environment. The initial scripts of the package were modified to meet the requirements of SS bodies' specific observations. In our case, the internal positional accuracy of the reduction lies in the range $\sigma_{\text{об}}=0.10''$, the accuracy of photometric estimations is better than $\sigma_B = 0.2^m$. Table 2 contains the results of processing 16 plates with Neptune, Uranus and its satellite Oberon, Pluto, and five Saturn's moons. The catalog of observed topocentric positions and the results of their comparison with theoretic data is given in Table 3. The observations which have the discrepancies with the theory more than ± 2.5 arcsec were not included to the catalog. The plates required the more accurate moments of observations were excluded as well.

3. Conclusions

The first 47 topocentric positions of major planets and their satellites were obtained from DAZ observations. The processing of photographic observational data was made using algorithms of digital data reduction and the software developed in MAO NAS of Ukraine. Earlier, the same technique was tested and proved for the search for asteroids and satellites of major planets (Protsyuk, 2017; Shatokhina, 2016; Shatokhina, 2017; Yizhakevych, 2014; Yizhakevych, 2015; Yizhakevych, 2016; Yizhakevych, 2017a; Yizhakevych, 2017b). The comparison of observed positions of objects with those of online ephemeris data of IMCCE demonstrates the good agreement of the theory and observations.

In the future, we plan to go on with the processing of photographic plates from UBAI glass collection containing the images of Solar system bodies obtained in Uzbekistan on two astrographs.

References

- Andruk V.M., Pakuliak L.K., Golovnia V.V. et al.: 2015, *Odessa Astron. Publ.*, **28**, 192.
 Andruk V.M., Golovnia V.V., Ivanov G.A. et al.: 2016, *Kinem. Phys. Cel. Bodies*, **32**, N1, 38.
 Andruk V.M., Pakuliak L.K., Golovnia V.V. et al.: 2016, *Kinem. Phys. Cel. Bodies*, **32**, N5, 260.
 Andruk V.M., Pakuliak L.K., Golovnia V.V. et al.: 2017, *Science and Innovation*, **13a**, 17.
 Andruk V., Yuldoshev Q., Eglitis I. et al.: 2017, *Odessa Astron. Publ.*, **30**, 159.
 Eglitis I., Andruk V.: 2017, *Open Astronomy*, 26, N1, 7.
 Kolchinsky I.G., Onegina A.B.: 1977, *Astrometry and Astrophysics*, **33**, 11.
 Pakuliak L.K., Andruk V.M., Golovnia V.V. et al.: 2016, *Odessa Astron. Publ.*, **29**, 132.
 Protsyuk Yu.I., Andruk V.N., Muminov M.M. et al.: 2014, *Odessa Astron. Publ.*, **27**, 61.

Table 2. The statistical data of the reduction of SS bodies observations made in Kitab (DAZ):

1 – object name; 2-years of observations; 3 – number of plates /number of observational nights;
 4 – number of positions, 5 – photographic stellar magnitude; 6,8,10 – standard deviation; 7,9 – (O-C) on right
 ascension and declination; 11, 12,13 – RMS – internal error of the reduction;
 14 – number of reference stars from Tycho-2.

| Obj | Range | N pl. /N nights | N pos. | Bph | Sd Bph | O-C R.A. | Sd R.A. | O-C Del. | Sd Del | RMS | | | n |
|-----------------------|------------------------|-----------------------|-----------|------|-----------|-------------|------------|-------------|-----------|-----|-----|-----|------|
| | | | | | | | | | | Bph | R.A | Del | |
| 1 | 2 | 3 | 4 | 5 | 6 | 7 | 8 | 9 | 10 | 11 | 12 | 13 | 14 |
| SATURN'S MOONS | | | | | | | | | | | | | |
| S5 | 1983, 1990 | 4/4 | 8 | 10.3 | .44 | -0.53 | .77 | +0.36 | .56 | .29 | .08 | .09 | 1277 |
| S6 | 1983, 1986, 1990 | 6/6 | 10 | 9.9 | .19 | +0.13 | .59 | -0.04 | .36 | .28 | .09 | .09 | 1194 |
| S7 | 1990 | 3/3 | 3 | 15.0 | .20 | -0.00 | .35 | -0.09 | .14 | .28 | .07 | .08 | 1725 |
| S8 | 1990 | 4/4 | 6 | 12.8 | .20 | +0.05 | .22 | -0.19 | .31 | .29 | .09 | .10 | 1676 |
| S9 | 1990 | 1/1 | 1 | 16.6 | | +3.96 | | +1.04 | | .28 | .06 | .07 | 1675 |
| Σ | 1983- 1990 | 6/6 | 27 | | | | | | | | | | |
| URANUS | | | | | | | | | | | | | |
| Ura- nus | 1983, 1985 | 3/3 | 6 | 7.5 | 1.34 | -0.13 | .57 | -0.35 | .34 | .33 | .13 | .14 | 630 |
| U4 | 1979, 1983 1985 | 4/4 | 4 | 13.9 | 0.72 | +0.13 | .94 | +0.44 | .82 | .30 | .08 | .08 | 729 |
| Σ | 1979- 1985 | 7/7 | 10 | | | | | | | | | | |
| NEPTUNE | | | | | | | | | | | | | |
| Nep- tune | 1983, 1984 | 4/4 | 9 | 8.4 | 0.48 | +0.05 | .64 | 0.11 | .45 | .33 | .13 | .14 | 2245 |
| PLUTO | | | | | | | | | | | | | |
| Plu- to | 1990 | 2/2 | 3 | 13.7 | 0.15 | -0.19 | .05 | -0.25 | .19 | .29 | .06 | .07 | 527 |

Table 3. The catalog of topocentric positions of major planets and their satellites from observations on DAZ astrograph in Kitab:

1 – Date+UT in fractions of day; 2 – Right Ascension (h,m,sec); 3 – Declination (degrees, min.,arcsec); 4 – exposure (min.);
 5 – photographic magnitude; 6,7 – (O-C) on Right Ascension and Declination (arcsec); 8 – number of plate.

| Date, UT | | | RA | | | DEC | | | Exp. | B _{ph} | (O-C) _α | (O-C) _δ | NPI. |
|----------------|----|-----------|----|----|--------|-----|----|--------|------|-----------------|--------------------|--------------------|------|
| 1 | | | 2 | | | 3 | | | 4 | 5 | 6 | 7 | 8 |
| Y | M | Day | h | m | s | ° | ' | " | min | mag | " | " | |
| NEPTUNE | | | | | | | | | | | | | |
| 1983 | 09 | 11.656048 | 17 | 45 | 44.237 | -22 | 10 | 49.307 | 15 | 8.7 | 1.06 | 0.10 | 17 |
| 1984 | 06 | 21.762796 | 18 | 01 | 4.906 | -22 | 13 | 29.341 | 2 | 8.6 | 0.22 | 0.64 | 1645 |
| 1984 | 06 | 21.769491 | 18 | 01 | 4.904 | -22 | 13 | 29.758 | 15 | 7.6 | 0.91 | 0.23 | 1645 |
| 1984 | 06 | 21.775954 | 18 | 01 | 4.822 | -22 | 13 | 30.408 | 2 | 8.6 | 0.37 | -0.42 | 1645 |
| 1984 | 06 | 24.795219 | 18 | 00 | 43.611 | -22 | 13 | 32.322 | 2 | 8.8 | -0.62 | -0.10 | 1753 |
| 1984 | 06 | 24.801625 | 18 | 00 | 43.592 | -22 | 13 | 32.551 | 15 | 7.6 | -0.22 | -0.33 | 1753 |
| 1984 | 06 | 24.814891 | 18 | 00 | 43.552 | -22 | 13 | 31.947 | 2 | 8.7 | 0.59 | 0.29 | 1753 |
| 1984 | 06 | 27.781188 | 18 | 00 | 22.902 | -22 | 13 | 34.920 | 36 | 8.8 | 1.20 | -0.28 | 1718 |
| 1984 | 06 | 27.800493 | 18 | 00 | 22.762 | -22 | 13 | 33.755 | 5 | 8.5 | 1.15 | 0.90 | 1718 |
| PLUTO | | | | | | | | | | | | | |
| 1990 | 06 | 13.778986 | 15 | 10 | 36.276 | -01 | 17 | 4.240 | 30 | 13.9 | -0.23 | -0.47 | 1822 |
| 1990 | 07 | 17.722097 | 15 | 08 | 38.607 | -01 | 25 | 31.984 | 21 | 13.6 | -0.22 | -0.14 | 1850 |
| 1990 | 07 | 17.725559 | 15 | 08 | 38.613 | -01 | 25 | 32.081 | 21 | 13.7 | -0.13 | -0.14 | 1850 |

| U4 OBERON | | | | | | | | | | | | | |
|-------------|----|-----------|----|----|--------|-----|----|--------|----|------|-------|-------|------|
| 1979 | 07 | 14.693111 | 14 | 59 | 34.990 | -16 | 41 | 24.500 | 15 | 13.5 | -0.60 | 1.44 | 470 |
| 1983 | 07 | 2.686363 | 16 | 16 | 37.989 | -21 | 12 | 50.224 | 15 | 13.8 | -0.52 | -0.56 | 1529 |
| 1985 | 09 | 5.651112 | 16 | 51 | 39.235 | -22 | 32 | 55.360 | 15 | 15.0 | 0.12 | 0.38 | 1376 |
| URANUS | | | | | | | | | | | | | |
| 1983 | 04 | 14.934433 | 16 | 28 | 57.093 | -21 | 41 | 18.023 | 17 | 5.6 | 0.23 | -0.60 | 1619 |
| 1983 | 04 | 14.941162 | 16 | 28 | 56.967 | -21 | 41 | 17.559 | 3 | 6.6 | -0.98 | -0.23 | 1619 |
| 1983 | 07 | 2.686366 | 16 | 16 | 36.535 | -21 | 13 | 28.697 | 15 | 9.0 | 0.40 | -0.92 | 1529 |
| 1985 | 09 | 5.641802 | 16 | 51 | 36.362 | -22 | 33 | 9.358 | 2 | 7.5 | 0.43 | -0.13 | 1376 |
| 1985 | 09 | 5.644533 | 16 | 51 | 36.313 | -22 | 33 | 9.422 | 2 | 7.5 | -0.42 | -0.18 | 1376 |
| 1985 | 09 | 5.648381 | 16 | 51 | 36.323 | -22 | 33 | 9.324 | 15 | 9.0 | -0.44 | -0.06 | 1376 |
| S5 RHEA | | | | | | | | | | | | | |
| 1983 | 04 | 13.862186 | 14 | 03 | 3.460 | -09 | 34 | 28.083 | 3 | 10.3 | -0.20 | 0.14 | 1433 |
| 1983 | 04 | 13.864896 | 14 | 03 | 3.422 | -09 | 34 | 27.878 | 3 | 10.3 | -0.27 | 0.15 | 1433 |
| 1983 | 04 | 13.867666 | 14 | 03 | 3.376 | -09 | 34 | 27.794 | 3 | 10.3 | -0.44 | 0.04 | 1433 |
| 1990 | 07 | 14.744142 | 19 | 35 | 42.985 | -21 | 32 | 58.089 | 15 | 10.3 | -0.24 | 0.31 | 1842 |
| 1990 | 07 | 16.766385 | 19 | 34 | 53.635 | -21 | 34 | 23.908 | 15 | 10.7 | 0.40 | -0.24 | 1847 |
| 1990 | 07 | 19.774135 | 19 | 34 | 6.618 | -21 | 37 | 16.724 | 1 | 10.5 | -0.75 | 0.22 | 1862 |
| 1990 | 07 | 19.780367 | 19 | 34 | 6.362 | -21 | 37 | 15.775 | 15 | 9.3 | -2.26 | 1.60 | 1862 |
| 1990 | 07 | 19.786600 | 19 | 34 | 6.326 | -21 | 37 | 17.137 | 1 | 10.7 | -0.46 | 0.68 | 1862 |
| S6 TITAN | | | | | | | | | | | | | |
| 1983 | 04 | 13.862186 | 14 | 02 | 47.294 | -09 | 34 | 22.163 | 3 | 9.9 | 0.07 | -0.12 | 1433 |
| 1983 | 04 | 13.864896 | 14 | 02 | 47.259 | -09 | 34 | 21.608 | 3 | 9.9 | 0.16 | 0.13 | 1433 |
| 1983 | 04 | 13.867666 | 14 | 02 | 47.177 | -09 | 34 | 21.522 | 3 | 9.9 | -0.44 | -0.09 | 1433 |
| 1986 | 06 | 29.724425 | 16 | 11 | 20.692 | -19 | 05 | 53.813 | 1 | 9.7 | 1.58 | -0.10 | 1425 |
| 1990 | 07 | 14.744142 | 19 | 35 | 24.083 | -21 | 32 | 47.862 | 15 | 9.8 | 0.07 | -0.09 | 1842 |
| 1990 | 07 | 15.732411 | 19 | 35 | 5.256 | -21 | 33 | 6.876 | 15 | 9.8 | -0.15 | 0.18 | 1844 |
| 1990 | 07 | 16.766385 | 19 | 34 | 47.665 | -21 | 33 | 31.633 | 15 | 9.8 | 0.16 | -0.17 | 1847 |
| 1990 | 07 | 19.774135 | 19 | 34 | 5.029 | -21 | 35 | 39.340 | 1 | 9.8 | -0.13 | 0.74 | 1862 |
| 1990 | 07 | 19.780367 | 19 | 34 | 4.986 | -21 | 35 | 41.142 | 15 | 9.9 | 0.51 | -0.68 | 1862 |
| 1990 | 07 | 19.786600 | 19 | 34 | 4.830 | -21 | 35 | 40.987 | 1 | 10.4 | -0.54 | -0.15 | 1862 |
| S7 HYPERION | | | | | | | | | | | | | |
| 1990 | 07 | 14.744142 | 19 | 35 | 24.110 | -21 | 31 | 48.484 | 15 | 15.2 | 0.17 | -0.22 | 1842 |
| 1990 | 07 | 15.732411 | 19 | 35 | 8.372 | -21 | 32 | 18.102 | 15 | 15.0 | -0.41 | 0.06 | 1844 |
| 1990 | 07 | 19.780367 | 19 | 34 | 10.289 | -21 | 35 | 37.961 | 15 | 14.8 | 0.23 | -0.09 | 1862 |
| S8 IAPETUS | | | | | | | | | | | | | |
| 1990 | 07 | 14.744142 | 19 | 36 | 13.530 | -21 | 33 | 20.375 | 15 | 12.7 | -0.02 | -0.18 | 1842 |
| 1990 | 07 | 15.732411 | 19 | 35 | 55.746 | -21 | 34 | 14.853 | 15 | 12.8 | 0.36 | 0.17 | 1844 |
| 1990 | 07 | 16.766385 | 19 | 35 | 36.792 | -21 | 35 | 12.787 | 15 | 12.7 | -0.18 | -0.76 | 1847 |
| 1990 | 07 | 19.774135 | 19 | 34 | 40.299 | -21 | 37 | 54.795 | 1 | 12.7 | -0.04 | -0.07 | 1862 |
| 1990 | 07 | 19.780367 | 19 | 34 | 40.199 | -21 | 37 | 55.180 | 15 | 12.9 | 0.28 | -0.12 | 1862 |
| 1990 | 07 | 19.786600 | 19 | 34 | 40.054 | -21 | 37 | 55.598 | 1 | 13.2 | -0.07 | -0.21 | 1862 |
| S9 Phoebe | | | | | | | | | | | | | |
| 1983 | 07 | 11.689238 | 16 | 15 | 30.593 | -21 | 10 | 49.381 | 15 | 9.5 | 3.63 | 1.86 | 1614 |

- Protsyuk Yu.I., Kovylianska O.E., Protsyuk S.V. et al.: 2017, *Science and Innovation*, **13a**, 89.
- Relke E., Protsyuk Yu.I., Andruk V.M.: 2015, *Odessa Astron. Publ.*, **28**, 211.
- Shatokhina S.V., Kazantseva L.V., Yizhakevych O.M. et al.: 2017, *Odessa Astron. Publ.*, **30**, 198.
- Shatokhina S.V., Kazantseva L.V., Yizhakevych O.M. et al.: 2018, *Kinem. Phys. Cel. Bodies*, **34**, N5, 70.
- Vavilova I.B., Pakulyak L.K., Shlyapnikov A.A. et al.: 2012, *Kinem. Phys. Cel. Bodies*, **28**, N2, 85.
- Vavilova I.B., Pakuliak L.K., Protsyuk Yu.I. et al.: 2012, *Baltic Ast.*, **21**, N3, 356.
- Vavilova, I.B., Golovnya, V.V., Andruk, V.M. et al.: 2014., *Odessa Astron. Publ.*, **27**, 132.
- Vavilova I.B.: 2016, *Odessa Astron. Publ.*, **29**, 109.
- Vavilova I.B., Yatskiv Ya.S., Pakuliak L.K. et al.: 2017, *IAUS*, **325**, 361.
- Yizhakevych O.M., Andruk V.M., Pakuliak L.K. et al.: 2014, *Odessa Astron Publ.*, **27**, 67.
- Yizhakevych O.M., Andruk V.M., Pakuliak L.K. 2015, *Odessa Astron Publ.*, **28**, 213.
- Yizhakevych O.M., Andruk V.M., Pakuliak L.K. 2016, *Odessa Astron Publ.*, **29**, 155.
- Yizhakevych O.M., Andruk V.M., Pakuliak L.K. 2017, *Odessa Astron Publ.*, **30**, 201.
- Yizhakevych O.M., Andruk V.M., Pakuliak L.K. 2017, *Kinem. Phys. Cel. Bodies*, **33**, N3, 142.
- Yuldoshev Q.X., Muminov M.M., Ehgamberdiev Sh.A. et al.: 2016, *Odessa Astron Publ.*, **29**, 160.
- Yuldoshev Q.X., Muminov M.M., Ehgamberdiev Sh.A. et al.: 2017, *Odessa Astron Publ.*, **30**, 205.
- Yuldoshev Q.X., Ehgamberdiev Sh.A., Muminov M.M. et al.: 2017, *Kinem. Phys. Cel. Bodies*, **33**, N5, 250.

Наукове видання

Одеські Астрономічні Публікації

том 31 (2018)

Англійською мовою

Технічний редактор *В. В. Ковтюх*
Комп'ютерна верстка *С. Л. Страхова*

Підписано до друку 14.12.18.
Формат 60x84/8. Папір офсетний. Друк різнограф.
Ум. друк. арк. 29,53. Обл.-вид. арк. 28.0. Тираж 300 екз. Зам. № 230.

Друкарня ТОВ Компанія ВАІТЕ
01402, Київ, вул. П. Лумумби, 7
Свідоцтво про внесення до Держреєстру суб'єкта видавничої справи
серія ДК №2570 від 27.07.2006 р.